Snelle en nauwkeurige modellering van elektromagnetische kristallen

Fast and Accurate Modeling of Electromagnetic Crystals

Davy Pissoort

Promotoren: prof. dr. ir. F. Olyslager, prof. dr. ir. D. De Zutter
Proefschrift ingediend tot het behalen van de graad van
Doctor in de Toegepaste Wetenschappen: Elektrotechniek

Vakgroep Informatietechnologie
Voorzitter: prof. dr. ir. P. Lagasse
Faculteit Toegepaste Wetenschappen
Academiejaar 2004 - 2005

UNIVERSITEIT
GENT

ISBN 90-8578-009-8
NUR 959, 928
Wettelijk depot: D/2005/10.500/9

Dankwoord

Een zondagmorgen, halfweg april 2005. Eindelijk begin ik aan het allerbelangrijkste en meest gelezen onderdeel van mijn proefschrift: het dankwoord! Mijn geschiedenis binnen de Elektromagnetisme groep begon nu bijna vijf jaar geleden, toen ik net na de paasvakantie als student burgerlijk ingenieur voor de levensbelangrijke, maar oh zo moeilijke keuze stond welk eindwerk ik zou gaan kiezen. Als eeuwige twijfelaar heeft het dan niet veel gescheeld of ik ging een 'low-noise amplifier' ontwerpen op verdieping -3 van het Technicum. Op het allerlaatste nippertje besloot ik toch maar om enkele verdiepingen hoger een poging te wagen om de wereld een stukje veiliger te maken en de ultieme antenne te ontwerpen om landmijnen te detecteren. Enkele maanden later keerde ik huiswaarts met in mijn rugzak twee boeken: een boek over hoe antennes kunnen ontworpen worden via genetische algoritmes, waarvan een zekere Eric Michielssen mede-auteur was, en een boek over programmeren in C. Rond nieuwjaar bleek dat al dat programmeren nog best meeviel en was de beslissing snel gemaakt om binnen de Elektromagnetisme groep te gaan doctoreren, weliswaar niet meer over landmijnen, maar wel over elektromagnetische kristallen.

In de afgelopen vier jaar heb ik het me eigenlijk nog geen enkel moment beklaagd dat ik toen de keuze heb gemaakt om bij Frank en Daniël, de promotoren van dit werk, te gaan doctoreren. In hun geval beschrijft het woord *promotor* nog niet de helft van wat ze doen en betekenen voor hun doctoraatsstudenten. Frank en Daniël, bedankt dat jullie me steeds de vrijheid hebben gegeven om dit onderzoek uit te voeren zoals dat mij het best lag, maar ook bedankt om me als het nodig was weer in de goede richting op weg te zetten.

Dit onderzoek zou uiteraard nooit mogelijk geweest zijn zonder de ondersteuning die binnen de vakgroep wordt gegeven. Hierbij gaat mijn dank uit naar iedereen binnen INTEC en vooral naar Paul Lagasse, de voorzitter van INTEC.

Toen ik indertijd terug naar huis ging met het boek over genetische algoritmes, kon ik absoluut nog niet vermoeden dat ik op een zaterdagavond een paar jaar later bij diezelfde Eric Michielssen en diens vrouw Lut thuis een pizza ging zitten eten. Eric, bedankt om Dries en mezelf een zestal weken in Urbana-Champaign op te vangen als je eigen doctoraatsstudenten, bedankt voor de vele telefoons en e-mails die u aan mij al hebt besteed en bedankt om mij in uw eigen stijl beter Engels en vooral een kritische kijk op wat ik neerschrijf aan te leren.

Een heel belangrijk iemand binnen de Elektromagnetisme groep is prof. dr. ir. Hendrik Rogier, de vertrouwenspersoon voor velen. Ik vermoed dat Hendrik

wel nog in een aantal andere dankwoorden expliciet zal vermeld worden. Hendrik, Dries omschreef je in zijn dankwoord als zijn mentor, ik zou je mijn grote broer binnen de Elektromagnetisme groep willen noemen. Ik heb het voorrecht gehad om drie keer met jou de VS te kunnen verkennen. Bedankt voor je aangenaam gezelschap zowel op reis als in Gent, bedankt voor je vele grappen, maar bovenal: bedankt voor alle goede raad die je me in de afgelopen jaren hebt gegeven.

Ook vele andere (ex-)collega's wil ik bedanken voor de heel aangename sfeer binnen de Elektromagnetisme groep en vooral voor de vele *soft-meetings* die meestal rond vier uur in de namiddag plaatsvinden: Ignace Bogaert, Kristof Cools, Bart Denecker, Jurgen De Zaeytijd, Ann Franchois, Roald Goossens, Luc Knockaert, Peter Lewyllie, Gunther Lippens, Eric Laermans, Lieven Meert, Pia Perriello, Liesbeth Vandamme, Stephan Van Damme, Dries Vande Ginste, Isabelle Van der Elstraeten en Ward Wallyn.

Dries, jouw naam komt sowieso een aantal keer terug als mede-auteur van sommige hoofdstukken in dit proefschrift. Alleen daardoor is het al duidelijk dat jouw bijdrage aan dit proefschrift groot is. In de eerste plaats: bedankt voor je MLFMA-code. Daarnaast ook bedankt dat ik je mocht vergezellen naar Urbana-Champaign. Voor ons vertrek zag ik mezelf al veroordeeld tot het zes weken verorberen van niets anders dan hamburgers. Mijn opluchting was groot toen je direct instemde met de taakverdeling die ik had voorgesteld: jij koken en ik afwassen. Zo kon ik ginds toch ook eens genieten van een aantal typisch Vlaamse gerechten. Vooral je spaghetti in tomatensaus geserveerd met tonijn uit blik is een aanrader!

Peter, heel erg bedankt voor al die keren dat je mij bent komen helpen toen mijn PC weer eens niet deed wat ik wou dat hij zou doen. Het moet voor jou wel frustrerend geweest zijn dat je me voor de zoveelste keer moest komen tonen hoe ik die VNC-viewer weer moest heropstarten.

Stephan, aka *Snellen Eddy uit Hoboken*, wij zijn samen afgestudeerd als burgerlijk ingenieur en we zijn ongeveer samen begonnen aan ons doctoraat. Binnen een paar maand dien jij ook je proefschrift in. Met je typisch Antwerpse humor zorgde jij ervoor dat er elke dag heel veel kon gelachen worden in onze vroegere bureau. Bedankt voor je hulp bij diverse practica en numerieke opgaves, bedankt voor je tof gezelschap in Nice en Pisa en bedankt om de hele Elektromagnetisme groep een snelcursus wijnproeven te geven!

Jarenlang is de Elektromagnetisme groep onlosmakelijk verbonden geweest met de Cable & Wireless groep, alleen al omdat we tot voor kort één grote bureau deelden, waarbij we enkel gescheiden waren door een rij kasten. De volgende mensen *van over de kast* wil ik dan ook heel hartelijk bedanken voor de talloze plezierige momenten in de bureau of in het studentenrestaurant: Wout Joseph, Christof Olivier, Nobby Stevens, Günter Vermeeren en Leen Verloock. En Nobby, ik denk niet dat ik ooit nog iemand zal tegenkomen die zo bezorgd is om Beauty.

Peter Bienstman wil ik bedanken voor zijn hulp bij de mode-matching met PMLs en het ter beschikking stellen van zijn simulatietool CAMFR.

Dit dankwoord geeft me eindelijk ook eens de gelegenheid om mijn vrienden te bedanken: Koen, Tinneke, Gert, Wendy, Steven, Natalie en Tom. Bedankt voor de vele keren dat we zijn gaan fietsen, poolen, snookeren of bowlen. Bedankt

voor de etentjes, verjaardagsfeestjes en barbecues. Bedankt voor de weekends aan zee of in de ardennen. Uiteraard ontbraken op al die uitstapjes de nodige gezelschapsspelletjes niet (Cluedo, Trivial Pursuit, armworstelen,...). En ik zal het nu maar toegeven: ik kan inderdaad moeilijk tegen mijn verlies. Daarnaast wil ik ook Wouter Haerick en Hilde expliciet bedanken.

Herman en Anita, jullie verdienen ook een speciale vermelding in dit dankwoord. Jullie zijn twee prachtige mensen bij wie ik me onmiddellijk thuis voelde. Bedankt dat jullie er altijd zijn om naar mij te luisteren.

Ma en pa, ik heb dit proefschrift speciaal aan jullie opgedragen. Jullie mogen terecht fier zijn dat jullie erin geslaagd zijn om Johan, Eddy en mij de kansen te geven die jullie zelf nooit hebben gekregen. Jullie staan nog altijd voor ons alledrie klaar, niet alleen met raad maar vooral ook met daad. Bedankt voor de warme thuis die jullie ons hebben gegeven! Johan, bedankt om altijd thuis mijn computerproblemen op te lossen. Eddy, bedankt voor al die keren dat we samen zijn gaan vissen of met de vinken gaan spelen. Wietjewie!

En tenslotte is er nog een heel speciaal iemand die ik absoluut niet mag vergeten bedanken. Nele: mijn fitnessmaatje, mijn danspartner, mijn persoonlijke styliste, mijn keukenprinses, mijn favoriete reisgezel, maar vooral al bijna anderhalf jaar mijn steun en toeverlaat. Nele, hoewel we elkaar nog niet zo heel erg lang kennen, hebben we toch al het een en het ander beleefd: samen overwonnen we de Thaise jungle, samen kregen we een ongeplande, extra rondleiding in het Phyathai ziekenhuis in Bangkok, samen trotseerden we in Edinburgh de verschrikkelijke McKenzie poltergeist. Maar het belangrijkste wat ik van jou al geleerd heb: nooit opgeven! Nele, bedankt om gewoon Nele te zijn!

Davy Pissoort
april 2005

voor mijn ouders

Contents

Nederlandse Samenvatting

1 Inleiding

Steeds meer en meer informatie vertrekt vanaf onze computers via het Internet of vanaf onze mobiele telefoons naar allerlei plaatsen ter wereld. Aan een modern informatiesysteem worden twee eenvoudige maar fundamentele vereisten gesteld. Ten eerste moet het systeem snel zijn, zodat grote hoeveelheden informatie op korte tijd kunnen worden overgebracht. Ten tweede moeten de toestellen van de gebruikers klein zijn. Zoals voorspeld door de wet van Moore [1] verdubbelt het aantal elektronische componenten dat op één microchip kan geïntegreerd worden om de achttien maanden, waardoor computers in dezelfde periode qua snelheid verdubbelen of equivalent halveren in prijs. In tegenstelling hiermee is de hoeveelheid fotonische componenten die op een microchip kunnen geïntegreerd worden beperkt gebleven. Dit komt voornamelijk doordat de traditionele optische golfgeleiders teveel oppervlakte innemen. Deze traditionele golfgeleiders bestaan uit een kern met een hoge diëlektrische permittiviteit omgeven door een materiaal met een lagere diëlektrische permittiviteit, waarbij het licht zich bij voorkeur voortplant in de kern. Dit is echter slechts een zwakke insluiting en in bijvoorbeeld scherpe bochten treden belangrijke stralingsverliezen op. Golfgeleiders gebaseerd op zogenaamde *fotonische* of *elektromagnetische kristallen* [2], dit zijn materialen waarin de permittiviteit en/of permeabiliteit een periodiek verloop hebben, kunnen hiervoor een oplossing bieden en tot een verdere miniaturisatie leiden.

2 Elektromagnetische kristallen

Het gedrag van elektromagnetische golven in een elektromagnetisch kristal kan het best begrepen worden via de analogie met de beweging van elektronen en gaten in een halfgeleider. In een halfgeleider zijn de atomen geordend volgens een regelmatig rooster. Wanneer elektronen bewegen doorheen dit rooster voelen ze een periodieke potentiaal. Hierdoor ontstaan toegelaten en verboden energiezones. Indien het rooster perfect is kan geen enkel elektron een energie bezitten uit de verboden energiezone. Voor reële materialen is het rooster echter niet perfect. Er zullen zogenaamde defecten, bijvoorbeeld ontbrekende, verplaatste of andere types atomen, aanwezig zijn in het rooster. Hierdoor kunnen elektronen toch welbepaalde energieniveaus uit de verboden zone bezitten.

Veronderstel nu dat een elektromagnetische golf propageert doorheen een diëlektrisch en/of magnetisch materiaal (het achtergrondmedium) dat een aantal kleine elementen be-

vat die bestaan uit een ander diëlektrisch/magnetisch materiaal en die geordend zijn volgens een periodiek rooster. Dit periodiek contrast in permitiviteit/permeabiliteit wordt door de elektromagnetische golf op precies dezelfde manier ervaren als de periodieke potentiaal door een elektron in een halfgeleider. Er ontstaan toegelaten en verboden frequentiegebieden. Voor frequenties binnen de verboden zone zal een perfect elektromagnetisch kristal alle elektromagnetische golven blokkeren. Net zoals in halfgeleiders kunnen gelokaliseerde modes worden gegenereerd door het verbreken van de periodiciteit van het rooster.

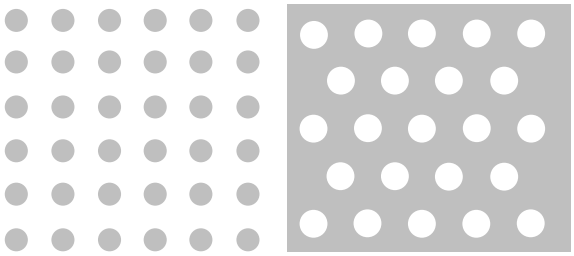

Figuur 1: Twee types 2D elektromagnetische kristallen.

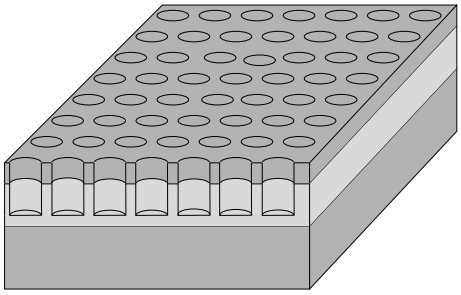

Figuur 2: Gelaagd elektromagnetisch kristal.

Met 3D elektromagnetische kristallen, dit zijn kristallen waarin de periodiciteit zich in drie dimensies uitstrekt, kunnen de elektromagnetische golven in alle richtingen gecontroleerd worden. Helaas zijn dergelijke 3D elektromagnetische kristallen moeilijk te fabriceren en te integreren op een microchip. Vandaar dat er in de literatuur heel wat aandacht wordt besteed aan 2D elektromagnetische kristallen. De twee meest voorkomende geometrieën zijn dan een regelmatig rooster van oneindig lange, diëlektrische cilinders in lucht of een regelmatig rooster van gaten in een diëlektrisch achtergrondmedium (Fig. 1). Het rooster kan vierkant of hexagonaal zijn. Defecten kunnen worden aangebracht door bijvoorbeeld het verwijderen of toevoegen van cilinders/gaten op welbepaalde plaatsen in het kristal of door het veranderen van de parameters van sommige cilinders/gaten. Door een volledige rij cilinders/gaten te verwijderen ontstaat een golfgeleider. Aangezien voor frequenties in de verboden zone de elektromagnetische golven niet kunnen ontsnappen

via het kristal, biedt dit type van golfgeleiders de mogelijkheid om elektromagnetische golven met lage verliezen doorheen scherpe bochten te sturen [3–5]. In de praktijk moet er een mechanisme voorzien worden dat de elektromagnetische golven ook controleert in de derde dimensie, parallel aan de cilinders/gaten. Hiertoe worden de 2D elektromagnetische kristallen ingebouwd in een gelaagd medium (Fig. 2). In dergelijke gelaagde elektromagnetische kristallen worden de elektromagnetische velden in het vlak parallel aan de lagen gecontroleerd via het elektromagnetisch kristal, terwijl ze in de richting loodrecht op de lagen ingesloten blijven door de eigenschappen van het gelaagd medium. Een voorbeeld van zo'n structuur is een regelmatig rooster van gaten geëtst in een GaAs-AlGaAs lagenstructuur of in een Silicium-Op-Isolator structuur [6].

3 Overzicht

De nadruk ligt in dit doctoraatswerk op de ontwikkeling van efficiënte simulatiemethodes voor de karakterisatie van 2D elektromagnetisch-kristalstructuren en gelaagde elektromagnetische kristallen. In Sectie 4 worden de belangrijkste eigenschappen van algemene periodieke golfgeleiders afgeleid door te steunen op het Lorentz reciprociteitstheorema. Vervolgens worden in Sectie 5 de basisvergelijkingen afgeleid voor de klassieke meervoudige-verstrooiingstechniek. Daarna wordt een nieuwe absorberende randvoorwaarde beschreven, gebaseerd op perfect aangepaste lagen, waarmee periodieke golfgeleiders kunnen worden afgesloten in integraalvergelijkingstechnieken. Het belangrijkste nadeel van de klassieke meervoudige-verstrooiingstechniek is dat deze methode uiteindelijk vereist dat een volledig gevuld stelsel wordt opgelost. Om de rekencomplexiteit en de geheugenvereisten te beperken wordt dit stelsel iteratief opgelost waarbij bovendien de nodige matrix-vector vermenigvuldigingen worden uitgevoerd via een snel en efficiënt vermenigvuldigingsschema. Sectie 6 beschrijft twee snelle vermenigvuldigingsschema's, namelijk het meervoudige niveau snelle multipool algoritme en een schema gebaseerd op een snelle Fouriertransformatie. Helaas is de totale rekencomplexiteit ook evenredig met het aantal iteraties dat nodig is om een voldoend nauwkeurige oplossing te bekomen. De karakterisatie van realistische elektromagnetisch-kristalstructuren vereist vaak een groot aantal iteraties. In Sectie 7 worden drie types preconditioners vergeleken. In Sectie 8 wordt een nieuwe en snelle meervoudige-verstrooiingstechniek, speciaal aangepast aan de karakterisatie van 2D elektromagnetisch-kristalstructuren, geïntroduceerd. Doordat deze techniek gebruik maakt van de Greense functie van het kristal, moet uiteindelijk een dunbezet stelsel met een heel specifieke vorm worden opgelost wat snel en efficiënt kan gebeuren met een multifrontale methode. Tenslotte beschrijft Sectie 9 hoe de 2D meervoudige-verstrooiingstechniek door combinatie met een cilindrische mode-aanpassing uitgebreid kan worden naar de simulatie van golfpropagatie in gelaagde elektromagnetische kristallen.

Alle 2D voorbeelden in deze Nederlandse samenvatting bestaan uit structuren gevormd in een elektromagnetisch kristal dat bestaat uit diëlektrische cilinders met relatieve permittiviteit 11.56 en straal $0.18a$ die gerangschikt zijn volgens een periodiek rooster met vierkante eenheidscel met zijde a - a noemt men de roosterconstante. Het achtergrondmedium is lucht. Voor de TM_z-polarisatie, waarbij het elektrisch veld enkel een component heeft parallel aan de cilinders, heeft dit kristal een verboden zone van $k_1 = 0.604\frac{\pi}{a}$ tot

$k_1 = 0.886\frac{\pi}{a}$, met k_1 het golfgetal in lucht.

4 Eigenmodes van periodieke golfgeleiders

Door de interessante eigenschappen van golfgeleiders in elektromagnetische kristallen is er een hernieuwde interesse in de eigenschappen van periodieke golfgeleiders. De propagatie in periodieke golfgeleiders kan het best bestudeerd worden via de analyse van de eigenmodes. Deze eigenmodes zijn gedefinieerd als de oplossingen van de vergelijkingen van Maxwell in een bronloos gebied van de golfgeleider. Hoewel er in de literatuur heel wat kan teruggevonden worden over de eigenschappen van niet-periodieke golfgeleiders [7] en over verstrooiing aan periodieke structuren [8], blijkt een rigoureuze analyse van de eigenmodes van algemene periodieke golfgeleiders te ontbreken.

Analoog aan hoe de eigenschappen van de eigenmodes van gewone golfgeleiders worden afgeleid in [7], worden in wat volgt de belangrijkste eigenschappen van de eigenmodes in periodieke golfgeleiders aangetoond door te vertrekken van het Lorentz reciprociteitstheorema. Een periodieke golfgeleider wordt hierbij gedefinieerd als een structuur waarvoor de materiaalparameters een periodiek verloop met periode T kennen in één richting (de propagatierichting) en een willekeurig verloop in het vlak loodrecht op deze richting. Als de z-richting de propagatierichting is en als $\boldsymbol{\rho} = x\boldsymbol{u}_x + y\boldsymbol{u}_y$ een willekeurige punt in het xy-vlak voorstelt, betekent dit dat $\epsilon(\boldsymbol{\rho}, z+T) = \epsilon(\boldsymbol{\rho}, z)$ en $\mu(\boldsymbol{\rho}, z+T) = \mu(\boldsymbol{\rho}, z)$. Volgens het Floquet-Bloch theorema kunnen de velden in zo'n periodieke golfgeleider geschreven worden als quasi-periodieke functies

$$\boldsymbol{e}(\boldsymbol{\rho}, z) = [\boldsymbol{E}_t(\boldsymbol{\rho}, z) + E_z(\boldsymbol{\rho}, z)\boldsymbol{u}_z]\, e^{-\gamma z}, \quad (1)$$

$$\boldsymbol{h}(\boldsymbol{\rho}, z) = [\boldsymbol{H}_t(\boldsymbol{\rho}, z) + H_z(\boldsymbol{\rho}, z)\boldsymbol{u}_z]\, e^{-\gamma z}, \quad (2)$$

waarbij

$$\boldsymbol{E}_t(\boldsymbol{\rho}, z+T) + E_z(\boldsymbol{\rho}, z+T)\boldsymbol{u}_z = \boldsymbol{E}_t(\boldsymbol{\rho}, z) + E_z(\boldsymbol{\rho}, z)\boldsymbol{u}_z, \quad (3)$$

$$\boldsymbol{H}_t(\boldsymbol{\rho}, z+T) + H_z(\boldsymbol{\rho}, z+T)\boldsymbol{u}_z = \boldsymbol{H}_t(\boldsymbol{\rho}, z) + H_z(\boldsymbol{\rho}, z)\boldsymbol{u}_z. \quad (4)$$

periodieke functies zijn. Het subscript 't' duidt op de transversale of xy-componenten van de velden. Niet-triviale oplossingen van de bronloze vergelijkingen van Maxwell van de vorm (1)-(2) bestaan enkel voor welbepaalde waarden van de propagatieconstante γ. Deze oplossingen worden precies de eigenmodes genoemd.

4.1 Lorentz reciprociteitstheorema

Beschouw een bronloos gedeelte van een periodieke golfgeleider gelegen tussen de twee vlakken $S(z_1)$ en $S(z_2)$ (Fig. 3). Het volume begrensd door deze twee vlakken wordt aangeduid door V. Voor een *gesloten* golfgeleider, dit is een golfgeleider die eindig is in het xy-vlak, wordt het volume V transversaal begrensd door het oppervlak S_o. Voor een *open* golfgeleider bevindt dit oppervlak S_o zich geheel of gedeeltelijk op oneindig. Het totale oppervlak van V wordt aangeduid als S: $S = S(z_1) + S(z_2) + S_o$. Het Lorentz reciprociteitstheorema stelt dat voor twee onafhankelijke oplossingen $(\boldsymbol{e}_a, \boldsymbol{h}_a)$

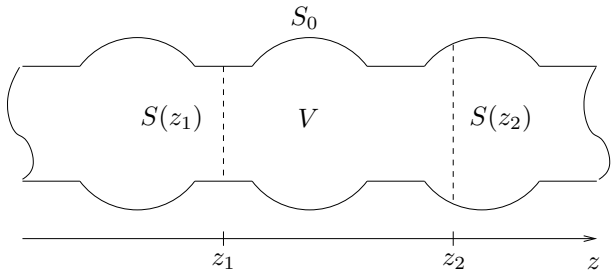

Figuur 3: Gedeelte van een periodieke golfgeleider relevant voor het Lorentz reciprociteitstheorema.

en $(\boldsymbol{e}_b, \boldsymbol{h}_b)$ van de vergelijkingen van Maxwell in het bronloos volume V geldt dat

$$\int_S (\boldsymbol{e}_a \times \boldsymbol{h}_b - \boldsymbol{e}_b \times \boldsymbol{h}_a) \cdot \boldsymbol{u}_n dS = 0, \tag{5}$$

met $\boldsymbol{u}_n$ de naar buiten gerichte normaal op S.

4.2 Orthogonaliteit

De orthogonaliteitsrelatie voor de eigenmodes wordt bekomen door het Lorentz reciprociteitstheorema (5) toe te passen op twee eigenmodes. Veronderstel dat de a-velden een eigenmode zijn met subscript i

$$\boldsymbol{e}_a(\boldsymbol{\rho}, z) = [\boldsymbol{E}_{i,t}(\boldsymbol{\rho}, z) + E_{i,z}(\boldsymbol{\rho}, z)\boldsymbol{u}_z]\, e^{-\gamma_i z}, \tag{6}$$
$$\boldsymbol{h}_a(\boldsymbol{\rho}, z) = [\boldsymbol{H}_{i,t}(\boldsymbol{\rho}, z) + H_{i,z}(\boldsymbol{\rho}, z)\boldsymbol{u}_z]\, e^{-\gamma_i z}, \tag{7}$$

en de b-velden een eigenmode met subscript j

$$\boldsymbol{e}_b(\boldsymbol{\rho}, z) = [\boldsymbol{E}_{j,t}(\boldsymbol{\rho}, z) + E_{j,z}(\boldsymbol{\rho}, z)\boldsymbol{u}_z]\, e^{-\gamma_j z}, \tag{8}$$
$$\boldsymbol{h}_b(\boldsymbol{\rho}, z) = [\boldsymbol{H}_{j,t}(\boldsymbol{\rho}, z) + H_{j,z}(\boldsymbol{\rho}, z)\boldsymbol{u}_z]\, e^{-\gamma_j z}. \tag{9}$$

De integratie over het oppervlak S_o geeft geen bijdrage: voor gesloten golfgeleiders is dit een rechtstreeks gevolg van de randvoorwaarden op dit oppervlak, voor open golfgeleiders wordt verondersteld dat de velden voldoend snel afnemen [7]. Indien bovendien $z_2 = z_1 + T$ wordt gekozen, herleidt het Lorentz reciprociteitstheorema zich tot

$$\int_{S(z_1)} [\boldsymbol{E}_{i,t}(\boldsymbol{\rho}, z_1) \times \boldsymbol{H}_{j,t}(\boldsymbol{\rho}, z_1) - \boldsymbol{E}_{j,t}(\boldsymbol{\rho}, z_1) \times \boldsymbol{H}_{i,t}(\boldsymbol{\rho}, z_1)] \cdot \boldsymbol{u}_z dS \times \{e^{-(\gamma_i+\gamma_j)T} - 1\} = 0. \tag{10}$$

Als enkel propagatieconstanten in de eerste Brillouin zone $[-\frac{\pi}{T}, +\frac{\pi}{T}]$ worden beschouwd, dan geldt dat indien $\gamma_i \neq -\gamma_j$ twee eigenmodes orthogonaal zijn:

$$\int_{S(z)} [\boldsymbol{E}_{i,t}(\boldsymbol{\rho}, z) \times \boldsymbol{H}_{j,t}(\boldsymbol{\rho}, z) - \boldsymbol{E}_{j,t}(\boldsymbol{\rho}, z) \times \boldsymbol{H}_{i,t}(\boldsymbol{\rho}, z)] \cdot \boldsymbol{u}_z dS = 0. \tag{11}$$

Indien men als b-veld de eigenmode kiest met de tegengestelde propagatieconstante van het a-veld,

$$\boldsymbol{e}_b(\boldsymbol{\rho}, z) = \left[\tilde{\boldsymbol{E}}_{i,t}(\boldsymbol{\rho}, z) + \tilde{E}_{i,z}(\boldsymbol{\rho}, z)\boldsymbol{u}_z\right] e^{\gamma_i z}, \quad (12)$$

$$\boldsymbol{h}_b(\boldsymbol{\rho}, z) = \left[\tilde{\boldsymbol{H}}_{i,t}(\boldsymbol{\rho}, z) + \tilde{H}_{i,z}(\boldsymbol{\rho}, z)\boldsymbol{u}_z\right] e^{\gamma_i z}, \quad (13)$$

bekomt men

$$\int_{S(z)} \left[\boldsymbol{E}_{i,t}(\boldsymbol{\rho}, z) \times \tilde{\boldsymbol{H}}_{i,t}(\boldsymbol{\rho}, z) - \tilde{\boldsymbol{E}}_{i,t}(\boldsymbol{\rho}, z) \times \boldsymbol{H}_{i,t}(\boldsymbol{\rho}, z)\right] \cdot \boldsymbol{u}_z dS = c, \quad (14)$$

met c een z-onafhankelijke constante.

4.3 Bidirectionaliteit

Een golfgeleider is bidirectionaal indien er voor elke (voorwaartse) eigenmode met propagatieconstante γ een andere (achterwaartse) eigenmode bestaat met propagatieconstante $-\gamma$. Een *symmetrische* periodieke golfgeleider, dit is een periodieke golfgeleider waarvoor de oorsprong $z = 0$ zodanig kan gekozen worden dat $\epsilon(\boldsymbol{\rho}, -z) = \epsilon(\boldsymbol{\rho}, z)$ en $\mu(\boldsymbol{\rho}, -z) = \mu(\boldsymbol{\rho}, z)$, is duidelijk bidirectionaal. Figuur 3 toont een voorbeeld van een dergelijke symmetrische periodieke golfgeleider. Bovendien bestaat er voor deze golfgeleiders een direct verband tussen beide eigenmodes. Inderdaad, indien γ, $\boldsymbol{E}_t(\boldsymbol{\rho}, z)$, $E_z(\boldsymbol{\rho}, z)$, $\boldsymbol{H}_t(\boldsymbol{\rho}, z)$, $H_z(\boldsymbol{\rho}, z)$ een eigenmode is, dan is $-\gamma$, $\boldsymbol{E}_t(\boldsymbol{\rho}, -z)$, $-E_z(\boldsymbol{\rho}, -z)$, $-\boldsymbol{H}_t(\boldsymbol{\rho}, -z)$, $H_z(\boldsymbol{\rho}, -z)$ ook een eigenmode.

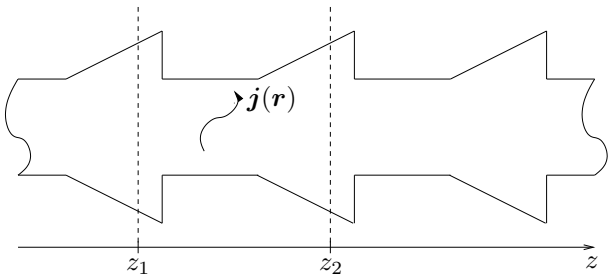

Figuur 4: Periodieke golfgeleider geëxciteerd door een stroomdichtheid $\boldsymbol{j}(\boldsymbol{r})$.

Voor een *niet-symmetrische* periodieke golfgeleider, zoals bijvoorbeeld diegene getoond in Fig. 4, is het niet onmiddellijk duidelijk dat deze golfgeleider bidirectionaal is. Dit kan evenwel bewezen worden door te starten van een symmetrische golfgeleider. De materiaalparameters van deze symmetrische golfgeleider worden dan aangepast zodanig dat deze op een continue wijze verandert van de symmetrische periodieke golfgeleider naar de beschouwde niet-symmetrische periodieke golfgeleider. Veronderstel dat deze overgang kan gekarakteriseerd worden aan de hand van een continue variabele α, waarbij de symmetrische situatie overeenstemt met $\alpha = \alpha_0$. Aangezien deze symmetrische periodieke golfgeleider bidirectionaal is, geldt dat

$$\gamma_f(\alpha_0) + \gamma_b(\alpha_0) = 0. \quad (15)$$

Hier duiden de subscripts $'f'$ and $'b'$ respectievelijk op de voorwaartse en de achterwaartse eigenmode. Door een gelijkaardige redenering te volgen als in Sectie 4.2, toont men makkelijk aan dat

$$\left[e^{-[\gamma_f(\alpha)+\gamma_b(\alpha)]T} - 1\right] I(\alpha) \quad = \quad 0, \tag{16}$$

waarbij de volgende notatie werd ingevoerd:

$$I(\alpha) = \int_{S(z)} [\boldsymbol{E}_{f,t}(\boldsymbol{\rho}, z, \alpha) \times \boldsymbol{H}_{b,t}(\boldsymbol{\rho}, z, \alpha) - \boldsymbol{E}_{b,t}(\boldsymbol{\rho}, z, \alpha) \times \boldsymbol{H}_{f,t}(\boldsymbol{\rho}, z, \alpha)] \cdot \boldsymbol{u}_z dS. \tag{17}$$

Uit (14) volgt dat $I(\alpha_0) = 1$ kan gekozen worden. Door vergelijking (16) verschillende keren af te leiden naar α, toont men aan dat

$$\left.\frac{\partial^n \gamma_f}{\partial \alpha^n}\right|_{\alpha=\alpha_0} + \left.\frac{\partial^n \gamma_b}{\partial \alpha^n}\right|_{\alpha=\alpha_0} \quad = \quad 0 \text{ voor } n = 1, 2 \cdots + \infty. \tag{18}$$

Samen met (15) betekent dit dat $\gamma_f(\alpha) + \gamma_b(\alpha)$ nul is voor alle α indien tenminste $\gamma_f(\alpha) + \gamma_b(\alpha)$ een analytische functie is van α. Indien bij de verandering van α plots een nieuwe eigenmode ontstaat of indien een eigenmode opsplitst in twee eigenmodes (bifurcatie), dan geldt dit bewijs niet meer voor deze eigenmodes. In deze gevallen kan men misschien zonder deze fenomenen de uiteindelijke niet-symmetrische periodieke golfgeleider bereiken door te vertrekken van een andere symmetrische periodieke golfgeleider. Dit bewijs illustreert duidelijk het verband tussen reciprociteit en bidirectionaliteit.

4.4 Excitatie

Veronderstel dat een periodieke golfgeleider wordt geëxciteerd door een stroomdichtheid $\boldsymbol{j}(\boldsymbol{r})$, gesitueerd tussen $z = z_1$ en $z = z_2$ (Fig. 4). Voor $z = z_1$ kunnen de velden geschreven worden als de superpositie van alle eigenmodes die in de negatieve z-richting propageren

$$\boldsymbol{e}(\boldsymbol{\rho}, z_1) = \sum_i K_i^- \left[\tilde{\boldsymbol{E}}_{i,t}(\boldsymbol{\rho}, z_1) + \tilde{E}_{i,z}(\boldsymbol{\rho}, z_1)\boldsymbol{u}_z\right] e^{\gamma_i z_1}, \tag{19}$$

$$\boldsymbol{h}(\boldsymbol{\rho}, z_1) = \sum_i K_i^- \left[\tilde{\boldsymbol{H}}_{i,t}(\boldsymbol{\rho}, z_1) + \tilde{H}_{i,z}(\boldsymbol{\rho}, z_1)\boldsymbol{u}_z\right] e^{\gamma_i z_1}, \tag{20}$$

en voor $z = z_2$ als de superpositie van alle eigenmodes die propageren in de positieve z-richting

$$\boldsymbol{e}(\boldsymbol{\rho}, z_2) = \sum_i K_i^+ \left[\boldsymbol{E}_{i,t}(\boldsymbol{\rho}, z_2) + E_{i,z}(\boldsymbol{\rho}, z_2)\boldsymbol{u}_z\right] e^{-\gamma_i z_2}, \tag{21}$$

$$\boldsymbol{h}(\boldsymbol{\rho}, z_2) = \sum_i K_i^+ \left[\boldsymbol{H}_{i,t}(\boldsymbol{\rho}, z_2) + H_{i,z}(\boldsymbol{\rho}, z_2)\boldsymbol{u}_z\right] e^{-\gamma_i z_2}. \tag{22}$$

Hierbij wordt verondersteld dat de eigenmodes een complete set vormen.

De coëfficiënten K_i^- en K_i^+ kunnen gevonden worden door opnieuw te vertrekken van het Lorentz reciprociteitstheorema. Nu stellen de a-velden echter de oplossingen voor van de vergelijkingen van Maxwell tengevolge van de stroomdichtheid $\boldsymbol{j}(\boldsymbol{r})$ binnen het volume V. Het Lorentz reciprociteitstheorema is dan

$$\int_S (\boldsymbol{e}_a \times \boldsymbol{h}_b - \boldsymbol{e}_b \times \boldsymbol{h}_a) \cdot \boldsymbol{u}_n dS = \int_V \boldsymbol{e}_b \cdot \boldsymbol{j} dV. \tag{23}$$

Door het b-veld gelijk te nemen aan een eigenmode met propagatieconstante $-\gamma_j$

$$\boldsymbol{e}_b(\boldsymbol{\rho}, z) = \left[\tilde{\boldsymbol{E}}_{j,t}(\boldsymbol{\rho}, z) + \tilde{E}_{j,z}(\boldsymbol{\rho}, z)\boldsymbol{u}_z\right] e^{\gamma_j z}, \tag{24}$$

$$\boldsymbol{h}_b(\boldsymbol{\rho}, z) = \left[\tilde{\boldsymbol{H}}_{j,t}(\boldsymbol{\rho}, z) + \tilde{H}_{j,z}(\boldsymbol{\rho}, z)\boldsymbol{u}_z\right] e^{\gamma_j z}, \tag{25}$$

vindt men door rekening te houden met de orthogonaliteitsrelatie (11) dat

$$K_j^+ = -\frac{\int_V \left[\tilde{\boldsymbol{E}}_{j,t}(\boldsymbol{\rho}, z) + \tilde{E}_{j,z}(\boldsymbol{\rho}, z)\boldsymbol{u}_z\right] \cdot \boldsymbol{j}(\boldsymbol{r}) e^{\gamma_j z} dV}{\int_{S(z)} \left[\boldsymbol{E}_{j,t}(\boldsymbol{\rho}, z) \times \tilde{\boldsymbol{H}}_{j,t}(\boldsymbol{\rho}, z) - \tilde{\boldsymbol{E}}_{j,t}(\boldsymbol{\rho}, z) \times \boldsymbol{H}_{j,t}(\boldsymbol{\rho}, z)\right] \cdot \boldsymbol{u}_z dS}. \tag{26}$$

Gelet op (14) is K_j^+ wel degelijk onafhankelijk van z. Analoog vindt men door als b-veld een eigenmode te nemen met propagatieconstante γ_j, de volgende uitdrukking voor K_j^-:

$$K_j^- = -\frac{\int_V \left[\boldsymbol{E}_{j,t}(\boldsymbol{\rho}, z) + E_{j,z}(\boldsymbol{\rho}, z)\boldsymbol{u}_z\right] \cdot \boldsymbol{j}(\boldsymbol{r}) e^{-\gamma_j z} dV}{\int_{S(z)} \left[\tilde{\boldsymbol{E}}_{j,t}(\boldsymbol{\rho}, z) \times \boldsymbol{H}_{j,t}(\boldsymbol{\rho}, z) - \boldsymbol{E}_{j,t}(\boldsymbol{\rho}, z) \times \tilde{\boldsymbol{H}}_{j,t}(\boldsymbol{\rho}, z)\right] \cdot \boldsymbol{u}_z dS}. \tag{27}$$

Veronderstel nu dat de periodieke golfgeleider wordt geëxciteerd door een extern invallend veld ($\boldsymbol{e}^{\mathrm{i}}(\boldsymbol{r})$, $\boldsymbol{h}^{\mathrm{i}}(\boldsymbol{r})$). Beschouw het gedeelte van deze golfgeleider gelegen tussen de oppervlakken $S(z_1)$ en $S(z_2)$ (Fig. 5). Introduceer ook een cilindrisch oppervlak S parallel met de z-richting dat de oppervlakken $S(z_1)$ en $S(z_2)$ verbindt. Dit oppervlak verdeelt de ruimte in een intern gebied V_{int} en een extern gebied V_{ext}. Het verschil tussen het totale veld ($\boldsymbol{e}(\boldsymbol{r})$, $\boldsymbol{h}(\boldsymbol{r})$) en het invallend veld ($\boldsymbol{e}^{\mathrm{i}}(\boldsymbol{r})$, $\boldsymbol{h}^{\mathrm{i}}(\boldsymbol{r})$) wordt het verstrooide veld ($\boldsymbol{e}^{\mathrm{s}}(\boldsymbol{r})$, $\boldsymbol{h}^{\mathrm{s}}(\boldsymbol{r})$) genoemd. Dit verstrooide veld is enkel gedefinieerd in het extern gebied. Zoals in (19)–(22) kan het totale veld ontbonden worden als een superpositie van alle eigenmodes. Indien verondersteld wordt dat de invallende velden gelokaliseerd zijn, zodat ze verwaarloosbaar zijn op $S_{\text{ext}}(z_1)$ en $S_{\text{ext}}(z_2)$, volgt uit het Lorentz reciprociteitstheorema dat

$$K_j^+ = -\frac{\int_S \left[\tilde{\boldsymbol{E}}_j(\boldsymbol{\rho}, z) \times \boldsymbol{h}^{\mathrm{i}}(\boldsymbol{\rho}, z) - \boldsymbol{e}^{\mathrm{i}}(\boldsymbol{\rho}, z) \times \tilde{\boldsymbol{H}}_j(\boldsymbol{\rho}, z)\right] \cdot \boldsymbol{u}_n e^{\gamma_j z} dS}{\int_{S(z)} \left[\boldsymbol{E}_{j,t}(\boldsymbol{\rho}, z) \times \tilde{\boldsymbol{H}}_{j,t}(\boldsymbol{\rho}, z) - \tilde{\boldsymbol{E}}_{j,t}(\boldsymbol{\rho}, z) \times \boldsymbol{H}_{j,t}(\boldsymbol{\rho}, z)\right] \cdot \boldsymbol{u}_z dS}, \tag{28}$$

$$K_j^- = -\frac{\int_S \left[\boldsymbol{E}_j(\boldsymbol{\rho}, z) \times \boldsymbol{h}^{\mathrm{i}}(\boldsymbol{\rho}, z) - \boldsymbol{e}^{\mathrm{i}}(\boldsymbol{\rho}, z) \times \boldsymbol{H}_j(\boldsymbol{\rho}, z)\right] \cdot \boldsymbol{u}_n e^{-\gamma_j z} dS}{\int_{S(z)} \left[\tilde{\boldsymbol{E}}_{j,t}(\boldsymbol{\rho}, z) \times \boldsymbol{H}_{j,t}(\boldsymbol{\rho}, z) - \boldsymbol{E}_{j,t}(\boldsymbol{\rho}, z) \times \tilde{\boldsymbol{H}}_{j,t}(\boldsymbol{\rho}, z)\right] \cdot \boldsymbol{u}_z dS}. \tag{29}$$

Merk op dat de kennis van het invallend veld volstaat om deze coëfficiënten te berekenen. Bovendien is er een grote vrijheid wat betreft de keuze van dit invallend veld.

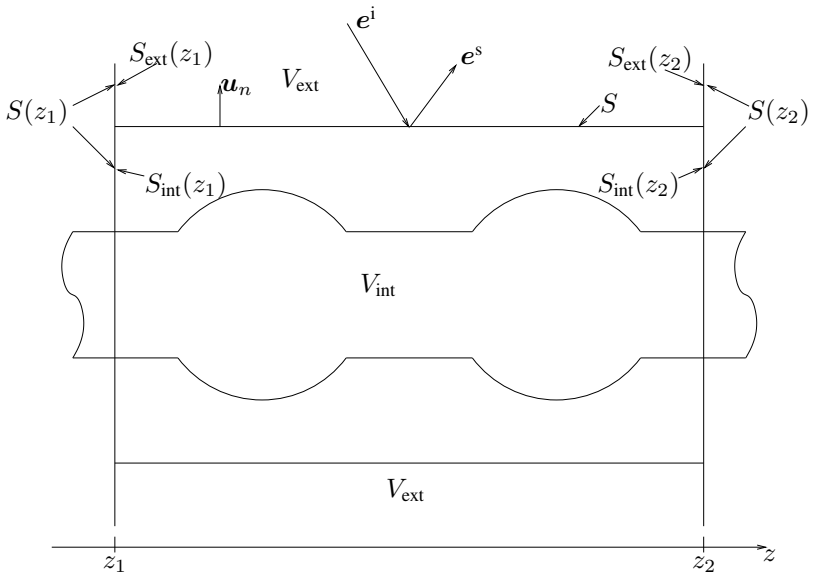

Figuur 5: Excitatie van een periodieke golfgeleider door een invallend veld.

5 Analyse van 2D elektromagnetisch-kristalstructuren

Recent werden in de literatuur heel wat numerieke technieken beschreven voor de analyse van elektromagnetisch-kristalstructuren. De meest gebruikte techniek blijft echter de *eindige-differentie-in-de-tijd* (FDTD - Finite Difference Time Domain) methode [9] omwille van zijn eenvoud en flexibiliteit. Aangezien dit een tijdsdomein methode is verkrijgt men via één enkele simulatie gevolgd door een Fouriertransformatie onmiddellijk informatie over een brede frequentieband. Omwille van de kleine afmetingen van de objecten in elektromagnetische kristallen in vergelijking met de golflengte is echter een fijne discretisatie van de ruimte noodzakelijk. Hierdoor zijn de geheugenvereisten wanneer gewone FDTD wordt gebruikt voor de analyse van elektromagnetische kristallen gauw excessief. Bovendien moet om stabiliteitsredenen ook een kleine tijdsstap gebruikt worden, met een langere simulatietijd tot gevolg. Deze problemen kunnen grotendeels opgelost worden door gebruik te maken van subdomein-modellen. Dit betekent dat de vergelijkingen in FDTD lokaal worden aangepast aan de kennis van het gedrag van de elektromagnetische velden nabij de kleine objecten. Op deze manier kan voor het gebied buiten de objecten een grovere discretisatie gebruikt worden en wordt de tijdsstap hoofdzakelijk bepaald door deze grovere discretisatie. In [10] werd een techniek beschreven die automatisch zulke subdomein-modellen genereert in FDTD voor willekeurige objecten. Bovendien zijn ook de geheugenvereisten beperkt door het reduceren van het aantal interne variabelen. Een blijvend nadeel van FDTD is dat in deze techniek onvermijdelijk fasefouten optreden bij de analyse van grote structuren.

Een tweede veelgebruikte methode is de *eigenmode expansie* (EME - Eigenmode Expansion) techniek [11, 12]. Deze methode deelt de te simuleren structuur op in een aantal lagen waarbinnen de materiaalparameters constant zijn in de propagatierichting. Vervol-

gens worden de totale velden in elke laag geschreven als een superpositie van de eigenmodes van de desbetreffende laag. De onbekende coëfficiënten worden bepaald door mode-aanpassing toe te passen aan de scheidingsoppervlakken tussen de verschillende laagjes. Voor structuren waarin een welbepaalde laag zeer frequent wordt herhaald, is de rekencomplexiteit van deze methode zeer gering. Bovendien kan vrij gemakkelijk de reflectiematrix berekend worden van een halfoneindige elektromagnetisch-kristalgolfgeleider. Deze reflectiematrix kan dan aangewend worden om in de simulaties ongewenste reflecties aan de poorten van de elektromagnetisch-kristalstructuur te vermijden. De mode-aanpassing vereist echter dat elke laag gekarakteriseerd kan worden met een discreet aantal modes. De gehele structuur wordt hiertoe typisch afgesloten met een perfect geleidend omhulsel. Dit leidt tot parasitaire reflecties. Een betere oplossing bestaat erin om meer geavanceerde randvoorwaarden toe te passen, zoals perfect aangepaste lagen (PMLs - Perfectly Matched Layers).

Een derde veel gebruikte techniek is de *meervoudige-verstrooiingstechniek* (MST - Multiple Scattering Technique) [13, 14]. Deze techniek lost integraalvergelijkingen op in functie van onbekende stromen die vloeien op het oppervlak van de cilinders in het elektromagnetisch kristal. Bovendien wordt het feit dat de cilinders rond zijn uitgebuit door deze oppervlaktestromen in een Fourierreeks te ontbinden. De elektromagnetische velden veroorzaakt door deze stromen kunnen dan analytisch berekend worden en geven aanleiding tot Bessel/Hankelfuncties. Op deze manier kunnen zeer nauwkeurige simulatieresultaten bekomen worden met een beperkt aantal onbekenden per cilinder. Het belangrijkste nadeel is dat deze methode uiteindelijk de oplossing van een volledig gevuld lineair stelsel vereist waarvan de dimensie recht evenredig is met het aantal cilinders in de elektromagnetisch-kristalstructuur.

5.1 Meervoudige-verstrooiingstechniek

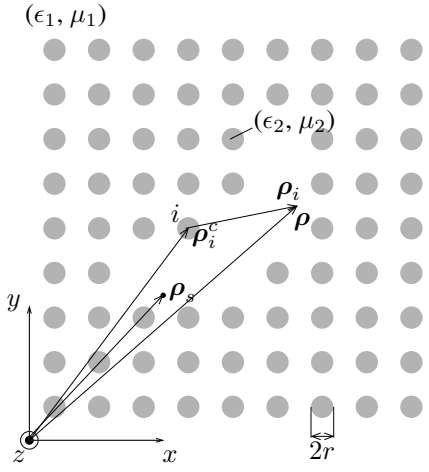

Figuur 6: Elektromagnetisch-kristalstructuur.

In deze sectie wordt de klassieke meervoudige-verstrooiingstechniek voor de karak-

terisatie van eindige elektromagnetisch-kristalstructuren beschreven. De vergelijkingen voor deze methode worden in de Engelstalige tekst op drie verschillende manieren bekomen:

- via een equivalente randimpedantie;
- via het veld-equivalentietheorema [15];
- via rechtstreekse eliminatie van het intern probleem.

Beschouw een algemene elektromagnetisch-kristalstructuur zoals getoond in Fig. 6. Deze structuren bestaan uit N_c oneindig lange, z-invariante, homogene, diëlektrische/magnetische, ronde cilinders met straal r and materiaalparameters (ϵ_2, μ_2) die ingebed zijn in een homogeen achtergrondmedium met materiaalparameters (ϵ_1, μ_1). Om de notatie niet te overladen worden alle cilinders identiek verondersteld. In de Engelstalige tekst wordt ook de uitbreiding naar verschillende cilinders behandeld. Bovendien wordt enkel de TM$_z$-polarisatie behandeld. De vergelijkingen voor de TE$_z$-polarisatie, waarvoor het magnetisch veld enkel een z-component heeft, kunnen op een gelijkaardige manier afgeleid worden.

In wat volgt stelt $\boldsymbol{\rho} = x\boldsymbol{u}_x + y\boldsymbol{u}_y = (\rho, \phi)$ een globale positievector voor in het xy-vlak; $\boldsymbol{\rho}_j = (\rho_j, \phi_j)$ is een lokale positievector vertrekkend uit het middelpunt $\boldsymbol{\rho}_j^c$ van cilinder j, $j = 1, \ldots, N_c$. Het veld dat door de opgelegde bronnen wordt gegenereerd in afwezigheid van de cilinders wordt het invallend veld $E_z^{\mathrm{i}}(\boldsymbol{\rho})\boldsymbol{u}_z$ genoemd. In de aanwezigheid van de cilinders wordt het totale veld $E_z^{\mathrm{t}}(\boldsymbol{\rho})\boldsymbol{u}_z$ waargenomen. Het verschil tussen beide wordt het verstrooide veld $E_z^{\mathrm{s}}(\boldsymbol{\rho})\boldsymbol{u}_z$ genoemd: $E_z^{\mathrm{t}}(\boldsymbol{\rho}) = E_z^{\mathrm{i}}(\boldsymbol{\rho}) + E_z^{\mathrm{s}}(\boldsymbol{\rho})$.

5.1.1 Via een equivalente randimpedantie

Op het oppervlak S_j van elke cilinder j wordt een set van equivalente, z-gerichte, elektrische stromen $J_z^j(\boldsymbol{\rho})\boldsymbol{u}_z$ geïntroduceerd, $j = 1, \ldots, N_c$. Het veld dat uitgestraald wordt door $J_z^j(\boldsymbol{\rho})\boldsymbol{u}_z$ in een homogene ruimte met materiaalparameters (ϵ_1, μ_1) wordt aangeduid met $E_z^{\mathrm{s},j}(\boldsymbol{\rho})\boldsymbol{u}_z$. De algemene uitdrukking voor dit veld is

$$E_z^{\mathrm{s},j}(\boldsymbol{\rho}) \quad = \quad \int_{\boldsymbol{\rho}' \in S_j} G(\boldsymbol{\rho}|\boldsymbol{\rho}') J_z^j(\boldsymbol{\rho}') d\boldsymbol{\rho}', \tag{30}$$

met $G(\boldsymbol{\rho}|\boldsymbol{\rho}')$ de Greense functie in het achtergrondmedium:

$$G(\boldsymbol{\rho}|\boldsymbol{\rho}') \quad = \quad -\frac{\omega\mu_1}{4} H_0^{(2)}(k_1|\boldsymbol{\rho} - \boldsymbol{\rho}'|). \tag{31}$$

Hierbij is $k_1 = \omega\sqrt{\epsilon_1\mu_1}$ het golfgetal in het achtergrondmedium. Het totale veld buiten de cilinders is gelijk aan de som van het invallend veld en alle velden gegenereerd door de (voorlopig onbekende) oppervlaktestromen. Indien alle cilinders perfect geleidend zijn kunnen deze oppervlaktestromen bekomen worden door te eisen dat het totale elektrisch veld verdwijnt op het oppervlak van elke cilinder. Voor dielektrische/magnetische cilinders kan een gepaste randimpedantie Z^i voor elke cilinder i bepaald worden. De randvoorwaarde op het oppervlak S_i van cilinder i wordt dan

$$E_z^{\mathrm{i}}(\boldsymbol{\rho}) + \sum_{j=1}^{N_c} E_z^{\mathrm{s},j}(\boldsymbol{\rho}) \quad = \quad Z^i J_z^i(\boldsymbol{\rho}), \ \text{ voor } \boldsymbol{\rho} \in S_i, \ i = 1, \ldots, N_c. \tag{32}$$

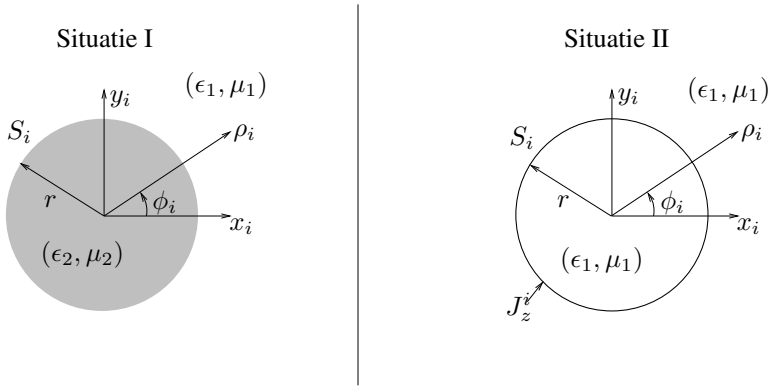

Figuur 7: Twee situaties voor de berekening van de randimpedantie.

Het circulair karakter van elke cilinder wordt uitgebuit door $J_z^j(\boldsymbol{\rho})$ te ontbinden in een Fourierreeks in de lokale cilindrische coördinaten[1]:

$$J_z^j(\boldsymbol{\rho}) \quad = \quad \sum_{n=-K}^{K} \frac{I_n^j}{2\pi r J_n(k_1 r)} e^{jn\phi_j} \delta(\rho_j - r). \tag{33}$$

In deze uitdrukking stelt $J_n(\cdot)$ de Besselfunctie van de eerste soort en orde n voor; $H_n^{(2)}(\cdot)$ stelt de Hankelfunctie van de tweede soort en orde n voor. Omdat de straal van de cilinders klein is ten opzichte van de golflengte, kan het aantal Fouriercomponenten steeds beperkt worden tot $n = -K, \ldots, K$, met K een klein, positief geheel getal. In alle voorbeelden in deze Nederlandse samenvatting wordt convergentie al bereikt met $K = 1$. Nu kan men makkelijk een analytische uitdrukking vinden voor $E_z^{\mathrm{s},j}(\boldsymbol{\rho})$:

$$E_z^{\mathrm{s},j}(\boldsymbol{\rho}) \quad = \quad -\frac{\omega\mu_1}{4} \sum_{n=-K}^{K} H_n^{(2)}(k_1\rho_j) I_n^j e^{jn\phi_j}, \ \text{ als } \rho_j > r. \tag{34}$$

Analoog kan vergelijking (32) herschreven worden als

$$E_z^{\mathrm{i}}(\boldsymbol{\rho}) + \sum_{j=1}^{N_c} E_z^{\mathrm{s},j}(\boldsymbol{\rho}) = \quad \sum_{n=-K}^{K} \frac{Z_n^i I_n^i}{2\pi r J_n(k_1 r)} e^{jn\phi_i}, \ \text{ voor } \boldsymbol{\rho} \in S_i, \ i = 1, \ldots, N_c. \tag{35}$$

De randimpedanties Z_n^i worden bekomen door het vergelijken van de volgende twee configuraties (Fig. 7):

- een diëlektrische/magnetische cilinder met straal r en materiaalparameters (ϵ_2, μ_2) in een homogeen achtergrondmedium met materiaalparameters (ϵ_1, μ_1),

[1] In vergelijking met de Engelstalige tekst werd hier een extra normalisatiefactor $J_n(k_1 r)$ gebruikt in deze expansie. Hierdoor zijn de finale uitdrukkingen voor de elementen van de interactiematrix en de excitatievector voor de drie afleidingswijzes identiek.

- de onbekende stromen $\sum_{n=-K}^{K} \frac{I_n^i}{2\pi r J_n(k_1 r)} e^{jn\phi_i}\delta(\rho_i - r)$ in een homogeen achtergrondmedium met materiaalparameters (ϵ_1, μ_1).

In de eerste situatie kunnen de velden net binnen de cilinder geschreven worden als

$$E_z^{\mathrm{I}}(r^-, \phi_i) = \sum_{n=-K}^{K} A_n J_n(k_2 r) e^{jn\phi_i}, \tag{36}$$

$$j\omega\mu_2 H_{\phi_i}^{\mathrm{I}}(r^-, \phi_i) = k_2 \sum_{n=-K}^{K} A_n J_n'(k_2 r) e^{jn\phi_i}, \tag{37}$$

met $k_2 = \omega\sqrt{\epsilon_2\mu_2}$ het golfgetal in de cilinder. In de tweede situatie kunnen de velden net buiten de cilinder geschreven worden als

$$E_z^{\mathrm{II}}(r^+, \phi_i) = \sum_{n=-K}^{K} B_n J_n(k_1 r) e^{jn\phi_i}, \tag{38}$$

$$j\omega\mu_1 H_{\phi_i}^{\mathrm{II}}(r^+, \phi_i) = k_1 \sum_{n=-K}^{K} B_n J_n'(k_1 r) e^{jn\phi_i} + j\omega\mu_1 \sum_{n=-K}^{K} \frac{I_n^i}{2\pi r J_n(k_1 r)} e^{jn\phi_i}. \tag{39}$$

De randimpedantie Z_n^i is gedefinieerd als

$$E_z^{\mathrm{II}}(r^+, \phi_i) = \sum_{n=-K}^{K} \frac{Z_n^i I_n^i}{2\pi r J_n(k_1 r)} e^{jn\phi_i} \tag{40}$$

en kan bekomen worden door te eisen dat $E_z^{\mathrm{I}}(r^-, \phi_i) = E_z^{\mathrm{II}}(r^+, \phi_i)$ en $H_{\phi_i}^{\mathrm{I}}(r^-, \phi_i) = H_{\phi_i}^{\mathrm{II}}(r^+, \phi_i)$. Men bekomt

$$Z_n^i = J_n(k_1 r)\left[\frac{k_2 J_n'(k_2 r)}{\mu_2 J_n(k_2 r)} - \frac{k_1 J_n'(k_1 r)}{\mu_1 J_n(k_1 r)}\right]^{-1}. \tag{41}$$

Invullen van de uitdrukkingen (34) en (41) in (35) en wegen van de resulterende vergelijking met de testfuncties $T_m^i(\boldsymbol{\rho}) = \frac{1}{2\pi r J_m(k_1 r)} e^{-jm\phi_i}\delta(\rho_i - r)$ resulteert in een lineair stelsel van vergelijkingen

$$\boldsymbol{Z}\boldsymbol{I} = \boldsymbol{E}. \tag{42}$$

In wat volgt wordt de bovenstaande weging aangeduid via $\langle\cdot,\cdot\rangle$. De elementen Z_{mn}^{ij} van de interactiematrix $\boldsymbol{Z}$ zijn

$$Z_{mn}^{ij} = \begin{cases} -\frac{\omega\mu_1}{4}\frac{k_2\mu_1 H_n^{(2)}(k_1 r) J_n'(k_2 r) - k_1\mu_2 H_n^{(2)\prime}(k_1 r) J_n(k_2 r)}{k_2\mu_1 J_n(k_1 r) J_n'(k_2 r) - k_1\mu_2 J_n'(k_1 r) J_n(k_2 r)} & \text{als } \begin{cases} i = j \\ m = n \end{cases} \\ 0 & \text{als } \begin{cases} i = j \\ m \neq n \end{cases} \\ -\frac{\omega\mu_1}{4} H_{n-m}^{(2)}(k_1 R_{ij}) e^{j(m-n)\Phi_{ij}} & \text{als } i \neq j. \end{cases} \tag{43}$$

Hier zijn R_{ij} and Φ_{ij} respectievelijk de lengte en de hoek ten opzichte van de positieve x-as van de vector $\boldsymbol{\rho}_{ij}^c = \boldsymbol{\rho}_j^c - \boldsymbol{\rho}_i^c$ die de middelpunten van de cilinders i en j verbindt. Voor sommige invallende velden bestaan er ook analytische uitdrukkingen voor de elementen $E_m^i = \langle T_m^i(\boldsymbol{\rho}), -E_z^{\rm i}(\boldsymbol{\rho})\rangle$ van de excitatievector $\boldsymbol{E}$. Indien $E_z^{\rm i}(\boldsymbol{\rho})$ veroorzaakt wordt door een Dirac lijnbron op het punt $\boldsymbol{\rho}_s$, dan is

$$E_m^i = -\frac{\omega\mu_1}{4}(-1)^m H_m^{(2)}(k_1 R_{si}) e^{jm\Phi_{si}}, \tag{44}$$

met R_{si} en Φ_{si} de lengte en de hoek van de vector $\boldsymbol{\rho}_{si}^c = \boldsymbol{\rho}_i^c - \boldsymbol{\rho}_s$.

5.1.2 Via het veld-equivalentietheorema

Om $E_z^{\rm s}(\boldsymbol{\rho})$ en $E_z^{\rm t}(\boldsymbol{\rho})$ te beschrijven worden hier twee sets van equivalente elektrische en magnetische stromen, aangeduid door de index $\alpha = 1, 2$, ingevoerd op het oppervlak S_j van elke cilinder. Indien deze stromen verbonden zijn met het totale elektrische veld op S_j via

$$J_\alpha^j(\boldsymbol{\rho})\boldsymbol{u}_z = -s_\alpha \frac{j}{\omega\mu_\alpha} \left.\frac{\partial E_z^{\rm t}(\boldsymbol{\rho})}{\partial \rho_j}\right|_{\boldsymbol{\rho}\in S_j} \delta(\rho_j - r)\boldsymbol{u}_z, \tag{45}$$

$$K_\alpha^j(\boldsymbol{\rho})\boldsymbol{u}_{\phi_j} = s_\alpha \left. E_z^{\rm t}(\boldsymbol{\rho})\right|_{\boldsymbol{\rho}\in S_j} \delta(\rho_j - r)\boldsymbol{u}_{\phi_j}, \tag{46}$$

met $s_1 = 1$, $s_2 = -1$, dan volgt uit het veld-equivalentietheorema dat

(i) de elektrische en magnetische stromen $\displaystyle\sum_{j=1}^{N_c} J_1^j(\boldsymbol{\rho})\boldsymbol{u}_z$ in $\displaystyle\sum_{j=1}^{N_c} K_1^j(\boldsymbol{\rho})\boldsymbol{u}_{\phi_j}$ samen met de opgelegde bronnen in een homogeen medium met materiaalparameters (ϵ_1, μ_1) een veld veroorzaken dat nul is binnen elk oppervlak S_j en gelijk is $E_z^{\rm t}(\boldsymbol{\rho})$ buiten alle S_j;

(ii) de elektrische en magnetische stromen $J_2^j(\boldsymbol{\rho})\boldsymbol{u}_z$ en $K_2^j(\boldsymbol{\rho})\boldsymbol{u}_{\phi_j}$ in een homogeen medium met materiaalparameters (ϵ_2, μ_2) een veld veroorzaken dat nul is buiten S_j en $E_z^{\rm t}(\boldsymbol{\rho})$ binnen S_j.

Indien $E_\alpha^{{\rm s},j}(\boldsymbol{\rho})\boldsymbol{u}_z$ het elektrisch veld voorstelt dat wordt veroorzaakt door de stromen $J_\alpha^j(\boldsymbol{\rho})\boldsymbol{u}_z$ en $K_\alpha^j(\boldsymbol{\rho})\boldsymbol{u}_{\phi_j}$ in een homogeen medium met materiaalparameters (ϵ_α, μ_α), dan volgt uit het bovenstaande dat

$$E_z^{\rm i}(\boldsymbol{\rho}) + \sum_{j=1}^{N_c} E_1^{{\rm s},j}(\boldsymbol{\rho}) = 0 \text{ voor } \boldsymbol{\rho}\in S_i^-,\ i = 1,\ldots,N_c, \tag{47}$$

$$E_2^{{\rm s},j}(\boldsymbol{\rho}) = 0 \text{ voor } \boldsymbol{\rho}\in S_j^+,\ j = 1,\ldots,N_c. \tag{48}$$

Hier duiden S_j^- en S_j^+ oppervlaktes aan die respectievelijk net binnen en net buiten S_j gelegen zijn. De elektrische en magnetische stromen worden opnieuw in een Fourierreeks

ontbonden:

$$J_\alpha^j(\boldsymbol{\rho}) = s_\alpha \sum_{n=-K}^{K} \frac{C_n I_n^j}{2\pi r} e^{jn\phi_j}\delta(\rho_j - r), \tag{49}$$

$$K_\alpha^j(\boldsymbol{\rho}) = s_\alpha \sum_{n=-K}^{K} \frac{C_n M_n^j}{2\pi r} e^{jn\phi_j}\delta(\rho_j - r), \tag{50}$$

met

$$C_n = \frac{k_2\mu_1 J_n'(k_2 r)}{k_2\mu_1 J_n(k_1 r)J_n'(k_2 r) - k_1\mu_2 J_n'(k_1 r)J_n(k_2 r)}. \tag{51}$$

Vergelijkingen (47) en (48) kunnen samen opgelost worden naar alle onbekenden I_n^j en M_n^j, $j = 1, \ldots, N_c$; $n = -K, \ldots, K$. Het is echter voordeliger om eerst enkel (48) op te lossen. Dit levert het volgende verband op:

$$\frac{I_n^j}{M_n^j} = -j\sqrt{\frac{\epsilon_2}{\mu_2}}\frac{J_n'(k_2 r)}{J_n(k_2 r)}. \tag{52}$$

Dit verband kan nu aangewend worden om alle magnetische onbekenden M_n^j in (47) te elimineren. Rekening houdend met (52) kan het veld $E_1^{s,j}(\boldsymbol{\rho})$ uitgedrukt worden als

$$E_1^{s,j}(\boldsymbol{\rho}) = \sum_{n=-K}^{K} G_n(\boldsymbol{\rho}_j) I_n^j, \tag{53}$$

met

$$G_n(\boldsymbol{\rho}_j) = \begin{cases} -\dfrac{\omega\mu_1}{4} H_n^{(2)}(k_1\rho_j)e^{jn\phi_j} & \text{als } \rho_j > r, \\ -\dfrac{\omega\mu_1}{4} \dfrac{k_2\mu_1 H_n^{(2)}(k_1 r)J_n'(k_2 r) - k_1\mu_2 H_n^{(2)'}(k_1 r)J_n(k_2 r)}{k_2\mu_1 J_n(k_1 r)J_n'(k_2 r) - k_1\mu_2 J_n'(k_1 r)J_n(k_2 r)} \times & \\ \qquad J_n(k\rho_j)e^{jn\phi_j} & \text{als } \rho_j < r. \end{cases} \tag{54}$$

De grootheid $G_n(\boldsymbol{\rho}_j)$ stelt de Greense functie voor van een Huygens bron met respectievelijke elektrische en magnetische componenten $\frac{C_n^j}{2\pi r}e^{jn\phi_j}\delta(\rho_j - r)\boldsymbol{u}_z$ en $\frac{jC_n}{2\pi r}\sqrt{\frac{\mu_2}{\epsilon_2}}$ $\frac{J_n(k_2 r)}{J_n'(k_2 r)}e^{jn\phi_j}\delta(\rho_j - r)\boldsymbol{u}_{\phi_j}$ die samen stralen in een homogeen medium met materiaalparameters (ϵ_1, μ_1). Na invullen van uitdrukking (54) in (47) en na weging van de resulterende vergelijking met de testfuncties $T_m^i(\boldsymbol{\rho})$ bekomt men opnieuw een linear stelsel met matrixelementen $Z_{mn}^{ij} = \langle T_m^i(\boldsymbol{\rho}), G_n(\boldsymbol{\rho}_j)\rangle$ gegeven door (43). Indien de excitatie een Dirac lijnbron is op plaats $\boldsymbol{\rho}_s$, zijn de elementen van de excitatievector opnieuw gegeven door (44).

5.1.3 Via rechtstreekse eliminatie van het intern probleem

Indien $E_z^{\mathrm{s},j}(\boldsymbol{\rho})\boldsymbol{u}_z$ hier het elektrisch veld voorstelt dat verstrooid wordt door cilinder j wanneer er een veld op invalt, dan kan dit verstrooide veld uitgedrukt worden als

$$E_z^{\mathrm{s},j}(\boldsymbol{\rho}) \quad = \quad -\frac{\omega\mu_1}{4}\sum_{n=-K}^{K} A_n^j H_n^{(2)}(k_1\rho_j)e^{jn\phi_j}, \ \text{ als } \rho_j > r. \tag{55}$$

Analoog kan het totale veld binnen cilinder j uitgedrukt worden als

$$E_z^{\mathrm{t}}(\boldsymbol{\rho}) \quad = \quad -\frac{\omega\mu_2}{4}\sum_{n=-K}^{K} B_n^j J_n(k_2\rho_j)e^{jn\phi_j}, \ \text{ als } \rho_j < r. \tag{56}$$

Tenslotte kan een willekeurig invallend veld in de buurt van cilinder j uitgedrukt worden in functie van het cilindrisch coördinatenstelsel van deze cilinder als

$$E_z^{\mathrm{i}}(\boldsymbol{\rho}) \quad = \quad -\frac{\omega\mu_1}{4}\sum_{n=-K}^{K} C_n^j J_n(k\rho_j)e^{jn\phi_j}. \tag{57}$$

In (55) worden enkel Hankelfuncties gebruikt omdat het verstrooide veld een veld voorstelt dat weg van de cilinder propageert. In (56) en (57) daarentegen worden enkel Besselfuncties gebruikt omdat het totale en het invallend veld eindig moeten blijven voor $\rho_j = 0$. De onbekende coëfficiënten A_n^j en B_n^j kunnen gevonden worden in functie van de gegeven coëfficiënten C_n^j door te eisen dat het totale tangentieel elektrisch en magnetisch veld continu moeten zijn op het oppervlak van elke cilinder:

$$E_z^{\mathrm{i}}(\boldsymbol{\rho})\big|_{\boldsymbol{\rho}\in S_i^+} + \sum_{j=1}^{N_c} E_z^{\mathrm{s},j}(\boldsymbol{\rho})\big|_{\boldsymbol{\rho}\in S_i^+} \quad = \quad E_z^{\mathrm{t}}(\boldsymbol{\rho})\big|_{\boldsymbol{\rho}\in S_i^-}, \tag{58}$$

$$H_{\phi_i}^{\mathrm{i}}(\boldsymbol{\rho})\big|_{\boldsymbol{\rho}\in S_i^+} + \sum_{j=1}^{N_c} H_{\phi_i}^{\mathrm{s},j}(\boldsymbol{\rho})\Big|_{\boldsymbol{\rho}\in S_i^+} \quad = \quad H_{\phi_i}^{\mathrm{t}}(\boldsymbol{\rho})\big|_{\boldsymbol{\rho}\in S_i^-}. \tag{59}$$

Hiertoe wordt $E_z^{\mathrm{s},j}(\boldsymbol{\rho})$ eerst herschreven in functie van het cilindrisch coördinatenstelsel van cilinder i met behulp van het additietheorema voor de Hankelfunctie ([16], p. 232, vgl. 5-103)

$$E_z^{\mathrm{s},j}(\boldsymbol{\rho}) = \quad -\frac{\omega\mu_1}{4}\sum_{n=-K}^{K} A_n^j \sum_{m=-K}^{K} H_{m-n}^{(2)}(k_1R_{ij})e^{j(n-m)\Phi_{ij}} J_m(k_1\rho_i)e^{jm\phi_i}, \tag{60}$$

met R_{ij} en Φ_{ij} de lengte en de hoek ten opzichte van de positieve x-as van de vector $\boldsymbol{\rho}_{ij}^c = \boldsymbol{\rho}_j^c - \boldsymbol{\rho}_i^c$. Hieruit kan dan de ϕ_i-component van het magnetisch veld verstrooid door cilinder j bekomen worden via

$$H_{\phi_i}^{\mathrm{s},j}(\boldsymbol{\rho}) \quad = \quad \frac{1}{j\omega\mu_1}\frac{\partial E_z^{\mathrm{s},j}(\boldsymbol{\rho})}{\partial\rho_i}. \tag{61}$$

Op gelijkaardige wijze berekent men de ϕ_i-component van het invallend magnetisch veld. Door te steunen op de orthogonaliteit van de $e^{jn\phi_i}$-functies kunnen (58) en (59)

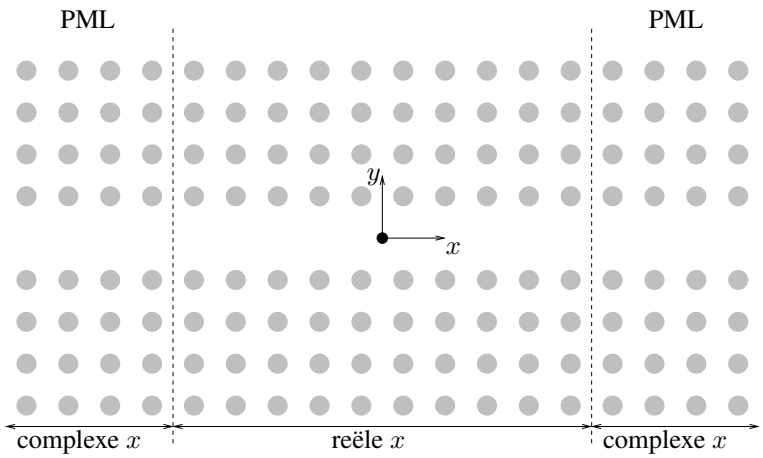

Figuur 8: Elektromagnetisch-kristalgolfgeleider met PML randvoorwaarden.

omgevormd worden tot een lineair stelsel van $2(2K+1)N_c$ vergelijking in de onbekenden A_n^j en B_n^j, $n = -K, \ldots, K$; $j = 1, \ldots, N_c$. De onbekenden B_n^j kunnen echter makkelijk geëlimineerd worden zodat er slechts $(2K+1)N_c$ vergelijkingen overblijven in de onbekenden A_n^j. In matrixvorm wordt dit linear stelsel van vergelijkingen genoteerd als

$$\boldsymbol{Z}\boldsymbol{A} \;=\; \boldsymbol{C}. \tag{62}$$

De elementen van de matrix $\boldsymbol{Z}$ worden gegeven door (43). Indien het invallend veld veroorzaakt wordt door een Dirac lijnbron in $\boldsymbol{\rho}_s$, dan is $C_m^i = E_m^i$ zoals gedefinieerd in (44).

5.1.4 Complexe coördinaten

Met de hierboven beschreven techniek kunnen enkel eindige elektromagnetisch-kristalstructuren gekarakteriseerd worden. Deze structuren kunnen aanzien worden als een N-poort waarbij de poorten periodieke golfgeleiders zijn. Meestal is men bij de simulaties niet geïnteresseerd in reflecties ten gevolge van een abrupt einde van deze golfgeleiders. Het is daarom voordelig om, via een aangepaste randvoorwaarde, elektromagnetisch-kristalgolfgeleiders te kunnen modelleren die oneindig doorlopen in de propagatierichting. Recent werd in [17] een dergelijke randvoorwaarde voorgesteld voor FDTD. Het basisidee is om de elektromagnetisch-kristalgolfgeleider te laten doorlopen in een PML. Door te steunen op de interpretatie van een PML met behulp van complexe coördinaten [18, 19], kan een gelijkaardige randvoorwaarde voor integraalvergelijkingstechnieken geïmplementeerd worden door de elektromagnetisch-kristalgolfgeleiders over een aantal periodes te laten doorlopen in de PML. Men kan zeggen dat de golfgeleider een bocht maakt in het complexe vlak. Dit betekent dat de middelpunten van de cilinders in de PML complexe coördinaten hebben (Fig. 8). In deze sectie worden complexe coördinaten en afstanden aangeduid met een tilde. Indien de propagatierichting van de elektromagnetisch-

kristalgolfgeleider die wordt afgesloten door de PML randvoorwaarde de positieve x-richting is, dan zijn de x-coördinaten van de middelpunten van de cilinders in de PML complex, terwijl hun y-coördinaten reëel blijven:

$$\tilde{x}_i^c = x_i^{\text{re}} + jx_i^{\text{im}}. \tag{63}$$

De afstand tussen 2 cilinders i en j wordt ook complex indien ten minste één van beiden zich in de PML bevindt:

$$\begin{aligned} \tilde{R}_{ij} &= R_{ij}^{\text{re}} + jR_{ij}^{\text{im}} \\ &= \left[(\tilde{x}_i^c - \tilde{x}_j^c)^2 + (y_i^c - y_j^c)^2\right]^{\frac{1}{2}}. \end{aligned} \tag{64}$$

Indien alle middelpunten reëel zouden zijn, is $\tilde{R}_{ij} = R_{ij}^{\text{re}} \geq 0$. Voor complexe afstanden wordt ook geëist dat $R_{ij}^{\text{re}} \geq 0$. Uit het gedrag van de Hankelfunctie voor grote argumenten

$$\lim_{|k_1\tilde{R}_{ij}|>>0} H_0^{(2)}(k_1\tilde{R}_{ij}) = \left(\frac{2}{\pi k_1 \tilde{R}_{ij}}\right)^{\frac{1}{2}} e^{-jk_1(R_{ij}^{\text{re}} - \frac{\pi}{4})} e^{k_1 R_{ij}^{\text{im}}}, \tag{65}$$

volgt bovendien dat R_{ij}^{im} negatief moet zijn om een exponentiële demping te bekomen. Deze vaststelling bepaalt de vertakkingslijn voor (64). Dit betekent ook dat indien $(x_i^{\text{re}} - x_j^{\text{re}})$ positief is, $(x_i^{\text{im}} - x_j^{\text{im}})$ negatief moet zijn en omgekeerd.

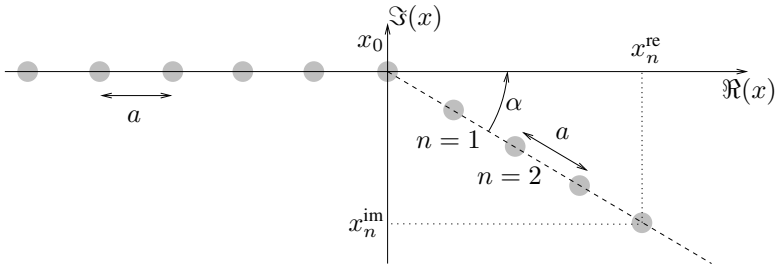

Figuur 9: Lineaire PML.

De performantie van de voorgestelde randvoorwaarde hangt sterk af van de wijze waarop de overgang van reële naar complexe coördinaten gebeurt. Beschouw hiertoe de configuratie getoond in Fig. 8. Deze configuratie omvat een rechte elektromagnetisch-kristalgolfgeleider met N_{wav} gewone periodes. Voor en na deze gewone periodes, zijn er nog N_{PML} extra periodes waarvoor de cilinders complexe x-coördinaten hebben. Twee verschillende manieren waarop de golfgeleider in het complex vlak kan binnentreden worden hier bekeken, namelijk:

- de overgang naar complexe coördinaten gebeurt lineair (Fig. 9). De complexe x-coördinaat voor een cilinder in de n^{de} periode in de PML is

  $$\tilde{x}_n^c = x_0 + na\cos(\alpha) - jna\sin(\alpha), \tag{66}$$

  met $n = 1, \ldots, N_{\text{PML}}$ en x_0 de x-coordinaat van de laatste periode van de golfgeleider die zich net niet in de PML bevindt.

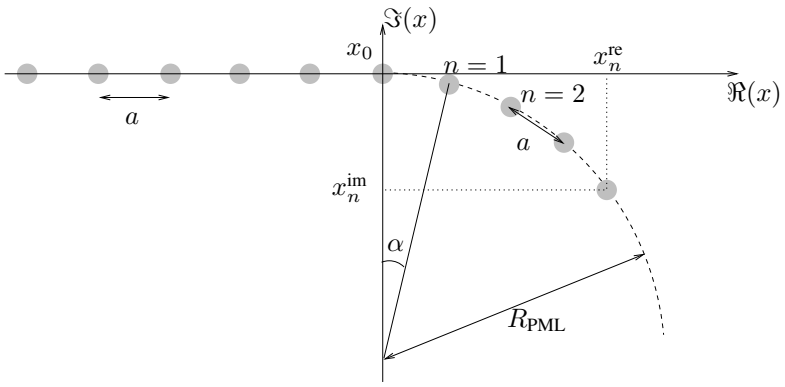

Figuur 10: Circulaire PML.

- de overgang naar complexe coördinaten gebeurt circulair (Fig. 10). De complexe x-coördinaat voor een cilinder in de n^{de} periode in de PML is nu

$$\tilde{x}_n^c \quad = \quad x_0 + R_{\text{PML}} \sin(n\alpha) - jR_{\text{PML}}(1 - \cos(n\alpha)), \tag{67}$$

  met $\alpha = 2 \arcsin(\frac{a}{2R_{\text{PML}}})$.

In beide gevallen is de absolute waarde van de complexe afstand tussen twee opeenvolgende periodes gelijk aan de roosterconstante a.

In Fig. 11 wordt de absolute waarde van het totale elektrische veld getoond in vier gewone periodes voor verschillende PMLs en vergeleken met de oplossing voor een oneindige golfgeleider. Ook het geval waarbij de golfgeleiders abrupt worden afgebroken is getoond in deze figuur. Voor de lineaire PML met $\alpha = \pi/6$ en $N_{\text{PML}} = 11$, blijft er een vrij sterke reflectie bestaan. De verstoring in de periodiciteit is in dit geval te groot. Door de overgang naar het complex vlak meer geleidelijk aan te laten verlopen, kunnen deze reflecties sterk gereduceerd worden. Als $\alpha = \pi/90$ en $N_{\text{PML}} = 40$ is er bijna geen verschil meer te merken met het geval van de oneindige golfgeleider. Met een circulaire PML kan hetzelfde bereikt worden met $R_{\text{PML}} = 10a$ en slechts $N_{\text{PML}} = 7$ extra periodes.

Als tweede, meer geavanceerd voorbeeld wordt de twee-kanaals multiplexer-demultiplexer [20, 21] uit Fig. 12 beschouwd met interactielengte $l = 48a$. Aan elke poort wordt een circulaire PML met $R_{\text{PML}} = 10a$ en $N_{\text{PML}} = 7$ toegevoegd. Aan elke poort wordt de uitgaande flux berekend en vergeleken met die van een rechte golfgeleider met dezelfde excitatie en PML randvoorwaarden. De transmissie naar elke poort is dan gelijk aan de verhouding van beide fluxen. In Fig. 13 worden de resultaten van deze berekening vergeleken met die uit [20].

5.1.5 Rekencomplexiteit en geheugenvereisten

Het belangrijkste nadeel van de meervoudige-verstrooiingstechniek is dat het uiteindelijk de oplossing vereist van een volledig gevuld lineair stelsel van vergelijkingen. Grofweg kan men stellen dat dit stelsel op twee manieren kan opgelost worden: (i) via een *directe* methode, zoals bijvoorbeeld Gauss eliminatie of LU-decompositie, of (ii) via een

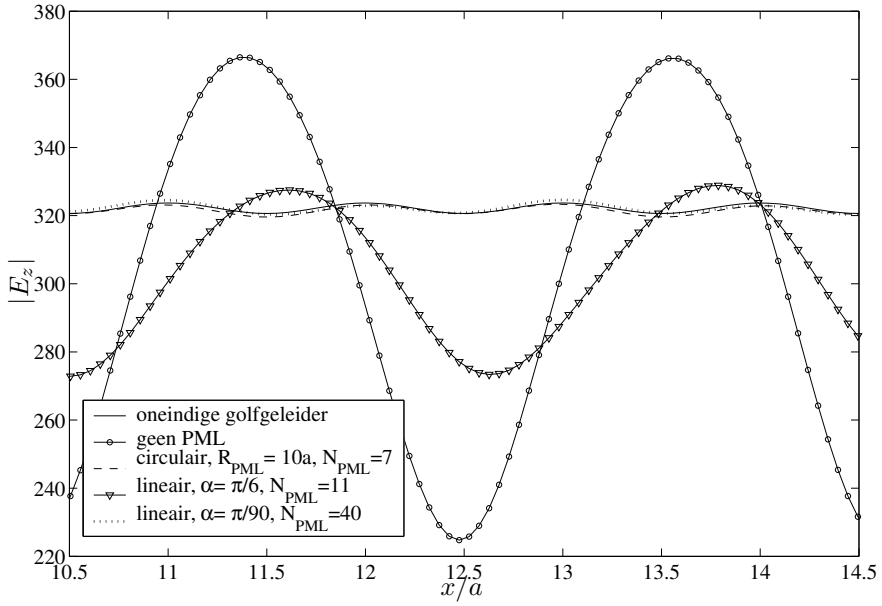

Figuur 11: Vergelijking van de performantie van verschillende PMLs.

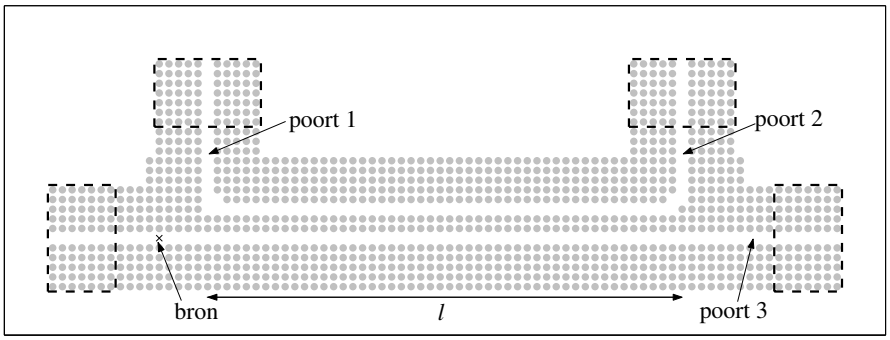

Figuur 12: Two-kanaals multiplexer-demultiplexer.

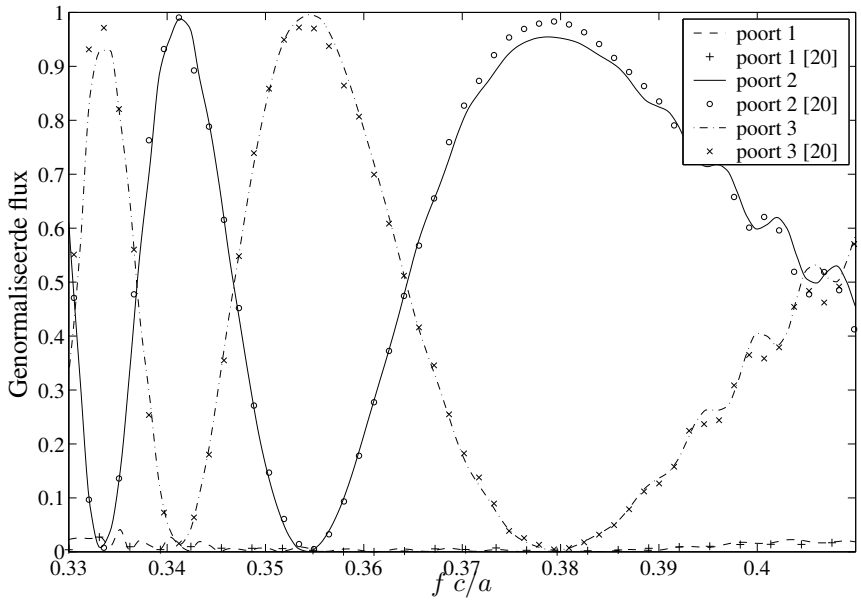

Figuur 13: Transmissiespectrum van de twee-kanaals multiplexer-demultiplexer met $l = 48a$.

iteratieve methode. Het aantal onbekenden in (42) is $(2K + 1)N_c$. Aangezien het aantal Fouriercomponenten $2K + 1$ niet afhangt van de grootte van de elektromagnetisch-kristalstructuur, zullen er om dit stelsel op te lossen via een directe methode $O(N_c^3)$ operaties nodig zijn. De geheugenvereisten schalen als $O(N_c^2)$. Een iteratieve methode probeert een benadering te vinden voor de echte oplossing. In elke iteratie wordt een nieuwe testoplossing $\tilde{\boldsymbol{I}}$ voorgesteld door de iteratieve oplossingsmethode. Deze testoplossing wordt dan vermenigvuldigd met de interactiematrix $\boldsymbol{Z}$ en het resultaat $\tilde{\boldsymbol{E}} = \boldsymbol{Z}\tilde{\boldsymbol{I}}$ hiervan wordt vergeleken met de excitatievector $\boldsymbol{E}$. Indien het verschil tussen beide 'voldoende klein' is, wordt $\tilde{\boldsymbol{I}}$ aanvaard als oplossing van het lineair stelsel. Indien dit niet het geval is, wordt een nieuwe testoplossing voorgesteld door de iteratieve methode en wordt de hele cyclus herhaald. Het is duidelijk dat voor het oplossen van een lineair stelsel met een iteratieve methode veel matrix-vector vermenigvuldigingen moeten berekend worden. Indien deze vermenigvuldigingen op de klassieke manier worden berekend, vraagt één zo'n matrix-vermenigvuldiging $O(N_c^2)$ operaties. Als een voldoend nauwkeurige oplossing gevonden wordt na P iteraties schaalt de totale rekencomplexiteit bijgevolg als $O(PN_c^2)$. Uiteraard schalen de geheugenvereisten nog altijd als $O(N_c^2)$.

6 Klassieke efficiënte vermenigvuldigingsschema's

In deze sectie worden de basisprincipes besproken van twee klassieke schema's om de nodige matrix-vector vermenigvuldigingen tijdens het iteratief oplossen van het lineair stelsel (42) te versnellen en de geheugenvereisten te reduceren, namelijk het meervoudige

niveau snelle multipool algoritme (MLFMA - Multilevel Fast Multipole Algorithm) en een schema gebaseerd op een snelle Fouriertransformatie (FFT - Fast Fourier Transform).

De snelle multipool methode (FMM - Fast Multipole Method) werd voor het eerst toegepast door Rohklin om statische integraalvergelijkingen snel op te lossen [22–24]. Deze methode werd door vele onderzoekers uitgebreid naar elektromagnetische problemen, zowel voor twee als voor drie dimensies. Door FMM te gaan toepassen op meerdere niveaus (MLFMA) kunnen de rekencomplexiteit en de geheugenvereisten teruggebracht worden tot vrijwel $O(N_c)$.

Vermenigvuldigingsschema's die gebaseerd zijn FFTs zijn bijzonder geschikt voor elektromagnetisch-kristalstructuren waarin alle cilinders geordend zijn volgens een regelmatig rooster. Voor deze structuren kan een matrix-vector vermenigvuldiging als een twee-dimensionale convolutie geschreven worden. Indien deze convolutie berekenend wordt met FFTs, vereist één matrix-vector vermenigvuldiging $O(N_c \log_2 N_c)$ operaties. De geheugenvereisten voor FFT-gebaseerde schema's schalen als $O(N_c)$.

6.1 FMM en MLFMA

6.1.1 FMM

In FMM worden de rekencomplexiteit en de geheugenvereisten gereduceerd door de N_c cilinders van de elektromagnetisch-kristalstructuur te verdelen in groepen die elk ongeveer M_c cilinders bevatten. De snelheids- en geheugenwinst wordt bekomen door in plaats van elke interactie tussen twee onbekenden afzonderlijk te berekenen, alle interacties tussen twee groepen in één keer te berekenen. Vereenvoudigd kan men stellen dat elke groep beheerd wordt door zijn centrum. Communicatie of interactie tussen twee groepen gebeurt dan via de centra. Op hun beurt communiceren/interageren deze centra met de onbekenden in hun groep. Dit idee van groep-naar-groep interacties kan helaas alleen toegepast worden als twee groepen voldoend ver uit elkaar gelegen zijn. Bijgevolg wordt elke matrix-vector vermenigvuldiging opgesplitst in twee bijdragen:

$$\boldsymbol{Z}\tilde{\boldsymbol{I}} \quad = \quad \boldsymbol{Z}_{\text{nf}}\tilde{\boldsymbol{I}} + \boldsymbol{Z}_{\text{ff}}\tilde{\boldsymbol{I}}. \tag{68}$$

De matrix $\boldsymbol{Z}_{\text{nf}}$ is een dunbezette matrix die alle *nabije* interacties bevat waarvoor FMM niet kan toegepast worden. Aangezien deze matrix slechts $O(N_c)$ elementen bevat, kan $\boldsymbol{Z}_{\text{nf}}\tilde{\boldsymbol{I}}$ in $O(N_c)$ bewerkingen berekend worden. De matrix $\boldsymbol{Z}_{\text{ff}}$ bevat alle overige, *verre* interacties waarvoor FMM wel kan toegepast worden.

Er zal nu aangetoond worden hoe de verre interacties sneller kunnen berekend worden via groep-naar-groep interacties. Beschouw hiertoe eerst de situatie voorgesteld in Fig. 14. Het elektrisch veld in $\boldsymbol{\rho}$ veroorzaakt door een Dirac lijnbron geplaatst in $\boldsymbol{\rho}'$ is

$$\begin{aligned} E_z(\boldsymbol{\rho}) &= -\frac{\omega\mu_1}{4} H_0^{(2)}(k_1|\boldsymbol{\rho}-\boldsymbol{\rho}'|) \\ &= -\frac{\omega\mu_1}{4}\text{nf}(\boldsymbol{\rho}). \end{aligned} \tag{69}$$

De punten $\boldsymbol{\rho}' = (\rho', \phi')$ en $\boldsymbol{\rho} = (\rho, \phi)$ worden respectievelijk de bron en de waarnemer genoemd. Indien de afstand tussen de bron en de waarnemer voldoend groot is, kan deze

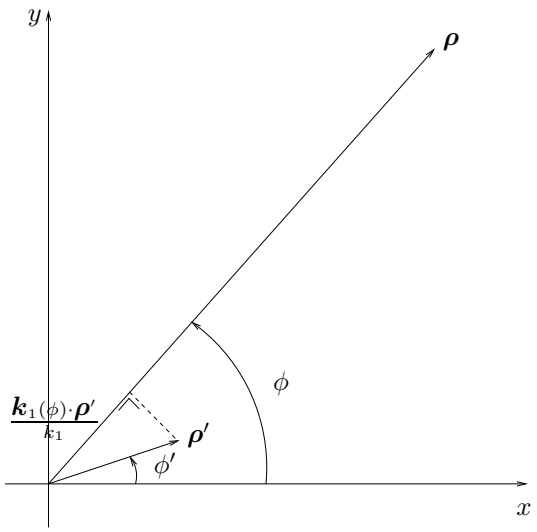

Figuur 14: Bron $\boldsymbol{\rho}'$ en waarnemer $\boldsymbol{\rho}$.

afstand benaderd worden als

$$|\boldsymbol{\rho} - \boldsymbol{\rho}'| \approx \rho - \frac{\boldsymbol{k}_1(\phi) \cdot \boldsymbol{\rho}'}{k_1}, \tag{70}$$

met

$$\boldsymbol{k}_1(\phi) \quad = \quad k_1[\cos(\phi)\boldsymbol{u}_x + \sin(\phi)\boldsymbol{u}_y]. \tag{71}$$

Gelet op het gedrag van de Hankelfunctie voor grote argumenten, kan men via een aantal opeenvolgende benaderingen afleiden dat

$$\text{nf}(\boldsymbol{\rho}) \quad \approx \quad \sqrt{\frac{2}{\pi k_1 \rho}} \frac{e^{-j(k_1\rho - \frac{\pi}{4})}}{2Q+1} \sum_{q=-Q}^{Q} \sum_{q'=-Q}^{Q} \text{ff}(\phi_{q'}) e^{jq(\phi - \phi_{q'})} \text{ als } \rho \gg \rho'. \tag{72}$$

In deze uitdrukking stelt $\text{ff}(\phi) = e^{j\boldsymbol{k}_1(\phi)\cdot\boldsymbol{\rho}'}$ het verre veld voor van de Dirac lijnbron. De hoeken ϕ_q zijn gedefinieerd als

$$\phi_q \quad = \quad \frac{2\pi q}{2Q+1},\ q = -Q, \ldots, Q. \tag{73}$$

De grootheid $2Q+1$ noemt men de bemonsteringsgraad. Anderzijds ziet men via de meest algemene oplossing van de vergelijkingen van Maxwell in cilindercoördinaten in het bronloos gebied nabij de waarnemer in dat

$$\begin{aligned} \text{nf}(\boldsymbol{\rho}) \quad &= \quad \sum_{q=-\infty}^{+\infty} a_q H_q^{(2)}(k_1\rho) e^{jq\phi} \\ &\approx \quad \sum_{q=-Q}^{Q} a_q \sqrt{\frac{2}{\pi k_1 \rho}} e^{-j(k_1\rho - \frac{q\pi}{2} - \frac{\pi}{4})} \text{ als } \rho \rightarrowtail \infty. \end{aligned} \tag{74}$$

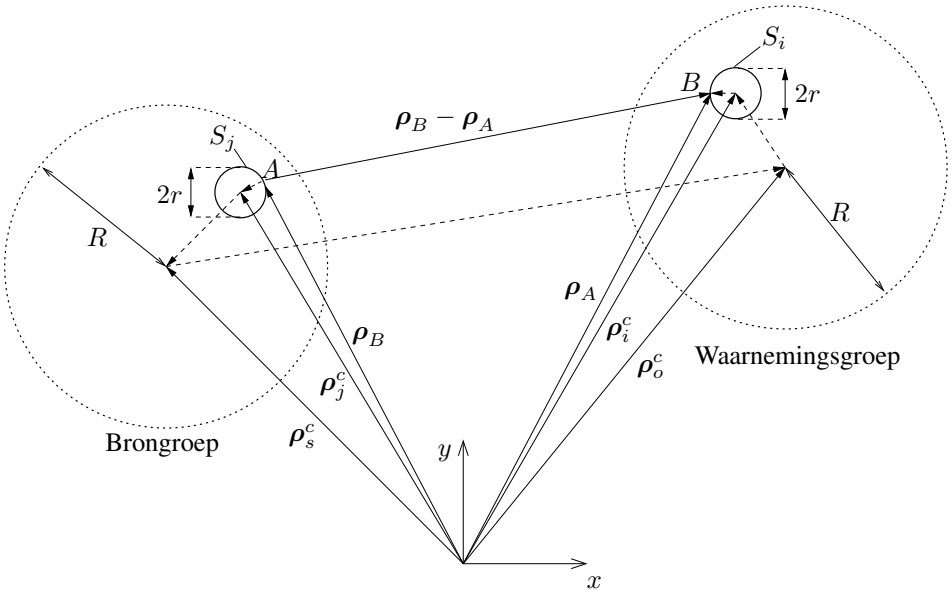

Figuur 15: Bron- en waarnemingsgroep.

Door identificatie van (72) en (74) kunnen de coëfficiënten a_q bepaald worden. Uiteindelijk bekomt men het volgende verband

$$\text{nf}(\boldsymbol{\rho}) \approx \sum_{q=-Q}^{Q} \text{ff}(\phi_q) T_q(k_1, \rho, \phi) \text{ als } \rho \gg \rho', \tag{75}$$

met

$$T_q(k_1, \rho, \phi) = \frac{1}{2Q+1} \sum_{q'=-Q}^{Q} H_{q'}^{(2)}(k_1\rho) e^{jq'(\phi - \phi_q - \frac{\pi}{2})}. \tag{76}$$

Uitdrukking (75) laat toe om het nabije veld in $\boldsymbol{\rho}$ ten gevolge van de lijnbron in $\boldsymbol{\rho}'$ te bepalen uit de kennis van het bemonsterd verre veld van deze lijnbron.

Beschouw vervolgens de situatie voorgesteld in Fig. 15. Deze configuratie omvat twee circulaire groepen met straal R die voldoend ver uit elkaar liggen. In de brongroep met centrum $\boldsymbol{\rho}_s^c$ bevindt er zich één cilinder i met straal r, centrum $\boldsymbol{\rho}_i^c$ en oppervlak S_i; in de waarnemingsgroep met centrum $\boldsymbol{\rho}_o^c$ bevindt er zich eveneens één cilinder j met straal r, centrum $\boldsymbol{\rho}_j^c$ en oppervlak S_j. De vectoren $\boldsymbol{\rho}_A$ en $\boldsymbol{\rho}_B$ duiden respectievelijk punten aan op S_i en S_j. De vector $\boldsymbol{\rho}_B - \boldsymbol{\rho}_A$ kan geschreven worden als

$$\boldsymbol{\rho}_B - \boldsymbol{\rho}_A = \boldsymbol{\rho} - \boldsymbol{\rho'}, \tag{77}$$

met

$$\boldsymbol{\rho} = \boldsymbol{\rho}_o^c - \boldsymbol{\rho}_s^c, \tag{78}$$

$$\boldsymbol{\rho'} = (\boldsymbol{\rho}_j^c - \boldsymbol{\rho}_s^c) + (\boldsymbol{\rho}_A - \boldsymbol{\rho}_j^c) - (\boldsymbol{\rho}_B - \boldsymbol{\rho}_i^c) - (\boldsymbol{\rho}_i^c - \boldsymbol{\rho}_o^c). \tag{79}$$

Uit Sectie 5.1.1 volgt dat Z_{mn}^{ij} gedefinieerd is als

$$Z_{mn}^{ij} = \frac{1}{4\pi^2 r^2 J_n(k_1 r) J_m(k_1 r)} \int_{\boldsymbol{\rho}_B \in S_i} \int_{\boldsymbol{\rho}_A \in S_j} G(\boldsymbol{\rho}_B|\boldsymbol{\rho}_A) e^{-jm\phi_i} e^{jn\phi_j} d\boldsymbol{\rho}_B d\boldsymbol{\rho}_A, \tag{80}$$

met de Greense functie $G(\boldsymbol{\rho}_B|\boldsymbol{\rho}_A)$ gedefinieerd in (31). Rekening houdend met de benadering (75), vindt men na integratie

$$\begin{aligned} Z_{mn}^{ij} \quad \approx \quad & -\frac{\omega\mu_1}{4} \sum_{q=-Q}^{Q} \underbrace{e^{-j[\boldsymbol{k}_1(\phi_q)\cdot(\boldsymbol{\rho}_i^c - \boldsymbol{\rho}_o^c) + m(\phi_q + \frac{\pi}{2})]}}_{1} \times \\ & \underbrace{T_q(k_1, \rho_{so}^c, \phi_{so}^c)}_{2} \underbrace{e^{j[\boldsymbol{k}_1(\phi_q)\cdot(\boldsymbol{\rho}_j^c - \boldsymbol{\rho}_s^c) + n(\phi_q + \frac{\pi}{2})]}}_{3}. \end{aligned} \tag{81}$$

Hier zijn ρ_{so}^c en ϕ_{so}^c respectievelijk de lengte en de hoek ten opzichte van de positieve x-as van de vector $\boldsymbol{\rho}_{so}^c = \boldsymbol{\rho}_o^c - \boldsymbol{\rho}_s^c$. De eerste term in (81) is de complex toegevoegde van het bemonsterd stralingspatroon van de waarnemingsgroep, de tweede term is de (diagonale) translatie-operator, de derde term is het bemonsterd stralingspatroon van de brongroep. In [25, 26] wordt aangetoond dat de bemonsteringsgraad om een voldoende nauwkeurigheid te bereiken schaalt als

$$2Q + 1 \quad = \quad 4kR + C. \tag{82}$$

De constante C brengt in rekening dat het verre veld slechts *quasi* bandbeperkt is. Hierdoor moet de bemonsteringsgraad iets groter zijn dan de waarde $4kR$ die voorspeld wordt door het Nyquist theorema.

Beschouw tenslotte de situatie waarbij er zich M_s cilinders bevinden in de brongroep en M_o cilinders in de waarnemingsgroep. Uitbreiding van de redenering uit de voorgaande paragraaf toont aan dat de groep-naar-groep interactie van de bron- naar de waarnemingsgroep kan uitgedrukt worden als

$$\begin{aligned} \sum_{j=1}^{M_s} \sum_{n=-K}^{K} Z_{mn}^{ij} \tilde{I}_n^j \quad \approx \quad & -\frac{\omega\mu_1}{4} \sum_{q=-Q}^{Q} e^{-j[\boldsymbol{k}_1(\phi_q)\cdot(\boldsymbol{\rho}_i^c - \boldsymbol{\rho}_o^c) + m(\phi_q + \frac{\pi}{2})]} \times \\ & T_q(k_1, \rho_{so}^c, \phi_{so}^c) \times \\ & \sum_{j=1}^{M_s} \sum_{n=-K}^{K} e^{j[\boldsymbol{k}_1(\phi_q)\cdot(\boldsymbol{\rho}_j^c - \boldsymbol{\rho}_s^c) + n(\phi_q + \frac{\pi}{2})]} \tilde{I}_n^j, \end{aligned} \tag{83}$$

voor $i = 1, \ldots, M_o$ en $m = -K, \ldots, K$. Zo'n groep-naar-groep interactie wordt dus berekend in drie stappen. Eerst worden de zogenaamde *uitgaande vlakke golven* van de brongroep bepaald via

$$\text{OPW}_q = \quad \sum_{j=1}^{M_s} \sum_{n=-K}^{K} e^{j[\boldsymbol{k}_1(\phi_q)\cdot(\boldsymbol{\rho}_j^c - \boldsymbol{\rho}_s^c) + n(\phi_q + \frac{\pi}{2})]} \tilde{I}_n^j, \; q = -Q, \ldots, +Q. \tag{84}$$

Deze uitgaande vlakke golven worden in een tweede stap via de diagonale translatie-operator omgezet in zogenaamde *inkomende vlakke golven* voor de waarnemingsgroep:

$$\text{IPW}_q \quad = \quad T_q(k_1, \rho_{so}^c, \phi_{so}^c)\text{OPW}_q,\ q = -Q, \ldots, +Q. \tag{85}$$

Tenslotte worden deze inkomende vlakke golven geprojecteerd op elke cilinder i in de waarnemingsgroep om zo het gewogen veld ten gevolge van alle stromen in de brongroep te bekomen:

$$\mathcal{E}_m^i \quad = \quad -\frac{\omega\mu_1}{4} \sum_{q=-Q}^{Q} e^{-j[\boldsymbol{k}_1(\phi_q)\cdot(\boldsymbol{\rho}_i^c - \boldsymbol{\rho}_o^c) + m(\phi_q + \frac{\pi}{2})]}\text{IPW}_q, \tag{86}$$

voor $i = 1, \ldots, M_o$ en $m = -K, \ldots, K$.

6.1.2 MLFMA

Een grote snelheidswinst wordt bekomen door het FMM schema te gaan toepassen op meerdere niveaus. Hiertoe wordt de elektromagnetisch-kristalstructuur eerst ingesloten in het kleinst mogelijke vierkant dat de volledige structuur kan bevatten. Dit vierkant stemt overeen met niveau 1. Niveau 2 wordt gevormd door dit vierkant onder te verdelen in vier gelijke vierkanten. Op zijn beurt wordt elke vierkant van niveau 2 opnieuw onderverdeeld in vier gelijke vierkanten (niveau 3). Dit proces wordt herhaald tot de zijde van de nieuwe vierkanten ongeveer 0.2λ tot 0.5λ is (niveau L). Nadien worden alle vierkanten genummerd. Hierbij worden echter enkel niet lege vierkanten overgehouden. Vierkanten op niveau $l+1$ worden de *kinderen* genoemd van het groter vierkant op niveau l waarvan ze een onderverdeling zijn. Analoog noemt men dit groter vierkant hun *ouder*.

Twee vierkanten b en b' zijn op een bepaald niveau l voldoende ver uit elkaar gelegen als de afstand tussen hun centra voldoet aan

$$|\boldsymbol{\rho}_b^c - \boldsymbol{\rho}_{b'}^c| \geq \beta R_l, \tag{87}$$

met R_l de halve lengte van de diagonaal van een vierkant op niveau l; een typische waarde voor de constante β is 4 tot 6. Aangezien twee vierkanten op niveau 1 of 2 nooit voldoend ver uit elkaar gelegen zijn, beschouwt men eerst de vierkanten op niveau 3. Voor vierkanten op niveau 3 die voldoend ver uit elkaar gelegen zijn kan men de bijhorende interacties berekenen via FMM. Daarna beschouwt men de vierkanten op niveau 4. Indien twee vierkanten voldoend ver zijn op dit niveau en indien de bijhorende interacties nog niet berekend zijn op niveau 3, berekent men deze interacties op dit niveau via FMM. Dit proces wordt herhaald tot niveau L wordt bereikt. Op dit niveau blijven dan uiteindelijk de nabije interacties over die op de klassieke manier moeten berekend worden.

6.1.3 Nauwkeurigheid

Hoewel FMM slechts een benaderende methode is, is de fout ervan toch onder controle en kan elke gewenste nauwkeurigheid bereikt worden. Beschouw de configuratie getoond in Fig. 16. Op het oppervlak van de bron- en waarnemingsgroep bevinden zich telkens M

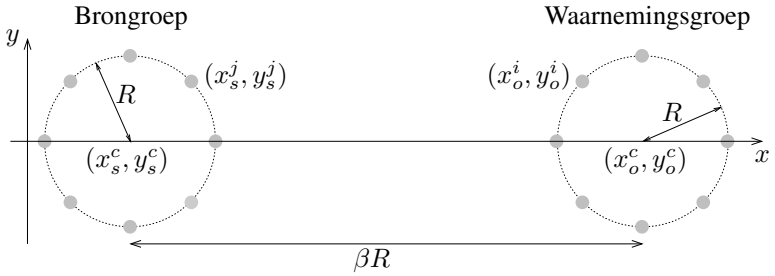

Figuur 16: Bron- en waarnemingsgroep voor het testen van de nauwkeurigheid met reële coördinaten.

cilinders. De relatieve fout δ wordt gedefinieerd als

$$\delta \quad = \quad \max_{i,j} \left| \frac{(Z_{mn}^{ij})_{\text{FMM}} - (Z_{mn}^{ij})_{\text{Klass}}}{(Z_{mn}^{ij})_{\text{Klass}}} \right|. \tag{88}$$

De indices i en j duiden hier een cilinder aan op respectievelijk het oppervlak van

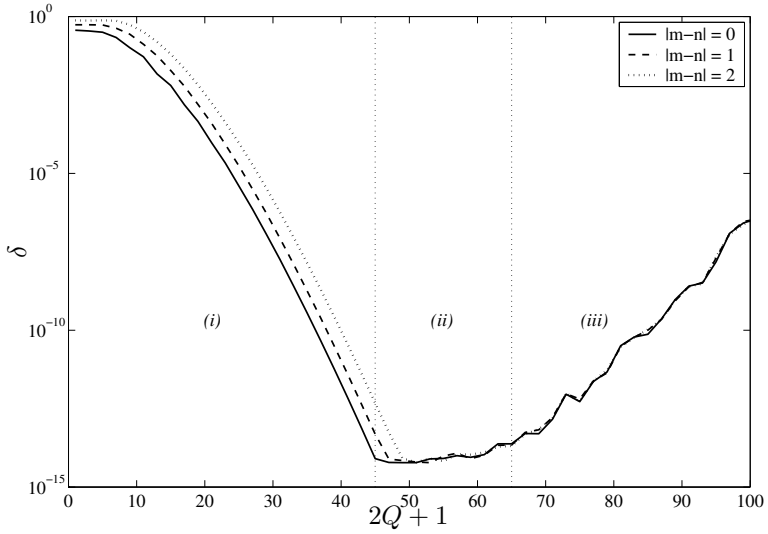

Figuur 17: Relatieve fout voor $k_1 = 0.72\frac{\pi}{a}$, $R = \frac{\lambda}{2}$, $\beta = 12$ en $M = 16$.

de waarnemings- en brongroep; $(Z_{mn}^{ij})_{\text{Klass}}$ is de interactie tussen twee cilinders berekend op de klassieke manier; $(Z_{mn}^{ij})_{\text{FMM}}$ is dezelfde interactie, maar berekend met FMM. Figuur 17 toont deze relatieve fout in functie van de bemonsteringsgraad voor $k_1 = 0.72\frac{\pi}{a}$, $R = \frac{\lambda}{2}$, $\beta = 12$ en $M = 16$. Men kan drie gebieden onderscheiden. Eerst daalt de relatieve fout met stijgende bemonsteringsgraad. Indien β voldoend groot is, wordt de maximale nauwkeurigheid bereikt die overeenstemt met de computernauwkeurigheid. Tenslotte wordt de relatieve fout weer groter ten gevolge van numerieke

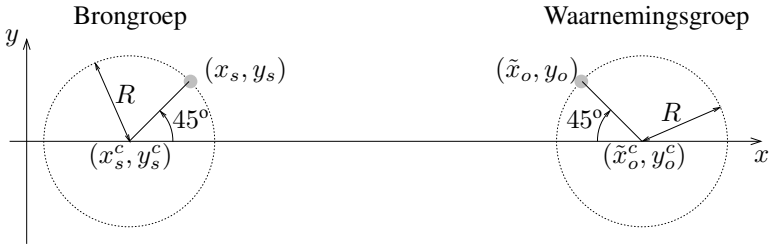

Figuur 18: Bron- en waarnemingsgroep voor het testen van de nauwkeurigheid met complexe coördinaten.

instabiliteiten in het FMM schema. De relatieve fout vertoont hetzelfde gedrag voor verschillende waardes van het verschil tussen m en n. Als dit verschil stijgt, moet de bemonsteringsgraad iets hoger genomen worden om toch dezelfde nauwkeurigheid te bereiken.

6.1.4 Rekencomplexiteit

Om de rekencomplexiteit te reduceren worden de uitgaande vlakke golven enkel op niveau L berekend via (84). Vergelijking (84) op elk niveau toepassen zou teveel operaties vereisen aangezien zowel het aantal onbekenden binnen één vierkant als de bemonsteringsgraad toenemen bij de overgang van niveau $l+1$ naar niveau l. In plaats daarvan worden de uitgaande vlakke golven van een vierkant op niveau l berekend door eerst de uitgaande golven van de kinderen van dit vierkant te interpoleren met een FFT, ze daarna op te tellen en tenslotte de resulterende vlakke golven te verschuiven naar het centrum van het vierkant op niveau l. Voor de inkomende vlakken wordt een analoge werkwijze gevolgd.

Het blijkt dat de rekencomplexiteit en de geheugenvereisten precies bepaald worden door de berekening van de uitgaande en inkomende vlakke golven. Bovendien moet er een onderscheid gemaakt worden tussen volledige gevulde en langgerekte elektromagnetisch-kristalstructuren. Voor de eerstgenoemde structuren schalen zowel de rekencomplexiteit als de geheugenvereisten volgens $O(N_c)$. Voor de laatstgenoemde structuren schaalt de rekencomplexiteit volgens $O(N_c \log_2^2 N_c)$, terwijl de geheugenvereisten schalen volgens $O(N_c \log_2 N_c)$. De rekencomplexiteit en de geheugenvereisten van realistische elektromagnetisch-kristalstructuren situeren zich ergens tussen beide grenswaarden.

6.1.5 Complexe coördinaten

In deze sectie wordt het MLFMA schema uitgebreid naar het gebruik van complexe coördinaten, zoals geïntroduceerd in Sectie 5.1.4. Veronderstel eerst dat voor de opdeling van de elektromagnetisch-kristalstructuur in vierkanten enkel rekening wordt gehouden met het reëel deel van de coördinaten van de middelpunten. Dit betekent dat de centra van alle vierkanten ook zuiver reële coördinaten hebben en dat er geen complexe afstanden optreden in de translatie-operatoren (76). Beschouw de configuratie getoond in Fig 18. Nu bevindt er zich op het oppervlak van de bron- en waarnemingsgroep telkens maar één

cilinder met coördinaten

$$x_s = x_s^c + \frac{R}{\sqrt{2}}, \tag{89}$$

$$y_s = y_s^c + \frac{R}{\sqrt{2}}, \tag{90}$$

$$\tilde{x}_o = x_s^c + \beta R - \frac{R}{\sqrt{2}} - j\alpha_o R, \tag{91}$$

$$y_o = y_s. \tag{92}$$

Figuur 19 toont de relatieve fout in functie van Q voor stijgend imaginair deel van de x-coördinaat van de cilinder op het oppervlak van de waarnemingsgroep. Het is duidelijk dat in vergelijking met reële coördinaten de bemonsteringsgraad veel hoger moet gekozen worden om dezelfde nauwkeurigheid te bereiken. Bovendien daalt de maximaal bereikbare nauwkeurigheid met stijgend imaginair deel.

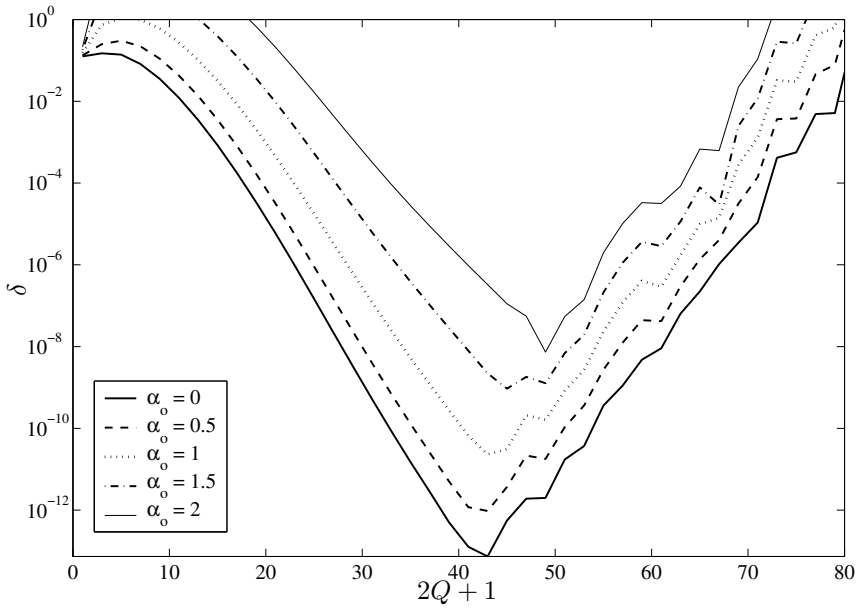

Figuur 19: Relatieve fout voor $k_1 = 0.72\frac{\pi}{a}$, $R = \frac{\lambda}{2}$ en $\beta = 6$ met reële coördinaten voor de groepscentra.

Een beter resultaat wordt bereikt door toe te laten dat de coördinaten van de groepscentra ook complex zijn:

$$\tilde{x}_o^c = x_s^c + \beta R - j\alpha_o^c R, \tag{93}$$

$$y_o^c = y_s^c. \tag{94}$$

Figuur 20 toont de relatieve fout in functie van Q voor $\alpha_o = 2$ en voor toenemende waarden van α_o^c. Nu kan wel dezelfde nauwkeurigheid bereikt worden als bij zuiver

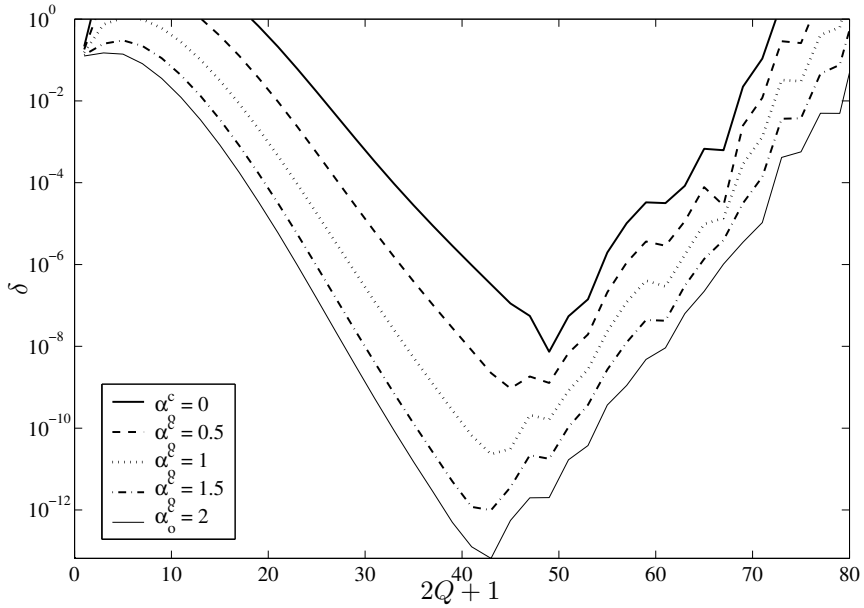

Figuur 20: Relatieve fout voor $k_1 = 0.72\frac{\pi}{a}$, $R = \frac{\lambda}{2}$ en $\beta = 6$ met complexe coördinaten voor de groepscentra.

reële coördinaten. In de praktijk wordt dit gerealiseerd door de centra van de vierkanten hetzelfde pad te laten volgen als de middelpunten van de cilinders in de PML, bijvoorbeeld (66) voor een lineaire PML en (67) voor een circulaire PML. Hiertoe wordt een nieuwe reële coördinaat s ingevoerd die dit pad volgt, zoals getoond in Fig. 21 voor een circulaire PML. Eerst worden de s-coördinaten van de middelpunten van alle cilinders bepaald en op basis van deze reële coördinaten wordt de gehele structuur in vierkanten opgedeeld. Daarna worden de s-coördinaten van de centra van de vierkanten weer omgerekend naar complexe coördinaten.

6.1.6 Voorbeelden

Als eerste voorbeeld beschouwen we de twee-kanaals multiplexer-demultiplexer getoond in Fig. 12 met $l = 3010a$. Aan elke poort wordt een circulaire PML toegevoegd met $R_{\text{PML}} = 10a$ en $N_{\text{PML}} = 7$. Voor dit voorbeeld, dat 91752 onbekenden omvat, duurt één matrix-vector vermenigvuldiging 3 s op een 2.4GHz Pentium IV PC. Om het nodig aantal iteraties te beperken wordt een blok-diagonale preconditioner (zie Sectie 7) toegepast. Met BICGSTAB als iteratieve solver zijn er per frequentiepunt ongeveer 320 iteraties nodig om een residuele fout te bekomen die kleiner is dan 10^{-4}. De totale rekentijd per frequentiepunt is ongeveer 1 uur. De geheugenvereiste is 600Mb. Figuur 22 toont het transmissiespectrum voor deze elektromagnetisch-kristalstructuur met $a = 540nm$. Het valt op dat de transmissie veel kleiner is dan 1 omwille van lekken langs de zijkanten van de elektromagnetisch-kristalgolfgeleiders. Als tweede voorbeeld beschouwen we de elektromagnetisch-kristalstructuur uit Fig. 23. Deze configuratie bestaat uit vier

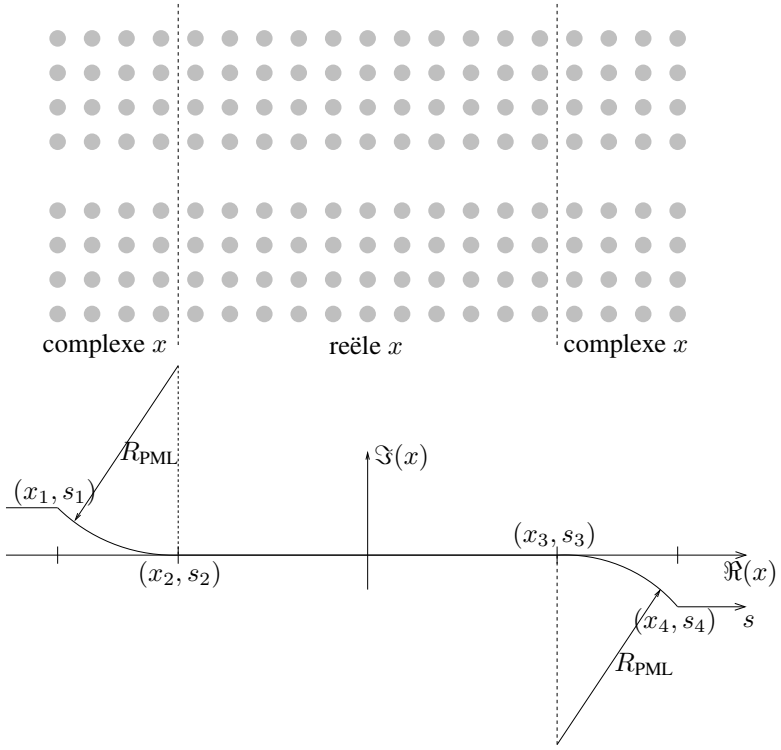

Figuur 21: Nieuwe reële coördinaat s.

elektromagnetisch-kristalhoornantennes [27,28] gecombineerd met een voedingsnetwerk. Merk op dat aan de randen van de hoornantennes de cilinders zich niet op hun normale plaats in het rooster bevinden. Dit voorbeeld omvat 10800 onbekenden. Het stralingspatroon voor $k_1 = 0.784\frac{\pi}{a}$ ervan is getoond in Fig. 24. Eén matrix-vector vermenigvuldiging op een 2.4GHz Pentium IV PC duurt 0.5 s. Om het aantal iteraties te reduceren wordt voor dit voorbeeld een afgeschermde-blok preconditioner toegepast. Met TFQMR als iteratieve oplossingsmethode zijn er 50 iteraties nodig om de residuele fout te reduceren tot 10^{-4}. De totale rekentijd is 71 s. De geheugenvereisten zijn 130 Mb.

6.2 FFT-gebaseerd schema

In veel elektromagnetisch-kristalstructuren zijn alle cilinders geordend volgens een regelmatig 2D rooster. Voor dergelijke structuren kunnen de rekencomplexiteit en de geheugenvereisten gereduceerd worden door de matrix-vector vermenigvuldigingen via FFTs te berekenen. Beschouw bijvoorbeeld een rechthoekig kristal van N_x+1 op N_y+1 cilinders geordend volgens een vierkant rooster met roosterconstante a (Fig. 25). De matrix-vector vermenigvuldiging $\tilde{\boldsymbol{E}} = \boldsymbol{Z}\tilde{\boldsymbol{I}}$ kan herschreven worden als

$$\tilde{\boldsymbol{E}}_m = \sum_{n=-K}^{K} \tilde{\boldsymbol{E}}_{mn} = \sum_{n=-K}^{K} \boldsymbol{Z}_{mn}\tilde{\boldsymbol{I}}_n, \quad m = -K, \ldots, K. \tag{95}$$

De deelmatrix $\boldsymbol{Z}_{mn}$ bevat alle elementen Z^{ij}_{mn} met dezelfde m en n. Analoog bevat de subvector $\tilde{\boldsymbol{I}}_n$ alle elementen van $\tilde{\boldsymbol{I}}$ met dezelfde index n in de Fourierontwikkeling van de stromen op de cilinders. Tenslotte bevat de subvector $\tilde{\boldsymbol{E}}_m$ het veld veroorzaakt door alle stromen $\tilde{\boldsymbol{I}}$ gewogen met de testfunctie $T^i_m(\boldsymbol{\rho})$. Voor vaste m en n hangt Z^{ij}_{mn} enkel af van de relatieve afstand tussen de centra van de cilinders i en j gemeten in roosterconstantes langs de x en y-as. In deze sectie stelt $Z_{mn}(l_x, l_y)$ de interactie voor tussen twee cilinders die l_x en l_y roosterconstantes uit elkaar staan langs de x en y-richting. Analoog is $\tilde{I}_n(l_x, l_y)$ de benadering voor de n^{de} Fouriercomponent van de stroom op de cilinder die gecentreerd is rond $\boldsymbol{\rho}^c_{l_x l_y} = l_x a\boldsymbol{u}_x + l_y a\boldsymbol{u}_y$. Hierbij is verondersteld dat de cilinder in de linkerbenedenhoek van het rechthoekig kristal gecentreerd is rond de oorsprong. Indien tenslotte $E_{mn}(l_x, l_y)$ het veld voorstelt veroorzaakt door alle stromen $\tilde{\boldsymbol{I}}_n$ en gewogen met $T^i_m(\boldsymbol{\rho})$ op de cilinder gecentreerd rond $\boldsymbol{\rho}^c_{l_x l_y}$, dan is

$$\tilde{E}_{mn}(l_x, l_y) \quad = \quad \sum_{p_x=0}^{N_x-1} \sum_{p_y=0}^{N_y-1} Z_{mn}(l_x - p_x, l_y - p_y)\tilde{I}_n(p_x, p_y), \tag{96}$$

voor $0 \leq l_x \leq N_x$, $0 \leq l_y \leq N_y$ en $m = -K, \ldots, K$. Deze twee-dimensionale convolutie kan als volgt berekend worden:

(i) $\tilde{I}(l_x, l_y)$ wordt aangevuld met nullen, zodat deze grootheid gedefinieerd is voor $-N_x \leq l_x \leq N_x$ en $-N_y \leq l_y \leq N_y$;

(ii) de twee-dimensionale Fouriertransformaties van $Z_{mn}(l_x, l_y)$ en $\tilde{I}_n(l_x, l_y)$ worden berekend. Deze Fouriertransformaties worden hier genoteerd als $\hat{Z}_{mn}(\hat{l}_x, \hat{l}_y)$ en $\hat{I}_n(\hat{l}_x, \hat{l}_y)$;

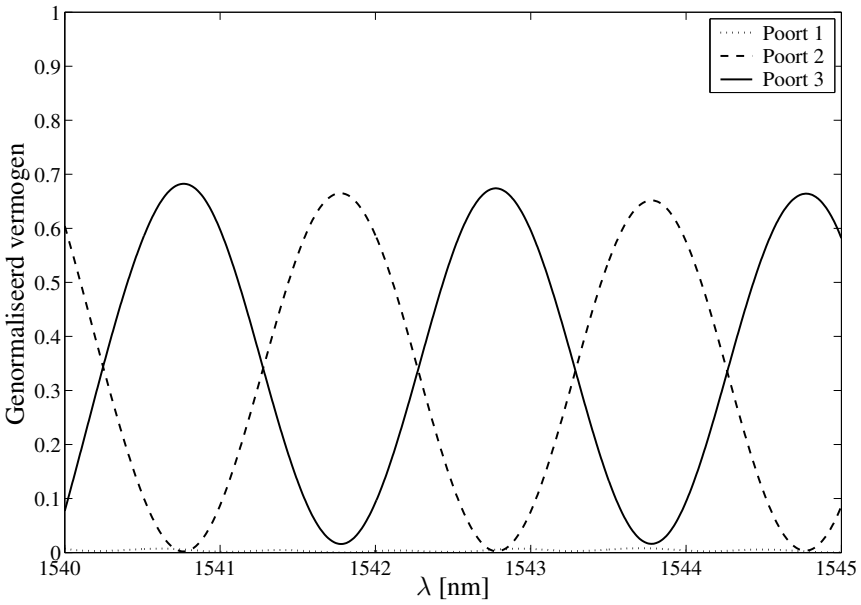

Figuur 22: Transmissiespectrum van een twee-kanaals multiplexer-demultiplexer met $l = 3010a$ berekend met MLFMA.

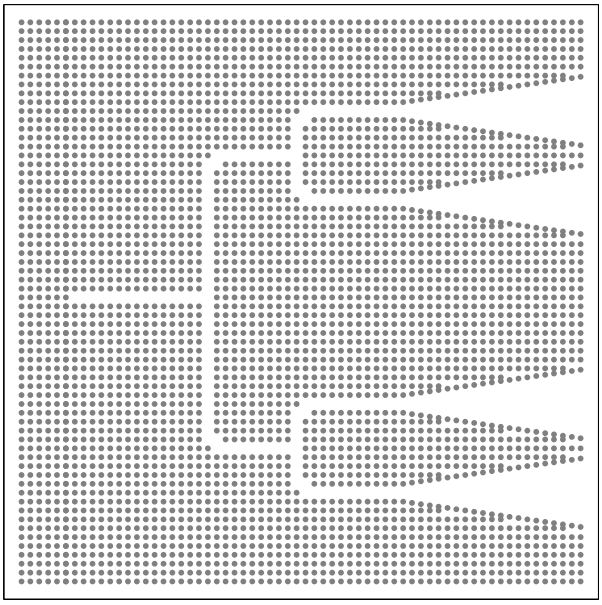

Figuur 23: Rooster van elektromagnetisch-kristalhoornantennes.

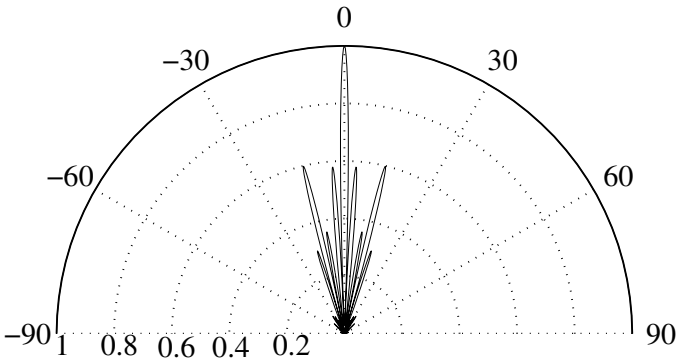

Figuur 24: Stralingspatroon van het rooster van elektromagnetisch-kristalhoornantennes.

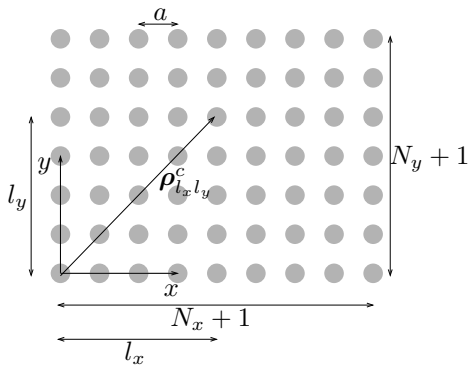

Figuur 25: Eindig rechthoekig elektromagnetisch kristal.

(iii) de twee-dimensionale inverse Fourier transformatie van $\hat{Z}_{mn}(\hat{l}_x, \hat{l}_y)\hat{I}_n(\hat{l}_x, \hat{l}_y)$ wordt berekend;

(iv) van deze inverse Fourier transformatie worden enkel de elementen overgehouden voor $0 \leq l_x \leq N_x$ en $0 \leq l_y \leq N_y$.

Voor een elektromagnetisch-kristalstructuur die wordt bekomen door N_r cilinders uit dit rechthoekig kristal te verwijderen, stelt men altijd dat de onbekenden op de weggelaten cilinders nul zijn. In stap (iv) van bovenstaand schema houdt men dan enkel de elementen over die overeenstemmen met de niet-weggelaten cilinders. Indien de twee-dimensionale Fouriertransformaties worden uitgevoerd met FFTs, schaalt de rekencomplexiteit als $O(N_c \log_2 N_c)$. De geheugenvereisten schalen volgens $O(N_c)$.

7 Preconditioners

Indien het lineair stelsel (42) wordt opgelost via een iteratieve methode, schaalt de totale rekencomplexiteit ook recht evenredig met het aantal iteraties P dat nodig is om de residuele fout tot beneden een vooropgestelde waarde te reduceren. Helaas blijkt uit numerieke voorbeelden dat voor realistische elektromagnetisch-kristalstructuren het aantal iteraties vrij hoog kan zijn, zeker wanneer deze structuren elektromagnetisch-kristalgolfgeleiders bevatten. Om dit op te lossen moet men zijn toevlucht nemen naar preconditioners. Alle preconditioners die hier worden besproken, worden gebruikt als *linkse* preconditioners. Dit betekent dat in plaats van het lineair stelsel (42), een equivalent lineair stelsel

$$\boldsymbol{MZI} \quad = \quad \boldsymbol{ME} \tag{97}$$

iteratief wordt opgelost. Hierbij benadert de preconditioner $\boldsymbol{M}$ de inverse $\boldsymbol{Z}^{-1}$ van de interactiematrix $\boldsymbol{Z}$. Uiteraard mag de rekencomplexiteit nodig om $\boldsymbol{M}$ te berekenen en om $\boldsymbol{M}$ te vermenigvuldigen met een vector, de rekencomplexiteit van het gebruikte matrix-vector vermenigvuldigingsschema niet overschrijden. De volgende drie types preconditioners zullen hier vergeleken worden:

- diagonale preconditioner $\boldsymbol{M}_{\mathrm{d}}$: de preconditioner is een diagonale matrix waarbij de elementen op de hoofddiagonaal gelijk zijn aan de inverse van de elementen op de hoofddiagonaal van $\boldsymbol{Z}$.

- blok-diagonale preconditioner $\boldsymbol{M}_{\mathrm{bd}}$: de elektromagnetisch-kristalstructuur wordt eerst onderverdeeld in N_g groepen en de inverse van de kleine interactiematrix van elke groep wordt berekend via een directe methode. De blok-diagonale preconditioner bestaat dan uit de verzameling van al deze kleine inverse matrices.

- afgeschermde-blok preconditioner $\boldsymbol{M}_{\mathrm{sb}}$: net als bij de blok-diagonale preconditioner, wordt de elektromagnetisch-kristalstructuur onderverdeeld in N_g groepen. Nu wordt echter voor elke groep een iets grotere interactiematrix geïnverteerd, namelijk de interactiematrix van de desbetreffende groep met een *afscherming* eromheen. Deze afscherming kan bijvoorbeeld bestaan uit een aantal rijen cilinders rondom de groep. Om de preconditioner te vormen worden enkel de rijen uit deze inverse overgenomen die corresponderen met de onbekenden in de groep zelf.

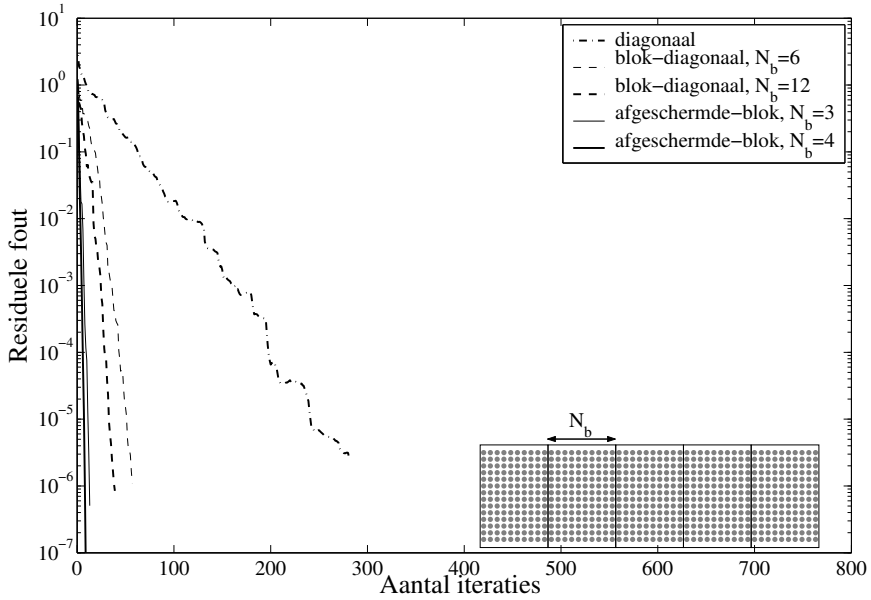

Figuur 26: Residuele fout voor een defectloos, rechthoekig elektromagnetisch kristal.

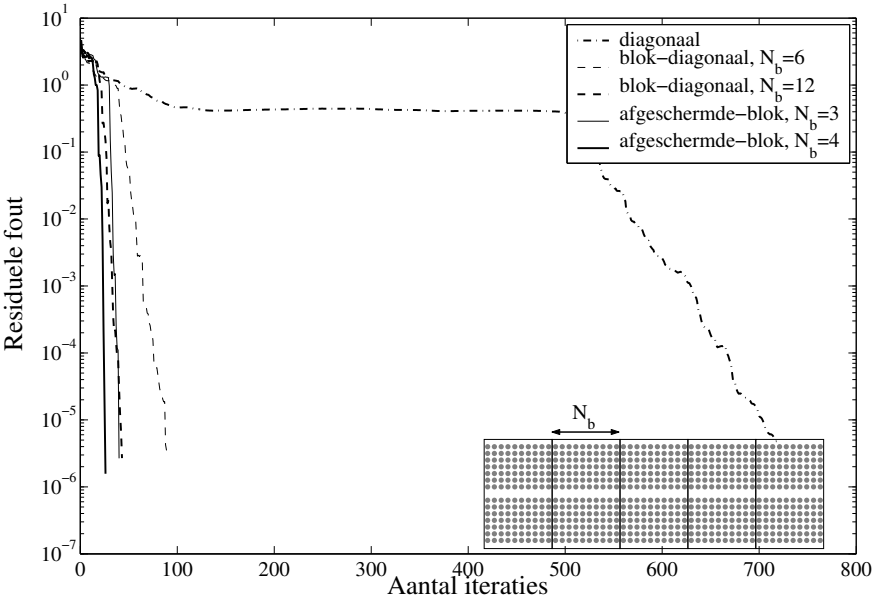

Figuur 27: Residuele fout voor een elektromagnetisch-kristalgolfgeleider.

Deze preconditioners worden getest op twee eenvoudige configuraties, namelijk een defectloos rechthoekig elektromagnetisch kristal en een elektromagnetisch-kristalgolfgeleider. Het verloop van de residuele fout in functie van het aantal iteraties wordt voor deze configuraties weergegeven in Fig. 26 en 27 voor de drie types preconditioners en voor verschillende afmetingen van de groepen. Elke groep bestaat hier uit N_b opeenvolgende periodes van de elektromagnetisch-kristalstructuur. Voor de afgeschermde-blok preconditioner bestaat de afscherming uit de buurgroepen van elke groep. Opvallend is dat voor dezelfde residuele fout het aantal iteraties voor de elektromagnetisch-kristalgolfgeleider groter is dan voor het defectloos kristal. Wanneer enkel een diagonale preconditioner wordt gebruikt blijft voor de elektromagnetisch-kristalgolfgeleider de residuele fout vrijwel constant gedurende vele iteraties. De twee andere preconditioners verhelpen dit probleem tot op zekere hoogte. Voor beide configuraties presteert de afgeschermde-blok preconditioner het best aangezien er voor deze preconditioner vrijwel geen verschil is tussen de onbekenden aan de rand en de onbekenden rond het centrum van elke groep. Via een grondige studie van de ligging van de eigenwaarden van de geprecondition eerde interactiematrix van beide structuren, kan men echter inzien dat het aantal nodige iteraties voor een elektromagnetisch-kristalstructuur met golfgeleiders altijd groter zal zijn dan voor een elektromagnetisch-kristalstructuur zonder golfgeleiders. Om dezelfde performantie te bereiken zou het golfgeleiderkarakter volledig opgelost moeten worden, wat vrijwel onmogelijk is met een preconditioner.

8 Analyse via de Greense functie van het kristal

In deze sectie wordt een nieuwe, snelle techniek beschreven voor de karakterisatie van golfpropagatie in elektromagnetisch-kristalstructuren. Op een beperkt aantal andere defecten na, worden deze elektromagnetisch-kristalstructuren gevormd door uit een oneindig, defectloos, perfect geordend 2D kristal een aantal cilinders te verwijderen. In tegenstelling tot de klassieke meervoudige-verstrooiingstechniek lost deze methode integraalvergelijkingen op in functie van equivalente stromen op het (fictieve) oppervlak van de *verwijderde* cilinders. Uiteraard kunnen stralingsverliezen door het afbreken van het kristal via deze methode niet in rekening gebracht worden. Daarentegen heeft deze methode een aantal belangrijke voordelen ten opzichte van de klassieke meervoudige-verstrooiingstechniek. Ten eerste leidt deze methode uiteindelijk tot een dunbezet stelsel dat wegens zijn specifieke vorm snel kan opgelost worden via een multi-frontale methode. Daarnaast kunnen de propagerende eigenmodes van elektromagnetisch-kristalgolfgeleiders heel makkelijk berekend worden, wat tot een eenvoudig schema leidt om de S-parameters van een elektromagnetisch-kristalstructuur te berekenen. Bovendien kunnen ook een beperkt aantal andere defecten, bijvoorbeeld cilinders die verplaatst zijn of die andere parameters hebben, eveneens efficiënt in rekening worden gebracht.

8.1 Basisvergelijkingen

De afleiding van de basisvergelijkingen van deze nieuwe techniek is heel nauw verwant met de afleiding van de klassieke meervoudige-verstrooiingstechniek via het veld-equivalentietheorema (Sectie 5.1.2). Beschouw een 2D elektromagnetisch-kristalstructuur

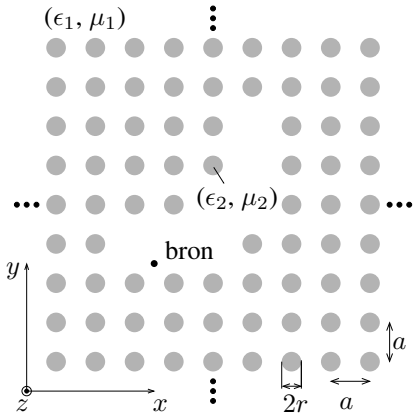

Figuur 28: Typische elektromagnetisch-kristalstructuur voor de analyse via de Greense functie van het kristal.

die bekomen wordt door N_r cilinders te verwijderen uit een oneindig, defectloos kristal met vierkante éénheidscel met zijde a. Alle cilinders hebben dezelfde straal r en materiaalparameters (ϵ_2, μ_2) en zijn ingebed in een achtergrondmedium met materiaalparameters (ϵ_1, μ_1). De notatie in deze sectie stemt overeen met die uit Sectie 5.1, behalve dat er tildes worden gebruikt voor symbolen die verwijzen naar velden, stromen en oppervlakken geassocieerd met de verwijderde cilinders. Bovendien wordt er expliciet verondersteld dat ω zich in de verboden zone van het kristal bevindt. Het invallend veld $\tilde{E}_z^{\mathrm{i}}(\boldsymbol{\rho})\boldsymbol{u}_z$ is hier gedefinieerd als het veld dat wordt gegenereerd door de opgelegde bronnen *in het oneindig, defectloos kristal*. Indien de N_r cilinders verwijderd worden, wordt het totale veld $\tilde{E}_z^{\mathrm{t}}(\boldsymbol{\rho})\boldsymbol{u}_z$ waargenomen. Het verschil tussen beide velden is het verstrooide veld $\tilde{E}_z^{\mathrm{s}}(\boldsymbol{\rho})\boldsymbol{u}_z$: $\tilde{E}_z^{\mathrm{t}}(\boldsymbol{\rho}) = \tilde{E}_z^{\mathrm{i}}(\boldsymbol{\rho}) + \tilde{E}_z^{\mathrm{s}}(\boldsymbol{\rho})$. Om $\tilde{E}_z^{\mathrm{s}}(\boldsymbol{\rho})$ en $\tilde{E}_z^{\mathrm{t}}(\boldsymbol{\rho})$ te beschrijven worden twee sets ($\alpha = 1, 2$) van equivalente elektrische en magnetische stromen geïntroduceerd op het oppervlak $\tilde{S}_j$ van elke *verwijderde* cilinder, $j = 1, \ldots, N_r$. Indien deze stromen verbonden zijn met het totale elektrische veld op $\tilde{S}_j$ via

$$\tilde{J}_\alpha^j(\boldsymbol{\rho})\boldsymbol{u}_z = -s_\alpha \frac{j}{\omega\mu_1} \left.\frac{\partial \tilde{E}_z^{\mathrm{t}}(\boldsymbol{\rho})}{\partial \rho_j}\right|_{\boldsymbol{\rho}\in\tilde{S}_j} \delta(\rho_j - r)\boldsymbol{u}_z, \tag{98}$$

$$\tilde{K}_\alpha^j(\boldsymbol{\rho})\boldsymbol{u}_{\phi_j} = s_\alpha \left.\tilde{E}_z^{\mathrm{t}}(\boldsymbol{\rho})\right|_{\boldsymbol{\rho}\in\tilde{S}_j} \delta(\rho_j - r)\boldsymbol{u}_{\phi_j}, \tag{99}$$

dan volgt uit het veld-equivalentietheorema dat

(i) de elektrische en magnetische stromen $\displaystyle\sum_{j=1}^{N_r} \tilde{J}_1^j(\boldsymbol{\rho})\boldsymbol{u}_z$ en $\displaystyle\sum_{j=1}^{N_r} \tilde{K}_1^j(\boldsymbol{\rho})\boldsymbol{u}_{\phi_j}$ samen met de opgelegde bronnen *in het oneindig, defectloos kristal* een veld veroorzaken dat nul is binnen elk oppervlak $\tilde{S}_j$ en gelijk is aan $\tilde{E}_z^{\mathrm{t}}(\boldsymbol{\rho})$ buiten alle $\tilde{S}_j$;

(ii) de elektrische en magnetische stromen $\tilde{J}_2^j(\boldsymbol{\rho})\boldsymbol{u}_z$ en $\tilde{K}_2^j(\boldsymbol{\rho})\boldsymbol{u}_{\phi_j}$ in een homogeen medium met materiaalparameters (ϵ_1, μ_1) een veld veroorzaken dat nul is buiten $\tilde{S}_j$

en $\tilde{E}_z^{\rm t}(\boldsymbol{\rho})$ binnen $\tilde{S}_j$.

Als $\tilde{E}_\alpha^{{\rm s},j}\boldsymbol{u}_z$ het elektrisch veld voorstelt dat wordt veroorzaakt door de stromen $\tilde{J}_\alpha^j(\boldsymbol{\rho})\boldsymbol{u}_z$ en $\tilde{K}_\alpha^j(\boldsymbol{\rho})\boldsymbol{u}_{\phi_j}$ in het oneindig, defectloos kristal als $\alpha = 1$ en in een homogeen medium met materiaalparameters (ϵ_1, μ_1) als $\alpha = 2$, dan volgt uit het bovenstaande dat

$$\tilde{E}_z^{\rm i}(\boldsymbol{\rho}) + \sum_{j=1}^{N_r} \tilde{E}_1^{{\rm s},j}(\boldsymbol{\rho}) = 0 \text{ voor } \boldsymbol{\rho} \in \tilde{S}_i^-,\ i = 1, \ldots, N_r, \tag{100}$$

$$\tilde{E}_2^{{\rm s},j}(\boldsymbol{\rho}) = 0 \text{ voor } \boldsymbol{\rho} \in \tilde{S}_j^+,\ j = 1, \ldots, N_r. \tag{101}$$

De elektrische en magnetische stromen worden ontbonden in een Fourierreeks:

$$\tilde{J}_\alpha^j(\boldsymbol{\rho}) = s_\alpha \sum_{n=-K}^{K} \frac{C_n \tilde{I}_n^j}{2\pi r} e^{jn\phi_j} \delta(\rho_j - r), \tag{102}$$

$$\tilde{K}_\alpha^j(\boldsymbol{\rho}) = s_\alpha \sum_{n=-K}^{K} \frac{C_n \tilde{M}_n^j}{2\pi r} e^{jn\phi_j} \delta(\rho_j - r), \tag{103}$$

met C_n gedefinieerd in (51). Oplossen van vergelijking (101) levert het volgende verband op:

$$\frac{\tilde{I}_n^j}{\tilde{M}_n^j} = -j\sqrt{\frac{\epsilon_1}{\mu_1}} \frac{J_n'(k_1 r)}{J_n(k_1 r)}. \tag{104}$$

In vergelijking met (52) is de index 2 veranderd in de index 1. Via dit verband kan het veld $\tilde{E}_1^{{\rm s},j}$ uitgedrukt worden in functie van enkel de elektrische onbekenden als:

$$\tilde{E}_1^{{\rm s},j}(\boldsymbol{\rho}) = \sum_{n=-K}^{K} \tilde{G}_n(\boldsymbol{\rho}_j) \tilde{I}_n^j. \tag{105}$$

De grootheid $\tilde{G}_n(\boldsymbol{\rho}_j)$ stelt de Greense functie voor van een Huygens bron met respectievelijke elektrische en magnetische componenten $\frac{C_n}{2\pi r} e^{jn\phi_j} \delta(\rho_j - r)\boldsymbol{u}_z$ en $\frac{jC_n}{2\pi r}\sqrt{\frac{\epsilon_1}{\mu_1}}$ $\frac{J_n(k_1 r)}{J_n'(k_1 r)} e^{jn\phi_j} \delta(\rho_j - r)\boldsymbol{u}_{\phi_j}$ die samen stralen *in het oneindig, defectloos kristal*. Helaas bestaat er voor deze Greense functie van het kristal geen analytische uitdrukking. Na invullen van (105) in (100) en na weging van de resulterende vergelijking met de testfuncties $\tilde{T}_m^i(\boldsymbol{\rho}) = \dfrac{1}{2\pi r J_m(k_2\rho)} e^{jm\phi_i} \delta(\rho_i - r)$ bekomt men het linear stelsel

$$\tilde{\boldsymbol{Z}}\tilde{\boldsymbol{I}} = \tilde{\boldsymbol{E}}, \tag{106}$$

met $\tilde{Z}_{mn}^{ij} = \langle \tilde{T}_m^i(\boldsymbol{\rho}), \tilde{G}_n(\boldsymbol{\rho}_j) \rangle$ en $\tilde{E}_m^i = \langle \tilde{T}_m^i(\boldsymbol{\rho}), -\tilde{E}^{\rm i}(\rho) \rangle$.

De lineaire stelsels (42) en (106) verschillen op twee belangrijke punten. Ten eerste is voor de meeste elektromagnetisch-kristalstructuren $N_r \ll N_c$. Ten tweede is de matrix $\tilde{\boldsymbol{Z}}$ dunbezet. Inderdaad, aangezien ω in de verboden zone ligt, is de Greense functie $\tilde{G}_n(\boldsymbol{\rho})$ exponentieel gedempt in functie van de afstand ρ. Bijgevolg interageert elke verwijderde cilinder slechts met de verwijderde cilinders in zijn nabije omgeving. In Fig. 29 wordt de typische vorm getoond van $\tilde{\boldsymbol{Z}}$ voor een elektromagnetisch-kristalstructuur bestaande uit een aantal golfgeleiders. Dergelijk matrices kunnen zeer snel en efficiënt opgelost worden met zogenaamde multi-frontale methodes [29].

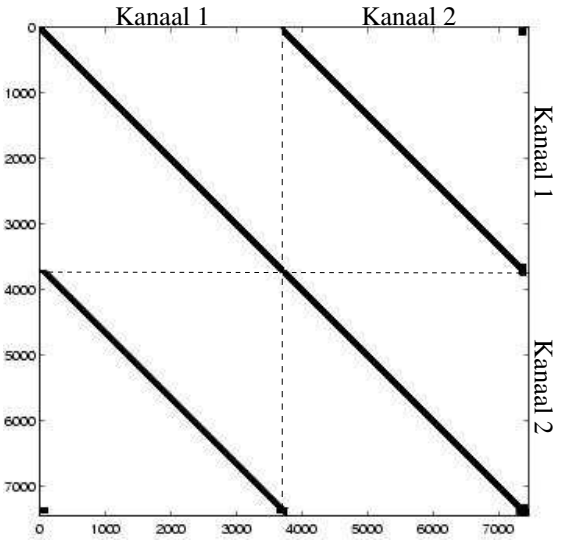

Figuur 29: Interactiematrix $\tilde{\boldsymbol{Z}}$ voor de twee-kanaals multiplexer-demultiplexer met $l = 1200a$.

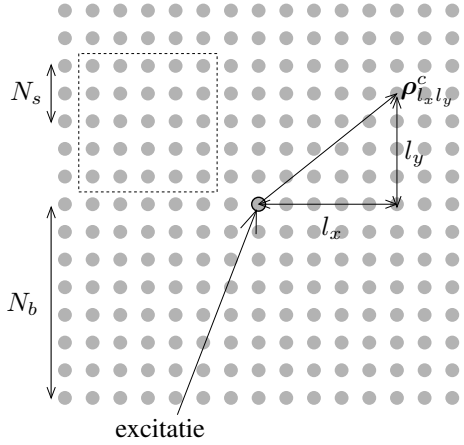

Figuur 30: Berekening van $\tilde{G}_n(\boldsymbol{\rho})$.

8.2 Berekening van de Greense functie van het kristal

De Greense functie van een oneindig, defectloos kristal kan helaas niet analytisch berekend worden. Aangezien $\tilde{G}_n(\boldsymbol{\rho})$ echter exponentieel gedempt is, kan ze makkelijk numeriek berekend worden via de klassieke meervoudige-verstrooiingstechniek. Hiertoe beschouwt men een eindig kristal van $(2N_b+1)$ op $(2N_b+1)$ cilinders dat gecentreerd is rond de oorsprong en dat centraal wordt geëxciteerd door een Huygens bron met respectievelijke elektrische en magnetische componenten $\frac{C_n}{2\pi r}e^{jn\phi}\delta(\rho-r)\boldsymbol{u}_z$ en $\frac{jC_n}{2\pi r}\sqrt{\frac{\epsilon_1}{\mu_1}}\frac{J_n(k_1 r)}{J_n'(k_1 r)}e^{jn\phi}\delta(\rho-r)\boldsymbol{u}_\phi$ (Fig. 30). De parameter N_b wordt voldoend groot gekozen zodanig dat het totale veld veroorzaakt door deze bron verwaarloosbaar is buiten het eindig kristal. Bovendien kan het lineair stelsel (42) voor een dergelijk defectloos kristal efficiënt iteratief worden opgelost met een afgeschermde-blok preconditioner in combinatie met een FFT-gebaseerd matrix-vector vermenigvuldigingsschema. Indien $I_{mn}(l_x,l_y)$, $l_x,l_y=-N_b,\ldots,N_b$; $m,n=-K,\ldots,K$, de m^{de} Fouriercomponent voorstelt van de stroom op de cilinder gecentreerd rond $\boldsymbol{\rho}^c_{l_x l_y}=l_x a\boldsymbol{u}_x+l_y a\boldsymbol{u}_y$ als antwoord op de zonet beschreven excitatie, dan is

$$\tilde{Z}_{mn}(l_x,l_y) \quad = \quad \frac{\omega\mu_2}{4}\frac{2jC_m}{\pi k_2 r J_m'(k_2 r)}I_{mn}(l_x,l_y), \tag{107}$$

waarbij $\tilde{Z}_{mn}(l_x,l_y)$ het matrixelement $\tilde{Z}^{ij}_{mn}$ voorstelt tussen twee verwijderde cilinders i en j die l_x en l_y roosterconstantes van elkaar verwijderd zijn langs respectievelijk de x en y-richting.

8.3 Excitatie en berekening van de S-parameters

Aangezien het invallend veld $\tilde{E}^{\text{i}}_z(\boldsymbol{\rho})$ gedefinieerd is als het veld veroorzaakt door de opgelegde bronnen *in het oneindig, defectloos kristal*, moet dit veld op een analoge manier berekend worden als de Greense functie van het kristal, namelijk door via de klassieke meervoudige-verstrooiingstechniek de stromen te berekenen op een eindig, defectloos kristal rond de bron.

De nieuwe techniek laat echter toe om zeer eenvoudig de S-parameters van een elektromagnetisch-kristalstructuur te bepalen door de propagerende eigenmodes van de gepaste elektromagnetisch-kristalgolfgeleiders te gebruiken als excitatie en als exacte absorberende randvoorwaarde. Veronderstel voor de eenvoud dat de golfgeleider wordt bekomen door het verwijderen van één rij cilinders, parallel aan de x-as, uit een oneindig, defectloos kristal. Volgens het Floquet-Bloch theorema voldoet het elektrisch veld van ν^{de} voorwaarts propagerende eigenmode aan

$$\tilde{E}_\nu(\boldsymbol{\rho}) \quad = \quad \tilde{e}_\nu(\boldsymbol{\rho})e^{-j\beta_\nu x}. \tag{108}$$

Hier geldt dat $\tilde{e}_\nu(\boldsymbol{\rho}+a\boldsymbol{u}_x)=\tilde{e}_\nu(\boldsymbol{\rho})$; β_ν is de reëel veronderstelde propagatieconstante van deze eigenmode. De equivalente stromen op de verwijderde cilinders voldoen eveneens aan (108). Bijgevolg moeten deze stromen slechts voor één periode berekend worden. De expansiecoëfficiënten $\tilde{I}^{\beta_\nu}_n$, $n=-K,\ldots,K$, kunnen gevonden worden uit

$$\sum_{n=-K}^{K}\left[\sum_{l_x=-N_b}^{N_b}\tilde{Z}_{mn}(l_x,0)e^{-j\beta_\nu l_x a}\right]\tilde{I}^{\beta_\nu}_n \quad = \quad 0, \text{ voor } m=-K,\ldots,K. \tag{109}$$

Merk op dat wegens de exponentiële demping van de Greense functie van het kristal in deze som slechts $2N_b + 1$ periodes in rekening moeten gebracht worden. De propagatieconstanten β_ν worden gevonden als de nulpunten van de determinant van het homogeen linear stelsel (109). De bijhorende oplossing $\tilde{I}_n^{\beta_\nu}$ bepaalt het mode-profiel.

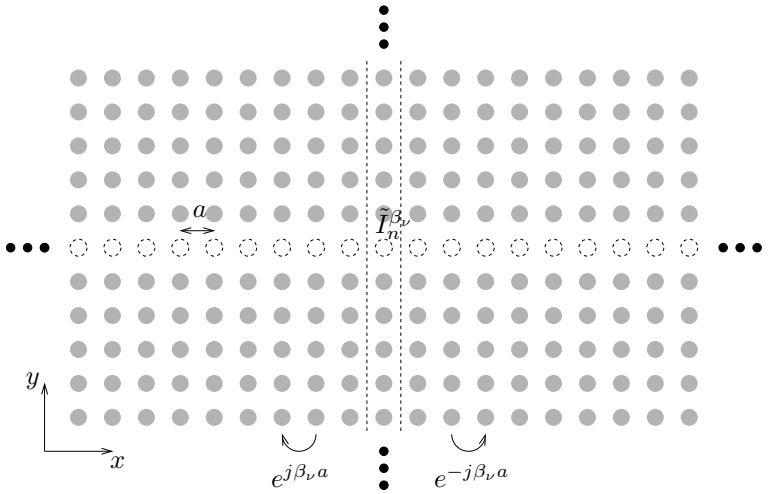

Figuur 31: Berekening van de eigenmodes van een elektromagnetisch-kristalgolfgeleider.

Beschouw een elektromagnetisch-kristalstructuur die eindigt in N_p identieke halfoneindige elektromagnetisch-kristalgolfgeleiders (Fig. 32). Veronderstel bovendien dat deze golfgeleiders slechts één propagerende eigenmode met propagatieconstante β hebben. Op voldoend verre afstand van de elektromagnetisch-kristalstructuur kan het veld in elke golfgeleider beschreven worden via enkel een naar buiten propagerende eigenmode. Dit betekent dat men kan stellen dat vanaf een bepaalde cilinder in de golfgeleider de stromen evenredig zijn met $\tilde{I}_n^\beta$ en dat de stromen voor opeenvolgende cilinders voldoen aan (108). Naar al deze cilinders wordt gerefereerd als de cilinders van poort j, $j = 1, \ldots, N_p$. De stromen op alle cilinders van poort j kunnen dus gekenmerkt worden door één enkele amplitude A_j. Deze amplitudes zijn N_p extra onbekenden. Vergelijking (100) dient vervangen te worden door

$$\tilde{E}_z^{\mathrm{i}}(\boldsymbol{\rho}) + \sum_{j=1}^{N_r} \tilde{E}_1^{\mathrm{s},j}(\boldsymbol{\rho}) + \sum_{j=1}^{N_p} \tilde{E}_1^{\mathrm{s},p_j}(\boldsymbol{\rho}) = 0, \quad \text{voor } \boldsymbol{\rho} \in \tilde{S}_i^-,\ i = 1, \ldots, N_r + N_p. \quad (110)$$

Hierbij stelt $\tilde{E}_1^{\mathrm{s},p_j}$ het veld voor veroorzaakt door alle stromen in poort j. Een eerste set van N_r vergelijkingen wordt bekomen door (110) te wegen op de N_r gewone, verwijderde cilinders. De tweede term in (110) geeft aanleiding tot de matrixelementen (107). Indien poort j gericht is volgens de positieve x-richting dan zal weging op van $\tilde{E}_1^{\mathrm{s},p_j}$ op een cilinder die in de x-richting $-l_x$ ($l_x > 0$) en in de y-richting l_y roosterconstantes

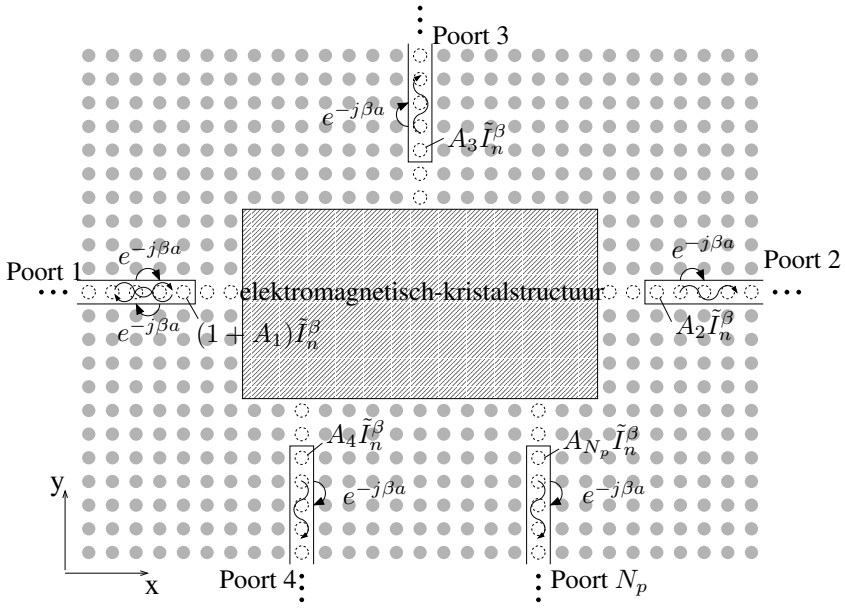

Figuur 32: Eigenmodes als excitatie en absorberende randvoorwaarden.

verwijderd is van de eerste cilinder van poort j, aanleiding geven tot een matrix-element

$$\tilde{Z}_{mp_j}(-l_x, l_y) = \sum_{l_s=0}^{N_b} \sum_{n=-K}^{K} \tilde{Z}_{mn}(-l_x + l_s, l_y)\tilde{I}_n^\beta e^{-j\beta l_s a} \quad m = -K, \ldots, K. \tag{111}$$

Een tweede set van N_p vergelijkingen wordt gevonden door (110) te wegen met $\tilde{T}_0^i(\boldsymbol{\rho})$ op het oppervlak van de eerste cilinder van elke poort. De eerste term geeft weer aanleiding tot de matrix-elementen (107) en de tweede tot de matrix-elementen (111). Op analoge manier kan men ook het gewogen veld berekenen dat wordt veroorzaakt door een propagerende eigenmode die invalt op de elektromagnetisch-kristalstructuur langs één van de poorten, bijvoorbeeld poort 1. Wanneer alle golfgeleiders identiek zijn en wanneer de amplitude van de invallende mode gelijk is aan 1, dan corresponderen de amplitudes van de naar buiten propagerende eigenmodes onmiddellijk met de S-parameters van de elektromagnetisch-kristalstructuur: $S_{1j} = A_j$.

8.4 Andere defecten

Veel elektromagnetisch-kristalstructuren bevatten naast verwijderde cilinders ook andere defecten, zoals bijvoorbeeld verplaatste cilinders of cilinders met andere parameters dan de cilinders uit het elektromagnetisch kristal. De methode uit Sectie 8.1 blijft nog altijd geldig als er zulke speciale defecten aanwezig zijn, alleen moet voor de verwijderde cilinders nabij dit speciaal defect een andere Greense functie worden gebruikt die het speciaal defect in rekening brengt. Deze Greense functies kunnen berekend worden zoals de gewone Greense functie van het kristal, waarbij echter een eindig kristal wordt beschouwd

waarin het speciaal defect aanwezig is (Fig. 33). Al deze Greense functies expliciet op

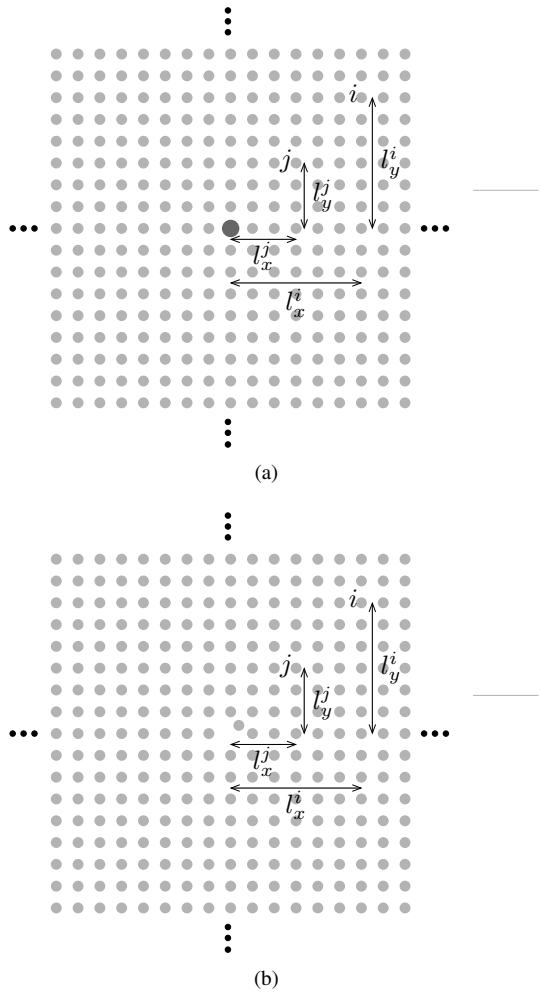

Figuur 33: Speciale Greense functies.

deze manier berekenen zou echter teveel tijd vergen. Gelukkig is de rang van het verschil tussen de matrix $\hat{\boldsymbol{Z}}$ die de interacties beschrijft in het eindig kristal met het speciaal defect erin en de matrix $\boldsymbol{Z}$ die de interacties beschrijft in het defectloos kristal, laag:

$$\hat{\boldsymbol{Z}} \quad = \quad \boldsymbol{Z} + \boldsymbol{U}\boldsymbol{V}^T. \tag{112}$$

Gelet op de formule van Sherman-Morrison [30] is de rang van het verschil tussen $\hat{\boldsymbol{Y}} = \hat{\boldsymbol{Z}}^{-1}$ en $\boldsymbol{Y} = \boldsymbol{Z}^{-1}$ ook laag:

$$\hat{\boldsymbol{Y}} \quad = \quad \boldsymbol{Y} - \boldsymbol{Y}\boldsymbol{U}(\mathbf{1} + \boldsymbol{V}^T\boldsymbol{Y}\boldsymbol{U})^{-1}\boldsymbol{V}^T\boldsymbol{Y}, \tag{113}$$

met $\mathbf{1}$ de éénheidsmatrix. Bijgevolg kan $\hat{\boldsymbol{Y}}$ en dus ook de speciale Greense functie snel berekend worden zonder een nieuw stelsel te moeten oplossen. Hier wordt enkel het geval

behandeld waarbij het special defect bestaat uit een cilinder met afwijkende parameters (Fig. 33(a)). In de Engelstalige tekst wordt ook het geval van een verplaatste cilinder beschreven (Fig. 33(b)). Bovendien wordt er voor de eenvoud verondersteld dat $K = 0$.

Veronderstel dat het speciaal defect gecentreerd is rond het midden van het eindig kristal en dat de index van deze cilinder in de klassieke meervoudige-verstrooiingstechniek 1 is, dan is

$$\boldsymbol{U} = \begin{pmatrix} 1 \\ 0 \\ \vdots \\ 0 \end{pmatrix}, \; \boldsymbol{V} = \begin{pmatrix} \Delta \\ 0 \\ \vdots \\ 0 \end{pmatrix}, \tag{114}$$

met $\Delta = \hat{Z}_{00}^{11} - Z_{00}^{11}$. Aangezien $\tilde{G}_n(\boldsymbol{\rho})$ via een iteratieve methode wordt berekend, is $\boldsymbol{Y}$ niet expliciet gekend. Er bestaat echter een rechtstreeks verband tussen het element Y_{00}^{ij} en de stroom op cilinder i wanneer het eindig kristal wordt geëxciteerd met een Huygens bron op cilinder j met elektrische en magnetische componenten $\frac{C_n}{2\pi r} e^{jn\phi_j} \delta(\rho_j - r) \boldsymbol{u}_z$ en $\frac{jC_n}{2\pi r} \sqrt{\frac{\epsilon_1}{\mu_1}} \frac{J_n(k_1 r)}{J_n'(k_1 r)} e^{jn\phi_j} \delta(\rho_j - r) \boldsymbol{u}_{\phi_j}$, namelijk

$$Y_{00}^{ij} = \frac{4}{\omega\mu_1} \frac{\pi k_1 r J_0'(k_1 r)}{2jC_0} I_{00}(l_x^i - l_x^j, l_y^i - l_y^j). \tag{115}$$

Aangezien $\boldsymbol{YU}$ correspondeert met de eerste kolom van $\boldsymbol{Y}$ en $\boldsymbol{V}^T\boldsymbol{Y}$ correspondeert met Δ keer de eerste rij van $\boldsymbol{Y}$, volgt er uit (113) dat

$$\hat{Y}_{00}^{ij} = Y_{00}^{ij} - Y_{00}^{i1}(1 + \Delta Y_{00}^{11})^{-1} \Delta Y_{00}^{1j}. \tag{116}$$

Combinatie van (107), (115) en (116) geeft

$$\begin{aligned} \tilde{Z}_{00}^{ij} = \frac{\omega\mu_2}{4} \frac{2jC_0}{\pi k_2 r J_0'(k_2 r)} \Big[& I_{00}(l_x^i - l_x^j, l_y^i - l_y^j) \\ & + I_{00}(l_x^i, l_y^i) \frac{\Delta D_0}{1 + \Delta D_0 I_{00}(0,0)} I_{00}(-l_x^j, -l_y^j) \Big], \end{aligned} \tag{117}$$

waarbij $\tilde{Z}_{00}^{ij}$ het matrix-element is in de dunbezette matrix $\tilde{\boldsymbol{Z}}$ dat in de interactie beschrijft tussen twee cilinders i en j die respectievelijk (l_x^i, l_y^i) en (l_x^j, l_y^j) roosterconstantes verwijderd zijn van het speciaal defect langs de x en de y-richting. Dit toont aan dat alle nodige matrix-elementen snel kunnen berekend worden uit de kennis van enkel de Greense functie van het defectloos kristal.

8.5 Voorbeelden

De volledige methode werd geïmplementeerd in Matlab. Om het dunbezette lineaire stelsel (106) op te lossen werd UMFPACK Versie 4.3 gebruikt [31]. Het berekenen van de Greense functie aan de hand van een eindig kristal van 31 op 31 cilinders en met $K = 1$, duurt op een 2GHz PC slechts 4 s indien BICGSTAB wordt gebruikt als iteratieve oplossingsmethode in combinatie met een afgeschermde-blok preconditioner en een FFT-gebaseerd vermenigvuldigingsschema.

Figuur 34 toont het transmissiespectrum van een twee-kanaals multiplexer-demultiplexer met $l = 1200a$ ($a = 540nm$) berekend met de nieuwe methode. In totaal zijn er in dit voorbeeld 7465 onbekenden. Voor één frequentiepunt duurt het 12.5 s om de dunbezette matrix op te vullen en 3.8 s om het lineair systeem (106) op te lossen. De totale rekentijd per frequentiepunt, het berekenen van de Greense functie inbegrepen, is dus slechts 20 s.

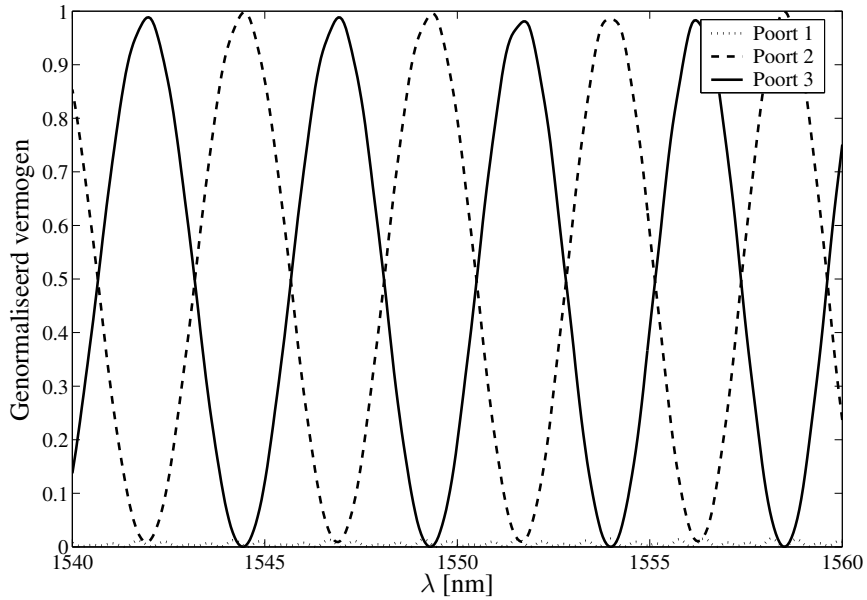

Figuur 34: Transmissiespectrum van een twee-kanaals multiplexer-demultiplexer met $l = 1200a$ berekend via de Greense functie van het kristal.

De correctheid van de theorie uit Sectie 8.4 wordt bewezen aan de hand van de filterstructuur getoond in Fig. 35. Deze filter bestaat uit een elektromagnetisch-kristalgolfgeleider waarin een caviteit, gevormd door twee of drie cilinders, is geplaatst. Hierdoor zal een signaal slechts doorgelaten worden in de smalle frequentieband waarvoor de caviteit in resonantie komt. Twee situaties werden gesimuleerd. In de eerste situatie bestaat de caviteit uit twee gewone cilinders, in de tweede situatie wordt in het midden van de caviteit een extra, afwijkende cilinder toegevoegd. De straal van deze cilinder is vier keer kleiner dan die van de gewone cilinders. Figuur 36 toont het transmissiespectrum voor beide gevallen, berekend met zowel de klassieke meervoudige-verstrooiingstechniek als met de nieuwe methode.

9 Analyse van gelaagde elektromagnetische kristallen

Tot nu toe werden enkel zuiver 2D elektromagnetische kristallen besproken waarbij er expliciet verondersteld wordt dat de cilinders zich oneindig uitstrekken in de derde richting (z-richting). Om de velden ook in de z-richting ingesloten te houden, wordt in de

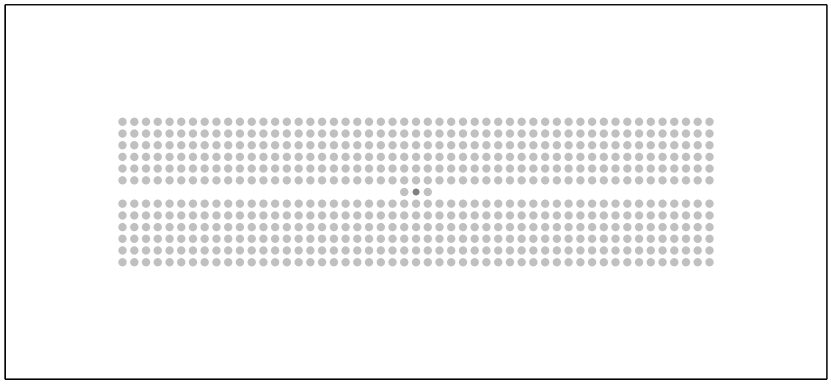

Figuur 35: Elektromagnetisch-kristalfilter.

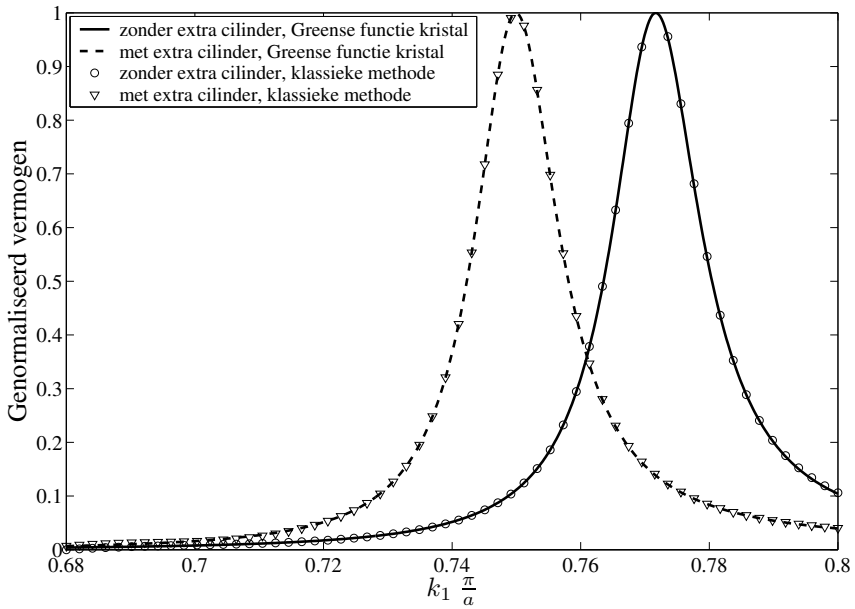

Figuur 36: Transmissiespectrum van de elektromagnetisch-kristalfilter.

praktijk zo'n 2D elektromagnetisch kristal ingebouwd in een gelaagd medium, bijvoorbeeld door in het gelaagd medium gaten te etsen (Fig. 37). Voor de correcte karakterisatie van deze gelaagde elektromagnetische kristallen is het belangrijk om de stralingsverliezen uit het vlak parallel aan de lagen (xy-vlak) in rekening te brengen. In deze sec-

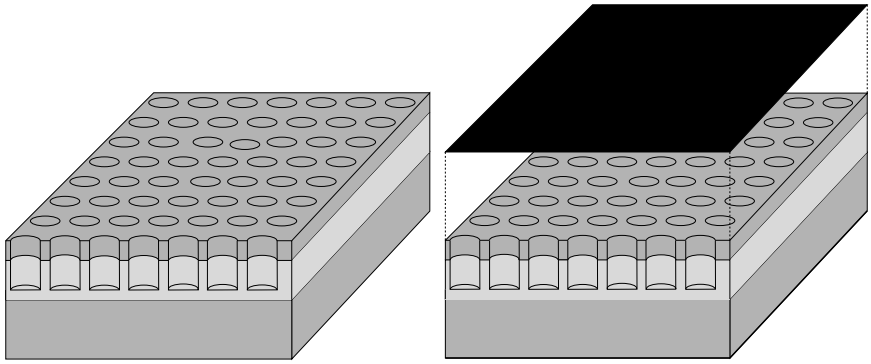

(a) (b)

Figuur 37: Gelaagd elektromagnetisch kristal.

tie wordt een nieuwe techniek besproken voor de karakterisatie van golfpropagatie in gelaagde elektromagnetische kristallen. Deze techniek combineert de 2D meervoudige-verstrooiingstechniek in het xy-vlak met een (cilindrische) mode-aanpassing langs de z-richting. Omdat voor de mode-aanpassing een volledig discreet spectrum van eigenmodes vereist is, wordt het *open* gelaagd medium beschreven aan de hand van een *gesloten* gelaagd medium. Hiertoe worden de buitenste lagen afgesloten met perfecte geleidende vlakken. De parasitaire reflecties die hierdoor ontstaan worden geminimaliseerd door net voor deze geleiders PMLs te plaatsen. Uit vroeger onderzoek volgt dat de buitenste lagen in dit geval kunnen beschouwd worden als één homogene, isotrope laag met een *complexe* dikte [18, 19]. Bovendien blijven formules voor gewone gelaagde media zonder PMLs geldig: men moet enkel voor de dikte van de buitenste lagen de correcte complexe waarde invullen [32].

9.1 Longitudinale en radiale eigenmodes

In deze sectie wordt het verband gegeven tussen de longitudinale en radiale eigenmodes van een algemeen gesloten gelaagd medium (Fig. 38). Deze media bestaan uit L homogene en isotrope lagen, evenwijdig aan het xy-vlak, met dikte d_i en materiaalparameters (ϵ_i, μ_i), $i = 1, \ldots, L$. De volledige structuur bevindt zich tussen twee perfect geleidende vlakken. Bovendien kan de dikte van de buitenste lagen complex zijn: $\tilde{d}_1 = d_1^{\text{re}} + jd_1^{\text{im}}$ en $\tilde{d}_L = d_L^{\text{re}} + jd_L^{\text{im}}$. Om absorptie te bekomen moet het imaginair deel van deze complexe diktes negatief zijn.

De *longitudinale* eigenmodes worden hier gedefinieerd als de algemene oplossingen van de bronloze vergelijkingen van Maxwell in deze media waarbij er verondersteld wordt

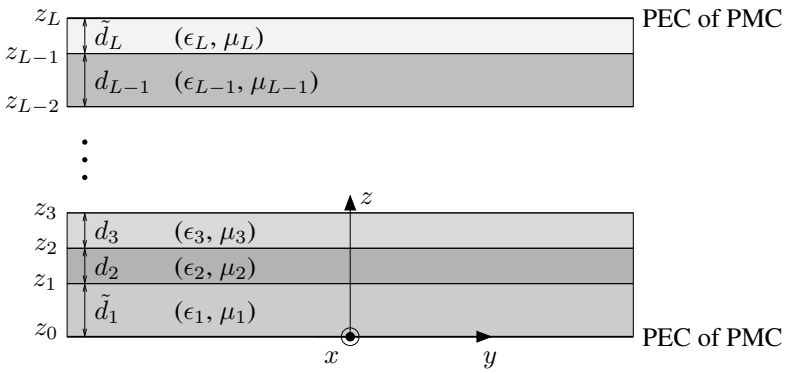

Figuur 38: Gesloten gelaagd medium.

dat de velden onafhankelijk zijn van x en een $e^{-j\beta y}$ verloop hebben in de y-richting:

$$\boldsymbol{e}(y,z) = \sum_{m=1}^{+\infty} \boldsymbol{E}_m(z) e^{-j\beta_m y}, \tag{118}$$

$$\boldsymbol{h}(y,z) = \sum_{m=1}^{+\infty} \boldsymbol{H}_m(z) e^{-j\beta_m y}. \tag{119}$$

Deze longitudinale eigenmodes kunnen opgesplitst worden in twee onafhankelijke sets. Voor de eerste set heeft het magnetisch veld geen z-component (TM$_z$-polarisatie), voor de tweede set heeft het elektrisch veld geen z-component (TE$_z$-polarisatie).

De *radiale* eigenmodes worden gedefinieerd als de oplossingen van de bronloze vergelijkingen van Maxwell in cilindercoördinaten waarbij er expliciet wordt verondersteld dat de velden een $e^{jk\phi}$ afhankelijkheid hebben:

$$\hat{\boldsymbol{e}}(\rho,\phi,z) = \sum_{k=-\infty}^{+\infty} \sum_{m=1}^{+\infty} \hat{\boldsymbol{E}}_{mk}(\rho,z) e^{jk\phi}, \tag{120}$$

$$\hat{\boldsymbol{h}}(\rho,\phi,z) = \sum_{k=-\infty}^{+\infty} \sum_{m=1}^{+\infty} \hat{\boldsymbol{H}}_{mk}(\rho,z) e^{jk\phi}. \tag{121}$$

Voor de duidelijkheid worden in deze sectie velden in functie van cilindercoördinaten aangeduid met een hoedje. Deze radiale eigenmodes kunnen eveneens onderverdeeld worden in een TM$_z$ en TE$_z$-polarisatie.

Er bestaat een nauw verband tussen de longitudinale en de radiale eigenmodes. Voor

de TM$_z$-polarisatie is dit

$$\hat{E}^{\text{TM}}_{z,mk}(\rho,z) = R^{\text{TM}}_{mk}(\beta^{\text{TM}}_m\rho)E_{z,m}(z), \quad (122)$$
$$\hat{E}^{\text{TM}}_{\rho,mk}(\rho,z) = jR^{\text{TM}\,\prime}_{mk}(\beta^{\text{TM}}_m\rho)E_{y,m}(z), \quad (123)$$
$$\hat{E}^{\text{TM}}_{\phi,mk}(\rho,z) = -\frac{k}{\beta^{\text{TM}}_m\rho}R^{\text{TM}}_{mk}(\beta^{\text{TM}}_m\rho)E_{y,m}(z), \quad (124)$$
$$\hat{H}^{\text{TM}}_{\rho,mk}(\rho,z) = -\frac{k}{\beta^{\text{TM}}_m\rho}R^{\text{TM}}_{mk}(\beta^{\text{TM}}_m\rho)H_{x,m}(z), \quad (125)$$
$$\hat{H}^{\text{TM}}_{\phi,mk}(\rho,z) = -jR^{\text{TM}\,\prime}_{mk}(\beta^{\text{TM}}_m\rho)H_{x,m}(z). \quad (126)$$

Hier is β^{TM}_m de propagatieconstante van de m^{de} longitudinale TM$_z$ eigenmode. De meest algemene uitdrukking voor $R^{\text{TM}}_{mk}(\beta^{\text{TM}}_m\rho)$ is

$$R^{\text{TM}}_{mk}(\beta^{\text{TM}}_m\rho) = A^{\text{TM}}_{mk}J_k(\beta^{\text{TM}}_m\rho) + B^{\text{TM}}_{mk}H^{(2)}_k(\beta^{\text{TM}}_m\rho). \quad (127)$$

Het analoog verband voor de TE$_z$-polarisatie is

$$\hat{H}^{\text{TE}}_{z,mk}(\rho,z) = R^{\text{TE}}_{mk}(\beta^{\text{TE}}_m\rho)H_{z,m}(z), \quad (128)$$
$$\hat{E}^{\text{TE}}_{\rho,mk}(\rho,z) = -\frac{k}{\beta^{\text{TE}}_m\rho}R^{\text{TE}}_{mk}(\beta^{\text{TE}}_m\rho)E_{x,m}(z), \quad (129)$$
$$\hat{E}^{\text{TE}}_{\phi,mk}(\rho,z) = -jR^{\text{TE}\,\prime}_{mk}(\beta^{\text{TE}}_m\rho)E_{x,m}(z), \quad (130)$$
$$\hat{H}^{\text{TE}}_{\rho,mk}(\rho,z) = jR^{\text{TE}\,\prime}_{mk}(\beta^{\text{TE}}_m\rho)H_{y,m}(z), \quad (131)$$
$$\hat{H}^{\text{TE}}_{\phi,mk}(\rho,z) = -\frac{k}{\beta^{\text{TE}}_m\rho}R^{\text{TE}}_{mk}(\beta^{\text{TE}}_m\rho)H_{y,m}(z), \quad (132)$$

met β^{TE}_m de propagatieconstante van de m^{de} longitudinale TE$_z$ eigenmode en

$$R^{\text{TE}}_{mk}(\beta^{\text{TE}}_m\rho) = A^{\text{TE}}_{mk}J_k(\beta^{\text{TE}}_m\rho) + B^{\text{TE}}_{mk}H^{(2)}_k(\beta^{\text{TE}}_m\rho). \quad (133)$$

9.2 Verstrooiingsmatrix

In deze sectie wordt beschreven hoe de verstrooiingsmatrix van een gelaagde cilinder die ingebed is in een ander gelaagd medium kan berekend worden (Fig. 39). De eigenmodes van het gelaagd medium binnenin de cilinder worden aangeduid met het subscript '1' en de bijhorende propagatieconstanten zijn ζ^{TX}_m, waarbij TX staat voor TM of TE. De eigenmodes van het extern gelaagd medium worden aangeduid met het subscript '2' en hun propagatieconstanten zijn β^{TX}_m. Het invallend veld $(\hat{\boldsymbol{e}}^{\text{i}}, \hat{\boldsymbol{h}}^{\text{i}})$ is gedefinieerd als het veld dat gegenereerd wordt door opgelegde bronnen in het extern gelaagd medium in afwezigheid van de cilinder. In aanwezigheid van de cilinder wordt het totale veld $(\hat{\boldsymbol{e}}^{\text{t}}, \hat{\boldsymbol{h}}^{\text{t}})$ waargenomen. Het verschil tussen beide is het verstrooide veld $(\hat{\boldsymbol{e}}^{\text{s}}, \hat{\boldsymbol{h}}^{\text{s}})$. Veronderstel dat het invallend veld bestaat uit de superpositie van $(2K+1)M$ radiale TM$_z$ en $(2K+1)M$

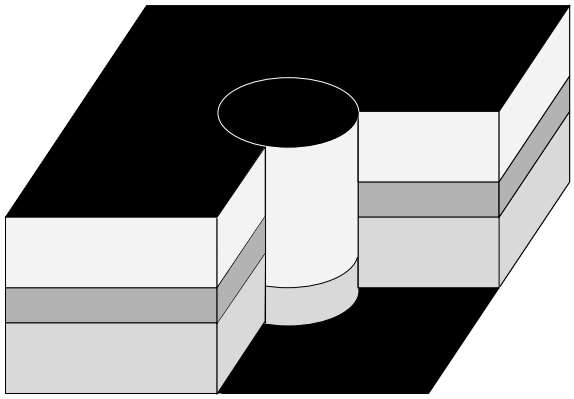

Figuur 39: Berekening van verstrooiingsmatrix van één gelaagde cilinder, ingebed in een ander gelaagd medium.

radiale TE_z eigenmodes:

$$\hat{e}_z^{\mathrm{i}}(\rho,\phi,z) = \sum_{k=-K}^{K}\sum_{m=1}^{M} C_{mk}^{\mathrm{TM}} \frac{J_k(\beta_m^{\mathrm{TM}}\rho)}{J_k(\beta_m^{\mathrm{TM}}r)} E_{z,m}^1(z)e^{jk\phi}, \tag{134}$$

$$\hat{h}_z^{\mathrm{i}}(\rho,\phi,z) = \sum_{k=-K}^{K}\sum_{m=1}^{M} C_{mk}^{\mathrm{TE}} \frac{J_k(\beta_m^{\mathrm{TE}}\rho)}{J_k(\beta_m^{\mathrm{TE}}r)} H_{z,m}^1(z)e^{jk\phi}, \tag{135}$$

met C_{mk}^{TX} gekende coëfficiënten. De andere componenten van het invallend veld kunnen hieruit afgeleid worden via (123)-(126) en (129)-(132). Daar het invallend veld eindig moet blijven voor $\rho = 0$, worden in (134) en (135) Besselfuncties $J_k(\cdot)$ gebruikt. Ook het verstrooide en het totale veld kunnen uitgedrukt worden als de superpositie van $(2K+1)M$ radiale TM_z en $(2K+1)M$ radiale TE_z eigenmodes:

$$\hat{e}_z^{\mathrm{s}}(\rho,\phi,z) = \sum_{k=-K}^{K}\sum_{m=1}^{M} B_{mk}^{\mathrm{TM}} \frac{H_k^{(2)}(\beta_m^{\mathrm{TM}}\rho)}{H_k^{(2)}(\beta_m^{\mathrm{TM}}r)} E_{z,m}^1(z)e^{jk\phi} \text{ voor } \rho > r, \tag{136}$$

$$\hat{h}_z^{\mathrm{s}}(\rho,\phi,z) = \sum_{k=-K}^{K}\sum_{m=1}^{M} B_{mk}^{\mathrm{TE}} \frac{H_k^{(2)}(\beta_m^{\mathrm{TE}}\rho)}{H_k^{(2)}(\beta_m^{\mathrm{TE}}r)} H_{z,m}^1(z)e^{jk\phi} \text{ voor } \rho > r, \tag{137}$$

$$\hat{e}_z^{\mathrm{t}}(\rho,\phi,z) = \sum_{k=-K}^{K}\sum_{m=1}^{M} A_{mk}^{\mathrm{TM}} \frac{J_k(\zeta_m^{\mathrm{TM}}\rho)}{J_k(\zeta_m^{\mathrm{TM}}r)} E_{z,m}^2(z)e^{jk\phi} \text{ voor } \rho < r, \tag{138}$$

$$\hat{h}_z^{\mathrm{t}}(\rho,\phi,z) = \sum_{k=-K}^{K}\sum_{m=1}^{M} A_{mk}^{\mathrm{TE}} \frac{J_k(\zeta_m^{\mathrm{TE}}\rho)}{J_k(\zeta_m^{\mathrm{TE}}r)} H_{z,m}^2(z)e^{jk\phi} \text{ voor } \rho < r, \tag{139}$$

met A_{mk}^{TX} en B_{mk}^{TX} onbekende coëfficiënten. In (136) en (137) worden enkel Hankelfuncties $H_k^{(2)}(\cdot)$ gebruikt omdat het verstrooide veld weg van de cilinder propageert; in (138) en (139) worden Besselfuncties $J_k(\cdot)$ gebruikt omdat het totale veld eindig is voor $\rho = 0$.

De verstrooiingsmatrix $\boldsymbol{S}$ geeft per definitie het verband tussen de coëfficiënten B_{mk}^{TX} en C_{mk}^{TX}:

$$\boldsymbol{B} \;=\; \boldsymbol{S}\boldsymbol{C}. \tag{140}$$

Deze verstrooiingsmatrix wordt gevonden door uit te drukken dat de z en de ϕ-componenten van het totale elektrisch en magnetisch veld continu zijn op het oppervlak van de gelaagde cilinder:

$$\left[\hat{\boldsymbol{e}}^{\mathrm{i}}(r^+,\phi,z)+\hat{\boldsymbol{e}}^{\mathrm{s}}(r^+,\phi,z)\right]\times\boldsymbol{u}_\rho \;=\; \hat{\boldsymbol{e}}^{\mathrm{t}}(r^-,\phi,z)\times\boldsymbol{u}_\rho, \tag{141}$$

$$\left[\hat{\boldsymbol{h}}^{\mathrm{i}}(r^+,\phi,z)+\hat{\boldsymbol{h}}^{\mathrm{s}}(r^+,\phi,z)\right]\times\boldsymbol{u}_\rho \;=\; \hat{\boldsymbol{h}}^{\mathrm{t}}(r^-,\phi,z)\times\boldsymbol{u}_\rho. \tag{142}$$

Hier duiden r^+ en r^- stralen aan die respectievelijk infinitesimaal groter en kleiner zijn dan r. Door vergelijking (141) te wegen met het magnetisch veld van elke radiale eigenmode van het extern medium en door analoog vergelijking (142) te wegen met het elektrisch veld van elke radiale eigenmode van het extern medium, ziet men in dat $\boldsymbol{S}$ een blok-diagonale matrix is:

$$\boldsymbol{S} \;=\; \begin{pmatrix} \boldsymbol{S}_{-K} & & & & \\ & \ddots & & & \\ & & \boldsymbol{S}_0 & & \\ & & & \ddots & \\ & & & & \boldsymbol{S}_K \end{pmatrix}. \tag{143}$$

De submatrix $\boldsymbol{S}_k$ heeft dimensie $2M\times 2M$ en geeft het verband tussen de vectors $\boldsymbol{B}_k$ en $\boldsymbol{C}_k$ die alle coëfficënten B_{mk}^{TX} en C_{mk}^{TX} bevatten met dezelfde k. Analoog bevat de vector $\boldsymbol{A}_k$ alle coëfficënten A_{mk}^{TX} met dezelfde k. Uit de weging van (141) en (142) volgt het volgende verband:

$$\begin{pmatrix} \boldsymbol{Z}_{11}^k & -\boldsymbol{I} \\ \boldsymbol{Z}_{21}^k & \boldsymbol{Z}_{22}^k \end{pmatrix}\begin{pmatrix} \boldsymbol{A}_k \\ \boldsymbol{B}_k \end{pmatrix} \;=\; \begin{pmatrix} \boldsymbol{I} \\ \boldsymbol{Y}_2^k \end{pmatrix}\boldsymbol{C}_k, \tag{144}$$

met $\boldsymbol{I}$ de eenheidsmatrix. De exacte uitdrukkingen voor de elementen van elke submatrix zijn terug te vinden in de Engelstalige tekst. Eliminatie van $\boldsymbol{A}_k$ in (144) geeft

$$\boldsymbol{S}_k=\left[\boldsymbol{I}+(\boldsymbol{Y}_2^k)^{-1}\boldsymbol{Z}_{22}^k\right]^{-1}\left[\boldsymbol{Z}_{11}^k-(\boldsymbol{Y}_2^k)^{-1}\boldsymbol{Z}_{21}^k\right]\left[\boldsymbol{Z}_{22}^k\boldsymbol{Z}_{11}^k+\boldsymbol{Z}_{21}^k\right]^{-1}\left[\boldsymbol{Z}_{22}^k+\boldsymbol{Y}_2^k\right]. \tag{145}$$

Indien de vector $\boldsymbol{C}$ is gegeven, dan is via (140) de vector $\boldsymbol{B}$ ook gekend. Hieruit kan $\boldsymbol{A}$ berekend worden via

$$\boldsymbol{A}_k \;=\; \left[\boldsymbol{Y}_2^k\boldsymbol{Z}_{11}^k-\boldsymbol{Z}_{21}^k\right]^{-1}[\boldsymbol{Z}_{22}^k+\boldsymbol{Y}_2^k]\boldsymbol{B}_k. \tag{146}$$

Bijgevolg is het totale veld zowel binnen als buiten de cilinder gekend.

9.3 Gelaagde elektromagnetische kristallen

Beschouw het gelaagde elektromagnetisch kristal uit Fig. 37 bekomen door het etsen van N_c gaten in een gelaagd medium. Na afsluiten van de buitenste lagen met PMLs en perfect geleidende vlakken, kan elke gat gezien worden als de cilinder uit Fig. 39. De verstrooiingsmatrix $\boldsymbol{S}^i$ van cilinder i geeft per definitie het verband tussen het veld dat invalt op deze cilinder en het veld dat verstrooid wordt door deze cilinder. Het veld dat invalt op een cilinder bestaat uit het invallende veld genereert door de opgelegde bronnen in het extern gelaagd medium in afwezigheid van alle cilinders en uit de som van de verstrooide velden van alle andere cilinders. Het invallend veld kan in de buurt van cilinder i geschreven worden als de superpositie van $(2K+1)M$ radiale TM_z en $(2K+1)M$ radiale TE_z eigenmodes:

$$\hat{e}_z^{\text{i}}(\rho_i,\phi_i,z) = \sum_{k=-K}^{K}\sum_{m=1}^{M} C_{mk}^{\text{TM},i}\frac{J_k(\beta_m^{\text{TM}}\rho_i)}{J_k(\beta_m^{\text{TM}}r_i)}E_{z,m}^1(z)e^{jk\phi_i}, \tag{147}$$

$$\hat{h}_z^{\text{i}}(\rho_i,\phi_i,z) = \sum_{k=-K}^{K}\sum_{m=1}^{M} C_{mk}^{\text{TE},i}\frac{J_k(\beta_m^{\text{TE}}\rho_i)}{J_k(\beta_m^{\text{TE}}r_i)}H_{z,m}^1(z)e^{jk\phi_i}, \tag{148}$$

met $C_{mk}^{\text{TX},i}$ gekende coëfficiënten en r_i de straal van cilinder i. Analoog wordt het veld verstrooid door cilinder j uitgedrukt als

$$\hat{e}_z^{\text{s},j}(\rho_j,\phi_j,z) = \sum_{k=-K}^{K}\sum_{m=1}^{M} B_{mk}^{\text{TM},j}\frac{H_k^{(2)}(\beta_m^{\text{TM}}\rho_j)}{H_k^{(2)}(\beta_m^{\text{TM}}r_j)}E_{z,m}^1(z)e^{jk\phi_j} \text{ voor } \rho_j > r_j, \tag{149}$$

$$\hat{h}_z^{\text{s},j}(\rho_j,\phi_j,z) = \sum_{k=-K}^{K}\sum_{m=1}^{M} B_{mk}^{\text{TE},j}\frac{H_k^{(2)}(\beta_m^{\text{TE}}\rho_j)}{H_k^{(2)}(\beta_m^{\text{TE}}r_j)}H_{z,m}^1(z)e^{jk\phi_j} \text{ voor } \rho_j > r_j. \tag{150}$$

Via het additietheorema van de Hankelfunctie ([16], p. 232, vgl. 5-103) kan men (149) en (150) herschrijven in functie van het cilindrisch coördinatensysteem van cilinder i. Sommeren van al deze verstrooide velden geeft

$$\sum_{j\neq i}\hat{e}_z^{\text{s},j}(\rho_i,\phi_i,z) = \sum_{k=-K}^{K}\sum_{m=1}^{M} \check{B}_{mk}^{\text{TM},i}\frac{J_k(\beta_m^{\text{TM}}\rho_i)}{J_k(\beta_m^{\text{TM}}r_i)}E_{z,m}^1(z)e^{jk\phi_i}, \tag{151}$$

$$\sum_{j\neq i}\hat{h}_z^{\text{s},j}(\rho_i,\phi_i,z) = \sum_{k=-K}^{K}\sum_{m=1}^{M} \check{B}_{mk}^{\text{TE},i}\frac{J_k(\beta_m^{\text{TE}}\rho_i)}{J_k(\beta_m^{\text{TE}}r_i)}H_{z,m}^1(z)e^{jk\phi_i}. \tag{152}$$

De coëfficiënten $\check{B}_{mk}^{(TX),i}$ zijn verbonden met de coëfficiënten $B_{mk}^{\text{TX},j}$ via

$$\check{B}_{mk}^{\text{TX},i} = \sum_{j\neq i}\sum_{p=-K}^{+K} \boldsymbol{Z}_{kp}^{ij}(\beta_m^{\text{TX}})B_{mp}^{\text{TX},j}, \tag{153}$$

met

$$\boldsymbol{Z}_{kp}^{ij}(\beta) = \frac{H_{p-k}^{(2)}(\beta R_{ij})J_k(\beta r_i)e^{j(k-p)\Phi_{ij}}}{H_p^{(2)}(\beta r_j)}. \tag{154}$$

Dit matrixelement vertoont grote gelijkenis met de matrixelementen uit de 2D klassieke meervoudige-verstrooiingstechniek.

Aangezien de verstrooiingsmatrix per definitie het verband geeft tussen het veld verstrooid door cilinder i en het totale invallende veld, bekomt men het lineaire stelsel

$$\boldsymbol{B}^i \quad = \quad \boldsymbol{S}^i \left[\check{\boldsymbol{B}}^i + \boldsymbol{C}^i \right], \;\; i = 1, \ldots, N_c. \tag{155}$$

Dit stelsel kan efficiënt opgelost worden met behulp van een iteratieve oplossingsmethode. De nodige matrix-vector vermenigvuldigingen worden hierbij in twee stappen uitgevoerd. In de eerste stap berekent men via (153) de coëfficiënten $\check{B}^{\mathrm{TX},i}_{mk}$. Aangezien hiervoor eigenmodes met een verschillende propagatieconstante niet interageren, herleidt deze operatie zich tot $2M$ kleinere matrix-vector vermenigvuldigingen waarop telkens een snel 2D matrix-vector vermenigvuldigingsschema kan worden toegepast. Zodra de vector $\check{\boldsymbol{B}}^i$ is berekend, wordt in de tweede stap deze vector vermenigvuldigd met $\boldsymbol{S}^i$. Aangezien $\boldsymbol{S}^i$ een blok-diagonale matrix is, valt deze stap uiteen in $(2K+1)N_c$ kleinere matrix-vector vermenigvuldigingen. Bovendien zal in de meeste gelaagde elektromagnetische kristallen dezelfde cilinder vaak terugkeren, zodat slechts een beperkt aantal verstrooiingsmatrices moet berekend en opgeslagen worden.

9.4 Voorbeelden

Beschouw het gelaagd elektromagnetisch kristal getoond in Fig. 40. Het gelaagd medium bestaat uit een kernlaag met hoge relatieve permittiviteit omgeven door twee oneindig dikke luchtlagen. Doorheen dit gelaagd medium zijn gaten geëtst volgens een hexagonaal

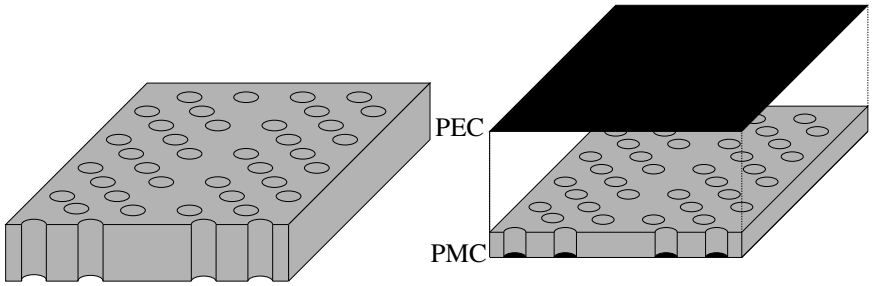

Figuur 40: Symmetrisch gelaagd elektromagnetisch kristal.

rooster met roosterconstante a. De relatieve permittiviteit van de kernlaag is 12.25 en zijn dikte is $0.6a$. De straal van de cilinders is $0.3a$. Dit gelaagd elektromagnetisch kristal heeft een verboden zone tussen $k_1 = 0.504\frac{\pi}{a}$ en $k_1 = 0.656\frac{\pi}{a}$, met k_1 het golfgetal in de vrije ruimte [33].

Ten gevolge van de symmetrie van dit gelaagd elektromagnetisch kristal kan de karakterisatie ervan opgesplitst worden in een even en oneven situatie. Voor de *even* situatie zijn de ρ en ϕ-componenten van het elektrisch veld symmetrisch in de z-richting; voor de *oneven* situatie zijn deze componenten oneven functies in de z-richting. Aangezien de excitatie in de onderstaande voorbeelden steeds even is, kan het simulatiegebied gehalveerd

worden. Het symmetrievlak in het midden van de kernlaag kan voor de even situatie immers vervangen worden door een perfect magnetisch geleidend vlak (Fig. 40(b)). De complexe dikte van de luchtlaag is $(6 - 0.3j)a$. Alle nodige propagatieconstanten en modeprofielen werden berekend met CAMFR [34].

De correctheid van de verstrooiingsmatrix wordt getest door één gat te beschouwen waarop de propagerende TE_z longitudinale eigenmode invalt volgens de positieve y-richting. Figuren 41 en 42 tonen de z-component van het magnetisch veld net buiten en net binnen de cilinder in functie van z en ϕ en dit voor $k_1 = 0.6\frac{\pi}{a}$, $K = 4$ en $M = 20$.

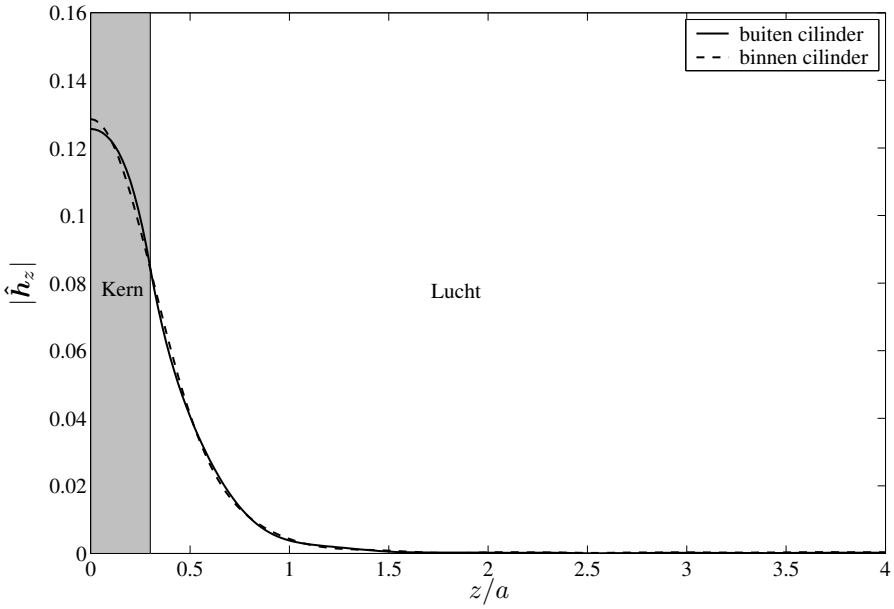

Figuur 41: Cilindrische mode-aanpassing voor één cilinder: $|\hat{\boldsymbol{h}}_z(z)|$ in functie van z.

De volledige methode wordt getest via de karakterisatie van een gelaagde elektromagnetisch-kristalgolfgeleider met twee bochten van 60^{o}. Als excitatie vertrekt de fundamentele radiale TE_z eigenmode cilindrisch vanuit een punt $\boldsymbol{\rho}_s$. Figuur 43 toont de absolute waarde van het magnetisch veld in het symmetrievlak van het gelaagd medium voor $k_1 = 0.6\frac{\pi}{a}$. Figuur 44 toont dezelfde veldcomponent volgens de as van de golfgeleider in het symmetrievlak. Een aanzienlijk verlies treedt op in de bochten, wat de noodzaak aantoont van het optimaliseren van het ontwerp van de bochten. Met $K = 4$ en $M = 20$ zijn er in totaal 232560 onbekenden in dit voorbeeld. Eén matrix-vector vermenigvuldiging, versneld via een FFT-gebaseerd schema, duurt 12 s. Het lineair stelsel (155) kan met BICGSTAB opgelost worden tot een tolerantie van 10^{-5} in 196 iteraties. De totale rekentijd is 2 uur en 35 minuten. De geheugenvereisten zijn 450Mb.

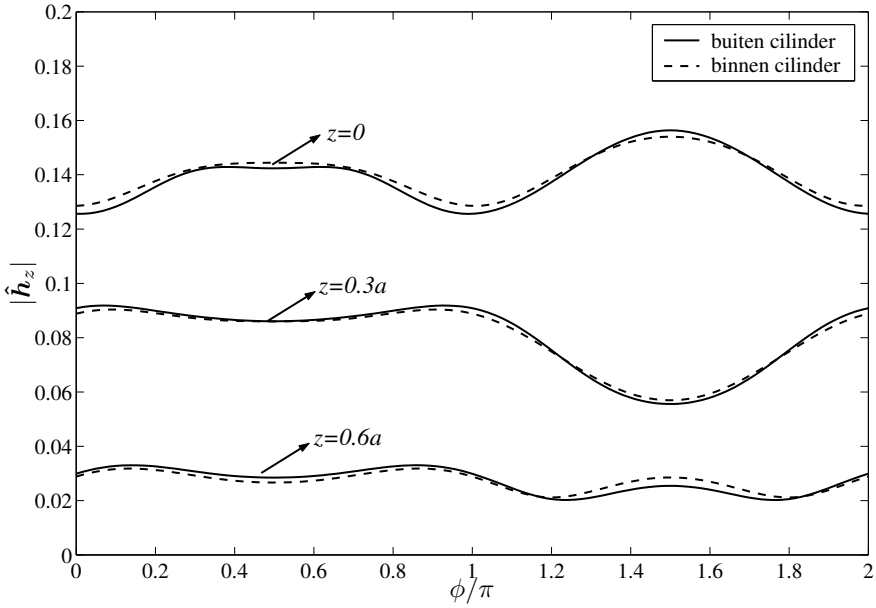

Figuur 42: Cilindrische mode-aanpassing voor één cilinder: $|\hat{\boldsymbol{h}}_z(z)|$ in functie van ϕ.

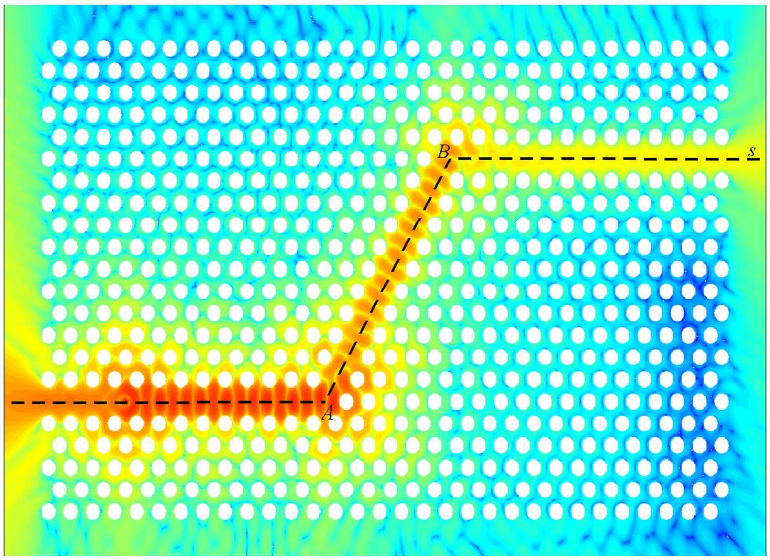

Figuur 43: Gelaagde elektromagnetisch-kristalgolfgeleider met twee bochten, magnetisch veld in het symmetrievlak.

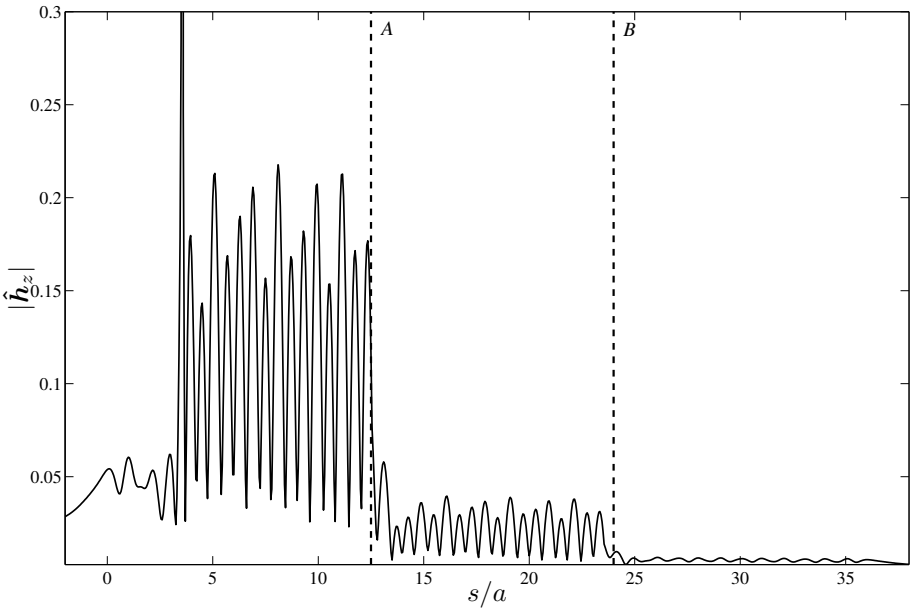

Figuur 44: Gelaagde elektromagnetisch-kristalgolfgeleider met twee bochten, magnetisch veld in het symmetrievlak volgens de as van de golfgeleider.

10 Besluit

In dit werk werden verschillende snelle en efficiënte technieken geïntroduceerd voor de simulatie van golfpropagatie in elektromagnetisch-kristalstructuren.

Ten eerste werden de eigenschappen van de eigenmodes van algemene periodieke golfgeleiders op een rigoureuze manier afgeleid door te vertrekken van het Lorentz reciprociteitstheorema. Naast de orthogonaliteit van deze eigenmodes, werd ook de bidirectionaliteit voor algemene periodieke golfgeleiders bewezen, een eigenschap die voorheen meestal zonder bewijs werd aangenomen in de literatuur. Hierop steunend konden formules worden afgeleid voor de excitatiecoëfficiënten van de eigenmodes wanneer een periodieke golfgeleider wordt geëxciteerd via een stroomdichtheid of via een extern invallend veld.

Om realistische 2D elektromagnetische-kristalstructuren te karakteriseren, werd geopteerd om een integraalvergelijkingstechniek te gebruiken, namelijk de meervoudige-verstrooiingstechniek. Deze techniek lost integraalvergelijkingen op in functie van equivalente stromen op het oppervlak van de cilinders. In vergelijking met de vaak gebruikte FDTD methode, heeft de meervoudige-verstrooiingstechniek geen last van fasefouten en is de nauwkeurigheid veel beter onder controle. Om ongewenste reflecties aan de poorten van elektromagnetisch-kristalstructuren te vermijden, werd een nieuwe absorberende randvoorwaarde, gebaseerd op PMLs, voorgesteld. Via deze absorberende randvoorwaarde wil men modelleren dat de elektromagnetisch-kristalstructuur eindigt in periodieke golfgeleiders die oneindig doorlopen in de propagatierichting. Door te steunen op de interpretatie van een PML met complexe coördinaten kan een periodieke golfgeleider

afgesloten worden door het toevoegen van een aantal extra periodes in het complexe vlak. Om enerzijds voldoende absorptie te bekomen en om anderzijds de periodiciteit niet teveel te verstoren, moet de overgang van reële naar complexe coördinaten zorgvuldig gekozen worden. De performantie van de randvoorwaarde werd bekeken voor zowel een lineaire als een ciculaire overgang door de simulatieresultaten te vergelijken met de exacte oplossing voor oneindige golfgeleiders zoals afgeleid uit het Lorentz reciprociteitstheorema. De beste resultaten worden bekomen met een circulaire overgang.

Omdat de meervoudige-verstrooiingstechniek uiteindelijk vereist dat een volledig gevuld stelsel wordt opgelost, zijn de rekencomplexiteit en de geheugenvereisten voor de analyse van realistische 2D elektromagnetisch-kristalstructuren vrij hoog, zeker wanneer dit stelsel via een directe methode wordt opgelost. In dat geval schalen de rekencomplexiteit en de geheugenvereisten immers respectievelijk als $O(N_c^3)$ en $O(N_c^2)$. Door het stelsel iteratief op te lossen in combinatie met een snel matrix-vector vermenigvuldigingsschema kan de rekencomplexiteit sterk gereduceerd worden. In deze tekst werden twee snelle vermenigvuldigingsschema's bestudeerd, namelijk MLFMA en een FFT-gebaseerd schema.

Via MLFMA kan de rekencomplexiteit gereduceerd worden tot $O(N_c \log_2^2 N_c)$ voor langgerekte structuren en zelfs tot $O(N_c)$ voor volle structuren. De bijhorende geheugenvereisten zijn respectievelijk $O(N_c \log_2 N_c)$ en $O(N_c)$. Dit schema is breed toepasbaar aangezien er vrijwel geen veronderstellingen worden gemaakt over de elektromagnetisch-kristalstructuur. Wanneer MLFMA wordt toegepast op elektromagnetisch-kristalstructuren die worden afgesloten met de nieuwe absorberende randvoorwaarde, wordt een extra reële coördinaat ingevoerd die als het ware de golfgeleiders volgt in het complexe vlak.

Voor structuren waarin alle cilinders geordend zijn volgens een regelmatig rooster, kan elke matrix-vector vermenigvuldiging geschreven worden als een twee-dimensionale convolutie. Via FFTs kunnen de rekencomplexiteit en de geheugenvereisten dan gereduceerd worden tot respectievelijk $O(N_c \log_2 N_c)$ en $O(N_c)$.

Helaas blijkt uit numerieke voorbeelden dat het aantal vereiste iteraties voor de karakterisatie van realistische elektromagnetisch-kristalstructuren, en bijgevolg ook de totale rekencomplexiteit, vrij hoog kan zijn, waardoor men zijn toevlucht moet nemen tot preconditioners. Drie verschillende types preconditioners werden vergeleken, namelijk een diagonale, blok-diagonale en afgeschermde-blok preconditioner. Vooral de afgeschermde-blok preconditioner reduceert het nodige aantal iteraties drastisch. Helaas is er wat dit betreft een belangrijk verschil tussen een defectloos kristal en een structuur met golfgeleiders. Voor de laatstgenoemde structuren zal het aantal nodige iteraties altijd hoger zijn. Om dezelfde efficiëntie te bereiken als een defectloos kristal, moet het golfgeleiderkarakter op de een of andere manier opgelost worden, wat vrijwel onmogelijk is met een iteratieve oplossingsmethode in combinatie met een preconditioner.

Voor elektromagnetisch-kristalstructuren die bekomen worden door, op een beperkt aantal afwijkende defecten na, cilinders te verwijderen uit een oneindig, defectloos kristal, kunnen de bovenstaande problemen omzeild worden door enkel equivalente stromen te beschouwen op verwijderde cilinders en hun interactie te beschrijven via de Greense functie van het kristal. Voor frequenties in de verboden zone van het kristal, is deze Greense functie exponentieel gedempt in functie van de afstand. Bijgevolg interageert elke onbekende slechts met de onbekenden in zijn nabije omgeving en moet uiteindelijk een dunbezet stelsel worden opgelost. Door de specifieke vorm van dit stelsel, kan het zeer

snel en efficiënt opgelost worden met een multi-frontale methode. Er werd aangetoond dat deze methode bijzonder geschikt is om de S-parameters van een elektromagnetisch-kristalstructuur te berekenen. De eigenmodes van de gepaste elektromagnetisch-kristal-golfgeleiders kunnen immers gemakkelijk bepaald worden en aangewend worden als excitatie of exacte absorberende randvoorwaarde.

Hoewel de bovenstaande technieken in dit werk enkel werden toegepast voor de TM_z-polarisatie op elektromagnetische kristallen waarin de cilinders gerangschikt zijn volgens een vierkant rooster, is de toepassing ervan op de TE_z-polarisatie of op hexagonale roosters triviaal. Ook elektromagnetische kristallen waarin de elementen niet-circulaire objecten zijn kunnen behandeld worden door gebruik te maken van hun verstrooiingsmatrices.

Tenslotte werd de klassieke meervoudige-verstrooiingstechniek uitgebreid voor de karakterisatie van gelaagde elektromagnetische kristallen bestaande uit gaten geëtst in een gelaagd medium. Door gebruik te maken van PMLs die afgesloten worden met perfecte geleiders, kan het open gelaagd medium gemodelleerd worden via een gesloten gelaagd medium met (vrijwel) hetzelfde elektromagnetisch gedrag. Via een circulaire mode-aanpassing kan de verstrooiingsmatrix van elk gat berekend worden. De matrix-elementen die de interacties tussen de verschillende gaten beschrijven zijn zeer nauw verwant aan de interacties uit de klassieke 2D meervoudige-verstrooiingstechniek. Hoewel het aantal onbekenden voor een realistisch gelaagd elektromagnetisch kristal groot is, zijn de rekencomplexiteit en de geheugenvereisten in deze methode toch beperkt indien het resulterend lineair stelsel via een iteratieve methode wordt opgelost. De nodige matrix-vector vermenigvuldigingen kunnen immers in twee stappen berekend worden. De eerste stap stemt overeen met het uitvoeren van een $2M$ 2D matrix-vermenigvuldigingen, waarvoor de rekencomplexiteit en de geheugenvereisten kunnen gereduceerd worden via de snelle en efficiënte matrix-vector vermenigvuldigingsschema's. In de tweede stap worden de onbekenden van elk gat vermenigvuldigd met de correcte verstrooiingsmatrix. Aangezien er meestal maar een beperkt aantal verschillende types gaten zijn, moeten er ook slechts een beperkt aantal verstrooiingsmatrices berekend en opgeslagen worden.

De resultaten van dit onderzoek werden opgenomen in tal van publicaties. Een overzicht van alle publicaties kan teruggevonden worden op het eind van de Engelstalige tekst.

Bibliografie

[1] R. R. Schaller, "Moore's law: Past, present and future," *IEEE Spectrum*, pp. 53–59, June 1997.

[2] J. D. Joannopoulos, R. D. Meade, and J. N. Winn, *Photonic Crystals, Molding the Flow of Light*. N.J.: Princeton Univ. Press, 1995.

[3] A. Mekis, J. Chen, I. Kurland, S. Fan, P. Villeneuve, and J. Joannopoulos, "High transmission through sharp bends in photonic crystal waveguides," *Phys. Rev. Lett*, vol. 77, no. 18, pp. 3787–3790, Oct. 1996.

[4] A. Chutinan and S. Noda, "Waveguides and waveguide bends in two-dimensional photonic crystal slabs," *Phys. Rev. B*, vol. 62, no. 7, pp. 4488–4492, Aug. 2000.

[5] H. Benisty, C. Weisbuch, M. Agio, M. Kafesaki, C. Soukoulis, M. Qiu, M. Swillo, A. Karlsson, B. Jaskorzynska, A. Talneau, J. Moosburger, M. Kamp, A. Forchell, R. Ferrini, R. Houdré, and U. Oesterle, "Models and measurements for the transmission of submicron-width waveguide bends defined in two-dimensional photonic crystals," *IEEE J. Quantum Electron.*, vol. 38, no. 7, pp. 770–785, July 2002.

[6] W. Bogaerts, "Nanophotonic waveguides and photonic crystals in silicon-on-insulator," Phd thesis, INTEC-Ghent University, Ghent, Belgium, 2003-2004.

[7] F. Olyslager, *Electromagnetic Waveguides and Transmission Lines*, ser. Oxford Engineering Science Series. Oxford: Clarendon Press, 1999.

[8] C. Elachi, "Waves in active and passive periodic structures: A review," *Proc. IEEE*, vol. 64, no. 12, pp. 1666–1698, Dec. 1976.

[9] A. Taflove, *Computational Electrodynamics: The Finite-Difference Time Domain Method*. Norwood: Artech House, 1995.

[10] B. Denecker, F. Olyslager, L. Knockaert, and D. D. Zutter, "Generation of FDTD subcell equations by means of reduced order modelling," *IEEE Trans. Antennas Propag.*, vol. 51, no. 8, pp. 1806–1817, Aug. 2003.

[11] H. Derudder, D. D. Zutter, and F. Olyslager, "A new way to analyse waveguide discontinuities using perfectly matched layers," *IEE Electronic Letters*, vol. 34, no. 22, pp. 2138–2140, Oct. 1998.

[12] P. Bienstman and R. Baets, "Optical modelling of photonic crystals and VCSELs using eigenmode expansion and perfectly matched layers," *Opt. Quantum Electron.*, vol. 33, no. 4-5, pp. 327–341, April 2001.

[13] G. Tayeb and D. Maystre, "Rigorous theoretical study of finite-size two-dimensional photonic crystals doped by microcavities," *J. Opt. Soc. Am. A*, vol. 14, no. 12, pp. 3323–3332, Dec. 1997.

[14] D. Pissoort, D. De Zutter, and F. Olyslager, "Efficient semi-analytical analysis of two-dimensional photonic crystals," in *IEEE AP-S Int. Symp.*, vol. 3, Columbus, OH, USA, June 2003, pp. 994–997.

[15] R. E. Collin, *Field Theory of Guided Waves*. New-York: IEEE Press, 1991.

[16] R. F. Harrington, *Time-Harmonic Electromagnetic Fields*, ser. Electrical and Electronic Engineering Series. New York: McGraw-Hill, 1961.

[17] M. Koshiba, Y. Tsuji, and S. Sasaki, "High-performance absorbing boundary conditions for photonic crystal waveguide simulations," *IEEE Microwave Wireless Comp. Lett.*, vol. 11, no. 4, pp. 152–154, April 2001.

[18] W. C. Chew and W. H. Weedon, "A 3D perfectly matched medium from modified Maxwell's equations in stretched coordinates," *Microwave Opt. Technol. Lett.*, vol. 7, no. 13, pp. 599–604, Sept. 1994.

[19] W. C. Chew, J. M. Jin, and E. Michielssen, "Complex coordinate stretching as a generalized absorbing boundary condition," *Microwave Opt. Technol. Lett.*, vol. 15, no. 6, pp. 363–369, Aug. 1997.

[20] M. Koshiba, "Wavelength division multiplexing and demultiplexing with photonic crystal waveguide couplers," *Journal of Lightwave Technology*, vol. 19, no. 12, pp. 1970–1975, Dec. 2001.

[21] S. Boscolo, M. Midrio, and C. G. Someda, "Coupling and decoupling of electromagnetic waves in parallel 2D photonic crystal waveguides," *IEEE J. Quantum Electron.*, vol. 1, no. 38, pp. 47–53, Jan. 2002.

[22] V. Rokhlin, "Rapid solution of integral equations of classical potential theory," *J. Comput. Phys.*, vol. 60, pp. 187–207, 1985.

[23] L. Greenhard and V. Rokhlin, "A fast algorithm for particle simulations," *J. Comput. Phys.*, vol. 73, pp. 325–348, 1987.

[24] L. G. J. Carrier and V. Rokhlin, "A fast adaptive multipole algorithm for particle simulations," *SIAM J. Sci. Stat. Comput.*, vol. 9, pp. 669–686, 1988.

[25] D. Vande Ginste, "Perfectly matched layer based fast multipole methods for planar microwave structures," Phd thesis, INTEC-Ghent University, Ghent, Belgium, 2004-2005.

[26] W. C. Chew, J. M. Jin, E. Michielssen, and J. Song, *Fast and Efficient Algorithms in Computational Electromagnetics*. Boston: Artech House, 2001.

[27] C. Chen, S. Shi, D. Prather, and A. Sharkawy, "Beam steering with photonic crystal horn radiators," *Optical Engineering*, vol. 68, pp. 174–180, Jan. 2004.

[28] A. Weily, K. Esselle, and B. Sanders, "Photonic crystal horn and array antennas," *Physical Review E*, vol. 68, 2003, paper no. 016609.

[29] I. Duff and J. Reid, "The multifrontal solution of unsymmetric sets of linear equations," *SIAM J. Sci. Comput.*, vol. 5, pp. 633–641, 1984.

[30] G. H. Golub and C. F. Van Loan, *Matrix Computations*. Baltimore, Maryland: The Johns Hopkins University Press, 1983.

[31] "http://www.cise.ufl.edu/ davis/."

[32] H. Derudder, F. Olyslager, D. De Zutter, and S. Van den Berghe, "Efficient mode-matching analysis of discontinuities in finite planar substrates using perfectly matched layers," *IEEE Trans. Antennas Propag.*, vol. 49, no. 2, pp. 1985–195, Feb. 2001.

[33] S. Shi, C. Chen, and D. Prather, "Plane-wave expansion method for calculating band structure of photonic crystal slabs with perfectly matched layers," *J. Opt. Soc. Am. A*, vol. 21, no. 9, pp. 1769–1774, Sep. 1999.

[34] "http://camfr.sourceforge.net."

English Text

Chapter 1

Introduction

1.1 Background

Technology is providing people all over the world with much better ways of communication than ever before. Increasing amounts of information flow from our computers through the Internet and from our mobile phones to places all over the world. Two simple but fundamental requirements are put on a modern information system. First of all, it must be fast so that large volumes of information can be transferred in a short time. Second, the user's apparatus must be small so that there is room for it in offices, homes, briefcases, or pockets. The invention of integrated electronic circuits brought an industrial revolution in all modern technology. Since the 1970s the number of electronic components that can be fitted onto a microchip has doubled every eighteen months, as predicted by Moore's law [1], allowing computers to double in speed, or half in price, during the same period.

The basic principles of digital communication are simple. To send, for example, a phone message or a picture, it is first encoded as a series of binary bits. These digital data packets are transmitted and decoded at the other end of the communication link to recreate the message or picture. The ones and zeroes are created by turning some signal on or off. In the past, the signal has been electrical, but nowadays it is most often composed of light pulses. In comparison to electrical signals, light pulses can be transmitted with less attenuation along an optical-fibre network. By consequence, in current communication systems, optical fibres have replaced electrical connections throughout most of the long-distance communication backbone infrastructure. In contrast to this, routing and regeneration are still done mainly electronically, resulting in a need for optoelectronic conversions.

Many different signals can be transmitted using a single wavelength by interweaving data packets from different sources, a technique known as *time division multiplexing*. A simple way of increasing the amount of data that can be transmitted by a single optical fibre is to make the pulses as short as possible. Another way to increase the capacity is to add new signals at other wavelengths, a method known as *wavelength division multiplexing*. However, in this case, the equipment for the optoelectronic conversions becomes highly complex. To circumvent this problem, photonic components should be integrated on chip. Such integration raises other problems, as there is then a need to develop small-

scale optical interconnects. These tiny planar waveguides should be able to steer light round tight corners. Traditionally, the guiding of light is achieved in dielectric structures, where the light is confined in a material with a higher dielectric permittivity than the surrounding material. When a large non-uniformity occurs in such a conventional waveguide, significant radiation losses appear. These radiation losses take place, for example, in sharp waveguide bends and in waveguide branches with large splitting angles. These problems severely limit the density of integration that can be achieved in an integrated optical circuit. Hence, unlike microelectronics, integrated photonic devices have remained approximately the same size over the past fifteen years. *Photonic* or *electromagnetic crytals* (ECs) [2], i.e., materials consisting of a periodic arrangement of dielectric/magnetic elements, could address some of the difficulties that currently limit the speed and capacity of optical-communications networks.

1.2 Electromagnetic crystals

The easiest way to understand the behavior of electromagnetic waves in an EC is to compare it with the movement of electrons and holes in a semiconductor. In a silicon crystal, for example, the atoms are arranged in a diamond-lattice structure. Electrons moving through this lattice experience a periodic potential as they interact with the silicon nuclei via the Coulomb force. This interaction results in the formation of allowed and forbidden energy states. For pure and perfect silicon crystals, no electrons will be found in an energy range called the forbidden energy gap or bandgap. However, the situation is different for real materials: electrons can have an energy within the bandgap if the periodicity of the lattice is broken by a missing silicon atom or by an impurity atom occupying a silicon site, or if the material contains interstitial impurities, viz. additional atoms located at non-lattice sites.

Now consider electromagnetic waves propagating through a block of dielectric/magnetic material (the background medium) that contains small elements of another dielectric/magnetic material arranged according to a periodic lattice. For an electromagnetic wave, the contrast in constitutive parameters between the background medium and the elements looks just like the periodic potential that an electron experiences when travelling through a silicon crystal. Indeed, if their is a large contrast in constitutive parameters between the two materials, then most of the electromagnetic waves will be confined within either the background material or in the elements. This confinement results in the existence of allowed frequency regions separated by a forbidden region - the so-called electromagnetic bandgap. The patterned dielectric material will block electromagnetic waves for frequencies in the electromagnetic bandgap, while for other frequencies, the electromagnetic waves can pass freely. As in semiconductors, it is possible to create localized electromagnetic modes in the electromagnetic bandgap by breaking the periodicity of the lattice.

A rough estimate of the spacing between the elements (or the lattice size) is given by the free-space wavelength divided by the square root of the relative dielectric permittivity of the background medium. To be able to create ECs for optical devices, state-of-the-art semiconductor-microfabrication techniques with their associated high production costs and investments have to be used. For this reason computer modeling of prospective

electromagnetic crystal structures is a very important area of research, as it may prevent expensive fabrication errors later.

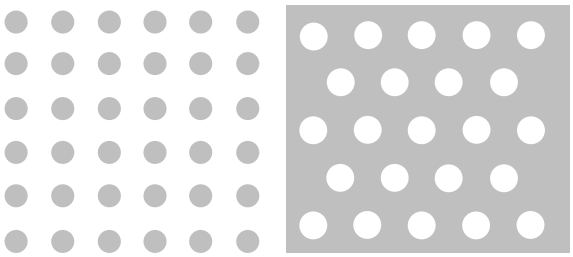

Figure 1.1: Basic geometries of 2D ECs.

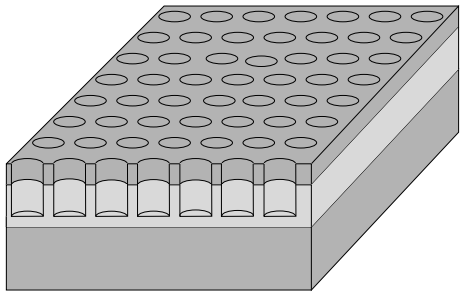

Figure 1.2: Electromagnetic crystal slab.

This work focusses on the development of efficient simulation techniques for the accurate characterization of ECs. With 3D ECs, viz. ECs which are periodic in all three directions, electromagnetic waves can be controlled in all directions. Unfortunately, these are difficult to fabricate and by consequence much attention is paid in the literature to 2D ECs. The two most common geometries are an array of dielectric cylinders surrounded by air and an array of air holes in a dielectric background medium (Fig. 1.1). The defects in 2D ECs are formed by adding or removing cylinders at one or more well defined positions in the lattice or by changing the material parameters of some of the cylinders. For example, a single point defect, made by changing one cylinder in the perfect lattice, can be used to define a high-Q cavity. A line defect can be obtained by removing a row of cylinders. In its turn, such a line defect can be used as a low-loss waveguide. The EC waveguides open the possibility to steer electromagnetic waves around very sharp bends with very low losses [3–5], because for frequencies in the electromagnetic bandgap, the electromagnetic waves cannot escape through the crystal.

In order to implement these devices in a realistic system, it is necessary to provide a mechanism to confine the electromagnetic waves also in the third direction. Therefore, the so-called EC slabs [6] have been presented (Fig. 1.2). The confinement in the third direction is in this case provided by a layered waveguide, while in the plane, propagation

is dictated by the properties of the 2D EC. These EC slabs are much more easily realized. The layered waveguide can be made by growing or depositing a layer structure, while the EC can be formed by etching, for example, air holes through the layered medium [7].

1.3 Numerical techniques

As stated in the previous section, because of the high production costs, the design of ECs asks for an accurate and efficient modelling of their electromagnetic behavior. Because of the constant increase of the data rates and the clock speeds, high-frequency phenomena play an ever more important role. Consider, for example, an interconnect. At low frequencies, this interconnect behaves as a perfect short circuit and allows the propagation of a signal from one point to another, without disturbing other interconnects or circuits. However, high-frequency signals, propagating along this interconnect, will be a source of crosstalk, resulting in a spurious signal in other interconnects or circuits. Because of reciprocity, the interconnect itself also becomes more susceptible to noise signals. Moreover, because of transmission line effects, the signals are delayed and distorted. It is not possible to predict these high-frequency phenomena with the so-called *circuit simulators*, e.g., SPICE, based on Kirchoff's laws. High-speed circuits must be analyzed using electromagnetic field theory. Many so-called *field simulators*, i.e., computer aided design tools based on the Maxwell equations have been proposed, where each technique has its own merits and reason for existence. An overview can be found in [8]. The most popular are the finite-elements method (FEM), the finite difference time domain (FDTD) method, and the boundary integral equation methods solved with the Method of Moments (MoM). More details on these methods can be found in [9] and the references therein.

1.4 Outline of this work

The organization of this work is as follows. In Chapter 2, a number of properties of the eigenmodes in general periodic waveguides are studied using the Lorentz reciprocity theorem. Although there is abundant literature on the theory of non-periodic waveguides and on the scattering of waves at periodic structures, such a consistent analysis of the eigenmodes of periodic waveguides seemed to be missing. First of all, the orthogonality relation between the eigenmodes is obtained together with another interesting integral relation that is satisfied by the modal fields in a periodic waveguide. The intimate relation between reciprocity and the bidirectionality of a periodic waveguide is proven. Based on orthogonality and bidirectionality, expressions for the excitation coefficients of the eigenmodes are given for an excitation comprising a source density or an incident field. Moreover, this analysis is generalized to include periodic waveguides composed of anisotropic or bianisotropic materials.

In recent years, many computational schemes for the characterization of EC devices have been proposed. In Chapter 3, three methods for the efficient simulation of 2D EC structures are compared, namely, a multiple scattering technique, an eigenmode expansion technique, and a Finite Difference Time Domain (FDTD) technique in combination with Reduced-Order Modelling (ROM). The main advantages and disadvantages of every

method are discussed. The basis principles of the three simulation techniques are summarized and some additional improvements over published results are presented. Finally, some EC filter structures are simulated and the results obtained with the different schemes are compared and discussed.

Many EC devices can be seen as N-ports for which the ports are periodic waveguides. When simulating such structures, these waveguides have to be terminated at a certain point in such a way that reflections are limited. In Chapter 4, a new way for the termination of periodic waveguides in integral equation like techniques is presented. Exploiting the complex coordinate interpretation of a Perfectly Matched Layer (PML), the periodic waveguides are terminated by adding a couple of periods in the complex plane, which means that the coordinate, corresponding to the direction of propagation, becomes complex. If the transition from real to complex coordinates happens smoothly, the reflections caused by the periodicity disturbance are very low and at the same time a significant absorption is achieved. The validity of this approach is demonstrated by comparison with the rigorous method based on the calculation of the excitation coefficients of the eigenmodes in a periodic waveguide as given in Chapter 2. Also a more complex EC device, namely, a two-channel multiplexer-demultiplexer, is considered.

The main disadvantage of the multiple scattering technique is that it requires the solution of a dense linear system of equations whose dimension scales proportional to the number of cylinders in the EC device, denoted by N_c. The cost of directly solving this system scales as $O(N_c^3)$. However, recently there has been a considerable interest in the development of fast schemes to iteratively solve such systems. The common goal of these fast schemes is to construct matrix-vector multiplication schemes characterized by a computational complexity and memory requirements lower than the $O(N_c^2)$ complexity of the classical matrix-vector multiplication scheme. In Chapter 5, the basic principles of two fast schemes for the simulation of wave propagation in 2D EC devices are described, namely, the multilevel fast multipole algorithm (MLFMA), which is the multilevel version of the fast multipole method (FMM), and a Fast Fourier Transform (FFT) based scheme. With the MLFMA the computational complexity for one iteration is reduced to $O(N_c \log_2^2 N_c)$ or even $O(N_c)$. This scheme is extended to the use of the complex coordinates that appear when using the PML based absorbing boundary conditions of Chapter 4. Multiplication schemes based on FFTs are very well suited for EC devices for which all cylinders are arranged according to a regular grid. These schemes exploit the convolutional nature of the matrix-vector multiplication to reduce the computational complexity to $O(N_c \log_2 N_c)$.

Unfortunately, the overall cost for the iterative solution of the linear system also scales proportional to the total number of iterations P required for the residual error to fall below a preset threshold. Numerical experiments show that the analysis of realistic EC devices often requires a high number of iterations. Hence, preconditioning is a must. Chapter 6 discusses the effectiveness of three preconditioners, namely, a diagonal, block-diagonal, and shielded-block preconditioner. These preconditioners, especially the shielded-block preconditioner, effectively reduce the required number of iterations to characterize defect-less ECs, this contrary to the characterization of EC devices containing waveguide components. Even with a state-of-the-art preconditioner, the number of iterations for the analysis of an EC waveguide will be higher than that for a defect-less EC. To obtain the same computational complexity, the waveguiding character of the EC device has to be

resolved.

In Chapter 7, a novel and fast multiple scattering technique for analyzing electromagnetic wave propagation in 2D EC devices is presented. A small number of irregular defects aside, the targeted devices are obtained by removing cylinders from infinite, doubly periodic, and defect-less ECs. This new multiple scattering technique solves integral equations in terms of equivalent currents residing on the surfaces of the removed cylinders. The interactions between these currents are modeled via a Green function innate to the surrounding infinite EC. As for frequencies in the bandgap, the EC Green function decays exponentially with distance, it can be computed using the conventional multiple scattering technique. The sparse system that results upon discretizing the integral equations can be solved efficiently by a multi-frontal method. This new scheme is ideally suited to compute the EC device's S-parameters, as it permits imposing modal excitations and absorbing boundary conditions. It is shown that the proposed method also applies to EC devices with a small number of other defects, e.g., cylinders with center positions, radii, and/or material parameters that do not conform to those of the EC background. It will be shown that these devices can be characterized by Green functions that are low-rank perturbations of that of the defect-less EC.

Finally, in Chapter 8, a new technique for analyzing wave propagation in EC slabs, consisting of air holes in an open layered medium, is presented. This new technique combines a cylindrical mode-matching technique with the 2D multiple scattering technique. The characterization of the open layered medium is transformed into the characterization of a closed one with (almost) the same electromagnetic behavior by terminating the outermost layers with PMLs, backed by perfectly conducting plates. The scattering matrix of every air hole can be easily obtained using a cylindrical mode-matching technique at its surface. The interactions between the different air holes are described by matrix elements similar to those in the 2D multiple scattering technique. The resulting linear system of equations is solved iteratively. By performing the matrix-vector multiplications in two steps, the computational complexity and the memory requirements can be kept low. The versatility of the new technique is demonstrated via its application to the analysis of a straight hexagonal EC waveguide and a hexagonal EC waveguide with two 60^{o} bends.

Most chapters in this work are papers that are either already published (Chapters 2, 3 and 4) or that are submitted for publication (Chapter 7). Chapters 5 and 6 are both enlarged versions of conference papers with some extra information. Chapter 8 is in preparation for submission. Because of this approach, every chapter can be understood very easily without having to read all the previous chapters. A disadvantage is that the notation may differ slightly and that the basic principles of the multiple scattering technique are repeated a few times.

Bibliography

[1] R. R. Schaller, "Moore's law: Past, present and future," *IEEE Spectrum*, pp. 53–59, June 1997.

[2] J. D. Joannopoulos, R. D. Meade, and J. N. Winn, *Photonic Crystals, Molding the Flow of Light*. N.J.: Princeton Univ. Press, 1995.

[3] A. Mekis, J. Chen, I. Kurland, S. Fan, P. Villeneuve, and J. Joannopoulos, "High transmission through sharp bends in photonic crystal waveguides," *Phys. Rev. Lett*, vol. 77, no. 18, pp. 3787–3790, Oct. 1996.

[4] A. Chutinan and S. Noda, "Waveguides and waveguide bends in two-dimensional photonic crystal slabs," *Phys. Rev. B*, vol. 62, no. 7, pp. 4488–4492, Aug. 2000.

[5] H. Benisty, C. Weisbuch, M. Agio, M. Kafesaki, C. Soukoulis, M. Qiu, M. Swillo, A. Karlsson, B. Jaskorzynska, A. Talneau, J. Moosburger, M. Kamp, A. Forchell, R. Ferrini, R. Houdré, and U. Oesterle, "Models and measurements for the transmission of submicron-width waveguide bends defined in two-dimensional photonic crystals," *IEEE J. Quantum Electron.*, vol. 38, no. 7, pp. 770–785, July 2002.

[6] S. Johnson, S. Fan, P. Villeneuve, and J. Joannopoulos, "Guided modes in photonic crystal slabs," *Phys. Rev. B*, vol. 60, no. 8, pp. 5751–5758, Aug. 1999.

[7] W. Bogaerts, "Nanophotonic waveguides and photonic crystals in silicon-on-insulator," Phd thesis, INTEC-Ghent University, Ghent, Belgium, 2003-2004.

[8] "http://www.emclab.umr.edu/csoft.html."

[9] H. Rogier, "Numerieke oplossing van de Maxwell vergelijkingen door combinatie van eindige differenties of eindige elementen met integraalvergelijkingen," Phd thesis, Ghent-University, Gent, Belgium, 1998–1999.

Chapter 2

Study of Eigenmodes in Periodic Waveguides Using the Lorentz Reciprocity Theorem

Davy Pissoort and Frank Olyslager

Published in IEEE Transactions on Microwave Theory and Techniques, Vol. 52, no. 2, pp. 542–553, February 2004

Abstract

Photonic crystals, frequency selective surfaces, gratings, and many so-called metamaterials are composed of periodic arrangements of objects. Such an arrangement of objects quickly forms a periodic waveguide. In this paper, we investigate a number of properties of the eigenmodes in general periodic waveguides using the Lorentz reciprocity theorem. Such an analysis seems to be missing in the literature. We present an original proof for the intimate relation between bidirectionality of a periodic waveguide and reciprocity. We also derive compact expressions for the excitation coefficients of the eigenmodes when the waveguide is excited by a source density or an incident field. The analysis is generalized to include periodic waveguides composed of anisotropic and bianisotropic materials.

2.1 Introduction

The interesting properties and the fabrication of photonic bandgap (PBG) materials or electromagnetic crystals (ECs) [1] have increased the interest in periodic waveguides. The propagation in a sourceless region in a periodic waveguide can be decomposed in the propagation of the eigenmodes of the waveguide. In this paper, we want to proof a number of properties of these eigenmodes using the Lorentz reciprocity theorem. It seems that in

the literature such a consistent analysis is missing. However, there is abundant literature on the theory of non-periodic waveguides and also on the scattering of waves at periodic structures. An overview up to 1975 can be found in [2]. In the optical literature, photonic bandgap structures are usually treated from the crystal viewpoint [1] and not so much from the waveguide viewpoint.

In [3], the properties of eigenmodes in regular waveguides were studied using the Lorentz reciprocity theorem. In this paper, we extend this to general periodic waveguides. A periodic waveguide is defined as a structure where the material parameters have a periodic dependence on one coordinate and an arbitrary dependence on the other two coordinates. This covers a very wide range of structures.

First we derive the orthogonality relation between the eigenmodes. Such an analysis is certainly not new [4, 5], but we need the results for further analysis, and apart from the orthogonality relations we obtain another integral relation that is satisfied by the modal fields in a periodic waveguide.

Then we consider periodic waveguides that have a symmetry plane perpendicular to the propagation direction in each period. In such symmetric waveguides, the eigenmodes come in pairs consisting of an eigenmode and its mirror image propagating in the opposite direction. A waveguide is said to be 'bidirectional' if for each mode with propagation coefficient γ there exists another mode with propagation coefficient $-\gamma$. A symmetric waveguide clearly is bidirectional. However, for a non-symmetric periodic waveguide this is less obvious. The Lorentz reciprocity theorem allows us to prove this. What is remarkable is that the modal fields of modes that propagate in opposite directions are not easily related as in the symmetric case. In [6], some allusion is made to bidirectionality, however without any proof. In [5], the bidirectionality property of a rectangular waveguide, periodically filled by a sinusoidally dielectric, is studied. The results follow from an analytical solution of the governing wave equation. Note that the studied waveguide is also a symmetric periodic waveguide, trivially implying bidirectionality. A more rigorous treatment of bidirectionality can be found in [4]. There closed waveguides with periodic walls in which the material parameters are constant in each cross section are studied. In each cross section, the waveguide is a non-periodic homogeneously filled waveguide that allows TE (Transverse Electric) and TM (Transverse Magnetic) modes. The introduction of a circuit representation for these modes allows the derivation of the bidirectionality property using circuit analysis techniques and reciprocity properties. In [7], bidirectionality in a periodic arrangement of electrical four ports is studied.

An isotropic non-periodic waveguide obviously is bidirectional. However, when the materials become reciprocal anisotropic or bianisotropic, this is less obvious as it is less obvious for an isotropic periodic waveguide. The bidirectionality of regular, anisotropic waveguides was studied in [8] and [9] based on circuit concepts. However, as is shown in [3, 10], the proof of Harrington and Villeneuve has its limitations. In [3, 10], a rigorous proof based on the Lorentz reciprocity theorem is presented. The proof in this paper for periodic waveguides is inspired by the proof in [3, 10]. Bidirectionality due to symmetry properties in reciprocal and non-reciprocal waveguides were studied in [11].

As stated earlier, in the optical literature periodic structures are treated as crystals, i.e., as periodic arrangements of objects or motives. When studying the photonic bandgap structures, one usually does not discuss its bidirectionality property, but one just assumes it without a motivation. This is usually correct because the motives are highly symmetric,

such as cylinders, resulting in symmetric waveguides. For nonsymmetric objects, the assumption is correct but not obvious, as will be proven in this paper.

We also consider the excitation of a periodic waveguide, i.e., we determine by what amount the eigenmodes are excited by a source density in the structure or by an incident field on the structure. The excitation, be it by a source density or an incident wave, of periodic structures and periodic waveguides in particular has been studied frequently. However, most often, the total fields generated by the sources are evaluated immediately, see, e.g., [2]. In the present contribution, using again the Lorentz reciprocity theorem, we immediately derive compact expressions for the excitation coefficients of the eigenmodes in periodic waveguides as a function of the exciting source densities or incident fields. This then also yields a series representation for the Green dyadics in a periodic waveguide. It is also interesting that it is not necessary to solve first the full scattering problem of an incident wave on a waveguide; knowledge of the modal and incident fields suffice to calculate the excitation coefficients.

The properties of waveguides in [3, 10] were not only studied in isotropic waveguides but also in anisotropic and even bianisotropic waveguides. In this paper, we also generalize the properties of eigenmodes in periodic waveguides to periodic waveguides composed of isotropic and bianisotropic materials. This requires the introduction of the concept of adjoint waveguides [12]. This extension is motivated by the increasing importance of these type of media. Think for example about metamaterials [13], such as the negative index or backward wave media that have been fabricated recently [14]. Many of these metamaterials are periodic structures on a microscopic level and behave as anisotropic or bianisotropic media on a macroscopic level.

To illustrate and numerically test our findings, some examples of periodically loaded rectangular waveguides and electromagnetic crystal waveguides are added.

2.2 Properties of eigenmodes in a periodic waveguide

Let us consider an isotropic medium where we assume that the material parameters $\epsilon(\boldsymbol{r})$ and $\mu(\boldsymbol{r})$ have an arbitrary dependence on the x and y coordinates and are periodic with periodicity T in the z direction, i.e., $\epsilon(\boldsymbol{\rho}, z+T) = \epsilon(\boldsymbol{\rho}, z)$ and $\mu(\boldsymbol{\rho}, z+T) = \mu(\boldsymbol{\rho}, z)$, where $\boldsymbol{\rho} = x\boldsymbol{u}_x + y\boldsymbol{u}_y$. This defines a periodic waveguide. According to the Floquet-Bloch theorem, the fields in such a periodic waveguide can be written as quasi-periodic functions

$$\boldsymbol{e}(\boldsymbol{\rho}, z) = [\boldsymbol{E}_t(\boldsymbol{\rho}, z) + E_z(\boldsymbol{\rho}, z)\boldsymbol{u}_z]\, e^{-\gamma z}, \tag{2.1}$$

$$\boldsymbol{h}(\boldsymbol{\rho}, z) = [\boldsymbol{H}_t(\boldsymbol{\rho}, z) + H_z(\boldsymbol{\rho}, z)\boldsymbol{u}_z]\, e^{-\gamma z}, \tag{2.2}$$

with

$$\boldsymbol{E}_t(\boldsymbol{\rho}, z+T) + E_z(\boldsymbol{\rho}, z+T)\boldsymbol{u}_z = \boldsymbol{E}_t(\boldsymbol{\rho}, z) + E_z(\boldsymbol{\rho}, z)\boldsymbol{u}_z, \tag{2.3}$$

$$\boldsymbol{H}_t(\boldsymbol{\rho}, z+T) + H_z(\boldsymbol{\rho}, z+T)\boldsymbol{u}_z = \boldsymbol{H}_t(\boldsymbol{\rho}, z) + H_z(\boldsymbol{\rho}, z)\boldsymbol{u}_z. \tag{2.4}$$

The subscript $'t'$ indicates the transverse part or xy-components of the fields. The source-free Maxwell equations will yield non-trivial solutions of the form (2.1) and (2.2) only for discrete values of the propagation coefficient γ.

Let us now expand the periodic functions in (2.1) and (2.2) into a Fourier series with periodicity T as follows:

$$\boldsymbol{e}(\boldsymbol{\rho},z) = \sum_{n=-\infty}^{+\infty} [\boldsymbol{E}_t^n(\boldsymbol{\rho}) + E_z^n(\boldsymbol{\rho})\boldsymbol{u}_z]\, e^{-\frac{j2\pi nz}{T}} e^{-\gamma z}, \tag{2.5}$$

$$\boldsymbol{h}(\boldsymbol{\rho},z) = \sum_{n=-\infty}^{+\infty} [\boldsymbol{H}_t^n(\boldsymbol{\rho}) + H_z^n(\boldsymbol{\rho})\boldsymbol{u}_z]\, e^{-\frac{j2\pi nz}{T}} e^{-\gamma z}, \tag{2.6}$$

and similarly for $\epsilon(\boldsymbol{\rho},z)$ and $\mu(\boldsymbol{\rho},z)$ as

$$\epsilon(\boldsymbol{\rho},z) = \sum_{n=-\infty}^{+\infty} \epsilon^n(\boldsymbol{\rho}) e^{-\frac{j2\pi nz}{T}}, \tag{2.7}$$

$$\mu(\boldsymbol{\rho},z) = \sum_{n=-\infty}^{+\infty} \mu^n(\boldsymbol{\rho}) e^{-\frac{j2\pi nz}{T}}. \tag{2.8}$$

Substituting (2.5)–(2.8) into the source-free Maxwell curl equations and equating Fourier components of the same order yields the following infinite set of equations:

$$\boldsymbol{\nabla}_t \times E_z^n(\boldsymbol{\rho})\boldsymbol{u}_z - \gamma^n \boldsymbol{u}_z \times \boldsymbol{E}_t^n(\boldsymbol{\rho}) = -j\omega \sum_{l=-\infty}^{+\infty} \mu^{n-l}(\boldsymbol{\rho})\boldsymbol{H}_t^l(\boldsymbol{\rho}), \tag{2.9}$$

$$\boldsymbol{\nabla}_t \times \boldsymbol{E}_t^n(\boldsymbol{\rho}) = -j\omega \sum_{l=-\infty}^{+\infty} \mu^{n-l}(\boldsymbol{\rho}) H_z^l(\boldsymbol{\rho})\boldsymbol{u}_z, \tag{2.10}$$

$$\boldsymbol{\nabla}_t \times H_z^n(\boldsymbol{\rho})\boldsymbol{u}_z - \gamma^n \boldsymbol{u}_z \times \boldsymbol{H}_t^n(\boldsymbol{\rho}) = j\omega \sum_{l=-\infty}^{+\infty} \epsilon^{n-l}(\boldsymbol{\rho})\boldsymbol{E}_t^l(\boldsymbol{\rho}), \tag{2.11}$$

$$\boldsymbol{\nabla}_t \times \boldsymbol{H}_t^n(\boldsymbol{\rho}) = j\omega \sum_{l=-\infty}^{+\infty} \epsilon^{n-l}(\boldsymbol{\rho}) E_z^l(\boldsymbol{\rho})\boldsymbol{u}_z, \tag{2.12}$$

with $n = -\infty, \cdots, -1, 0, 1, \cdots, +\infty$ and $\gamma^n = \gamma + j\dfrac{2\pi n}{T}$. The non-trivial solutions of this set of equations, corresponding to specific values of γ, are called the eigenmodes.

2.2.1 Orthogonality

Now we will investigate some properties of these eigenmodes using the Lorentz reciprocity theorem. Consider a piece of a periodic waveguide located between the plane $S(z_1)$ at $z = z_1$ and the plane $S(z_2)$ at $z = z_2$. Let V denote the volume bounded by the planes $S(z_1)$ and $S(z_2)$, as indicated in Fig. 2.1. If the waveguide is not an open waveguide, i.e., if it is bounded in the xy-plane (e.g., with a perfectly conducting shell), then the volume V is also transversely bounded by a surface S_o. For an open waveguide, S_o is located entirely or partly at infinity. Hence, the surface S of the volume V consists

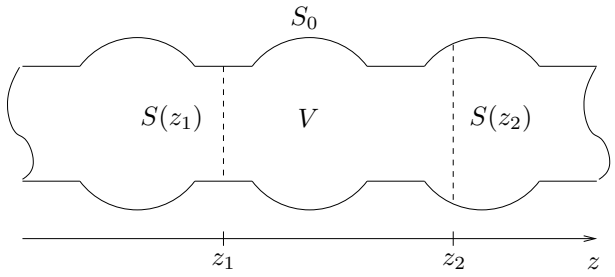

Figure 2.1: A piece of a periodic waveguide relevant to the Lorentz reciprocity theorem.

of $S(z_1)$, $S(z_2)$, and S_o. Let us now apply the Lorentz reciprocity theorem to the volume V for two independent solutions $(\boldsymbol{e}_a, \boldsymbol{h}_a)$ and $(\boldsymbol{e}_b, \boldsymbol{h}_b)$ of the Maxwell equations

$$\int_S (\boldsymbol{e}_a \times \boldsymbol{h}_b - \boldsymbol{e}_b \times \boldsymbol{h}_a) \cdot \boldsymbol{u}_n dS = 0, \tag{2.13}$$

where we assume that there are no sources for these fields inside the volume V. One now easily proves that two different modes are orthogonal. Assume that the a-fields in (2.13) are a mode with subscript i as follows:

$$\boldsymbol{e}_a(\boldsymbol{\rho}, z) = [\boldsymbol{E}_{i,t}(\boldsymbol{\rho}, z) + E_{i,z}(\boldsymbol{\rho}, z)\boldsymbol{u}_z]\, e^{-\gamma_i z}, \tag{2.14}$$

$$\boldsymbol{h}_a(\boldsymbol{\rho}, z) = [\boldsymbol{H}_{i,t}(\boldsymbol{\rho}, z) + H_{i,z}(\boldsymbol{\rho}, z)\boldsymbol{u}_z]\, e^{-\gamma_i z}, \tag{2.15}$$

and the b-fields a mode with subscript j as follows:

$$\boldsymbol{e}_b(\boldsymbol{\rho}, z) = [\boldsymbol{E}_{j,t}(\boldsymbol{\rho}, z) + E_{j,z}(\boldsymbol{\rho}, z)\boldsymbol{u}_z]\, e^{-\gamma_j z}, \tag{2.16}$$

$$\boldsymbol{h}_b(\boldsymbol{\rho}, z) = [\boldsymbol{H}_{j,t}(\boldsymbol{\rho}, z) + H_{j,z}(\boldsymbol{\rho}, z)\boldsymbol{u}_z]\, e^{-\gamma_j z}. \tag{2.17}$$

The part in the Lorentz reciprocity theorem that corresponds to the integration on S_o equals zero for a closed waveguide due to the boundary condition on S_o; for an open waveguide it is assumed that the fields decrease fast enough [3]. By consequence, the Lorentz reciprocity theorem reduces to

$$\begin{aligned} &- \int_{S(z_1)} [\boldsymbol{E}_{i,t}(\boldsymbol{\rho}, z_1) \times \boldsymbol{H}_{j,t}(\boldsymbol{\rho}, z_1) - \boldsymbol{E}_{j,t}(\boldsymbol{\rho}, z_1) \times \boldsymbol{H}_{i,t}(\boldsymbol{\rho}, z_1)] \cdot \boldsymbol{u}_z dS e^{-(\gamma_i+\gamma_j)z_1} \\ &+ \int_{S(z_2)} [\boldsymbol{E}_{i,t}(\boldsymbol{\rho}, z_2) \times \boldsymbol{H}_{j,t}(\boldsymbol{\rho}, z_2) - \boldsymbol{E}_{j,t}(\boldsymbol{\rho}, z_2) \times \boldsymbol{H}_{i,t}(\boldsymbol{\rho}, z_2)] \cdot \boldsymbol{u}_z dS e^{-(\gamma_i+\gamma_j)z_2} \\ &= 0. \end{aligned} \tag{2.18}$$

Take $z_2 = z_1 + T$, then $\boldsymbol{E}(\boldsymbol{\rho}, z_2) = \boldsymbol{E}(\boldsymbol{\rho}, z_1)$ and $\boldsymbol{H}(\boldsymbol{\rho}, z_2) = \boldsymbol{H}(\boldsymbol{\rho}, z_1)$. This yields

$$\begin{aligned} \int_{S(z_1)} [\boldsymbol{E}_{i,t}(\boldsymbol{\rho}, z_1) \times \boldsymbol{H}_{j,t}(\boldsymbol{\rho}, z_1) - \boldsymbol{E}_{j,t}(\boldsymbol{\rho}, z_1) \times \boldsymbol{H}_{i,t}(\boldsymbol{\rho}, z_1)] \cdot \boldsymbol{u}_z dS \times \\ \{e^{-(\gamma_i+\gamma_j)T} - 1\} = \quad 0. \end{aligned} \tag{2.19}$$

If we only look for the propagation coefficients in the first Brillouin zone $[-\frac{\pi}{T}, +\frac{\pi}{T}]$ and assume that $\gamma_i \neq -\gamma_j$, we obtain

$$\int_{S(z)} [\boldsymbol{E}_{i,t}(\boldsymbol{\rho}, z) \times \boldsymbol{H}_{j,t}(\boldsymbol{\rho}, z) - \boldsymbol{E}_{j,t}(\boldsymbol{\rho}, z) \times \boldsymbol{H}_{i,t}(\boldsymbol{\rho}, z)] \cdot \boldsymbol{u}_z dS = 0, \tag{2.20}$$

which is the orthogonality relation for the modes in a periodic waveguide.

It is now possible to obtain another interesting property from the Lorentz reciprocity theorem. Assume that there is a mode with propagation coefficient γ_i and another mode with propagation coefficient $\tilde{\gamma}_i = -\gamma_i$. We take these modes as the 'a' and 'b'-fields in the reciprocity theorem (2.13), i.e.,

$$\begin{aligned}
\boldsymbol{e}_a(\boldsymbol{\rho}, z) &= [\boldsymbol{E}_{i,t}(\boldsymbol{\rho}, z) + E_{i,z}(\boldsymbol{\rho}, z)\boldsymbol{u}_z]\, e^{-\gamma_i z}, && (2.21)\\
\boldsymbol{h}_a(\boldsymbol{\rho}, z) &= [\boldsymbol{H}_{i,t}(\boldsymbol{\rho}, z) + H_{i,z}(\boldsymbol{\rho}, z)\boldsymbol{u}_z]\, e^{-\gamma_i z}, && (2.22)\\
\boldsymbol{e}_b(\boldsymbol{\rho}, z) &= \left[\tilde{\boldsymbol{E}}_{i,t}(\boldsymbol{\rho}, z) + \tilde{E}_{i,z}(\boldsymbol{\rho}, z)\boldsymbol{u}_z\right] e^{\gamma_i z}, && (2.23)\\
\boldsymbol{h}_b(\boldsymbol{\rho}, z) &= \left[\tilde{\boldsymbol{H}}_{i,t}(\boldsymbol{\rho}, z) + \tilde{H}_{i,z}(\boldsymbol{\rho}, z)\boldsymbol{u}_z\right] e^{\gamma_i z}. && (2.24)
\end{aligned}$$

From (2.13), it follows that

$$\begin{aligned}
&\int_{S(z_1)} \left[\boldsymbol{E}_{i,t}(\boldsymbol{\rho}, z_1) \times \tilde{\boldsymbol{H}}_{i,t}(\boldsymbol{\rho}, z_1) - \tilde{\boldsymbol{E}}_{i,t}(\boldsymbol{\rho}, z_1) \times \boldsymbol{H}_{i,t}(\boldsymbol{\rho}, z_1)\right] \cdot \boldsymbol{u}_z dS \quad =\\
&\int_{S(z_2)} \left[\boldsymbol{E}_{i,t}(\boldsymbol{\rho}, z_2) \times \tilde{\boldsymbol{H}}_{i,t}(\boldsymbol{\rho}, z_2) - \tilde{\boldsymbol{E}}_{i,t}(\boldsymbol{\rho}, z_2) \times \boldsymbol{H}_{i,t}(\boldsymbol{\rho}, z_2)\right] \cdot \boldsymbol{u}_z dS, \qquad (2.25)
\end{aligned}$$

which means that

$$\int_{S(z)} \left[\boldsymbol{E}_{i,t}(\boldsymbol{\rho}, z) \times \tilde{\boldsymbol{H}}_{i,t}(\boldsymbol{\rho}, z) - \tilde{\boldsymbol{E}}_{i,t}(\boldsymbol{\rho}, z) \times \boldsymbol{H}_{i,t}(\boldsymbol{\rho}, z)\right] \cdot \boldsymbol{u}_z dS \quad = \quad c, \tag{2.26}$$

with c a z-independent constant.

2.2.2 Bidirectionality for a symmetric periodic waveguides

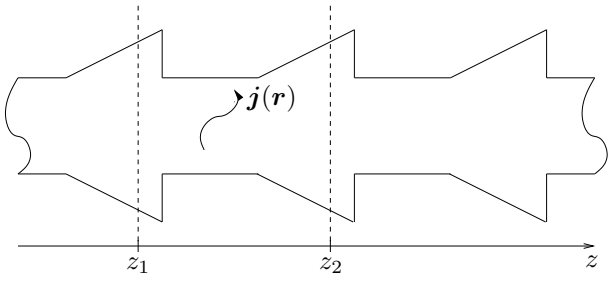

Figure 2.2: Periodic waveguide excited by a current source density $\boldsymbol{j}(\boldsymbol{r})$.

Consider a periodic waveguide in which it is possible to choose the origin $z = 0$ such that $\mu(\boldsymbol{\rho}, -z) = \mu(\boldsymbol{\rho}, z)$ and $\epsilon(\boldsymbol{\rho}, -z) = \epsilon(\boldsymbol{\rho}, z)$, i.e., $z = 0$ is a symmetry plane of the

waveguide. Figure 2.1 is an example of such a waveguide. Figure 2.2 is a counterexample. We will now show for such a waveguide that, if γ, $\boldsymbol{E}_t(\boldsymbol{\rho}, z)$, $E_z(\boldsymbol{\rho}, z)$, $\boldsymbol{H}_t(\boldsymbol{\rho}, z)$, $H_z(\boldsymbol{\rho}, z)$ is a solution, then $-\gamma$, $\boldsymbol{E}_t(\boldsymbol{\rho}, -z)$, $-E_z(\boldsymbol{\rho}, -z)$, $-\boldsymbol{H}_t(\boldsymbol{\rho}, -z)$, $H_z(\boldsymbol{\rho}, -z)$ is also a solution. Let us write the forward mode as

$$\begin{aligned}
\boldsymbol{e}^+(\boldsymbol{\rho}, z) &= [\boldsymbol{E}_t(\boldsymbol{\rho}, z) + E_z(\boldsymbol{\rho}, z)\boldsymbol{u}_z]\, e^{-\gamma z} \\
&= \sum_n [\boldsymbol{E}_t^n(\boldsymbol{\rho}) + E_z^n(\boldsymbol{\rho})\boldsymbol{u}_z]\, e^{-(\gamma + \frac{j2\pi n}{T})z}, \qquad (2.27) \\
\boldsymbol{h}^+(\boldsymbol{\rho}, z) &= [\boldsymbol{H}_t(\boldsymbol{\rho}, z) + H_z(\boldsymbol{\rho}, z)\boldsymbol{u}_z]\, e^{-\gamma z} \\
&= \sum_n [\boldsymbol{H}_t^n(\boldsymbol{\rho}) + H_z^n(\boldsymbol{\rho})\boldsymbol{u}_z]\, e^{-(\gamma + \frac{j2\pi n}{T})z}, \qquad (2.28)
\end{aligned}$$

and the backward mode as

$$\begin{aligned}
\boldsymbol{e}^-(\boldsymbol{\rho}, z) &= \left[\tilde{\boldsymbol{E}}_t(\boldsymbol{\rho}, z) + \tilde{E}_z(\boldsymbol{\rho}, z)\boldsymbol{u}_z\right] e^{\tilde{\gamma} z} \\
&= \sum_n \left[\tilde{\boldsymbol{E}}_t^n(\boldsymbol{\rho}) + \tilde{E}_z^n(\boldsymbol{\rho})\boldsymbol{u}_z\right] e^{(\tilde{\gamma} - \frac{j2\pi n}{T})z}, \qquad (2.29) \\
\boldsymbol{h}^-(\boldsymbol{\rho}, z) &= \left[\tilde{\boldsymbol{H}}_t(\boldsymbol{\rho}, z) + \tilde{H}_z(\boldsymbol{\rho}, z)\boldsymbol{u}_z\right] e^{\tilde{\gamma} z} \\
&= \sum_n \left[\tilde{\boldsymbol{H}}_t^n(\boldsymbol{\rho}) + \tilde{H}_z^n(\boldsymbol{\rho})\boldsymbol{u}_z\right] e^{(\tilde{\gamma} - \frac{j2\pi n}{T})z}. \qquad (2.30)
\end{aligned}$$

The forward mode satisfies equations (2.9)–(2.12), while the backward mode satisfies

$$\begin{aligned}
\boldsymbol{\nabla}_t \times \tilde{E}_z^n(\boldsymbol{\rho})\boldsymbol{u}_z + \tilde{\gamma}^n \boldsymbol{u}_z \times \tilde{\boldsymbol{E}}_t^n(\boldsymbol{\rho}) &= -j\omega \sum_{l=-\infty}^{+\infty} \mu^{n-l}(\boldsymbol{\rho})\tilde{\boldsymbol{H}}_t^l(\boldsymbol{\rho}), \qquad (2.31) \\
\boldsymbol{\nabla}_t \times \tilde{\boldsymbol{E}}_t^n(\boldsymbol{\rho}) &= -j\omega \sum_{l=-\infty}^{+\infty} \mu^{n-l}(\boldsymbol{\rho})\tilde{H}_z^l(\boldsymbol{\rho})\boldsymbol{u}_z, \qquad (2.32) \\
\boldsymbol{\nabla}_t \times \tilde{H}_z^n(\boldsymbol{\rho})\boldsymbol{u}_z + \tilde{\gamma}^n \boldsymbol{u}_z \times \tilde{\boldsymbol{H}}_t^n(\boldsymbol{\rho}) &= j\omega \sum_{l=-\infty}^{+\infty} \epsilon^{n-l}(\boldsymbol{\rho})\tilde{\boldsymbol{E}}_t^l(\boldsymbol{\rho}), \qquad (2.33) \\
\boldsymbol{\nabla}_t \times \tilde{\boldsymbol{H}}_t^n(\boldsymbol{\rho}) &= j\omega \sum_{l=-\infty}^{+\infty} \epsilon^{n-l}(\boldsymbol{\rho})\tilde{E}_z^l(\boldsymbol{\rho})\boldsymbol{u}_z, \qquad (2.34)
\end{aligned}$$

with $\tilde{\gamma}^n = \tilde{\gamma} - \dfrac{j2\pi n}{T}$. If we replace n by $-n$, $\tilde{\boldsymbol{E}}_t^{-n}(\boldsymbol{\rho})$ by $\boldsymbol{E}_t^n(\boldsymbol{\rho})$, $\tilde{E}_z^{-n}(\boldsymbol{\rho})$ by $-E_z^n(\boldsymbol{\rho})$, $\tilde{\boldsymbol{H}}_t^{-n}(\boldsymbol{\rho})$ by $-\boldsymbol{H}_t^n(\boldsymbol{\rho})$, $\tilde{H}_z^{-n}(\boldsymbol{\rho})$ by $H_z^n(\boldsymbol{\rho})$, and $\tilde{\gamma}$ by γ, and if we notice that $\mu(\boldsymbol{\rho}, -z) = \mu(\boldsymbol{\rho}, z)$ and $\epsilon(\boldsymbol{\rho}, -z) = \epsilon(\boldsymbol{\rho}, z)$ is equivalent to $\mu^{-n}(\boldsymbol{\rho}) = \mu^n(\boldsymbol{\rho})$ and $\epsilon^{-n}(\boldsymbol{\rho}) = \epsilon^n(\boldsymbol{\rho})$, then (2.31)–(2.34) becomes again (2.9)–(2.12). This means we can write for the backward

mode

$$\begin{aligned}
\boldsymbol{e}^{-}(\boldsymbol{\rho},z) &= \sum_n \left[\boldsymbol{E}_t^{-n}(\boldsymbol{\rho}) - E_z^{-n}(\boldsymbol{\rho})\boldsymbol{u}_z\right] e^{(\gamma - \frac{j2\pi n}{T})z} \\
&= \left[\boldsymbol{E}_t(\boldsymbol{\rho},-z) - E_z(\boldsymbol{\rho},-z)\boldsymbol{u}_z\right] e^{\gamma z}, \qquad (2.35)\\
\boldsymbol{h}^{-}(\boldsymbol{\rho},z) &= \sum_n \left[-\boldsymbol{H}_t^{-n}(\boldsymbol{\rho}) + H_z^{-n}(\boldsymbol{\rho})\boldsymbol{u}_z\right] e^{(\gamma - \frac{j2\pi n}{T})(z)} \\
&= \left[-\boldsymbol{H}_t(\boldsymbol{\rho},-z) + H_z(\boldsymbol{\rho},-z)\boldsymbol{u}_z\right] e^{\gamma z}. \qquad (2.36)
\end{aligned}$$

Note that $\mu(\boldsymbol{\rho},-z) = \mu(\boldsymbol{\rho},z)$ and $\epsilon(\boldsymbol{\rho},-z) = \epsilon(\boldsymbol{\rho},z)$ do not automatically imply $\boldsymbol{E}(\boldsymbol{\rho},-z) = \boldsymbol{E}(\boldsymbol{\rho},z)$ or $\boldsymbol{H}(\boldsymbol{\rho},-z) = \boldsymbol{H}(\boldsymbol{\rho},z)$.

From the orthogonality relation (2.20) for a periodic waveguide with a symmetry plane, we obtain ($i \neq j$)

$$\int_{S(z)} \left[\boldsymbol{E}_{i,t}(\boldsymbol{\rho},z) \times \boldsymbol{H}_{j,t}(\boldsymbol{\rho},-z) + \boldsymbol{E}_{j,t}(\boldsymbol{\rho},-z) \times \boldsymbol{H}_{i,t}(\boldsymbol{\rho},z)\right] \cdot \boldsymbol{u}_z dS = 0. \qquad (2.37)$$

Using (2.26), we further find

$$\begin{aligned}
&\int_{S(z)} \left[\boldsymbol{E}_{i,t}(\boldsymbol{\rho},z) \times \boldsymbol{H}_{i,t}(\boldsymbol{\rho},-z) + \boldsymbol{E}_{i,t}(\boldsymbol{\rho},-z) \times \boldsymbol{H}_{i,t}(\boldsymbol{\rho},z)\right] \cdot \boldsymbol{u}_z dS \\
= &\int_{S(z)} \left[\boldsymbol{E}_{i,t}(\boldsymbol{\rho},-z) \times \boldsymbol{H}_{i,t}(\boldsymbol{\rho},z) + \boldsymbol{E}_{i,t}(\boldsymbol{\rho},z) \times \boldsymbol{H}_{i,t}(\boldsymbol{\rho},-z)\right] \cdot \boldsymbol{u}_z dS \\
= &\; 2\int_{S(0)} \left[\boldsymbol{E}_{i,t}(\boldsymbol{\rho},0) \times \boldsymbol{H}_{i,t}(\boldsymbol{\rho},0)\right] \cdot \boldsymbol{u}_z dS = c. \qquad (2.38)
\end{aligned}$$

Since the amplitude of an eigenmode is arbitrary we can take $c = 1$, except for eigenmodes for which c vanishes. These eigenmodes will be excluded further on.

2.2.3 Bidirectionality for a general periodic waveguide

In a periodic waveguide without a symmetry plane, such as the one in Fig. 2.2, it is not obvious that for each mode propagating in one direction with propagation coefficient $\gamma_f = \gamma$ there is a mode propagating in the opposite direction with propagation coefficient $\gamma_b = -\gamma$, i.e., it is not obvious that a general periodic waveguide is bidirectional. Let us nevertheless prove this bidirectionality property. Start from a waveguide with a symmetry plane. According to (2.26) and (2.38), we can assume for every mode that

$$\int_{S(z)} \left[\boldsymbol{E}_{f,t}(\boldsymbol{\rho},z) \times \boldsymbol{H}_{b,t}(\boldsymbol{\rho},z) - \boldsymbol{E}_{b,t}(\boldsymbol{\rho},z) \times \boldsymbol{H}_{f,t}(\boldsymbol{\rho},z)\right] \cdot \boldsymbol{u}_z dS = 1. \qquad (2.39)$$

Now change the material parameters or, in other words, the geometry of this waveguide such that the waveguide loses its symmetry plane and, e.g., migrates continuously from the waveguide in Fig. 2.1 to the waveguide in Fig. 2.2. Assume that this change in material parameters can be expressed by a continuous variable 'α' and that the symmetrical waveguide corresponds to $\alpha = \alpha_0$ for which

$$\gamma_f(\alpha_0) + \gamma_b(\alpha_0) = 0. \qquad (2.40)$$

Using the reciprocity theorem, one finds for every α that

$$\left[e^{-[\gamma_f(\alpha)+\gamma_b(\alpha)]T}-1\right] I(\alpha) \quad = \quad 0, \tag{2.41}$$

where we introduced the following notation:

$$I(\alpha)=\int_{S(z)}[\boldsymbol{E}_{f,t}(\boldsymbol{\rho},z,\alpha)\times\boldsymbol{H}_{b,t}(\boldsymbol{\rho},z,\alpha)-\boldsymbol{E}_{b,t}(\boldsymbol{\rho},z,\alpha)\times\boldsymbol{H}_{f,t}(\boldsymbol{\rho},z,\alpha)]\cdot\boldsymbol{u}_z dS. \tag{2.42}$$

From (2.39) it follows that $I(\alpha_0)=1$. Taking the first derivative of (2.41), gives us

$$\begin{aligned} -e^{-[\gamma_f(\alpha)+\gamma_b(\alpha)]T}\left(\frac{\partial\gamma_f(\alpha)}{\partial\alpha}+\frac{\partial\gamma_b(\alpha)}{\partial\alpha}\right)TI(\alpha) & \\ +\left[e^{-(\gamma_f(\alpha)+\gamma_b(\alpha))T}-1\right]\frac{\partial I(\alpha)}{\partial\alpha} \quad &= \quad 0. \end{aligned} \tag{2.43}$$

At $\alpha=\alpha_0$, this reduces to

$$\left.\frac{\partial\gamma_f}{\partial\alpha}\right|_{\alpha=\alpha_0}+\left.\frac{\partial\gamma_b}{\partial\alpha}\right|_{\alpha=\alpha_0} \quad = \quad 0. \tag{2.44}$$

Taking the second derivative of (2.41), gives us

$$\begin{aligned} e^{-[\gamma_f(\alpha)+\gamma_b(\alpha)]T}\left(\frac{\partial\gamma_f(\alpha)}{\partial\alpha}+\frac{\partial\gamma_b(\alpha)}{\partial\alpha}\right)^2T^2I(\alpha) & \\ -e^{-[\gamma_f(\alpha)+\gamma_b(\alpha)]T}\left(\frac{\partial^2\gamma_f(\alpha)}{\partial\alpha^2}+\frac{\partial^2\gamma_b(\alpha)}{\partial\alpha^2}\right)TI(\alpha) & \\ -2e^{-[\gamma_f(\alpha)+\gamma_b(\alpha)]T}\left(\frac{\partial\gamma_f(\alpha)}{\partial\alpha}+\frac{\partial\gamma_b(\alpha)}{\partial\alpha}\right)T\frac{\partial I(\alpha)}{\partial\alpha} & \\ +\left[e^{-[\gamma_f(\alpha)+\gamma_b(\alpha)]T}-1\right]\frac{\partial^2 I(\alpha)}{\partial\alpha^2} \quad &= \quad 0. \end{aligned} \tag{2.45}$$

At $\alpha=\alpha_0$, this reduces to

$$\left.\frac{\partial^2\gamma_f}{\partial\alpha^2}\right|_{\alpha=\alpha_0}+\left.\frac{\partial^2\gamma_b}{\partial\alpha^2}\right|_{\alpha=\alpha_0} \quad = \quad 0. \tag{2.46}$$

Following the same way of reasoning for the higher order derivatives, it is obvious that

$$\gamma_f(\alpha_0)+\gamma_b(\alpha_0) \quad = \quad 0, \tag{2.47}$$

$$\left.\frac{\partial^n\gamma_f}{\partial\alpha^n}\right|_{\alpha=\alpha_0}+\left.\frac{\partial^n\gamma_b}{\partial\alpha^n}\right|_{\alpha=\alpha_0} \quad = \quad 0 \text{ for } n=1,2\cdots+\infty, \tag{2.48}$$

which means that $\gamma_f(\alpha)+\gamma_b(\alpha)$ equals zero for all α if we assume that $\gamma_f(\alpha)+\gamma_b(\alpha)$ is an analytic function of α. This proves the bidirectionality for a general, periodic waveguide. This proof depends on the existence of a parameter α such that $\gamma_f(\alpha)+\gamma_b(\alpha)$

is an analytic function. If, by changing α, suddenly a mode comes into existence or if there is a bifurcation, then this proof is invalid for these eigenmodes. However, in such cases one can perhaps reach the requested eigenmode by starting from another symmetric waveguide and by using a different parameter α in order to proof its bidirectionality. In exceptional cases, this might be impossible. Obviously, one has a large choice of initial symmetric configurations. This proof also shows the intimate relation between reciprocity and bidirectionality.

2.2.4 Excitation

Now we excite the eigenmodes in a periodic waveguide by a current density source. Assume that the current density source $\boldsymbol{j}(\boldsymbol{r})$ is located between $z = z_1$ and $z = z_2$ (Fig. 2.2). The fields at $z = z_1$ can then be written as a series of the modes propagating in the negative z direction as follows:

$$\boldsymbol{e}(\boldsymbol{\rho}, z_1) = \sum_i K_i^- \left[\tilde{\boldsymbol{E}}_{i,t}(\boldsymbol{\rho}, z_1) + \tilde{E}_{i,z}(\boldsymbol{\rho}, z_1)\boldsymbol{u}_z\right] e^{\gamma_i z_1}, \tag{2.49}$$

$$\boldsymbol{h}(\boldsymbol{\rho}, z_1) = \sum_i K_i^- \left[\tilde{\boldsymbol{H}}_{i,t}(\boldsymbol{\rho}, z_1) + \tilde{H}_{i,z}(\boldsymbol{\rho}, z_1)\boldsymbol{u}_z\right] e^{\gamma_i z_1}, \tag{2.50}$$

in the same way the fields at $z = z_2$ can be written as a sum of the modes propagating in the positive z direction as

$$\boldsymbol{e}(\boldsymbol{\rho}, z_2) = \sum_i K_i^+ \left[\boldsymbol{E}_{i,t}(\boldsymbol{\rho}, z_2) + E_{i,z}(\boldsymbol{\rho}, z_2)\boldsymbol{u}_z\right] e^{-\gamma_i z_2}, \tag{2.51}$$

$$\boldsymbol{h}(\boldsymbol{\rho}, z_2) = \sum_i K_i^+ \left[\boldsymbol{H}_{i,t}(\boldsymbol{\rho}, z_2) + H_{i,z}(\boldsymbol{\rho}, z_2)\boldsymbol{u}_z\right] e^{-\gamma_i z_2}. \tag{2.52}$$

We assume here that the eigenmodes form a complete set. This can be proven for lossless media, but for lossy media we have to accept an assumed completeness [3, 15, 16]. If there is no completeness then the presented analysis for the determination of the excitation coefficients is still valid but the sum on the right hand side of, e.g., (2.49) and (2.50), will not completely represent the fields $\boldsymbol{e}(\rho, z_1)$ and $\boldsymbol{h}(\rho, z_1)$.

The definition of direction of propagation of a mode is not unambiguous and can be made in different ways [3, 16]. One can take the direction of the phase velocity or that of the group velocity. In lossy systems, it is obvious to assume that the mode is exponentially damped in the direction of propagation. The lossless case can then be treated as a limit for losses going to zero resulting in still another definition of the direction of propagation. Each choice corresponds to a different behavior at infinity and means that the modes in the sums (2.49)-(2.52) will be exchanged. The presented analysis can also be easily generalized to a case where the waveguide is terminated by two perfectly conducting plates by considering all modes propagating in both directions in both the sums (2.49)-(2.52).

Let us now determine the expansion coefficients K_i^- and K_i^+, using again the Lorentz reciprocity theorem

$$\int_S (\boldsymbol{e}_a \times \boldsymbol{h}_b - \boldsymbol{e}_b \times \boldsymbol{h}_a) \cdot \boldsymbol{u}_n dS = \int_V \boldsymbol{e}_b \cdot \boldsymbol{j}_a dV \tag{2.53}$$

where we assume that the 'a'-fields have sources $\boldsymbol{j}_a$ inside the volume V. We take the fields (2.49)-(2.52) as the 'a'-fields with sources $\boldsymbol{j}_a = \boldsymbol{j}$.

To find K_j^+, the excitation coefficient of the 'a'-mode with propagation coefficient γ_j, we choose the mode with propagation coefficient $-\gamma_j$ as the 'b'-field, i.e.,

$$\boldsymbol{e}_b(\boldsymbol{\rho}, z) = \left[\tilde{\boldsymbol{E}}_{j,t}(\boldsymbol{\rho}, z) + \tilde{E}_{j,z}(\boldsymbol{\rho}, z)\boldsymbol{u}_z\right] e^{\gamma_j z}, \tag{2.54}$$

$$\boldsymbol{h}_b(\boldsymbol{\rho}, z) = \left[\tilde{\boldsymbol{H}}_{j,t}(\boldsymbol{\rho}, z) + \tilde{H}_{j,z}(\boldsymbol{\rho}, z)\boldsymbol{u}_z\right] e^{\gamma_j z}. \tag{2.55}$$

Equation (2.53) yields

$$\begin{aligned}\sum_i K_i^- \int_{S(z_1)} \left[\tilde{\boldsymbol{E}}_{i,t}(\boldsymbol{\rho}, z_1) \times \tilde{\boldsymbol{H}}_{j,t}(\boldsymbol{\rho}, z_1) - \tilde{\boldsymbol{E}}_{j,t}(\boldsymbol{\rho}, z_1) \times \tilde{\boldsymbol{H}}_{i,t}(\boldsymbol{\rho}, z_1)\right] \cdot \boldsymbol{u}_z dS \times \\ e^{(\gamma_i+\gamma_j)z_1} \\ -\sum_i K_i^+ \int_{S(z_2)} \left[\boldsymbol{E}_{i,t}(\boldsymbol{\rho}, z_2) \times \tilde{\boldsymbol{H}}_{j,t}(\boldsymbol{\rho}, z_2) - \tilde{\boldsymbol{E}}_{j,t}(\boldsymbol{\rho}, z_2) \times \boldsymbol{H}_{i,t}(\boldsymbol{\rho}, z_2)\right] \cdot \boldsymbol{u}_z dS \times \\ e^{-(\gamma_i-\gamma_j)z_2} \\ = \int_V \left[\tilde{\boldsymbol{E}}_{j,t}(\boldsymbol{\rho}, z) + \tilde{E}_{j,z}(\boldsymbol{\rho}, z)\boldsymbol{u}_z\right] \cdot \boldsymbol{j}(\boldsymbol{r}) e^{\gamma_j z} dV.\end{aligned} \tag{2.56}$$

With (2.20), this reduces to

$$\begin{aligned}K_j^+ &= -\frac{\int_V \left[\tilde{\boldsymbol{E}}_{j,t}(\boldsymbol{\rho}, z) + \tilde{E}_{j,z}(\boldsymbol{\rho}, z)\boldsymbol{u}_z\right] \cdot \boldsymbol{j}(\boldsymbol{r}) e^{\gamma_j z} dV}{\int_{S(z)} \left[\boldsymbol{E}_{j,t}(\boldsymbol{\rho}, z) \times \tilde{\boldsymbol{H}}_{j,t}(\boldsymbol{\rho}, z) - \tilde{\boldsymbol{E}}_{j,t}(\boldsymbol{\rho}, z) \times \boldsymbol{H}_{j,t}(\boldsymbol{\rho}, z)\right] \cdot \boldsymbol{u}_z dS} \\ &= -\frac{\int_V \left[\tilde{\boldsymbol{e}}_{j,t}(\boldsymbol{\rho}, z) + \tilde{e}_{j,z}(\boldsymbol{\rho}, z)\boldsymbol{u}_z\right] \cdot \boldsymbol{j}(\boldsymbol{r}) dV}{\int_{S(z)} \left[\boldsymbol{e}_{j,t}(\boldsymbol{\rho}, z) \times \tilde{\boldsymbol{h}}_{j,t}(\boldsymbol{\rho}, z) - \tilde{\boldsymbol{e}}_{j,t}(\boldsymbol{\rho}, z) \times \boldsymbol{h}_{j,t}(\boldsymbol{\rho}, z)\right] \cdot \boldsymbol{u}_z dS}.\end{aligned} \tag{2.57}$$

At first sight, one may think that K_j^+ is a function of z, but in view of (2.26) this obviously is not the case. By considering the mode with propagation coefficient γ_j as the 'b-field, one finds

$$\begin{aligned}K_j^- &= -\frac{\int_V \left[\boldsymbol{E}_{j,t}(\boldsymbol{\rho}, z) + E_{j,z}(\boldsymbol{\rho}, z)\boldsymbol{u}_z\right] \cdot \boldsymbol{j}(\boldsymbol{r}) e^{-\gamma_j z} dV}{\int_{S(z)} \left[\tilde{\boldsymbol{E}}_{j,t}(\boldsymbol{\rho}, z) \times \boldsymbol{H}_{j,t}(\boldsymbol{\rho}, z) - \boldsymbol{E}_{j,t}(\boldsymbol{\rho}, z) \times \tilde{\boldsymbol{H}}_{j,t}(\boldsymbol{\rho}, z)\right] \cdot \boldsymbol{u}_z dS} \\ &= -\frac{\int_V \left[\boldsymbol{e}_{j,t}(\boldsymbol{\rho}, z) + e_{j,z}(\boldsymbol{\rho}, z)\boldsymbol{u}_z\right] \cdot \boldsymbol{j}(\boldsymbol{r}) dV}{\int_{S(z)} \left[\tilde{\boldsymbol{e}}_{j,t}(\boldsymbol{\rho}, z) \times \boldsymbol{h}_{j,t}(\boldsymbol{\rho}, z) - \boldsymbol{e}_{j,t}(\boldsymbol{\rho}, z) \times \tilde{\boldsymbol{h}}_{j,t}(\boldsymbol{\rho}, z)\right] \cdot \boldsymbol{u}_z dS}.\end{aligned} \tag{2.58}$$

For a periodic waveguide with a symmetry plane this can be written more compactly as

$$\begin{aligned}K_j^\pm &= -\frac{1}{2}\frac{\int_V \left[\boldsymbol{E}_{j,t}(\boldsymbol{\rho}, \mp z) \mp E_{j,z}(\boldsymbol{\rho}, \mp z)\boldsymbol{u}_z\right] \cdot \boldsymbol{j}(\boldsymbol{r}) e^{\pm\gamma_j z} dV}{\int_{S(0)} \left[\boldsymbol{E}_{j,t}(\boldsymbol{\rho}, 0) \times \boldsymbol{H}_{j,t}(\boldsymbol{\rho}, 0)\right] \cdot \boldsymbol{u}_z dS} \\ &= -\frac{1}{2}\frac{\int_V \left[\boldsymbol{e}_{j,t}(\boldsymbol{\rho}, \mp z) \mp e_{j,z}(\boldsymbol{\rho}, -\mp z)\boldsymbol{u}_z\right] \cdot \boldsymbol{j}(\boldsymbol{r}) dV}{\int_{S(0)} \left[\boldsymbol{e}_{j,t}(\boldsymbol{\rho}, 0) \times \boldsymbol{h}_{j,t}(\boldsymbol{\rho}, 0)\right] \cdot \boldsymbol{u}_z dS}.\end{aligned} \tag{2.59}$$

The denominators in (2.57)–(2.59) drop if c in (2.26) is taken to be equal to 1.

We can now easily write down a series expansion for the Green dyadics in the periodic waveguide, e.g., the electric-electric Green dyadic $\overline{\overline{G}}(\boldsymbol{r}|\boldsymbol{r'})$ defined as follows:

$$\boldsymbol{e}(\boldsymbol{r}) \quad = \quad \int_V \overline{\overline{G}}(\boldsymbol{r}|\boldsymbol{r'})\boldsymbol{j}(\boldsymbol{r'})dV', \tag{2.60}$$

can be expressed conveniently as

$$\overline{\overline{G}}(\boldsymbol{r}|\boldsymbol{r'}) = \quad -\sum_j \frac{\boldsymbol{E}_j(\boldsymbol{r})\tilde{\boldsymbol{E}}_j(\boldsymbol{r'})e^{-\gamma_j(z-z')}}{\int_{S(z)}\left[\tilde{\boldsymbol{E}}_{j,t}(\boldsymbol{r})\times\boldsymbol{H}_{j,t}(\boldsymbol{r}) - \boldsymbol{E}_{j,t}(\boldsymbol{r})\times\tilde{\boldsymbol{H}}_{j,t}(\boldsymbol{r})\right]\cdot\boldsymbol{u}_z dS}, \tag{2.61}$$

if $z > z'$.

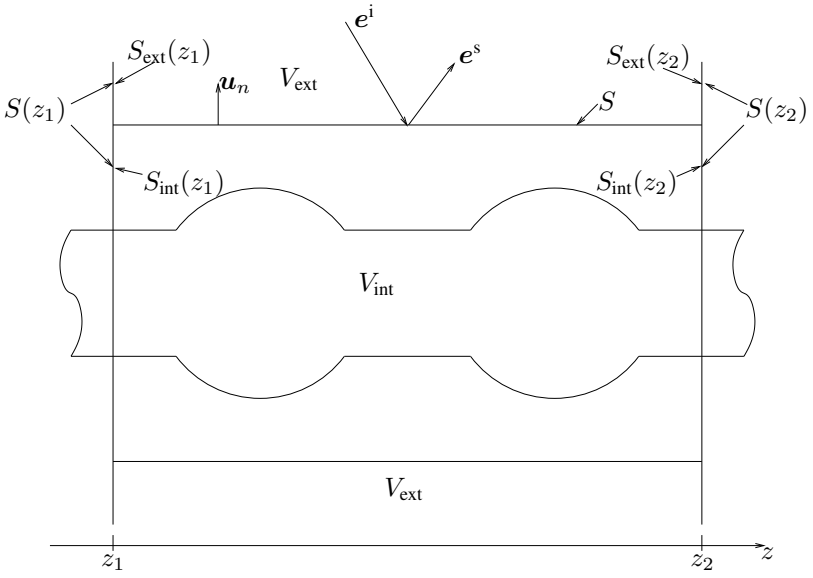

Figure 2.3: Excitation of a periodic waveguide by an incident field.

Instead of placing a source density inside the waveguide, we can also excite the eigenmodes by an external incident field $\boldsymbol{e}^{\mathrm{i}}(\boldsymbol{r})$ and $\boldsymbol{h}^{\mathrm{i}}(\boldsymbol{r})$, e.g., an incident light beam. Now consider a part of the periodic waveguide located between the cross sections $S(z_1)$ and $S(z_2)$ (Fig. 2.3). Introduce a cylindrical surface S parallel to the z-axis which connects the cross sections $S(z_1)$ and $S(z_2)$. The surface S, with external normal $\boldsymbol{u}_n$, divides space into an internal region V_{int} and an external region V_{ext}. The differences between the total fields ($\boldsymbol{e}(\boldsymbol{r})$, $\boldsymbol{h}(\boldsymbol{r})$) in the external region V_{ext} and the incident fields ($\boldsymbol{e}^{\mathrm{i}}(\boldsymbol{r})$, $\boldsymbol{h}^{\mathrm{i}}(\boldsymbol{r})$) are called the scattered fields ($\boldsymbol{e}^{\mathrm{s}}(\boldsymbol{r})$, $\boldsymbol{h}^{\mathrm{s}}(\boldsymbol{r})$). These scattered fields are only defined in the external region V_{ext}.

First apply the Lorentz reciprocity theorem in the external region. Take a mode ($\boldsymbol{e}_j(\boldsymbol{r})$, $\boldsymbol{h}_j(\boldsymbol{r})$) of the waveguide as the a-fields and as the b-fields take the scattered fields ($\boldsymbol{e}^{\mathrm{s}}(\boldsymbol{r})$,

$\boldsymbol{h}^{\mathrm{s}}(\boldsymbol{r})$) as follows:

$$\begin{aligned} -\int_S [\boldsymbol{e}_j(\boldsymbol{r}) \times \boldsymbol{h}^{\mathrm{s}}(\boldsymbol{r}) - \boldsymbol{e}^{\mathrm{s}}(\boldsymbol{r}) \times \boldsymbol{h}_j(\boldsymbol{r})] \cdot \boldsymbol{u}_n dS \\ +\int_{S_{\mathrm{ext}}(z_2)} [\boldsymbol{e}_j(\boldsymbol{r}) \times \boldsymbol{h}^{\mathrm{s}}(\boldsymbol{r}) - \boldsymbol{e}^{\mathrm{s}}(\boldsymbol{r}) \times \boldsymbol{h}_j(\boldsymbol{r})] \cdot \boldsymbol{u}_z dS \\ -\int_{S_{\mathrm{ext}}(z_1)} [\boldsymbol{e}_j(\boldsymbol{r}) \times \boldsymbol{h}^{\mathrm{s}}(\boldsymbol{r}) - \boldsymbol{e}^{\mathrm{s}}(\boldsymbol{r}) \times \boldsymbol{h}_j(\boldsymbol{r})] \cdot \boldsymbol{u}_z dS &= 0. \end{aligned} \tag{2.62}$$

Then apply the Lorentz reciprocity theorem to the internal region, with the mode ($\boldsymbol{e}_j(\boldsymbol{r})$, $\boldsymbol{h}_j(\boldsymbol{r})$) as the a-fields and the total fields ($\boldsymbol{e}(\boldsymbol{r})$, $\boldsymbol{h}(\boldsymbol{r})$) as the b-fields as follows:

$$\begin{aligned} \int_S [\boldsymbol{e}_j(\boldsymbol{r}) \times \boldsymbol{h}(\boldsymbol{r}) - \boldsymbol{e}(\boldsymbol{r}) \times \boldsymbol{h}_j(\boldsymbol{r})] \cdot \boldsymbol{u}_n dS \\ +\int_{S_{\mathrm{int}}(z_2)} [\boldsymbol{e}_j(\boldsymbol{r}) \times \boldsymbol{h}(\boldsymbol{r}) - \boldsymbol{e}(\boldsymbol{r}) \times \boldsymbol{h}_j(\boldsymbol{r})] \cdot \boldsymbol{u}_z dS \\ -\int_{S_{\mathrm{int}}(z_1)} [\boldsymbol{e}_j(\boldsymbol{r}) \times \boldsymbol{h}(\boldsymbol{r}) - \boldsymbol{e}(\boldsymbol{r}) \times \boldsymbol{h}_j(\boldsymbol{r})] \cdot \boldsymbol{u}_z dS &= 0. \end{aligned} \tag{2.63}$$

Combining (2.62) and (2.63) with the continuity relations at the common surface S of V_{ext} and V_{int}, after some manipulations, yields

$$\begin{aligned} -\int_{S_{\mathrm{ext}}(z_2)} \left[\boldsymbol{e}_{t,j}(\boldsymbol{r}) \times \boldsymbol{h}_t^{\mathrm{i}}(\boldsymbol{r}) - \boldsymbol{e}_t^{\mathrm{i}}(\boldsymbol{r}) \times \boldsymbol{h}_{t,j}(\boldsymbol{r})\right] \cdot \boldsymbol{u}_z dS \\ +\int_{S_{\mathrm{ext}}(z_1)} \left[\boldsymbol{e}_{t,j}(\boldsymbol{r}) \times \boldsymbol{h}_t^{\mathrm{i}}(\boldsymbol{r}) - \boldsymbol{e}_t^{\mathrm{i}}(\boldsymbol{r}) \times \boldsymbol{h}_{t,j}(\boldsymbol{r})\right] \cdot \boldsymbol{u}_z dS \\ +\int_S \left[\boldsymbol{e}_j(\boldsymbol{r}) \times \boldsymbol{h}^{\mathrm{i}}(\boldsymbol{r}) - \boldsymbol{e}^{\mathrm{i}}(\boldsymbol{r}) \times \boldsymbol{h}_j(\boldsymbol{r})\right] \cdot \boldsymbol{u}_n dS \\ +\int_{S(z_2)} [\boldsymbol{e}_{t,j}(\boldsymbol{r}) \times \boldsymbol{h}_t(\boldsymbol{r}) - \boldsymbol{e}_t(\boldsymbol{r}) \times \boldsymbol{h}_{t,j}(\boldsymbol{r})] \cdot \boldsymbol{u}_z dS \\ -\int_{S(z_1)} [\boldsymbol{e}_{t,j}(\boldsymbol{r}) \times \boldsymbol{h}_t(\boldsymbol{r}) - \boldsymbol{e}_t(\boldsymbol{r}) \times \boldsymbol{h}_{t,j}(\boldsymbol{r})] \cdot \boldsymbol{u}_z dS &= 0. \end{aligned} \tag{2.64}$$

Now assume that the incident fields are localized, so that they can be neglected on the surfaces $S_{\mathrm{ext}}(z_1)$ and $S_{\mathrm{ext}}(z_2)$. This yields

$$\begin{aligned} \int_S \left[\boldsymbol{e}_j(\boldsymbol{r}) \times \boldsymbol{h}^{\mathrm{i}}(\boldsymbol{r}) - \boldsymbol{e}^{\mathrm{i}}(\boldsymbol{r}) \times \boldsymbol{h}_j(\boldsymbol{r})\right] \cdot \boldsymbol{u}_n dS \\ +\int_{S(z_2)} [\boldsymbol{e}_{t,j}(\boldsymbol{r}) \times \boldsymbol{h}_t(\boldsymbol{r}) - \boldsymbol{e}_t(\boldsymbol{r}) \times \boldsymbol{h}_{t,j}(\boldsymbol{r})] \cdot \boldsymbol{u}_z dS \\ -\int_{S(z_1)} [\boldsymbol{e}_{t,j}(\boldsymbol{r}) \times \boldsymbol{h}_t(\boldsymbol{r}) - \boldsymbol{e}_t(\boldsymbol{r}) \times \boldsymbol{h}_{t,j}(\boldsymbol{r})] \cdot \boldsymbol{u}_z dS &= 0. \end{aligned} \tag{2.65}$$

In a last step, we expand the total fields in the eigenmodes of the waveguide, as was done in (2.49)–(2.52). If we take for the mode ($\boldsymbol{e}_j(\boldsymbol{r})$, $\boldsymbol{h}_j(\boldsymbol{r})$) consecutively a mode

propagating in the positive z direction and a mode propagating in the negative z direction, and if we use the relations (2.20) and (2.26), we find

$$K_j^+ = -\frac{\int_S \left[\tilde{\boldsymbol{e}}_j(\boldsymbol{\rho},z)\times\boldsymbol{h}^{\mathrm{i}}(\boldsymbol{\rho},z) - \boldsymbol{e}^{\mathrm{i}}(\boldsymbol{\rho},z)\times\tilde{\boldsymbol{h}}_j(\boldsymbol{\rho},z)\right]\cdot\boldsymbol{u}_n dS}{\int_{S(z)}\left[\boldsymbol{e}_{j,t}(\boldsymbol{\rho},z)\times\tilde{\boldsymbol{h}}_{j,t}(\boldsymbol{\rho},z) - \tilde{\boldsymbol{e}}_{j,t}(\boldsymbol{\rho},z)\times\boldsymbol{h}_{j,t}(\boldsymbol{\rho},z)\right]\cdot\boldsymbol{u}_z dS}, \tag{2.66}$$

$$K_j^- = -\frac{\int_S \left[\boldsymbol{e}_j(\boldsymbol{\rho},z)\times\boldsymbol{h}^{\mathrm{i}}(\boldsymbol{\rho},z) - \boldsymbol{e}^{\mathrm{i}}(\boldsymbol{\rho},z)\times\boldsymbol{h}_j(\boldsymbol{\rho},z)\right]\cdot\boldsymbol{u}_n dS}{\int_{S(z)}\left[\tilde{\boldsymbol{e}}_{j,t}(\boldsymbol{\rho},z)\times\boldsymbol{h}_{j,t}(\boldsymbol{\rho},z) - \boldsymbol{e}_{j,t}(\boldsymbol{\rho},z)\times\tilde{\boldsymbol{h}}_{j,t}(\boldsymbol{\rho},z)\right]\cdot\boldsymbol{u}_z dS}. \tag{2.67}$$

It is important to remark that the total field is not necessary to calculate the excitation coefficients with (2.66) and (2.67), but that the incident fields suffice. There is a lot of freedom in the choice of these incident fields. The most common and simplest situation occurs when V_{ext} is a homogeneous medium, in which case the incident field can be chosen as a field solution in homogeneous space. For more dicussion on these choices, we refer to [3]. In [3], also the situation when the incident fields are not negligible at $S_{\text{ext}}(z_1)$ and $S_{\text{ext}}(z_2)$ is treated, however for a non-periodic waveguide. The theory in the present paper could also be extended to include this situation.

2.3 Properties of eigenmodes in anisotropic and bianisotropic periodic waveguides

Assume that the media in the waveguide are described by tensors $\overline{\overline{\epsilon}}(\boldsymbol{\rho},z+T) = \overline{\overline{\epsilon}}(\boldsymbol{\rho},z)$ and $\overline{\overline{\mu}}(\boldsymbol{\rho},z+T) = \overline{\overline{\mu}}(\boldsymbol{\rho},z)$. In an anisotropic medium, the Lorentz reciprocity theorem takes the following form [3, 17]:

$$\int_S \left(\boldsymbol{e}_a\times\boldsymbol{h}_b^A - \boldsymbol{e}_b^A\times\boldsymbol{h}_a\right)\cdot\boldsymbol{u}_n dS \;=\; \int_V \left(\boldsymbol{e}_b^A\cdot\boldsymbol{j}_a - \boldsymbol{e}_a\cdot\boldsymbol{j}_b^A\right) dV, \tag{2.68}$$

where $(\boldsymbol{e}_a, \boldsymbol{h}_a, \boldsymbol{j}_a)$ are the fields and sources in the medium $(\overline{\overline{\epsilon}},\overline{\overline{\mu}})$ and where $(\boldsymbol{e}_b^A, \boldsymbol{h}_b^A, \boldsymbol{j}_b^A)$ are the fields and sources in the adjoint medium $(\overline{\overline{\epsilon}}^T, \overline{\overline{\mu}}^T)$. A reciprocal medium $(\overline{\overline{\epsilon}} = \overline{\overline{\epsilon}}^T$, $\overline{\overline{\mu}} = \overline{\overline{\mu}}^T)$ is self-adjoint.

Using the reciprocity theorem (2.68), one can readily show that the orthogonality relation (2.20) now becomes a biorthogonality relation [12]

$$\int_{S(z)}\left[\boldsymbol{E}_{i,t}(\boldsymbol{\rho},z)\times\boldsymbol{H}_{j,t}^A(\boldsymbol{\rho},z) - \boldsymbol{E}_{j,t}^A(\boldsymbol{\rho},z)\times\boldsymbol{H}_{i,t}(\boldsymbol{\rho},z)\right]\cdot\boldsymbol{u}_z dS = 0, \tag{2.69}$$

if $\gamma_i \neq -\gamma_j^A$, and that the integral relation (2.26) becomes

$$\int_{S(z)}\left[\boldsymbol{E}_{i,t}(\boldsymbol{\rho},z)\times\tilde{\boldsymbol{H}}_{i,t}^A(\boldsymbol{\rho},z) - \tilde{\boldsymbol{E}}_{i,t}^A(\boldsymbol{\rho},z)\times\boldsymbol{H}_{i,t}(\boldsymbol{\rho},z)\right]\cdot\boldsymbol{u}_z dS = c, \tag{2.70}$$

if $\gamma_i = -\tilde{\gamma}_i^A$. For reciprocal media, the superscript A can be deleted in (2.69) and (2.70).

Assume a symmetric periodic waveguide in which we can choose an origin $z = 0$ such that $\overline{\overline{\epsilon}}(\boldsymbol{\rho}, -z) = \overline{\overline{\epsilon}}(\boldsymbol{\rho}, z)$ and $\overline{\overline{\mu}}(\boldsymbol{\rho}, -z) = \overline{\overline{\mu}}(\boldsymbol{\rho}, z)$. Assume further that $\overline{\overline{\epsilon}}(\boldsymbol{\rho}, z)$ and $\overline{\overline{\mu}}(\boldsymbol{\rho}, z)$ are of the form

$$\overline{\overline{\epsilon}}(\boldsymbol{\rho}, z) = \begin{bmatrix} \overline{\overline{\epsilon}}_{tt}(\boldsymbol{\rho}, z) & 0 \\ 0 & \epsilon_{zz}(\boldsymbol{\rho}, z) \end{bmatrix}, \tag{2.71}$$

$$\overline{\overline{\mu}}(\boldsymbol{\rho}, z) = \begin{bmatrix} \overline{\overline{\mu}}_{tt}(\boldsymbol{\rho}, z) & 0 \\ 0 & \mu_{zz}(\boldsymbol{\rho}, z) \end{bmatrix}, \tag{2.72}$$

with $\overline{\overline{\epsilon}}^T_{tt}(\boldsymbol{\rho}, z) = \overline{\overline{\epsilon}}_{tt}(\boldsymbol{\rho}, z)$ and $\overline{\overline{\mu}}^T_{tt}(\boldsymbol{\rho}, z) = \overline{\overline{\mu}}_{tt}(\boldsymbol{\rho}, z)$. As in the isotropic case, one can again prove that, if γ, $\boldsymbol{E}_t(\boldsymbol{\rho}, z)$, $E_z(\boldsymbol{\rho}, z)$, $\boldsymbol{H}_t(\boldsymbol{\rho}, z)$, $H_z(\boldsymbol{\rho}, z)$ is an eigenmode, then $-\gamma$, $\boldsymbol{E}_t(\boldsymbol{\rho}, -z)$, $-E_z(\boldsymbol{\rho}, -z)$, $-\boldsymbol{H}_t(\boldsymbol{\rho}, -z)$, $H_z(\boldsymbol{\rho}, -z)$ is also an eigenmode. In a symmetric anisotropic waveguide satisfying (2.71), the relation (2.38) remains valid.

Using the reciprocity theorem (2.68) and repeating the steps (2.40)–(2.48), one can show that an anisotropic waveguide and its adjoint waveguide are mutual bidirectional irrespective of symmetry properties. In particular, this means that a periodic waveguide filled with reciprocal anisotropic media is bidirectional. Finally, (2.57) and (2.58) for the excitation coefficients now generalize to

$$\begin{aligned} K_j^+ &= -\frac{\int_V \left[\tilde{\boldsymbol{E}}^A_{j,t}(\boldsymbol{\rho}, z) + \tilde{E}^A_{j,z}(\boldsymbol{\rho}, z)\boldsymbol{u}_z\right] \cdot \boldsymbol{j}(\boldsymbol{r}) e^{\gamma_j z} dV}{\int_{S(z)} \left[\boldsymbol{E}_{j,t}(\boldsymbol{\rho}, z) \times \tilde{\boldsymbol{H}}^A_{j,t}(\boldsymbol{\rho}, z) - \tilde{\boldsymbol{E}}^A_{j,t}(\boldsymbol{\rho}, z) \times \boldsymbol{H}_{j,t}(\boldsymbol{\rho}, z)\right] \cdot \boldsymbol{u}_z dS} \\ &= -\frac{\int_V \left[\tilde{\boldsymbol{e}}^A_{j,t}(\boldsymbol{\rho}, z) + \tilde{e}^A_{j,z}(\boldsymbol{\rho}, z)\boldsymbol{u}_z\right] \cdot \boldsymbol{j}(\boldsymbol{r}) dV}{\int_{S(z)} \left[\boldsymbol{e}_{j,t}(\boldsymbol{\rho}, z) \times \tilde{\boldsymbol{h}}^A_{j,t}(\boldsymbol{\rho}, z) - \tilde{\boldsymbol{e}}^A_{j,t}(\boldsymbol{\rho}, z) \times \boldsymbol{h}_{j,t}(\boldsymbol{\rho}, z)\right] \cdot \boldsymbol{u}_z dS}, \end{aligned} \tag{2.73}$$

$$\begin{aligned} K_j^- &= -\frac{\int_V \left[\boldsymbol{E}_{j,t}(\boldsymbol{\rho}, z) + E_{j,z}(\boldsymbol{\rho}, z)\boldsymbol{u}_z\right] \cdot \boldsymbol{j}(\boldsymbol{r}) e^{-\gamma_j z} dV}{\int_{S(z)} \left[\tilde{\boldsymbol{E}}^A_{j,t}(\boldsymbol{\rho}, z) \times \boldsymbol{H}_{j,t}(\boldsymbol{\rho}, z) - \boldsymbol{E}_{j,t}(\boldsymbol{\rho}, z) \times \tilde{\boldsymbol{H}}^A_{j,t}(\boldsymbol{\rho}, z)\right] \cdot \boldsymbol{u}_z dS} \\ &= -\frac{\int_V \left[\boldsymbol{e}_{j,t}(\boldsymbol{\rho}, z) + e_{j,z}(\boldsymbol{\rho}, z)\boldsymbol{u}_z\right] \cdot \boldsymbol{j}(\boldsymbol{r}) dV}{\int_{S(z)} \left[\tilde{\boldsymbol{e}}^A_{j,t}(\boldsymbol{\rho}, z) \times \boldsymbol{h}_{j,t}(\boldsymbol{\rho}, z) - \boldsymbol{e}_{j,t}(\boldsymbol{\rho}, z) \times \tilde{\boldsymbol{h}}^A_{j,t}(\boldsymbol{\rho}, z)\right] \cdot \boldsymbol{u}_z dS}, \end{aligned} \tag{2.74}$$

and in the symmetric case, satisfying (2.71) to

$$\begin{aligned} K_j^\pm &= -\frac{1}{2}\frac{\int_V \left[\boldsymbol{E}_{j,t}(\boldsymbol{\rho}, \mp z) \mp E_{j,z}(\boldsymbol{\rho}, \mp z)\boldsymbol{u}_z\right] \cdot \boldsymbol{j}(\boldsymbol{r}) e^{\pm\gamma_j z} dV}{\int_{S(0)} \left[\boldsymbol{E}_{j,t}(\boldsymbol{\rho}, 0) \times \boldsymbol{H}_{j,t}(\boldsymbol{\rho}, 0)\right] \cdot \boldsymbol{u}_z dS} \\ &= -\frac{1}{2}\frac{\int_V \left[\boldsymbol{e}_{j,t}(\boldsymbol{\rho}, \mp z) \mp e_{j,z}(\boldsymbol{\rho}, \mp z)\boldsymbol{u}_z\right] \cdot \boldsymbol{j}(\boldsymbol{r}) dV}{\int_{S(0)} \left[\boldsymbol{e}_{j,t}(\boldsymbol{\rho}, 0) \times \boldsymbol{h}_{j,t}(\boldsymbol{\rho}, 0)\right] \cdot \boldsymbol{u}_z dS}. \end{aligned} \tag{2.75}$$

Most of the results of this section remain valid if one generalizes further to bianisotropic media characterized by ($\overline{\overline{\epsilon}}$, $\overline{\overline{\mu}}$, $\overline{\overline{\zeta}}$, $\overline{\overline{\xi}}$) [17]. The adjoint medium is ($\overline{\overline{\epsilon}}^A = \overline{\overline{\epsilon}}^T$, $\overline{\overline{\mu}}^A = \overline{\overline{\mu}}^T$, $\overline{\overline{\zeta}}^A = -\overline{\overline{\zeta}}^T$, $\overline{\overline{\xi}}^A = -\overline{\overline{\xi}}^T$). The only changes occur in a symmetric periodic waveguide with $\overline{\overline{\epsilon}}(\boldsymbol{\rho}, -z) = \overline{\overline{\epsilon}}(\boldsymbol{\rho}, z)$, $\overline{\overline{\mu}}(\boldsymbol{\rho}, -z) = \overline{\overline{\mu}}(\boldsymbol{\rho}, z)$, $\overline{\overline{\zeta}}(\boldsymbol{\rho}, -z) = \overline{\overline{\zeta}}(\boldsymbol{\rho}, z)$ and

$\overline{\overline{\xi}}(\boldsymbol{\rho},-z) = \overline{\overline{\xi}}(\boldsymbol{\rho},z)$. If $\overline{\overline{\epsilon}}$ and $\overline{\overline{\mu}}$ are of the form (2.71) with $\overline{\overline{\epsilon}}^T_{tt}(\boldsymbol{\rho},z) = \overline{\overline{\epsilon}}_{tt}(\boldsymbol{\rho},z)$ and $\overline{\overline{\mu}}^T_{tt}(\boldsymbol{\rho},z) = \overline{\overline{\mu}}_{tt}(\boldsymbol{\rho},z)$ and if $\overline{\overline{\zeta}}(\boldsymbol{\rho},z)$ and $\overline{\overline{\xi}}(\boldsymbol{\rho},z)$ are of the form [3]

$$\overline{\overline{\zeta}}(\boldsymbol{\rho},z) = \begin{bmatrix} \overline{\overline{\zeta}}_{tt}(\boldsymbol{\rho},z) & \boldsymbol{\zeta}_{tz}(\boldsymbol{\rho},z) \\ \boldsymbol{\zeta}^T_{zt}(\boldsymbol{\rho},z) & \zeta_{zz}(\boldsymbol{\rho},z) \end{bmatrix}, \tag{2.76}$$

$$\overline{\overline{\xi}}(\boldsymbol{\rho},z) = \begin{bmatrix} \overline{\overline{\xi}}_{tt}(\boldsymbol{\rho},z) & \boldsymbol{\xi}_{tz}(\boldsymbol{\rho},z) \\ \boldsymbol{\xi}^T_{zt}(\boldsymbol{\rho},z) & \xi_{zz}(\boldsymbol{\rho},z) \end{bmatrix}, \tag{2.77}$$

with $\zeta_{zz}(\boldsymbol{\rho},z) = \xi_{zz}(\boldsymbol{\rho},z)$, $\overline{\overline{\zeta}}_{tt}(\boldsymbol{\rho},z) = \overline{\overline{\xi}}_{tt}(\boldsymbol{\rho},z)$, $\boldsymbol{\zeta}_{tz}(\boldsymbol{\rho},z) = -\boldsymbol{\xi}_{tz}(\boldsymbol{\rho},z)$ and $\boldsymbol{\zeta}_{zt}(\boldsymbol{\rho},z) = -\boldsymbol{\xi}_{zt}(\boldsymbol{\rho},z)$ and if γ, $\boldsymbol{E}_t(\boldsymbol{\rho},z)$, $E_z(\boldsymbol{\rho},z)$, $\boldsymbol{H}_t(\boldsymbol{\rho},z)$, $H_z(\boldsymbol{\rho},z)$ is an eigenmode in the waveguide, then $-\gamma$, $\boldsymbol{E}_t(\boldsymbol{\rho},-z)$, $-E_z(\boldsymbol{\rho},-z)$, $-\boldsymbol{H}_t(\boldsymbol{\rho},-z)$, $H_z(\boldsymbol{\rho},-z)$ is an eigenmode in the *adjoint* waveguide.

2.4 Example I: Periodic Loaded Rectangular Waveguide

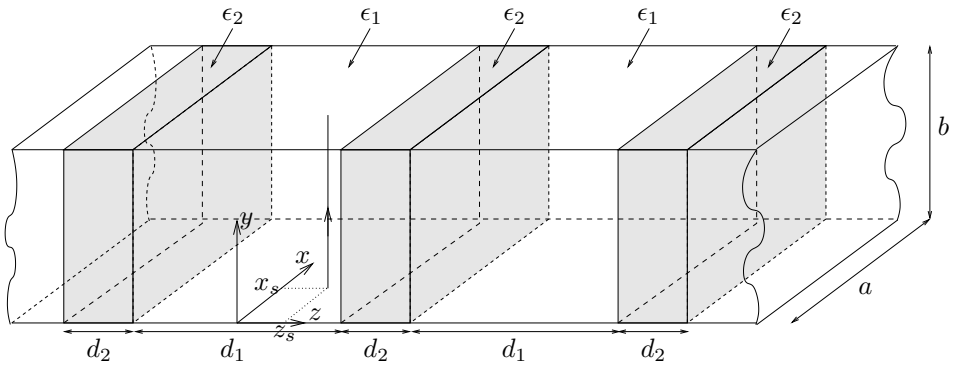

Figure 2.4: Periodic loaded rectangular waveguide with $N = 2$.

As a simple example, we consider a rectangular waveguide with width a and height b periodically loaded with dielectrics. Each period consists of N dielectrics with permittivity ϵ_i and length d_i ($i = 1, 2, \ldots, N$). Hence, the periodicity of the waveguide is given by $T = \sum_{i=1}^{N} d_i$. Figure 2.4 shows an example with $N = 2$.

2.4.1 Modal analysis

In this section, the TE_z modes of this periodic loaded rectangular waveguide are analyzed with a mode-matching technique. The fields in region i are written as a sum of the forward and backward modes of the homogeneously filled rectangular waveguide with permittivity ϵ_i. Because the cross section of the periodic rectangular waveguide remains constant, no mix of the modes of each homogeneous region occurs at the interface between two such

regions. This means that the TE$_z$ fields in region i in the periodic loaded rectangular waveguide can be written as

$$\begin{aligned} \boldsymbol{e}_t^{mn}(\boldsymbol{r}) &= [F^{mn}(z) + B^{mn}(z)]\, \boldsymbol{E}_{t,i}^{mn}(\boldsymbol{\rho}) && (2.78)\\ \boldsymbol{h}_t^{mn}(\boldsymbol{r}) &= [F^{mn}(z) - B^{mn}(z)]\, \boldsymbol{H}_{t,i}^{mn}(\boldsymbol{\rho}) && (2.79)\\ h_z^{mn}(\boldsymbol{r}) &= [F^{mn}(z) + B^{mn}(z)]\, H_{z,i}^{mn}(\boldsymbol{\rho}) && (2.80) \end{aligned}$$

with $\boldsymbol{E}_{t,i}^{mn}(\boldsymbol{\rho})$, $\boldsymbol{H}_{t,i}^{mn}(\boldsymbol{\rho})$ and $\boldsymbol{H}_{z,i}^{mn}(\boldsymbol{\rho})$ the TE$_z$ modes of the rectangular waveguide homogeneously filled by the medium of region i.

In each region i, we can write the functions $F^{mn}(z)$ and $B^{mn}(z)$ as

$$F^{mn}(z) = F_i^{mn} e^{-\gamma_i^{mn} z} \quad (2.81)$$

$$B^{mn}(z) = B_i^{mn} e^{\gamma_i^{mn} z} \quad (2.82)$$

with $\gamma_i^{mn} = \sqrt{\frac{n^2\pi^2}{a^2} + \frac{m^2\pi^2}{b^2} - \omega^2\epsilon_i\mu_i}$. Using a classic scattering formalism, one can obtain

$$\begin{bmatrix} F^{mn}(z+T) \\ B^{mn}(z+T) \end{bmatrix} = \begin{bmatrix} A & B \\ C & D \end{bmatrix} \begin{bmatrix} F^{mn}(z) \\ B^{mn}(z) \end{bmatrix}. \quad (2.83)$$

Requesting that $F^{mn}(z+T) = e^{-\gamma^{mn}T} F^{mn}(z)$ and $B^{mn}(z+T) = e^{-\gamma^{mn}T} B^{mn}(z)$ according to the Floquet-Bloch theorem results in an eigenvalue system for the coefficients γ^{mn}. For each value of mn, there will be two solutions for γ^{mn} corresponding to a forward and a backward propagating mode.

2.4.2 Periodic loaded rectangular waveguide with $N = 2$

Consider a periodic loaded rectangular waveguide with $N = 2$ as shown in Fig. 2.4. This is an example of a periodic waveguide with a symmetry plane. The origin $z = 0$ is chosen in the middle of region 1 with permittivity ϵ_1. We consider a waveguide with parameters $a = 2cm$, $b = 1cm$, $d_1 = 1cm$, $d_2 = 0.5cm$, $\epsilon_{r1} = 9$, and $\epsilon_{r2} = 1$.

Let us excite the waveguide by a line current I parallel to the y-axis situated at $z_s = \frac{d_1}{4}$ and $x_s = \frac{a}{4}$, i.e.,

$$\boldsymbol{j}(\boldsymbol{r}) = I\delta(x - x_s)\delta(z - z_s)\boldsymbol{u}_y \quad (2.84)$$

In this case only modes with $m = 0$ and $n \geq 1$ are excited. From (2.49)–(2.52), and (2.59), we find for $z > z_s$

$$\begin{aligned} h_z(\boldsymbol{r}) &= -\sum_{n=1}^{+\infty} \frac{n\pi}{\gamma_1^{0n} a^2} \sin(\frac{n\pi x_s}{a}) \cos(\frac{n\pi x}{a}) \times \\ &\quad \frac{[F^{0n}(-z_s) + B^{0n}(-z_s)][F^{0n}(z) + B^{0n}(z)]}{F^{0n}(0)^2 - B^{0n}(0)^2}, \end{aligned} \quad (2.85)$$

and for $z < z_s$

$$\begin{aligned} h_z(\boldsymbol{r}) &= -\sum_{n=1}^{+\infty} \frac{n\pi}{\gamma_1^{0n} a^2} \sin(\frac{n\pi x_s}{a}) \cos(\frac{n\pi x}{a}) \times \\ &\quad \frac{[F^{0n}(z_s) + B^{0n}(z_s)][F^{0n}(-z) + B^{0n}(-z)]}{F^{0n}(0)^2 - B^{0n}(0)^2}. \end{aligned} \quad (2.86)$$

In region 1, we have $F^{0n}(z) = F^{0n}(0)e^{-\gamma_1^{0n}z}$ and $B^{0n}(z) = F^{0n}(0)e^{\gamma_1^{0n}z}$. If R^{0n} is the reflection coefficient for the TE_{0n} mode in region 1 at $z = -\frac{d_1}{2}$ for the stack of regions in the interval $-\infty < z < -\frac{d_1}{2}$, then we have that $B_1^{0n} = R^{0n}F_1^{0n}e^{-\gamma_1^{0n}d_1}$. This allows us to express the fields excited by the source in region 1 as given in the following:

$$h_z(\boldsymbol{r}) = -\sum_{n=1}^{+\infty} \frac{n\pi}{\gamma_1^{0n}a^2} \sin(\frac{n\pi x_s}{a}) \cos(\frac{n\pi x}{a}) \times \frac{[e^{\gamma_1^{0n}z_s} + R^{0n}e^{-\gamma_1^{0n}(z_s+d_1)}][e^{-\gamma_1^{0n}z} + R^{0n}e^{\gamma_1^{0n}(z-d_1)}]}{1-(R^{0n})^2e^{-2\gamma_1^{0n}d_1}}, \quad (2.87)$$

for $\frac{d_1}{2} > z > z_s$, and as follows:

$$h_z(\boldsymbol{r}) = -\sum_{n=1}^{+\infty} \frac{n\pi}{\gamma_1^{0n}a^2} \sin(\frac{n\pi x_s}{a}) \cos(\frac{n\pi x}{a}) \times \frac{[e^{-\gamma_1^{0n}z_s} + R^{0n}e^{\gamma_1^{0n}(z_s-d_1)}][e^{\gamma_1^{0n}z} + R^{0n}e^{-\gamma_1^{0n}(z+d_1)}]}{1-(R^{0n})^2e^{-2\gamma_1^{0n}d_1}}, \quad (2.88)$$

for $-\frac{d_1}{2} < z < z_s$.

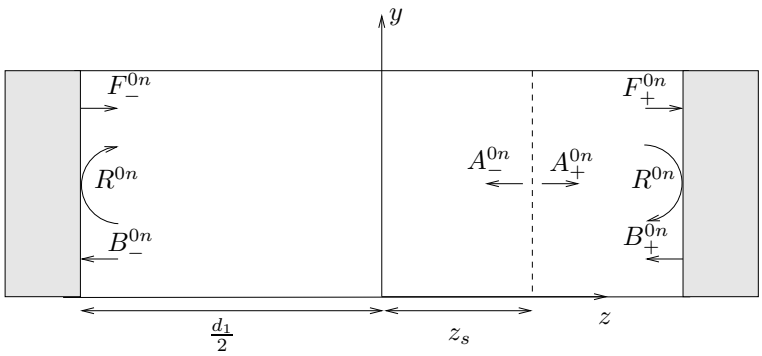

Figure 2.5: Alternative method for the calculation of the excitation coefficients.

For this special case, we can calculate the fields excited by the source in an alternative way (Fig. 2.5). Let A_{0n}^+ and A_{0n}^- be the amplitudes of the forward and the backward propagating TE_{0n} mode, respectively, when the source is placed at $z = z_s$ in a homogeneously filled waveguide with permittivity ϵ_1. From Fig. 2.5, we can easily derive the following relations

$$F_+^{0n} = \frac{R^{0n}A_-^{0n}e^{-\gamma_1^{0n}(z_s+d_1)} + A_+^{0n}e^{\gamma_1^{0n}z_s}}{1-(R^{0n})^2e^{-2\gamma_1^{0n}d_1}} e^{-\gamma_1^{0n}\frac{d_1}{2}}, \quad (2.89)$$

$$B_-^{0n} = \frac{R^{0n}A_+^{0n}e^{\gamma_1^{0n}(z_s-d_1)} + A_-^{0n}e^{-\gamma_1^{0n}z_s}}{1-(R^{0n})^2e^{-2\gamma_1^{0n}d_1}} e^{-\gamma_1^{0n}\frac{d_1}{2}}, \quad (2.90)$$

where A_+^{0n} and A_-^{0n} are given by

$$A_+^{0n} = -\frac{(\frac{n\pi}{a})\sin(\frac{n\pi x_s}{a})}{\gamma_1^{0n} a}, \tag{2.91}$$

$$A_-^{0n} = -\frac{(\frac{n\pi}{a})\sin(\frac{n\pi x_s}{a})}{\gamma_1^{0n} a}. \tag{2.92}$$

We find for the field in $-\frac{d_1}{2} < z \leq z_s$

$$\begin{aligned} h_z(\boldsymbol{r}) &= \sum_{n=1}^{+\infty} e^{\gamma_1^{0n}\frac{d_1}{2}}(e^{\gamma_1^{0n} z} + R^{0n} e^{-\gamma_1^{0n}(z+d_1)}) B_-^{0n} \cos(\frac{n\pi x}{a}) \\ &= -\sum_{n=1}^{+\infty} \frac{n\pi}{\gamma_1^{0n} a^2} \sin(\frac{n\pi x_s}{a}) \cos(\frac{n\pi x}{a}) \times \\ &\quad \frac{[R^{0n} e^{\gamma_1^{0n}(z_s - d_1)} + e^{-\gamma_1^{0n} z_s}][e^{\gamma_1^{0n} z} + R^{0n} e^{-\gamma_1^{0n}(z+d_1)}]}{1 - (R^{0n})^2 e^{-2\gamma_1^{0n} d_1}}, \end{aligned} \tag{2.93}$$

and for the field in $z_s \leq z < \frac{d_1}{2}$

$$\begin{aligned} h_z(\boldsymbol{r}) &= \sum_{n=1}^{+\infty} e^{\gamma_1^{0n}\frac{d_1}{2}}(e^{-\gamma_1^{0n} z} + R^{0n} e^{\gamma_1^{0n}(z-d_1)}) F_+^{0n} \cos(\frac{n\pi x}{a}) \\ &= -\sum_{n=1}^{+\infty} \frac{n\pi}{\gamma_1^{0n} a^2} \sin(\frac{n\pi x_s}{a}) \cos(\frac{n\pi x}{a}) \times \\ &\quad \frac{[R^{0n} e^{-\gamma_1^{0n}(z_s + d_1)} + e^{\gamma_1^{0n} z_s}][e^{\gamma_1^{0n} z} + R^{0n} e^{-\gamma_1^{0n}(z-d_1)}]}{1 - (R^{0n})^2 e^{-2\gamma_1^{0n} d_1}}. \end{aligned} \tag{2.94}$$

These formulas are exactly the same as (2.87) and (2.88). The amplitude of h_z^{01} for the TE_{01} mode is given in Fig.2.6 for two different z values.

2.4.3 Periodic loaded rectangular waveguide with N=3

Now consider a periodic waveguide with $N = 3$, which is an example of a waveguide without a symmetry plane. We calculated with (2.83) the propagation coefficients of the TE_{01}, TE_{10}, and TE_{11} modes for such a waveguide with parameters $a = 2cm$, $b = 1cm$, $d_1 = 0.5cm$, $d_2 = 0.3cm$, $d_3 = 0.1cm$, $\epsilon_{r1} = 9$, $\epsilon_{r2} = 4$, and $\epsilon_{r3} = 1$. The imaginary part of these propagation coefficients are shown for the first Brillouin zone in Fig. 2.7. This figure clearly shows the bidirectionality of this waveguide.

2.5 Example II: Metallic Electromagnetic Crystal Waveguide

In this section, we will calculate the propagation coefficients and the corresponding mode profiles of a two-dimensional electromagnetic crystal waveguide, consisting of perfectly

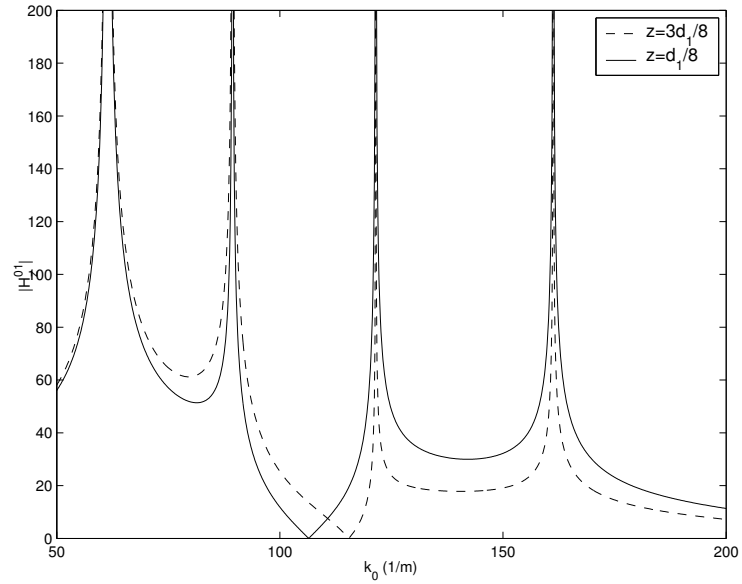

Figure 2.6: Amplitude of the TE_{01}-mode at $z = \frac{3d_1}{8}$ and at $z = \frac{d_1}{8}$.

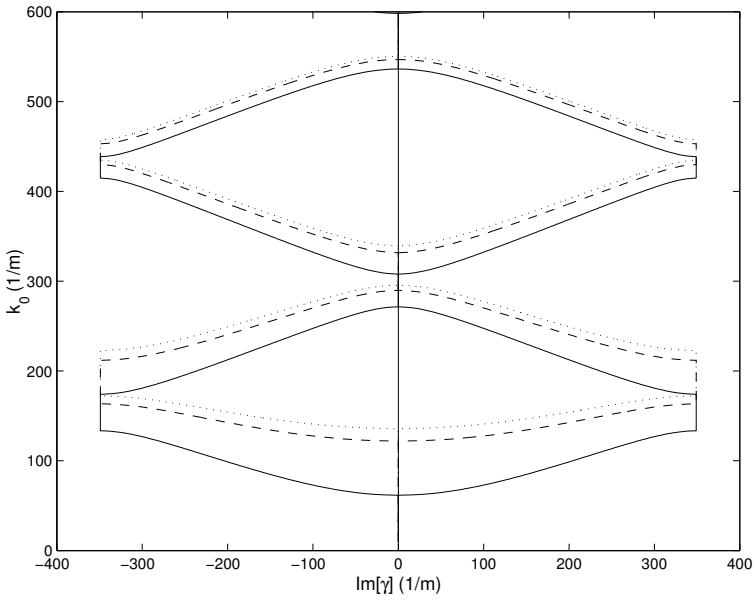

Figure 2.7: Propagation coefficient of the TE_{01} (solid line), TE_{10} (dashed line) and the TE_{11} (dotted line) modes for a periodic rectangular waveguide with $N = 3$.

electric conducting (PEC) cylinders embedded in air. All the cylinders have the same radius r. We will only consider the TM_y case, for which the electric field has only a y-component, parallel to the PEC cylinders.

2.5.1 Simulation technique

At the surface of every cylinder, we expand the unknown surface currents in a Fourier series

$$J_y^i(\phi_i) \quad = \quad \sum_{n=-\infty}^{+\infty} \frac{I_n^i}{2\pi r} e^{jn\phi_i} \tag{2.95}$$

The field generated by this current is then given by

$$E_y^{\mathrm{s},i}(\rho_i, \phi_i) \quad = \quad -\frac{\omega\mu_0}{4} \sum_{n=-\infty}^{+\infty} J_n(kr) H_n^{(2)}(k\rho_i) I_n^i e^{jn\phi_i} \tag{2.96}$$

The whole problem can be solved by demanding that the total electric field, which is the sum of the scattered fields of all cylinders, is zero on the surface of every cylinder. We enforce this boundary condition by imposing that the Fourier coefficients of the total electric field at the surface of each cylinder vanishes. The Floquet-Bloch theorem tells us that the currents change by a factor $e^{-\gamma T}$ when we proceed one period. This allows us to limit the unknowns to the expansions of the currents in one unit cell. According to the Floquet-Bloch theorem, we only have to calculate these surface currents in one unit cell. By truncating the Fourier expansions, we then obtain the following homogeneous linear system:

$$\boldsymbol{Z}(\gamma)\boldsymbol{I} \quad = \quad \mathbf{0}. \tag{2.97}$$

The elements of the matrix $\boldsymbol{Z}(\gamma)$ can be derived as an infinite series by using an addition theorem for the Hankel functions. These elements are a function of the propagation coefficient γ. This set of equations will only have nontrivial solutions for some discrete values of γ, which are found by the demand that $\det(\boldsymbol{Z}(\gamma))$ equals zero. Once γ is known, the surface currents and hence the corresponding mode profile, are easily calculated.

2.5.2 Numerical results

As a first example, we calculated the propagation coefficient γ of an eigenmode for the symmetric waveguide shown in Fig. 2.8. The radius r of every cylinder is $0.2T$. At $f = 0.36\frac{\pi}{T}$, there is only one propagating mode, and for this mode we obtained $\gamma_f = -\gamma_b = 1.479j$. In Fig. 2.9, the absolute value of the electric field E_y of both the forward and the backward propagating mode is shown at $x = 0$, between $z = 0$ and $z = T$. The other field components show similar behaviors. This figure illustrates the relation between both profiles, as derived in Section 2.2.2.

In order to validate the proof given in Section 2.2.3, we considered the asymmetric waveguide shown in Fig. 2.10. The radius r is now $0.06T$. At $f = 0.9\frac{\pi}{T}$, we find a mode with $\gamma_f = -\gamma_b = 0.063 + j0.678$. Although the forward and the backward propagating

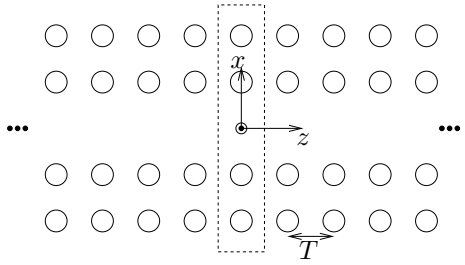

Figure 2.8: Photonic crystal channel waveguide.

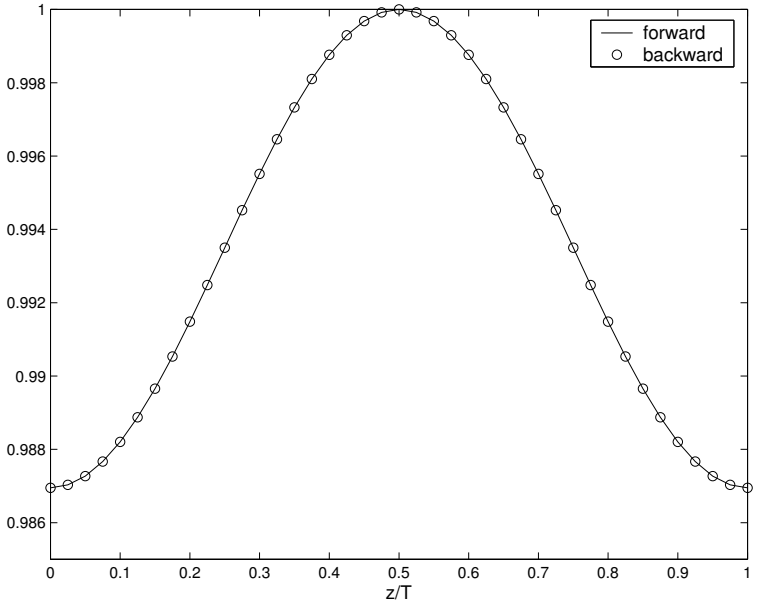

Figure 2.9: Forward and backward mode of a symmetric PC waveguide.

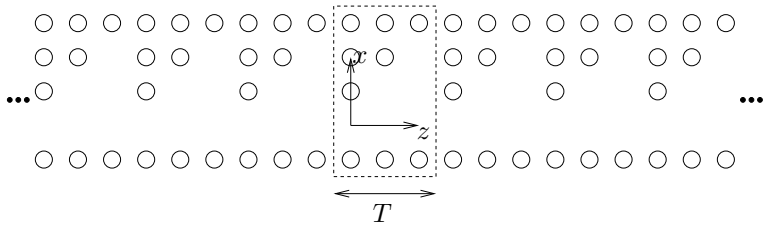

Figure 2.10: Asymmetric photonic crystal waveguide.

mode still have opposite propagation coefficients, as was expected from our proof, but the mode profiles no longer have a clear relation. This is illustrated in Fig. 2.11, where the absolute value of the electric field E_y is given at $x = 0$.

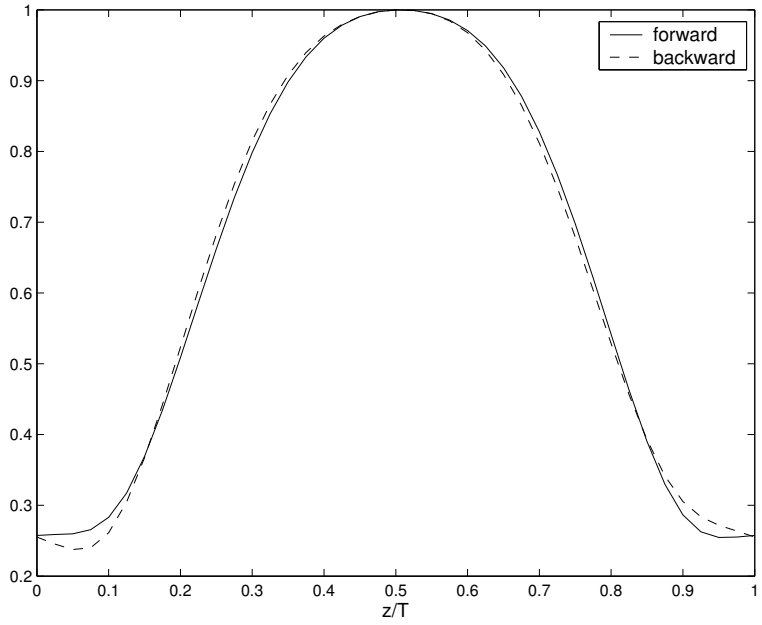

Figure 2.11: Forward and backward mode of an asymmetric PC waveguide.

2.6 Conclusion

A rigorous study has been presented of the properties of eigenmodes propagating in general periodic waveguides using the Lorentz reciprocity theorem. This has led to orthogonality relations that the modes satisfy. We have also provided a proof of the bidirectionality property of these waveguides and we have derived formulas to determine the excitation coefficients of the modes when the waveguide is excited by current source densities or externally incident waves. Finally, the whole analysis was generalized to periodic waveguides filled with reciprocal and non-reciprocal anisotropic and bianisotropic materials.

Bibliography

[1] J. Joannopoulos, R. Meade, and J. Winn, *Photonic Crystals: Molding the Flow of Light*. N.J.: Princeton Univ. Press, 1995.

[2] C. Elachi, "Waves in active and passive periodic structures: A review," *Proc. IEEE*, vol. 64, no. 12, pp. 1666–1698, Dec. 1976.

[3] F. Olyslager, *Electromagnetic Waveguides and Transmission Lines*, ser. Oxford Engineering Science Series. Oxford: Clarendon Press, 1999.

[4] K. Kurokawa, *An introduction to the theory of microwave circuits*. New York: Academic Press, 1969.

[5] R. E. Collin, *Field Theory of Guided Waves*. New-York: IEEE Press, 1991.

[6] D. Watkins, *Topics in electromagnetic theory*. New York: John Wiley & Sons, 1958.

[7] L. Brillouin, *Wave propagation in periodic structures*. New York: Dover Publications, 1953.

[8] R. Harrington and A. Villeneuve, "Reciprocity relations for gyrotropic media," *IRE Transactions on Microwave and Theory and Techniques*, vol. 6, pp. 308–310, 1958.

[9] A. Villeneuve, "Orthogonality relationships for waveguides and cavities with inhomogeneous anisotropic media," *IRE Transactions on Microwave and Theory and Techniques*, vol. 7, pp. 441–446, 1959.

[10] F. Olyslager, "Properties of and generalized full-wave transmission line models for hybrid (bi)(an)isotropic waveguides," *IEEE Trans. Microwave Theory Tech.*, vol. 44, no. 11, pp. 2064–2075, Nov. 1996.

[11] P. McIsaac, "Mode orthogonality in reciprocal and non-reciprocal waveguides," *IEEE Trans. Microwave Theory Tech.*, vol. 39, no. 11, pp. 1808–1816, Nov. 1991.

[12] C. Altman and K. Suchy, *Reciprocity, spatial mapping and time reversal in electromagnetics*, ser. Developments in Electromagnetic Theory and Application. Dordrecht: Kluwer Academic Publishers, 1991, vol. 9.

[13] R. Ziolkowski and N. Engheta, "Metamaterial special issue introduction," *IEEE Trans. Antennas Propag.*, vol. 51, pp. 2546–2549, Oct. 2003.

[14] R. Shelby, D. Smith, and S. Shultz, "Experimental verification of a negative index of refraction," *Science*, vol. 292, pp. 77–79, 2001.

[15] W. C. Chew, *Waves and Fields in Inhomogeneous Media*. New York: Van Nostrand Reinhold, 1990.

[16] L. Felsen and N. Marcuvitz, *Radiation and Scattering of Waves*. Oxford: Oxford University Press, 1994.

[17] I. V. Lindell, *Methods for Electromagnetic Field Analysis*, ser. Oxford Engineering Science Series. Oxford: Clarendon Press, 1992.

Chapter 3

A Comparative Study of Three Methods for the Simulation of 2D Photonic Crystals

**Davy Pissoort, Bart Denecker, Peter Bienstman,
Frank Olyslager, and Daniël De Zutter**

Published in Journal of the Optical Society of America A - Optics Image Science and Vision, Vol. 21, no. 11, pp. 2186–2195, November 2004

Abstract

Three methods for the efficient simulation of two-dimensional photonic crystal structures are compared, namely, a semi-analytical multiple scattering technique; a vectorial eigenmode expansion technique; and a FDTD-ROM technique. The basic principles of each method are presented. For the semi-analytical technique and for the vectorial eigenmode expansion technique, we show how reflections coming from abruptly terminated waveguides can be avoided. The main advantages and disadvantages of each method are discussed. Results from use of the three methods are compared for several photonic crystal structures.

3.1 Introduction

Photonic crystals (PCs) have aroused substantial interest because of their ability to control lightwave propagation [1]. Two-dimensional PCs consist of a set of parallel cylinders embedded in a homogeneous medium or a planar stratified medium. Because of the periodicity, a PC exhibits photonic band gaps in which electromagnetic fields cannot propagate in given directions. By creating different types of defects in a PC, it is possible to create

waveguides with sharp bends [2–4], lasers [5], multiplexers [6–8],...

To design and simulate PC circuits efficiently, many different numerical techniques have been proposed. Probably the most popular technique is the finite difference time domain technique (FDTD) owing to the simplicity of the algorithm and the flexibility regarding the structure and the materials. By means of this time-domain method, one can obtain information over a wide frequency range by performing a single simulation followed by a Fourier transform. However, as PCs consist of objects that are rather small compared with the wavelength, a small space step is required for a correct discretization. As a consequence, computer memory requirements rise excessively if the standard FDTD-method is used. The smaller time step that needs to be used also leads to excessive computing time. One way to overcome this problem is the use of subcell models, which means that on the basis of the knowledge of the analytical field behavior around small objects, one locally adapts the FDTD time-stepping equation. In this way the time step is dictated mainly by a coarse grid. In [9], a technique was presented that automatically generates such subcell models in the FDTD technique that can be used for arbitrarily shaped objects. Also, the memory requirements are kept small by reducing the number of internal variables in the subcell model by means of a reduced-order modeling (ROM) technique.

Another frequently used numerical method is the eigenmode expansion technique. This technique starts by slicing the structure into layers for which the index profile does not change in a given direction. For each layer, the fields are written as a sum of the so-called eigenmodes of that layer. The unknown expansion coefficients are obtained using the well-known mode-matching technique at the interfaces between the different layers. If a specific layer is frequently repeated, the computational complexity scales linearly or even logarithmically with the longitudinal dimension of the structure. By calculating the reflection matrix of a semi-infinite crystal, one can terminate the PC structure and avoid back reflections coming from abruptly terminated waveguides. However, the eigenmode expansion technique requires a discrete set of modes. Typically, this is achieved by enclosing the entire structure in a metal box. Unfortunately, this can create parasitic reflections. A better way is to make use of advanced boundary conditions, such as Perfectly Matched Layers (PMLs) [10–12]. This also speeds up the computation time, as the metal walls can now be placed much closer to the structure.

A third method is the multiple scattering technique [13–15], which is a rigorous semi-analytical technique. In contrast to FDTD and the eigenmode expansion technique, this method exploits the fact that the cylinders have a circular cross section by using the Bessel/Hankel functions, which are the 'natural' modes for cylindrical objects, i.e., scalar cylindrical harmonics. As a consequence, only a few unknowns per cylinder are required. We will show that this method is not only limited to finite PC structures. By adding some extra rows of cylinders in the complex plane, one can efficiently avoid the spurious reflections [16]. However, with this method the solution of a linear system whose dimension scales linearly with the number of cylinders is required. With a direct solver the computational complexity scales as the third power of the number of cylinders.

In Sections 3.2, 3.3, and 3.4 the basic principles of the three simulation techniques are summarized, and some additional improvements over published results are presented. The main advantages and disadvantages of each method are also discussed. In Section 3.5, some PC filter structures are simulated, and the results obtained with the different methods are compared and discussed.

3.2 Semi-analytical technique

In this section, a semi-analytical technique for computing the scattering by a large number of circular dielectric or perfectly conducting (PEC) cylinders is described. First the total field is written as the sum of the incident field due to the source and the field scattered by the cylinders. To calculate this scattered field we introduce surface currents at the surface of each cylinder. For PEC cylinders, these currents correspond with the physical surface currents, but for dielectric cylinders these currents are fictitious. The scattered field is then written as the sum of the fields due to these currents.

3.2.1 Field and current representation

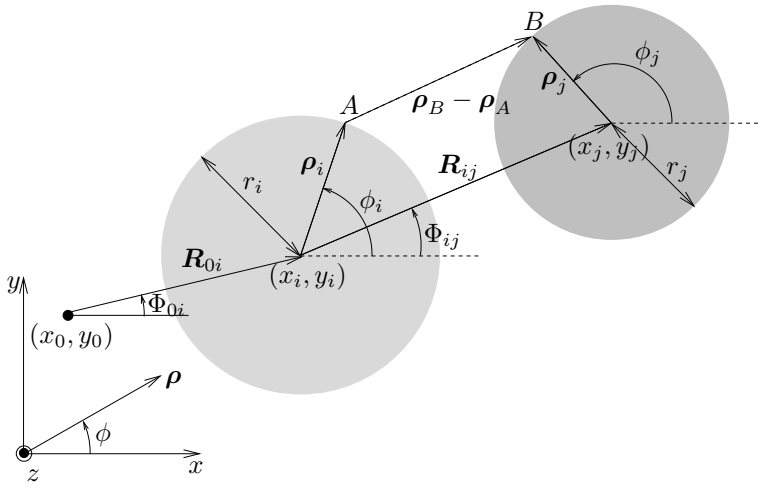

Figure 3.1: Multiple scattering.

At the surface of every cylinder i (Fig. 3.1) we define unknown surface currents

$$J_z^i(\rho_i, \phi_i) = \sum_{m=-\infty}^{+\infty} \frac{I_m^i}{2\pi r_i} e^{jm\phi_i} \delta(\rho_i - r_i), \tag{3.1}$$

with r_i the radius of cylinder i and (ρ_i, ϕ_i) the local cylindrical coordinates of this cylinder. These currents are placed in an infinite homogeneous medium with refractive index n_{ext}. The total electric field on the surface of cylinder i can also be written as a Fourier series

$$E_z^{\text{t}}(\rho_i = r_i, \phi_i) = \sum_{p=-\infty}^{+\infty} e_p^i e^{jp\phi_i}, \tag{3.2}$$

with

$$e_p^i = \frac{1}{2\pi} \int_{-\pi}^{\pi} E_z^{\text{t}}(\rho_i = r_i, \phi_i) e^{-jp\phi_i} d\phi_i. \tag{3.3}$$

The total field $E_z^{\mathrm{t}}(r_i, \phi_i)$ is the superposition of the following three contributions:

(i) the field generated by the surface currents on cylinder i,

$$E_z^{\mathrm{s},i}(\rho_i = r_i, \phi_i) = \sum_{p=-\infty}^{+\infty} e_p^{ii} e^{jp\phi_i}; \tag{3.4}$$

(ii) the field caused by the surface currents on the other cylinders,

$$E_z^{\mathrm{s},j}(\rho_i = r_i, \phi_i) = \sum_{p=-\infty}^{+\infty} \sum_{j \neq i} e_p^{ji} e^{jp\phi_i}; \tag{3.5}$$

(iii) the incident field caused by the source in absence of all cylinders,

$$E_z^{\mathrm{i}}(\rho_i = r_i, \phi_i) = \sum_{p=-\infty}^{+\infty} e_p^{0i} e^{jp\phi_i}. \tag{3.6}$$

One can easily verify that the first contribution is given by

$$e_p^{ii} = -(\frac{\omega\mu_0}{4}) H_p^{(2)}(kr_i) J_p(kr_i) I_p^i. \tag{3.7}$$

To calculate the contribution e_p^{ji}, we express the field caused by the currents on cylinder j in terms of the local coordinates of cylinder i by using the addition theorem of the Hankel functions [17]. We find that

$$e_p^{ji} = -\frac{\omega\mu_0}{4} \sum_{m=-\infty}^{+\infty} H_{p-m}^{(2)}(kR_{ij}) J_m(kr_j) J_p(kr_i) e^{j(m-p)\Phi_{ij}} I_m^j, \tag{3.8}$$

with R_{ij} and Φ_{ij} the distance and the angle between the centers of both cylinders (Fig. 3.1).

Again using the addition theorem of the Hankel functions, we can easily calculate the contribution of the source e_p^{0i}. For a line source situated at a point (x_0, y_0), the field at a point on the surface of cylinder i is given by

$$\begin{aligned} E_z^{\mathrm{i}}(\rho_i = r_i, \phi_i) &= -\frac{\omega\mu_0}{4} H_0^{(2)}(k|\boldsymbol{R}_{0i} + \boldsymbol{\rho}_i|) \\ &= -\frac{\omega\mu_0}{4} \sum_{n=-\infty}^{+\infty} (-1)^n H_n^{(2)}(kR_{0i}) J_n(kr_i) e^{jn(\Phi_{oi} - \phi_i)}, \end{aligned} \tag{3.9}$$

such that we obtain the source contribution

$$e_p^{0i} = -\frac{\omega\mu_0}{4} (-1)^p H_p^{(2)}(kR_{0i}) J_p(kr_i) e^{-jp\Phi_{oi}}. \tag{3.10}$$

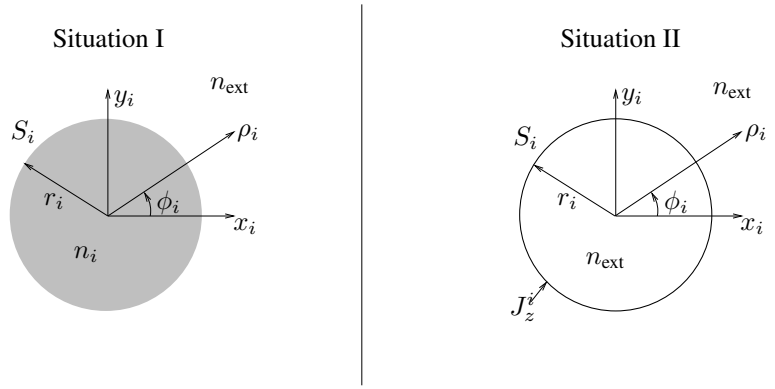

Figure 3.2: Two situations for the calculation of the boundary impedance.

3.2.2 Boundary Impedance

For the case of perfectly conducting cylinders, the whole problem can be solved by requiring that the total electric field be zero on the surface of all cylinders. This in turn leads to a set of equations for the unknown surface currents I_m^i in Eq. (3.1). For dielectric cylinders, internal fields have to be taken into account. Here, we circumvent this problem by continuing to use the surface current of Eq. (3.1) as our only unknown quantity, but now an appropriate boundary impedance has to be introduced that relates the total external electric field to this current. For the calculation of this boundary impedance, we consider two situations (Fig. 3.2):

I. The original situation with a dielectric cylinder with radius r_i and refractive index n_i placed in a homogeneous space with refractive index n_{ext}.

II. A homogeneous space with refractive index n_{ext} but with unknown currents $J_z^i = \sum_{n=-\infty}^{+\infty} \frac{I_n^i}{2\pi r_i} e^{jn\phi_i}$ placed on the now fictitious surface S_i of cylinder i.

In the first situation the fields inside the dielectric cylinder are given by

$$E_z^{\text{I}}(\rho_i \leq r_i, \phi_i) = \sum_{n=-\infty}^{+\infty} A_n J_n(k_0 n_i \rho_i) e^{jn\phi_i}, \tag{3.11}$$

$$j\omega\mu_0 H_{\phi_i}^{\text{I}}(\rho_i \leq r_i, \phi_i) = k_0 n_i \sum_{n=-\infty}^{+\infty} A_n J_n'(k_0 n_i \rho_i) e^{jn\phi_i}, \tag{3.12}$$

where A_n are unknown coefficients. In the second situation the fields at $\rho_i = r_i^+$ are given by

$$E_z^{\text{II}}(\rho_i = r_i^+, \phi_i) = \sum_{n=-\infty}^{+\infty} B_n J_n(k_0 n_{\text{ext}} r_i) e^{jn\phi_i}, \tag{3.13}$$

$$\begin{aligned} j\omega\mu_0 H_{\phi_i}^{\text{II}}(\rho_i = r_i^+, \phi_i) &= k_0 n_{\text{ext}} \sum_{n=-\infty}^{+\infty} B_n J_n'(k_0 n_{\text{ext}} r_i) e^{jn\phi_i} \\ &\quad + j\omega\mu_0 \sum_{n=-\infty}^{+\infty} \frac{I_n^i}{2\pi r_i} e^{jn\phi_i}. \end{aligned} \tag{3.14}$$

We define the boundary admittance $Y_n^i = \dfrac{1}{Z_n^i}$ as

$$\frac{I_n^i}{2\pi r_i} = Y_n^i e_n^{\text{II}}(r_i) = Y_n^i B_n J_n(k_0 n_{\text{ext}} r_i). \tag{3.15}$$

This boundary admittance can be determined by requiring that

$$E_z^{\text{I}}(r_i^-, \phi_i) = E_z^{\text{II}}(r_i^+, \phi_i) \tag{3.16}$$

$$H_{\phi_i}^{\text{I}}(r_i^-, \phi_i) = H_{\phi_i}^{\text{II}}(r_i^+, \phi_i). \tag{3.17}$$

This yields

$$Z_n^i = j\sqrt{\frac{\mu_0}{\epsilon_0}} \frac{J_n(k_0 n_{\text{ext}} r_i) J_n(k_0 n_i r_i)}{n_{\text{ext}} J_{n+1}(k_0 n_{\text{ext}} r_i) J_n(k_0 n_i r_i) - n_i J_{n+1}(k_0 n_i r_i) J_n(k_0 n_{\text{ext}} r_i)}. \tag{3.18}$$

A perfectly conducting cylinder corresponds to $\epsilon_i = \infty$ or $Z_n^i = 0$, as expected. The unknown surface currents are then determined by

$$E_z^{\text{t}}(\rho_i = r_i, \phi_i) - \sum_{n=-\infty}^{+\infty} Z_n^i \frac{I_n^i}{2\pi r_i} e^{jn\phi_i} = 0. \tag{3.19}$$

In practice, this infinite sum has to be truncated to a finite number of terms: n going from $-K$ to K. As will become clear in the examples, three terms for every cylinder (corresponding to $K = 1$) are usually sufficient. Similar formulas were derived in [13–15].

3.2.3 Modeling infinite crystals with a Perfectly Matched Layer

When designing PC devices, one is usually not interested in back reflections coming from an abruptly terminated photonic crystal. Therefore it is advantageous to be able to model PC waveguides that are infinitely long in the propagation direction. This can be achieved, e.g., by incorporating an appropriate boundary condition. Recently such a boundary condition has been proposed for FDTD simulations, namely, a PC-based-PML [6]. The main difference from a regular PML boundary condition is that the PC structure is maintained

in the PML. In [16], we introduced a similar boundary condition for integral-equation-like techniques. By exploiting the complex coordinate interpretation of a PML [18, 19], a PC structure can be terminated by adding a couple of periods in the complex plane. Although entering into the complex plane always causes a disturbance of the periodicity, the absorption in the PML region drastically reduces the reflections at the termination of the PC structure compared with a termination in real space. The remaining reflections due to the disturbance of the periodicity can be strongly reduced if the waveguide enters the complex plane smoothly. In [16], two different ways to enter the complex plane were compared, namely, a 'linear' PML and a 'circular' PML. It was shown that the circular PML outperforms the linear PML.

3.2.4 Advantages

The advantages of the semi-analytical method are as follows:

- Because this is a semi-analytical technique, the accuracy is very much under control, which makes this technique well suited as a bench-mark technique. No phase errors are introduced.
- For finite structures this technique does not rely on an absorbing boundary condition.
- This technique is suited for cylinders with arbitrary losses ranging from dielectric cylinders to perfectly conducting cylinders.

3.2.5 Disadvantages

The disadvantages of the semi-analytical method are as follows:

- CPU time is proportional to N^3; however, the number of unknowns N will be much smaller than with mode-matching.
- The technique is limited to circular wires. An extension to arbitrary shapes is possible, but at significant extra cost.

3.3 Vectorial eigenmode expansion

The general principles behind the vectorial eigenmode expansion method have already been described, e.g., in [11, 12] and references therein. For clarity, we will briefly review the main principles behind the method, as well as clarify its advantages and disadvantages when applied to the modeling of PC structures. In the following sections we will extend the method to deal with a source placed inside a structure and with PCs that extend infinitely in the propagation direction. CAMFR, our implementation of this model, is freely available from [20].

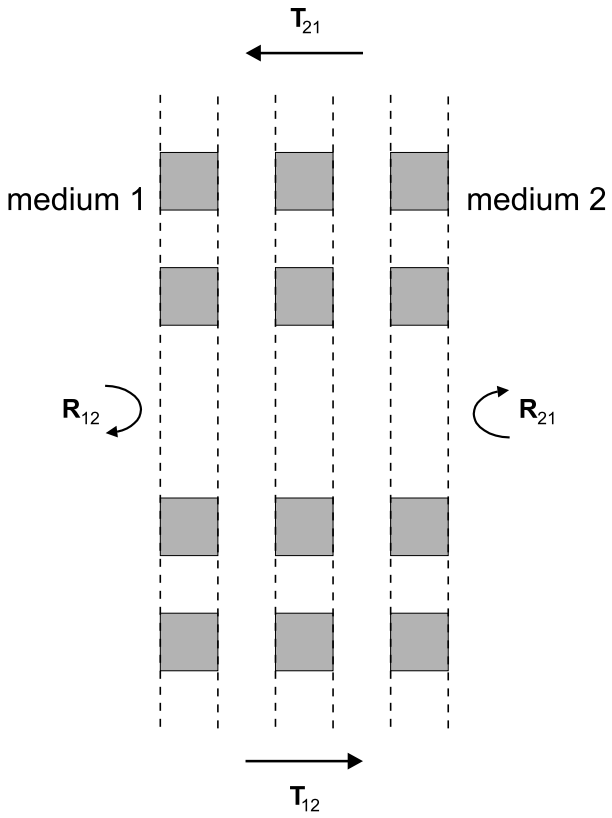

Figure 3.3: Reflection and transmission of a layered medium.

3.3.1 Overview of eigenmode expansion

The main philosophy of the eigenmode expansion method is to divide the structure of interest into a number of layers in which the refractive-index profile does not change in the propagation or z direction. If the geometry is not piecewise constant, a suitable staircase approximation can be chosen (Fig. 3.3). Subsequently, the vectorial eigenmodes of these waveguide sections are calculated and are used as basis functions for a field expansion. At the interface between two different layers, mode-matching is applied to derive the reflection and transmission matrices, which can be used to calculate the reflection and transmission matrices $\boldsymbol{R}_{12}$ and $\boldsymbol{T}_{12}$ of the entire structure. For an arbitrary incident field described by its expansion vector $\boldsymbol{A}_1$ in the eigenmodes, the reflected and transmitted fields are given by $\boldsymbol{R}_{12}\boldsymbol{A}_1$ and $\boldsymbol{T}_{12}\boldsymbol{A}_1$, respectively. Similar matrices $\boldsymbol{R}_{21}$ and $\boldsymbol{T}_{21}$ can be derived for incidence from the other side.

3.3.2 Source inside a structure

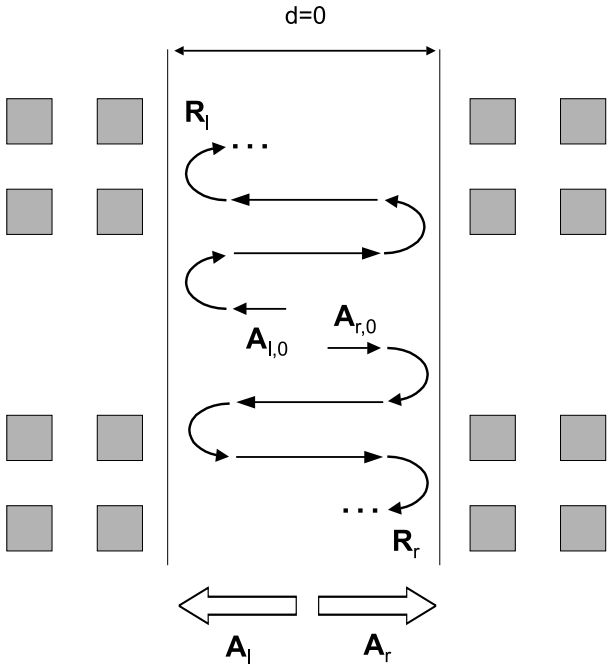

Figure 3.4: Source inside a layered medium.

The natural excitation of a structure in this formalism is an incident field expanded in eigenmodes and impinging on the structure from the outside. This field can even be a Bloch mode, which reduces the required computational domain, as no extra length of PC waveguide is needed to achieve an equilibrium field distribution. For a dipole current source as excitation, a longer waveguide would be needed to achieve this equilibrium.

However, it is also possible to calculate the response to a current source (or a more general source) placed inside the structure, as will now be shown.

The plane which contains the source divides the structure in a left and a right part, of which we can calculate the reflection matrices $\boldsymbol{R}_{\mathrm{r}}$ and $\boldsymbol{R}_{\mathrm{l}}$ (Fig. 3.4). The exact field pattern emitted by this source is arbitrary; only its expansion coefficients need to be known. In general, the source will radiate in both directions (right/forward and left/backward), so it is fully characterized by two expansion vectors $\boldsymbol{A}_{\mathrm{r},0}$ and $\boldsymbol{A}_{\mathrm{l},0}$.

Let us concentrate for the moment on the source term $\boldsymbol{A}_{\mathrm{r},0}$. This field distribution will keep on bouncing back and forth between the right and left part of the structure such that the equilibrium forward field distribution just to the right of the source will be

$$\boldsymbol{A}_{\mathrm{r},0} + \boldsymbol{R}_{\mathrm{l}}\boldsymbol{R}_{\mathrm{r}}\boldsymbol{A}_{\mathrm{r},0} + \boldsymbol{R}_{\mathrm{l}}\boldsymbol{R}_{\mathrm{r}}\boldsymbol{R}_{\mathrm{l}}\boldsymbol{R}_{\mathrm{r}}\boldsymbol{A}_{\mathrm{r},0} + ... \tag{3.20}$$

We can write this as

$$\sum_{i=0}^{\infty} \left(\boldsymbol{R}_{\mathrm{l}}\boldsymbol{R}_{\mathrm{r}}\right)^{i} \boldsymbol{A}_{\mathrm{r},0} \tag{3.21}$$

This sum converges to

$$\left(\boldsymbol{I} - \boldsymbol{R}_{\mathrm{l}}\boldsymbol{R}_{\mathrm{r}}\right)^{-1} \boldsymbol{A}_{\mathrm{r},0} \tag{3.22}$$

The other source term $\boldsymbol{A}_{\mathrm{l},0}$ also contributes to the total forward field. After reflecting at the left part, it goes through the same sequence of reflections as in (3.20). Therefore, the total forward equilibrium field can be written as

$$\boldsymbol{A}_{\mathrm{r}} = \left(\boldsymbol{I} - \boldsymbol{R}_{\mathrm{l}}\boldsymbol{R}_{\mathrm{r}}\right)^{-1} \left(\boldsymbol{A}_{\mathrm{r},0} + \boldsymbol{R}_{\mathrm{l}}\boldsymbol{A}_{\mathrm{l},0}\right) \tag{3.23}$$

Similarly, the total backward field just to the left of the source is

$$\boldsymbol{A}_{\mathrm{l}} = \left(\boldsymbol{I} - \boldsymbol{R}_{\mathrm{r}}\boldsymbol{R}_{\mathrm{l}}\right)^{-1} \left(\boldsymbol{A}_{\mathrm{l},0} + \boldsymbol{R}_{\mathrm{r}}\boldsymbol{A}_{\mathrm{r},0}\right) \tag{3.24}$$

Using these field distributions as excitations for, respectively, the right and the left part of the structure, we can calculate the total field at an arbitrary position. This completely characterizes the response of the structure to the source.

For the specific case of a dipole current source $\boldsymbol{J}_0\delta\left(\boldsymbol{r} - \boldsymbol{r}_0\right)$, we can calculate the source terms $\boldsymbol{A}_{\mathrm{r},0}$ and $\boldsymbol{A}_{\mathrm{l},0}$ based on the Lorentz reciprocity theorem [21] as

$$-2A_{l,m} = \boldsymbol{J}_0\boldsymbol{E}_{r,m}\left(\boldsymbol{r}_0\right) \tag{3.25}$$

$$-2A_{r,m} = \boldsymbol{J}_0\boldsymbol{E}_{l,m}\left(\boldsymbol{r}_0\right) \tag{3.26}$$

Here, m is the index of the mode.

3.3.3 Modeling infinite crystals

In the eigenmode expansion formalism another more exact method can be used in order to reduce reflections. That is, it is possible to calculate the reflection matrix $\boldsymbol{R}_{\infty}$ of a semi-infinite crystal, and then to use this matrix to terminate the structure in the propagation direction.

To calculate this matrix $\boldsymbol{R}_\infty$ we first calculate the blochmodes of the infinite crystal by solving the following generalized eigenvalue problem containing the scattering matrices of the basic period [22, 23]:

$$\begin{bmatrix} \boldsymbol{T}_{12} & \boldsymbol{R}_{21} \\ \boldsymbol{0} & \boldsymbol{I} \end{bmatrix} \begin{bmatrix} \boldsymbol{F}_1 \\ q\boldsymbol{B}_1 \end{bmatrix} = q \begin{bmatrix} \boldsymbol{I} & \boldsymbol{0} \\ \boldsymbol{R}_{12} & \boldsymbol{T}_{21} \end{bmatrix} \begin{bmatrix} \boldsymbol{F}_1 \\ q\boldsymbol{B}_1 \end{bmatrix} \tag{3.27}$$

Here, $\boldsymbol{F}_1$ and $\boldsymbol{B}_1$ are the forward and backward components of the Bloch mode at the left-hand side of the unit cell, and q is related to the Bloch vector β by $q = e^{-j\beta T}$, with T the length of the basic period. Equation 3.27 is more stable than more traditional methods based on calculating eigenvectors of the transfer matrix, because it does not contain any matrix inversions. For higher-order evanescent modes, the corresponding diagonal elements in $\boldsymbol{T}_{12}$ and $\boldsymbol{T}_{21}$ are close to zero. Therefore $\boldsymbol{T}_{12}$ and $\boldsymbol{T}_{21}$ are close to singular and cannot be inverted in a stable way. It is this inversion that Eq. (3.27) avoids.

For M modes retained in the series expansion, this method will give rise to $2M$ solutions, half of which are Bloch modes with a forward flux, the other half with a backward flux. We retain only those with forward flux and arrange their field profiles as column vectors in two matrices $\boldsymbol{F}^+$and $\boldsymbol{B}^+$. We can now calculate the reflection matrix of the semi-infinite stack as

$$\boldsymbol{R}_\infty = \boldsymbol{B}^+(\boldsymbol{F}^+)^{-1} \tag{3.28}$$

which is intuitively plausible as being a generalized ratio between a backward and a forward field. A similar idea was already put forward in [24].

3.3.4 Advantages

The advantages of the vectorial eigenmode expansion are the following:

- The calculation time is linear in the number of layers, and not in the total length of the structure, as the propagation through layers can be handled analytically.
- In modeling structures with a finite number of repetitions of a basic period (as is common in PC devices), calculation time for the scattering matrices is logarithmic in the number of periods rather than linear [11].
- PML boundary conditions [25,26] can be introduced trivially by allowing the cladding thickness to take on complex values [19]. In this way, structures with radiation losses can be handled.
- Abruptly terminating a photonic crystal will give rise to unwanted parasitic reflections from the end face. In eigenmode expansion it is possible to calculate analytically crystals that are infinite in the propagation direction, thereby solving this problem.

3.3.5 Disadvantages

The disadvantages of eigenmode expansion are the following:

- This technique behaves less advantageously if there is no repetition of layers, which would be the case when considering irregular structures.
- For curved non-rectangular objects, many layers are needed.
- This technique relies on an absorbing boundary condition.
- Considerable performance is lost if the structure is excited by waveguides that run along different directions.

3.4 The subdomain FDTD method

The FDTD technique has often been used to analyze PC structures [27–29]. One of the problems in doing so is the fine grid needed to capture the shape of the periodic unit cells. In [9], a scheme was developed to automatically generate new FDTD update equations for objects that are smaller than the grid step size. With this technique the simulation of PC structures by FDTD can be enhanced dramatically. Here, we will give a brief summary of the technique presented in [9] and at some time improve it in two respects.

Consider a part of a TM FDTD grid as shown in Fig. 3.5. We consider a local fine grid inside a contour C that encloses the small object that will be periodically repeated when used in a PC structure. Outside the contour C we use a coarse grid. The refinement ratio ξ is defined as $\xi = \frac{\Delta_c}{\Delta_f}$. In the fine grid the FDTD equations can be written as

$$\epsilon \frac{dE_z^{i+1/2,j+1/2}(t)}{dt} = \frac{H_y^{i+1,j+1/2}(t) - H_y^{i,j+1/2}(t)}{\Delta_f} - \frac{H_x^{i+1/2,j+1}(t) - H_x^{i+1/2,j}(t)}{\Delta_f} \tag{3.29}$$

$$\mu_0 \frac{dH_y^{i,j+1/2}(t)}{dt} = \frac{E_z^{i+1/2,j+1/2}(t) - E_z^{i-1/2,j+1/2}(t)}{\Delta_f} \tag{3.30}$$

$$\mu_0 \frac{dH_x^{i+1/2,j}(t)}{dt} = -\frac{E_z^{i+1/2,j+1/2}(t) - E_z^{i+1/2,j-1/2}(t)}{\Delta_f}, \tag{3.31}$$

where standard FDTD index notation was used and where Δ_f is the fine mesh grid step. In these equations time is still kept continuous. Taking all these equations together for all field variables inside the contour C yields the following system of first-order equations

$$\begin{cases} \begin{bmatrix} \epsilon_0 \boldsymbol{D}_\epsilon & \boldsymbol{0} \\ \boldsymbol{0} & \mu_0 \boldsymbol{I} \end{bmatrix} \begin{bmatrix} \dot{\boldsymbol{e}} \\ \dot{\boldsymbol{h}} \end{bmatrix} = -\frac{1}{\Delta_f} \begin{bmatrix} \boldsymbol{0} & \boldsymbol{K} \\ -\boldsymbol{K}^T & \boldsymbol{0} \end{bmatrix} \begin{bmatrix} \boldsymbol{e} \\ \boldsymbol{h} \end{bmatrix} + \frac{1}{\Delta_f} \begin{bmatrix} \boldsymbol{0} \\ \boldsymbol{B} \end{bmatrix} \boldsymbol{u} \\ \boldsymbol{y} = \begin{bmatrix} \boldsymbol{0} & \boldsymbol{L}^T \end{bmatrix} \begin{bmatrix} \boldsymbol{e} \\ \boldsymbol{h} \end{bmatrix} \end{cases}, \tag{3.32}$$

with $\boldsymbol{e}$ a vector with all variables $E_z^{i+1/2,j+1/2}$ inside C and $\boldsymbol{h}$ a vector with all variables $H_x^{i+1/2,j+1}$ and $H_y^{i+1,j+1/2}$ inside or on C; $\dot{\boldsymbol{e}}$ and $\dot{\boldsymbol{h}}$ denote the time derivatives of $\boldsymbol{e}$ and

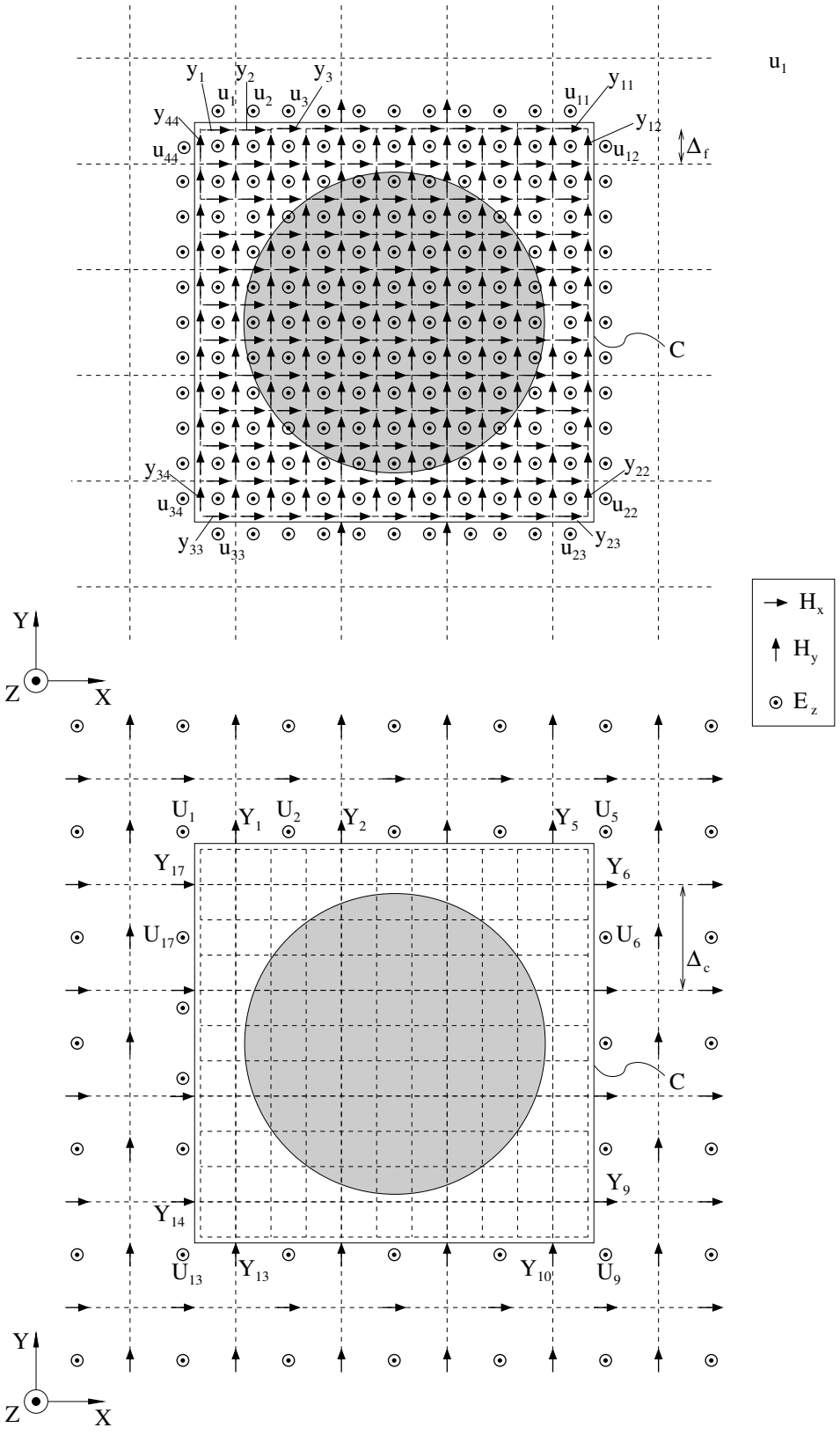

Figure 3.5: A coarse and a fine grid with refinement ratio, $\xi = \Delta_c/\Delta_f = 3$.

$\boldsymbol{h}$, and $\boldsymbol{u}$ is a vector with the variables $E_z^{i+1/2,j+1/2}$ just outside the fine grid as if the fine grid had been extended by one row of cells. The vector $\boldsymbol{y}$ contains the components $H_x^{i+1/2,j+1}$ and $H_y^{i+1,j+1/2}$ on the boundary C. The matrices $\boldsymbol{K}$ and $\boldsymbol{B}$ are sparse matrices with nonzero elements equal to ± 1. The matrix $\boldsymbol{D}_e$ is a diagonal matrix with the relative permittivities in each cell. The matrix $\boldsymbol{L}$ contains a few elements equal to 1 in order to pick the subset $\boldsymbol{y}$ from $\boldsymbol{x}$. Now we have to connect the fine grid variables $\boldsymbol{y}$ and $\boldsymbol{u}$ to the coarse grid variables $\boldsymbol{Y}$ and $\boldsymbol{U}$. This can be done in many different ways [9]. In general we can write

$$\begin{aligned} \boldsymbol{u} &= \boldsymbol{A}\boldsymbol{U} && (3.33)\\ \boldsymbol{Y} &= \boldsymbol{D}\boldsymbol{y}, && (3.34) \end{aligned}$$

with $\boldsymbol{U}$ the $E_z^{i+1/2,j+1/2}$ variables of the coarse grid just outside C and with $\boldsymbol{Y}$ the $H_x^{i+1/2,j+1}$ and $H_y^{i+1,j+1/2}$ variables of the coarse grid on C. In this way we can recast system (3.32) as

$$\begin{cases} \begin{bmatrix} \epsilon_0 \boldsymbol{D}_\epsilon & \boldsymbol{0} \\ \boldsymbol{0} & \mu_0 \boldsymbol{I} \end{bmatrix} \begin{bmatrix} \dot{\boldsymbol{e}} \\ \dot{\boldsymbol{h}} \end{bmatrix} = -\frac{1}{\Delta_f} \begin{bmatrix} \boldsymbol{0} & \boldsymbol{K} \\ -\boldsymbol{K}^T & \boldsymbol{0} \end{bmatrix} \begin{bmatrix} \boldsymbol{e} \\ \boldsymbol{h} \end{bmatrix} + \frac{1}{\Delta_f} \begin{bmatrix} \boldsymbol{0} \\ \boldsymbol{B'} \end{bmatrix} \boldsymbol{U} \\ \boldsymbol{Y} = \begin{bmatrix} \boldsymbol{0} & \boldsymbol{L'}^T \end{bmatrix} \begin{bmatrix} \boldsymbol{e} \\ \boldsymbol{h} \end{bmatrix} \end{cases}, \tag{3.35}$$

with $\boldsymbol{B'} = \boldsymbol{B}\boldsymbol{A}$ and $\boldsymbol{L'} = \boldsymbol{L}\boldsymbol{D}^T$.

In the next step we will use a ROM technique [30], characterized by an order of approximation q, to reduce the size of the vectors $\boldsymbol{e}$ and $\boldsymbol{h}$ drastically while still retaining the same dynamic behavior of the system (3.35) up to a certain frequency. The result is

$$\begin{cases} \begin{bmatrix} \epsilon_0 \boldsymbol{I} & \boldsymbol{0} \\ \boldsymbol{0} & \mu_0 \boldsymbol{I} \end{bmatrix} \begin{bmatrix} \dot{\boldsymbol{x}}_1 \\ \dot{\boldsymbol{x}}_2 \end{bmatrix} = -\frac{1}{\Delta_f} \begin{bmatrix} \boldsymbol{0} & \tilde{\boldsymbol{K}} \\ -\tilde{\boldsymbol{K}}^T & \boldsymbol{0} \end{bmatrix} \begin{bmatrix} \boldsymbol{x}_1 \\ \boldsymbol{x}_2 \end{bmatrix} + \frac{1}{\Delta_f} \begin{bmatrix} \boldsymbol{0} \\ \tilde{\boldsymbol{B}} \end{bmatrix} \boldsymbol{U} \\ \boldsymbol{Y} = \begin{bmatrix} \boldsymbol{0} & \tilde{\boldsymbol{L}}^T \end{bmatrix} \begin{bmatrix} \boldsymbol{x}_1 \\ \boldsymbol{x}_2 \end{bmatrix} \end{cases}. \tag{3.36}$$

We can enhance this further by diagonalyzing the full matrix $\tilde{\boldsymbol{K}}$ using a singular-value decomposition

$$\tilde{\boldsymbol{K}} = \tilde{\boldsymbol{U}}^T \boldsymbol{\Sigma} \tilde{\boldsymbol{V}}. \tag{3.37}$$

By changing the variables $\boldsymbol{z}_1 = \tilde{\boldsymbol{U}}\boldsymbol{x}_1$ and $\boldsymbol{z}_2 = \tilde{\boldsymbol{U}}\boldsymbol{x}_2$, we rewrite system (3.36) as

$$\begin{cases} \begin{bmatrix} \epsilon_0 \boldsymbol{I} & \boldsymbol{0} \\ \boldsymbol{0} & \mu_0 \boldsymbol{I} \end{bmatrix} \begin{bmatrix} \dot{\boldsymbol{z}}_1 \\ \dot{\boldsymbol{z}}_2 \end{bmatrix} = -\frac{1}{\Delta_f} \begin{bmatrix} \boldsymbol{0} & \boldsymbol{\Sigma} \\ -\boldsymbol{\Sigma}^T & \boldsymbol{0} \end{bmatrix} \begin{bmatrix} \boldsymbol{z}_1 \\ \boldsymbol{z}_2 \end{bmatrix} + \frac{1}{\Delta_f} \begin{bmatrix} \boldsymbol{0} \\ \tilde{\boldsymbol{V}}\tilde{\boldsymbol{B}} \end{bmatrix} \boldsymbol{u} \\ \boldsymbol{y} = \begin{bmatrix} \boldsymbol{0} & \tilde{\boldsymbol{L}}^T \tilde{\boldsymbol{V}}^T \end{bmatrix} \begin{bmatrix} \boldsymbol{z}_1 \\ \boldsymbol{z}_2 \end{bmatrix} \end{cases}. \tag{3.38}$$

This diagonalization was not introduced in [9]. The FDTD iteration process now proceeds as follows. Suppose everything is known until time step $t = (n - 1/2)\Delta_t$.

- First, we update the electric fields outside C in the coarse grid with the regular equation:

$$\begin{aligned} E_z^{i+1/2,j+1/2}(n) &= E_z^{i+1/2,j+1/2}(n-1) \\ &+ \frac{\Delta_t}{\epsilon\Delta_c}\left(H_y^{i+1,j+1/2}(n-1/2) - H_y^{i,j+1/2}(n-1/2)\right) \\ &- \frac{\Delta_t}{\epsilon\Delta_c}\left(H_x^{i+1/2,j+1}(n-1/2) - H_x^{i+1/2,j}(n-1/2)\right), \end{aligned} \tag{3.39}$$

  with Δ_t the time step and Δ_c the coarse grid step. Note that some of the magnetic fields on the right hand side are extracted from $\boldsymbol{y}(n-1/2)$ when $E_z^{i+1/2,j+1/2} \in \boldsymbol{u}$.

- Second, we update the magnetic fields outside C with the regular equations:

$$\begin{aligned} H_y^{i,j+1/2}(n+1/2) &= H_y^{i,j+1/2}(n-1/2) \\ &+ \frac{\Delta_t}{\mu\Delta_c}\left(E_z^{i+1/2,j+1/2}(n) - E_z^{i-1/2,j+1/2}(n)\right) \end{aligned} \tag{3.40}$$

  and similar for the H_x-components.

- Third, we discretize the state-space system (3.38) using an explicit scheme. The variables $\boldsymbol{z}_1$ are discretized around the same moment in time as the electric field variables, say $t = n\Delta_t$. The variables $\boldsymbol{z}_2$ are discretized around the same moment in time as the magnetic field variables, a half time step later than the electric field variables: $t = (n+1/2)\Delta_t$. This results in the following equations:

$$\boldsymbol{z}_1|^{n+1/2} = \boldsymbol{z}_1|^{n-1/2} - \frac{\Delta_t}{\epsilon_0\Delta_f}\boldsymbol{\Sigma}\boldsymbol{z}_2|^n \tag{3.41a}$$

$$\boldsymbol{z}_2|^{n+1} = \boldsymbol{z}_1|^n + \frac{\Delta_t}{\mu_0\Delta_f}\boldsymbol{\Sigma}^T\boldsymbol{z}_1|^{n+1/2} + \frac{\Delta_t}{\mu_0\Delta_f}\tilde{\boldsymbol{V}}\tilde{\boldsymbol{B}}\boldsymbol{u}|^{n+1/2} \tag{3.41b}$$

$$\boldsymbol{y}|^{n+1} = \tilde{\boldsymbol{L}}^T\tilde{\boldsymbol{V}}^T\boldsymbol{z}_2|^{n+1} \tag{3.41c}$$

  It can be shown that this scheme is stable for

$$\Delta_t < \frac{2}{c_0\sigma} \tag{3.42}$$

  with σ the largest eigenvalue of $\tilde{\boldsymbol{K}}$ or the largest element of $\boldsymbol{\Sigma}$. This is an explicit scheme and differs from the implicit scheme proposed in [9]. Although the implicit scheme in [9] is unconditionally stable, it suffers from late-time instabilities. The new scheme of Eqs. (3.41) has the stability condition of Eq. (3.42) related to it, and numerical experiments show that choosing

$$\Delta_t < \min\left\{\frac{2}{c_0\sigma}, \frac{\Delta_c}{\sqrt{2}c_0}\right\} \tag{3.43}$$

  results in a stable iteration scheme.

  It is clear that the model (3.38) can be calculated once and for all. Therefore the time consuming ROM and singular-value decomposition are performed in advance and depend only on the shape of the cell that is repeated in the photonic crystal.

3.4.1 Advantages

The advantages of the FDTD method are the following:

- The CPU-time and the memory requirements scale linearly with the number of cylinders.
- This approach is not limited to circular cylinders, and the numerical complexity does not increase when the shape of the periodic objects changes.
- The technique yields results over a wide frequency range in a single run.

3.4.2 Disadvantages

Disadvantages of the FDTD method are as follows:

- The accuracy is more difficult to control.
- The technique relies on absorbing boundary conditions.
- FDTD in general suffers from the accumulation of phase errors for larger structures, which could lead to a change in resonance frequencies.
- If there are many objects that are not repeated, this technique becomes costly in CPU time and memory.

3.5 Examples

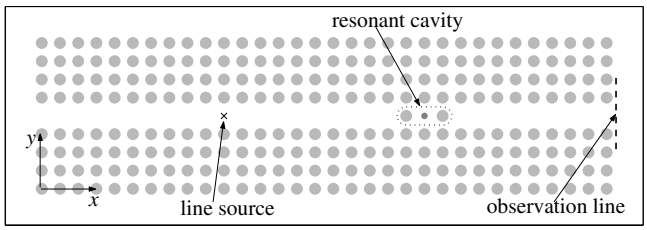

Figure 3.6: Geometry of the PC structure used for comparison of the three techniques.

In this section, the PC structure given in Fig. 3.6 is simulated with the three methods described in Sections 3.2, 3.3, and 3.4. The basic structure is a PC waveguide with a unit cell consisting of four dielectric cylinders at each side of the waveguide channel. This channel is actually formed by removing one row of cylinders. The radius of the cylinders of refractive index n is $0.18a$, with a the lattice constant, and they are placed in air. In the PC waveguide a resonant cavity is created by adding two or three cylinders. Because of this resonant cavity, the structure behaves as a filter. Only a small band around a certain frequency will be transmitted. Both finite and infinite PC structures are simulated. From this the effect of the reflections at the end surfaces of the PC waveguide becomes clear.

The finite PC waveguide consists of 32 unit cells. These unit cells are numbered from 1 up to 32. The two cylinders of the resonant cavity are placed in the middle of rows 21 and 23, as shown in Fig. 3.6. A line source is placed in the middle of unit cell 11. The transmission spectrum $T(f)$ of this finite structure is calculated as follows. The energy flux $\Phi = \iint_S [\boldsymbol{E} \times \boldsymbol{H}^*] \cdot \boldsymbol{u}_n dS$, with $\boldsymbol{u}_n$ the unit vector in the direction of propagation, is calculated at the outlet of the PC structure. This is done by integration along a line situated at a distance $a/2$ of the outlet of the waveguide (Fig. 3.6). This flux is calculated for two situations: for the filter structure (Φ_{filt}) and for the waveguide without a resonant cavity (Φ_{wg}). The transmission spectrum $T(f)$ is defined by

$$T(f) = \frac{\Phi_{\text{filt}}}{\Phi_{\text{wg}}} \tag{3.44}$$

In the FDTD simulations the electric and magnetic fields are only available in discrete points that are determined by the coarse grid used. Consequently, the electric and magnetic fields are not known at the same points. To calculate the energy flux, linear interpolation for the magnetic fields is used. The transmission spectrum for the finite PC

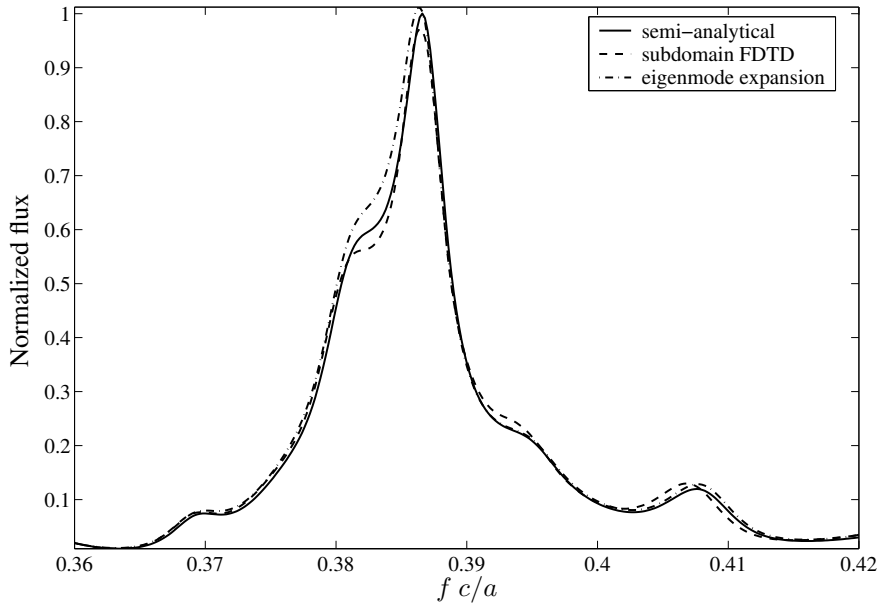

Figure 3.7: Transmission through the finite filter structure, with $n = 3.4$.

filter is given in Figs. 3.7 and 3.8 in the frequency range from $f = 0.36\frac{c}{a}$ to $f = 0.42\frac{c}{a}$ for $n = 3.4$ and $n = 2.83$, respectively. In the semi-analytical case technique, three unknowns per cylinder are used, which corresponds to $K = 1$ in (3.2). For the FDTD simulations, the refinement ratio ξ is chosen to be 9 and a ROM technique with approximation order $q = 1$ is used. The time step is $0.056\frac{a}{c}$. The thickness of the layers used in the vectorial eigenmode expansion technique is $\Delta = \frac{a}{20}$. Excellent agreement between the three methods is observed. Note that because of reflections at the end surfaces, $T(f)$ as defined in Eq. (3.44) can become larger than 1.

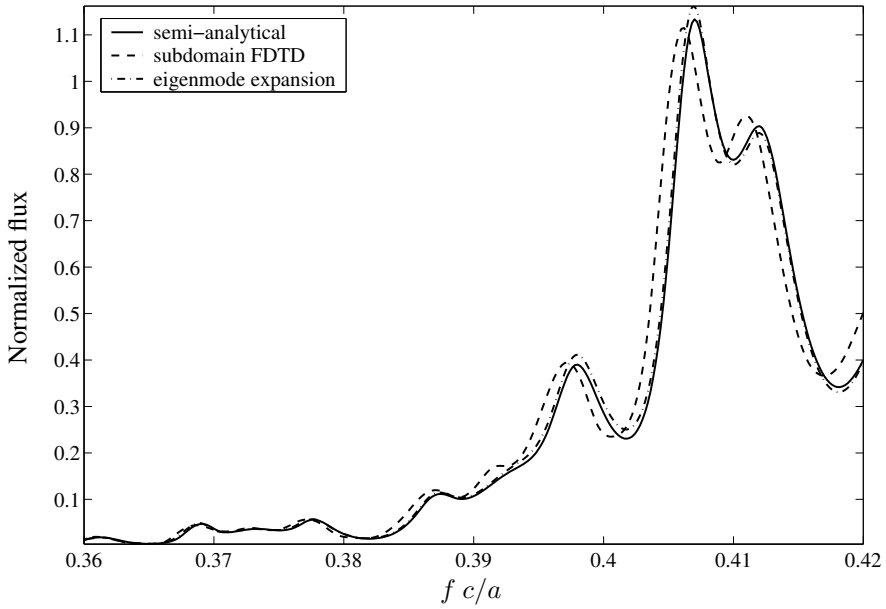

Figure 3.8: Transmission through the finite filter structure, with $n = 2.83$.

For the infinite structures, the relative position of the line source, the cavity, and the observation points remains the same as for the finite structure. In the simulations with the semi-analytical method of Section 3.2, a circular PML region with seven extra unit cells is added before and after the photonic crystal structure [16]. The x coordinates of these cylinders are made complex according to a circle with radius $R_{\text{PML}} = 10a$. For the PML region after the PC waveguide we can write

$$x_n^{\text{re}} = x_0 + R_{\text{PML}} \sin(n\alpha), \tag{3.45}$$

$$x_n^{\text{im}} = -R_{\text{PML}}(1 - \cos(n\alpha)), \tag{3.46}$$

with $\alpha = 2\arcsin(\frac{a}{2R_{\text{PML}}})$ and x_0 the x-coordinate of the last row in PC waveguide which is not yet in the PML. For the simulations with the subdomain FDTD method no extra boundary condition is added, but a very long waveguide with 100 extra unit cells before and after the original finite waveguide is calculated. In this way, the pulse that is transmitted through the resonant cavity can be easily separated from the pulse that is reflected by the end surface of the PC waveguide. The transmission spectrum for the infinite structures, with the same parameters as in the finite case are given in Figs. 3.9 and 3.10. When one compares these results with the previous ones, it becomes clear that the reflections on the end surfaces have a rather strong influence on the behavior of the structure, as could be expected. The results also show that the complex coordinate technique to terminate the waveguide in the semi-analytical technique works well. Note that $T(f)$ is now always smaller than 1. In Fig. 3.11, the electric field at the observation line is shown for the infinite PC waveguide with $n = 3.4$ at a frequency of $f = 0.36\frac{c}{a}$ and this for the three methods. Because the implementation of the source is not exactly the same for

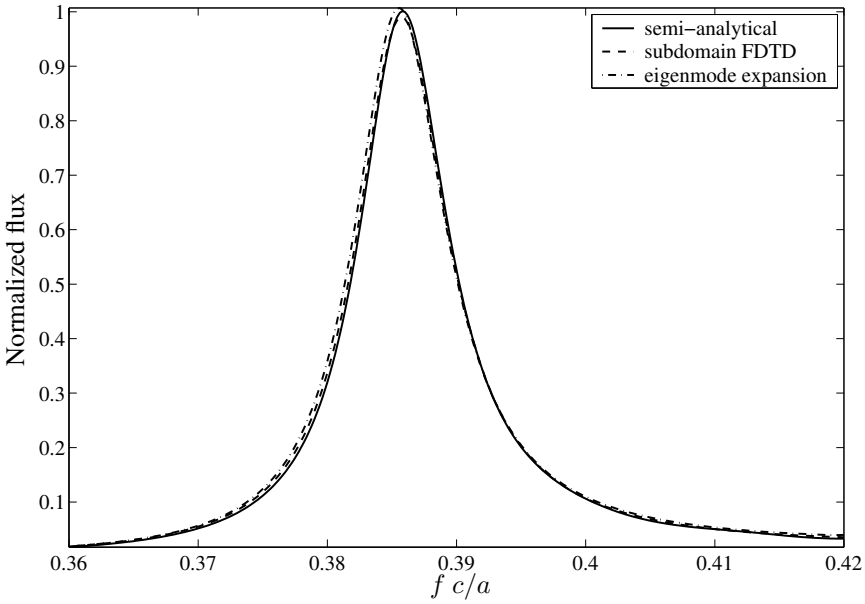

Figure 3.9: Transmission through the infinite filter structure, with $n = 3.4$.

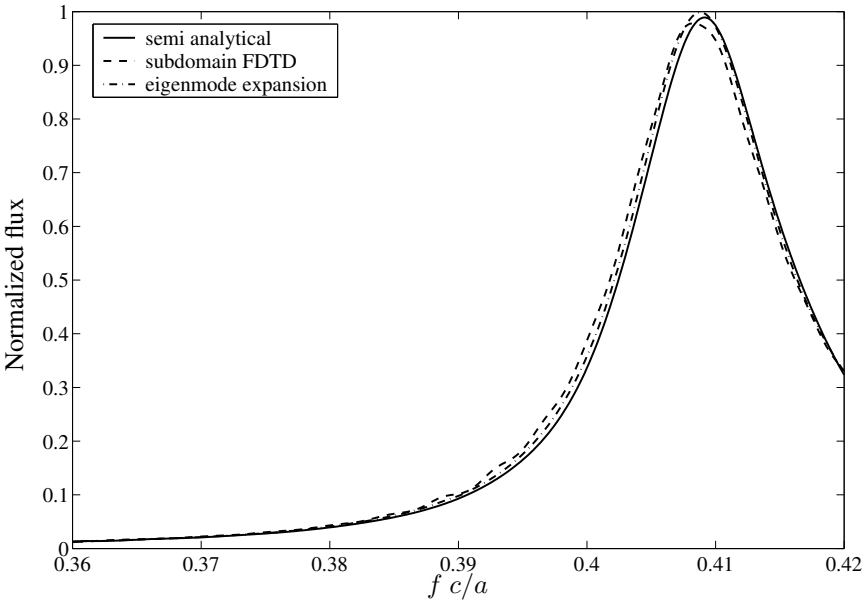

Figure 3.10: Transmission through the infinite filter structure, with $n = 2.83$.

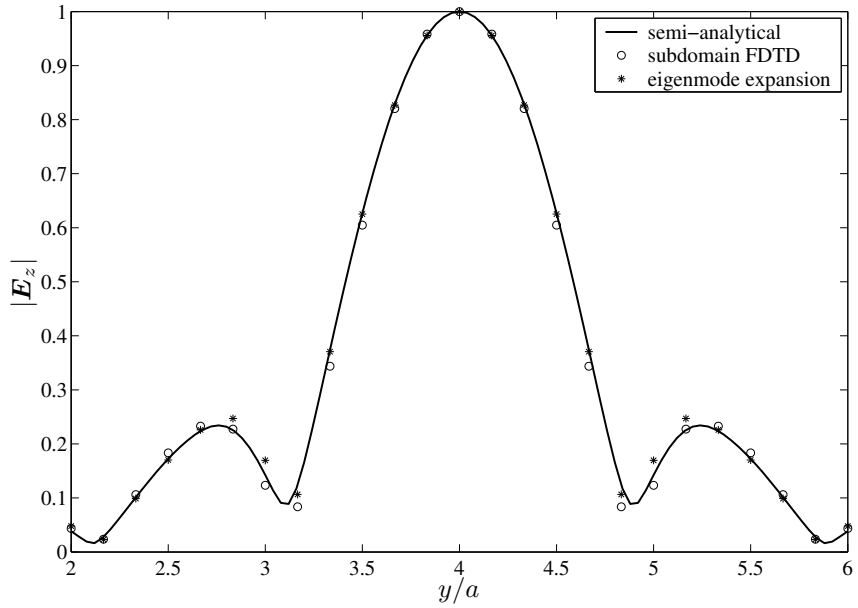

Figure 3.11: Electric field at the observation line shown in Fig. 3.6 for an infinite waveguide, with $n = 3.4$ and $f = 0.36\frac{c}{a}$.

the frequency domain techniques as for the time domain technique, this electric field is normalized to its value at the center of the waveguide channel. The central frequency of the filter can be tuned by placing an extra cylinder with a different radius and/or index of refraction, in the middle of the cavity. We simulated the infinite PC structure with an extra rod with radius $r/4 = 0.045a$ but with the same index of refraction as the 'regular' cylinders. For $n = 3.4$, the difference between the three schemes now becomes larger. This is due to the staircase approximation used in the FDTD and in the vectorial eigenmode expansion technique. This shows that the discretization used in the FDTD and in the vectorial eigenmode expansion technique has to be chosen very fine for accurate results. In Fig. 3.12, we show on the one hand that three unknowns are indeed sufficient in the semi-analytical technique and on the other hand that the results for the vectorial eigenmode expansion technique converge towards those of the semi-analytical technique if the grid size is decreased. This finer grid only has to be used in the region of the PC filter that contains the extra rod. For the other parts of the structure a coarser grid still suffices. The accuracy of the FDTD subdomain technique can be adjusted with three parameters: the refinement ratio ξ, the order of approximation q, and the time step Δ_t. In Fig. 3.13, the transmission spectrum $T(f)$ of the same PC filter as studied in Fig. 3.12 is shown for several combinations of these parameters. It is clear that it is not so obvious to predict which combination will yield the most accurate results, as was already mentioned in Section 3.4. In Fig. 3.14, the transmission spectrum is shown for the infinite filter with one extra rod for the situation where $n = 2.83$.

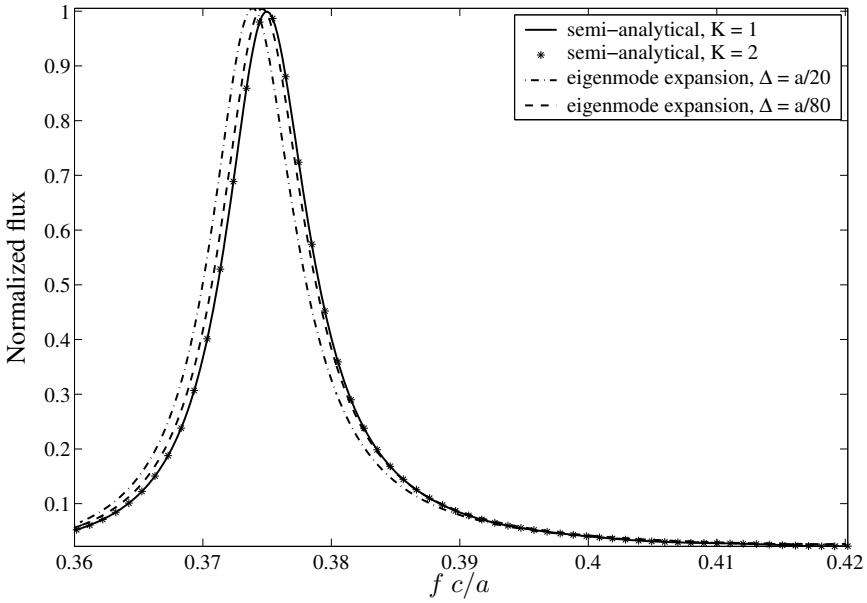

Figure 3.12: Transmission through the infinite filter structure with one extra rod, with $n = 3.4$, comparison of the vectorial eigenmode expansion technique with the semi-analytical technique.

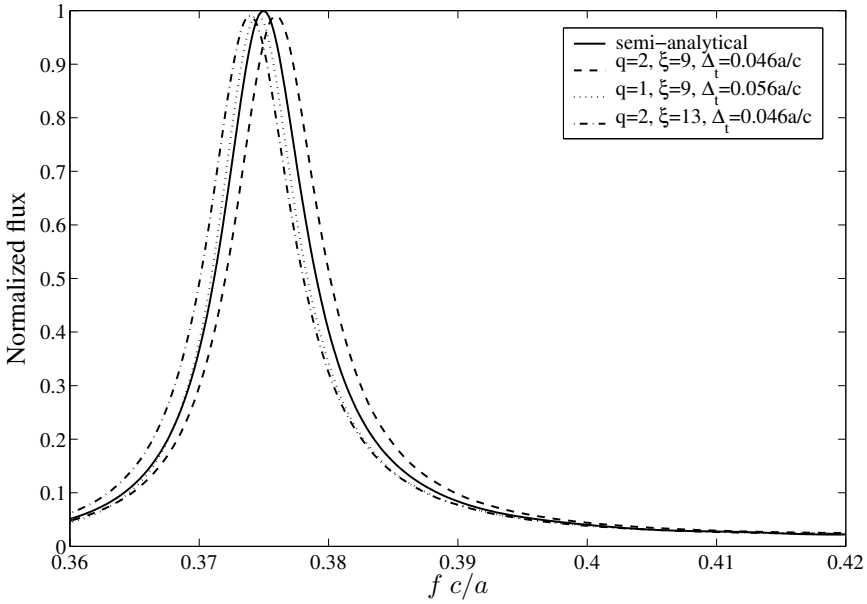

Figure 3.13: Transmission through the infinite filter structure with one extra rod, with $n = 3.4$, comparison of the subdomain FDTD technique with the semi-analytical technique.

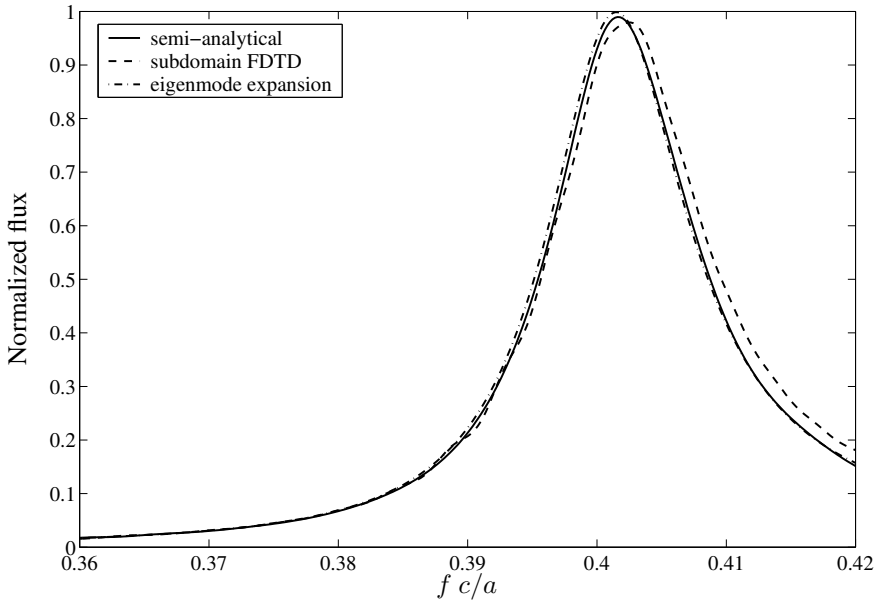

Figure 3.14: Transmission through the infinite filter structure with one extra rod, with $n = 2.83$.

3.6 Conclusion

We have presented and compared three techniques for the efficient simulation of 2D PC structures: a semi-analytical multiple scattering technique, a vectorial eigenmode expansion technique, and a FDTD-ROM technique. The semi-analytical technique yields accurate reference results, the vectorial eigenmode expansion technique is very fast, and the FDTD-ROM technique can give results over a wide frequency band in a single run.

Bibliography

[1] J. D. Joannopoulos, R. D. Meade, and J. N. Winn, *Photonic Crystals, Molding the Flow of Light*. N.J.: Princeton Univ. Press, 1995.

[2] A. Mekis, J. Chen, I. Kurland, S. Fan, P. Villeneuve, and J. Joannopoulos, "High transmission through sharp bends in photonic crystal waveguides," *Phys. Rev. Lett*, vol. 77, no. 18, pp. 3787–3790, Oct. 1996.

[3] A. Chutinan and S. Noda, "Waveguides and waveguide bends in two-dimensional photonic crystal slabs," *Phys. Rev. B*, vol. 62, no. 7, pp. 4488–4492, Aug. 2000.

[4] H. Benisty, C. Weisbuch, M. Agio, M. Kafesaki, C. Soukoulis, M. Qiu, M. Swillo, A. Karlsson, B. Jaskorzynska, A. Talneau, J. Moosburger, M. Kamp, A. Forchell, R. Ferrini, R. Houdré, and U. Oesterle, "Models and measurements for the transmission of submicron-width waveguide bends defined in two-dimensional photonic crystals," *IEEE J. Quantum Electron.*, vol. 38, no. 7, pp. 770–785, July 2002.

[5] O. Painter, R. Lee, A. Yariv, A. Sherer, J. O'Brian, P. Dapkus, and I. Kim, "Two-dimensional photonic bandgap defect mode laser," *Science*, vol. 284, no. 5421, pp. 1819–1821, June 1999.

[6] M. Koshiba, "Wavelength division multiplexing and demultiplexing with photonic crystal waveguide couplers," *Journal of Lightwave Technology*, vol. 19, no. 12, pp. 1970–1975, Dec. 2001.

[7] C. Jin, S. Han, X. Meng, B. Cheng, and D. Zhang, "Demultiplexer using directly resonant tunneling between point defects and waveguides in a photonic crystal," *J. Appl. Phys.*, vol. 91, pp. 4771–4773, 2002.

[8] S. Boscolo, M. Midrio, and C. G. Someda, "Coupling and decoupling of electromagnetic waves in parallel 2D photonic crystal waveguides," *IEEE J. Quantum Electron.*, vol. 1, no. 38, pp. 47–53, Jan. 2002.

[9] B. Denecker, F. Olyslager, L. Knockaert, and D. De Zutter, "Generation of FDTD subcell equations by means of reduced order modelling," *IEEE Trans. Antennas Propag.*, vol. 51, pp. 1806–1817, 2003.

[10] H. Derudder, D. D. Zutter, and F. Olyslager, "A new way to analyse waveguide discontinuities using perfectly matched layers," *IEE Electronic Letters*, vol. 34, no. 22, pp. 2138–2140, Oct. 1998.

[11] P. Bienstman and R. Baets, "Optical modelling of photonic crystals and VCSELs using eigenmode expansion and perfectly matched layers," *Opt. Quantum Electron.*, vol. 33, pp. 327–341, 2001.

[12] ——, "Advanced boundary conditions for eigenmode expansion models," *Opt. Quantum Electron.*, vol. 34, pp. 523–540, 2002.

[13] A. Z. Elsherbeni and A. A. Kishk, "Modelling of cylindrical objects by circular dielectric and conducting cylinders," *IEEE Trans. Antennas Propag.*, vol. 40, no. 1, pp. 96–99, 1992.

[14] A. Z. Elsherbeni, "A comparative study of two-dimensional multiple scattering techniques," *Radio Science*, vol. 29, no. 4, pp. 1023–1033, 1994.

[15] G. Tayeb and D. Maystre, "Rigorous theoretical study of finite-size two-dimensional photonic crystals doped by microcavities," *J. Opt. Soc. Am. A*, vol. 14, no. 12, pp. 3323–3332, Dec. 1997.

[16] D. Pissoort and F. Olyslager, "Termination of periodic waveguides by PMLs in time-harmonic integral equation like techniques," *Antennas and Wireless Propagation Letters*, vol. 2, pp. 281–284, 2003.

[17] W. Magnus, F. Oberhettinger, and R. Soni, *Formulas and Theorems for the Special Functions of Mathematical Physics*. Berlin: Springer Verlag, 1966.

[18] W. C. Chew and W. H. Weedon, "A 3D perfectly matched medium from modified Maxwell's equations in stretched coordinates," *Microwave Opt. Technol. Lett.*, vol. 7, no. 13, pp. 599–604, Sept. 1994.

[19] W. C. Chew, J. M. Jin, and E. Michielssen, "Complex coordinate stretching as a generalized absorbing boundary condition," *Microwave Opt. Technol. Lett.*, vol. 15, no. 6, pp. 363–369, Aug. 1997.

[20] "http://camfr.sourceforge.net."

[21] H. Derudder, F. Olyslager, and D. De Zutter, "An efficient series expansion for the 2D Green's function of a microstrip substrate using perfectly matched layers," *IEEE Microwave Guided Wave Lett.*, vol. 9, no. 12, pp. 505–507, Dec. 1999.

[22] K. Huang, P. Bienstman, J. Joannopoulos, K. Nelson, and S. Fan, "Phonon-polariton excitations in photonic crystals," *Physical Review B*, vol. 68, 2003, art. No. 075209.

[23] Q. Cao, P. Lalanne, and J. Hugonin, "Stable and efficient bloch-mode computational method for one-dimensional grating waveguides," *J. Opt. Soc. Am. A*, vol. 19, pp. 335–338, 2002.

[24] J. Ĉtyroký, S. Helfert, and R. Pregla, "Analysis of a deep waveguide Bragg grating," *Opt. Quantum Electron.*, vol. 30, pp. 343–358, 1998.

[25] J. P. Bérenger, "A perfectly matched layer for the absorption of electromagnetic waves," *Journ. Comput. Phys.*, vol. 114, no. 1, pp. 185–200, 1994.

[26] H. Derudder, F. Olyslager, D. De Zutter, and S. Van den Berghe, "Efficient mode-matching analysis of discontinuities in finite planar substrates using perfectly matched layers," *IEEE Trans. Antennas Propag.*, vol. 49, no. 2, pp. 1985–195, Feb. 2001.

[27] R. Ziolkowski and M. Tanaka, "FDTD analysis of PBG waveguides, power splitters and switches," *Opt. Quantum Electron.*, vol. 31, pp. 843–855, 1999.

[28] I. El-Kady, M. Sigalas, R. Biswas, and K. Ho, "Dielectric waveguide in two-dimensional photonic bandgap materials," *Journal of Lightwave Technology*, vol. 17, pp. 2042–2049, 1999.

[29] C. Seassal, Y. Désières, X. Letartre, P. Rojo-Romeo, P. Viktorovitch, and T. Benyattou, "Optical coupling between a two-dimensional photonic crystal-based microcavity and single-line defect waveguide on InP membranes," *IEEE Journal of Quantum Electronics*, vol. 38, pp. 811–815, 2002.

[30] L. Knockaert and D. De Zutter, "Laguerre-SVD reduced-order modelling," *IEEE Trans. Microwave Theory Tech.*, vol. 48, pp. 1469–1475, 2000.

Chapter 4

Termination of Periodic Waveguides by PMLs in Time-Harmonic Integral Equation Like Techniques

Davy Pissoort and Frank Olyslager

Published in IEEE Antennas and Wireless Propagation Letters, Vol. 2, no. 20, pp. 281–284, 2003

Abstract

In this letter, a new way for the termination of periodic waveguides in integral equation like simulation techniques is introduced. Exploiting the complex coordinate interpretation of a perfectly matched layer, we can terminate a periodic waveguide by adding a couple of periods in the complex plane. If the waveguide enters the complex plane in a smooth way, the reflections caused by the periodicity disturbance are very low and at the same time one achieves a significant absorption. This idea is applied to a two-dimensional electromagnetic crystal waveguide structure. The validity of our approach is demonstrated by comparison with a rigorous method based on the exact calculation of the excitation coefficients of the eigenmodes in the waveguide and by comparison of a more complex example (a two-channel multiplexer-demultiplexer) from literature.

4.1 Introduction

An electromagnetic crystal (EC) device typically can be seen as a N-port where the ports consist of periodic waveguides. When simulating such structures one has to terminate these waveguides at a certain point and in such a way that reflections are limited. When using integral equation techniques, one can avoid reflections by using a Green function of a semi-infinite line, but this is not very convenient. We will provide an alternative way to terminate periodic waveguides in integral equation techniques by means of a perfectly matched layer (PML). Apart from their use as an absorbing boundary condition in finite difference time domain (FDTD) and finite-elements methods (FEM), PMLs have been used successfully, for example, for the calculation of the Green function of a layered medium [1] and in mode-matching techniques [2, 3]. We will use the complex coordinate interpretation of a PML [4, 5] and terminate a periodic waveguide by continuing it a number of periods in the complex plane (Fig. 4.1). One could say that the periodic waveguide makes a 'bend' into the complex plane.

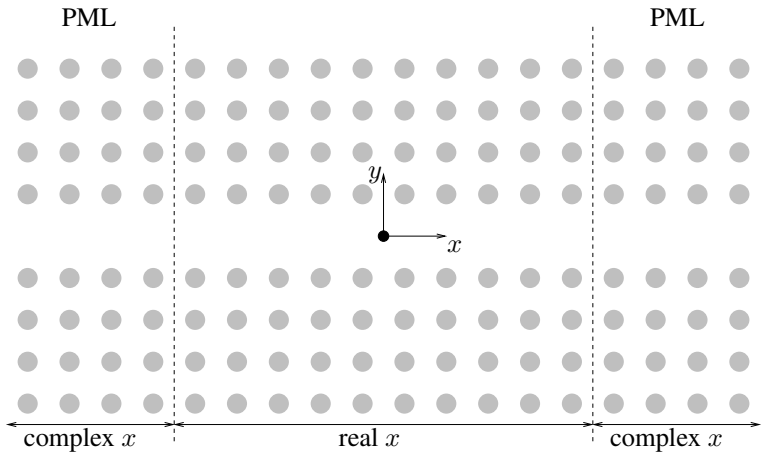

Figure 4.1: Electromagnetic crystal channel waveguide.

In this letter, this idea will be applied to a two-dimensional EC waveguide that consists of a set of parallel cylinders embedded in a homogeneous medium. By removing a row of cylinders, channel waveguides with low losses are created. Maintaining the periodicity throughout the PML means that for the middle points of the cylinders at the ends of the EC waveguide the coordinate, corresponding to the direction of propagation, becomes complex. This can be done in several ways and we will study how these choices influence the behavior of this absorbing boundary condition. Recently, a similar 'EC-based PML' was also introduced for FDTD and FEM simulations [6]. However, in those FDTD and FEM simulations the PML is described as an anisotropic medium.

In order to prove the validity of our approach, we will calculate the fields excited by a line source in an infinitely long EC waveguide with two different techniques: first, by calculating the eigenmodes of the waveguide and their excitation coefficients [7] and, second, by placing the cylinders at the end of the (finite) EC waveguide in the complex

plane. The EC waveguide is simulated with an integral equation that is solved in a semi-analytical manner similar as has been done in [8, 9]. In this analysis, the unknown field components at the boundary of each cylinder are expanded in a Fourier series, the terms of which generate cylindrical waves. The boundary conditions at the cylinders are enforced also by using a Fourier decomposition to obtain a linear set of equations. Solving the resulting matrix equation yields the unknown coefficients.

The organization of this letter is as follows. In Section 4.2 the main principles of the simulation technique are explained. Section 4.3 describes how the eigenmodes and their excitation coefficients are calculated. In Section 4.4, we describe how the cylinders must be placed in the complex plane to get absorption of the modes propagating in the waveguide. Finally, in Section 4.5, some numerical examples are given and the performance of several PMLs is compared.

4.2 Simulation technique

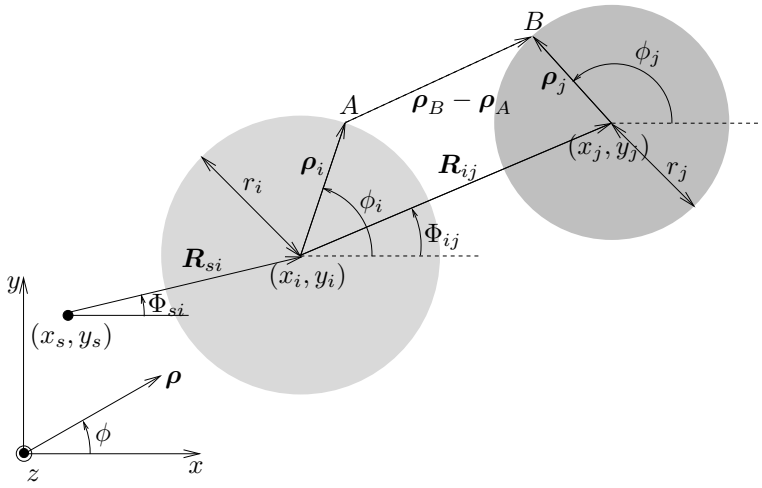

Figure 4.2: Multiple scattering.

We will consider the TM_z case, for which the electric field only has a z component. All the cylinders $i = 1, 2, \ldots, N_c$ in the EC waveguide are dielectric (with relative complex dielectric permittivity ϵ_{ri}) or perfectly electric conducting (PEC) and they are placed in air. At the center of the i^{th} cylinder, we define a local cylindrical coordinate system (ρ_i, ϕ_i) (Fig. 4.2). The total field E_z^{t} is the sum of the incident field E_z^{i} generated by the source and the scattered fields $E_z^{\mathrm{s},i}$, $i = 1, 2, \ldots, N_c$, of all cylinders. The waveguide is excited by a Dirac line source at (x_s, y_s). Using the following addition theorem for the Hankel function:

$$H_0^{(2)}(k_0|\boldsymbol{R}_{ij} + \boldsymbol{\rho}_i|) \quad = \quad \sum_{n=-\infty}^{+\infty} (-1)^n H_n^{(2)}(k_0 R_{ij}) J_n(k_0 \rho_i) e^{jn(\Phi_{ij} - \phi_i)}, \quad (4.1)$$

when $R_{ij} > \rho_i$, the electric field generated by this source can be written in terms of the local coordinates of the i^{th} cylinder as (Fig. 4.2)

$$E_z^{\text{i}}(\rho_i > r_i, \phi_i) = -\frac{\omega\mu_0}{4} \sum_{n=-\infty}^{+\infty} (-1)^n H_n^{(2)}(k_0 R_{si}) J_n(k_0\rho_i) e^{jn(\Phi_{si}-\phi_i)}, \quad (4.2)$$

with $k_0 = \omega\sqrt{\epsilon_0\mu_0}$ and r_i the radius of the i^{th} cylinder. For the calculation of the field 'generated', i.e., scattered, by the i^{th} cylinder, we introduce unknown surface currents on this cylinder. These surface currents are expanded in a Fourier series

$$J_z^i(\rho_i, \phi_i) = \sum_{n=-\infty}^{+\infty} \frac{I_n^i}{2\pi r_i} e^{jn\phi_i} \delta(\rho_i - r_i), \quad (4.3)$$

with unknown coefficients I_n^i. These unknown surface currents will be the only unknowns in our problem. The electric field radiated by the currents on the i^{th} cylinder can be expressed as

$$E_z^{\text{s},i}(\rho_i > r_i, \phi_i) = -\frac{\omega\mu_0}{4} \sum_{n=-\infty}^{+\infty} I_n^i H_n^{(2)}(k_0\rho_i) J_n(k_0 r_i) e^{jn\phi_i}. \quad (4.4)$$

Using the following addition theorem

$$H_n^{(2)}(k_0\rho_j) e^{jn\phi_j} = \sum_{m=-\infty}^{+\infty} J_m(k_0\rho_i) e^{jm\phi_i} H_{n-m}^{(2)}(k_0 R_{ij}) e^{j(m-n)\Phi_{ij}}, \quad (4.5)$$

the field scattered by cylinder j can be written in terms of the local coordinates of the i^{th} cylinder

$$E_z^{\text{s},j}(\rho_i > r_i, \phi_i) = -\frac{\omega\mu_0}{4} \sum_{n=-\infty}^{+\infty} J_n(k_0\rho_i) e^{jn\phi_i} \times \left(\sum_{m=-\infty}^{+\infty} I_m^i J_m(k_0 r_j) H_{n-m}^{(2)}(k_0 R_{ij}) e^{j(m-n)\Phi_{ij}} \right). \quad (4.6)$$

In the case of PEC cylinders, the currents (4.3) are the physical currents and they can be obtained by demanding that the total electric field E_z^{t} is zero on the surface of all cylinders. For dielectric cylinders, internal fields have to be taken into account. However, by introducing an appropriate boundary impedance it is still possible to solve the whole problem with the surface currents I_n^i as the sole unknowns. They are then determined from

$$E_z^{\text{t}}(r_i, \phi_i) = \sum_{n=-\infty}^{+\infty} Z_n^i \frac{I_n^i}{2\pi r_i} e^{jn\phi_i}. \quad (4.7)$$

These boundary impedances Z_n^i are found by comparing two situations:

- the original situation with a dielectric cylinder with radius r_i and relative dielectric permittivity ϵ_{ri};
- the unknown currents (4.3) placed on an air cylinder with radius r_i.

In the first situation the fields inside the dielectric cylinder can be expanded in full generality as

$$E_z^{\mathrm{I}}(\rho_i \leq r_i, \phi_i) = \sum_{n=-\infty}^{+\infty} A_n J_n(k_i \rho_i) e^{jn\phi_i}, \tag{4.8}$$

$$j\omega\mu_0 H_{\phi_i}^{\mathrm{I}}(\rho_i \leq r_i, \phi_i) = k_i \sum_{n=-\infty}^{+\infty} A_n J_n'(k_i \rho_i) e^{jn\phi_i}, \tag{4.9}$$

with unknown coefficients A_n. In the second situation the fields at $\rho_i = r_i^+$ are given by

$$E_z^{\mathrm{II}}(r_i^+, \phi_i) = \sum_{n=-\infty}^{+\infty} B_n J_n(k_0 r_i) e^{jn\phi_i}, \tag{4.10}$$

$$j\omega\mu_0 H_{\phi_i}^{\mathrm{II}}(r_i^+, \phi_i) = k_0 \sum_{n=-\infty}^{+\infty} B_n J_n'(k_0 r_i) e^{jn\phi_i} + j\omega\mu_0 \sum_{-\infty}^{+\infty} \frac{I_n^i}{2\pi r_i} e^{jn\phi_i}, \tag{4.11}$$

with another set of unknown coefficients B_n. As stated earlier, we have the following relation at $\rho_i = r_i^+$

$$E_z^{\mathrm{II}}(r_i^+, \phi_i) = \sum_{i=-\infty}^{+\infty} Z_n^i \frac{I_n^i}{2\pi r_i} e^{jn\phi_i} \tag{4.12}$$

The boundary impedances can now be determined by demanding that $E_z^{\mathrm{I}}(r_i^-, \phi_i) = E_z^{\mathrm{II}}(r_i^+, \phi_i)$ and that $H_{\phi_i}^{\mathrm{I}}(r_i^-, \phi_i) = H_{\phi_i}^{\mathrm{II}}(r_i^+, \phi_i)$. The result is

$$Z_n^i = j\sqrt{\frac{\mu_0}{\epsilon_0}} \frac{J_n(k_0 r_i) J_n(k_i r_i)}{J_{n+1}(k_0 r_i) J_n(k_i r_i) - \sqrt{\epsilon_{ri}} J_{n+1}(k_i r_i) J_n(k_0 r_i)}. \tag{4.13}$$

In practice, the infinite sums have to be truncated to a finite number of terms.

4.3 Eigenmodes

The eigenmodes of an EC waveguide are the eigensolutions that exist in an infinitely long EC waveguide without any sources. Assume that the x-axis is the direction of propagation in the EC waveguide. According to the Floquet-Bloch theorem, the eigenmodes in a periodic waveguide can be written as quasi-periodic functions, for example,

$$E_z(x, y) = e_z(x, y) e^{-j\beta x}, \tag{4.14}$$

with $e_z(x + a, y) = e_z(x, y)$, where a is the period of the waveguide and β is the propagation constant of this eigenmode. As a consequence, for an infinite EC waveguide the

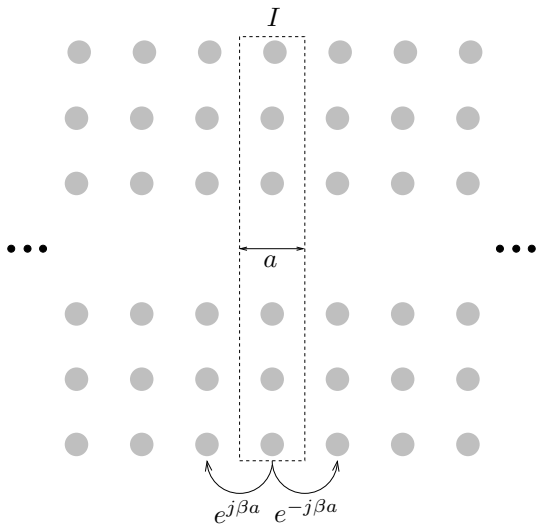

Figure 4.3: Floquet-Bloch theorem.

unknown surface currents, defined in Section 4.2, only have to be calculated in one unit cell. The other currents follow directly from these currents by using the Floquet-Bloch theorem, as is shown in Fig. 4.3 . However, the coefficients in the matrix equation will now be infinite sums where each term corresponds to the contribution of one cell. These coefficients are a function of the propagation constant β such that a homogeneous system of the following form is obtained:

$$\boldsymbol{Z}(\beta)\boldsymbol{I} \quad = \quad \mathbf{0}, \tag{4.15}$$

where $\boldsymbol{I}$ is a column vector that groups the unknowns I_n^i of one unit cell. This set of equations will only have nonzero solutions for discrete values of β, which are given by the demand that det($\boldsymbol{Z}(\beta)$) equals zero. Once β is known, the surface currents $\boldsymbol{I}$ and, hence, the mode profile can be calculated.

Assume that the waveguide is excited with a z directed line source placed at the origin (Fig. 4.1) and assume that there is only one mode propagating at the considered frequency. In that case, the z component of the electric field in the waveguide at a point (x, y) that is sufficiently far away from the source, will be given by $K^+E_z(x,y)$ if $x > 0$ or $K^-E_z(x,y)$ if $x < 0$, where $E_z(x,y)$ is the field of the eigenmode. In [7], it is shown that these excitation coefficients can be easily calculated, once the propagation constant and the mode profile of the eigenmode are known. For the line source placed at the origin, these excitation coefficients are given by

$$K^{\pm} \quad = \quad \frac{1}{2}\frac{E_z(0,0)}{\int_{-\infty}^{+\infty} E_z(0,y)H_y(0,y)dy}. \tag{4.16}$$

4.4 Complex coordinates

For a cylinder in the PML, the middle point has a complex x coordinate $(\tilde{x}_i,\, y_i)$, while the y coordinate remains real (Fig. 4.1)

$$\tilde{x}_i \;=\; x_i^{\text{re}} + j x_i^{\text{im}}. \tag{4.17}$$

As a consequence, the distance between rod i and j becomes complex

$$\begin{aligned} \tilde{R}_{ij} &= R_{ij}^{\text{re}} + j R_{ij}^{\text{im}} \\ &= \left[(\tilde{x}_i - \tilde{x}_j)^2 + (y_i - y_j)^2\right]^{\frac{1}{2}}. \end{aligned} \tag{4.18}$$

If all the middle points are real, $\tilde{R}_{ij} = R_{ij}^{\text{re}} \geq 0$. For complex distances, we also want that $R_{ij}^{\text{re}} \geq 0$. This defines the branch of the square in (4.18). Looking at the behavior of the Hankel function for large arguments

$$\lim_{|k\tilde{R}_{ij}|>>0} H_0^{(2)}(k\tilde{R}_{ij}) \;=\; \left(\frac{2}{\pi k \tilde{R}_{ij}}\right)^{\frac{1}{2}} e^{-jk(R_{ij}^{\text{re}} - \frac{\pi}{4})} e^{kR_{ij}^{\text{im}}}, \tag{4.19}$$

it becomes clear that R_{ij}^{im} has to be negative in order to obtain exponential decay. This demand has important consequences for the imaginary parts of the middle points in the PML:

$$\begin{aligned} (\tilde{R}_{ij})^2 &= (R_{ij}^{\text{re}})^2 - (R_{ij}^{\text{im}})^2 + 2jR_{ij}^{\text{re}} R_{ij}^{\text{im}} \\ &= (\tilde{x}_i - \tilde{x}_j)^2 + (y_i - y_j)^2 \\ &= (x_i^{\text{re}} - x_j^{\text{re}})^2 - (x_i^{\text{im}} - x_j^{\text{im}})^2 + (y_i - y_j)^2 \\ &\quad +2j(x_i^{\text{re}} - x_j^{\text{re}})(x_i^{\text{im}} - x_j^{\text{im}}). \end{aligned} \tag{4.20}$$

So, if $(x_i^{\text{re}} - x_j^{\text{re}}) > 0$, $(x_i^{\text{im}} - x_j^{\text{im}})$ has to be negative and if $(x_i^{\text{re}} - x_j^{\text{re}}) < 0$, $(x_i^{\text{im}} - x_j^{\text{im}})$ has to be positive. The angle $\tilde{\Phi}_{ij}$ is defined by

$$\tilde{\Phi}_{ij} = \arctan \frac{y_j - y_i}{\tilde{x}_j - \tilde{x}_i} \tag{4.21}$$

It is not obvious that the analysis in Section 4.2 is not in jeopardy when $\tilde{R}_{ij}$ and $\tilde{\Phi}_{ij}$ are complex. However, in [10] it is shown that for the aforementioned choice for $\tilde{R}_{ij}$ and $\tilde{\Phi}_{ij}$, the addition theorem for the Hankel function (4.1) remains valid and as a consequence the whole analysis in Section 4.2 remains valid.

4.5 Examples

In this section, it will be shown with a numerical example that the performance of the proposed PML boundary condition depends on the way the waveguide 'enters' the complex plane. The first configuration that is simulated is shown in Fig. 4.1 . It consists of a straight EC channel waveguide. The dielectric rods, with a radius $r = 0.2a$ and a relative

dielectric permittivity of 11.56, are embedded in air on a square array with lattice constant a. For the considered polarization, this EC has a bandgap from $f = 0.283\frac{c}{a}$ up to $f = 0.424\frac{c}{a}$. There are 50 'regular' rows of cylinders in the EC channel waveguide and a line source is placed in the center. Before and after these 50 rows there are N_{PML} extra rows for which the cylinders have complex x coordinates. Two different ways to enter the complex plane in these so-called PML regions, are studied, namely:

- the waveguide enters the complex plane in a linear way (Fig. 4.4), the complex x coordinate for the n^{th} row after the PC waveguide is then given by

$$x_n^{\text{re}} = x_0 + na\cos(\alpha) \tag{4.22}$$
$$x_n^{\text{im}} = -na\sin(\alpha), \tag{4.23}$$

  with $n = 1 \ldots N_{\text{PML}}$ and $x_0 = \frac{49a}{2}$ the x coordinate of the last row in the EC waveguide which is not in the PML.

- the waveguide enters the complex plane in a circular way (Fig. 4.5). The complex x coordinate for the n^{th} row can now be written as

$$x_n^{\text{re}} = x_0 + R_{\text{PML}}\sin(n\alpha), \tag{4.24}$$
$$x_n^{\text{im}} = -R_{\text{PML}}(1 - \cos(n\alpha)), \tag{4.25}$$

  with $\alpha = 2\arcsin(\frac{a}{2R_{\text{PML}}})$.

In both cases, the absolute value of the complex distance between two consecutive rows is equal to the lattice constant a.

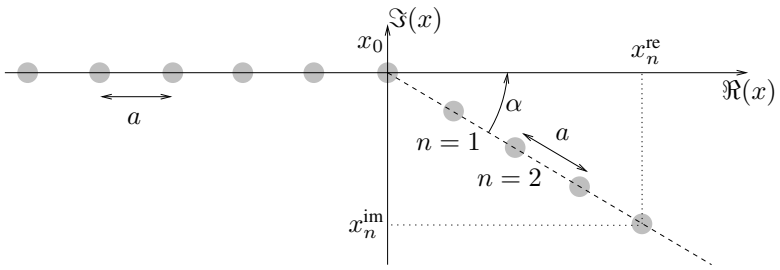

Figure 4.4: Linear PML.

In Fig. 4.6, the magnitude of the electrical field is given between $x = 10.5a$ and $x = 14.5a$ and at $y = 0$, for the infinite waveguide as well as for several kinds of PMLs. For the infinite waveguide, this field is calculated as discussed in Section 4.3. Also the electrical field for the case where the waveguide is abruptly terminated at $\pm x_0$ is shown. For the 'linear' PML with $\alpha = \pi/6$ and $N_{\text{PML}} = 11$ extra rows, there always remains a rather strong reflection. Using a higher number of rows in the PML regions, does not change the electrical fields. This is a consequence of the fact that entering the PML disturbs the periodicity. In fact, by entering into the complex space there will always be a disturbance in the periodicity. The complex distance between consecutive cylinders defined by (4.18) will differ from a. However, because of the absorption in the PML region

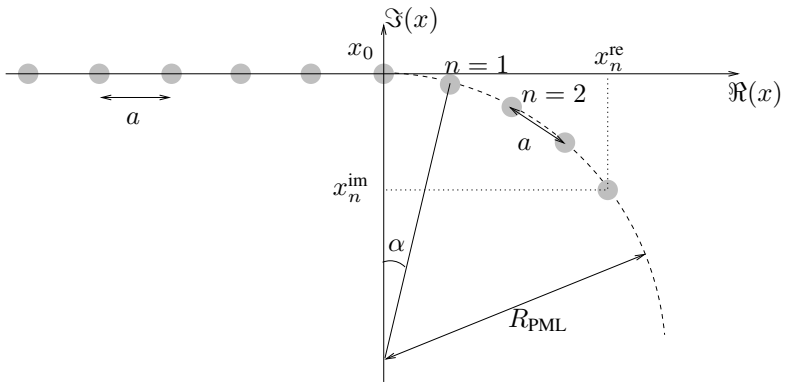

Figure 4.5: Circular PML.

at the termination of the waveguide these reflections are drastically reduced compared with the termination of the waveguide in real space. The reflections due to periodicity disturbance can be strongly reduced if the waveguide enters the complex plane in a more smooth way. If α for the linear PML is reduced to $\pi/90$, these reflections are almost zero. With $N_{\mathrm{PML}} = 40$ extra rows, one finds nearly the exact fields. The average relative error

$$\frac{1}{x_2 - x_1} \int_{x_1}^{x_2} \frac{|E_z^{\mathrm{PML}}(x,0) - E_z^{\mathrm{ref}}(x,0)|}{|E_z^{\mathrm{ref}}(x,0)|} dx, \tag{4.26}$$

with $x_1 = 10.5a$ and $x_2 = 14.5a$, is equal to 0.00179. Using a circular PML with $R_{\mathrm{PML}} = 10a$, it is possible to achieve the same accuracy with only seven extra rows. The average relative error is then 0.0018. With a circular PML, one enters smoothly in the complex plane and at the same time significant absorption is achieved.

As a more complex example, we consider a so-called two-channel multiplexer-demultiplexer, as shown in Fig. 4.7. The parameters of this structure are the same as in the example discussed above. The interaction length l is equal to $48a$. This configuration has already been simulated using a time-domain beam propagation method based on a finite element scheme and an EC-based PML in [11]. In our technique, we add at the end of every port some extra rows in the complex plane. For the input port and for port 3, the middle points of these extra cylinders have a complex x coordinate, but for the ports 1 and 2 they have a complex y coordinate. We used a circular PML with $R_{\mathrm{PML}} = 10a$ and for every port there were seven extra rows. A Dirac line source was placed at the input port. At every output port we calculated the outgoing flux. In order to obtain the transmission spectrum of the structure, we also calculated the flux in a straight waveguide with the same excitation. The transmission coefficient of every port is then given by the ratio of both fluxes and is shown in Fig. 4.8. The results are in very good agreement with [11]. Small differences, especially at the higher frequency side, are probably explained due accumulation of phase errors in FEM.

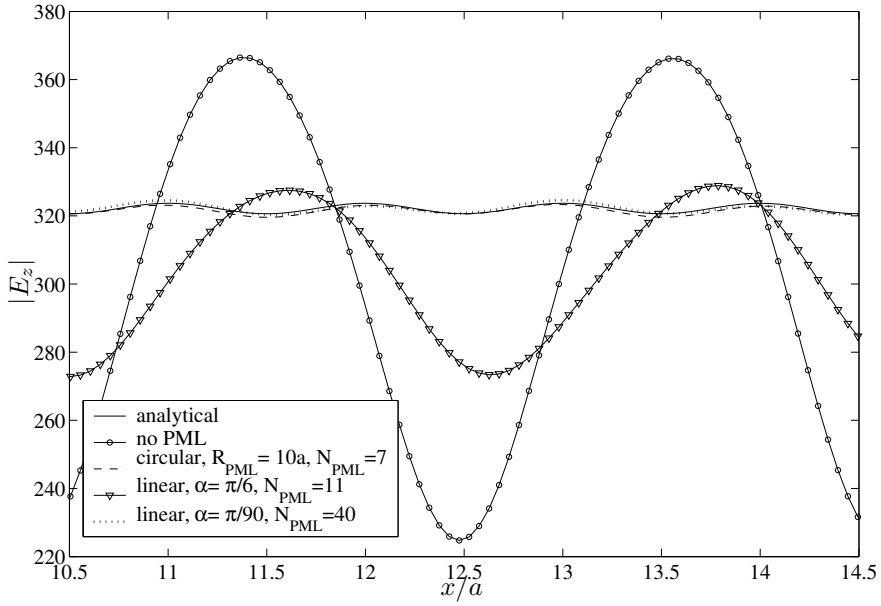

Figure 4.6: Comparison of several PMLs.

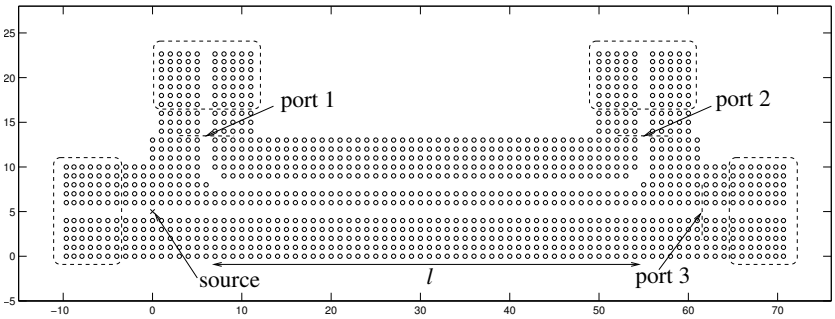

Figure 4.7: Two-channel multiplexer-demultiplexer.

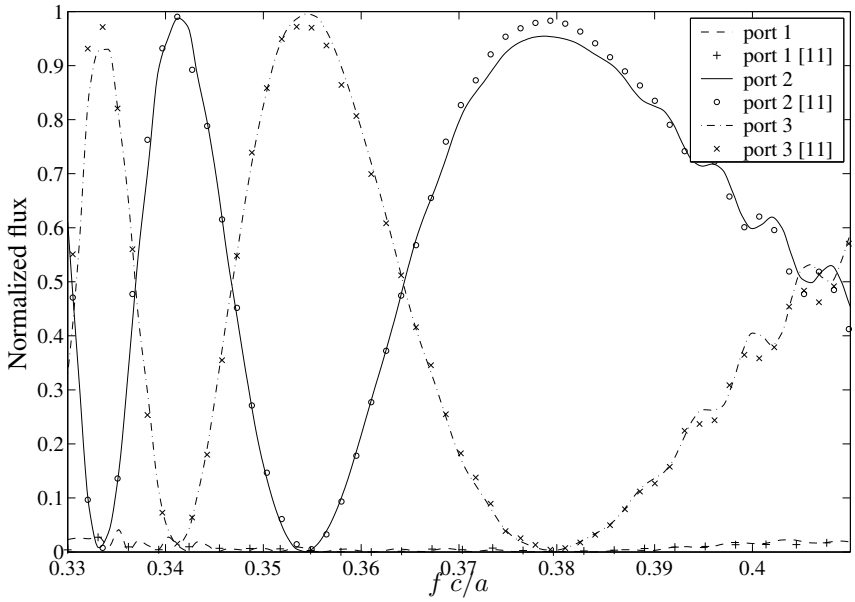

Figure 4.8: Transmission spectrum of the two-channel multiplexer-demultiplexer.

4.6 Conclusion

In this letter, we presented a technique to terminate a periodic waveguide without reflections by continuing the waveguide for a number of periods in the complex plane. This is based on the complex coordinate interpretation of PMLs. Although we demonstrated the validity of our technique for circular cylinders that allow a semi-analytical solution technique, it is clear that this is also valid for objects of more irregular shape requiring an integral equation solution technique. Two ways of entering the complex plane have been studied: a linear PML and a circular PML. With the circular PML one enters the complex plane in a very smooth way. As a consequence, the reflections caused by the periodicity disturbance are strongly reduced. Finally, this idea has been applied to the simulation of a two-channel multiplexer-demultiplexer.

Bibliography

[1] H. Derudder, F. Olyslager, and D. De Zutter, "An efficient series expansion for the 2D Green's function of a microstrip substrate using perfectly matched layers," *IEEE Microwave Guided Wave Lett.*, vol. 9, no. 12, pp. 505–507, Dec. 1999.

[2] H. Derudder, F. Olyslager, D. De Zutter, and S. Van den Berghe, "Efficient mode-matching analysis of discontinuities in finite planar substrates using perfectly matched layers," *IEEE Trans. Antennas Propag.*, vol. 49, no. 2, pp. 1985–195, Feb. 2001.

[3] P. Bienstman, H. Derudder, R. Baets, F. Olyslager, and D. De Zutter, "Analysis of cylindrical waveguide discontinuities using vectorial eigenmodes and perfectly matched layers," *IEEE Trans. Microwave Theory Tech.*, vol. 49, no. 2, pp. 349–354, Feb. 2001.

[4] W. C. Chew and W. H. Weedon, "A 3D perfectly matched medium from modified Maxwell's equations in stretched coordinates," *Microwave Opt. Technol. Lett.*, vol. 7, no. 13, pp. 599–604, Sept. 1994.

[5] W. C. Chew, J. M. Jin, and E. Michielssen, "Complex coordinate stretching as a generalized absorbing boundary condition," *Microwave Opt. Technol. Lett.*, vol. 15, no. 6, pp. 363–369, Aug. 1997.

[6] M. Koshiba, Y. Tsuji, and S. Sasaki, "High-performance absorbing boundary conditions for photonic crystal waveguide simulations," *IEEE Microwave Wireless Comp. Lett.*, vol. 11, no. 4, pp. 152–154, April 2001.

[7] D. Pissoort and F. Olyslager, "Study of eigenmodes in periodic waveguides using the Lorentz reciprocity theorem," *IEEE Trans. Microwave Theory Tech.*, vol. 52, pp. 542–553, 2004.

[8] A. Z. Elsherbeni and A. A. Kishk, "Modelling of cylindrical objects by circular dielectric and conducting cylinders," *IEEE Trans. Antennas Propag.*, vol. 40, no. 1, pp. 96–99, 1992.

[9] A. Z. Elsherbeni, "A comparative study of two-dimensional multiple scattering techniques," *Radio Science*, vol. 29, no. 4, pp. 1023–1033, 1994.

[10] W. Magnus, F. Oberhettinger, and R. Soni, *Formulas and Theorems for the Special Functions of Mathematical Physics*. Berlin: Springer Verlag, 1966.

[11] M. Koshiba, "Wavelength division multiplexing and demultiplexing with photonic crystal waveguide couplers," *Journal of Lightwave Technology*, vol. 19, no. 12, pp. 1970–1975, Dec. 2001.

Chapter 5

Classical Fast Multiplication Schemes

**Davy Pissoort, Dries Vande Ginste, Eric Michielssen,
Frank Olyslager, and Daniël De Zutter**

This chapter is an enlarged version of the following contributions:

D. Pissoort, D. Vande Ginste, F. Olyslager, D. De Zutter, and E. Michielssen, "A Multilevel Fast Multipole Algorithm for the Simulation of Wave Propagation in 2D Electromagnetic Crystals,"in *Proceedings of PIERS 2004*, Pisa, Italy, March 2004, pp. 28–31

D. Pissoort, D. Vande Ginste, F. Olyslager, and E. Michielssen, "Efficient Simulation of 2D Electromagnetic Crystal Structures with the Multilevel Fast Multipole Algorithm,"in *Proceedings of the URSI-EMT Conference*, vol.2, Pisa, Italy, May 2004, pp. 751–753

Abstract

The basic principles of two fast matrix-vector multiplication schemes to speed up the characterization of two-dimensional electromagnetic crystal devices with the multiple scattering technique are described. The multilevel fast multipole algorithm, which is the multilevel version of the fast multipole method, reduces the computational complexity to $O(N \log_2^2 N)$ or even $O(N)$ for a problem with N unknowns. This method is extended to the use of complex coordinates, which appear when extracting the S-parameters of the EC device with perfectly matched layer based absorbing boundary conditions. The second scheme is suited for finite EC devices in which all cylinders are arranged according to a regular grid. It exploits the convolutional nature of the matrix-vector multiplication for such EC devices by using a Fast Fourier Transform to reduce the computational complexity to $O(N \log_2 N)$.

5.1 Introduction

Electromagnetic crystals (ECs) are periodically arranged dielectric media that offer the possibility of controlling and manipulating electromagnetic waves at spatial scales smaller than achievable with classical fibers or optical waveguides [1]. The underlying periodic structure of an EC gives rise to the appearance of frequency ranges (*electromagnetic bandgaps*) for which the electromagnetic fields cannot propagate inside the crystal. Disruption of the crystal periodicity by introducing crystal defects induces a field localization that allows the design of various interesting devices. For instance, line defects may behave as waveguides and, since the electromagnetic fields cannot escape through the crystal, waveguide bends with very low losses can be designed.

A popular method for analyzing EC devices is the multiple scattering technique [2,3]. This frequency domain technique solves integral equations in terms of equivalent electric currents residing on the cylinders' surfaces. The drawback of this method is that it requires the solution of a dense linear system of equations whose dimension is proportional to the number of cylinders in the EC device, denoted by N_c. However, recently, there has been a considerable interest in the development of *fast* schemes to solve such systems. The common goal of these fast schemes is to construct matrix-vector multiplication algorithms characterized by a computational complexity and memory requirement lower than the $O(N_c^2)$ complexity of the classical matrix-vector multiplication scheme. This paper details the basic principles of two fast methods for simulating wave propagation in 2D EC devices, namely, a multilevel fast multipole based and a Fast Fourier Transform (FFT) based scheme.

The fast multipole method (FMM) was first introduced by Rokhlin et al. to rapidly solve static integral equations [4–6]. The FMM was extended by many researchers to solve electromagnetic scattering problems, both in two and three dimensions. A two-level FMM reduces both the computational complexity and memory requirement to $O(N_c^{1.5})$. The multilevel version of the FMM further reduces the computational complexity and memory requirements to (nearly) $O(N_c)$. In Section 5.3.1, the basic principles of the FMM when applied to EC devices are detailed. The multilevel version is described in Section 5.3.2. To calculate the S-parameters of the EC device, perfectly matched layer (PML) based absorbing boundary conditions were introduced in [7]. As a consequence, some cylinders are centered about *complex* coordinates. In Section 5.3.5, the FMM is extended to the use of such PML based absorbing boundary conditions for EC devices. Some examples are given to illustrate the versatility of this approach.

Fast Fourier Transform (FFT) based solvers are suited for EC devices for which all cylinders are arranged according to a regular grid, viz. the crystal defects comprise only removed cylinders or cylinders with a different radius and/or constitutive parameters. They exploit the convolutional nature of the integral equation operator to obtain the necessary matrix-vector multiplications with $O(N_c \log_2 N_c)$ operations and with a memory requirement that scales as $O(N_c)$. Section 5.4 briefly details the basic principles of a FFT-based scheme for the characterization of EC devices.

Notation: all sources and fields are assumed time-harmonic with angular frequency ω; temporal dependencies $e^{j\omega t}$ are suppressed.

5.2 Multiple scattering technique

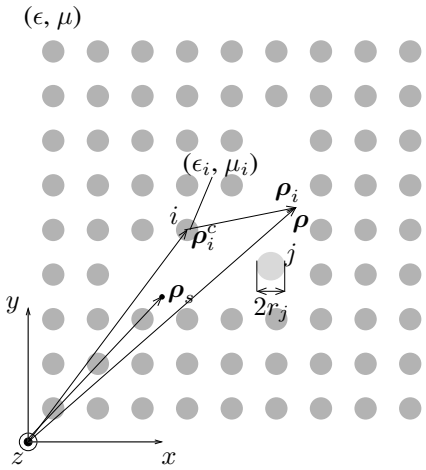

Figure 5.1: Electromagnetic crystal device.

This section briefly details the conventional multiple scattering technique, which is an integral equation based scheme for the characterization of wave propagation in 2D EC devices [2, 3]. The targeted EC structures (Fig. 5.1) comprise N_c infinite, z-invariant, homogeneous, dielectric/magnetic, circular cylinders with radius r_j and constitutive parameters (ϵ_j, μ_j), $j = 1, \ldots, N_c$, embedded in a homogeneous background medium with constitutive parameters (ϵ, μ). Here, only the TM_z polarization, for which the electric field is parallel to the cylinders (z direction), is considered. The incident field $E^{\mathrm{i}}(\boldsymbol{\rho})\boldsymbol{u}_z$, with $\boldsymbol{\rho} = (\rho, \phi)$ a global position vector in the xy-plane, is defined as the electric field generated by impressed sources in the absence of any cylinders. The difference between the total electric field $E^{\mathrm{t}}(\boldsymbol{\rho})\boldsymbol{u}_z$, defined as the field that is observed in the presence of the cylinders, and the incident field is called the scattered field $E^{\mathrm{s}}(\boldsymbol{\rho})\boldsymbol{u}_z$. To describe these electric fields, a set of equivalent z directed electric currents $J^j(\boldsymbol{\rho})\boldsymbol{u}_z$ are introduced on the surface S_j of every cylinder j, $j = 1, \ldots, N_c$. Let $E^{\mathrm{s},j}(\boldsymbol{\rho})\boldsymbol{u}_z$ denote for further reference the electric field generated by $J^j(\boldsymbol{\rho})\boldsymbol{u}_z$ in the unbounded medium with parameters (ϵ, μ). In the case of perfectly electric conducting cylinders, the total electric field would vanish on the surface of every cylinder. For dielectric/magnetic cylinders, appropriate boundary impedances Z^i can be proffered. The boundary condition on the surface S_i of the i^{th} cylinder can then be cast as

$$E^{\mathrm{i}}(\boldsymbol{\rho}) + \sum_{j=1}^{N_c} E^{\mathrm{s},j}(\boldsymbol{\rho}) \quad = \quad Z^i J^i(\boldsymbol{\rho}), \ \text{ for } \boldsymbol{\rho} \in S_i, \ i = 1, \ldots, N_c. \tag{5.1}$$

To solve (5.1), the surface currents are expanded into an angular Fourier series in a local cylindrical coordinate system $\boldsymbol{\rho}_j = (\rho_j, \phi_j)$ w.r.t. the center of the corresponding

cylinder:

$$J^j(\boldsymbol{\rho}) \quad = \quad \sum_{n=-\infty}^{+\infty} \frac{I_n^j}{2\pi r_j} e^{jn\phi_j} \delta(\rho_j - r_j). \tag{5.2}$$

Likewise, Eq. (5.1) can be re-expressed as

$$E^{\mathrm{i}}(\boldsymbol{\rho}) + \sum_{j=1}^{N_c} E^{\mathrm{s},j}(\boldsymbol{\rho}) \quad = \quad \sum_{n=-\infty}^{+\infty} Z_n^i \frac{I_n^i}{2\pi r_i} e^{jn\phi_i}, \ \text{ for } \boldsymbol{\rho} \in S_i, \ i = 1, \ldots, N_c, \tag{5.3}$$

with [3]

$$Z_n^i \quad = \quad \left[\frac{k_i J_n'(k_i r_i)}{\mu_i J_n(k_i r_i)} - \frac{k J_n'(k r_i)}{\mu J_n(k r_i)} \right]^{-1}. \tag{5.4}$$

Here, $k_i = \omega\sqrt{\epsilon_i \mu_i}$ and $k = \omega\sqrt{\epsilon\mu}$ are the wavenumber inside the i^{th} cylinder and in the background medium; $J_n(\cdot)$ is the n^{th}-order Bessel function of the first kind and $H_n^{(2)}(\cdot)$ is the n^{th}-order Hankel function of the second kind. In practice, the range of the modal index n can be restricted to $n = -K, \ldots, K$, with K a small positive integer. The scattered electric field $E^{\mathrm{s},j}(\boldsymbol{\rho})$ is given by

$$E^{\mathrm{s},j}(\boldsymbol{\rho}) \quad = \quad \int_{\boldsymbol{\rho}' \in S_j} G(\boldsymbol{\rho}|\boldsymbol{\rho}') J^j(\boldsymbol{\rho}') d\boldsymbol{\rho}', \tag{5.5}$$

with $G(\boldsymbol{\rho}|\boldsymbol{\rho}')$ the free-space Green function:

$$G(\boldsymbol{\rho}|\boldsymbol{\rho}') \quad = \quad -\frac{\omega\mu}{4} H_0^{(2)}(k|\boldsymbol{\rho} - \boldsymbol{\rho}'|). \tag{5.6}$$

Inserting (5.5) into (5.3), truncating the infinite sums to a finite number, and testing the resulting equation with $T_m^i(\rho) = \frac{1}{2\pi r_i} e^{-jm\phi_i} \delta(\rho_i - r_i)$, $m = -K, \ldots, K$; $i = 1, \ldots, N_c$, results in a linear system of equations:

$$\boldsymbol{Z}\boldsymbol{I} \quad = \quad \boldsymbol{E}. \tag{5.7}$$

The entries of the interaction matrix $\boldsymbol{Z}$ are

$$Z_{mn}^{ij} = \quad \frac{1}{4\pi^2 r_i r_j} \int_{\boldsymbol{\rho} \in S_i} \int_{\boldsymbol{\rho}' \in S_j} G(\boldsymbol{\rho}|\boldsymbol{\rho}') e^{-jm\phi_i} e^{jn\phi_j} d\boldsymbol{\rho} d\boldsymbol{\rho}' - \delta_{ij}\delta_{mn} Z_m^i \tag{5.8}$$

and those of the excitation vector $\boldsymbol{E}$ are

$$E_m^i \quad = \quad -\frac{1}{2\pi r_i} \int_{\boldsymbol{\rho} \in S_i} E^{\mathrm{i}}(\boldsymbol{\rho}) e^{-jm\phi_i} d\boldsymbol{\rho}. \tag{5.9}$$

The total number of unknowns in matrix equation (5.7) equals $(2K+1)N_c$. There are basically two ways to solve this dense system of equations: (i) a *direct* solver, which can be e.g. Gaussian elimination or LU-decomposition, or (ii) an *iterative* solver. A direct

solver seeks the inversion of the matrix equation. Because the number of azimuthal harmonics does not depend on the extent of the EC device, the number of operations when using such a direct solver is proportional to $O(N_c^3)$, while the matrix storage requirement is $O(N_c^2)$. An iterative solver tries to seek an approximation of the solution $\boldsymbol{I}$ in a number of successive iterations. In each iteration, a new test solution $\tilde{\boldsymbol{I}}$ is proposed as an approximation of the exact solution of the matrix equation. This approximation is multiplied with the interaction matrix $\boldsymbol{Z}$ and the resulting vector is compared with the excitation vector $\boldsymbol{E}$. If the difference between both vectors is 'small enough', $\tilde{\boldsymbol{I}}$ is accepted as the solution of the matrix equation. Otherwise, a new test solution is proposed and the cycle is repeated. It is clear that an iterative method requires many matrix-vector multiplications, which usually are the bottleneck of the computation. For dense matrices, such a matrix-vector multiplication requires $O(N_c^2)$ operations. If a satisfying approximation is found after P iterations, the computational cost is proportional to PN_c^2. Of course, the matrix storage requirement remains $O(N_c^2)$.

The next two sections detail two classical methods to minimize both the memory requirements and the computational complexity. Section 5.3 describes a multilevel fast multipole algorithm (MLFMA). This method is extended to the use of complex coordinates. Section 5.4 describes a Fast Fourier Transform (FFT) based method. All examples presented below involve ECs composed of dielectric cylinders with constitutive parameters (ϵ_i, μ_i) = (11.56ϵ_0, μ_0) and radius $r = 0.18a$ that are arranged on a Cartesian lattice with a square unit cell and lattice constant a. All cylinders reside in free space, viz. (ϵ, μ)=(ϵ_0, μ_0). This EC has a bandgap that extends from $k = 0.604\frac{\pi}{a}$ to $k = 0.886\frac{\pi}{a}$.

5.3 Multilevel fast multipole algorithm

5.3.1 Fast multipole method

In the fast multipole method (FMM), the computational complexity and the memory requirements are minimized by dividing the N_c cylinders into boxes, each of which contain about M_c cylinders. The crux of the FMM is that it considers *box-to-box* interactions in stead of *unknown-to-unknown* interactions. This can be seen as the manager-worker model. Basically, each box is managed by the center element, with the workers comprising the elements of the box. Communication/interaction among the boxes takes place through the managers, which, in turn, interact with the box elements. However, this idea of box-to-box interactions can only be applied if these two boxes are sufficiently separated. When this is not the case, the associated part of the matrix-vector multiplication has to be computed in the classical way, using unknown-to-unknown interactions. By consequence, the matrix-vector multiplication is decomposed in two contributions, namely, the *near field* and the *far field* contribution, as follows:

$$\boldsymbol{Z}\tilde{\boldsymbol{I}} \quad = \quad \boldsymbol{Z}_{\text{nf}}\tilde{\boldsymbol{I}} + \boldsymbol{Z}_{\text{ff}}\tilde{\boldsymbol{I}}. \tag{5.10}$$

The matrix $\boldsymbol{Z}_{\text{nf}}$ is a sparse matrix with $O(N_c)$ nonzero elements. Hence, the computational complexity to calculate $\boldsymbol{Z}_{\text{nf}}\tilde{\boldsymbol{I}}$ scales as $O(N_c)$.

It will now be shown how the far field contribution can be computed more efficiently using box-to-box interactions. Therefore, first consider the configuration depicted in

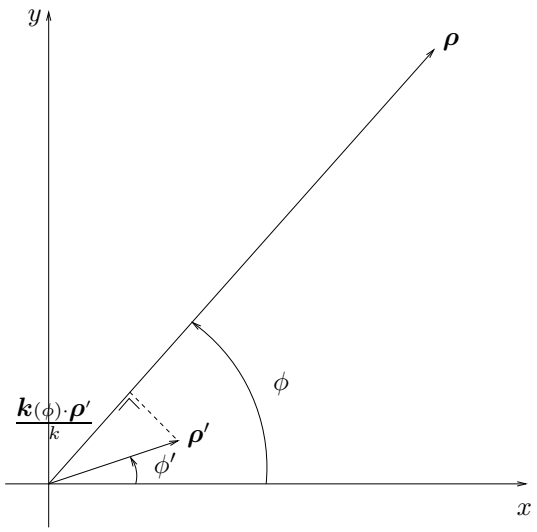

Figure 5.2: A source $\boldsymbol{\rho}'$ and an observer $\boldsymbol{\rho}$.

Fig 5.2. The z directed electric field radiated by a Dirac line source located at $\boldsymbol{\rho}' = (\rho', \phi')$ and observed in $\boldsymbol{\rho} = (\rho, \phi)$ is

$$\begin{aligned} E(\boldsymbol{\rho}) &= -\frac{\omega\mu}{4} H_0^{(2)}(k|\boldsymbol{\rho} - \boldsymbol{\rho}'|) \\ &= -\frac{\omega\mu}{4} \mathrm{nf}(\boldsymbol{\rho}). \end{aligned} \tag{5.11}$$

In this equation, 'nf' stands for near field. In what follows, $\boldsymbol{\rho}'$ and $\boldsymbol{\rho}$ are referred to as the source and the observer, respectively. Now, let the distance between the source and the observer increase. Because of the asymptotic behavior of the Hankel function [8], nf($\boldsymbol{\rho}$) reduces to

$$\mathrm{nf}(\boldsymbol{\rho}) \approx \sqrt{\frac{2}{\pi k \rho}} e^{-j(k|\boldsymbol{\rho}-\boldsymbol{\rho}'|-\frac{\pi}{4})} \text{ if } \rho \gg \rho'. \tag{5.12}$$

Under the same assumption, the distance $|\boldsymbol{\rho} - \boldsymbol{\rho}'|$ can be approximated as

$$|\boldsymbol{\rho} - \boldsymbol{\rho}'| \approx \rho - \frac{\boldsymbol{k}(\phi) \cdot \boldsymbol{\rho}'}{k}, \tag{5.13}$$

with

$$\boldsymbol{k}(\phi) = k[\cos(\phi)\boldsymbol{u}_x + \sin(\phi)\boldsymbol{u}_y]. \tag{5.14}$$

This allows to approximate (5.12) further as

$$\mathrm{nf}(\boldsymbol{\rho}) \approx \sqrt{\frac{2}{\pi k \rho}} e^{-j(k\rho-\frac{\pi}{4})} \mathrm{ff}(\phi) \text{ if } \rho \gg \rho'. \tag{5.15}$$

Here, $\text{ff}(\phi) = e^{j\boldsymbol{k}(\phi)\cdot\boldsymbol{\rho}'}$ is the far field radiated by the Dirac line source. In [9], it is proven that this far field is quasi-bandlimited. From the Nyquist sampling theorem, it follows that a real bandlimited signal can be perfectly reconstructed from its samples if the sampling rate is at least twice the highest frequency contributing to this signal. Although $\text{ff}(\phi)$ is only quasi-bandlimited, it can be approximated to an arbitrary accuracy from $2Q+1$ samples $\text{ff}(\phi_q)$ as follows:

$$\text{ff}(\phi) \approx \sum_{q=-Q}^{Q} \text{ff}(\phi_q) D(\phi - \phi_q). \tag{5.16}$$

Here,

$$\phi_q = \frac{2\pi q}{2Q+1},\ q = -Q, \ldots, Q \tag{5.17}$$

$$D(\phi) = \sum_{q=-Q}^{Q} \frac{e^{jq\phi}}{2Q+1}. \tag{5.18}$$

The so-called Dirichlet kernel $D(\phi - \phi_q)$ is a periodic function (period 2π) that is one for the sampling point ϕ_q and zero for the other sampling points. In [9, 10], it is argued that to accurately describe the far field at the observer, the sampling rate must obey

$$2Q + 1 = 2k\rho' + C. \tag{5.19}$$

In [9], the constant C is estimated using Lambert-W functions; in [10], it is found that $C \approx C_0[k\rho']^{\frac{1}{3}}$.

Combining (5.15), (5.18), and (5.16), yields

$$\text{nf}(\boldsymbol{\rho}) \approx \sqrt{\frac{2}{\pi k\rho}} \frac{e^{-j(k\rho - \frac{\pi}{4})}}{2Q+1} \sum_{q=-Q}^{Q} \sum_{q'=-Q}^{Q} \text{ff}(\phi_{q'}) e^{jq(\phi - \phi_{q'})} \text{ if } \rho \gg \rho'. \tag{5.20}$$

On the other hand, the most general solution of the source free Maxwell equations in cylindrical coordinates at the observer leads to the observation that

$$\begin{aligned} \text{nf}(\boldsymbol{\rho}) &= \sum_{q=-\infty}^{+\infty} a_q H_q^{(2)}(k\rho) e^{jq\phi} \\ &\approx \sum_{q=-Q}^{Q} a_q H_q^{(2)}(k\rho) e^{jq\phi} \\ &\approx \sum_{q=-Q}^{Q} a_q \sqrt{\frac{2}{\pi k\rho}} e^{-j(k\rho - \frac{q\pi}{2} - \frac{\pi}{4})} \text{ if } \rho \rightarrowtail \infty. \end{aligned} \tag{5.21}$$

Identification of (5.20) and (5.21) yields

$$a_q = \frac{1}{2Q+1} \sum_{q'=-Q}^{Q} \text{ff}(\phi_{q'}) e^{-jq(\phi_{q'} + \frac{\pi}{2})}. \tag{5.22}$$

Upon inserting (5.22) into (5.21) and interchanging the summation indices n and n', nf($\boldsymbol{\rho}$) can be re-expressed as

$$\text{nf}(\boldsymbol{\rho}) \approx \sum_{q=-Q}^{Q} \text{ff}(\phi_q) T_q(k, \rho, \phi) \text{ if } \rho \gg \rho'. \tag{5.23}$$

Here,

$$T_q(k, \rho, \phi) = \frac{1}{2Q+1} \sum_{q'=-Q}^{Q} H_{q'}^{(2)}(k\rho) e^{jq'(\phi - \phi_q - \frac{\pi}{2})}. \tag{5.24}$$

Equation (5.23) permits the reconstruction of the near field at $\boldsymbol{\rho}$ of the source located at $\boldsymbol{\rho}'$ from its far field samples.

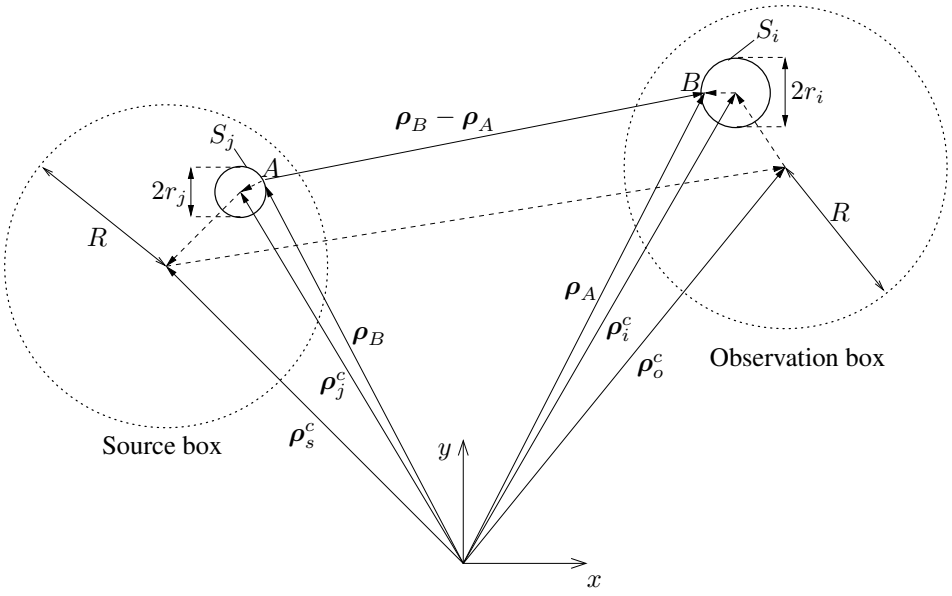

Figure 5.3: Source and observation box.

Now consider the configuration depicted in Fig. 5.3. It comprises two sufficiently separated circular boxes with radius R. The source box comprises one source cylinder i with surfaces S_i; the observation box comprises one observation cylinder j with surface S_j. Let $\boldsymbol{\rho}_A$ and $\boldsymbol{\rho}_B$ denote points A and B on S_j and S_i, respectively. Likewise, let $\boldsymbol{\rho}_j^c$ and $\boldsymbol{\rho}_i^c$ denote the centers of cylinder j and i. Finally, let $\boldsymbol{\rho}_s^c$ and $\boldsymbol{\rho}_o^c$ denote the centers of the source and the observation box. With these definitions, the vector $\boldsymbol{\rho}_{BA} = \boldsymbol{\rho}_B - \boldsymbol{\rho}_A$ can be expressed as

$$\boldsymbol{\rho}_B - \boldsymbol{\rho}_A = (\boldsymbol{\rho}_B - \boldsymbol{\rho}_i^c) + (\boldsymbol{\rho}_i^c - \boldsymbol{\rho}_o^c) + (\boldsymbol{\rho}_o^c - \boldsymbol{\rho}_s^c) - (\boldsymbol{\rho}_j^c - \boldsymbol{\rho}_s^c) - (\boldsymbol{\rho}_A - \boldsymbol{\rho}_j^c). \tag{5.25}$$

Define $\boldsymbol{\rho}$ and $\boldsymbol{\rho}'$ as

$$\begin{aligned} \boldsymbol{\rho} &= \boldsymbol{\rho}_o^c - \boldsymbol{\rho}_s^c, && (5.26)\\ \boldsymbol{\rho}' &= (\boldsymbol{\rho}_j^c - \boldsymbol{\rho}_s^c) + (\boldsymbol{\rho}_A - \boldsymbol{\rho}_j^c) - (\boldsymbol{\rho}_B - \boldsymbol{\rho}_i^c) - (\boldsymbol{\rho}_i^c - \boldsymbol{\rho}_o^c). && (5.27) \end{aligned}$$

From (5.8), (5.23), and (5.25), it follows

$$\begin{aligned} Z_{mn}^{ij} \approx & -\frac{\omega\mu}{16\pi^2}\sum_{q=-Q}^{Q}\int_{-\pi}^{\pi} e^{-j\boldsymbol{k}(\phi_q)\cdot(\boldsymbol{\rho}_B-\boldsymbol{\rho}_i^c)} e^{-jm\phi_i} d\phi_i e^{-j\boldsymbol{k}(\phi_q)\cdot(\boldsymbol{\rho}_i^c-\boldsymbol{\rho}_o^c)} \times \\ & T_q(k,\rho_{so}^c,\phi_{so}^c)\int_{-\pi}^{\pi} e^{j\boldsymbol{k}(\phi_q)\cdot(\boldsymbol{\rho}_A-\boldsymbol{\rho}_j^c)} e^{jn\phi_j} d\phi_j e^{j\boldsymbol{k}(\phi_q)\cdot(\boldsymbol{\rho}_j^c-\boldsymbol{\rho}_s^c)}. \quad (5.28) \end{aligned}$$

Here, ρ_{so}^c and ϕ_{so}^c are the length and the angle w.r.t. x-axis of the vector $\boldsymbol{\rho}_{so}^c = \boldsymbol{\rho}_o^c - \boldsymbol{\rho}_s^c$ connecting the centers of the observation and source box. With

$$\begin{aligned} \int_{-\pi}^{\pi} e^{-j\boldsymbol{k}(\phi_n)\cdot(\boldsymbol{\rho}_B-\boldsymbol{\rho}_i^c)} e^{-jm\phi_i} d\phi_i &= \int_{-\pi}^{\pi} e^{-jkr_i\cos(\phi_i-\phi_q)} e^{-jm\phi_i} d\phi_i \\ &= 2\pi e^{-jm(\phi_q+\frac{\pi}{2})} J_m(kr_i), && (5.29)\\ \int_{-\pi}^{\pi} e^{j\boldsymbol{k}(\phi_q)\cdot(\boldsymbol{\rho}_A-\boldsymbol{\rho}_j^c)} e^{jn\phi_j} d\phi_j &= \int_{-\pi}^{\pi} e^{jkr_j\cos(\phi_j-\phi_q)} e^{jn\phi_j} d\phi_j \\ &= 2\pi e^{jn(\phi_q+\frac{\pi}{2})} J_n(kr_j), && (5.30) \end{aligned}$$

eqn. (5.28) becomes

$$\begin{aligned} Z_{mn}^{ij} \approx & -\frac{\omega\mu}{4}\sum_{q=-Q}^{Q} \underbrace{J_m(kr_i) e^{-j[\boldsymbol{k}(\phi_q)\cdot(\boldsymbol{\rho}_i^c-\boldsymbol{\rho}_o^c)+m(\phi_q+\frac{\pi}{2})]}}_{1} \times \\ & \underbrace{T_q(k,\rho_{so}^c,\phi_{so}^c)}_{2} \underbrace{J_n(kr_j) e^{j[\boldsymbol{k}(\phi_q)\cdot(\boldsymbol{\rho}_j^c-\boldsymbol{\rho}_s^c)+n(\phi_q+\frac{\pi}{2})]}}_{3}. \quad (5.31) \end{aligned}$$

The first term is the complex conjugate of the sampled radiation pattern of the observation box, multiplied with a factor depending on the modal number m and the radius of the observation cylinder; the second term is the (diagonal) translation operator; the last term is the sampled far-field pattern of the source box, multiplied with a factor depending on the modal number n and the radius of the source cylinder. Since $\max\rho' = 2R + r_i + r_j$, it follows from (5.19) that the sampling rate scales as

$$2Q + 1 = 4kR + C. \quad (5.32)$$

Finally, consider the situation where there are M_s cylinders inside the source and M_o cylinders inside observation box. Let $\tilde{I}_n^j$ denote the approximation for the n^{th} modal unknown on cylinder j inside the source box, $j = 1,\ldots,M_s$; $n = -K,\ldots,K$, proffered by the iterative solver. Following the reasoning of the previous paragraph, the box-to-box

interaction from the source to the observation box can be expressed as

$$\sum_{j=1}^{M_s}\sum_{n=-K}^{K} Z_{mn}^{ij}\tilde{I}_n^j \approx -\frac{\omega\mu}{4}\sum_{q=-Q}^{Q} J_m(kr_i)e^{-j[\boldsymbol{k}(\phi_q)\cdot(\boldsymbol{\rho}_i^c-\boldsymbol{\rho}_o^c)+m(\phi_q+\frac{\pi}{2})]}\times T_q(k,\rho_{so}^c,\phi_{so}^c)\times \sum_{j=1}^{M_s}\sum_{n=-K}^{K} J_n(kr_j)e^{j[\boldsymbol{k}(\phi_q)\cdot(\boldsymbol{\rho}_j^c-\boldsymbol{\rho}_s^c)+n(\phi_q+\frac{\pi}{2})]}\tilde{I}_n^j, \quad (5.33)$$

for $i = 1,\ldots,M_o$ and $m = -K,\ldots,K$. Hence, the box-to-box interactions are calculated in three stages. First, the so-called *outgoing plane waves* of the source box are calculated:

$$\text{OPW}_q = \sum_{j=1}^{M_s}\sum_{n=-K}^{K} J_n(kr_j)e^{j[\boldsymbol{k}(\phi_q)\cdot(\boldsymbol{\rho}_j^c-\boldsymbol{\rho}_s^c)+n(\phi_q+\frac{\pi}{2})]}\tilde{I}_n^j,\ q=-Q,\ldots,+Q. \quad (5.34)$$

In the second step, these outgoing plane waves are transformed into so-called *incoming plane waves* for the observation box via the (diagonal) translation operator:

$$\text{IPW}_q = T_q(k,\rho_{so}^c,\phi_{so}^c)\text{OPW}_q,\ q=-Q,\ldots,+Q. \quad (5.35)$$

Finally, these incoming plane waves are projected onto each cylinder i inside the observation box, resulting in the weighted electric field on the surface of this cylinder radiated by all the currents inside the source box. If this weighted field is denoted by $\mathcal{E}_m^i$, then

$$\mathcal{E}_m^i = -\frac{\omega\mu}{4}\sum_{q=-Q}^{Q} J_m(kr_i)e^{-j[\boldsymbol{k}(\phi_q)\cdot(\boldsymbol{\rho}_i^c-\boldsymbol{\rho}_o^c)+m(\phi_q+\frac{\pi}{2})]}\text{IPW}_q, \quad (5.36)$$

for $i = 1,\ldots,M_o$ and $m = -K,\ldots,K$. Similarly, the far field contribution, as defined in (5.10), can be decomposed into three contributions as follows:

$$\boldsymbol{Z}_{\text{ff}}\tilde{\boldsymbol{I}} = -\frac{\omega\mu}{4}\boldsymbol{V}\boldsymbol{T}\boldsymbol{U}\tilde{\boldsymbol{I}}. \quad (5.37)$$

The matrices $\boldsymbol{V}$ and $\boldsymbol{U}$ are block-diagonal matrices, as is shown in Fig. 5.4(a) and Fig. 5.4(b). The sparsity pattern of the matrix $\boldsymbol{T}$ is shown in Fig. 5.4(c).

5.3.2 Multilevel algorithm

A straightforward implementation of the above described FMM reduces the computational cost to $O(N_c^{1.5})$. A further reduction of the computational complexity is possible by using a multilevel algorithm. To implement such a multilevel algorithm, the entire EC device is first enclosed in the smallest square box that can contain the EC. This box is referred to as the level 1 box. Then this box is divided into four square subboxes to form level 2. In its turn, each box of level 2 is divided into four square subboxes to generate the third level. This process is repeated until the finest level L, in which every box has a size

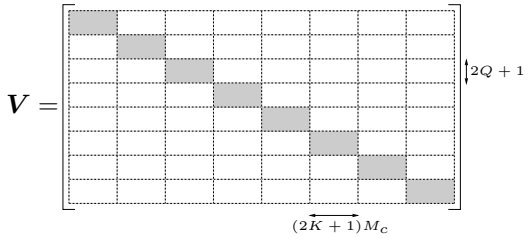

(a) Sparsity pattern of $\boldsymbol{V}$.

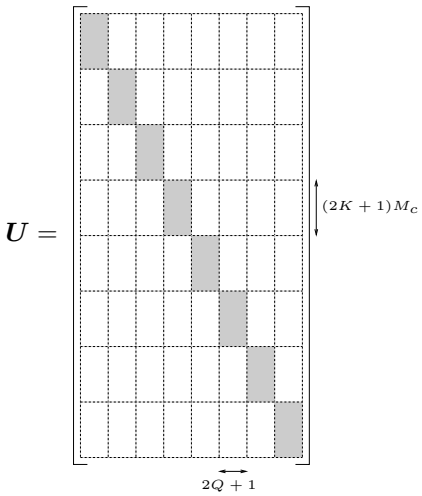

(b) Sparsity pattern of $\boldsymbol{U}$.

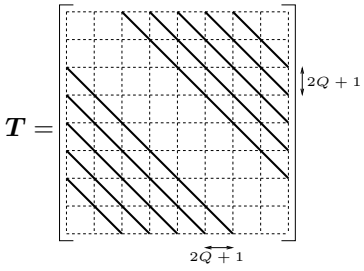

(c) Sparsity pattern of $\boldsymbol{T}$.

Figure 5.4: Decomposition of $\boldsymbol{Z}_{\text{ff}}$.

of $0.2\lambda \sim 0.5\lambda$, is reached. This procedure generates a quad-tree structure. After setting up the tree structure, boxes at all levels are indexed. However, only nonempty boxes are retained. Note that a cylinder is inside a box if its center resides in this box. Hence, the computational cost only depends on the nonempty boxes. In practice, the minimal box size Δ_{min} is chosen on beforehand and the size of the largest box, denoted by Δ_{max}, obeys

$$\Delta_{\text{max}} \quad = \quad \Delta_{\text{min}} 2^{L-1}. \tag{5.38}$$

The boxes on level $l+1$ are called the *child* boxes of the larger box on level l in which they are enclosed. Similarly, this large box on level l is called the *parent* box of its subboxes on level $l+1$.

In the multilevel algorithm, the boxes on level 3 are considered first. Note that all boxes on levels 1 and 2 are certainly near as all boxes touch each other. When two boxes are well separated on level 3, the corresponding part of the far field contribution is calculated on this level using the FMM approach described in Section 5.3.1. Two boxes b and b' on level l are well-separated when the distance between their centers satisfies

$$|\boldsymbol{\rho}_b^c - \boldsymbol{\rho}_{b'}^c| \geq \beta R_l. \tag{5.39}$$

Here, $\boldsymbol{\rho}_b^c$ and $\boldsymbol{\rho}_{b'}^c$ are the centers of the boxes b and b'; R_l is the radius of the circumscribed circle of a box at level l; β is a constant, typically chosen between 4 and 6. Next, interactions between boxes on level 4 are calculated. Of course, interactions between boxes on this level whose parent boxes are well separated on level 3, are no longer considered. If for the other boxes the inter-box spacing is sufficient on level 4, the corresponding interactions are calculated using FMM on level 4. This process continues until level L is reached. All the interactions that remain on this level are computed in the classical way and constitute the near field contribution.

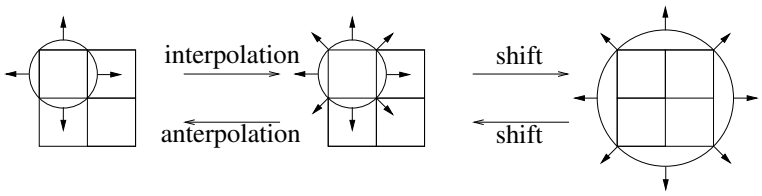

Figure 5.5: Calculating the outgoing and incoming plane waves on different levels.

Calculating box-to-box interactions with the FMM on a certain level l requires that the outgoing plane waves (5.34) are known for every box at each level. Unfortunately, calculating them by simply following Eq. (5.34) would become very expensive. Indeed, on the one hand, the number of unknowns inside a box increases as the box becomes larger. On the other hand, it follows from (5.32) that also the sampling rate Q roughly doubles when going from level $l+1$ to level l. To circumvent this problem, the outgoing plane waves are only calculated with (5.34) for level L. The outgoing plane waves of a box on level l are obtained by first interpolating the outgoing plane waves of its child boxes on level $l+1$ using a FFT, adding them, and finally shifting the resulting plane waves to the center of the box on level l. The incoming plane waves are treated in a

similar way. They are first calculated on the level with the largest possible boxes. These incoming plane waves are then shifted to the centers of the child boxes followed by an anterpolation using again a FFT. Both procedures are illustrated in Fig. 5.5. Finally, (5.36) is applied on level L, resulting in the complete far field contribution.

5.3.3 Computational complexity

For the calculation of the computational complexity and the memory requirements of the above described MLFMA, a distinction has to be made between densely and sparsely filled EC structures. Densely filled EC structures correspond to the best case scenario, as the tree structure in the MLFMA is a full quad tree, which means that every parent box has four non empty child boxes. The worst case scenario corresponds to one long line of cylinders. Then the tree is a binary tree, which means that every parent box only has two nonempty child boxes. The computational complexity and memory requirements for realistic EC devices will lie somewhere in between both cases.

5.3.3.1 Densely filled EC structure

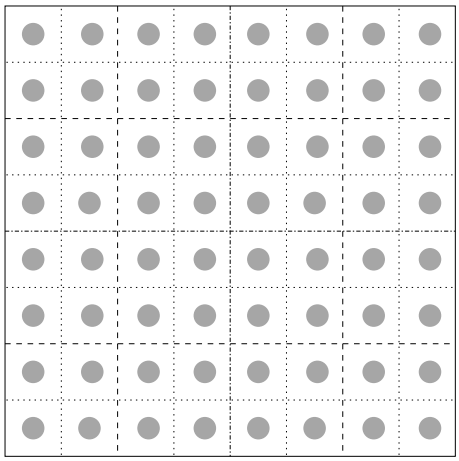

Figure 5.6: Densely filled EC structure.

Consider the densely filled EC structure depicted in Fig. 5.6. Suppose for simplicity that every box at level L contains exactly one cylinder. A box on level $L-1$ comprises 4 cylinders, a box on level $L-2$ comprises 16 cylinders, etc. Hence, a box on level l, $l = 1, \ldots, L$, contains $M_l = 2^{2(L-l)}$ cylinders. If N_c is the total number of cylinders in the EC device, the number of levels is

$$L = \frac{1}{2}\log_2 N_c + 1. \tag{5.40}$$

The number of nonempty boxes at level l is $\dfrac{N_c}{2^{2(L-l)}}$. As the size of a box roughly doubles when going from level $l+1$ to level l, it follows from (5.32) that the sampling rate also

roughly doubles:

$$Q_l \sim 2^{L-l}, \tag{5.41}$$

with Q_l the sampling rate at level l.

The outgoing and incoming plane waves are calculated following (5.34) and (5.35) for every box at level L. The cost to calculate all outgoing (incoming) plane waves for one box scales as $(2K+1) \times (2Q_L+1) \times M_L$. Since both the number of azimuthal harmonics as the sampling rate do not depend on the extent of the EC device, and because the number of boxes at level L is N_c, the workload for this step scales as $O(N_c)$. To obtain the outgoing (incoming) plane waves at other levels, interpolation (anterpolation) is applied. The cost for this step is dominated by the FFTs. The cost for one FFT of a vector with n elements is $n \log_2 n$. As there are $(2K+1) \times (2Q_l+1) \times M_l$ outgoing (incoming) plane waves for one box at level l, the cost for one FFT scales as $Q_l \log_2 Q_l$. However, this is only true if $l > 2$, as there are no far interactions at level 1 or 2. Hence, the total cost for the inter- and anterpolation scales as

$$\begin{aligned} \sum_{l=3}^{L} \frac{N_c}{2^{2(L-l)}} 2^{L-l} \log_2 2^{L-l} &= 2(N_c - \sqrt{N_c} \log_2 N_c) \\ &\approx O(N_c). \end{aligned} \tag{5.42}$$

Finally, the cost for the translation of the outgoing plane waves into incoming plane waves is proportional to the number of diagonal elements T_q. The latter scales as the sampling rate. Because the box-to-box interactions are always performed on the level with the largest possible boxes, the number of translations for a box on a certain level does not depend on the extent of the EC device, nor on the level number. If this number is noted by η, then the cost for all translations can be estimated as follows:

$$\begin{aligned} \sum_{l=3}^{L} \eta \frac{N_c}{2^{2(L-l)}} 2^{L-l} &= 2\eta N_c - 4\eta\sqrt{N_c} \\ &\approx O(N_c). \end{aligned} \tag{5.43}$$

Adding up these different costs leads to a total cost of $O(N_c)$ for densely filled EC structures. The memory requirements can be estimated following a similar reasoning. This also leads to an $O(N_c)$ behavior.

5.3.3.2 Sparsely filled EC structure

Consider one long line of N_c cylinders as shown in Fig. 5.7. Again, it is assumed that each nonempty box at level L comprises exactly one cylinder. As the tree structure is binary in this case, the number of cylinders inside a nonempty box at level l is $M_l = 2^{L-l}$. Moreover, the total number of levels is

$$L = \log_2 N_c + 1 \tag{5.44}$$

and on level l there are $\dfrac{N_c}{2^{L-l}}$ nonempty boxes. The sampling rate scales as (5.41).

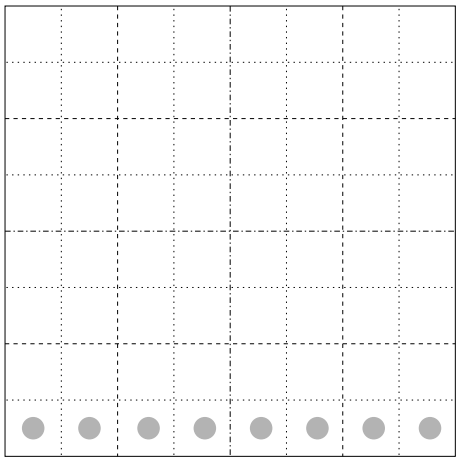

Figure 5.7: Sparsely filled EC structure.

In comparison with the developments of the previous section, only the costs for the inter- and anterpolation, and for the translations change. Now, the cost for the inter- and anterpolation is

$$\begin{aligned}\sum_{l=3}^{L} \frac{N_c}{2^{L-l}} 2^{L-l} \log_2 2^{L-l} &= \frac{N_c}{2}(\log_2^2 N_c - 3\log_2 N_c + 2) \\ &\approx O(N_c \log_2^2 N_c), \end{aligned} \tag{5.45}$$

and that for the translations is

$$\begin{aligned}\sum_{l=3}^{L} \eta \frac{N_c}{2^{L-l}} 2^{L-l} &= \eta N_c(\log_2 N_c - 1) \\ &\approx O(N_c \log_2 N_c). \end{aligned} \tag{5.46}$$

It is seen that the cost for the inter- and anterpolation is dominant. Hence, the total computational complexity also scales as $O(N_c \log_2^2 N_c)$.

The dominant cost with regard to the memory requirements is the cost to store the far field samples. This cost scales as

$$\begin{aligned}\sum_{l=3}^{L} \frac{N_c}{2^{L-l}} 2^{L-l} &= N_c(\log_2 N_c - 1) \\ &\approx O(N_c \log_2 N_c). \end{aligned} \tag{5.47}$$

5.3.4 Accuracy

As can be seen from the numerous '$\approx$'-symbols that appear in Section 5.3.1, the FMM is an *approximate* process for performing a matrix-vector multiplication. Nevertheless, as

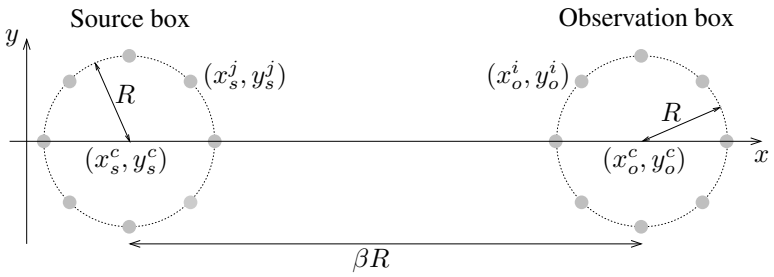

Figure 5.8: Source and observation box for testing the accuracy, real coordinates.

will be shown with some numerical examples in this section, the error can be controlled to be arbitrarily small. Consider a (circular) source and observation box as depicted in Fig. 5.8, both with radius R. The centers of both boxes are located on the x-axis and the distance between their centers is βR. On the surface of the source (observation) box, M source (observation) cylinders are placed. The coordinates of their middle points are

$$x_\nu^l = x_\nu^c + R\cos\left(\frac{2l\pi}{M}\right), \tag{5.48}$$

$$y_\nu^l = y_\nu^c + R\sin\left(\frac{2l\pi}{M}\right), \tag{5.49}$$

with $l = 0, \cdots, M-1$. The free-space wavenumber is $k = 0.72\frac{\pi}{a}$. Define the relative error δ as follows:

$$\delta = \max_{i,j}\left|\frac{(Z_{mn}^{ij})_{\text{FMM}} - (Z_{mn}^{ij})_{\text{Class}}}{(Z_{mn}^{ij})_{\text{Class}}}\right|. \tag{5.50}$$

Here, i and j account for all observers and sources, respectively; $(Z_{mn}^{ij})_{\text{Class}}$ is the interaction between the n^{th} modal unknown on the j^{th} source and the m^{th} modal unknown on the i^{th} observation cylinder calculated with (5.8); $(Z_{mn}^{ij})_{\text{FMM}}$ stands for the same interaction, but calculated using the FMM. Figure 5.9 shows the relative error δ versus the sampling rate for $R = \frac{\lambda}{2}$, $\beta = 12$, and $M = 16$. Figure 5.10 shows the same data for $R = \frac{\lambda}{2}$, $\beta = 6$, and $M = 16$. Three regions can be distinguished:

(i) The relative error decreases with increasing Q.

(ii) The highest possible accuracy, corresponding to the accuracy limit of the computer representation of the floating point numbers, is reached. However, this region only exists if β is large enough.

(iii) The relative error becomes larger again and tends to diverge for large Q. This is caused by numerical instabilities in the plane wave decomposition.

Moreover, δ only depends on the absolute value of the difference between m and n. The same behavior is observed for the different values of $|m-n|$. However, to obtain the same accuracy, the sampling rate has to be chosen slightly higher if $|m-n|$ increases.

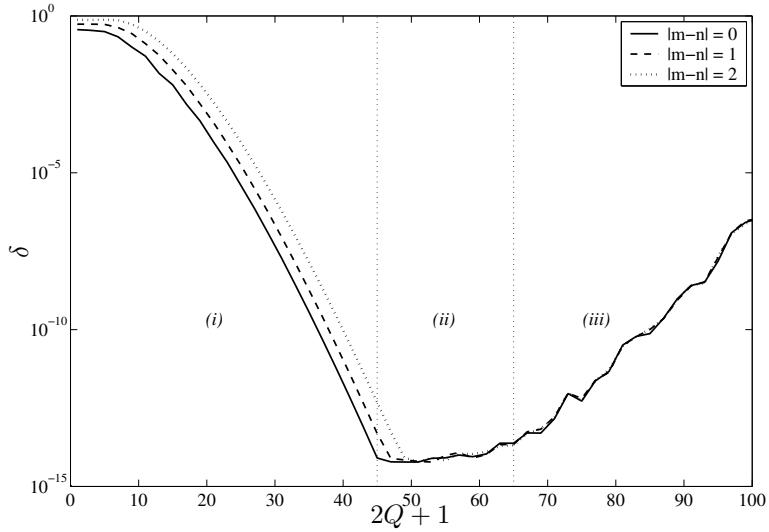

Figure 5.9: Accuracy for $R = \frac{\lambda}{2}$, $\beta = 12$, and $M = 16$.

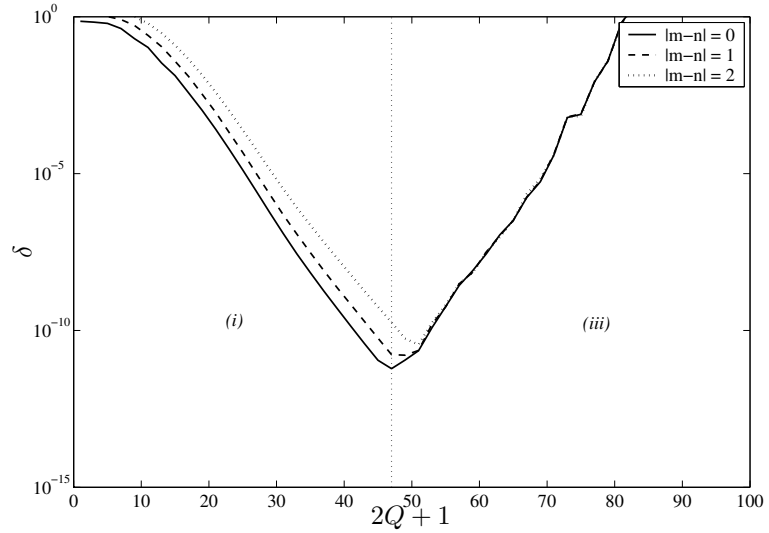

Figure 5.10: Accuracy for $R = \frac{\lambda}{2}$, $\beta = 6$, and $M = 16$.

In practice, a certain accuracy $\delta_{\max}$ is selected on beforehand. The sampling rate at each level is found by calculating δ at each level for increasing Q until the desired accuracy is obtained. Of course, these sampling rates can also be stored for later use.

5.3.5 Complex coordinates

Most often, the goal of the simulations is the knowledge of the S-parameters of the EC device. This can be achieved with the above described multiple scattering technique by terminating sufficiently long EC waveguide appendages by perfectly matched layer (PML) based absorbing boundary conditions [7]. Exploiting the complex coordinate interpretation of a PML, the EC waveguide appendages are terminated by adding N_{PML} periods in the complex plane, which means that their centers have complex coordinates. If the waveguide enters the complex plane in a smooth way, the reflections caused by the periodicity disturbance are low and at the same time a significant absorption is achieved. In [7], it was heuristically shown that a good absorption is obtained with a *circular* PML. This means that, for example, for an EC waveguide appendage in the positive x direction, the x coordinates of the cylinders in the complex plane become complex according to a circle with radius R_{PML}:

$$x = x_0 + R_{\text{PML}} \sin(n\alpha) - jR_{\text{PML}}[1 - \cos(n\alpha)], \tag{5.51}$$

with $\alpha = 2 \arcsin\left(\dfrac{a}{2R_{\text{PML}}}\right)$ and $n = 1, \cdots, N_{\text{PML}}$. Here, x_0 is the (real) x coordinate of the last period that is not in the PML region. Typical values for the different parameters of the PML region are $R_{\text{PML}} = 10a$ and $N_{\text{PML}} = 7$. This section will detail on how to incorporate these complex coordinates in the MLFMA framework.

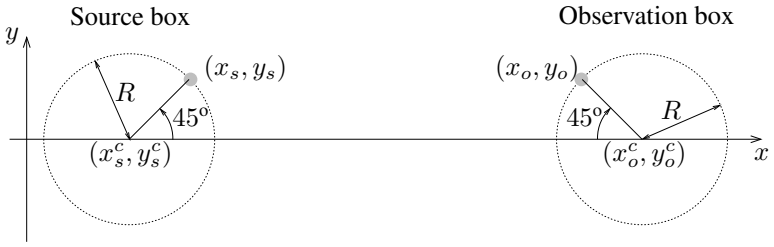

Figure 5.11: Source and observation box for testing the accuracy, complex coordinates.

First suppose that for the construction of the boxes and the MLFMA tree, only the real parts of the coordinates of the cylinders' centers are considered. In this case, a cylinder is inside a box if the real parts of its coordinates are located inside that box. It is obvious that also all box centers are real. As a consequence, no complex distances appear in the translation operators (5.24), but only in the outgoing and incoming plane waves, defined in (5.34) and (5.35). Consider the configuration depicted in Fig. 5.11. Again, it comprises a circular source and observation box with radius R. The distance between their centers is βR:

$$x_o^c = x_s^c + \beta R, \tag{5.52}$$

$$y_o^c = x_o^c. \tag{5.53}$$

As in Section 5.3.4, the relative error (5.50) is calculated, but now only one source and one observation cylinder are considered. Their coordinates are

$$x_s = x_s^c + \frac{R}{\sqrt{2}}, \tag{5.54}$$

$$y_s = y_s^c + \frac{R}{\sqrt{2}}, \tag{5.55}$$

$$x_o = x_s^c + \beta R - \frac{R}{\sqrt{2}} - j\alpha_o R, \tag{5.56}$$

$$y_o = y_s. \tag{5.57}$$

Note that this configuration does not necessarily correspond to the worst case scenario. Again the free-space wavenumber is $k = 0.72\frac{\pi}{a}$. Figure 5.12 shows the relative error versus the sampling rate for increasing imaginary part of the x coordinate of the observation cylinder with $R = \frac{\lambda}{2}$ and $\beta = 6$. The minimal achievable δ increases with increasing α_o and this minimum requires a higher Q. This yields some problems when choosing the optimal Q on each level in the MLFMA. If only real coordinates are used for this choice, the required accuracy will not be obtained for interactions involving complex coordinates. When considering also complex coordinates, the sampling rate will be much higher than necessary for the interactions with only real coordinates. Also, it is clear that for very large imaginary parts the FMM will break down.

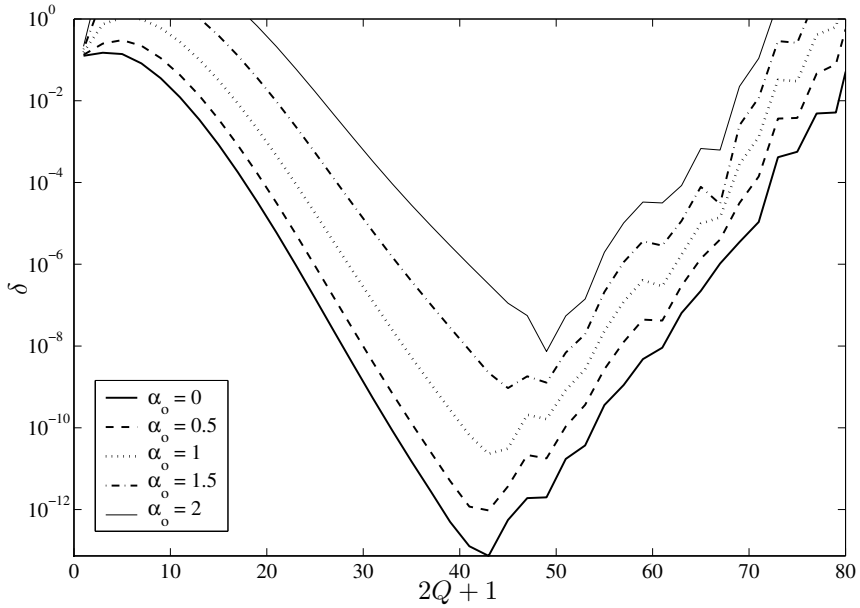

Figure 5.12: Accuracy for $R = \frac{\lambda}{2}$ and $\beta = 6$, real box centers ($\alpha_o^c = 0$).

To circumvent these difficulties, the coordinates of the boxes' centers will be allowed to be complex too. Then, complex distances appear in the translation operators. For the

above example, the coordinates of the source box remain real, but the coordinates of the observation box are

$$x_o^c = x_s^c + \beta R - j\alpha_o^c R, \tag{5.58}$$
$$y_o^c = y_s^c. \tag{5.59}$$

Figure 5.13 shows δ versus Q for $\alpha_o = 2$ and for increasing values of α_o^c. A better accuracy can be achieved and this for a sampling rate that is the same as for real coordinates. A disadvantage of this approach is the slightly higher memory requirement because more different translation operators have to be stored.

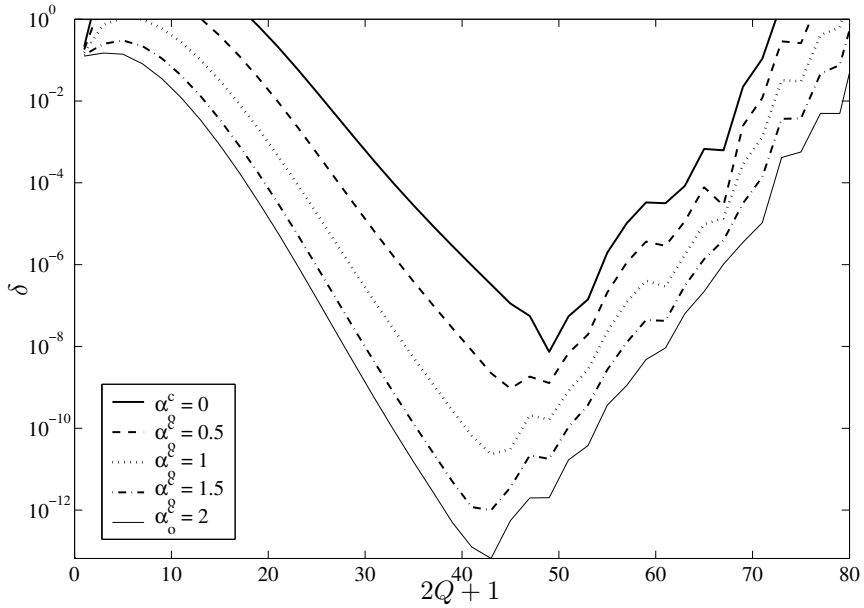

Figure 5.13: Accuracy for $R = \frac{\lambda}{2}$, $\beta = 6$, and $\alpha_o = 2$, complex box centers.

An issue that still remains to be solved is how to construct the boxes and the MLFMA tree when allowing complex coordinates for the box centers. Recall that the coordinates of the cylinders in the PML regions become complex according to a pre-described path, e.g., (5.51) for a circular PML in the positive x direction. The coordinates of the box centers will be chosen such that they also follow this path. Two sets of coordinates will be used: the first set comprises the regular (complex) coordinates of the cylinders, the second set is completely real and follows the path according to which the coordinates become complex. Consider, for example, the configuration depicted in Fig. 5.14. A straight EC waveguide parallel to the x direction is sandwiched between two circular PML regions with radius R_{PML}. A new real coordinate s is introduced. This coordinate follows the circles of the two PML regions, as indicated in Fig. 5.14. Here, $\Re(\cdot)$ and $\Im(\cdot)$ denote the real and imaginary part, respectively. These circles stop at the last cylinders in the complex plane and from these points on the parameters s follows a line parallel to the real x-axis. Both coordinate systems are related through

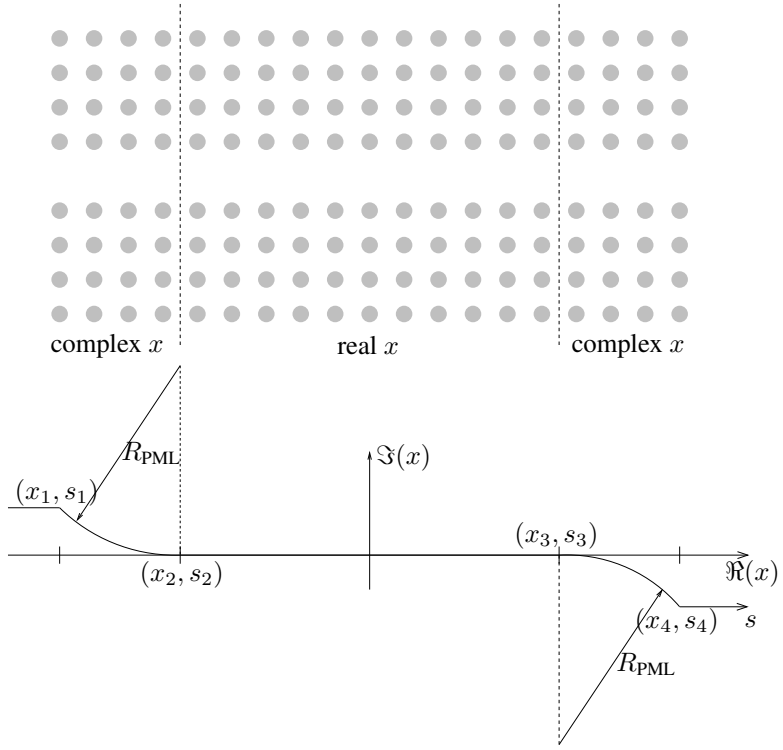

Figure 5.14: Transformation coordinate system.

- $\Re(x) < \Re(x_1)$ or $s < s_1$:

$$s = s_1 + \Re(x - x_1), \tag{5.60}$$
$$x = x_1 + s - s_1. \tag{5.61}$$

- $\Re(x_1) < \Re(x) < x_2$ or $s_1 < s < s_2$:

$$s = s_2 - \arctan\left(\frac{x_2 - \Re(x)}{R_{\text{PML}} - \Im(x)}\right), \tag{5.62}$$
$$x = x_2 - R_{\text{PML}} \sin\left(\frac{s_2 - s}{R_{\text{PML}}}\right) + jR_{\text{PML}}\left[1 - \cos\left(\frac{s_2 - s}{R_{\text{PML}}}\right)\right]. \tag{5.63}$$

- $x_2 < x < x_3$ or $s_2 < s < s_3$

$$s = x. \tag{5.64}$$

- $x_3 < \Re(x) < \Re(x_4)$ or $s_3 < s < s_4$:

$$s = s_3 + \arctan\left(\frac{\Re(x) - x_3}{R_{\text{PML}} + \Im(x)}\right), \tag{5.65}$$
$$x = x_3 + R_{\text{PML}} \sin\left(\frac{s - s_3}{R_{\text{PML}}}\right) + jR_{\text{PML}}\left[-1 + \cos\left(\frac{s - s_3}{R_{\text{PML}}}\right)\right]. \tag{5.66}$$

- $\Re(x) > \Re(x_4)$ or $s > s_4$

$$s = s_4 + \Re(x - x_4), \tag{5.67}$$
$$x = x_4 + s - s_4. \tag{5.68}$$

To construct the boxes and the MLFMA tree, the complex x coordinates of all cylinders are first transformed into the real s coordinates. The boxes are constructed based on these s coordinates. The corresponding complex x coordinates of the box centers can be easily calculated. The translation operators, the outgoing, and incoming plane waves are calculated using these complex coordinates.

5.3.6 Examples

The accuracy and the versatility of the MLFMA are demonstrated in this section via its application to the characterization of an EC waveguide coupler and an array of EC horn antennas. All calculations are performed on a Linux-based 2.4GHz Pentium IV PC. The accuracy and the overall performance are determined by the numerous parameters that appear in the MLFMA. More details about the influence of these parameters can be found in [9]. For the examples presented below, the following parameters are used: $\beta = 6$, minimal box size $\Delta_{\text{min}} = 0.5\lambda$, preset accuracy $\delta_{\text{max}} = 10^{-5}$.

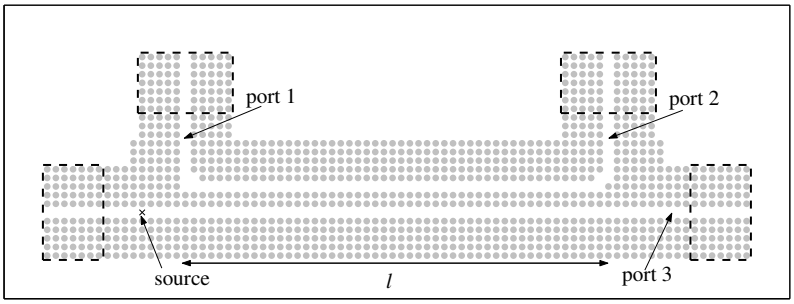

Figure 5.15: EC waveguide coupler.

5.3.6.1 EC waveguide coupler

As a first example, consider the ultra-compact two-channel multiplexer-demultiplexer depicted in Fig. 5.15 [11, 12]. This EC waveguide coupler is formed by removing two rows of cylinders separated by another two rows of cylinders. The combination of these two EC waveguides can support even and odd modes having different propagation constants β_e and β_o, respectively. As the mismatch between these propagation constants can be large, the coupling length, defined as $L = \frac{2\pi}{|\beta_e - \beta_o|}$, can become significantly smaller compared with that of conventional dielectric waveguide couplers. A field injected into one waveguide switches entirely to the other one if the length of the coupling region l is an odd integer multiple of L. In contrast, the field remains in the input waveguide if l is an integer multiple of L. The normalized output power at ports 1, 2, and 3 can be estimated using the coupled mode theory [11]:

$$P_1 = 0, \tag{5.69}$$
$$P_2 = \sin^2(\kappa l), \tag{5.70}$$
$$P_3 = \cos^2(\kappa l), \tag{5.71}$$

with $\kappa = \frac{\pi}{L} = \frac{|\beta_e - \beta_o|}{2}$. Contrary to the multiple scattering technique, coupled mode theory cannot account for reflections from the 90^{o} waveguide bends. Figures 5.16 and 5.17 show the transmission spectra calculated with the coupled mode theory and the multiple scattering technique in combination with the MLFMA for a coupling length of $l = 310a$, assuming that $a = 540nm$. All waveguides are lined by 5 rows of cylinders. When characterizing the EC waveguide coupler with the multiple scattering technique, circular PML regions with $N_{\text{PML}} = 7$ and $R_{\text{PML}} = 10a$ are added at the output ports and the MLFMA is adopted as described in Section 5.3.5. The device is excited by a Dirac line source situated at the input port. The transmission spectrum is obtained by calculating the flux at the different ports of the EC device and comparing it with that of a straight EC waveguide. This example comprises 10752 unknowns and one matrix-vector multiplication takes 0.3 s. Unfortunately, the required number of iterations is high, so preconditioning is a must. Instead of solving system $\boldsymbol{ZI} = \boldsymbol{E}$, an equivalent system $\boldsymbol{MZI} = \boldsymbol{ME}$ is solved. Here, a *block-diagonal preconditioner* was used. To construct such a preconditioner, the EC device is first divided into groups. The inverse of the small interaction matrix that describes the interactions inside one group is calculated with a direct method and used to

form an approximate inverse of $\boldsymbol{Z}$. Here, one group comprises 15 rows of the EC waveguide coupler perpendicular to the propagation direction. With this preconditioner, the BICGSTAB iterative solver requires about 200 iterations to solve the system of equations (5.7) to a tolerance of 10^{-4}. This takes about 240 s for one frequency point. The memory requirements are 74Mb.

When comparing Figs. 5.16 and 5.17, it is noted that the normalized output power calculated with the MLFMA is smaller than one. This is due to leakage from the sides of the EC waveguides. Longer couplers exhibit even more leakage. Figures 5.18 and 5.19 show the transmission spectra for $l = 3010a$. This example comprises 91752 unknowns and one matrix-vector multiplication takes 3 s. The required number of iterations to reduce the residual error below 10^{-4} is about 320. The total calculation time for one frequency point is about 1 hour. The memory requirements are 600 Mb.

5.3.6.2 EC horn antenna array

Electromagnetic crystals have introduced new possibilities in the design of radiating structures. The bandgap property of ECs has been widely applied in the design of the substrate of microwave antennas to reduce the surface wave loss or modify the radiation pattern. Recently, yet another application of ECs has been presented, namely, that of radiating horn antennas and arrays for optical beam steering [13, 14]. Optical beam steering is required in numerous applications, such as optical interconnection, optical communication, optical routing, and optical switching. An EC horn antenna is obtained from an EC defect waveguide. At one end, the EC waveguide is gradually tapered to a larger opening to form the radiating aperture of the horn antenna. The advantages of such EC horn antennas in comparison with classical horn antennas are a large operating bandwidth, high directivity, low loss, and scalability.

Consider the EC horn array device depicted in Fig 5.20. It comprises four basic EC horn antennas and a feed network of EC waveguides. The structure is excited by a Dirac line source situated at the beginning of the feed network. The basic EC horn antenna was presented in [14] and was analyzed using FDTD. The taper length and the taper angle are $21a$ and $\arctan(\frac{4}{21})$, respectively. Near the inner edges of the horn antennas the cylinders are displaced from their regular place in the EC. The complete EC horn array comprises 3600 cylinders, which corresponds to 10800 unknowns ($K = 1$). The radiation pattern for $k = 0.784\frac{\pi}{a}$ is given in Fig. 5.21. To reduce the required number of iterations, a *shielded-block preconditioner* is used. Similar to the block diagonal preconditioner that was applied for the simulation of the EC waveguide couplers, the EC device is first divided into groups. However, now a larger submatrix is inverted, namely, the submatrix describing the interactions of the group itself and a shield around it. Here, this shield are the direct neighbors of the center group. From this inverse, only those rows are retained that correspond to the unknowns of the center group. For this example, the groups to form the shielded-block preconditioner were squares of four by four lattice constants. One matrix-vector multiplication takes 0.5 s. The iterative solver is TFQMR and with the above described preconditioner, the solution of the system of equations (5.7) to a tolerance of 10^{-4} requires 50 iterations and takes 71 s. The memory requirements are 130 Mb.

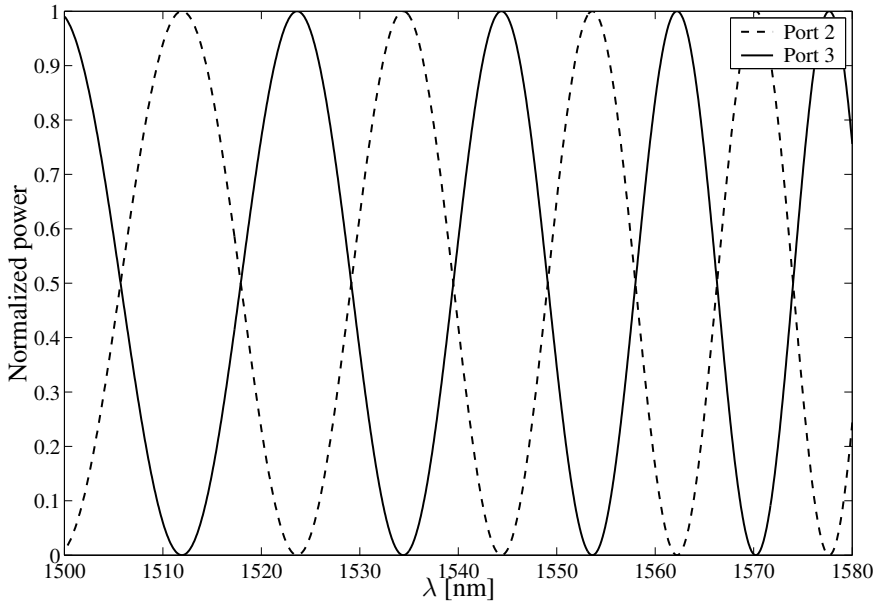

Figure 5.16: Transmission spectrum of an EC coupler with $l = 310a$ calculated with the coupled mode theory.

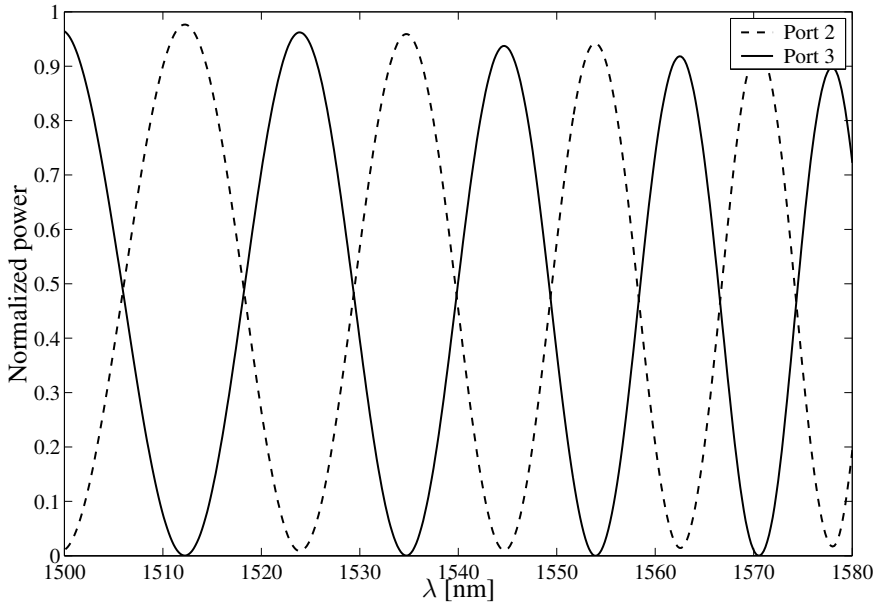

Figure 5.17: Transmission spectrum of an EC coupler with $l = 310a$ calculated with the MLFMA.

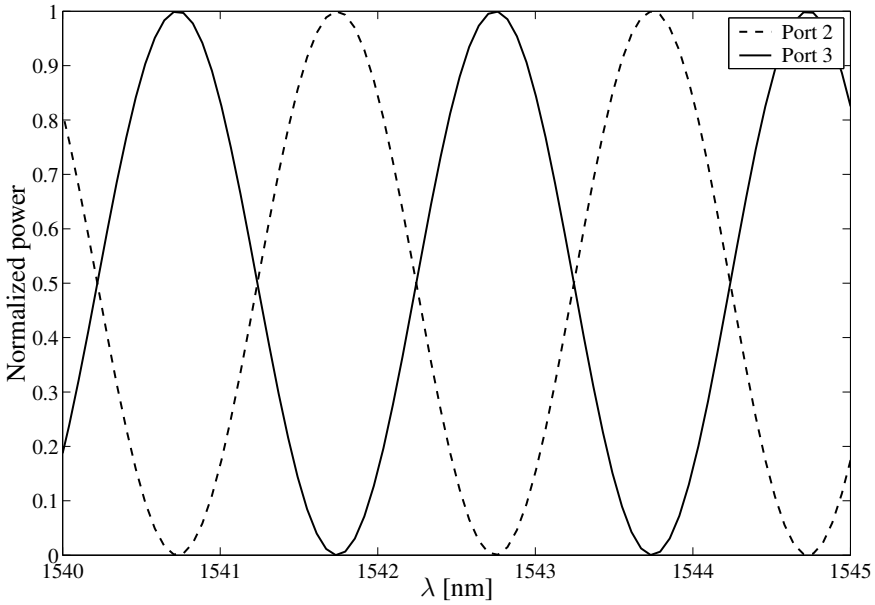

Figure 5.18: Transmission spectrum of an EC coupler with $l = 3010a$ calculated with the coupled mode theory.

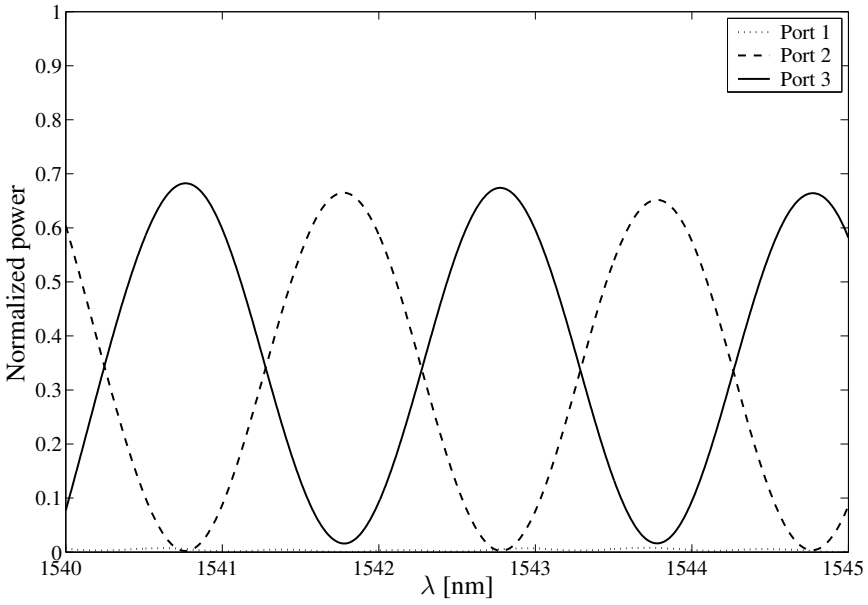

Figure 5.19: Transmission spectrum of an EC coupler with $l = 3010a$ calculated with the MLFMA.

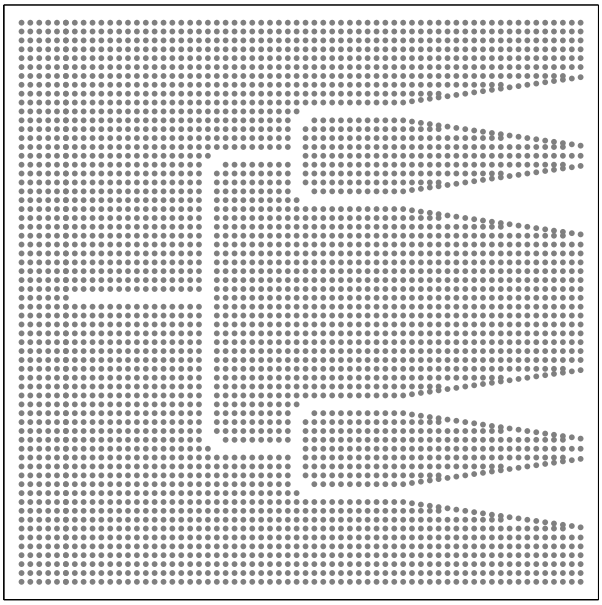

Figure 5.20: EC horn array device.

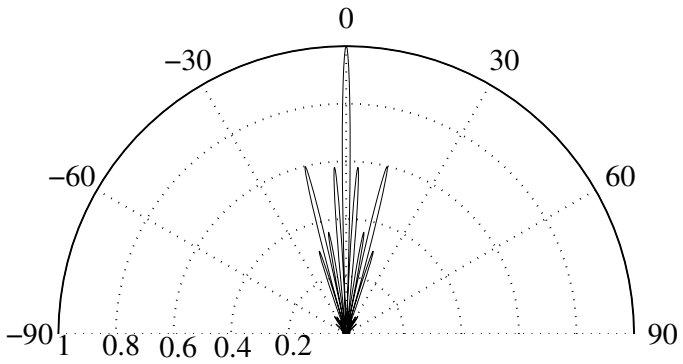

Figure 5.21: Radiation pattern of the EC horn array device.

5.4 Fast Fourier Transform based scheme

In many EC devices all cylinders snap to a regular 2D lattice, e.g., a square or a hexagonal lattice. For such structures, the computational complexity and memory requirements can be reduced using 2D FFTs. This section will only consider the basic principles for this multiplication scheme for a square lattice. However, the extension to EC devices defined on a hexagonal lattice is straightforward.

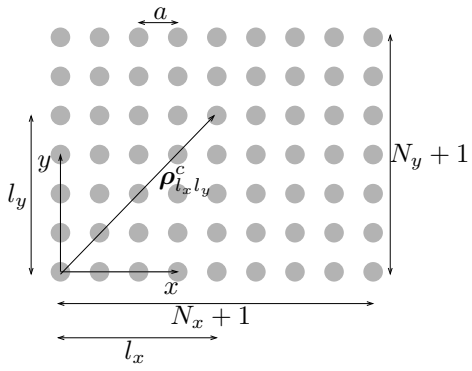

Figure 5.22: Finite rectangular EC.

First consider a finite EC with a square unit cell (lattice constant a) of $N_x + 1$ by $N_y + 1$ cylinders (Fig.5.22). Let $\boldsymbol{Z}_{mn}$ denote the submatrix that describes the interactions obtained by weighting the field caused by electric currents with modal index n with the test functions $T^i_m(\boldsymbol{\rho})$, $m = -K, \ldots, K$; $n = -K, \ldots, K$. Likewise, let $\tilde{\boldsymbol{I}}_n$ denote the subvectors comprising all entries of $\tilde{\boldsymbol{I}}$ with the same modal index n. The matrix vector multiplication $\tilde{\boldsymbol{E}} = \boldsymbol{Z}\tilde{\boldsymbol{I}}$ can then be re-expressed as follows:

$$\tilde{\boldsymbol{E}}_m = \sum_{n=-K}^{K} \tilde{\boldsymbol{E}}_{mn} = \sum_{n=-K}^{K} \boldsymbol{Z}_{mn}\tilde{\boldsymbol{I}}_n, \quad m = -K, \ldots, K. \tag{5.72}$$

For fixed m and n, the entries of the submatrix $\boldsymbol{Z}_{mn}$ only depend on the relative distances along the x- and y-axis between two cylinders. Let $Z_{mn}(l_x, l_y)$ denote the entry of this submatrix describing the interaction between two cylinders separated $l_x a$ and $l_y a$ apart along the x and y directions. Likewise let $\tilde{I}_n(l_x, l_y)$ denote the unknown on the cylinder centered about $\boldsymbol{\rho}^c_{l_x l_y} = l_x a \boldsymbol{u}_x + l_y a \boldsymbol{u}_y$. Here, it is assumed that the cylinder at the left bottom corner of the EC is centered about the origin $\boldsymbol{\rho} = \boldsymbol{0}$. Finally, let $E_{mn}(l_x, l_y)$ denote the field caused by all currents $\tilde{\boldsymbol{I}}_n$ weighted with $T^i_m(\boldsymbol{\rho})$ on the cylinder centered about $\boldsymbol{\rho}^c_{l_x l_y}$. It follows that

$$\tilde{E}_{mn}(l_x, l_y) \quad = \quad \sum_{p_x=0}^{N_x-1} \sum_{p_y=0}^{N_y-1} Z_{mn}(l_x - p_x, l_y - p_y)\tilde{I}_n(p_x, p_y), \tag{5.73}$$

for $0 \leq l_x \leq N_x$, $0 \leq l_y \leq N_y$, and $m = -K, \ldots, K$. From (5.73), it is seen that there are only $(2N_x + 1) \times (2N_y + 1)$ different entries in $\boldsymbol{Z}_{mn}$, i.e., $Z_{mn}(l_x, l_y)$ is defined for

$-N_x \leq l_x \leq N_x$ and $-N_y \leq l_y \leq N_y$. In contrast to this, the above defined unknowns $\tilde{I}_n(l_x, l_y)$ are only defined for $0 \leq l_x \leq N_x$ and $0 \leq l_y \leq N_y$. Therefore, zeros are added at the beginning of this vector:

$$\tilde{I}_n(l_x, l_y) \quad = \quad 0 \text{ for } -N_x \leq l_x \leq -1 \text{ and } -N_y \leq l_y \leq -1. \tag{5.74}$$

The 2D Fourier transform of $Z_{mn}(l_x, l_y)$ and $\tilde{I}_n(l_x, l_y)$ are defined as:

$$\hat{Z}_{mn}(\hat{l}_x, \hat{l}_y) \quad = \quad \sum_{l_x=-N_x}^{N_x} \sum_{l_y=-N_y}^{N_y} Z_{mn}(l_x, l_y) e^{-j2\pi\left(\frac{l_x \hat{l}_x}{2N_x+1} + \frac{l_y \hat{l}_y}{2N_y+1}\right)}, \tag{5.75}$$

$$\hat{I}_n(\hat{l}_x, \hat{l}_y) \quad = \quad \sum_{l_x=-N_x}^{N_x} \sum_{l_y=-N_y}^{N_y} \tilde{I}_n(l_x, l_y) e^{-j2\pi\left(\frac{l_x \hat{l}_x}{2N_x+1} + \frac{l_y \hat{l}_y}{2N_y+1}\right)}, \tag{5.76}$$

for $-N_x \leq \hat{l}_x \leq N_x$ and $-N_y \leq \hat{l}_x \leq N_y$. The 2D inverse Fourier transform of $\hat{Z}_{mn}(\hat{l}_x, \hat{l}_y)\hat{I}_n(\hat{l}_x, \hat{l}_y)$ is

$$\begin{aligned}
&\frac{1}{2N_x+1}\frac{1}{2N_y+1} \sum_{\hat{l}_x=-N_x}^{N_x} \sum_{\hat{l}_y=-N_y}^{N_y} \hat{Z}_{mn}(\hat{l}_x, \hat{l}_y)\hat{I}_n(\hat{l}_x, \hat{l}_y) e^{j2\pi\left(\frac{l_x \hat{l}_x}{2N_x+1} + \frac{l_y \hat{l}_y}{2N_y+1}\right)} = \\
&\sum_{p_x=-N_x}^{N_x} \sum_{p'_x=-N_x}^{N_x} \sum_{p_y=-N_x}^{N_x} \sum_{p'_y=-N_x}^{N_x} Z_{mn}(p'_x, p'_y)\tilde{I}_n(p_x, p_y) \times \\
&\frac{1}{2N_x+1} \sum_{\hat{l}_x=-N_x}^{N_x} e^{-j2\pi \frac{\hat{l}_x(p_x+p'_x-l_x)}{2N_x+1}} \times \\
&\frac{1}{2N_y+1} \sum_{\hat{l}_y=-N_y}^{N_y} e^{-j2\pi \frac{\hat{l}_y(p_y+p'_y-l_y)}{2N_y+1}} = \\
&\sum_{p_x=-N_x}^{N_x} \sum_{p_y=-N_y}^{N_y} Z_{mn}(l_x - p_x, l_y - p_y)\tilde{I}_n(p_x, p_y) = \\
&\sum_{p_x=0}^{N_x} \sum_{p_y=0}^{N_y} Z_{mn}(l_x - p_x, l_y - p_y)\tilde{I}_n(p_x, p_y).
\end{aligned} \tag{5.77}$$

Here, the following identity was invoked:

$$\sum_{n=-N}^{N} e^{-j2\pi \frac{nm}{2N+1}} \quad = \quad \begin{cases} 2N+1 & \text{if } m = 0, \\ 0 & \text{otherwise.} \end{cases} \tag{5.78}$$

It can be concluded from the above that $\boldsymbol{Z}_{mn}\tilde{\boldsymbol{I}}_n$ can be obtained by:

(i) extending $\tilde{I}_n(l_x, l_y)$ with zeros, such that it is defined for $-N_x \leq l_x \leq N_x$ and $-N_y \leq l_y \leq N_y$;

(ii) taking the 2D Fourier transforms of $Z_{mn}(l_x, l_y)$ and $I_n(l_x, l_y)$;

(iii) calculating the 2D inverse Fourier transform of $\hat{Z}_{mn}(\hat{l}_x, \hat{l}_y)\hat{I}_n(\hat{l}_x, \hat{l}_y)$;

(iv) retaining the samples of this 2D inverse Fourier transform corresponding to $0 \leq l_x \leq N_x$ and $0 \leq l_y \leq N_y$.

The total number of matrix elements that have to be stored in this scheme is $(2N_x + 1) \times (2N_y + 1)$. As there are in total $N_c = (N_x + 1) \times (N_y + 1)$ cylinders in the finite EC, the memory requirements scale as $O(N_c)$. Step (iii) in the above described scheme requires $(2N_x + 1) \times (2N_y + 1)$ or $O(N_c)$ multiplications. When handled properly, the required 2D (inverse) Fourier transform can be obtained with discrete FFTs with a computational complexity that scales as $O(N_c \log_2 N_c)$. Hence, the total computational complexity also scales as $O(N_c \log_2 N_c)$.

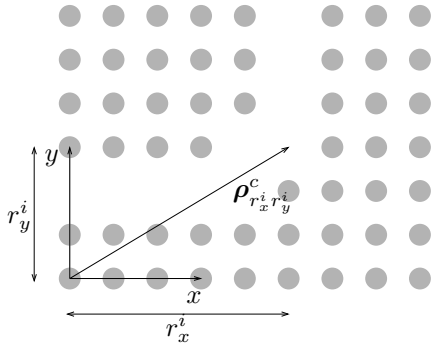

Figure 5.23: Electromagnetic crystal device.

Finally, consider an EC device obtained by removing N_r cylinders from the above finite EC (Fig. 5.23). Let ($r_x^i a$, $r_y^i a$) denote the coordinates of the removed cylinders, $i = 1, \ldots, N_r$. The required matrix-vector multiplications for this structure can be easily obtained with the FFT-based scheme by simply stating that the unknowns associated with the *removed* cylinders are always zero: $\tilde{I}(r_x^i, r_y^i) = 0$, $i = 1, \ldots, N_r$. Furthermore, in step (iv) the elements of the 2D inverse Fourier transform at (r_x^i, r_y^i) are not retained.

5.5 Conclusion

Two classical fast multiplication schemes have been applied to the multiple scattering technique for the characterization of 2D EC devices. The MLFMA reduces the computational complexity to $O(N_c \log_2^2 N_c)$ for sparsely filled EC devices and to $O(N_c)$ for densely filled EC devices. The corresponding memory requirements scale as $O(N_c \log_2 N_c)$ and $O(N_c)$, respectively. This scheme is very versatile as it makes no assumptions about the EC device under study. It can be even applied to EC devices with waveguide appendages that are terminated by PML based absorbing boundary conditions. For EC devices in which all cylinders are arranged according to a regular grid, FFTs can be applied to reduce the computational complexity to $O(N_c \log_2 N_c)$ and the memory requirements

to $O(N_c)$. Although this paper only considered EC devices defined on a square Cartesian lattice and TM_z polarized fields, extensions to EC devices on a hexagonal lattice and/or TE_z polarized fields are straightforward.

Bibliography

[1] J. D. Joannopoulos, R. D. Meade, and J. N. Winn, *Photonic Crystals, Molding the Flow of Light*. N.J.: Princeton Univ. Press, 1995.

[2] G. Tayeb and D. Maystre, "Rigorous theoretical study of finite-size two-dimensional photonic crystals doped by microcavities," *J. Opt. Soc. Am. A*, vol. 14, no. 12, pp. 3323–3332, Dec. 1997.

[3] D. Pissoort, B. Denecker, P. Bienstman, F. Olyslager, and D. De Zutter, "Comparative study of three methods for the simulation of two-dimensional photonic crystals," *J. Opt. Soc. Am. A*, vol. 21, pp. 2186–2195, Nov. 2004.

[4] V. Rokhlin, "Rapid solution of integral equations of classical potential theory," *J. Comput. Phys.*, vol. 60, pp. 187–207, 1985.

[5] L. Greenhard and V. Rokhlin, "A fast algorithm for particle simulations," *J. Comput. Phys.*, vol. 73, pp. 325–348, 1987.

[6] L. G. J. Carrier and V. Rokhlin, "A fast adaptive multipole algorithm for particle simulations," *SIAM J. Sci. Stat. Comput.*, vol. 9, pp. 669–686, 1988.

[7] D. Pissoort and F. Olyslager, "Termination of periodic waveguides by PMLs in time-harmonic integral equation like techniques," *Antennas and Wireless Propagation Letters*, vol. 2, pp. 281–284, 2003.

[8] M. Abramowitz and I. A. Stegun, *Handbook of Mathematical Functions with Formulas, Graphs and Mathematical Tables*, ser. Advanced Mathematics. New York: Dover Publications, Inc., 1965.

[9] D. Vande Ginste, "Perfectly matched layer based fast multipole methods for planar microwave structures," Phd thesis, INTEC-Ghent University, Ghent, Belgium, 2004-2005.

[10] W. C. Chew, J. M. Jin, E. Michielssen, and J. Song, *Fast and Efficient Algorithms in Computational Electromagnetics*. Boston: Artech House, 2001.

[11] M. Koshiba, "Wavelength division multiplexing and demultiplexing with photonic crystal waveguide couplers," *Journal of Lightwave Technology*, vol. 19, no. 12, pp. 1970–1975, Dec. 2001.

[12] S. Boscolo, M. Midrio, and C. G. Someda, "Coupling and decoupling of electromagnetic waves in parallel 2D photonic crystal waveguides," *IEEE J. Quantum Electron.*, vol. 1, no. 38, pp. 47–53, Jan. 2002.

[13] C. Chen, S. Shi, D. Prather, and A. Sharkawy, "Beam steering with photonic crystal horn radiators," *Optical Engineering*, vol. 68, pp. 174–180, Jan. 2004.

[14] A. Weily, K. Esselle, and B. Sanders, "Photonic crystal horn and array antennas," *Physical Review E*, vol. 68, 2003, paper no. 016609.

Chapter 6

Comparison of Different Preconditioners for the Efficient Simulation of Electromagnetic Crystal Devices

Davy Pissoort, Dries Vande Ginste, Eric Michielssen, and Frank Olyslager

This chapter is an enlarged version of the following contribution:

D. Pissoort, D. Vande Ginste, F. Olyslager, and E. Michielssen, "Different preconditioning techniques for the efficient simulation of 2D EC structures ,"IEEE Antennas and Propagation Society Symposium, Monterey, California, June 2004, Vol. 2, pp. 2131–2134

Abstract

When analyzing wave propagation in electromagnetic crystal devices using the multiple scattering technique in combination with an iterative solver, the total number of iterations for the solver to converge often is large. This paper discusses the effectiveness of three preconditioners, namely, a diagonal, block-diagonal, and shielded-block preconditioner. Numerical examples show that these preconditioners work well for a defect-less crystal, this contrary to EC devices containing waveguiding structures.

6.1 Introduction

Electromagnetic crystals (ECs) become more and more studied because of their ability to control electromagnetic/optical waves. The ECs studied in this paper consist of parallel, homogeneous, dielectric/magnetic cylinders that snap to a periodic lattice and that reside in a homogeneous background medium. These crystals are characterized by their electromagnetic bandgaps. For a frequency within this bandgap, no electromagnetic fields can propagate through the crystal. This characteristic can be used to create EC waveguides, for example, by removing cylinders from the EC. As no fields can escape through the crystal, these waveguides can exhibit sharp bends [1, 2]. Various other applications have been demonstrated, such as multiplexers [3–5], superprisms [6], etc.

As these structures are often electromagnetically large, usage of computationally efficient methods is imperative to their analysis. In [7, 8], a multiple scattering technique was introduced for the characterization of 2D EC devices. The main disadvantage of this technique is that it requires the solution of a dense linear system of equations whose dimension scales linearly with the number of cylinders. The cost for solving this system directly scales cubically in the number of cylinders. Carrying out this operation using an iterative solvers, reduces this cost to scale (nearly) linearly or quadratically in the number of cylinders, depending on whether or not fast matrix-vector multiplication schemes are employed [9]. Unfortunately, the overall cost of the iterative solver also scales proportional to the total number of iterations required for its residual error to fall below a preset threshold. Numerical experiments show that the analysis of realistic ECs often requires a high number of iterations. This observation necessitates the use of preconditioners. In this paper, three different types of preconditioners are compared on their performance and overall merits, namely, (i) a simple diagonal preconditioner, (ii) a block-diagonal preconditioner, and (iii) a shielded-block preconditioner. These preconditioners, especially the shielded-block preconditioner, effectively reduce the required number of iterations to characterize defect-less ECs, this contrary to the characterization of EC devices containing waveguide components.

Notation: all sources and fields are assumed time-harmonic with angular frequency ω; temporal dependencies $e^{j\omega t}$ are suppressed.

6.2 Multiple Scattering Technique

This section briefly details the multiple scattering technique (MST) for characterizing EC devices comprising arbitrarily positioned dielectric/magnetic cylinders. Consider a finite 2D EC device composed of N_c identical, infinite and z-invariant, homogeneous, dielectric/magnetic circular cylinders with radius r and constitutive parameters (ϵ_2, μ_2) (permittivity, permeability) that reside in a homogeneous background medium with constitutive parameters (ϵ_1, μ_1). Let $\boldsymbol{\rho} = (\rho, \phi)$ denote a global position vector in the xy-plane. Likewise, let $\boldsymbol{\rho}_j = (\rho_j, \phi_j)$ denote a local position vector with respect to the center $\boldsymbol{\rho}_j^c$ of cylinder j, $j = 1, \ldots, N_c$. Let $E_z^{\mathrm{i}}(\boldsymbol{\rho})\boldsymbol{u}_z$ denote the incident TM_z polarized electric field generated by impressed sources (assumed to reside outside the cylinders) *in the absence of any cylinders*. In the presence of the cylinders, the total field $E_z^{\mathrm{t}}(\boldsymbol{\rho})\boldsymbol{u}_z$ is observed. The difference between the total and incident fields is the scattered field $E_z^{\mathrm{s}}(\boldsymbol{\rho})\boldsymbol{u}_z$, viz.

$E_z^{\rm t}(\boldsymbol{\rho}) = E_z^{\rm i}(\boldsymbol{\rho}) + E_z^{\rm s}(\boldsymbol{\rho})$. The electric field *scattered* by cylinder j, further denoted as $E_z^{{\rm s},j}(\boldsymbol{\rho})\boldsymbol{u}_z$, can be expressed as

$$E_z^{{\rm s},j}(\boldsymbol{\rho}) \;=\; -\frac{\omega\mu_1}{4}\sum_{n=-\infty}^{+\infty} A_n^j H_n^{(2)}(k_1\rho_j)e^{jn\phi_j}, \;\text{ for } \rho_j > r. \tag{6.1}$$

Likewise, the *total* electric field inside the $j^{\rm th}$ cylinder can be expressed as

$$E_z^{\rm t}(\boldsymbol{\rho}) \;=\; -\frac{\omega\mu_2}{4}\sum_{n=-\infty}^{+\infty} B_n^j J_n(k_2\rho_j)e^{jn\phi_j}, \;\text{ for } \rho_j < r. \tag{6.2}$$

In the above equations, $k_\alpha = \omega\sqrt{\epsilon_\alpha\mu_\alpha}$ ($\alpha = 1, 2$) is the wavenumber of the unbounded medium with constitutive parameters (ϵ_α, μ_α); $J_n(\cdot)$ and $H_n^{(2)}(\cdot)$ are the $n^{\rm th}$ order Bessel function of the first kind and the $n^{\rm th}$ order Hankel function of the second kind; A_n^j and B_n^j are unknown coefficients related to cylinder j.

On the surface S_i of every cylinder i, $i = 1, \ldots, N_c$, the total tangential electric and magnetic fields are continuous

$$E_z^{\rm i}(\boldsymbol{\rho})\big|_{\boldsymbol{\rho}\in S_i^+} + \sum_{j=1}^{N_c} E_z^{{\rm s},j}(\boldsymbol{\rho})\big|_{\boldsymbol{\rho}\in S_i^+} \;=\; E_z^{\rm t}(\boldsymbol{\rho})\big|_{\boldsymbol{\rho}\in S_i^-}, \tag{6.3}$$

$$H_{\phi_i}^{\rm i}(\boldsymbol{\rho})\big|_{\boldsymbol{\rho}\in S_i^+} + \sum_{j=1}^{N_c} H_{\phi_i}^{{\rm s},j}(\boldsymbol{\rho})\Big|_{\boldsymbol{\rho}\in S_i^+} \;=\; H_{\phi_i}^{\rm t}(\boldsymbol{\rho})\big|_{\boldsymbol{\rho}\in S_i^-}. \tag{6.4}$$

Here, S_i^+ and S_i^- denote surfaces residing just outside and inside cylinder i, respectively. To solve (6.3) and (6.4) for the unknown expansion coefficients A_n^j and B_n^j, $E_z^{{\rm s},j}(\boldsymbol{\rho})$ is first written in terms of the local cylindrical coordinate system of cylinder i making use of the addition theorem for the Hankel function ([10], p. 232, Eq. 5-103)

$$E_z^{{\rm s},j}(\boldsymbol{\rho}) = \; -\frac{\omega\mu_1}{4}\sum_{n=-\infty}^{+\infty} A_n^j \sum_{m=-\infty}^{+\infty} H_{m-n}^{(2)}(k_1R_{ij})e^{j(n-m)\Phi_{ij}} J_m(k_1\rho_i)e^{jm\phi_i} \tag{6.5}$$

Here, $R_{ij} = |\boldsymbol{\rho}_{ij}^c|$ and $\Phi_{ij} = \arctan\left(\dfrac{\boldsymbol{\rho}_{ij}^c\cdot\boldsymbol{u}_y}{\boldsymbol{\rho}_{ij}^c\cdot\boldsymbol{u}_x}\right)$ are the length and the angle w.r.t. the positive x-axis of the vector $\boldsymbol{\rho}_{ij}^c = \boldsymbol{\rho}_j^c - \boldsymbol{\rho}_i^c$ connecting the centers of cylinders i and j. After that, the ϕ_i-component of the magnetic field scattered by cylinder j is obtained as

$$H_{\phi_i}^{{\rm s},j}(\boldsymbol{\rho}) \;=\; \frac{1}{j\omega\mu_1}\frac{\partial E_z^{{\rm s},j}(\boldsymbol{\rho})}{\partial\rho_i}. \tag{6.6}$$

An arbitrary incident electric field can be rewritten in terms of the cylindrical coordinates of cylinder i using the above-referenced addition theorem:

$$E_z^{\rm i}(\boldsymbol{\rho}) \;=\; -\frac{\omega\mu_1}{4}\sum_{n=-\infty}^{+\infty} C_n^i J_n(k_1\rho_i)e^{jn\phi_i}, \tag{6.7}$$

with C_n^i known coefficients. The ϕ_i-component of the incident magnetic field is found by invoking (6.6) in which $E_z^{\mathrm{s},j}(\boldsymbol{\rho})$ is of course replaced by $E_z^{\mathrm{i}}(\boldsymbol{\rho})$.

As the cylinder radius r is small compared with the wavelength and because the cylinders are assumed sufficiently separated from one another as well as from the impressed sources, the range of the modal index n can always be restricted to $n = -K, \ldots, K$, with K a small positive integer. Following the above procedure and invoking the orthogonality of the $e^{jn\phi_i}$-functions, (6.3) and (6.4) reduce to a linear set of $2(2K+1)N_c$ equations that can be solved for A_n^j and B_n^j, $n = -K, \ldots, K$; $j = 1, \ldots, N_c$, by brute force. Alternatively, all the unknowns B_n^j can be easily eliminated in favor of the unknowns A_n^j, leaving only $(2K+1)N_c$ linear equations:

$$\sum_{j=1}^{N_c} \sum_{n=-K}^{K} Z_{mn}^{ij} A_n^j = C_m^i, \; i = 1, \ldots, N_c; m = -K, \ldots, K \;\text{ or }\; \boldsymbol{ZA} = \boldsymbol{C}, \tag{6.8}$$

with

$$Z_{mn}^{ij} = \begin{cases} -\dfrac{\omega\mu_1}{4} \dfrac{k_2\mu_1 H_n^{(2)}(k_1 r) J_n'(k_2 r) - k_1\mu_2 H_n^{(2)'}(k_1 r) J_n(k_2 r)}{k_2\mu_1 J_n(k_1 r) J_n'(k_2 r) - k_1\mu_2 J_n'(k_1 r) J_n(k_2 r)} & \text{if } \begin{cases} i = j \\ m = n \end{cases} \\ 0 & \text{if } \begin{cases} i = j \\ m \neq n \end{cases} \\ -\dfrac{\omega\mu_1}{4} H_{n-m}^{(2)}(k_1 R_{ij}) e^{j(m-n)\Phi_{ij}} & \text{if } i \neq j. \end{cases} \tag{6.9}$$

All the examples presented in the next sections involve ECs composed of dielectric cylinders with constitutive parameters $(\epsilon_2, \mu_2) = (11.56\epsilon_0, \mu_0)$ and radius $r = 0.18a$ that are arranged on a Cartesian lattice with a square unit cell of size a, where a denotes the lattice constant. The cylinders reside in free space, viz. (ϵ_1, μ_1)=(ϵ_0, μ_0). This EC has a TM_z bandgap that extends from $k_1 = 0.604\frac{\pi}{a}$ to $k_1 = 0.886\frac{\pi}{a}$. When characterizing EC devices, convergence is already reached for $K = 1$.

6.3 Preconditioning

The number of unknowns in system (6.8) is $(2K+1)N_c$. The number of azimuthal harmonics per cylinder, $2K+1$, does not depend on N_c, the extent of the EC device. As the latter grows, the cost of solving (6.8) using a direct solver thus scales as $O(N_c^3)$. By using classical iterative solvers, this cost can be reduced to $O(PN_c^2)$; here P is the number of iterations. The cost can be further reduced to $O(PN_c \log N_c)$ or even $O(PN_c)$ by using fast multiplication schemes, such as multilevel fast multipole or Fast Fourier Transform (FFT) based methods. Unfortunately, as shown in this section, numerical experiments demonstrate that for the analysis of realistic EC devices, P can be very high. As a consequence, preconditioning is a must. All the preconditioners discussed below will be used as *left* preconditioners. That is, in stead of solving (6.8), the equivalent system of equations

$$\boldsymbol{MZA} \;=\; \boldsymbol{MC} \tag{6.10}$$

is solved iteratively. Let $\tilde{\boldsymbol{Z}}$ and $\tilde{\boldsymbol{C}}$ denote the preconditioned interaction matrix $\boldsymbol{MZ}$ and the preconditioned excitation vector $\boldsymbol{MC}$, respectively. The preconditioner $\boldsymbol{M}$ approximates $\boldsymbol{Z}^{-1}$, the inverse of the interaction matrix $\boldsymbol{Z}$. When employing fast multiplication schemes, the complexity to calculate these preconditioners should not jeopardize the $O(N_c)$-complexity. The following three preconditioners will be compared on their performance and overall merits:

- Diagonal preconditioner $\boldsymbol{M}_{\mathrm{d}}$: only the diagonal elements of the interaction matrix $\boldsymbol{Z}$ are retained and $\boldsymbol{M}_{\mathrm{d}}$ is the inverse of this diagonal matrix.

- Block-diagonal preconditioner $\boldsymbol{M}_{\mathrm{bd}}$: the EC device is first divided into N_g groups and the inverse of the small interaction matrix $\boldsymbol{Z}_j$ describing the interactions only inside group j, $j = 1, \ldots, N_g$, is calculated by a direct method. The block-diagonal preconditioner $\boldsymbol{M}_{\mathrm{bd}}$ is formed by combining these small inverses to construct an approximation of $\boldsymbol{Z}^{-1}$, viz.

$$\boldsymbol{M}_{\mathrm{bd}} = \begin{pmatrix} \boldsymbol{Z}_1^{-1} & & & \\ & \boldsymbol{Z}_2^{-1} & & \\ & & \ddots & \\ & & & \boldsymbol{Z}_{N_g}^{-1} \end{pmatrix}. \tag{6.11}$$

- Shielded-block preconditioner $\boldsymbol{M}_{\mathrm{sb}}$: similarly to the calculation of $\boldsymbol{M}_{\mathrm{bd}}$, the EC device is divided into N_g groups. However, now, for each group, the submatrix $\hat{\boldsymbol{Z}}_j$, describing the interaction of the j^{th} group itself with a *shield* around it is inverted. The approximate inverse $\boldsymbol{M}_{\mathrm{sb}}$ is constructed by retaining from $\hat{\boldsymbol{Z}}_j^{-1}$ only those rows that correspond to unknowns in group j. The shield can be chosen in many variants. For example, the shield might comprise some extra rows of cylinders round about every group.

Typical sparsity patterns for each of these preconditioners are shown in Fig. 6.1.

The effectiveness of the above-described preconditioners is tested on two simple EC devices, namely, a rectangular, defect-less EC and a straight EC waveguide that is formed by removing a single row of cylinders from an otherwise defect-less EC. As an iterative solver, the quasi-minimal residual (QMR) routine of Matlab is used. Figures 6.2 and 6.3 show the evolution of the residual error versus the iteration count for these EC devices (both with 2160 unknowns) for the three types of preconditioners and for different sizes of the groups used to construct $\boldsymbol{M}_{\mathrm{b}}$ and $\boldsymbol{M}_{\mathrm{sb}}$. Each group comprises N_b consecutive rows of the EC device, as indicated in both figures. Here, $\boldsymbol{M}_{\mathrm{sb}}$ is calculated by inverting the small interaction matrix describing each group along with its direct neighbor group(s) and retaining only those rows corresponding to the center group. When using only a diagonal preconditioner, the residual error quasi-stagnates for many iterations. The block-diagonal and the shielded-block preconditioner alleviate this phenomenon drastically. For both configurations, the shielded-block preconditioner outperforms the other two. For this preconditioner there is no difference between unknowns residing at the edge of each group and those near the center. Unfortunately, the little 'plateau' in the residual error – iteration count graph always remains present for the EC waveguide.

$\boldsymbol{M}_{\mathrm{d}} =$ 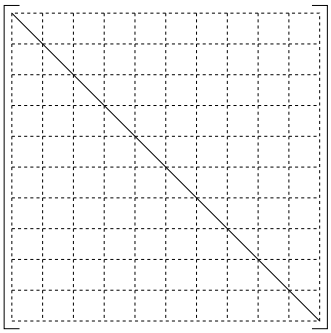

(a) Sparsity pattern of $\boldsymbol{M}_{\mathrm{d}}$.

$\boldsymbol{M}_{\mathrm{bd}} =$ 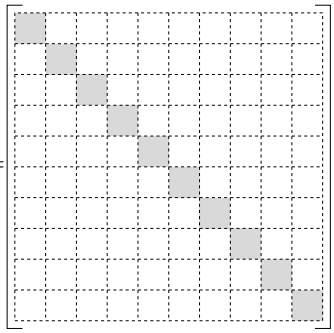

(b) Sparsity pattern of $\boldsymbol{M}_{\mathrm{bd}}$.

$\boldsymbol{M}_{\mathrm{sb}} =$ 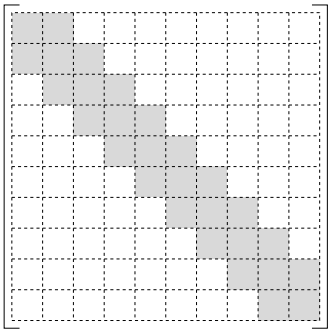

(c) Sparsity pattern of $\boldsymbol{M}_{\mathrm{sb}}$.

Figure 6.1: Sparsity pattern of the preconditioners.

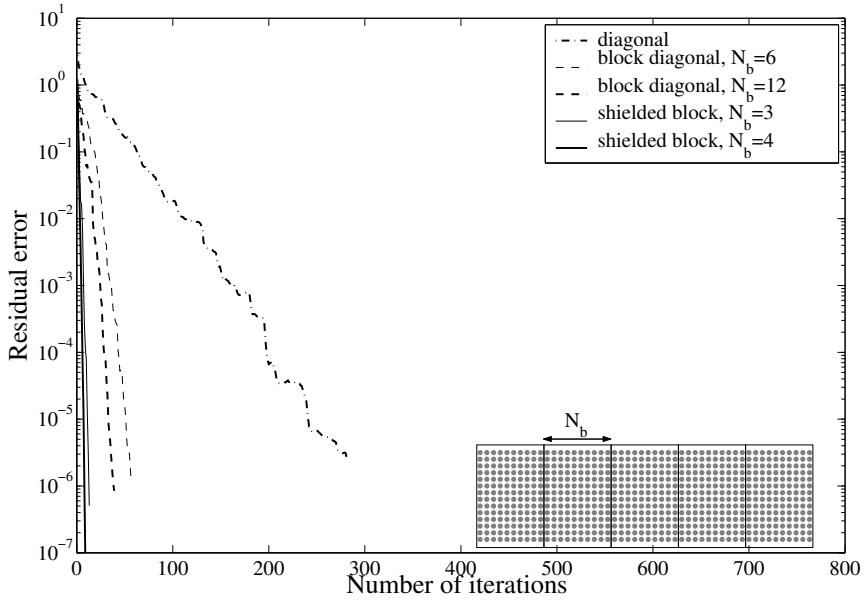

Figure 6.2: Residual error for a rectangular, defect-less EC.

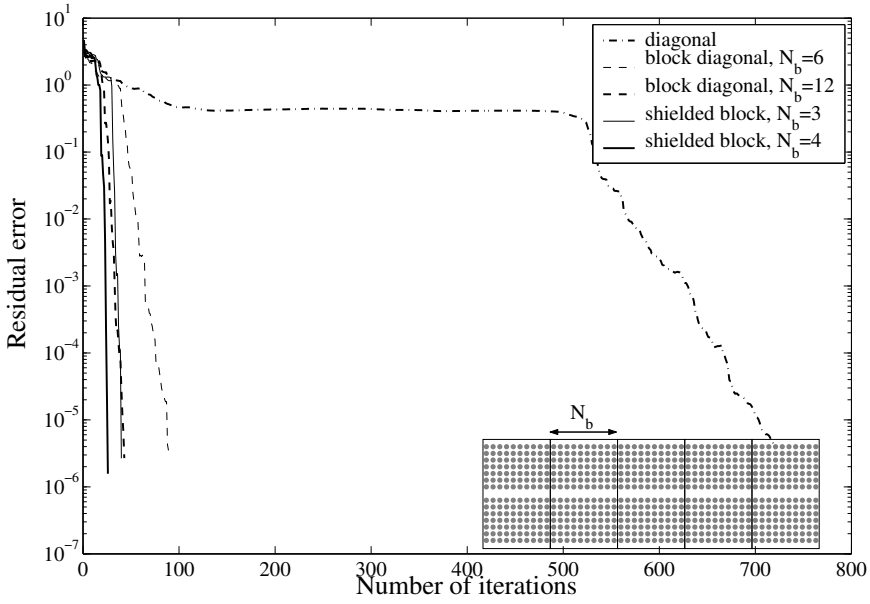

Figure 6.3: Residual error for an EC waveguide.

To obtain a deeper understanding of the physics behind this different convergence behavior, the eigenvalues and corresponding eigenvectors of both the unpreconditioned interaction matrix $\boldsymbol{Z}$ as the preconditioned interaction matrix $\tilde{\boldsymbol{Z}}$, when using the shielded-block preconditioner, are calculated. Figure 6.4 shows the distribution of these eigenvalues in the complex plane for a defect-less rectangular EC. The gray-scaled figures show some typical eigenvectors. The eigenvalues/vectors of $\boldsymbol{Z}$ correspond basically to two different physical interpretations. The eigenvalues near the imaginary axis correspond to eigenvectors that are mainly located inside the EC. The other eigenvalues are more or less positioned on circles and the corresponding eigenvectors are more located at the edges of the EC. The shielded-block preconditioner clusters all these eigenvalues around 1, which explains the rapid convergence when solving system (6.8) iteratively for a defect-less EC. Figure 6.5 shows the distribution of the eigenvalues of the unpreconditioned interaction matrix $\boldsymbol{Z}$ describing an EC waveguide. The distribution of these eigenvalues is similar to those for the defect-less EC, except that near the origin there is an extra line of eigenvalues. The corresponding eigenvectors are all located at the edges of the EC waveguide's channel. The other eigenvalues/vectors exhibit the same behavior as the eigenvalues/vectors for the defect-less EC: eigenvectors corresponding to eigenvalues near the imaginary axis are located mainly inside the EC, while those of eigenvalues residing on circles further away from the imaginary axis are located more near the outer edges of the EC. Figure 6.6 shows the distribution of the eigenvalues of the preconditioned matrix $\tilde{\boldsymbol{Z}}$ for the EC waveguide. All the eigenvectors with eigenvalues located inside or at the outer edges of the EC waveguide are clustered around 1, similar to the eigenvalues of the defect-less EC. However, the special eigenvalues with eigenvectors residing more near the edges of the EC waveguide's channel are not. Even when a state of the art preconditioner is used, the number of iterations required for the analysis of an EC waveguide will be higher than for the analysis of a defect-less EC. To obtain the same computational complexity, the waveguiding character of the EC device has to be resolved. However, this is not possible using the above method in conjunction with an iterative solver.

6.4 Conclusion

Several preconditioners have been compared on their performance and overall merits for the simulation of wave propagation in 2D EC devices. The shielded-block preconditioner outperforms the block-diagonal and the simple preconditioner. However, this reduction of the iteration count is much less for EC devices containing waveguiding structures. Further reduction of the iteration count requires to resolve the waveguiding character of the EC device.

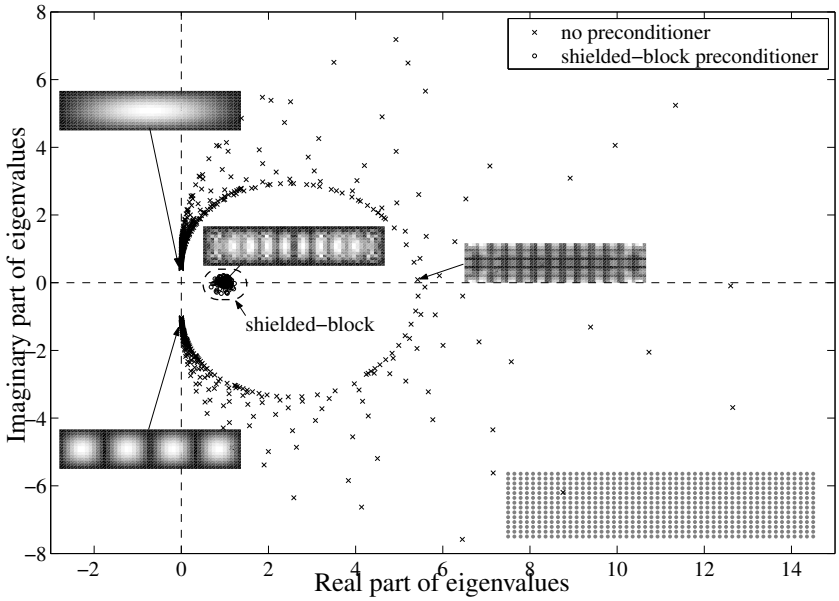

Figure 6.4: Eigenvalues/vectors for a rectangular, defect-less EC.

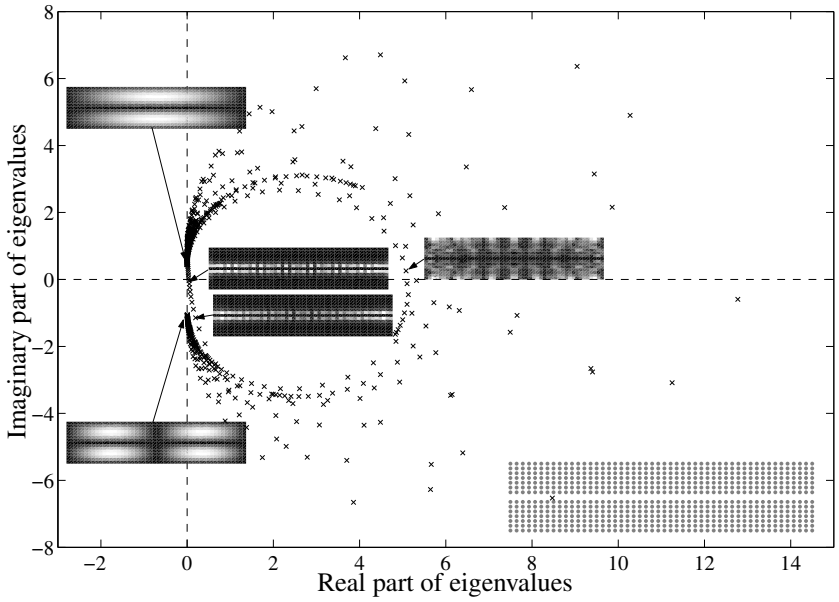

Figure 6.5: Eigenvalues/vectors for an EC waveguide, no preconditioner.

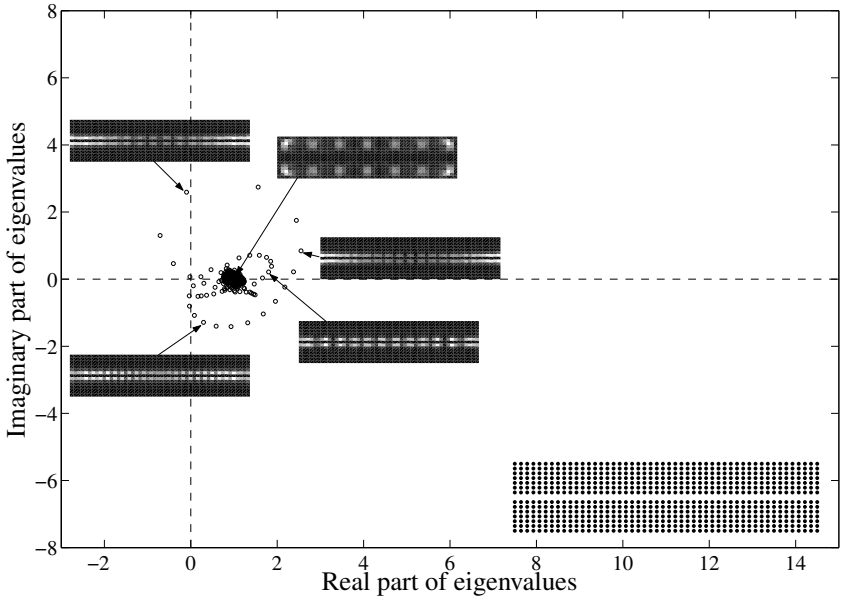

Figure 6.6: Eigenvalues/vectors for an EC waveguide, shielded-block preconditioner.

Bibliography

[1] A. Mekis, J. Chen, I. Kurland, S. Fan, P. Villeneuve, and J. Joannopoulos, "High transmission through sharp bends in photonic crystal waveguides," *Phys. Rev. Lett*, vol. 77, no. 18, pp. 3787–3790, Oct. 1996.

[2] H. Benisty, C. Weisbuch, M. Agio, M. Kafesaki, C. Soukoulis, M. Qiu, M. Swillo, A. Karlsson, B. Jaskorzynska, A. Talneau, J. Moosburger, M. Kamp, A. Forchell, R. Ferrini, R. Houdré, and U. Oesterle, "Models and measurements for the transmission of submicron-width waveguide bends defined in two-dimensional photonic crystals," *IEEE J. Quantum Electron.*, vol. 38, no. 7, pp. 770–785, July 2002.

[3] M. Koshiba, "Wavelength division multiplexing and demultiplexing with photonic crystal waveguide couplers," *Journal of Lightwave Technology*, vol. 19, no. 12, pp. 1970–1975, Dec. 2001.

[4] S. Boscolo, M. Midrio, and C. G. Someda, "Coupling and decoupling of electromagnetic waves in parallel 2D photonic crystal waveguides," *IEEE J. Quantum Electron.*, vol. 1, no. 38, pp. 47–53, Jan. 2002.

[5] C. Jin, S. Han, X. Meng, B. Cheng, and D. Zhang, "Demultiplexer using directly resonant tunneling between point defects and waveguides in a photonic crystal," *Jounal of Applied Physics*, vol. 91, no. 7, pp. 4771–4773, April 2002.

[6] L. Wu, M. Mazilu, T. Karle, and T. Krauss, "Superprism phenomena in planar photonic crystals," *IEEE J. Quantum Electron.*, vol. 38, no. 7, pp. 915–918, July 2002.

[7] G. Tayeb and D. Maystre, "Rigorous theoretical study of finite-size two-dimensional photonic crystals doped by microcavities," *J. Opt. Soc. Am. A*, vol. 14, no. 12, pp. 3323–3332, Dec. 1997.

[8] D. Pissoort, D. De Zutter, and F. Olyslager, "Efficient semi-analytical analysis of two-dimensional photonic crystals," in *IEEE AP-S Int. Symp.*, vol. 3, Columbus, OH, USA, June 2003, pp. 994–997.

[9] W. C. Chew, J. M. Jin, E. Michielssen, and J. Song, *Fast and Efficient Algorithms in Computational Electromagnetics*. Boston: Artech House, 2001.

[10] R. F. Harrington, *Time-Harmonic Electromagnetic Fields*, ser. Electrical and Electronic Engineering Series. New York: McGraw-Hill, 1961.

Chapter 7

Fast Analysis of 2D Electromagnetic Crystal Devices Using a Periodic Green Function Approach

Davy Pissoort, Eric Michielssen, Frank Olyslager, and Daniël De Zutter

Accepted for publication in IEEE Journal of Lightwave Technology

Abstract

A novel integral equation-based method for simulating wave propagation in two-dimensional electromagnetic crystal devices is presented. A small number of irregular defects aside, the targeted devices are obtained by removing cylinders from infinite, doubly periodic, and defect-less electromagnetic crystals. Integral equations in terms of equivalent currents that reside on the surfaces of the voids left by the removed cylinders are constructed by using Green functions innate to the defect-less electromagnetic crystal. The sparse system of equations that results upon discretizing these integral equations is solved efficiently by a multi-frontal method. The scheme is ideally suited to extract electromagnetic crystal device S-parameters, as it permits imposing modal excitations and exact absorbing boundary conditions. The scheme is applied to the analysis of two multiplexer-demultiplexer devices, a filter, and a bended EC waveguide, thereby demonstrating its versatility and computational efficiency.

7.1 Introduction

Recently, electromagnetic crystals (ECs) have been studied widely as their careful design enables the manipulation of electromagnetic/optical waves on spatial scales smaller than achievable by classical fiber structures [1]. Two-dimensional ECs consist of parallel homogeneous dielectric cylinders residing on a periodic lattice in a homogeneous background. These ECs exhibit electromagnetic bandgaps, viz. ranges of frequencies for which no electromagnetic propagation is allowed. By removing/adding cylinders from/to an otherwise perfect EC, an EC device capable of supporting localized electromagnetic modes may result. This phenomenon can be exploited to create low loss waveguides with sharp bends [2, 3], multiplexers [4–6], superprisms [7], etc.

In recent years, many computational schemes for simulating EC devices have been proposed. At present, the finite difference time domain method (FDTD) [8], which relates spatial samples of electromagnetic field variables on a staggered Cartesian grid via a temporal leapfrog scheme, is the most popular among them. As the FDTD method operates directly in the time-domain, it permits the wideband characterization of an EC device via a single simulation. Unfortunately, as ECs often contain small elements, their FDTD discretization and analysis requires small spatial cells and time steps. Even though the ensuing computational burden can be partially alleviated by using subcell models [9], FDTD methods remain computationally expensive, especially when high accuracies are required and phase dispersion is to be controlled. The eigenmode expansion method (EME) [10, 11] constitutes another frequently used technique for analyzing EC devices. The EME method slices up an EC device into sections with constant index profile along the propagation direction. Next, it expresses EC fields as a sum over each section's eigenmodes and determines the latter's expansion coefficients by mode matching at the section interfaces. While the EME method is very attractive when analyzing regular structures, its application becomes unwieldy when many different section types or curved structures are involved. The multiple scattering technique (MST) [12, 13] is a third popular method for analyzing EC devices. The MST solves integral equations in terms of equivalent currents that reside on the EC cylinders' surfaces. Often, the MST exploits the cylinders' circular nature by expanding surface currents in angular Fourier series, which permits their fields to be cast in terms of Bessel/Hankel functions. With this method, high accuracy can be obtained with only a few unknowns per cylinder. The MST's principal disadvantage is that it requires the solution of a dense linear system of equations whose dimension scales linearly with the number of cylinders. The cost of directly solving this system scales cubically in the numbers of cylinders. When using iterative solvers, this cost per iteration scales (nearly) linearly or quadratically in the number of cylinders depending on whether or not fast matrix-vector multiplication schemes are employed [14]. Unfortunately, the overall cost of the iterative solver also scales proportional to the total number of iterations required for its residual error to fall below a preset threshold. Numerical experiments have shown that for many realistic EC devices this number of iterations can be very high, especially when they contain waveguide components [15].

This paper describes a novel and fast MST for analyzing electromagnetic wave propagation in EC devices. A small number of defects aside, the targeted devices are obtained by removing cylinders from doubly periodic, defect-less, and infinite ECs. The proposed method expressly cannot model radiation and mismatch effects caused by EC truncation,

nor can it analyze devices carved out of non-ideal and perturbed ECs. Just like the conventional MST, the new MST solves integral equations in terms of equivalent currents that reside on cylindrical surfaces. However, contrary to conventional MST, which associates currents with the surfaces of all physical cylinders that define the EC device and then subsequently describes their interactions using a free-space Green function, the new method considers unknown currents on the surfaces of fictitious, removed cylinders and then models their interaction via a Green function innate to the surrounding infinite EC. For frequencies in the electromagnetic bandgap, this EC Green function decays exponentially with distance. Its pre-computation can be achieved using the conventional MST by considering a centrally excited, finite, and small EC. Knowledge of the EC Green function permits the fast assembly of the novel MST's system of equations comprising a sparse interaction matrix and a localized excitation that can be solved rapidly by multi-frontal methods. Pre-computation of the EC Green function also permits calculation of the modes of the semi-infinite waveguides that terminate the EC device. Knowledge of these modes in turn can be used to compute the EC device's S-parameters as it enables the implementation of exact modal excitations and absorbing boundary conditions. Unfortunately, many EC devices do not fit the above mold. That is, they cannot be constructed by simply removing cylinders from an otherwise defect-less and infinite EC as they contain defects, e.g., cylinders with center positions, radii, and/or material parameters that do not conform to those of the EC background. It will be shown that the proposed method applies to these structures as well, as they can be characterized by special Green functions that are low-rank perturbations of that of the defect-less EC.

Notation: all sources and fields are assumed time-harmonic with angular frequency ω; temporal dependencies $e^{j\omega t}$ are suppressed.

7.2 Analysis of EC devices using the free-space Green function MST

This section details the conventional MST for the characterization of finite EC devices comprising arbitrarily positioned dielectric/ magnetic cylinders. This integral equation based scheme uses a free-space Green function to describe interactions between equivalent currents on the cylinder surfaces. The field-equivalence principle [16] is invoked to elucidate symmetries between this conventional MST and the proposed novel MST (Section 7.3).

Consider a finite 2D EC device (Fig.7.1(a)) comprising N_c identical, infinite and z-invariant, homogeneous, dielectric/magnetic circular cylinders with radius r and constitutive parameters (ϵ_2, μ_2) (permittivity, permeability) that reside in a homogeneous background medium with constitutive parameters (ϵ_1, μ_1). Let $\boldsymbol{\rho} = (\rho, \phi)$ denote a global position vector. Likewise, let $\boldsymbol{\rho}_j = (\rho_j, \phi_j)$ denote a local position vector w.r.t. the center $\boldsymbol{\rho}_j^c$ of cylinder j, $j = 1, \ldots, N_c$. Let $E^{\mathrm{i}}(\boldsymbol{\rho})\boldsymbol{u}_z$ denote the incident TM$_z$ polarized electric field generated by impressed sources (assumed to reside outside the cylinders) *in the absence of any cylinders*. In the presence of the cylinders, the total field $E^{\mathrm{t}}(\boldsymbol{\rho})\boldsymbol{u}_z$ is observed. The difference between the total and incident fields is the scattered field $E^{\mathrm{s}}(\boldsymbol{\rho})\boldsymbol{u}_z$, viz. $E^{\mathrm{t}}(\boldsymbol{\rho}) = E^{\mathrm{i}}(\boldsymbol{\rho}) + E^{\mathrm{s}}(\boldsymbol{\rho})$. To describe $E^{\mathrm{s}}(\boldsymbol{\rho})$ and $E^{\mathrm{t}}(\boldsymbol{\rho})$, two sets of equivalent electric and magnetic currents are introduced on the surface S_j of every cylinder j,

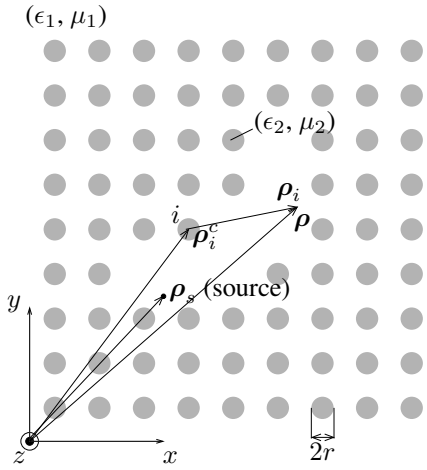

(a) Original configuration.

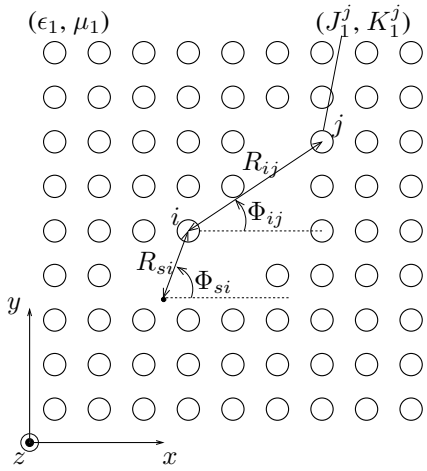

(b) Exterior problem.

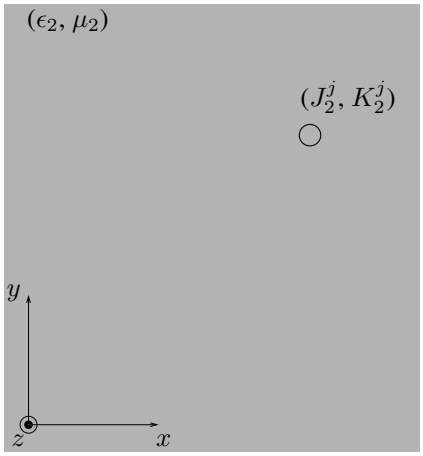

(c) Interior problem.

Figure 7.1: Field-equivalence theorem applied to the simulation of finite EC devices using the free-space Green function approach.

$j = 1, \ldots, N_c$. These sets, labelled by subscripts $\alpha = 1$ and 2, relate to the total field on S_j as

$$J_\alpha^j(\boldsymbol{\rho})\boldsymbol{u}_z = -s_\alpha \frac{j}{\omega\mu_\alpha} \left.\frac{\partial E^{\mathrm{t}}(\boldsymbol{\rho})}{\partial \rho_j}\right|_{\boldsymbol{\rho}\in S_j} \delta(\rho_j - r)\boldsymbol{u}_z, \tag{7.1}$$

$$K_\alpha^j(\boldsymbol{\rho})\boldsymbol{u}_{\phi_j} = s_\alpha \left. E^{\mathrm{t}}(\boldsymbol{\rho})\right|_{\boldsymbol{\rho}\in S_j} \delta(\rho_j - r)\boldsymbol{u}_{\phi_j}, \tag{7.2}$$

with $s_1 = 1$ and $s_2 = -1$. It follows from the field-equivalence theorem that (Fig. 7.1):

(i) The electric and magnetic currents $\sum_{j=1}^{N_c} J_1^j(\boldsymbol{\rho})\boldsymbol{u}_z$ and $\sum_{j=1}^{N_c} K_1^j(\boldsymbol{\rho})\boldsymbol{u}_{\phi_j}$, when radiating alongside the impressed sources in an unbounded medium with constitutive parameters (ϵ_1, μ_1), generate zero fields inside the (now fictitious) surface S_j of every cylinder and the total electric field $E^{\mathrm{t}}(\boldsymbol{\rho})\boldsymbol{u}_z$ outside all S_j.

(ii) The electric and magnetic currents $J_2^j(\boldsymbol{\rho})\boldsymbol{u}_z$ and $K_2^j(\boldsymbol{\rho})\boldsymbol{u}_{\phi_j}$, when radiating in an unbounded medium with constitutive parameters (ϵ_2, μ_2), generate zero fields outside S_j and $E^{\mathrm{t}}(\boldsymbol{\rho})\boldsymbol{u}_z$ inside S_j.

Therefore, knowledge of $J_\alpha^j(\boldsymbol{\rho})$ and $K_\alpha^j(\boldsymbol{\rho})$ suffices to reconstruct all fields, scattered and/or total, both inside and outside the cylinders. If $E_\alpha^{\mathrm{s},j}\boldsymbol{u}_z$ denotes the electric field radiated jointly by $J_\alpha^j(\boldsymbol{\rho})\boldsymbol{u}_z$ and $K_\alpha^j(\boldsymbol{\rho})\boldsymbol{u}_{\phi_j}$ in an unbounded medium with constitutive parameters (ϵ_α, μ_α), then the above statements can be cast as

$$E^{\mathrm{i}}(\boldsymbol{\rho}) + \sum_{j=1}^{N_c} E_1^{\mathrm{s},j}(\boldsymbol{\rho}) = 0 \text{ for } \boldsymbol{\rho} \in S_i^-,\ i = 1, \ldots, N_c, \tag{7.3}$$

$$E_2^{\mathrm{s},j}(\boldsymbol{\rho}) = 0 \text{ for } \boldsymbol{\rho} \in S_j^+,\ j = 1, \ldots, N_c. \tag{7.4}$$

Here, S_j^- and S_j^+ denote surfaces residing just inside and outside cylinder j, respectively. To solve (integral equations) (7.3)-(7.4), $J_\alpha^j(\boldsymbol{\rho})$ and $K_\alpha^j(\boldsymbol{\rho})$ are expanded into an angular Fourier series as

$$J_\alpha^j(\boldsymbol{\rho}) = s_\alpha \sum_{n=-K}^{K} \frac{C_n I_n^j}{2\pi r} e^{jn\phi_j}\delta(\rho_j - r), \tag{7.5}$$

$$K_\alpha^j(\boldsymbol{\rho}) = s_\alpha \sum_{n=-K}^{K} \frac{C_n M_n^j}{2\pi r} e^{jn\phi_j}\delta(\rho_j - r). \tag{7.6}$$

The constant

$$C_n = \frac{k_2\mu_1 J_n'(k_2 r)}{k_2\mu_1 J_n(k_1 r)J_n'(k_2 r) - k_1\mu_2 J_n'(k_1 r)J_n(k_2 r)}, \tag{7.7}$$

with $k_\alpha = \omega\sqrt{\epsilon_\alpha\mu_\alpha}$, is introduced to simplify the derivations and equations that follow. Because the cylinder radius r is small compared to the wavelength and because the cylinders are assumed sufficiently separated from one another as well as from the impressed

sources, the range of the modal index n always can be restricted to $n = -K, \ldots, +K$, with K a small positive integer. It is readily verified that the scattered field $E_\alpha^{s,j}(\boldsymbol{\rho})$ is given by

$$E_\alpha^{s,j}(\boldsymbol{\rho}) = \begin{cases} -s_\alpha \displaystyle\sum_{n=-K}^{K} \left[\frac{\omega\mu_\alpha}{4} J_n(k_\alpha r) I_n^j + \frac{jk_\alpha}{4} J_n'(k_\alpha r) M_n^j \right] \times \\ \qquad C_n H_n^{(2)}(k_\alpha \rho_j) e^{jn\phi_j} & \text{if } \rho_j > r, \\ -s_\alpha \displaystyle\sum_{n=-K}^{K} \left[\frac{\omega\mu_\alpha}{4} H_n^{(2)}(k_\alpha r) I_n^j + \frac{jk_\alpha}{4} H_n^{(2)'}(k_\alpha r) M_n^j \right] \times \\ \qquad C_n J_n(k_\alpha \rho_j) e^{jn\phi_j} & \text{if } \rho_j < r. \end{cases} \tag{7.8}$$

Here, $J_n(\cdot)$ is the n^{th}-order Bessel function of the first kind and $H_n^{(2)}(\cdot)$ is the n^{th}-order Hankel function of the second kind.

Upon inserting expansion (7.8) into Eqs. (7.3) and (7.4), and testing them using $T_m^i(\boldsymbol{\rho}) = \dfrac{1}{2\pi r J_m(k_1 r)} e^{-jm\phi_i} \delta(\rho_i - r)$, $i = 1, \ldots, N_c$; $m = -K, \ldots, K$, the resulting set of linear equations can be solved for I_n^j and M_n^j, $j = 1, \ldots, N_c$; $n = -K, \ldots, K$, by brute force. Alternatively, all the magnetic unknowns M_n^j can be eliminated in favor of their electric counterparts I_n^j by first solving the (interior) equation (7.4), thereby leaving only the (exterior) equation (7.3) and electric unknowns I_n^j to be considered. This strategy is adopted here. Inserting (7.8) with $\alpha = 2$ into Eq. (7.4) yields

$$\frac{I_n^j}{M_n^j} = -j\sqrt{\frac{\epsilon_2}{\mu_2}} \frac{J_n'(k_2 r)}{J_n(k_2 r)}. \tag{7.9}$$

Using (7.9), Eq. (7.8) with $\alpha = 1$ can be re-expressed as

$$E_1^{s,j}(\boldsymbol{\rho}) = \sum_{n=-K}^{K} G_n(\boldsymbol{\rho}_j) I_n^j, \tag{7.10}$$

where

$$G_n(\boldsymbol{\rho}_j) = \begin{cases} -\dfrac{\omega\mu_1}{4} H_n^{(2)}(k_1\rho_j) e^{jn\phi_j} & \text{if } \rho_j > r, \\ -\dfrac{\omega\mu_1}{4} \dfrac{k_2\mu_1 H_n^{(2)}(k_1 r) J_n'(k_2 r) - k_1\mu_2 H_n^{(2)'}(k_1 r) J_n(k_2 r)}{k_2\mu_1 J_n(k_1 r) J_n'(k_2 r) - k_1\mu_2 J_n'(k_1 r) J_n(k_2 r)} \times \\ \qquad J_n(k_1\rho_j) e^{jn\phi_j} & \text{if } \rho_j < r. \end{cases} \tag{7.11}$$

Quantity $G_n(\boldsymbol{\rho}_j)$ is the (generalized) free-space Green function for a Huygens source with distributed electric and magnetic components $\frac{C_n}{2\pi r} e^{jn\phi_j} \delta(\rho_j - r) \boldsymbol{u}_z$ and $\frac{jC_n}{2\pi r} \sqrt{\frac{\mu_2}{\epsilon_2}} \frac{J_n(k_2 r)}{J_n'(k_2 r)}$ $e^{jn\phi_j} \delta(\rho_j - r) \boldsymbol{u}_{\phi_j}$ radiating jointly in an unbounded medium with constitutive parameters (ϵ_1, μ_1).

To solve for the unknowns I_n^j, expansion (7.10) is inserted into (7.3) and the resulting equation is tested by $T_m^i(\boldsymbol{\rho})$, $i = 1, \ldots, N_c$; $m = -K, \ldots, K$, giving rise to the matrix equation

$$\boldsymbol{Z}\boldsymbol{I} \quad = \quad \boldsymbol{E}. \tag{7.12}$$

The entries of the matrix $\boldsymbol{Z}$ as well as the vector $\boldsymbol{E}$ are $Z_{mn}^{ij} = \langle T_m^i(\boldsymbol{\rho}), G_n(\boldsymbol{\rho}_j)\rangle$ and $E_m^i = \langle T_m^i(\boldsymbol{\rho}), -E^{\mathrm{i}}(\boldsymbol{\rho})\rangle$. Here $\langle\cdot,\cdot\rangle$ stands for the standard inner product. Making use of the addition theorem for the Hankel function ([17], p. 232, Eq. 5-103), it can be shown that the entries of the matrix $\boldsymbol{Z}$ are

$$Z_{mn}^{ij} = \begin{cases} -\dfrac{\omega\mu_1}{4}\dfrac{k_2\mu_1 H_n^{(2)}(k_1 r)J_n'(k_2 r) - k_1\mu_2 H_n^{(2)'}(k_1 r)J_n(k_2 r)}{k_2\mu_1 J_n(k_1 r)J_n'(k_2 r) - k_1\mu_2 J_n'(k_1 r)J_n(k_2 r)} & \text{if } \begin{cases} i = j \\ m = n \end{cases} \\ 0 & \text{if } \begin{cases} i = j \\ m \neq n \end{cases} \\ -\dfrac{\omega\mu_1}{4} H_{n-m}^{(2)}(k_1 R_{ij}) e^{j(m-n)\Phi_{ij}} & \text{if } i \neq j. \end{cases} \tag{7.13}$$

Here $R_{ij} = |\boldsymbol{\rho}_{ij}^c|$ and $\Phi_{ij} = \arctan\left(\frac{\boldsymbol{\rho}_{ij}^c \cdot \boldsymbol{u}_y}{\boldsymbol{\rho}_{ij}^c \cdot \boldsymbol{u}_x}\right)$ are the length and angle with respect to the positive x-axis of the vector $\boldsymbol{\rho}_{ij}^c = \boldsymbol{\rho}_j^c - \boldsymbol{\rho}_i^c$ connecting the centers of the cylinders i and j (Fig. 7.1(b)). For certain types of fields $E^{\mathrm{i}}(\boldsymbol{\rho})$, closed-form expressions of the entries of $\boldsymbol{E}$ exist, too. For example, if $E^{\mathrm{i}}(\boldsymbol{\rho})$ is due to a unit strength electric line current located at $\boldsymbol{\rho}_s$, that is, if $E^{\mathrm{i}}(\boldsymbol{\rho}) = -\dfrac{\omega\mu_1}{4} H_0^{(2)}(k_1|\boldsymbol{\rho} - \boldsymbol{\rho}_s|)$, then use of the above-referenced addition formula permits E_m^i to be expressed as

$$E_m^i \quad = \quad -\frac{\omega\mu_1}{4}(-1)^m H_m^{(2)}(k_1 R_{si}) e^{jm\Phi_{si}}. \tag{7.14}$$

Here, $R_{si} = |\boldsymbol{\rho}_{si}^c|$ and $\Phi_{si} = \arctan\left(\frac{\boldsymbol{\rho}_{si}^c \cdot \boldsymbol{u}_y}{\boldsymbol{\rho}_{si}^c \cdot \boldsymbol{u}_x}\right)$ are the length and angle of the vector $\boldsymbol{\rho}_{si}^c = \boldsymbol{\rho}_i^c - \boldsymbol{\rho}_s$ (Fig. 7.1(b)).

The above "free-space Green function"MST does not preclude the characterization of EC devices with semi-infinite waveguide attachments. Indeed, such characterization can be achieved by terminating sufficiently long EC device waveguide appendages by absorbing/resistive sections, e.g. by perfectly matched layer based absorbing boundary conditions for integral equation solvers [18]. The resulting scheme, potentially used in conjunction with computational de-embedding methods, then permits EC device S-parameter extraction.

Unfortunately, the above scheme's computational cost is high. The number of unknown electric current coefficients in the system (7.12) is $(2K + 1)N_c$; here, $2K + 1$, the number of azimuthal harmonics per cylinder, does not depend on N_c, the extent of the crystal. As the latter grows, the cost of solving (7.12) using a direct solver thus scales as $O(N_c^3)$. By using classical iterative solvers, this cost can be reduced to $O(PN_c^2)$; here, P is the number of iterations. The cost can be further reduced to $O(PN_c \log N_c)$ or even $O(PN_c)$ by using Fast Fourier Transform (FFT) or multilevel fast multipole based methods [14]. Unfortunately, numerical experiments have demonstrated that when the

EC device contains waveguiding components, P can be very high, even when a good preconditioner is used [15]. This precludes application of this free-space Green function MST – even in conjunction with state-of-the-art accelerators – to the analysis of all but the simplest EC devices.

7.3 Analysis of EC devices using the EC Green function MST

This section details a novel and fast scheme for characterizing (semi-in)finite EC devices. A small number of defects aside, these devices are obtained by removing cylinders from an otherwise infinitely periodic and defect-less EC. Contrary to the scheme described in the previous section, which characterized ECs by using a free-space Green function to describe interactions between equivalent currents on physical cylinders, the new scheme describes ECs by using a Green function innate to the defect-less EC to model interactions between equivalent currents on removed cylinders.

7.3.1 Formulation

Consider a 2D EC device (Fig. 7.2(a)) obtained by removing N_r cylinders from an infinite and defect-less EC comprising identical, infinite and z-invariant, homogeneous, dielectric/magnetic circular cylinders with radius r and constitutive parameters (ϵ_2, μ_2) that are spaced by Δ_x and Δ_y from center to center along the x and y directions and that reside in a homogeneous background medium with constitutive parameters (ϵ_1, μ_1). The nomenclature in this section generally adheres to that used in Section 7.2, with the exception that tilde's appear on symbols referring to fields, currents, and surfaces of removed cylinders. It is assumed that ω lies within the EC bandgap. Let $\tilde{E}^{\rm i}(\boldsymbol{\rho})\boldsymbol{u}_z$ denote the incident electric field generated by impressed sources that radiate *in the presence of the defect-less EC*, viz. the infinite EC without any cylinders removed. Upon removal of the cylinders, the total field $\tilde{E}^{\rm t}(\boldsymbol{\rho})\boldsymbol{u}_z$ is observed. The difference between the total and incident fields is the scattered field $\tilde{E}^{\rm s}(\boldsymbol{\rho})\boldsymbol{u}_z$, viz. $\tilde{E}^{\rm t}(\boldsymbol{\rho}) = \tilde{E}^{\rm i}(\boldsymbol{\rho}) + \tilde{E}^{\rm s}(\boldsymbol{\rho})$. To describe $\tilde{E}^{\rm s}(\boldsymbol{\rho})$ and $\tilde{E}^{\rm t}(\boldsymbol{\rho})$, two sets ($\alpha = 1, 2$) of equivalent electric and magnetic currents are introduced on the surface $\tilde{S}_j$ of every *removed* cylinder j, $j = 1, \ldots, N_r$. Both sets are related to the total field on $\tilde{S}_j$ by

$$\tilde{J}^j_\alpha(\boldsymbol{\rho})\boldsymbol{u}_z = -s_\alpha \frac{j}{\omega\mu_1} \left.\frac{\partial \tilde{E}^{\rm t}(\boldsymbol{\rho})}{\partial \rho_j}\right|_{\boldsymbol{\rho}\in\tilde{S}_j} \delta(\rho_j - r)\boldsymbol{u}_z, \tag{7.15}$$

$$\tilde{K}^j_\alpha(\boldsymbol{\rho})\boldsymbol{u}_{\phi_j} = s_\alpha \left.\tilde{E}^{\rm t}(\boldsymbol{\rho})\right|_{\boldsymbol{\rho}\in\tilde{S}_j} \delta(\rho_j - r)\boldsymbol{u}_{\phi_j}. \tag{7.16}$$

It follows from the field-equivalence theorem that (Fig. 7.2):

(i) The electric and magnetic currents $\sum_{j=1}^{N_r} \tilde{J}^j_1(\boldsymbol{\rho})\boldsymbol{u}_z$ and $\sum_{j=1}^{N_r} \tilde{K}^j_1(\boldsymbol{\rho})\boldsymbol{u}_{\phi_j}$, when radiating alongside the impressed sources *in the unbounded and defect-less EC*, generate

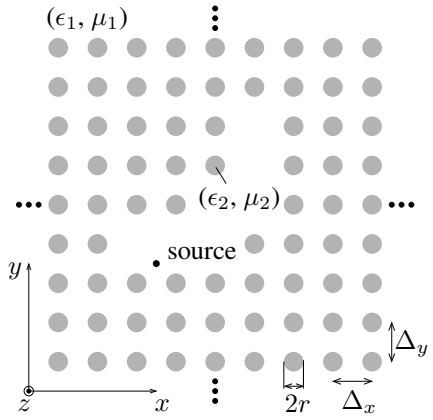

(a) Original configuration.

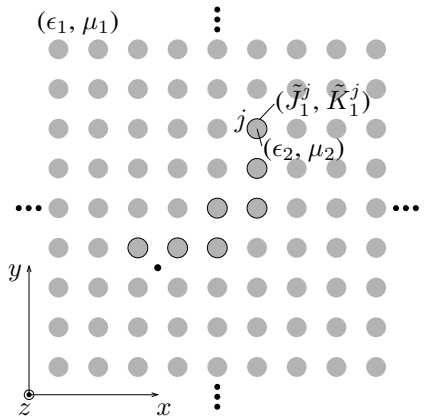

(b) Exterior problem.

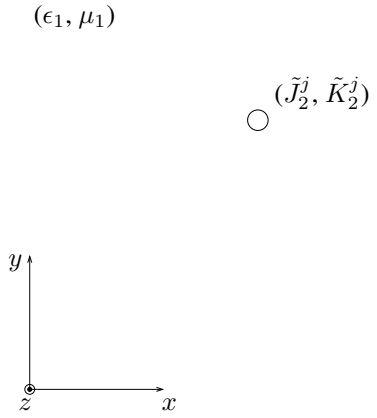

(c) Interior problem.

Figure 7.2: Field-equivalence theorem applied to the simulation of an EC device using the EC Green function approach.

zero fields inside the surface $\tilde{S}_j$ of every cylinder that was originally removed, and the total electric field $\tilde{E}^{\rm t}(\boldsymbol{\rho})\boldsymbol{u}_z$ outside all $\tilde{S}_j$.

(ii) The electric and magnetic currents $\tilde{J}_2^j(\boldsymbol{\rho})\boldsymbol{u}_z$ and $\tilde{K}_2^j(\boldsymbol{\rho})\boldsymbol{u}_{\phi_j}$, when radiating in an unbounded medium with constitutive parameters (ϵ_1, μ_1), generate zero fields outside $\tilde{S}_j$ and $\tilde{E}^{\rm t}(\boldsymbol{\rho})\boldsymbol{u}_z$ inside $\tilde{S}_j$.

If $\tilde{E}_\alpha^{{\rm s},j}(\boldsymbol{\rho})$ denotes the amplitude of the z directed electric field radiated jointly by $\tilde{J}_\alpha^j(\boldsymbol{\rho})\boldsymbol{u}_z$ and $\tilde{K}_\alpha^j(\boldsymbol{\rho})\boldsymbol{u}_{\phi_j}$ in the unbounded and defect-less EC when $\alpha = 1$ or in the unbounded medium with constitutive parameters (ϵ_1, μ_1) when $\alpha = 2$, then the above statements can be cast as

$$\tilde{E}^{\rm i}(\boldsymbol{\rho}) + \sum_{j=1}^{N_r} \tilde{E}_1^{{\rm s},j}(\boldsymbol{\rho}) = 0 \text{ if } \boldsymbol{\rho} \in \tilde{S}_i^-,\ i = 1, \ldots, N_r, \tag{7.17}$$

$$\tilde{E}_2^{{\rm s},j}(\boldsymbol{\rho}) = 0 \text{ if } \boldsymbol{\rho} \in \tilde{S}_j^+,\ j = 1, \ldots, N_r. \tag{7.18}$$

To solve equations (7.17)-(7.18), $\tilde{J}_\alpha^j(\boldsymbol{\rho})$ and $\tilde{K}_\alpha^j(\boldsymbol{\rho})$ are expanded as

$$\tilde{J}_\alpha^j(\boldsymbol{\rho}) = s_\alpha \sum_{n=-K}^{K} \frac{C_n \tilde{I}_n^j}{2\pi r} e^{jn\phi_j} \delta(\rho_j - r), \tag{7.19}$$

$$\tilde{K}_\alpha^j(\boldsymbol{\rho}) = s_\alpha \sum_{n=-K}^{K} \frac{C_n \tilde{M}_n^j}{2\pi r} e^{jn\phi_j} \delta(\rho_j - r). \tag{7.20}$$

Solving the (interior) Eq. (7.18) now leads to

$$\frac{\tilde{I}_n^j}{\tilde{M}_n^j} = -j\sqrt{\frac{\epsilon_1}{\mu_1}} \frac{J_n'(k_1 r)}{J_n(k_1 r)}. \tag{7.21}$$

Note the change in material index from 2 to 1 when comparing this ratio to that appearing in (7.9). This relationship permits $\tilde{E}_1^{{\rm s},j}(\boldsymbol{\rho})$, the amplitude of the z directed electric field radiated jointly by $\tilde{J}_1^j(\boldsymbol{\rho})$ and $\tilde{K}_1^j(\boldsymbol{\rho})$ *in the defect-less and unbounded EC*, to be expressed solely in terms of electric unknowns as

$$\tilde{E}_1^{{\rm s},j}(\boldsymbol{\rho}) = \sum_{n=-K}^{K} \tilde{G}_n(\boldsymbol{\rho}_j) \tilde{I}_n^j. \tag{7.22}$$

Quantity $\tilde{G}_n(\boldsymbol{\rho}_j)$ is the (generalized) EC Green function for a Huygens source with distributed electric and magnetic components $\frac{C_n}{2\pi r} e^{jn\phi_j}\delta(\rho_j - r)\boldsymbol{u}_z$ and $\frac{jC_n}{2\pi r}\sqrt{\frac{\epsilon_1}{\mu_1}}\frac{J_n(k_1 r)}{J_n'(k_1 r)}$ $e^{jn\phi_j}\delta(\rho_j - r)\boldsymbol{u}_{\phi_j}$ radiating jointly in the *defect-less and unbounded EC*. Unfortunately, contrary to the developments in the previous section, no closed-form expressions for $\tilde{G}_n(\boldsymbol{\rho}_j)$ exist.

To solve for the unknowns $\tilde{I}_n^j$, expansion (7.22) is inserted into (7.17) and the resulting equation is tested by $\tilde{T}_m^i(\boldsymbol{\rho}) = \frac{1}{2\pi r J_m(k_2 r)} e^{-jm\phi_i}\delta(\rho_i - r)$, resulting in the matrix equation

$$\tilde{\boldsymbol{Z}}\tilde{\boldsymbol{I}} = \tilde{\boldsymbol{E}}, \tag{7.23}$$

where $\tilde{Z}^{ij}_{mn} = \langle \tilde{T}^i_m(\boldsymbol{\rho}), \tilde{G}_n(\boldsymbol{\rho}_j)\rangle$ and $\tilde{E}^i_m = \langle \tilde{T}^i_m(\boldsymbol{\rho}), -\tilde{E}^{\mathrm{i}}(\rho)\rangle$. Sections 7.3.2 and 7.3.3 detail techniques for evaluating the entries of $\tilde{\boldsymbol{Z}}$ and $\tilde{\boldsymbol{E}}$.

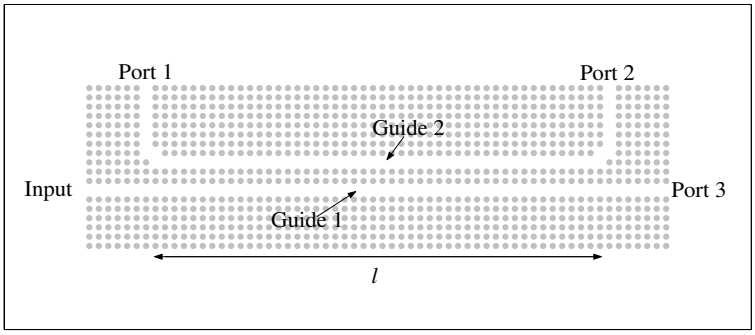

Figure 7.3: EC waveguide coupler.

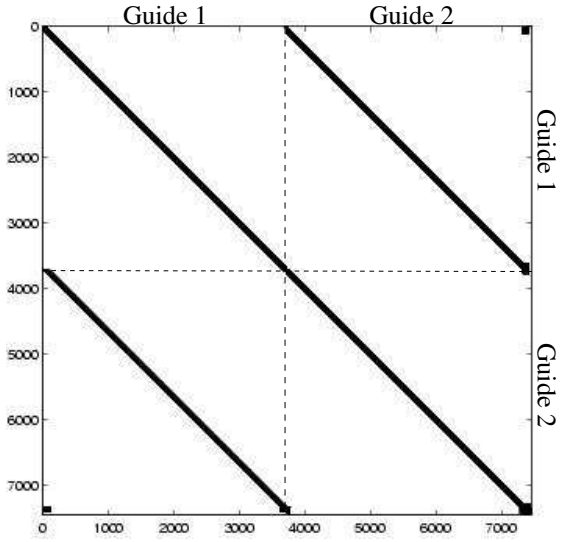

Figure 7.4: Sparsity pattern of $\tilde{\boldsymbol{Z}}$ for the EC Coupler of Fig. 7.3 with $l = 1200a$.

Matrix equations (7.12) and (7.23) differ in two important respects. First, for the vast majority of EC devices, $N_r \ll N_c$. Second, whereas $\boldsymbol{Z}$ is dense, $\tilde{\boldsymbol{Z}}$ is essentially sparse. To see why, recall that $\tilde{G}_n(\boldsymbol{\rho}_j)$ is the EC Green function for a cylindrical Huygens source that radiates in the *defect-less and unbounded EC*. Because ω is assumed to lie within the EC bandgap, $\tilde{G}_n(\boldsymbol{\rho}_j)$ decays exponentially with $|\boldsymbol{\rho}_j|$ – this fact also will be demonstrated via numerical examples in Section 7.4. Therefore, each and every removed cylinder only interacts with its near neighbors, thereby rendering vanishingly small all entries of $\tilde{\boldsymbol{Z}}$ describing interactions between sufficiently separated removed cylinders. Consider, for

example, the EC coupler depicted in Fig. 7.3. Figure 7.4 shows the sparsity pattern of the corresponding interaction matrix $\tilde{\boldsymbol{Z}}$. Recently, significant advances in direct methods for inverting such sparse matrices have been reported, e.g., the multi-frontal method by Duff and Reid [19]. This method organizes the numerical factorization of a sparse matrix into a number of steps, each involving the formation of a dense smaller frontal matrix, followed by its partial factorization. The multi-frontal method in the past already has been used for electromagnetic problems, e.g., in [20], and is adopted here to invert (7.23), thereby avoiding excessive iteration counts often encountered when analyzing EC devices using iterative solvers.

7.3.2 Calculation of the EC Green function $\tilde{G}_n(\boldsymbol{\rho})$ and the entries of $\tilde{\boldsymbol{Z}}$

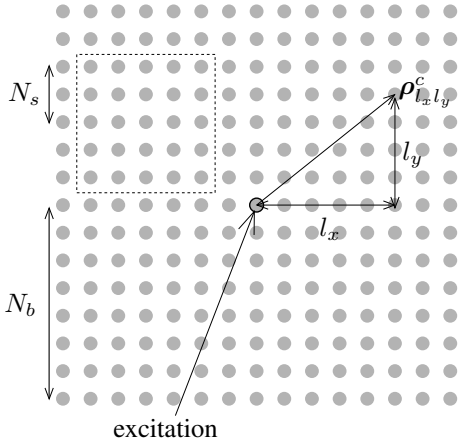

Figure 7.5: Calculation of $\tilde{G}_n(\boldsymbol{\rho})$ using a centrally excited finite EC of $(2N_b + 1)$ by $(2N_b + 1)$ cylinders.

The EC Green function $\tilde{G}_n(\boldsymbol{\rho}_j)$ for a cylindrical Huygens source that radiates in the *defect-less and unbounded EC* cannot be evaluated analytically. Its numerical evaluation is aided by two facts, however. First, because the EC is periodic, $\tilde{G}_n(\boldsymbol{\rho}_j)$ does not depend on the cylinder index j. Second, as already mentioned above, $\tilde{G}_n(\boldsymbol{\rho})$ decays exponentially with $|\boldsymbol{\rho}|$. As a result, $\tilde{G}_n(\boldsymbol{\rho})$ can be evaluated using the conventional MST scheme detailed in Section 7.2 by considering a finite square EC of $N_c = (2N_b + 1)^2$ cylinders wherein the central cylinder, which is assumed centered about the spatial origin $\boldsymbol{\rho} = \boldsymbol{0}$, is excited by a Huygens source with electric and magnetic components $\frac{C_n}{2\pi r} e^{jn\phi}\delta(\rho - r)\boldsymbol{u}_z$ and $\frac{jC_n}{2\pi r}\sqrt{\frac{\epsilon_1}{\mu_1}}\frac{J_n(k_1 r)}{J'_n(k_1 r)} e^{jn\phi}\delta(\rho - r)\boldsymbol{u}_\phi$ (Fig. 7.5). It follows from (7.8), (7.18), and (7.21) that this source, when radiating in the background medium (ϵ_1, μ_1), produces null fields for $\rho > r$ and

$$E^{\mathrm{i}}(\boldsymbol{\rho}) \quad = \quad -\frac{\omega\mu_1}{4}\frac{2jC_n}{\pi k_1 r J'_n(k_1 r)} J_n(k_1\rho)e^{jn\phi}, \tag{7.24}$$

for $\rho < r$. The parameter N_b is chosen to be large enough such that outside this square EC the total field produced by this Huygens source essentially vanishes. Let $I_{mn}(l_x, l_y)$, $l_x, l_y = -N_b, \ldots, N_b$; $m, n = -K, \ldots, +K$, denote the unknown describing the electric current's m^{th} harmonic that flows on the cylinder centered about $\boldsymbol{\rho}^c_{l_x l_y} = l_x \Delta_x \boldsymbol{u}_x + l_y \Delta_y \boldsymbol{u}_y$ in response to excitation by the above-described Huygens source (Fig. 7.5). Likewise, let $E_{mn}(l_x, l_y)$ denote the element of the excitation vector $\boldsymbol{E}$ in the formulation of Section 7.2 obtained by using the m^{th} harmonic testing function $T^i_m(\boldsymbol{\rho})$ on the fields produced by the Huygens source. It follows from (7.24)

$$E_{mn}(l_x, l_y) \quad = \quad \begin{cases} \dfrac{\omega\mu_1}{4} \dfrac{2jC_n}{\pi k_1 r J'_n(k_1 r)} & \text{if } l_x = l_y = 0 \text{ and } m = n, \\ 0 & \text{otherwise.} \end{cases} \tag{7.25}$$

Upon solving (7.12), with right-hand side (7.25) for $I_{mn}(l_x, l_y)$, it is seen that $\tilde{G}_n(\boldsymbol{\rho})$ can be expressed as

$$\tilde{G}_n(\boldsymbol{\rho}) = \begin{cases} \dfrac{\omega\mu_2}{4} \displaystyle\sum_{m=-K}^{K} \frac{2jC_m}{\pi k_2 r J'_m(k_2 r)} I_{mn}(l_x, l_y) J_m(k_2 \rho_{l_x l_y}) e^{jm\phi_{l_x l_y}} & \text{if } \rho_{l_x l_y} < r, \\ \displaystyle\sum_{l_x=-N_b}^{N_b} \sum_{l_y=-N_b}^{N_b} \sum_{m=-K}^{K} G_m(\boldsymbol{\rho}_{l_x l_y}) I_{mn}(l_x, l_y) & \text{if } \rho_{l_x l_y} > r \text{ for all } l_x, l_y, \end{cases} \tag{7.26}$$

with $\boldsymbol{\rho}_{l_x l_y}$ the position vector in the local cylindrical coordinate system centered about $\boldsymbol{\rho}^c_{l_x l_y}$. For future reference, let $\tilde{Z}_{mn}(l_x, l_y)$ denote the matrix element describing interactions between modes (m, n) on cylinders centered $l_x \Delta_x$ and $l_y \Delta_y$ apart along the x and y directions, respectively. It follows from (7.26) that $\tilde{Z}_{mn}(l_x, l_y)$ is

$$\tilde{Z}_{mn}(l_x, l_y) \quad = \quad \frac{\omega\mu_2}{4} \frac{2jC_m}{\pi k_2 r J'_m(k_2 r)} I_{mn}(l_x, l_y). \tag{7.27}$$

Note that all non-vanishing elements of the matrix $\tilde{\boldsymbol{Z}}$ in Eq. (7.23) are described by Eq. (7.27).

Matrix equation (7.12) for the centrally excited square EC with right hand side (7.25) can be solved efficiently by using an iterative, preconditioned, FFT-accelerated method. It was shown in [15] that the use of a left 'shielded-block preconditioner' effectively reduces the number of iterations to characterize finite and defect-less ECs, this contrary to EC devices with waveguiding structures. Instead of solving system $\boldsymbol{ZI} = \boldsymbol{E}$ to construct $\tilde{G}_n(\boldsymbol{\rho})$, system $\boldsymbol{M}_{\text{sb}}\boldsymbol{ZI} = \boldsymbol{M}_{\text{sb}}\boldsymbol{E}$ is solved. The preconditioner $\boldsymbol{M}_{\text{sb}}$ is formed by selecting, out of $\boldsymbol{Z}$, for each and every cylinder, a small $2N_s + 1$ by $2N_s + 1$ interaction matrix ($N_s < N_b$) of nearest interactions (Fig. 7.5). This reduced interaction matrix is inverted and the rows corresponding to the targeted cylinder extracted and inserted into $\boldsymbol{M}_{\text{sb}}$.

7.3.3 Computation of the EC impressed field $\tilde{E}^{\mathrm{i}}(\boldsymbol{\rho})$ and the entries of $\tilde{\boldsymbol{E}}$ - Modal excitation/absorbing boundary conditions of the semi-infinite EC

The z-component of the electric field generated by impressed sources that radiate *in the presence of the defect-less EC*, $\tilde{E}^{\mathrm{i}}(\boldsymbol{\rho})$, cannot be evaluated analytically. If the impressed source is a z directed electric line current at $\boldsymbol{\rho}_s$ (assumed to reside outside all the physical and removed cylinders) then $\tilde{E}^{\mathrm{i}}(\boldsymbol{\rho})$ can, just like $\tilde{G}_n(\boldsymbol{\rho})$, be computed using the free-space Green function MST of Section 7.2. Indeed, in this case, $\tilde{E}^{\mathrm{i}}(\boldsymbol{\rho})$ comprises $E^{\mathrm{i}}(\boldsymbol{\rho}) = -\frac{\omega\mu_1}{4}H_0^{(2)}(k_1|\boldsymbol{\rho}-\boldsymbol{\rho}_s|)$ plus the field scattered by the cylinders. The latter can be calculated using (7.10), following the computation of the currents on cylinders near the source. To this end, consider a finite EC comprising $N_c = (2N_b+1)^2$ cylinders centered about the origin, which is also assumed near $\boldsymbol{\rho}_s$. Let $I_{ms}(l_x, l_y)$ denote the electric current's m^{th} harmonic that flows on the cylinder centered about $\boldsymbol{\rho}^c_{l_x l_y}$ in this finite EC when excited with the field of the electric line current. These coefficients $I_{ms}(l_x, l_y)$ are obtained by solving (7.12) with the entries of the excitation vector $\boldsymbol{E}$ given by (7.14), which leads to

$$\tilde{E}^{\mathrm{i}}(\rho) = \begin{cases} \dfrac{\omega\mu_2}{4}\displaystyle\sum_{m=-K}^{K}\frac{2jC_m}{\pi k_2 r J'_m(k_2 r)} I_{ms}(l_x,l_y)J_m(k_2\rho_{l_x l_y})e^{jm\phi_{l_x l_y}} & \text{if } \rho_{l_x l_y} < r, \\ E^{\mathrm{i}}(\boldsymbol{\rho}) + \displaystyle\sum_{l_x=-N_b}^{N_b}\sum_{l_y=-N_b}^{N_b}\sum_{m=-K}^{K} G_m(\boldsymbol{\rho}_{l_x l_y})I_{ms}(l_x,l_y) & \\ \qquad\qquad \text{if } \rho_{l_x l_y} > r \text{ for all } l_x, l_y. \end{cases} \tag{7.28}$$

Hence, the entries of the excitation vector $\tilde{\boldsymbol{E}}$ are

$$\tilde{E}_{ms}(l_x,l_y) \quad = \quad \frac{\omega\mu_2}{4}\frac{2jC_m}{\pi k_2 r J'_m(k_2 r)} I_{ms}(l_x,l_y). \tag{7.29}$$

The above EC Green function MST with line source excitation can be used to characterize the effects of semi-infinite waveguides attached to finite EC devices by terminating sufficiently long waveguide appendages by resistive sections. The scheme, when used in conjunction with computational de-embedding techniques, then permits EC S-parameter extraction.

The EC Green function scheme however allows for an intriguing alternative to find the EC's S-parameters, as it allows for an easy identification of the propagating EC defect/waveguide modes and their subsequent use as modal excitations and boundary conditions when constructing system (7.23). To see how the EC Green function method can be used to find an EC waveguide's eigenmodes, let $\tilde{E}_\nu(\boldsymbol{\rho})\boldsymbol{u}_z$ denote the z directed electric field of the ν-th forward propagating eigenmode in an infinitely long, x directed EC waveguide. To simplify the ensuing discussion, assume that this waveguide is formed by removing a single x directed row of cylinders from an unbounded, defect-less EC (Fig. 7.6). According to the Floquet-Bloch theorem, $\tilde{E}_\nu(\boldsymbol{\rho})$ satisfies

$$\tilde{E}_\nu(\boldsymbol{\rho}) \quad = \quad \tilde{e}_\nu(\boldsymbol{\rho})e^{-j\beta_\nu x}, \tag{7.30}$$

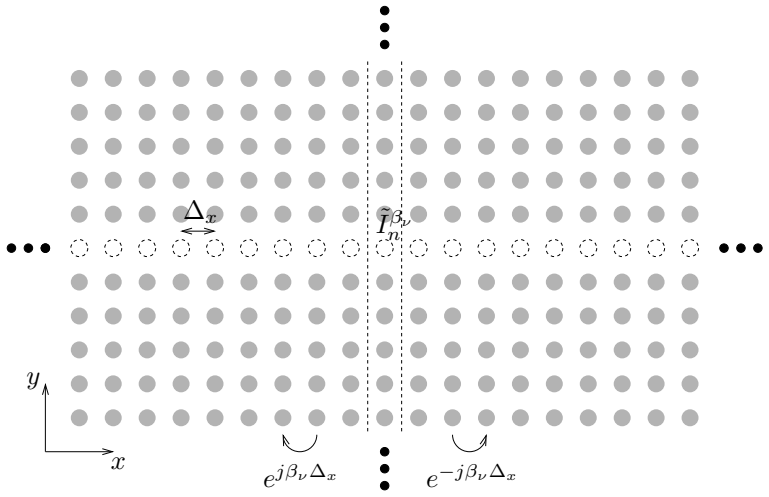

Figure 7.6: Calculation of an EC waveguide's eigenmodes.

where $\tilde{e}_\nu(\boldsymbol{\rho} + \Delta_x \boldsymbol{u}_x) = \tilde{e}_\nu(\boldsymbol{\rho})$ and β_ν is the mode's (assumed real) propagation constant. Of course, $\tilde{E}_\nu(\boldsymbol{\rho})$ can be characterized in terms of equivalent electric and magnetic currents on the surfaces of the removed cylinders. Moreover, the evolution of these currents' amplitudes along the waveguide channel is dictated by that of the fields they were derived from - viz. (7.30), and, hence, equivalent currents in only one unit cell suffice to fully characterize the modal field distribution. Mirroring the derivations in Section 7.3.1, it follows that the electric current expansion coefficients $\tilde{I}_n^{\beta_\nu}$, $n = -K, \ldots, K$, on the removed cylinder in the unit cell satisfy

$$\sum_{n=-K}^{K} \left[\sum_{l_x=-N_b}^{N_b} \tilde{Z}_{mn}(l_x, 0) e^{-j\beta_\nu l_x \Delta_x} \right] \tilde{I}_n^{\beta_\nu} \quad = \quad 0, \text{ for } m = -K, \ldots, K. \quad (7.31)$$

Note that in (7.31) only currents of $2N_b + 1$ cells symmetrically placed to the left and right of the cell in which currents $\tilde{I}_n^{\beta_\nu}$ are measured, are accounted for - this once again is possible only because ω lies in the EC bandgap. Setting the β_ν-dependent determinant of the matrix derived from system (7.31) to zero allows the waveguide's propagation constants to be determined. Once the propagation constants of the various modes are found, their transverse profiles are described by the null-space of (7.31) with fixed β_ν.

Once the waveguide modes have been characterized, they can be used, within the framework of the EC Green function MST, to terminate/excite the EC device in/from semi-infinite waveguides. To illustrate this procedure, consider an EC device connected to a set of N_p identical semi-infinite waveguides (Fig. 7.7) – to simplify the presentation, the assumption that these waveguides are formed by removing one row of cylinders from the EC remains in effect. To implement an exact absorbing boundary condition assume that these waveguides support only one propagating mode with propagation constant β. Far enough away from all discontinuities, the fields propagating away from the EC device in each of these waveguides are adequately described by a single outward propagating mode.

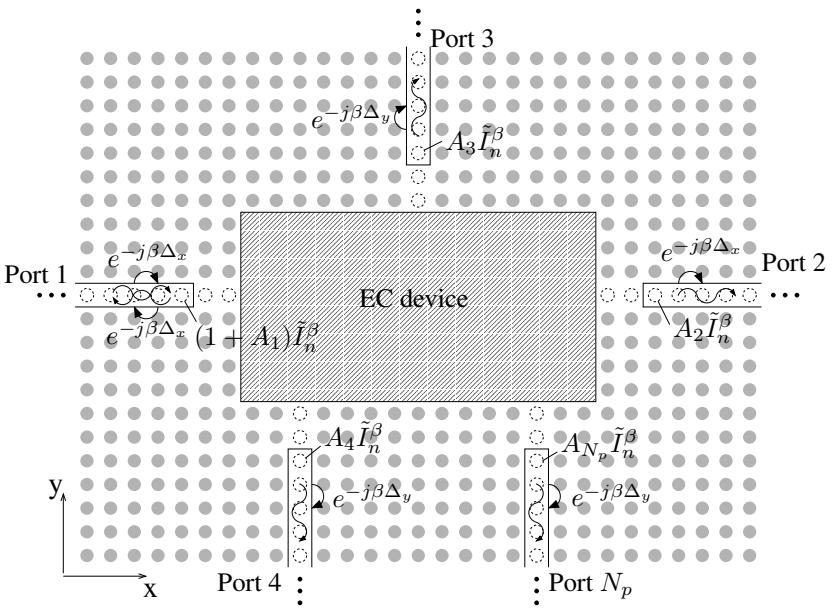

Figure 7.7: Modal absorbing boundary conditions and excitation.

Let the currents on the first cylinder in the waveguide where this behavior is believed to hold true be denoted by $A_j\tilde{I}_n^\beta$; A_j is referred to as the waveguide j outgoing mode's amplitude. This cylinder, along with all that follow, are referred to as the "cylinders of port j"– in what follows, they are to be distinguished from the N_r "regularly removed cylinders"that define the EC device. The current expansion coefficients for the cylinders of port j are related to one another by the Floquet-Bloch theorem (7.30), as indicated in Fig. 7.7. The unknowns now comprise $(2K+1)N_r$ electric current unknowns $\tilde{I}_n^j$, $j=1,...,N_r$; $j=-K,\ldots,K$, and N_p amplitudes A_j, $j=1,\ldots,N_p$, of the outgoing modes. To account for the outgoing modal fields, eq. (7.17) now is changed to

$$\tilde{E}^{\mathrm{i}}(\boldsymbol{\rho})+\sum_{j=1}^{N_r}\tilde{E}_1^{\mathrm{s},j}(\boldsymbol{\rho})+\sum_{j=1}^{N_p}\tilde{E}_1^{\mathrm{s},p_j}(\boldsymbol{\rho})=0,\ \text{ for } \boldsymbol{\rho}\in\tilde{S}_i^-,\ i=1,\ldots,N_r+N_p. \quad (7.32)$$

Here, $\tilde{E}_1^{\mathrm{s},p_j}(\boldsymbol{\rho})$ represents the sum of the fields produced by all the currents on the cylinders of port j. A first set of $(2K+1)N_r$ equations is obtained by testing (7.32) on the surfaces of all N_r regularly removed cylinders with $\tilde{T}_m^i(\boldsymbol{\rho})$, $i=1,...,N_r$; $m=-K,\ldots,K$. The matrix elements describing interactions between regularly removed cylinders resulting from this procedure are still described by (7.27). Assuming that port j consists of a $+x$ directed waveguide, weighting $\tilde{E}_1^{\mathrm{s},p_j}(\boldsymbol{\rho})$ on a cylinder whose center is located $-l_x\Delta_x$ ($l_x>0$) and $l_y\Delta_y$ away from the center of the first cylinder of port j along the x- and the

y direction respectively, yields a contribution

$$\tilde{Z}_{mp_j}(-l_x, l_y)A_j = A_j \sum_{l_s=0}^{N_b} \sum_{n=-K}^{K} \tilde{Z}_{mn}(-l_x + l_s, l_y)\tilde{I}_n^{\beta} e^{-j\beta l_s \Delta_x} \quad m = -K, \ldots, K, \tag{7.33}$$

where $\tilde{Z}_{mp_j}(l_x, l_y)$ denotes the effective matrix element describing the interaction of port p_j with a regularly removed cylinder. A second set of N_p equations are found by weighting (7.32) on the surface of the first cylinder of every port with $\tilde{T}_0^i(\boldsymbol{\rho})$. Weighting the second term of (7.32) leads to the matrix elements $\tilde{Z}_{0n}(l_x, l_y)$, while weighting the third term of (7.32) again leads to the effective matrix elements $\tilde{Z}_{0p_j}(l_x, l_y)$ defined in (7.33). Similar arguments and expressions can be proffered for ports associated with waveguides leaving the EC device in other directions.

To illustrate how to impose modal excitations within the EC Green function MST framework, assume that the EC device is excited by a propagating mode coming from the semi-infinite waveguide 1. The incident field $\tilde{E}^{\text{i}}(\boldsymbol{\rho})$ is the sum of the fields produced by all the currents on the cylinders of port 1, with the current expansion coefficients on the first cylinder equal to $\tilde{I}_n^{\beta}$ and those for consecutive cylinders related by the Floquet-Bloch theorem. For example, assume that port 1 is -x directed, which means that a mode that is incoming into the EC device propagates in the +x direction. Following the same reasoning as for the absorbing boundary condition, it can be readily seen that weighting the incident field on the surface of a cylinder whose center is $l_x\Delta_x$ and $l_y\Delta_y$ apart from that of the first cylinder of port 1 in the x- and the y direction, gives the following entries for the excitation vector $\tilde{\boldsymbol{E}}$

$$\tilde{E}_m(l_x, l_y) = \sum_{l_s=0}^{N_b} \sum_{n=-K}^{K} \tilde{Z}_{mn}(l_x - l_s, l_y)\tilde{I}_n^{\beta} e^{-j\beta l_s \Delta_x} \quad m = -K, \ldots, K. \tag{7.34}$$

Note that when all the semi-infinite waveguides are identical, the amplitudes of the outgoing modes correspond immediately with the S-parameters of the EC device: $S_{1j} = A_j$. The reasoning followed in this section can be generalized to waveguides with more than one cylinder across and/or to different types of semi-infinite waveguide appendages.

7.3.4 Special defects in the EC

The scheme detailed in Subsections 7.3.1–7.3.3 only permits the characterization of EC devices that are obtained by removing cylinders from defect-less ECs. However, many practical EC devices also contain defects other than removed cylinders. For example, filters sometimes contain special cylinders whose radius and/or constitutive parameters differ from those of the background EC elements to create resonant cavities. And EC devices with bended waveguides often contain special cylinders that are displaced from the background EC lattice to minimize reflections. In this section, it will be shown that ECs with (a few) special defects can be treated by a simple extension of the scheme of Subsections 7.3.1–7.3.3.

Generally speaking, the scheme of Subsection 7.3.1 wholesale applies to ECs with special defects, provided that their presence is reflected in the Green function. That is,

when sources and/or observers reside near a special defect, a Green function different from that computed in Subsection 7.3.2 must be used (Fig. 7.8). Recall that the scheme described in Subsection 7.3.2 for computing the EC Green function involved the construction (and conceptual inversion) of a conventional MST interaction matrix $\boldsymbol{Z}$ for a finite, square, and defect-less EC. Of course, the computation of the Green function for an EC with special defects can be effected by very similar techniques, provided that the finite EC considered now contains the special defect. Fortunately, the conventional MST interaction matrix for a finite EC with special defect, further denoted as $\hat{\boldsymbol{Z}}$, is a low-rank update of the interaction matrix for the defect-less finite ED:/Users/Davy

$$\hat{\boldsymbol{Z}} \quad = \quad \boldsymbol{Z} + \boldsymbol{U}\boldsymbol{V}^T. \tag{7.35}$$

According to the Sherman-Morrison–formula [21], $\hat{\boldsymbol{Y}} = \hat{\boldsymbol{Z}}^{-\mathbf{1}}$ also is a low-rank update of $\boldsymbol{Y} = \boldsymbol{Z}^{-\mathbf{1}}$:

$$\hat{\boldsymbol{Y}} \quad = \quad \boldsymbol{Y} - \boldsymbol{Y}\boldsymbol{U}(\mathbf{1} + \boldsymbol{V}^T\boldsymbol{Y}\boldsymbol{U})^{-1}\boldsymbol{V}^T\boldsymbol{Y} \tag{7.36}$$

In (7.36), $\mathbf{1}$ stands for the identity matrix. Therefore, $\hat{\boldsymbol{Y}}$ can be calculated very fast without resorting to solving a new linear system. Below, the vectors $\boldsymbol{U}$ and $\boldsymbol{V}$ are described for two important cases: special defects involving (i) a cylinder with modified constitutive parameters and/or radius and (ii) a cylinder displaced from its background lattice position. To simplify notation, only cases involving one special defect and ECs in which currents on cylinders are modeled by one unknown ($K = 0$), are considered; extensions to more complicated scenarios are straightforward.

(i) A cylinder with modified constitutive parameters and/or radius situated on a regular lattice node (Fig. 7.8(a)).

In this case, it follows from (7.13), that the matrices $\hat{\boldsymbol{Z}}$ and $\boldsymbol{Z}$ only differ by one element, namely the self-interaction of the special cylinder. Suppose the index of this cylinder is 1 and that this cylinder corresponds with the central cylinder in the finite EC that is used to calculate the Green function. With $\Delta = \hat{Z}_{00}^{11} - Z_{00}^{11}$, $\boldsymbol{U}$ and $\boldsymbol{V}$ read:

$$\boldsymbol{U} = \begin{pmatrix} 1 \\ 0 \\ \vdots \\ 0 \end{pmatrix}, \; \boldsymbol{V} = \begin{pmatrix} \Delta \\ 0 \\ \vdots \\ 0 \end{pmatrix}. \tag{7.37}$$

Because the Green function is calculated using an iterative method, $\boldsymbol{Y}$ is not explicitly known. In Section 7.3.2, it was shown that the excitation vector $\boldsymbol{E}$ completely consists of zeros except for the element corresponding with the central cylinder (cylinder 1). This means that $\boldsymbol{I}$ is proportional to the first column of $\boldsymbol{Y}$. If i is the index of the cylinder centered about $l_x^i\Delta_x\boldsymbol{u}_x + l_y^i\Delta_y\boldsymbol{u}_y$, then

$$Y_{00}^{i1} \quad = \quad D_0 I_{00}(l_x^i, l_y^i), \tag{7.38}$$

with

$$D_0 \quad = \quad \frac{4}{\omega\mu_1}\frac{\pi k_1 r J_0'(k_1 r)}{2jC_0}. \tag{7.39}$$

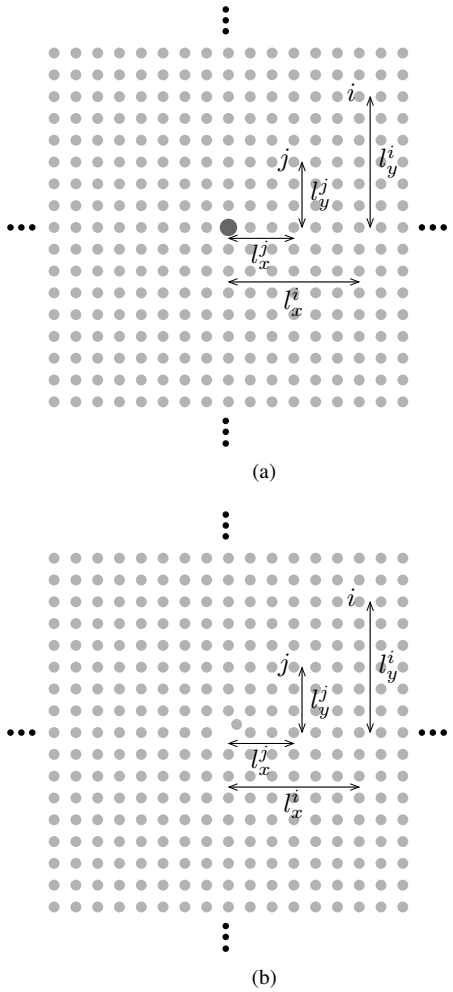

Figure 7.8: Special Green functions.

Although the iterative solution of (7.13) only gives the first column of $\boldsymbol{Y}$, all the elements of this matrix are known if it is kept in mind that in fact the Green function for an infinite EC is calculated. Indeed, Y_{00}^{ij} is proportional to the current on cylinder i, when the excitation is on cylinder j. For an infinite EC, the solution corresponding to the excitation on cylinder j can be derived from that of exciting cylinder 1 by a shift operation, and hence

$$Y_{00}^{ij} = D_0 I_{00}(l_x^i - l_x^j, l_y^i - l_y^j). \tag{7.40}$$

Suppose that $\tilde{Z}_{00}^{ij}$, the element in the sparse interaction matrix of the new method that describes the interaction between cylinder i and cylinder j that reside ($l_x^i\Delta_x$, $l_y^i\Delta_y$) and ($l_x^j\Delta_x$, $l_y^j\Delta_y$) apart along the x and y direction from the special cylinder, has to be calculated (Fig. 7.8). Note that $\boldsymbol{YU}$ corresponds with the first column of $\boldsymbol{Y}$ and that $\boldsymbol{V}^T\boldsymbol{Y}$ corresponds with Δ times the first row of $\boldsymbol{Y}$. According to (7.36),

$$\hat{Y}_{00}^{ij} = Y_{00}^{ij} - Y_{00}^{i1}(1 + \Delta Y_{00}^{11})^{-1}\Delta Y_{00}^{1j}. \tag{7.41}$$

Combination of (7.27), (7.40), and (7.41) yields

$$\begin{aligned}\tilde{Z}_{00}^{ij} = \frac{\omega\mu_2}{4}\frac{2jC_0}{\pi k_2 r J_0'(k_2 r)}\Big[&I_{00}(l_x^i - l_x^j, l_y^i - l_y^j) \\ &+ I_{00}(l_x^i, l_y^i)\frac{\Delta D_0}{1 + \Delta D_0 I_{00}(0,0)} I_{00}(-l_x^j, -l_y^j)\Big].\end{aligned} \tag{7.42}$$

(ii) A cylinder displaced from its background lattice position (with the same constitutive parameters and radius as those of the background EC lattice) (Fig. 7.8(b)).

Now, $\hat{\boldsymbol{Z}}$ and $\boldsymbol{Z}$ differ by the whole first column and row, except for the diagonal element. So, $\boldsymbol{U}$ and $\boldsymbol{V}$ can be expressed as

$$\boldsymbol{U} = \begin{pmatrix} 1 & 0 \\ 0 & \Delta_{21} \\ \vdots & \vdots \\ 0 & \Delta_{N_c 1} \end{pmatrix} = \begin{pmatrix} \boldsymbol{U}_1 & \boldsymbol{U}_2 \end{pmatrix}, \tag{7.43}$$

$$\boldsymbol{V} = \begin{pmatrix} 0 & 1 \\ \Delta_{12} & 0 \\ \vdots & \vdots \\ \Delta_{1N_c} & 0 \end{pmatrix} = \begin{pmatrix} \boldsymbol{V}_1 & \boldsymbol{V}_2 \end{pmatrix}. \tag{7.44}$$

with $\Delta_{ij} = \hat{Z}_{00}^{ij} - Z_{00}^{ij}$. The calculation of $\boldsymbol{YU}_1$ and $\boldsymbol{V}_2^T\boldsymbol{Y}$ has already been treated above. Let U_{2i} denote the i-th element of the vector $\boldsymbol{U}_2$. To calculate $\boldsymbol{YU}_2$, note

that

$$\boldsymbol{Y}\begin{pmatrix} U_{21} \\ U_{22} \\ \vdots \\ \vdots \\ U_{2N_c} \end{pmatrix} = U_{21}\boldsymbol{Y}\begin{pmatrix} 1 \\ 0 \\ \vdots \\ \vdots \\ 0 \end{pmatrix} + U_{22}\boldsymbol{Y}\begin{pmatrix} 0 \\ 1 \\ 0 \\ \vdots \\ 0 \end{pmatrix} + \ldots + U_{2N_c}\boldsymbol{Y}\begin{pmatrix} 0 \\ \vdots \\ \vdots \\ 0 \\ 1 \end{pmatrix}. \tag{7.45}$$

With $U_2(l_x^i, l_y^i) = U_{2i}$ and following the above reasoning, it is seen that the i-th element of $\boldsymbol{Y}\boldsymbol{U}_2$ is nothing but

$$(\boldsymbol{Y}\boldsymbol{U}_2)_i \quad = \quad D_0 \sum_{j=1}^{N_c} U_2(l_x^j, l_y^j) I_{00}(l_x^i - l_x^j, l_y^i - l_y^j). \tag{7.46}$$

Similarly,

$$(\boldsymbol{V}_1^T\boldsymbol{Y})_i \quad = \quad D_0 \sum_{j=1}^{N_c} V_1(l_x^j, l_y^j) I_{00}(l_x^j - l_x^i, l_y^j - l_y^i), \tag{7.47}$$

with $V_1(l_x^i, l_y^i) = V_{1i}$. Equations (7.46) and (7.47) show that $\boldsymbol{Y}\boldsymbol{U}_2$ and $\boldsymbol{V}_1^T\boldsymbol{Y}$ are discrete two-dimensional convolutions and, hence, can be calculated quickly using a 2D FFT. However, if one wants to know $\boldsymbol{Y}\boldsymbol{U}_2$ and $\boldsymbol{V}_1^T\boldsymbol{Y}$ inside a square EC of $2N_b + 1$ by $2N_b + 1$ cylinders, $\boldsymbol{U}_2$ and $\boldsymbol{V}_1$ have to be calculated for a square of $4N_b+1$ by $4N_b+1$ cylinders, so, $N_c = (4N_b+1)^2$; $l_x^i, l_x^j, l_y^i, l_y^j = -2N_b, \ldots, 2N_b$ in (7.46) and (7.47). By definition, $I_{00}(l_x, l_y) = 0$ if $|l_x| > N_b$ or $|l_y| > N_b$. This proves that although only I is known, the updates to obtain all the necessary elements of $\tilde{\boldsymbol{Z}}$ can be computed quickly without ever having to solve a new linear system.

7.4 Examples

All examples presented below involve ECs composed of dielectric cylinders with constitutive parameters $(\epsilon_2, \mu_2) = (11.56\epsilon_0, \mu_0)$ and radius $r = 0.18a$ that are arranged on a Cartesian lattice with $\Delta_x = \Delta_y = a$ – a is termed the lattice constant. The cylinders reside in free space, viz. (ϵ_1, μ_1)=(ϵ_0, μ_0). This EC has a TM_z bandgap that extends from $k_1 = 0.604\frac{\pi}{a}$ to $k_1 = 0.886\frac{\pi}{a}$. All calculations are carried out in Matlab on a 2GHz PC; the multi-frontal package used to solve system (7.23) is UMFPACK Version 4.3 [22].

7.4.1 Green function

As outlined in Section 7.3.2, the EC Green function is calculated by considering a centrally excited finite EC comprising $(2N_b+1)$ by $(2N_b+1)$ cylinders with N_b large enough to render the Green function vanishingly small beyond the finite EC boundaries. Figure 7.9 demonstrates the exponential decay of the EC Green function $|\tilde{G}_0(\boldsymbol{\rho} = x\boldsymbol{u}_x)|$

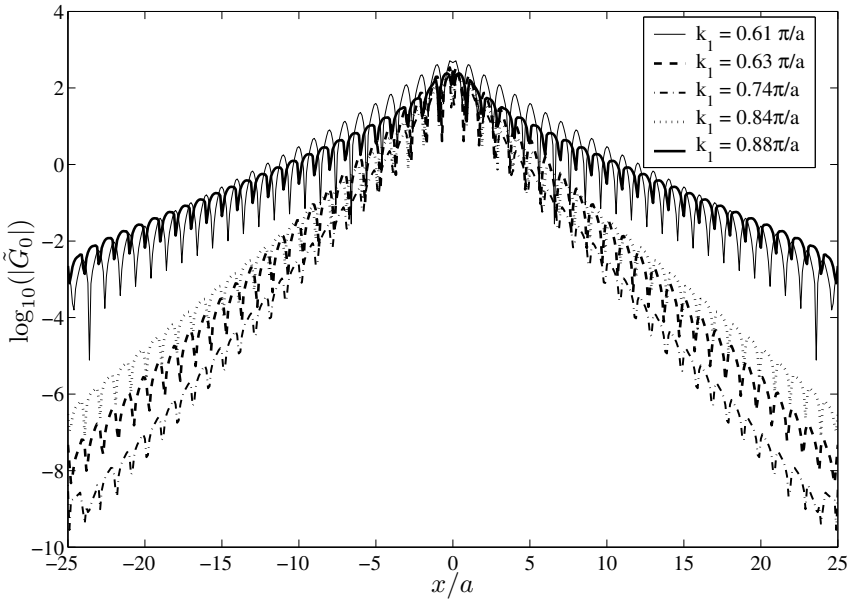

Figure 7.9: EC Green function.

with x and this for different frequencies inside the bandgap. The decay rate is larger for frequencies near the bandgap center than for frequencies near its edge. For example, for $k_1 = 0.74\frac{\pi}{a}$, $|\tilde{G}_0(\boldsymbol{\rho} = x\boldsymbol{u}_x)|$ decreases by eleven orders of magnitude from the spatial origin to $x = 25a$. In contrast, for $k_1 = 0.61\frac{\pi}{a}$ and $k_1 = 0.88\frac{\pi}{a}$, the EC Green function decays only by five orders of magnitude from the spatial origin to $x = 25a$. It suffices to focus on $|\tilde{G}_0(\boldsymbol{\rho} = x\boldsymbol{u}_x)|$ to determine the Green function decay rate as for $n \neq 0$ the decay is even faster. All examples reported below involve frequencies near the bandgap center.

For $K = 1$, using $N_b = 15$ with an $N_s = 3$ shielded-block preconditioner to accelerate convergence of the Matlab build-in BICGSTAB solver, the computation of the EC Green function takes just over 4 s.

7.4.2 Eigenmodes

As described in Section 7.3.3, the EC Green function can be used to characterize the propagating modes of an EC waveguide. Figure 7.10 shows the cross-sectional profile of the sole propagating mode in a waveguide that results upon removing one row of cylinders from the EC, obtained by using the proposed scheme with increasing values of K; convergence is reached for $K = 1$. This waveguide and K value are used for all other examples considered below. Figure 7.11 shows the propagation coefficient β as a function of frequency for the propagating mode of this waveguide.

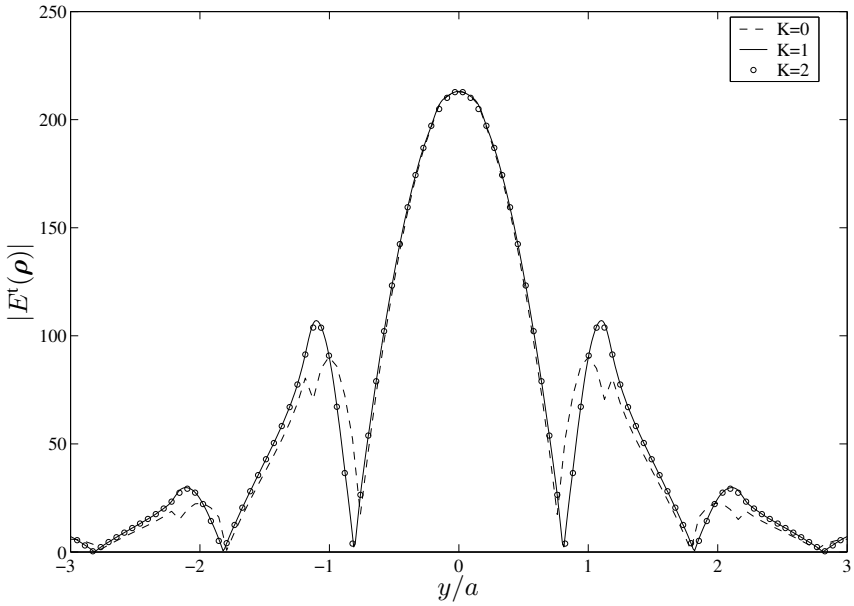

Figure 7.10: Mode profile for increasing value of K.

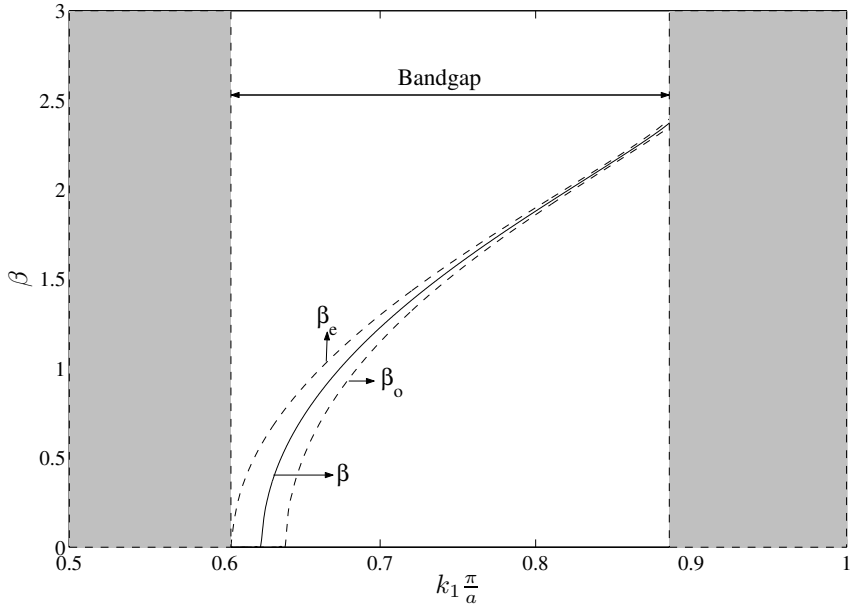

Figure 7.11: Dispersion curves, full line: single waveguide, dashed lines: two coupled waveguides.

7.4.3 EC waveguide couplers

The performance and accuracy of the proposed scheme are demonstrated via its application to the analysis of two EC waveguide couplers.

First, consider the ultra-compact wavelength multiplexer-demultiplexer depicted in Fig. 7.3 [4, 5]. The device comprises two identical and coupled EC waveguides that are separated by two rows of cylinders and that jointly support even and odd propagating modes. Figure 7.11 shows the dispersion curves of these even and odd modes' propagation constants β_e and β_o. A field injected into one waveguide will couple entirely into the other if the length of the coupling region l is an odd multiple of $L = \frac{2\pi}{|\beta_e - \beta_o|}$. The field however will exit from the output port attached to the input waveguide if l is an integer multiple of L. By using coupled-mode theory, the normalized output powers at ports 1, 2, and 3 defined in Fig. 7.3 are predicted to be

$$P_1 = 0, \tag{7.48}$$
$$P_2 = \sin^2(\kappa l), \tag{7.49}$$
$$P_3 = \cos^2(\kappa l), \tag{7.50}$$

with $\kappa = \frac{\pi}{L} = \frac{|\beta_e - \beta_o|}{2}$. The transmission spectrum calculated with coupled mode theory for a coupling length $l = 1200a$ is shown in Fig. 7.12, assuming that $a = 540nm$. Unfortunately, coupled mode theory cannot account for reflections from the 90^o waveguide bends. Figure 7.13 shows the same transmission spectra, but now calculated using the proposed scheme, which *does* account for these reflections. Note, for example, that the output power for port 1 is predicted to differ from zero. This example calls for 7465 unknown equivalent electric currents. For one frequency, it takes 12.5 s to fill the sparse interaction matrix (by selecting pertinent elements out of the pre-computed Green function matrix) and 3.8 s to solve system of equations (7.23). The total time to analyze the device, inclusive the Green function calculation, therefore is just over 20 s. Next, assume that the same device were analyzed using the classical scheme described in Section 7.2. Even if all EC waveguides were lined by only 5 rows of cylinders to prevent leakage, such analysis would call for 47262 unknowns. Not surprisingly, the CPU times required to solve system of equations (7.12) are several orders of magnitude larger than those for the new scheme, even if a fast matrix-vector multiplication method is used.

Second, consider the four-channel multiplexer-demultiplexer depicted in Fig. 7.14. The various waveguide coupling lengths are $l_1 = 41a$, $l_2 = 22a$, and $l_3 = 24a$. Using coupled mode theory, the normalized output powers at ports 1, 2, 3, and 4 defined in Fig. 7.14 are expressed as

$$P_1 = \sin^2(\kappa_2 l_1)\sin^2(\kappa_1 l_3), \tag{7.51}$$
$$P_2 = \sin^2(\kappa_2 l_1)\cos^2(\kappa_1 l_3), \tag{7.52}$$
$$P_3 = \cos^2(\kappa_2 l_1)\sin^2(\kappa_2 l_2), \tag{7.53}$$
$$P_4 = \cos^2(\kappa_2 l_1)\cos^2(\kappa_2 l_2), \tag{7.54}$$

with $\kappa_i = \frac{|\beta_{ei} - \beta_{oi}|}{2}$ and the subscript $i = 1$ or 2 depending in whether one or two rows of cylinders separate the EC guides. Figures 7.15 and 7.16 show the transmission spectra predicted by coupled mode theory and the proposed scheme, respectively. The

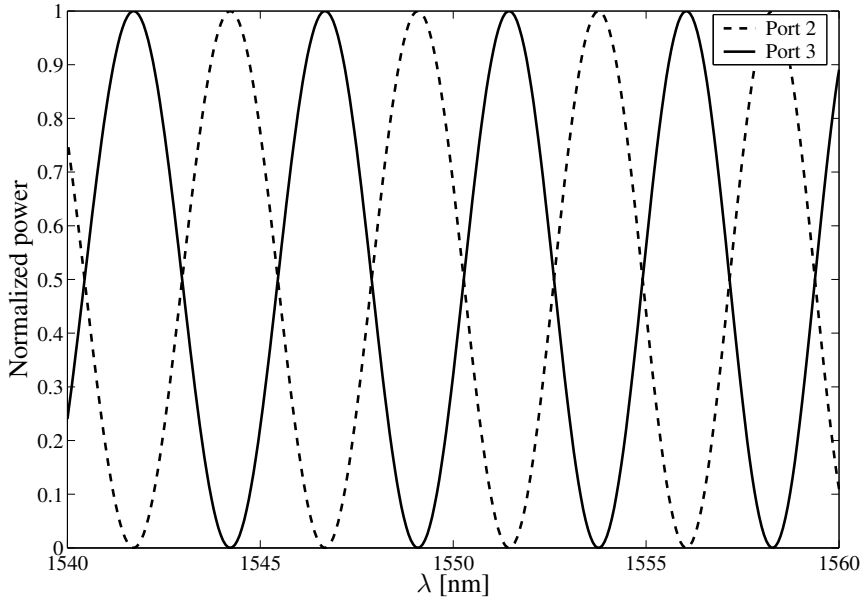

Figure 7.12: Transmission spectrum of an EC-coupler with $l = 1200a$ calculated with the coupled mode theory.

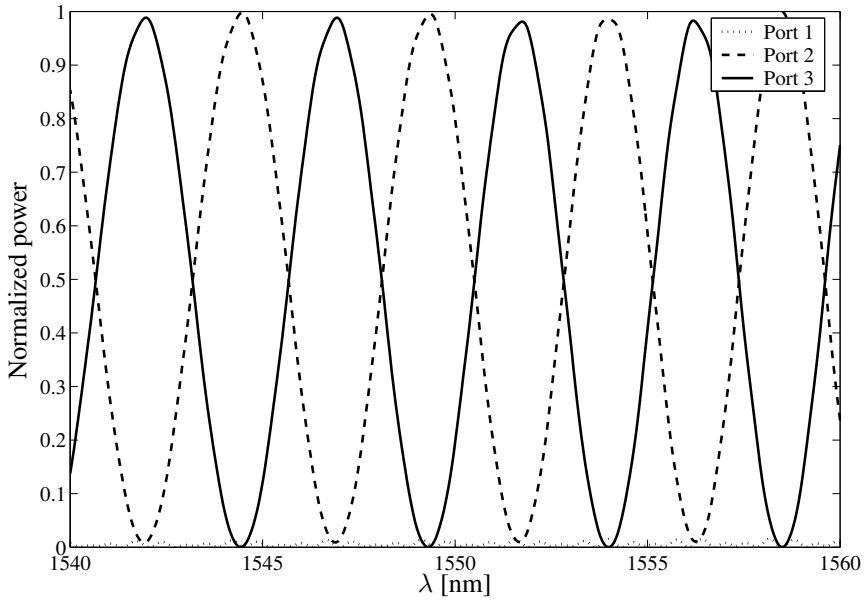

Figure 7.13: Transmission spectrum of an EC-coupler with $l = 1200a$ calculated with the new scheme.

proposed scheme uses 1066 unknowns to describe fields on removed cylinders. It takes only 2 s to fill in the interaction matrix (by selecting pertinent elements out of the pre-computed Green function matrix) and 0.6 s to solve system of equations (7.23). The total time to analyze the device, inclusive the Green function calculation, therefore is just over 6.6 s. If the EC waveguides are lined by 5 rows of cylinders on both sides, this device requires 4638 unknowns when modeled using the classical scheme of Section 7.2. Using a shielded-block preconditioner, the solution of system of equations (7.12) with BICGSTAB to a tolerance of 10^{-4} requires 345 iterations and takes 480 s.

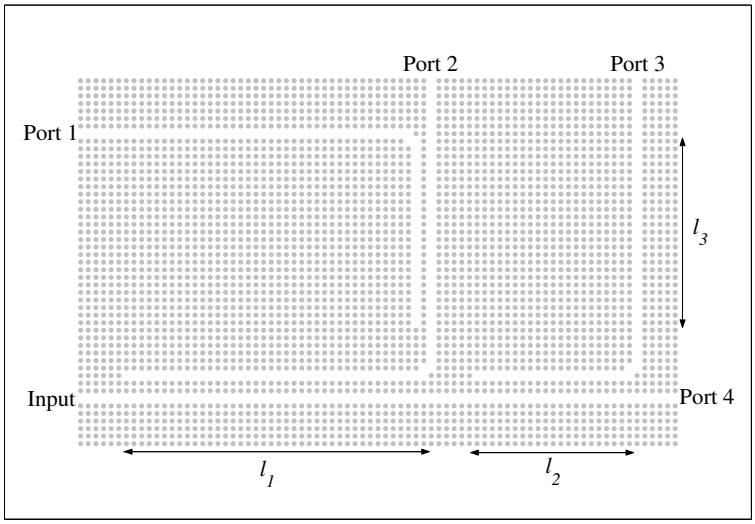

Figure 7.14: Four-channel MUX-DEMUX.

7.4.4 Other defects

To demonstrate the usefulness of the theory of Section 7.3.4, consider the EC waveguide filter depicted in Fig. 7.17 [18]. The filter comprises a waveguide that is loaded by two or three cylinders and transmits only signals in a narrow band of frequencies in which the load cylinders jointly resonate. Two configurations were simulated. In the first one, the obstruction consists of two (outer) cylinders separated by a cavity; in the second one, an extra (central) cylinder fills the cavity. The constitutive parameters of the outer and extra cylinders, and the radii of the outer cylinders, equal those of the EC cylinders. The radius of the extra cylinder is four times smaller than those of the EC cylinders ($r_{\text{extra}} = 0.045a$). Figure 7.18 shows the transmission spectra of both configurations calculated with the conventional, free space Green function and the novel, EC Green function MSTs; the conventional analysis uses perfectly matched layers to truncate the EC waveguide and mimic semi-infinite waveguide loads [23]. Excellent agreement between both data sets is observed. The new scheme calls for roughly 300 unknowns to describe the fields in the channels and uses 0.25 s and 0.3 s to fill in the interaction matrix and solve system of equations (7.23), respectively.

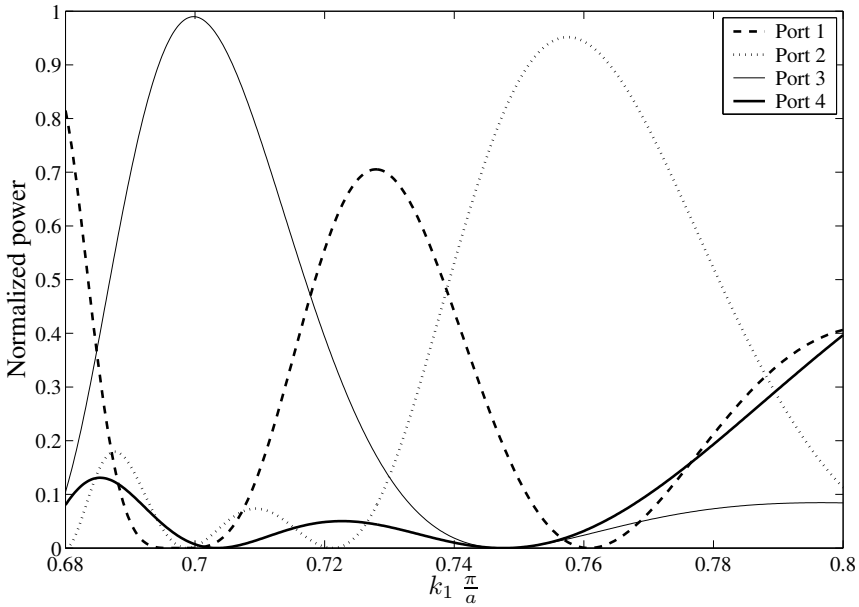

Figure 7.15: Transmission spectrum of the four-channel MUX-DEMUX calculated with the coupled mode theory.

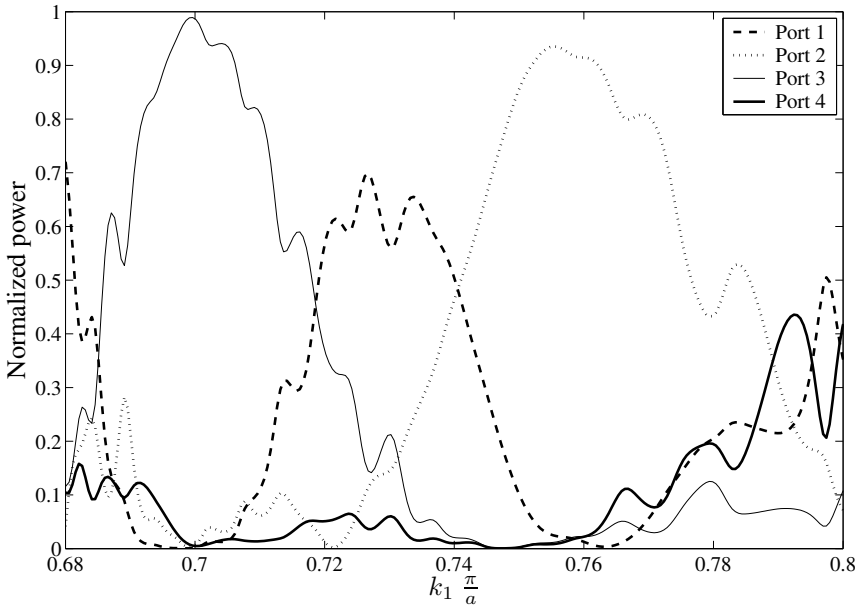

Figure 7.16: Transmission spectrum of the four-channel MUX-DEMUX calculated with the new scheme.

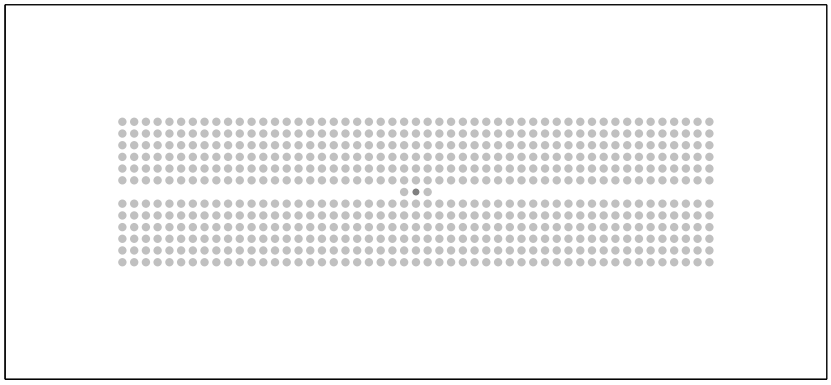

Figure 7.17: EC filter.

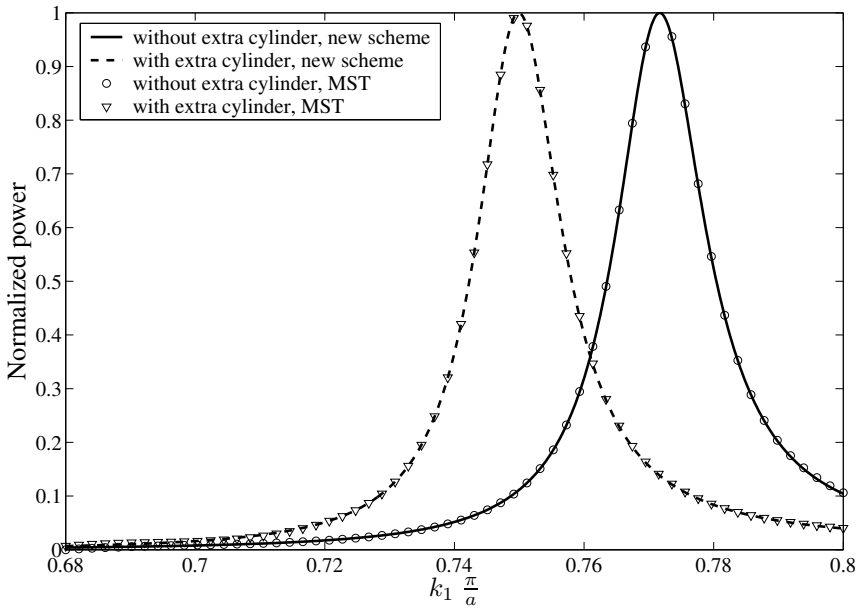

Figure 7.18: Transmission spectrum of the EC filter.

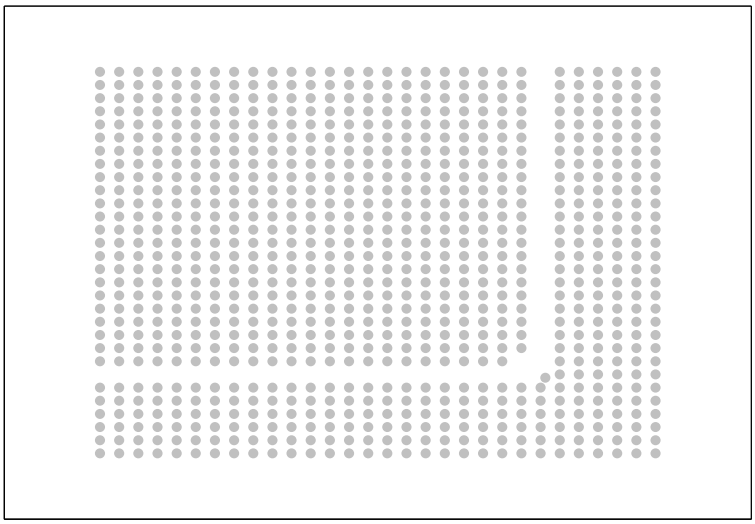

Figure 7.19: EC Bend.

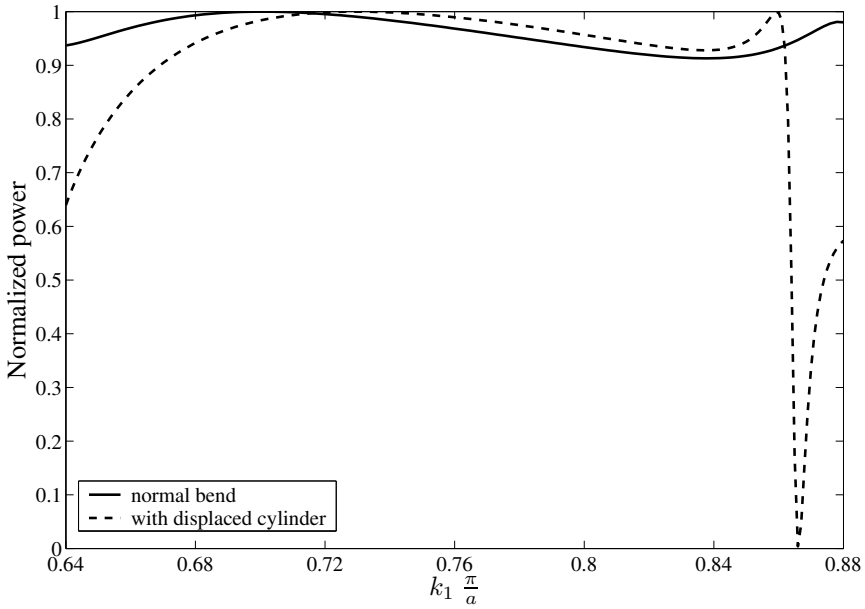

Figure 7.20: Transmission spectrum of the EC bend.

As a final example, consider the EC waveguide bend depicted in Fig. 7.19. To minimize reflections, one of the cylinders in the bend is displaced by $\Delta_x = 0.15a$ and $\Delta_y = -0.15a$. Figure 7.20 shows the transmission spectra of the bend with and without displaced cylinder, respectively. Both configurations require 305 unknown currents, 6.27 s to fill in the interaction matrix, and 0.5 s to solve system (7.23).

7.5 Conclusion

A novel method for simulating wave propagation in two-dimensional EC devices that, a small number of irregular defects aside, are obtained by removing cylinders from infinite doubly periodic and defect-less ECs, was presented. Integral equations in terms of equivalent currents that reside on the surfaces of removed cylinders were constructed by using Green functions innate to the defect-less EC, or low-rank perturbations thereof. The solution of the sparse system of equations that resulted upon discretizing these integral equations was effected using a multi-frontal method. The scheme was shown to be ideally suited for extracting EC device S-parameters, as it permits imposing modal excitations and exact boundary conditions. Although this paper only considered EC devices defined on a square Cartesian lattice that supports TM_z polarized fields, extensions of the proposed scheme to EC devices defined on a hexagonal lattice and/or supporting TE_z polarized fields are trivial. ECs formed by non-circular scatterers can be treated as well, by characterizing their interactions via scattering matrices.

Bibliography

[1] J. D. Joannopoulos, R. D. Meade, and J. N. Winn, *Photonic Crystals, Molding the Flow of Light*. N.J.: Princeton Univ. Press, 1995.

[2] A. Mekis, J. Chen, I. Kurland, S. Fan, P. Villeneuve, and J. Joannopoulos, "High transmission through sharp bends in photonic crystal waveguides," *Phys. Rev. Lett*, vol. 77, no. 18, pp. 3787–3790, Oct. 1996.

[3] H. Benisty, C. Weisbuch, M. Agio, M. Kafesaki, C. Soukoulis, M. Qiu, M. Swillo, A. Karlsson, B. Jaskorzynska, A. Talneau, J. Moosburger, M. Kamp, A. Forchell, R. Ferrini, R. Houdré, and U. Oesterle, "Models and measurements for the transmission of submicron-width waveguide bends defined in two-dimensional photonic crystals," *IEEE J. Quantum Electron.*, vol. 38, no. 7, pp. 770–785, July 2002.

[4] M. Koshiba, "Wavelength division multiplexing and demultiplexing with photonic crystal waveguide couplers," *Journal of Lightwave Technology*, vol. 19, no. 12, pp. 1970–1975, Dec. 2001.

[5] S. Boscolo, M. Midrio, and C. G. Someda, "Coupling and decoupling of electromagnetic waves in parallel 2D photonic crystal waveguides," *IEEE J. Quantum Electron.*, vol. 1, no. 38, pp. 47–53, Jan. 2002.

[6] C. Jin, S. Han, X. Meng, B. Cheng, and D. Zhang, "Demultiplexer using directly resonant tunneling between point defects and waveguides in a photonic crystal," *Jounal of Applied Physics*, vol. 91, no. 7, pp. 4771–4773, April 2002.

[7] L. Wu, M. Mazilu, T. Karle, and T. Krauss, "Superprism phenomena in planar photonic crystals," *IEEE J. Quantum Electron.*, vol. 38, no. 7, pp. 915–918, July 2002.

[8] A. Taflove, *Computational Electrodynamics: The Finite-Difference Time Domain Method*. Norwood: Artech House, 1995.

[9] B. Denecker, F. Olyslager, L. Knockaert, and D. D. Zutter, "Generation of FDTD subcell equations by means of reduced order modelling," *IEEE Trans. Antennas Propag.*, vol. 51, no. 8, pp. 1806–1817, Aug. 2003.

[10] H. Derudder, D. D. Zutter, and F. Olyslager, "A new way to analyse waveguide discontinuities using perfectly matched layers," *IEE Electronic Letters*, vol. 34, no. 22, pp. 2138–2140, Oct. 1998.

[11] P. Bienstman and R. Baets, "Optical modelling of photonic crystals and VCSELs using eigenmode expansion and perfectly matched layers," *Opt. Quantum Electron.*, vol. 33, no. 4-5, pp. 327–341, April 2001.

[12] G. Tayeb and D. Maystre, "Rigorous theoretical study of finite-size two-dimensional photonic crystals doped by microcavities," *J. Opt. Soc. Am. A*, vol. 14, no. 12, pp. 3323–3332, Dec. 1997.

[13] D. Pissoort, D. De Zutter, and F. Olyslager, "Efficient semi-analytical analysis of two-dimensional photonic crystals," in *IEEE AP-S Int. Symp.*, vol. 3, Columbus, OH, USA, June 2003, pp. 994–997.

[14] W. C. Chew, J. M. Jin, E. Michielssen, and J. Song, *Fast and Efficient Algorithms in Computational Electromagnetics*. Boston: Artech House, 2001.

[15] D. Pissoort, D. Vande Ginste, F. Olyslager, and E. Michielssen, "Different preconditioning techniques for the efficient simulation of 2D EC structures," in *IEEE AP-S Int. Symp.*, vol. 2, Monterey, CA, USA, June 2004, pp. 2131–2134.

[16] R. E. Collin, *Field Theory of Guided Waves*. New-York: IEEE Press, 1991.

[17] R. Harrington, *Time Harmonic Electromagnetic Fields*. New York: Mc Graw-Hill, 1961.

[18] D. Pissoort, B. Denecker, P. Bienstman, F. Olyslager, and D. De Zutter, "Comparative study of three methods for the simulation of two-dimensional photonic crystals," *J. Opt. Soc. Am. A*, vol. 21, pp. 2186–2195, Nov. 2004.

[19] I. Duff and J. Reid, "The multifrontal solution of unsymmetric sets of linear equations," *SIAM J. Sci. Comput.*, vol. 5, pp. 633–641, 1984.

[20] R. Cheng, D. Wang, E. Yung, and J. Jin, "Application of the multifrontal method to the vector FEM for analysis of microwave filters," *Microwave Opt. Technol. Lett.*, vol. 31, pp. 465–470, 2001.

[21] G. H. Golub and C. F. Van Loan, *Matrix Computations*. Baltimore, Maryland: The Johns Hopkins University Press, 1983.

[22] "http://www.cise.ufl.edu/ davis/."

[23] D. Pissoort and F. Olyslager, "Termination of periodic waveguides by PMLs in time-harmonic integral equation like techniques," *Antennas and Wireless Propagation Letters*, vol. 2, pp. 281–284, 2003.

Chapter 8

Fast and Efficient Analysis of Electromagnetic Crystal Slabs Using Perfectly Matched Layers

Davy Pissoort, Frank Olyslager, Daniël De Zutter, and Eric Michielssen

To be submitted

Abstract

A new technique for analyzing wave propagation in electromagnetic crystal slabs is presented. The proposed technique combines a cylindrical mode-matching technique with the multiple scattering technique. The open structure is transformed into a closed structure with the same electromagnetic behavior by terminating the outermost layers with perfectly matched layers, backed by perfectly electric or perfectly magnetic conducting plates. The resulting linear system of equations is solved iteratively. By performing the matrix-vector multiplications in two steps and by applying fast two-dimensional multiplication schemes, the computational complexity and memory requirements can be kept low. The versatility and the computational efficiency of the new technique are demonstrated via its application to the analysis of a straight hexagonal EC waveguide and an hexagonal EC waveguide with two 60^{o} bends.

8.1 Introduction

Recently, two-dimensional electromagnetic crystals (ECs) have received much attention because of their applicability to various optoelectronic devices [1]. In these structures, the dielectric constant is periodic in one plane (usually referred to as the xy-plane) and

extends infinitely in the third direction (z direction). Under specific conditions, electromagnetic bandgaps appear, viz. frequency regions in which wave propagation through the EC is forbidden. By removing/adding cylinders from/to an otherwise perfect EC, an EC device capable of supporting localized electromagnetic modes may result. This phenomenon can be exploited to create low loss waveguides with sharp bends [2,3], multiplexers [4–6], superprisms [7], etc. However, ideal 2D ECs extend infinitely in the z direction, a situation that cannot be realized in practice. Therefore, EC slabs have been proposed [8]. These structures combine an EC with 2D periodicity in the xy-plane with a slab waveguide in the z direction. Such an EC slab is typically realized by vertically etching an array of air holes through the slab waveguide. Electromagnetic fields guided in an EC slab line-defect waveguide are confined in the xy-plane within the line defect because of the electromagnetic bandgap property, while in the z direction the fields are confined by means of total internal reflection. Unfortunately, this confinement is imperfect: a continuum of radiation modes exists and this continuum can be excited by any point-defect, e.g. a bend. Because these out-of-plane radiation losses are of essential importance for future applications, they have to be taken into account when modeling EC devices. Hence, exact modeling of devices affected by such out-of-plane losses requires 3D calculations.

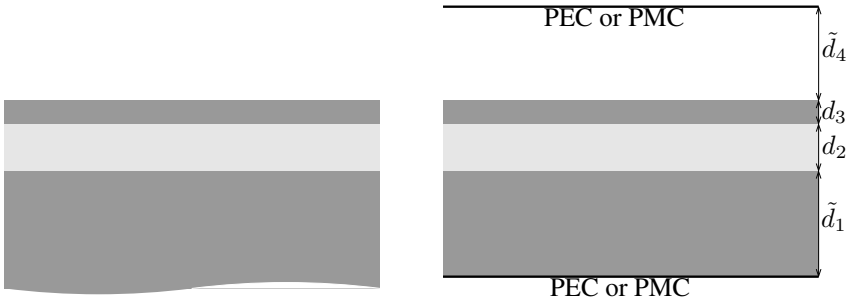

(a) Open layered medium. (b) Closed layered medium.

Figure 8.1: Transformation from an open to a closed layered medium.

A slab waveguide can be seen as an open layered medium comprising a set of parallel, isotropic layers (Fig. 8.1(a)). These media are called 'open' because both outermost layers are semi-infinite. Such an open layered medium has a discrete spectrum of surface waves and a continuous spectrum due to the semi-infinite layers [9]. The use of perfectly matched layers (PMLs), introduced by Bérenger [10], allows to transform the characterization of this open layered medium into the characterization of a closed one. Indeed, by terminating the outermost layers with PMLs, backed by perfectly electric or perfectly magnetic conducting (PEC or PMC) plates, the structure becomes closed (almost) without changing its electromagnetic behavior (Fig. 8.1(b)). Such a closed layered medium has a fully *discrete* spectrum of eigenmodes. Previous investigations have shown that, when terminating the outermost layers into a PEC or PMC backed layer, these layers can still be seen as one homogeneous and isotropic layer, but now with a *complex* thickness [11,12]. In what follows, complex thicknesses will be denoted by a tilde (Fig. 8.1(b)).

It also turns out that adding the PMLs does not complicate the eigenmode analysis of the closed layered medium: formulas obtained for regular closed layered media, i.e., without PMLs, remain valid by simply replacing the thicknesses of the outermost layers by the correct complex thicknesses [13]. This PML based technique, to turn an open structure into a closed structure without affecting the electromagnetic behavior, has already been used in the past to determine a series representation for the Green function of an open layered medium [14, 15] and to study waveguide discontinuities with a mode-matching technique [13, 16, 17]. In turn, the latter technique has already been applied to the characterization of 2D EC devices [18]. More recently, this PML concept in conjunction with the plane-wave expansion method has been applied to the calculation of the band structure of EC slabs [19].

This paper describes a new technique for analyzing electromagnetic wave propagation in EC slab devices. The proposed method combines a multiple scattering technique [20] in the xy-plane with a (cylindrical) mode-matching technique in the z direction. The open structure is first transformed into a closed one following the above described reasoning. Consider for example the EC slab depicted in Fig. 8.2(a) that consists of an open layered medium in which air holes are etched according to a regular lattice. This open structure is transformed into a closed structure by terminating the top and bottom layers by PEC or PMC backed PMLs. The air holes can now be thought of as layered circular cylinders embedded into another closed layered medium. Using a (cylindrical) mode-matching technique at the surface of every cylinder, the scattering matrix of this cylinder is easily obtained. The interactions between different cylinders are described by a technique similar to the multiple scattering technique that has been used in the past to characterize wave propagation in 2D EC devices [18, 21].

This paper is organized as follows. In Section 8.2, the main properties of the *longitudinal* eigenmodes of a general closed layered medium are described. Section 8.3 details the properties of the so-called *radial* eigenmodes of these media, i.e. solutions of the source free Maxwell equations with a $e^{jk\phi}$-dependence. These radial eigenmodes are intimately related to the longitudinal eigenmodes. In Section 8.4, the scattering matrix of a layered cylinder embedded in another closed layered medium is derived. Section 8.5 details how this scattering matrix in combination with the multiple scattering technique can be used to characterize wave propagation in EC slabs. Finally, the usefulness of the proposed method is validated in Section 8.6 with some illustrative examples.

Notation: all sources and fields are assumed time-harmonic with angular frequency ω; temporal dependencies $e^{j\omega t}$ are suppressed.

8.2 Longitudinal eigenmodes of a closed layered medium

This section details the most important properties of the *longitudinal* eigenmodes of closed layered media, a typical example of which is depicted in Fig. 8.3. The targeted media comprise L isotropic layers, parallel to the xy-plane, with thickness d_i and constitutive parameters (ϵ_i, μ_i) (permittivity, permeability), $i = 1, \ldots, L$. Moreover, the media are sandwiched between two ground planes, which can be either PEC or PMC. The thicknesses of the outermost layers can be complex: $\tilde{d}_1 = d_1^{\text{re}} + jd_1^{\text{im}}$ and $\tilde{d}_L = d_L^{\text{re}} + jd_L^{\text{im}}$. To obtain absorption of the electromagnetic fields in these layers, the imaginary part of

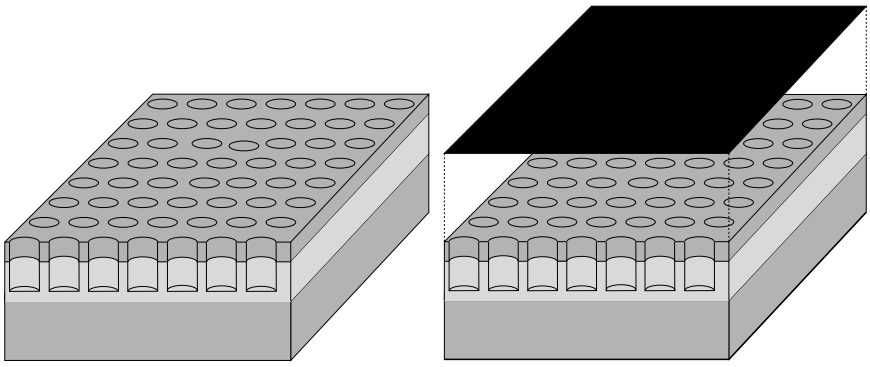

(a) (b)

Figure 8.2: Electromagnetic Crystal slab.

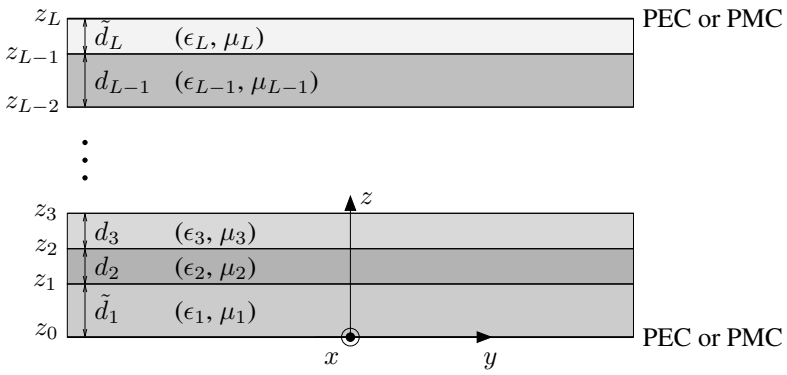

Figure 8.3: Closed layered medium.

their complex thicknesses has to be negative, viz. $d_1^{\text{im}} \leq 0$ and $d_L^{\text{im}} \leq 0$. Let $k_i = \omega\sqrt{\epsilon_i \mu_i}$ denote the wavenumber of the i^{th} layer. Further, let the z-coordinate of the bottom and top interface of layer i, $i = 1, \ldots, L$, be denoted by z_{i-1} and z_i, respectively.

In this paper, it is assumed that the longitudinal eigenmodes are invariant in the x direction and that they have an $e^{-j\beta y}$ dependence along the y direction:

$$\boldsymbol{e}(y,z) = \boldsymbol{E}(z)e^{-j\beta y}, \tag{8.1}$$
$$\boldsymbol{h}(y,z) = \boldsymbol{H}(z)e^{-j\beta y}. \tag{8.2}$$

Inserting (8.1) and (8.2) into the sourceless Maxwell's curl equations shows that these equations can be subdivided into two independent sets. For the first set, the magnetic field $\boldsymbol{h}(y,z)$ has no z-component and this set constitutes the longitudinal TM$_z$ eigenmodes. As for the second set the electric field $\boldsymbol{e}(y,z)$ has no z-component, this set constitutes the longitudinal TE$_z$ eigenmodes. Moreover, it is seen that for the longitudinal TM$_z$ (TE$_z$) eigenmodes, the electric (magnetic) field only has a y- and z-component, while the magnetic (electric) field only has an x-component.

8.2.1 TM$_z$-modes

Let $\boldsymbol{e}_m^{\text{TM}}(y,z)$ and $\boldsymbol{h}_m^{\text{TM}}(y,z)$ denote the electric and the magnetic field of the m^{th} longitudinal TM$_z$ eigenmode of the closed layered medium:

$$\boldsymbol{e}_m^{\text{TM}}(y,z) = \left[E_{y,m}(z)\boldsymbol{u}_y + E_{z,m}(z)\boldsymbol{u}_z\right] e^{-j\beta_m^{\text{TM}} y} \tag{8.3}$$
$$\boldsymbol{h}_m^{\text{TM}}(y,z) = H_{x,m}(z)\boldsymbol{u}_x e^{-j\beta_m^{\text{TM}} y}. \tag{8.4}$$

Here, β_m^{TM} is the corresponding propagation coefficient. Maxwell's curl equations lead to the following Helmholtz equation for $E_{z,m}(z)$:

$$\frac{d^2 E_{z,m}(z)}{dz^2} - (\gamma_{m,i}^{\text{TM}})^2 E_{z,m}(z) = 0, \tag{8.5}$$

with $\gamma_{m,i}^{\text{TM}} = \left[(\beta_m^{\text{TM}})^2 - k_i^2\right]^{1/2}$, $i = 1, \ldots, L$. Because the structure is closed the sign of this square root is of no importance. All other field components are related to $E_{z,m}(z)$ by

$$E_{y,m}(z) = \frac{1}{j\beta_m^{\text{TM}}} \frac{dE_{z,m}(z)}{dz}, \tag{8.6}$$
$$H_{x,m}(z) = \frac{\omega\epsilon_i}{\beta_m^{\text{TM}}} E_{z,m}(z). \tag{8.7}$$

It follows from (8.5) that

$$E_{z,m}(z) = a_{m,i}^{\text{TM}} e^{-\gamma_{m,i}^{\text{TM}} z} + b_{m,i}^{\text{TM}} e^{\gamma_{m,i}^{\text{TM}} z}, \;\; z_{i-1} < z < z_i, \; i = 1, \ldots, L. \tag{8.8}$$

The $2L$ unknown coefficients $a_{m,i}^{\text{TM}}$ and $b_{m,i}^{\text{TM}}$ are found from the boundary conditions at the layers' interfaces. A first set of $2L-2$ equations is obtained by expressing the continuity of $E_{y,m}(z)$ and $H_{x,m}(z)$ at the interface between two layers i and $i+1$, $i = 1, \ldots, L-1$. Two other equations are found by expressing that the layered medium is sandwiched

between two perfectly conducting planes, viz. $E_{y,m}(z_0) = 0$ or $H_{x,m}(z_0) = 0$ and $E_{y,m}(z_L) = 0$ or $H_{x,m}(z_L) = 0$ for a PEC or PMC plane, respectively. Setting the β-dependent determinant of the matrix derived from these $2L$ homogeneous linear equations to zero allows the propagation constants β_m^{TM} to be determined. Once the propagation constants of the various modes are found, the expansion coefficients $a_{m,i}^{\text{TM}}$ and $b_{m,i}^{\text{TM}}$ are obtained from the null space of the above linear system with fixed β.

8.2.2 TE$_z$-modes

Let $\boldsymbol{e}_m^{\text{TE}}(y,z)$ and $\boldsymbol{h}_m^{\text{TE}}(y,z)$ denote the electric and magnetic field of the m^{th} longitudinal TE$_z$ eigenmode of the closed layered medium:

$$\boldsymbol{e}_m^{\text{TE}}(y,z) = E_{x,m}(z)\boldsymbol{u}_x e^{-j\beta_m^{\text{TE}}y}, \tag{8.9}$$

$$\boldsymbol{h}_m^{\text{TE}}(y,z) = \left[H_{y,m}(z)\boldsymbol{u}_y + H_{z,m}(z)\boldsymbol{u}_z\right] e^{-j\beta_m^{\text{TE}}y}, \tag{8.10}$$

with β_m^{TE} the corresponding propagation coefficient. Maxwell's curl equations lead to the following Helmholtz equation for $H_{z,m}(z)$:

$$\frac{d^2H_{z,m}(z)}{dz^2} - (\gamma_{m,i}^{\text{TE}})^2 H_{z,m}(z) = 0, \tag{8.11}$$

with $\gamma_{m,i}^{\text{TE}} = \left[(\beta_m^{\text{TE}})^2 - k_i^2\right]$, $i = 1,\ldots,L$. All other field components are related to $H_{z,m}(z)$ by

$$H_{y,m}(z) = \frac{1}{j\beta_m^{\text{TE}}}\frac{dH_{z,m}(z)}{dz}, \tag{8.12}$$

$$E_{x,m}(z) = -\frac{\omega\mu_i}{\beta_m^{\text{TE}}}H_{z,m}(z). \tag{8.13}$$

Solving (8.11) shows that

$$H_{z,m}(z) = a_{m,i}^{\text{TE}}e^{-\gamma_{m,i}^{\text{TE}}z} + b_{m,i}^{\text{TE}}e^{\gamma_{m,i}^{\text{TE}}z}, \;\; z_{i-1} < z < z_i, \; i = 1,\ldots,L. \tag{8.14}$$

The propagations coefficients β_m^{TE} along with the expansion coefficients $a_{m,i}^{\text{TE}}$ and $b_{m,i}^{\text{TE}}$ are obtained via a similar procedure as described in Section 8.2.1, i.e., by expressing the continuity of $H_{y,m}(z)$ and $E_{x,m}(z)$ at the interfaces between two adjacent layers and by expressing the presence of a PEC or PMC plane at the top and bottom of the layered medium.

8.3 Radial eigenmodes of a closed layered medium

This section details the general solution of the source free Maxwell equations in terms of cylindrical coordinates for the closed layered media defined in Section 8.2. The notation in this section adheres mainly to that introduced in Section 8.2, except that hats appear on fields written in terms of cylindrical coordinates. Let $\boldsymbol{\rho} = x\boldsymbol{u}_x + y\boldsymbol{u}_y$ denote a global position vector in the xy-plane. By seperation of variables it is readily seen that the most

general solution of the source free Maxwell equations in terms of cylindrical coordinates can be expressed as follows:

$$\hat{\boldsymbol{e}}(\rho,\phi,z) = \sum_{k=-\infty}^{+\infty}\sum_{m=1}^{+\infty} \hat{\boldsymbol{e}}_{mk}(\rho,\phi,z) = \sum_{k=-\infty}^{+\infty}\sum_{m=1}^{+\infty} \hat{\boldsymbol{E}}_{mk}(\rho,z)e^{jk\phi}, \tag{8.15}$$

$$\hat{\boldsymbol{h}}(\rho,\phi,z) = \sum_{k=-\infty}^{+\infty}\sum_{m=1}^{+\infty} \hat{\boldsymbol{h}}_{mk}(\rho,\phi,z) = \sum_{k=-\infty}^{+\infty}\sum_{m=1}^{+\infty} \hat{\boldsymbol{H}}_{mk}(\rho,z)e^{jk\phi}. \tag{8.16}$$

The term in this summation with indices m and k is called the mk^{th} *radial* eigenmode of the closed layered medium. As will be shown in this section, the radial mode profiles $\hat{\boldsymbol{E}}_{mk}(\rho,z)$ and $\hat{\boldsymbol{H}}_{mk}(\rho,z)$ are closely related to the longitudinal ones discussed in Section 8.2. It is again possible to express a general electromagnetic field in terms of two separate sets of radial eigenmodes, namely, TM_z eigenmodes for which the magnetic field has no z-component and TE_z eigenmodes for which the electric field has no z-component:

$$\hat{\boldsymbol{e}}(\rho,\phi,z) = \sum_{k=-\infty}^{+\infty}\sum_{m=1}^{+\infty} \hat{\boldsymbol{E}}^{\text{TM}}_{mk}(\rho,z)e^{jk\phi} + \sum_{k=-\infty}^{+\infty}\sum_{m=1}^{+\infty} \hat{\boldsymbol{E}}^{\text{TE}}_{mk}(\rho,z)e^{jk\phi}, \tag{8.17}$$

$$\hat{\boldsymbol{h}}(\rho,\phi,z) = \sum_{k=-\infty}^{+\infty}\sum_{m=1}^{+\infty} \hat{\boldsymbol{H}}^{\text{TM}}_{mk}(\rho,z)e^{jk\phi} + \sum_{k=-\infty}^{+\infty}\sum_{m=1}^{+\infty} \hat{\boldsymbol{H}}^{\text{TE}}_{mk}(\rho,z)e^{jk\phi}. \tag{8.18}$$

Sections 8.3.1 and 8.3.2 detail the tight relation between the radial and longitudinal eigenmodes.

8.3.1 TM_z-modes

Recall that the radial TM_z eigenmodes are defined as the solutions of the source free Maxwell's equations when it is assumed that all field components have a $e^{jk\phi}$-dependence and that the magnetic field has no z-component. Let $\hat{\boldsymbol{e}}^{\text{TM}}_{mk}(\rho,\phi,z)$ and $\hat{\boldsymbol{h}}^{\text{TM}}_{mk}(\rho,\phi,z)$ denote the electric and magnetic field of the mk^{th} radial TM_z eigenmode:

$$\hat{\boldsymbol{e}}^{\text{TM}}_{mk}(\rho,\phi,z) = \left[\hat{E}^{\text{TM}}_{\rho,mk}(\rho,z)\boldsymbol{u}_\rho + \hat{E}^{\text{TM}}_{\phi,mk}(\rho,z)\boldsymbol{u}_\phi + \hat{E}^{\text{TM}}_{z,mk}(\rho,z)\boldsymbol{u}_z\right]e^{jk\phi}, \tag{8.19}$$

$$\hat{\boldsymbol{h}}^{\text{TM}}_{mk}(\rho,\phi,z) = \left[\hat{H}^{\text{TM}}_{\rho,mk}(\rho,z)\boldsymbol{u}_\rho + \hat{H}^{\text{TM}}_{\phi,mk}(\rho,z)\boldsymbol{u}_\phi\right]e^{jk\phi}. \tag{8.20}$$

Inserting (8.19) and (8.20) into Maxwell's curl equations leads to the following equation for $\hat{E}^{\text{TM}}_{z,mk}(\rho,z)$:

$$\frac{1}{\rho}\frac{\partial}{\partial\rho}\left(\rho\frac{\partial\hat{E}^{\text{TM}}_{z,mk}(\rho,z)}{\partial\rho}\right) + \left[k_i^2 + \frac{\partial^2}{\partial z^2} - \frac{k^2}{\rho^2}\right]\hat{E}^{\text{TM}}_{z,mk}(\rho,z) = 0. \tag{8.21}$$

All other field components are related to $\hat{E}^{\text{TM}}_{mk}(\rho,z)$ through

$$\left[k_i^2+\frac{\partial^2}{\partial z^2}\right]\hat{E}^{\text{TM}}_{\rho,mk}(\rho,z) = \frac{\partial^2\hat{E}^{\text{TM}}_{z,mk}(\rho,z)}{\partial\rho\partial z}, \tag{8.22}$$

$$\left[k_i^2+\frac{\partial^2}{\partial z^2}\right]\hat{E}^{\text{TM}}_{\phi,mk}(\rho,z) = \frac{jk}{\rho}\frac{\partial\hat{E}^{\text{TM}}_{z,mk}(\rho,z)}{\partial z}, \tag{8.23}$$

$$\left[k_i^2+\frac{\partial^2}{\partial z^2}\right]\hat{H}^{\text{TM}}_{\rho,mk}(\rho,z) = -\frac{\omega\epsilon_i k}{\rho}\hat{E}^{\text{TM}}_{z,mk}(\rho,z), \tag{8.24}$$

$$\left[k_i^2+\frac{\partial^2}{\partial z^2}\right]\hat{H}^{\text{TM}}_{\phi,mk}(\rho,z) = -j\omega\epsilon_i\frac{\partial\hat{E}^{\text{TM}}_{z,mk}(\rho,z)}{\partial\rho}. \tag{8.25}$$

Upon re-expressing $\hat{E}^{\text{TM}}_{z,mk}(\rho,z)$ as the product of two functions, the first one only depending on ρ and the second one only depending on z, viz. $\hat{E}^{\text{TM}}_{z,mk}=R(\rho)Z(z)$, Eq. (8.21) is separated into two coupled equations

$$\frac{1}{R(\rho)}\frac{1}{\rho}\frac{d}{d\rho}\left(\rho\frac{dR(\rho)}{d\rho}\right)-\frac{k^2}{\rho^2} = \sigma_m^2, \tag{8.26}$$

$$\frac{1}{Z(z)}\frac{d^2Z(z)}{dz^2}+k_i^2 = \sigma_m^2. \tag{8.27}$$

By choosing σ_m equal to β^{TM}_m, the propagation constant of the m-th *longitudinal* TM_z eigenmode, all the boundary conditions at the layers' interfaces can be fulfilled. Indeed, in that case, (8.27) reduces to (8.5) and $Z(z)$ is of the form (8.8). According to (8.8) and (8.22)–(8.25), all field components have the same $e^{\pm\gamma^{\text{TM}}_{m,i}z}$ dependence. By consequence, $k_i^2+\dfrac{\partial^2}{\partial z^2}$ in (8.22)–(8.25) is nothing but $(\beta^{\text{TM}}_m)^2$. Hence, it follows from (8.22)–(8.25) that expressing the continuity of $\hat{E}^{\text{TM}}_{\rho,mk}(\rho,z)$, $\hat{E}^{\text{TM}}_{\phi,mk}(\rho,z)$, $\hat{H}^{\text{TM}}_{\rho,mk}(\rho,z)$, and $\hat{H}^{\text{TM}}_{\phi,mk}(\rho,z)$ at $z=z_i$, $i=1,\ldots,L-1$, is equivalent to demanding the continuity of $Z(z)$ and $\frac{dZ(z)}{dz}$ at $z=z_i$, $i=1,\ldots,L-1$. Likewise, expressing that the layered medium is sandwiched between two perfectly conducting plates is equivalent to demanding that either $Z(z)$ or $\frac{dZ(z)}{dz}$ is zero at $z=z_0$ and $z=z_L$. Further, it follows from (8.6) and (8.7) that the boundary conditions for the *longitudinal* TM_z eigenmodes of Section 8.2.1 are also equivalent to expressing the continuity of $E_{z,m}(z)$ and $\frac{dE_{z,m}(z)}{dz}$ at $z=z_i$, $i=1,\ldots,L-1$, and expressing that $E_{z,m}(z)$ or $\frac{dE_{z,m}(z)}{dz}$ is zero at $z=z_0$ and $z=z_L$. From all the above, it is seen that $Z(z)$ must fulfill the same equation and boundary conditions as $E_{z,m}(z)$ and, hence, that $Z(z)=E_{z,m}(z)$.

Solving Eq. (8.26) with $\sigma_m=\beta^{\text{TM}}_m$ leads to

$$\begin{aligned}\hat{E}^{\text{TM}}_{z,mk}(\rho,z) &= \left[A^{\text{TM}}_{mk}J_k(\beta^{\text{TM}}_m\rho)+B^{\text{TM}}_{mk}H^{(2)}_k(\beta^{\text{TM}}_m\rho)\right]E_{z,m}(z)\\ &= R^{\text{TM}}_{mk}(\beta^{\text{TM}}_m\rho)E_{z,m}(z).\end{aligned} \tag{8.28}$$

Here, $J_k(\cdot)$ is the k^{th} order Bessel function of the first kind and $H^{(2)}_k(\cdot)$ is the k^{th} order Hankel function of the second kind; A^{TM}_{mk} and B^{TM}_{mk} are arbitrary coefficients. Combination of (8.6), (8.7), (8.22)–(8.25), and (8.28) proves the intimate relationship between the

radial and longitudinal TM_z eigenmodes:

$$\hat{E}^{\text{TM}}_{\rho,mk}(\rho,z) = jR^{\text{TM}\,\prime}_{mk}(\beta^{\text{TM}}_m\rho)E_{y,m}(z), \tag{8.29}$$

$$\hat{E}^{\text{TM}}_{\phi,mk}(\rho,z) = -\frac{k}{\beta^{\text{TM}}_m\rho}R^{\text{TM}}_{mk}(\beta^{\text{TM}}_m\rho)E_{y,m}(z), \tag{8.30}$$

$$\hat{H}^{\text{TM}}_{\rho,mk}(\rho,z) = -\frac{k}{\beta^{\text{TM}}_m\rho}R^{\text{TM}}_{mk}(\beta^{\text{TM}}_m\rho)H_{x,m}(z), \tag{8.31}$$

$$\hat{H}^{\text{TM}}_{\phi,mk}(\rho,z) = -jR^{\text{TM}\,\prime}_{mk}(\beta^{\text{TM}}_m\rho)H_{x,m}(z). \tag{8.32}$$

8.3.2 TE_z-modes

The radial TE_z eigenmodes are defined as the solutions of the source free Maxwell's equations when it is assumed that all field components have a $e^{jk\phi}$ dependence and that the electric field has no z-component. Let $\hat{\boldsymbol{e}}^{\text{TE}}_{mk}(\rho,\phi,z)$ and $\hat{\boldsymbol{h}}^{\text{TE}}_{mk}(\rho,\phi,z)$ denote the electric and magnetic field of the mk^{th} radial TE_z eigenmode:

$$\hat{\boldsymbol{e}}^{\text{TE}}_{mk}(\rho,\phi,z) = \left[\hat{E}^{\text{TE}}_{\rho,mk}(\rho,z)\boldsymbol{u}_\rho + \hat{E}^{\text{TE}}_{\phi,mk}(\rho,z)\boldsymbol{u}_\phi\right]e^{jk\phi}, \tag{8.33}$$

$$\hat{\boldsymbol{h}}^{\text{TE}}_{mk}(\rho,\phi,z) = \left[\hat{H}^{\text{TE}}_{\rho,mk}(\rho,z)\boldsymbol{u}_\rho + \hat{H}^{\text{TE}}_{\phi,mk}(\rho,z)\boldsymbol{u}_\phi + \hat{H}^{\text{TE}}_{z,mk}(\rho,z)\boldsymbol{u}_z\right]e^{jk\phi}. \tag{8.34}$$

Inserting (8.33) and (8.34) into Maxwell's curl equations leads to the following equation for $\hat{H}^{\text{TE}}_{z,mk}(\rho,z)$:

$$\frac{1}{\rho}\frac{\partial}{\partial\rho}\left(\rho\frac{\partial\hat{H}^{\text{TE}}_{z,mk}(\rho,z)}{\partial\rho}\right) + \left[k_i^2 + \frac{\partial^2}{\partial z^2} - \frac{k^2}{\rho^2}\right]\hat{H}^{\text{TE}}_{z,mk}(\rho,z) = 0. \tag{8.35}$$

All other field components are related to $\hat{H}^{\text{TE}}_{z,mk}(\rho,z)$ by

$$\left[k_i^2 + \frac{\partial^2}{\partial z^2}\right]\hat{E}^{\text{TE}}_{\rho,mk}(\rho,z) = \frac{\omega\mu_i k}{\rho}\hat{H}^{\text{TE}}_{z,mk}(\rho,z), \tag{8.36}$$

$$\left[k_i^2 + \frac{\partial^2}{\partial z^2}\right]\hat{E}^{\text{TE}}_{\phi,mk}(\rho,z) = j\omega\mu_i\frac{\partial\hat{H}^{\text{TE}}_{z,mk}(\rho,z)}{\partial\rho}, \tag{8.37}$$

$$\left[k_i^2 + \frac{\partial^2}{\partial z^2}\right]\hat{H}^{\text{TE}}_{\rho,mk}(\rho,z) = \frac{\partial^2\hat{H}^{\text{TE}}_{z,mk}(\rho,z)}{\partial z\partial\rho}, \tag{8.38}$$

$$\left[k_i^2 + \frac{\partial^2}{\partial z^2}\right]\hat{H}^{\text{TE}}_{\phi,mk}(\rho,z) = \frac{jk}{\rho}\frac{\partial\hat{H}^{\text{TE}}_{z,mk}(\rho,z)}{\partial z}. \tag{8.39}$$

By stating that $\hat{H}^{\text{TE}}_{z,mk}(\rho,z) = R(\rho)Z(z)$, eqn. (8.35) is separated into two coupled equations, one for the ρ-dependence and one for the z-dependence:

$$\frac{1}{R(\rho)}\frac{1}{\rho}\frac{d}{d\rho}\left(\rho\frac{dR(\rho)}{d\rho}\right) - \frac{k^2}{\rho^2} = \sigma_m^2 \tag{8.40}$$

$$\frac{1}{Z(z)}\frac{d^2Z(z)}{dz^2} + k_i^2 = \sigma_m^2 \tag{8.41}$$

Mirroring the reasoning followed in Section 8.3.1, it is seen that $\sigma_m = \beta_m^{\mathrm{TE}}$ and that $Z(z) = H_{z,m}(z)$. Combination with the solution of (8.40) yields

$$\begin{aligned} \hat{H}_{z,mk}^{\mathrm{TE}}(\rho, z) &= \left[A_{mk}^{\mathrm{TE}} J_k(\beta_m^{\mathrm{TE}}\rho) + B_{mk}^{\mathrm{TE}} H_k^{(2)}(\beta_m^{\mathrm{TE}}\rho) \right] H_{z,m}(z) \\ &= R_{mk}^{\mathrm{TE}}(\beta_m^{\mathrm{TE}}\rho) H_{z,m}(z) \end{aligned} \tag{8.42}$$

Combination of (8.12), (8.13), (8.36)–(8.39), and (8.42) proves the tight relation between the radial and the longitudinal TE_z modes:

$$\hat{E}_{\rho,mk}^{\mathrm{TE}}(\rho, z) = -\frac{k}{\beta_m^{\mathrm{TE}}\rho} R_{mk}^{\mathrm{TE}}(\beta_m^{\mathrm{TE}}\rho) E_{x,m}(z), \tag{8.43}$$

$$\hat{E}_{\phi,mk}^{\mathrm{TE}}(\rho, z) = -jR_{mk}^{\mathrm{TE}\,\prime}(\beta_m^{\mathrm{TE}}\rho) E_{x,m}(z), \tag{8.44}$$

$$\hat{H}_{\rho,mk}^{\mathrm{TE}}(\rho, z) = jR_{mk}^{\mathrm{TE}\,\prime}(\beta_m^{\mathrm{TE}}\rho) H_{y,m}(z), \tag{8.45}$$

$$\hat{H}_{\phi,mk}^{\mathrm{TE}}(\rho, z) = -\frac{k}{\beta_m^{\mathrm{TE}}\rho} R_{mk}^{\mathrm{TE}}(\beta_m^{\mathrm{TE}}\rho) H_{y,m}(z). \tag{8.46}$$

8.4 Scattering matrix

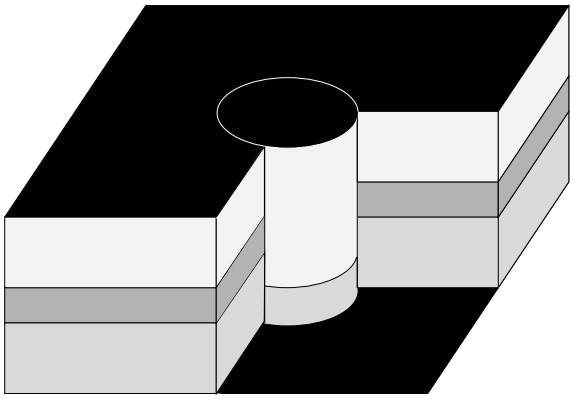

Figure 8.4: Scattering matrix of one cylinder.

Consider the configuration depicted in Fig. 8.4. A layered circular cylinder with radius r, centered about the spatial origin $\boldsymbol{\rho} = \mathbf{0}$, resides in another closed layered medium. In this section, expressions for the scattering matrix of such a layered cylinder will be derived. The longitudinal mode profiles of the layered medium outside the cylinder (medium 1) are denoted by $\boldsymbol{E}_m^1(z)$ and $\boldsymbol{H}_m^1(z)$. Their corresponding propagation coefficients are β_m^{TX} with TX either TE or TM. Likewise, the longitudinal mode profiles of the layered medium inside the cylinder (medium 2) are denoted by $\boldsymbol{E}_m^2(z)$ and $\boldsymbol{H}_m^2(z)$ with corresponding propagation coefficients ζ_m^{TX}. Let $\left(\hat{\boldsymbol{e}}^{\mathrm{i}}(\rho, \phi, z); \hat{\boldsymbol{h}}^{\mathrm{i}}(\rho, \phi, z)\right)$ denote the *incident* electric and magnetic field radiated by impressed sources in medium 1 *in the absence of the cylinder*. In the presence of the cylinder, the total electromagnetic field

$\left(\hat{\boldsymbol{e}}^{\mathrm{t}}(\rho,\phi,z);\hat{\boldsymbol{h}}^{\mathrm{t}}(\rho,\phi,z)\right)$ is observed. The difference between the total and incident field outside the cylinder is the scattered electromagnetic field $\left(\hat{\boldsymbol{e}}^{\mathrm{s}}(\rho,\phi,z),\hat{\boldsymbol{h}}^{\mathrm{s}}(\rho,\phi,z)\right)$, viz. $\hat{\boldsymbol{e}}^{\mathrm{t}}(\rho,\phi,z)=\hat{\boldsymbol{e}}^{\mathrm{i}}(\rho,\phi,z)+\hat{\boldsymbol{e}}^{\mathrm{s}}(\rho,\phi,z)$ and $\hat{\boldsymbol{h}}^{\mathrm{t}}(\rho,\phi,z)=\hat{\boldsymbol{h}}^{\mathrm{i}}(\rho,\phi,z)+\hat{\boldsymbol{h}}^{\mathrm{s}}(\rho,\phi,z)$. Assume that the incident field is the superposition of $(2K+1)M$ radial TM_z and $(2K+1)M$ radial TE_z eigenmodes. That is, the z-components of the incident electric and magnetic field are

$$\hat{e}_z^{\mathrm{i}}(\rho,\phi,z) = \sum_{k=-K}^{K}\sum_{m=1}^{M} C_{mk}^{\mathrm{TM}}\frac{J_k(\beta_m^{\mathrm{TM}}\rho)}{J_k(\beta_m^{\mathrm{TM}}r)}E_{z,m}^1(z)e^{jk\phi}, \tag{8.47}$$

$$\hat{h}_z^{\mathrm{i}}(\rho,\phi,z) = \sum_{k=-K}^{K}\sum_{m=1}^{M} C_{mk}^{\mathrm{TE}}\frac{J_k(\beta_m^{\mathrm{TE}}\rho)}{J_k(\beta_m^{\mathrm{TE}}r)}H_{z,m}^1(z)e^{jk\phi}, \tag{8.48}$$

with C_{mk}^{TX} known coefficients. In (8.47) and (8.48) only Bessel functions $J_k(\cdot)$ are used to describe the incident field because the incident field must be finite for $\rho=0$. All other field components of the incident field follow from (8.29)–(8.32) and (8.43)–(8.46). The scattered field outside the cylinder and the total field inside the cylinder are also expressed as the superposition of $(2K+1)M$ radial TM_z and $(2K+1)M$ radial TM_z modes:

$$\hat{e}_z^{\mathrm{s}}(\rho,\phi,z) = \sum_{k=-K}^{K}\sum_{m=1}^{M} B_{mk}^{\mathrm{TM}}\frac{H_k^{(2)}(\beta_m^{\mathrm{TM}}\rho)}{H_k^{(2)}(\beta_m^{\mathrm{TM}}r)}E_{z,m}^1(z)e^{jk\phi} \text{ for } \rho>r, \tag{8.49}$$

$$\hat{h}_z^{\mathrm{s}}(\rho,\phi,z) = \sum_{k=-K}^{K}\sum_{m=1}^{M} B_{mk}^{\mathrm{TE}}\frac{H_k^{(2)}(\beta_m^{\mathrm{TE}}\rho)}{H_k^{(2)}(\beta_m^{\mathrm{TE}}r)}H_{z,m}^1(z)e^{jk\phi} \text{ for } \rho>r, \tag{8.50}$$

$$\hat{e}_z^{\mathrm{t}}(\rho,\phi,z) = \sum_{k=-K}^{K}\sum_{m=1}^{M} A_{mk}^{\mathrm{TM}}\frac{J_k(\zeta_m^{\mathrm{TM}}\rho)}{J_k(\zeta_m^{\mathrm{TM}}r)}E_{z,m}^2(z)e^{jk\phi} \text{ for } \rho<r, \tag{8.51}$$

$$\hat{h}_z^{\mathrm{t}}(\rho,\phi,z) = \sum_{k=-K}^{K}\sum_{m=1}^{M} A_{mk}^{\mathrm{TE}}\frac{J_k(\zeta_m^{\mathrm{TE}}\rho)}{J_k(\zeta_m^{\mathrm{TE}}r)}H_{z,m}^2(z)e^{jk\phi} \text{ for } \rho<r. \tag{8.52}$$

Here, A_{mk}^{TX} and B_{mk}^{TX} are unknown expansion coefficients. In (8.49) and (8.50) only Hankel functions $H_k^{(2)}(\cdot)$ are used because the scattered field represents a field that radiates towards infinity, while in (8.51) and (8.52) Bessel functions $J_k(\cdot)$ are used because the total field is finite for $\rho=0$.

Let $\boldsymbol{A}$, $\boldsymbol{B}$, and $\boldsymbol{C}$ denote vectors with $2(2K+1)M$ entries A_{mk}^{TX}, B_{mk}^{TX}, and C_{mk}^{TX}, $m=1,\ldots,M$; $k=-K,\ldots,K$. By definition, the scattering matrix $\boldsymbol{S}$ is a $2(2K+1)M$ by $2(2K+1)M$ matrix relating the (unknown) vector $\boldsymbol{B}$ to the (given) vector $\boldsymbol{C}$ or, equivalently, relating the scattered field outside the cylinder to the incident field:

$$\boldsymbol{B} = \boldsymbol{S}\boldsymbol{C}. \tag{8.53}$$

This scattering matrix is obtained by expressing the continuity of the z- and ϕ-components of the total electric and magnetic field at $\rho=r$ and by weighting these equations in the appropriate way. Details about this procedure are given in Appendix B.

Let the entries of the vectors $\boldsymbol{A}$, $\boldsymbol{B}$, and $\boldsymbol{C}$ be arranged in such a way that all the coefficients with the same modal index k are collected, viz.

$$\boldsymbol{A} = \begin{pmatrix} \boldsymbol{A}_{-K} \\ \vdots \\ \boldsymbol{A}_0 \\ \vdots \\ \boldsymbol{A}_K \end{pmatrix}, \quad \boldsymbol{B} = \begin{pmatrix} \boldsymbol{B}_{-K} \\ \vdots \\ \boldsymbol{B}_0 \\ \vdots \\ \boldsymbol{B}_K \end{pmatrix}, \quad \boldsymbol{C} = \begin{pmatrix} \boldsymbol{C}_{-K} \\ \vdots \\ \boldsymbol{C}_0 \\ \vdots \\ \boldsymbol{C}_K \end{pmatrix}, \tag{8.54}$$

with $\boldsymbol{A}_k$, $\boldsymbol{B}_k$, and $\boldsymbol{C}_k$ vectors containing all expansion coefficients with modal index k. Because of the orthogonality of the $e^{jk\phi}$ functions, the scattering matrix $\boldsymbol{S}$ is a block-diagonal matrix, viz.

$$\boldsymbol{S} \;=\; \begin{pmatrix} \boldsymbol{S}_{-K} & & & & \\ & \ddots & & & \\ & & \boldsymbol{S}_0 & & \\ & & & \ddots & \\ & & & & \boldsymbol{S}_K \end{pmatrix}. \tag{8.55}$$

Here, $\boldsymbol{S}_k$ is a $2M$ by $2M$ matrix that relates the vectors $\boldsymbol{B}_k$ and $\boldsymbol{C}_k$. In Appendix B, it is shown that the vectors $\boldsymbol{A}_k$, $\boldsymbol{B}_k$, and $\boldsymbol{C}_k$ are related through

$$\begin{pmatrix} \boldsymbol{Z}_{11}^k & -\boldsymbol{I} \\ \boldsymbol{Z}_{21}^k & \boldsymbol{Z}_{22}^k \end{pmatrix} \begin{pmatrix} \boldsymbol{A}_k \\ \boldsymbol{B}_k \end{pmatrix} \;=\; \begin{pmatrix} \boldsymbol{I} \\ \boldsymbol{Y}_2^k \end{pmatrix} \boldsymbol{C}_k. \tag{8.56}$$

The submatrices $\boldsymbol{Z}_{11}^k$ and $\boldsymbol{Z}_{21}^k$ are dense matrices of dimension $2M$ by $2M$. The submatrices $\boldsymbol{Z}_{22}^k$ and Y_2^k are diagonal matrices of the same dimension. In (8.56), $\boldsymbol{I}$ denotes the $2M$ by $2M$ identity matrix. If the first M entries of $\boldsymbol{A}_k$, $\boldsymbol{B}_k$, and $\boldsymbol{C}_k$ are the coefficients of the TM_z eigenmodes and if the last M entries correspond to the TE_z eigenmodes, the following definitions for the entries of the submatrices in (8.56) are valid:

$$[\boldsymbol{Z}_{11}^k]_{nm} = \begin{cases} \int_0^d E_{z,m}^2 H_{x,n}^1 dz & \text{if } 1 \le n, m \le M, \\ -\int_0^d H_{z,m}^2 E_{x,n}^1 dz & \text{if } M+1 \le n, m \le 2M, \\ 0 & \text{otherwise.} \end{cases} \tag{8.57}$$

$$[\boldsymbol{Z}_{21}^k]_{nm} = \begin{cases} \int_0^d H_{x,m}^2 E_{z,n}^1 dz \frac{J_k'(\zeta_m^{\mathrm{TM}} r)}{J_k(\zeta_m^{\mathrm{TM}} r)} & \text{if } 1 \le n, m \le M, \\ \frac{k}{j\beta_n^{\mathrm{TM}} r} \left[\int_0^d H_{z,m}^2 E_{y,n}^1 dz + \frac{\beta_n^{\mathrm{TM}}}{\zeta_m^{\mathrm{TE}}} \int_0^d H_{y,m}^2 E_{z,n}^1 dz \right] & \\ \qquad\qquad \text{if } 1 \le n \le M \text{ and } M+1 \le m \le 2M, & \\ -\frac{k}{j\beta_n^{\mathrm{TE}} r} \left[\int_0^d E_{z,m}^2 H_{y,n}^1 dz + \frac{\beta_n^{\mathrm{TE}}}{\zeta_m^{\mathrm{TM}}} \int_0^d E_{y,m}^2 H_{z,n}^1 dz \right] & \\ \qquad\qquad \text{if } M+1 \le n \le 2M \text{ and } 1 \le m \le M & \\ -\int_0^d E_{x,m}^2 H_{z,n}^1 dz \frac{J_k'(\zeta_m^{\mathrm{TE}} r)}{J_k(\zeta_m^{\mathrm{TE}} r)} & \text{if } M+1 \le n, m \le 2M. \end{cases} \tag{8.58}$$

$$[\boldsymbol{Z}_{22}^k]_{nn} = \begin{cases} -\frac{H_k^{(2)\prime}(\beta_n^{\mathrm{TM}} r)}{H_k^{(2)}(\beta_n^{\mathrm{TM}} r)} & \text{if } 1 \le n \le M, \\ -\frac{H_k^{(2)\prime}(\beta_n^{\mathrm{TE}} r)}{H_k^{(2)}(\beta_n^{\mathrm{TE}} r)} & \text{if } M+1 \le n \le 2M. \end{cases} \tag{8.59}$$

$$[\boldsymbol{Y}_2^k]_{nn} = \begin{cases} -\frac{J_k'(\beta_n^{\mathrm{TM}} r)}{J_k(\beta_n^{\mathrm{TM}} r)} & \text{if } 1 \le n \le M, \\ -\frac{J_k'(\beta_n^{\mathrm{TE}} r)}{J_k(\beta_n^{\mathrm{TE}} r)} & \text{if } M+1 \le n \le 2M. \end{cases} \tag{8.60}$$

Elimination of $\boldsymbol{A}_k$ in (8.56) yields

$$\boldsymbol{S}_k = \left[\boldsymbol{I} + (\boldsymbol{Y}_2^k)^{-1}\boldsymbol{Z}_{22}^k\right]^{-1}\left[\boldsymbol{Z}_{11}^k - (\boldsymbol{Y}_2^k)^{-1}\boldsymbol{Z}_{21}^k\right]\left[\boldsymbol{Z}_{22}^k\boldsymbol{Z}_{11}^k + \boldsymbol{Z}_{21}^k\right]^{-1}\left[\boldsymbol{Z}_{22}^k + \boldsymbol{Y}_2^k\right]. \tag{8.61}$$

If $\boldsymbol{C}$ is given, $\boldsymbol{B}$ is known using (8.53), (8.55), and (8.61). Once $\boldsymbol{B}$ is known, $\boldsymbol{A}$ can be calculated from

$$\boldsymbol{A}_k \;=\; \left[\boldsymbol{Y}_2^k\boldsymbol{Z}_{11}^k - \boldsymbol{Z}_{21}^k\right]^{-1}[\boldsymbol{Z}_{22}^k + \boldsymbol{Y}_2^k]\boldsymbol{B}_k. \tag{8.62}$$

Hence, the total electromagnetic field inside and outside the cylinder is known.

8.5 Electromagnetic crystal slabs

Consider the EC slab depicted in Fig. 8.2(a), comprising N_c air holes etched in an open layered medium. To characterize such structures, PML regions backed by PEC or PMC plates are added at the bottom and top of this structure (Fig. 8.2(b)). In this way every air hole is described by the configuration considered in Section 8.4. Let $\boldsymbol{S}^i$ denote the scattering matrix of cylinder i, $i = 1, \ldots, N_c$. Recall that $\boldsymbol{S}^i$ relates the electromagnetic field scattered by cylinder i to the electromagnetic field that is incident on this cylinder. The field incident on cylinder i comprises the incident field $\left(\hat{\boldsymbol{e}}^{\mathrm{i}}(\rho,\phi,z); \hat{\boldsymbol{h}}^{\mathrm{i}}(\rho,\phi,z)\right)$ generated by the impressed sources and the field $\left(\hat{\boldsymbol{e}}^{\mathrm{s},j}(\rho,\phi,z); \hat{\boldsymbol{h}}^{\mathrm{s},j}(\rho,\phi,z)\right)$ scattered by all the other cylinders j, $j = 1, \ldots, N_c$, $j \neq i$. Let $\boldsymbol{\rho}_j = (\rho_j, \phi_j)$ denote a local position vector in the xy-plane with respect to the center $\boldsymbol{\rho}_j^c$ of cylinder j. Likewise, let r_j denote the radius of the j^{th} cylinder. Similarly to Section 8.4, assume that the incident field is the superposition of $(2K+1)M$ radial TM_z and $(2K+1)M$ radial TE_z modes. This incident field is first expressed in terms of the local cylindrical coordinates of cylinder i:

$$\hat{e}_z^{\mathrm{i}}(\rho_i,\phi_i,z) \;=\; \sum_{k=-K}^{K}\sum_{m=1}^{M} C_{mk}^{\mathrm{TM},i}\frac{J_k(\beta_m^{\mathrm{TM}}\rho_i)}{J_k(\beta_m^{\mathrm{TM}} r_i)}E_{z,m}^1(z)e^{jk\phi_i}, \tag{8.63}$$

$$\hat{h}_z^{\mathrm{i}}(\rho_i,\phi_i,z) \;=\; \sum_{k=-K}^{K}\sum_{m=1}^{M} C_{mk}^{\mathrm{TE},i}\frac{J_k(\beta_m^{\mathrm{TE}}\rho_i)}{J_k(\beta_m^{\mathrm{TE}} r_i)}H_{z,m}^1(z)e^{jk\phi_i}, \tag{8.64}$$

with $C_{mk}^{\mathrm{TX},i}$ known coefficients. The z-components of the electric and magnetic field scattered by cylinder j are

$$\hat{e}_z^{\mathrm{s},j}(\rho_j,\phi_j,z) = \sum_{k=-K}^{K}\sum_{m=1}^{M} B_{mk}^{\mathrm{TM},j}\frac{H_k^{(2)}(\beta_m^{\mathrm{TM}}\rho_j)}{H_k^{(2)}(\beta_m^{\mathrm{TM}}r_j)}E_{z,m}^1(z)e^{jk\phi_j} \text{ for } \rho_j > r_j, \quad (8.65)$$

$$\hat{h}_z^{\mathrm{s},j}(\rho_j,\phi_j,z) = \sum_{k=-K}^{K}\sum_{m=1}^{M} B_{mk}^{\mathrm{TE},j}\frac{H_k^{(2)}(\beta_m^{\mathrm{TE}}\rho_j)}{H_k^{(2)}(\beta_m^{\mathrm{TE}}r_j)}H_{z,m}^1(z)e^{jk\phi_j} \text{ for } \rho_j > r_j. \quad (8.66)$$

Invoking the addition theorem for the Hankel function ([22], p. 232, Eq. 5-103) permits to write (8.65) and (8.66) in terms of the local cylindrical coordinate system of cylinder i, e.g.,

$$\sum_{k=-K}^{K}\sum_{m=1}^{M} B_{mk}^{\mathrm{TM},j}\frac{H_k^{(2)}(\beta_m^{\mathrm{TM}}\rho_j)}{H_k^{(2)}(\beta_m^{\mathrm{TM}}r_j)}E_{z,m}^1(z)e^{jk\phi_j} = \sum_{k=-K}^{K}\sum_{m=1}^{M}\check{B}_{mk}^{\mathrm{TM},ij}\frac{J_k(\beta_m^{\mathrm{TM}}\rho_i)}{J_k(\beta_m^{\mathrm{TM}}r_i)}E_{z,m}^1(z)e^{jk\phi_i}, \quad (8.67)$$

with

$$\check{B}_{mk}^{\mathrm{TM},ij} = \sum_{p=-K}^{K} B_{mp}^{\mathrm{TM},j}\frac{H_{p-k}^{(2)}(\beta_m^{\mathrm{TM}}R_{ij})J_k(\beta_m^{\mathrm{TM}}r_i)e^{j(k-p)\Phi_{ij}}}{H_p^{(2)}(\beta_m^{\mathrm{TM}}r_j)}. \quad (8.68)$$

Here, $R_{ij} = |\boldsymbol{\rho}_{ij}^c|$ and $\Phi_{ij} = \arctan\left(\frac{\boldsymbol{\rho}_{ij}^c\cdot\boldsymbol{u}_y}{\boldsymbol{\rho}_{ij}^c\cdot\boldsymbol{u}_x}\right)$ are the length and the angle w.r.t. the positive x-axis of the vector $\boldsymbol{\rho}_{ij}^c = \boldsymbol{\rho}_j^c - \boldsymbol{\rho}_i^c$ connecting the centers of cylinders i and j. Similar expressions can be proffered for the TE$_z$ expansion coefficients. As mentioned above, the total field incident on cylinder i comprises the incident field given by (8.63) and (8.64), along with the field scattered by all other cylinders

$$\sum_{j\neq i}\hat{e}_z^{\mathrm{s},j}(\rho_i,\phi_i,z) = \sum_{k=-K}^{K}\sum_{m=1}^{M}\check{B}_{mk}^{\mathrm{TM},i}\frac{J_k(\beta_m^{\mathrm{TM}}\rho_i)}{J_k(\beta_m^{\mathrm{TM}}r_i)}E_{z,m}^1(z)e^{jk\phi_i}, \quad (8.69)$$

$$\sum_{j\neq i}\hat{h}_z^{\mathrm{s},j}(\rho_i,\phi_i,z) = \sum_{k=-K}^{K}\sum_{m=1}^{M}\check{B}_{mk}^{\mathrm{TE},i}\frac{J_k(\beta_m^{\mathrm{TE}}\rho_i)}{J_k(\beta_m^{\mathrm{TE}}r_i)}H_{z,m}^1(z)e^{jk\phi_i}, \quad (8.70)$$

with $\check{B}_{mk}^{\mathrm{TX},i} = \sum_{j\neq i}\check{B}_{mk}^{\mathrm{TX},ij}$. If $\boldsymbol{B}^i$ and $\check{\boldsymbol{B}}^i$ denote vectors comprising the coefficients $B_{mk}^{\mathrm{TX},i}$ and $\check{B}_{mk}^{\mathrm{TX},i}$ arranged as described in Section 8.4, then it follows from the definition of $\boldsymbol{S}^i$ that

$$\boldsymbol{B}^i = \boldsymbol{S}^i\left[\check{\boldsymbol{B}}^{\boldsymbol{i}} + \boldsymbol{C}^i\right],\ i = 1,\ldots,N_c. \quad (8.71)$$

Matrix equation (8.71) can be solved efficiently for the unknown vectors $\boldsymbol{B}^i$ using an iterative solver. The necessary matrix-vector multiplications are performed in two stages.

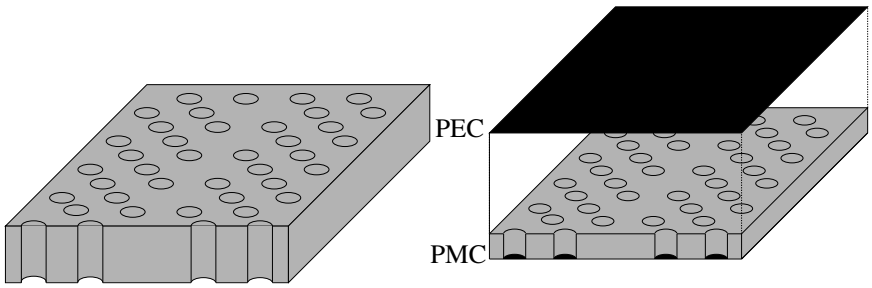

Figure 8.5: Electromagnetic Crystal slab waveguide.

First, the vectors $\boldsymbol{B}^i$ are transformed into the vectors $\check{\boldsymbol{B}}^i$. Define the β-dependent matrix element $\boldsymbol{Z}_{kp}^{ij}(\beta)$ as

$$\boldsymbol{Z}_{kp}^{ij}(\beta) \quad = \quad \frac{H_{p-k}^{(2)}(\beta R_{ij}) J_k(\beta r_i) e^{j(k-p)\Phi_{ij}}}{H_p^{(2)}(\beta r_j)}. \tag{8.72}$$

Note that this matrix element resembles the off-diagonal matrix elements from the multiple scattering technique used to characterize 2D EC devices [18, 21]. From the above, it follows that

$$\check{B}_{mk}^{\mathrm{TX},i} \quad = \quad \sum_{j \neq i} \sum_{p=-K}^{+K} \boldsymbol{Z}_{kp}^{ij}(\beta_m^{\mathrm{TX}}) B_{mp}^{\mathrm{TX},j}. \tag{8.73}$$

This shows that, when re-expressing the field scattered by cylinder j in terms of the local cylindrical coordinate system of cylinder i, radial modes with a different propagation coefficient do not interact. This means that this operation can be separately performed for TM_z and TE_z eigenmodes with different index m. So, the calculation of $\check{\boldsymbol{B}}^i$ out of $\boldsymbol{B}^i$ falls apart into $2M$ smaller matrix-vector multiplications, each comprising $(2K + 1)N_c$ expansion coefficients. These multiplications can be speeded up by using a (two-dimensional) fast multiplication scheme, e.g. a Fast Fourier Transform (FFT) based or a multilevel fast multipole based scheme [23]. Once the vector $\check{\boldsymbol{B}}^i$ is known, this vector is multiplied with $\boldsymbol{S}^i$. In most EC slabs, the same cylinder will re-appear many times, so only a few different scattering matrices (and most often even only one) will have to be calculated and stored. Moreover, recall that $\boldsymbol{S}^i$ in turn is a block-diagonal matrix. By consequence, this second step falls apart into $(2K + 1)N_c$ matrix-vector multiplications, each comprising $2M$ expansion coefficients. Although the total number of unknowns in the proposed method can be rather high, the computational complexity and memory requirements are low.

8.6 Examples

The usefulness of the proposed method is demonstrated via its application to the simulation of wave propagation through a (bended) line-defect waveguide in the EC slab depicted in Fig. 8.5(a). The EC slab consists of a high permittivity material surrounded by two air layers. Circular air holes are etched through this slab according to a hexagonal lattice with lattice constant a. Here, the relative permittivity of the slab is 12.25 and its thickness is $d_{\text{slab}} = 0.6a$. The radius of the air holes is $r = 0.3a$. In [19], it is shown that this EC slab has a bandgap between $k = 0.504\frac{\pi}{a}$ and $k = 0.656\frac{\pi}{a}$, with k the free-space wavenumber.

The modes of two-dimensional EC waveguides can be decomposed in two noninteracting polarizations, namely, TE_z and TM_z. Due to the lack of translational symmetry, this separation does not hold for EC slabs. However, for waveguides in EC slabs that are symmetrical with respect to the z direction, the modes can be classified in *even* and *odd* modes. For the *even* modes, the ρ- and ϕ-components of the electric field have even properties with respect to the plane bisecting the slab; for the *odd* modes these components are odd functions in the z direction. These even and odd modes are very similar to the TE_z and TM_z modes in two dimensions. In fact, in the mirror plane itself, the even and odd modes are purely TE_z and TM_z, respectively. As in all the examples presented below, the excitation will have an even symmetry in the z direction and because the even and odd modes do not interact, only the even modes have to be considered. This allows to reduce the computational domain and the number of unknowns by a factor two: the mirror plane ($z = 0$) for the even modes corresponds to a PMC plane (Fig. 8.5(b)). The complex thickness of the air layer is $\tilde{d}_{\text{air}} = (6 - 0.3j)a$. The imaginary part corresponds to a typical value previously used to characterize opto-electronic devices with mode-matching and PMLs [24, 25].

The longitudinal mode profiles and the propagation constants are calculated with CAMFR [26]. All other calculations are performed in Matlab on a Linux-based 2.4GHz Pentium IV PC.

First, the approach of Section 8.4 is tested by considering one air hole, centered about $\boldsymbol{\rho} = \mathbf{0}$. The incident field consist of the fundamental longitudinal TE_z eigenmode, propagating in the positive y direction:

$$\hat{e}_z^{\text{i}}(\rho, \phi, z) = 0, \tag{8.74}$$

$$\hat{h}_z^{\text{i}}(\rho, \phi, z) = e^{-j\beta_1^{\text{TE}} y} H_{z,1}^1(z). \tag{8.75}$$

Invoking the Fourier expansion

$$e^{-j\beta_1^{\text{TE}} y} = e^{-j\beta_1^{\text{TE}} \rho \sin\phi} = \sum_{k=-\infty}^{\infty} (-1)^n J_n(\beta_1^{\text{TE}}\rho) e^{jk\phi}, \tag{8.76}$$

yields the expansion coefficients C_{mk}^{TX}

$$C_{mk}^{\text{TM}} = 0 \tag{8.77}$$

$$C_{mk}^{\text{TE}} = \begin{cases} (-1)^k J_k(\beta_1^{\text{TE}} r) & \text{if } m = 1, \\ 0 & \text{otherwise.} \end{cases} \tag{8.78}$$

Figures 8.6 and 8.7 show the z-component of the magnetic field just outside and inside the cylinder as a function of z and ϕ and this for $k = 0.6\frac{\pi}{a}$, $K = 4$, and $M = 20$. These figures clearly prove the correctness of the formulas derived in Section 8.4.

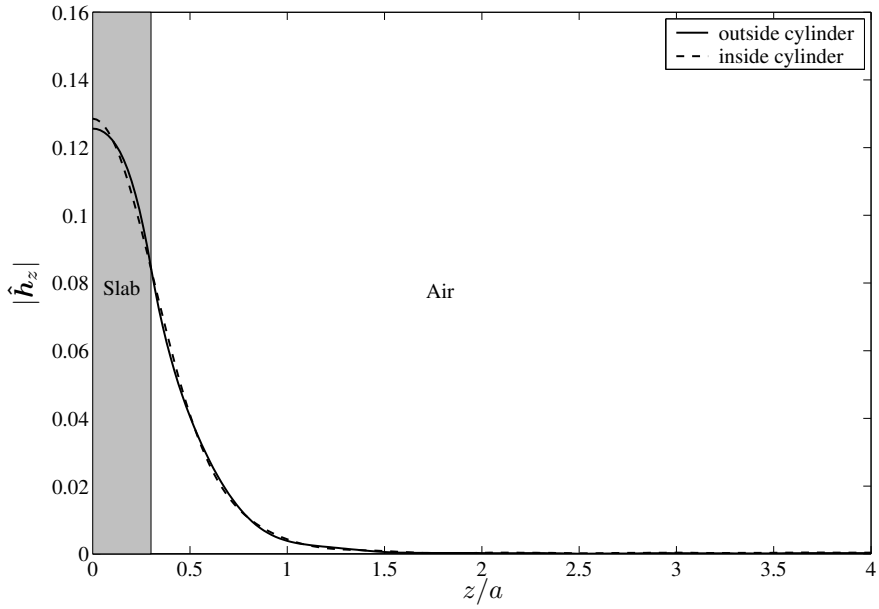

Figure 8.6: Cylindrical mode-matching at one cylinder: $|\hat{\boldsymbol{h}}_z(z)|$ as a function of z.

The scheme proposed in Section 8.5 is tested via its application to the simulation of two EC waveguide structures. In these examples, the excitation consists of the propagating TE$_z$ eigenmode that propagates cylindrically away from the point $\boldsymbol{\rho}_s$:

$$\hat{e}_z^{\mathrm{i}}(\rho,\phi,z) = 0, \tag{8.79}$$

$$\hat{h}_z^{\mathrm{i}}(\rho,\phi,z) = H_0^{(2)}(\beta_1^{\mathrm{TE}}|\boldsymbol{\rho}-\boldsymbol{\rho}_s|)H_{z,1}^1(z). \tag{8.80}$$

Using the addition theorem for the Hankel function, this incident field can be easily re-expressed in terms of the local cylindrical coordinate system of cylinder i, yielding

$$C_{mk}^{\mathrm{TM},i} = 0 \tag{8.81}$$

$$C_{mk}^{\mathrm{TE},i} = \begin{cases} (-1)^k H_k^{(2)}(\beta_1 R_{\mathrm{s}i})e^{jk\Phi_{\mathrm{s}i}}J_k(\beta_1 r_i) & \text{if } m=1, \\ 0 & \text{otherwise.} \end{cases} \tag{8.82}$$

Here, $R_{\mathrm{s}i} = |\boldsymbol{\rho}_{si}|$ and $\Phi_{\mathrm{s}i} = \arctan\left(\frac{\boldsymbol{\rho}_{si}^c\cdot\boldsymbol{u}_y}{\boldsymbol{\rho}_{si}^c\cdot\boldsymbol{u}_x}\right)$ are the length and angle of the vector $\boldsymbol{\rho}_{\mathrm{s}i}^c = \boldsymbol{\rho}_i^c - \boldsymbol{\rho}_s$.

Figure 8.8 shows the absolute value of the z-component of the magnetic field in the mirror plane for a straight EC waveguide. Fig. 8.10 shows the same field component at the middle of the waveguide channel. The free-space wavenumber is $k = 0.6\frac{\pi}{a}$. The total number of air holes in this example is $N_c = 200$. With $K = 4$ and $M = 20$, the

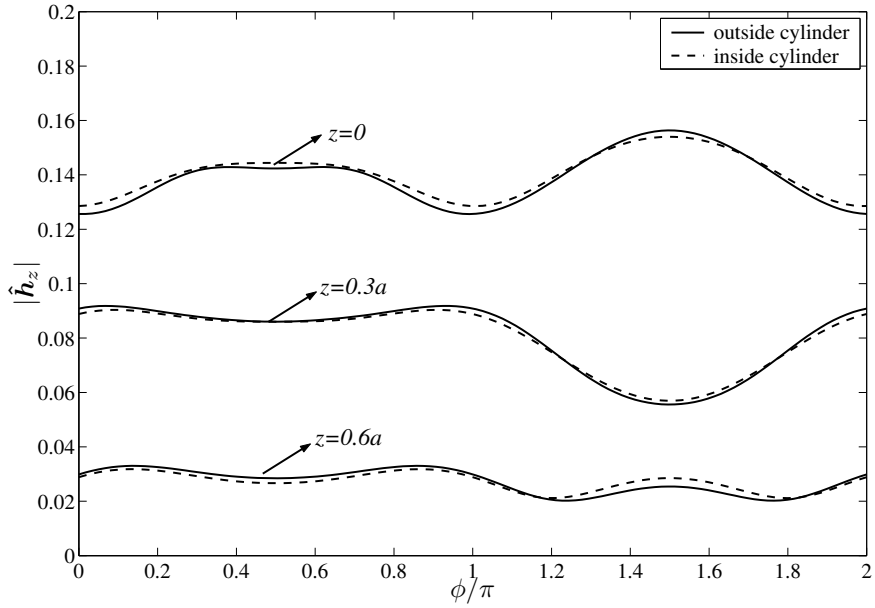

Figure 8.7: Cylindrical mode-matching at one cylinder: $|\hat{\boldsymbol{h}}_z(z)|$ as a function of ϕ.

total number of unknowns is 72000. One matrix-vector multiplication, accelerated using a FFT-based scheme, takes 2 s. The solution of the linear system of equations (8.71) with BICGSTAB to a tolerance of 10^{-5} requires 100 iterations. This takes about 12 mins. The memory requirements are 200Mb.

Figure 8.9 shows the same data for an EC waveguide with two (non-optimized) 60^{o} bends. Fig. 8.11 shows this field component at the middle of the waveguide channel. It is noted that considerable losses occur at the bends. By consequence, optimization of the EC waveguide bend is a must. The total number of air holes in this example is $N_c = 646$. With $K = 4$ and $M = 20$, the total number of unknowns is 232560. Here, one matrix-vector multiplication takes 12 s. The solution of the linear system of equations (8.71) with BICGSTAB to a tolerance of 10^{-5} requires 196 iterations. This takes about 2 h 35 mins. The memory requirements are 450Mb.

8.7 Conclusion

A new technique for analyzing wave propagation in EC slabs has presented. The open layered medium is described by a closed one by sandwiching it between two PEC or PMC backed PML layers. The scattering matrix of one air hole can be easily obtained following a cylindrical mode-matching. The interaction between the different air holes are very closely related to the interactions in the previously studied 2D multiple scattering technique. By solving the resulting linear system iteratively and performing the matrix-vector multiplications in two stages in combination with 2D fast multiplication schemes, the total computational complexity and memory requirements are low.

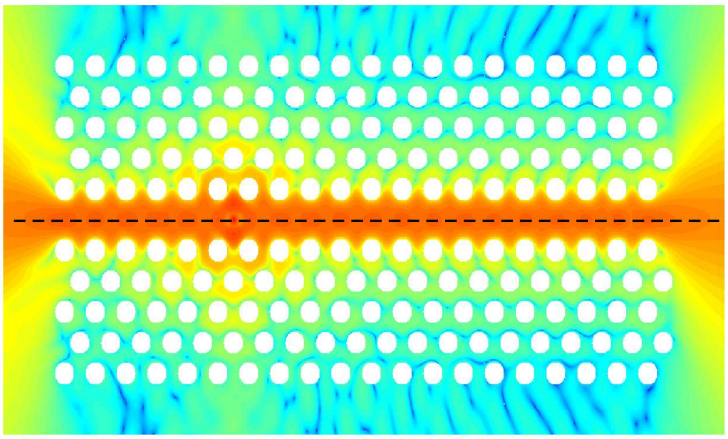

Figure 8.8: EC waveguide, magnetic field in mirror plane.

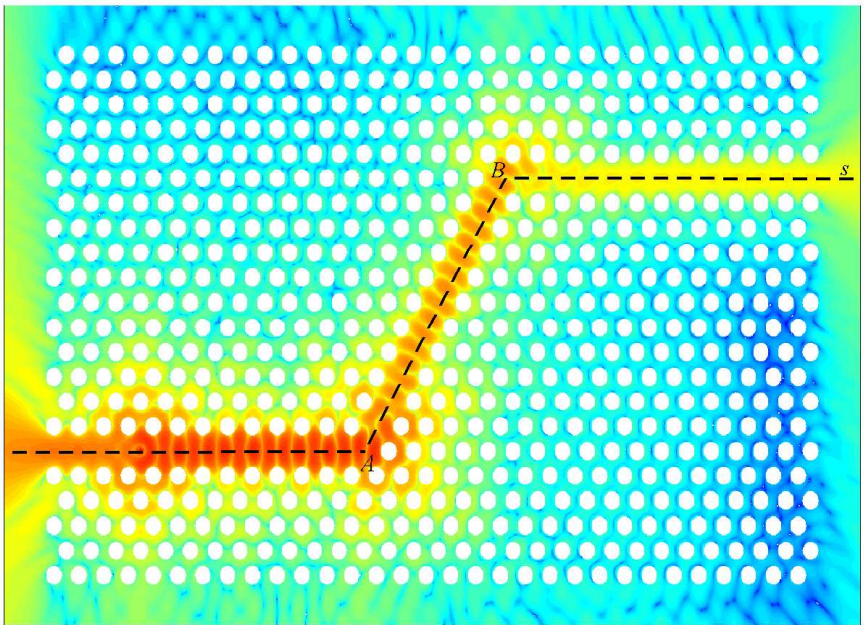

Figure 8.9: EC waveguide with two bends, magnetic field in mirror plane.

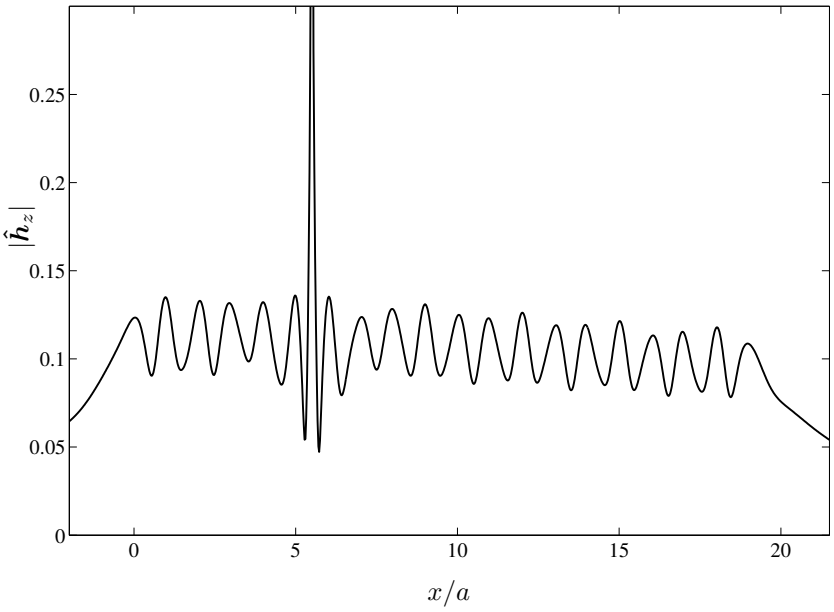

Figure 8.10: EC waveguide, magnetic field in the mirror plane at the middle of the waveguide.

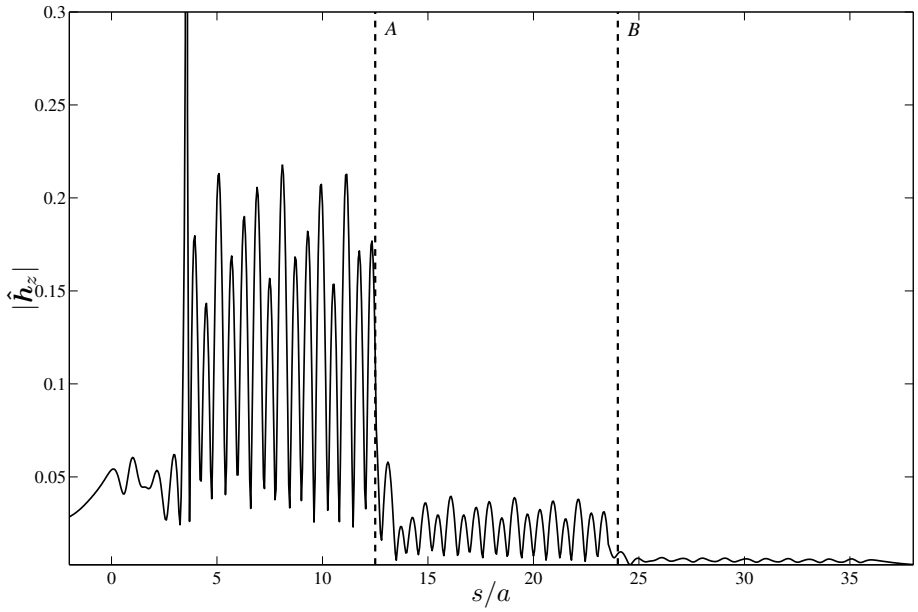

Figure 8.11: EC waveguide with two bends, magnetic field in the mirror plane at the middle of the waveguide.

Appendix A: Orthogonality

Invoking the Lorentz reciprocity theorem, it is easily proven that the longitudinal eigenmodes are orthogonal [9]. Moreover, as the mode profiles can always be multiplied with an arbitrary complex factor, these eigenmodes can be normalized such that

$$\int_0^d [\boldsymbol{E}_m(z) \times \boldsymbol{H}_n(z)] \cdot \boldsymbol{u}_y dz \quad = \quad \delta_{mn}. \tag{A.1}$$

For the TM$_z$ polarization this reduces to

$$\int_0^d E_{z,m}(z) H_{x,n}(z) dz \quad = \quad \delta_{mn} \tag{A.2}$$

and for the TE$_z$ polarization to

$$-\int_0^d E_{x,m}(z) H_{z,n}(z) dz \quad = \quad \delta_{mn}. \tag{A.3}$$

To prove the orthogonality of the radial eigenmodes, also another integral relationship between the m^{th} TM$_z$ and n^{th} TE$_z$ longitudinal eigenmodes will be used, namely

$$\int_0^d \left[\beta_n^{\text{TE}} E_{y,m}(z) H_{z,n}(z) + \beta_m^{\text{TM}} E_{z,m}(z) H_{y,n}(z)\right] dz \quad = \quad 0. \tag{A.4}$$

Indeed, Maxwell's curl equations lead to

$$E_{y,m}(z) \quad = \quad \frac{1}{j\omega\epsilon_i} \frac{dH_{x,m}(z)}{dz}, \tag{A.5}$$

$$\beta_m^{\text{TM}} E_{z,m}(z) \quad = \quad \omega\mu_i H_{x,m}(z) + j\frac{dE_{y,m}(z)}{dz}, \tag{A.6}$$

$$H_{y,n}(z) \quad = \quad -\frac{1}{j\omega\mu_i} \frac{dE_{x,n}(z)}{dz}, \tag{A.7}$$

$$\beta_n^{\text{TE}} H_{z,n}(z) \quad = \quad -\omega\epsilon_i E_{x,n}(z) + j\frac{dH_{y,n}(z)}{dz}, \tag{A.8}$$

which allows to rewrite the left hand side of (A.4) as

$$\begin{aligned} &\int_0^d \beta_n^{\text{TE}} E_{y,m}(z) H_{z,n}(z) + \beta_m^{\text{TM}} E_{z,m}(z) H_{y,n}(z) dz \quad = \\ &j\int_0^d \frac{d}{dz} \left[E_{x,m}(z) H_{x,m}(z) + E_{y,m}(z) H_{y,m}(z)\right] dz \quad = \\ &\qquad j\left[E_{x,m}(d) H_{x,m}(d) + E_{y,m}(d) H_{y,m}(d)\right. \\ &\qquad \left. -E_{x,m}(0) H_{x,m}(0) - E_{y,m}(0) H_{y,m}(0)\right] \end{aligned} \tag{A.9}$$

Because the layered medium is sandwiched between perfectly conducting planes, this integral equals zero as stated in (A.4).

Now, consider a circular cylindrical surface S parallel to the z-axis with radius ρ and centered about the spatial origin $\boldsymbol{\rho} = \mathbf{0}$. The orthogonality relationships for the radial eigenmodes follow from calculating

$$\int_S \left[\hat{\boldsymbol{e}}_{mk}(\rho,\phi,z) \times \hat{\boldsymbol{h}}_{nl}(\rho,\phi,z)\right] \cdot \boldsymbol{u}_\rho dS = \int_S \left[\hat{E}_{z,mk}(\rho,z)\hat{H}_{\phi,nl}(\rho,z) - \hat{E}_{\phi,mk}(\rho,z)\hat{H}_{z,nl}(\rho,z)\right] e^{j(k+l)\phi} dS \tag{A.10}$$

for two radial eigenmodes. If both eigenmodes are TM_z polarized, it follows from (A.2) that

$$\begin{aligned}\int_S \left[\hat{\boldsymbol{e}}^{\mathrm{TM}}_{mk}(\rho,\phi,z) \times \hat{\boldsymbol{h}}^{\mathrm{TM}}_{nl}(\rho,\phi,z)\right] \cdot \boldsymbol{u}_\rho dS &= \int_S \hat{E}^{\mathrm{TM}}_{z,mk}(\rho,z)\hat{H}^{\mathrm{TM}}_{\phi,nl}(\rho,z)e^{j(k+l)\phi} dS \\ &= -j\rho R^{\mathrm{TM}}_{mk}(\beta^{\mathrm{TM}}_m\rho)R^{\mathrm{TM}\prime}_{nl}(\beta^{\mathrm{TM}}_n\rho)\times \\ &\quad \int_0^d E_{z,m}(z)H_{x,n}(z)dz \int_0^{2\pi} e^{j(k+l)\phi}d\phi \\ &= -j\rho R^{\mathrm{TM}}_{mk}(\beta^{\mathrm{TM}}_m\rho)R^{\mathrm{TM}\prime}_{nl}(\beta^{\mathrm{TM}}_n\rho)\delta_{mn}\delta_{k;-l}.\end{aligned} \tag{A.11}$$

Similarly, if both eigenmodes are TE_z polarized, it is seen from (A.3) that

$$\begin{aligned}\int_S \left[\hat{\boldsymbol{e}}^{\mathrm{TE}}_{mk}(\rho,\phi,z) \times \hat{\boldsymbol{h}}^{\mathrm{TE}}_{nl}(\rho,\phi,z)\right] \cdot \boldsymbol{u}_\rho dS &= -\int_S \hat{E}^{\mathrm{TE}}_{\phi,mk}(\rho,z)\hat{H}^{\mathrm{TE}}_{z,nl}(\rho,z)e^{j(k+l)\phi} dS \\ &= j\rho R^{\mathrm{TE}\,\prime}_{mk}(\beta^{\mathrm{TE}}_m\rho)R^{\mathrm{TM}}_{nl}(\beta^{\mathrm{TE}}_n\rho)\times \\ &\quad \int_0^d E_{x,m}(z)H_{z,n}(z)dz \int_0^{2\pi} e^{j(k+l)\phi}d\phi \\ &= -j\rho R^{\mathrm{TE}\,\prime}_{mk}(\beta^{\mathrm{TE}}_m\rho)R^{\mathrm{TM}}_{nl}(\beta^{\mathrm{TE}}_n\rho)\delta_{mn}\delta_{k;-l}.\end{aligned} \tag{A.12}$$

If the first eigenmode is TE_z polarized and the second one is TM_z polarized, (A.10) obviously equals zero:

$$\int_S \left[\hat{\boldsymbol{e}}^{\mathrm{TE}}_{mk}(\rho,\phi,z) \times \hat{\boldsymbol{h}}^{\mathrm{TM}}_{nl}(\rho,\phi,z)\right] \cdot \boldsymbol{u}_\rho dS = 0 \tag{A.13}$$

Finally, if the first eigenmode is TM_z polarized and the second one is TE_z polarized, (A.10) reduces to

$$\begin{aligned}&\int_S \left[\hat{\boldsymbol{e}}^{\mathrm{TM}}_{mk}(\rho,\phi,z) \times \hat{\boldsymbol{h}}^{\mathrm{TE}}_{nl}(\rho,\phi,z)\right] \cdot \boldsymbol{u}_\rho dS = \\ &\int_S \left[\hat{E}^{\mathrm{TM}}_{z,mk}(\rho,z)\hat{H}^{\mathrm{TE}}_{\phi,nl}(\rho,z) - \hat{E}^{\mathrm{TM}}_{\phi,mk}(\rho,z)\hat{H}^{\mathrm{TE}}_{z,nl}(\rho,z)\right] e^{j(k+l)\phi} dS = \\ &R^{\mathrm{TM}}_{mk}(\beta^{\mathrm{TM}}_m\rho)R^{\mathrm{TE}}_{nl}(\beta^{\mathrm{TE}}_n\rho) \int_0^{2\pi} e^{j(k+l)\phi}d\phi\times \\ &\int_0^d \left[\frac{k}{\beta^{\mathrm{TM}}_m}E_{y,m}(z)H_{z,m}(z) - \frac{l}{\beta^{\mathrm{TE}}_n}E_{z,m}(z)H_{y,m}(z)\right] dz = 0.\end{aligned} \tag{A.14}$$

Indeed, if $k+l \neq 0$ the first integral is zero. If $k+l=0$, it follows from (A.4) that the second integral is zero. From (A.11), (A.12), (A.13), and (A.14), it can be concluded that the integral (A.10) only differs from zero if both modes have the same polarization, if $m=n$, and if $k=-l$.

Appendix B: Cylindrical mode-matching

This section details the (cylindrical) mode-matching technique used to obtain (8.56). As discussed in Section 8.4, the total field outside the cylinder is separated into the incident field and the scattered field. The z-component of both fields are given in (8.47)–(8.50). Using (8.30), (8.32), (8.44), and (8.46), it is readily seen that the ϕ-components of these fields are

$$\begin{aligned}
\hat{e}_\phi^{\mathrm{i}}(\rho,\phi,z) &= -\sum_{k=-K}^{K}\sum_{m=1}^{M} C_{mk}^{\mathrm{TM}} \frac{k}{\beta_m^{\mathrm{TM}}\rho}\frac{J_k(\beta_m^{\mathrm{TM}}\rho)}{J_k(\beta_m^{\mathrm{TM}}r)} E_{y,m}^1(z)e^{jk\phi} \\
&\quad -j\sum_{k=-K}^{K}\sum_{m=1}^{M} C_{mk}^{\mathrm{TE}} \frac{J_k'(\beta_m^{\mathrm{TE}}\rho)}{J_k(\beta_m^{\mathrm{TE}}r)} E_{x,m}^2(z)e^{jk\phi}, \qquad \text{(B.1)} \\
\hat{h}_\phi^{\mathrm{i}}(\rho,\phi,z) &= -j\sum_{k=-K}^{K}\sum_{m=1}^{M} C_{mk}^{\mathrm{TM}} \frac{J_k'(\beta_m^{\mathrm{TM}}\rho)}{J_k(\beta_m^{\mathrm{TM}}r)} H_{x,m}^1(z)e^{jk\phi} \\
&\quad -\sum_{k=-K}^{K}\sum_{m=1}^{M} C_{mk}^{\mathrm{TE}} \frac{k}{\beta_m^{\mathrm{TE}}\rho}\frac{J_k(\beta_m^{\mathrm{TE}}\rho)}{J_k(\beta_m^{\mathrm{TE}}r)} H_{y,m}^1(z)e^{jk\phi}, \qquad \text{(B.2)} \\
\hat{e}_\phi^{\mathrm{s}}(\rho,\phi,z) &= -\sum_{k=-K}^{K}\sum_{m=1}^{M} B_{mk}^{\mathrm{TM}} \frac{k}{\beta_m^{\mathrm{TM}}\rho}\frac{H_k^{(2)}(\beta_m^{\mathrm{TM}}\rho)}{H_k^{(2)}(\beta_m^{\mathrm{TM}}r)} E_{y,m}^1(z)e^{jk\phi} \\
&\quad -j\sum_{k=-K}^{K}\sum_{m=1}^{M} B_{mk}^{\mathrm{TE}} \frac{H_k^{(2)'}(\beta_m^{\mathrm{TE}}\rho)}{H_k^{(2)}(\beta_m^{\mathrm{TE}}r)} E_{x,m}^1(z)e^{jk\phi}, \qquad \text{(B.3)} \\
\hat{h}_\phi^{\mathrm{s}}(\rho,\phi,z) &= -j\sum_{k=-K}^{K}\sum_{m=1}^{M} B_{mk}^{\mathrm{TM}} \frac{H_k^{(2)'}(\beta_m^{\mathrm{TM}}\rho)}{H_k^{(2)}(\beta_m^{\mathrm{TM}}r)} H_{x,m}^1(z)e^{jk\phi} \\
&\quad -\sum_{k=-K}^{K}\sum_{m=1}^{M} B_{mk}^{\mathrm{TE}} \frac{k}{\beta_m^{\mathrm{TE}}\rho}\frac{H_k^{(2)}(\beta_m^{\mathrm{TE}}\rho)}{H_k^{(2)}(\beta_m^{\mathrm{TE}}r)} H_{y,m}^1(z)e^{jk\phi}. \qquad \text{(B.4)}
\end{aligned}$$

The z-components of the total electric and magnetic field inside the cylinder are given in (8.51) and (8.52). Hence, the ϕ-component of this electric and magnetic field are

$$\begin{aligned}
\hat{e}_\phi^{\mathrm{t}}(\rho,\phi,z) &= -\sum_{k=-K}^{K}\sum_{m=1}^{M} A_{mk}^{\mathrm{TM}} \frac{k}{\zeta_m^{\mathrm{TM}}\rho}\frac{J_k(\zeta_m^{\mathrm{TM}}\rho)}{J_k(\zeta_m^{\mathrm{TM}}r)} E_{y,m}^2(z)e^{jk\phi} \\
&\quad -j\sum_{k=-K}^{K}\sum_{m=1}^{M} A_{mk}^{\mathrm{TE}} \frac{J_k'(\zeta_m^{\mathrm{TE}}\rho)}{J_k(\zeta_m^{\mathrm{TE}}r)} E_{x,m}^2(z)e^{jk\phi}, \qquad \text{(B.5)}
\end{aligned}$$

$$\begin{aligned}\hat{h}_{\phi}^{\mathrm{t}}(\rho,\phi,z) &= -j\sum_{k=-K}^{K}\sum_{m=1}^{M} A_{mk}^{\mathrm{TM}}\frac{J_k'(\zeta_m^{\mathrm{TM}}\rho)}{J_k(\zeta_m^{\mathrm{TM}}r)}H_{x,m}^{2}(z)e^{jk\phi} \\ &\quad -\sum_{k=-K}^{K}\sum_{m=1}^{M} A_{mk}^{\mathrm{TE}}\frac{k}{\zeta_m^{\mathrm{TE}}\rho}\frac{J_k(\zeta_m^{\mathrm{TE}}\rho)}{J_k(\zeta_m^{\mathrm{TE}}r)}H_{y,m}^{2}(z)e^{jk\phi}. \qquad \text{(B.6)}\end{aligned}$$

A relationship between the unknown coefficients A_{mk}^{TX}, B_{mk}^{TX} and the given coefficients C_{mk}^{TX} can be found by demanding that the z- and ϕ-components of the total electric and magnetic field are continuous at $\rho = r$, which can be expressed as

$$\begin{aligned}\left[\hat{\boldsymbol{e}}^{\mathrm{i}}(r^+,\phi,z)+\hat{\boldsymbol{e}}^{\mathrm{s}}(r^+,\phi,z)\right]\times\boldsymbol{u}_\rho &= \hat{\boldsymbol{e}}^{\mathrm{t}}(r^-,\phi,z)\times\boldsymbol{u}_\rho, \qquad \text{(B.7)}\\ \left[\hat{\boldsymbol{h}}^{\mathrm{i}}(r^+,\phi,z)+\hat{\boldsymbol{h}}^{\mathrm{s}}(r^+,\phi,z)\right]\times\boldsymbol{u}_\rho &= \hat{\boldsymbol{h}}^{\mathrm{t}}(r^-,\phi,z)\times\boldsymbol{u}_\rho. \qquad \text{(B.8)}\end{aligned}$$

Here, r^+ and r^- denote radii that are infinitesimally larger and smaller then r, respectively. Weighting (B.7) by first taking the dot product with the magnetic field of a TM_z radial eigenmode $\hat{\boldsymbol{h}}_{nl}^{1,\mathrm{TM}}(\rho,\phi,z)$, $n = 1,\ldots,M$; $l = -K,\ldots,K$, of the outer layered medium and then integrating it over the whole boundary of the cylinder, yields with (A.11) the following linear equations

$$\sum_{m=1}^{M} A_{mk}^{\mathrm{TM}}\int_0^d E_{z,m}^{2}H_{x,n}^{1}dz = B_{nk}^{\mathrm{TM}}+C_{nk}^{\mathrm{TM}},\ n=1,\ldots,M,\ k=-K,\ldots,K. \qquad \text{(B.9)}$$

Similarly, equation (B.8) is weighted by taking the dot product with $\hat{\boldsymbol{e}}_{nl}^{1,\mathrm{TE}}(\rho,\phi,z)$, $l = 1,\ldots,M$; $l = -K,\ldots,K$, and integration over the boundary of the cylinder. Invoking the orthogonality relationship (A.12) leads to

$$-\sum_{m=1}^{M} A_{mk}^{\mathrm{TE}}\int_0^d H_{z,m}^{2}E_{x,n}^{1}dz = B_{nk}^{\mathrm{TE}}+C_{nk}^{\mathrm{TE}},\ n=1,\ldots,M,\ k=-K,\ldots,K. \qquad \text{(B.10)}$$

Equations (B.9) and (B.10) can be summarized as $\boldsymbol{Z}_{11}^{k}\boldsymbol{A}_k - \boldsymbol{B}_k = \boldsymbol{C}_k$, which explains (8.57). Taking the dot product of (B.8) with the electric field of a TM_z eigenmode $\hat{\boldsymbol{e}}_{nl}^{1,\mathrm{TM}}(\rho,\phi,z)$, $n = 1,\ldots,M$; $l = -K,\ldots,K$, of the outer medium and integrating this quantity over the cylinder's boundary gives, with orthogonality relations for the radial eigenmodes, the following equations

$$\begin{aligned}&\sum_{m=1}^{M} A_{mk}^{\mathrm{TM}}\int_0^d H_{x,m}^{2}E_{z,n}^{1}dz\frac{J_k'(\zeta_m^{\mathrm{TM}}r)}{J_k(\zeta_m^{\mathrm{TM}}r)} \\ &+\frac{k}{j\beta_n^{\mathrm{TM}}r}\sum_{m=1}^{M} A_{mk}^{\mathrm{TE}}\left[\int_0^d H_{z,m}^{2}E_{y,n}^{1}dz+\frac{\beta_n^{\mathrm{TM}}}{\zeta_m^{\mathrm{TE}}}\int_0^d H_{y,m}^{2}E_{z,n}^{1}dz\right] \\ &= B_{nk}^{\mathrm{TM}}\frac{H_k^{(2)\prime}(\beta_n^{\mathrm{TM}}r)}{H_k^{(2)}(\beta_n^{\mathrm{TM}}r)}+C_{nk}^{\mathrm{TM}}\frac{J_k'(\beta_n^{\mathrm{TM}}r)}{J_k(\beta_n^{\mathrm{TM}}r)},\ n=1,\ldots,M,\ k=-K,\ldots,K. \qquad \text{(B.11)}\end{aligned}$$

Finally, taking the dot product of (B.7) with $\hat{\boldsymbol{h}}_{nl}^{1,\mathrm{TE}}(\rho,\phi,z)$, $n=1,\ldots,M; l=-K,\ldots,K$, and integrating it over the boundary of the cylinder yields

$$
\begin{aligned}
&-\frac{k}{j\beta_n^{\mathrm{TE}}}\sum_{m=1}^{M}A_{mk}^{\mathrm{TM}}\left[\int_0^d E_{z,m}^2H_{y,n}^1dz+\frac{\beta_n^{\mathrm{TE}}}{\zeta_m^{\mathrm{TM}}}\int_0^d E_{y,m}^2H_{z,n}^1dz\right]\\
&-\sum_{m=1}^{M}A_{mk}^{\mathrm{TE}}\int_0^d E_{x,m}^2H_{z,n}^1dz\frac{J_k'(\zeta_m^{\mathrm{TE}}r)}{J_k(\zeta_m^{\mathrm{TE}}r)}\\
&=B_{nk}^{\mathrm{TE}}\frac{H_k^{(2)'}(\beta_n^{\mathrm{TE}}r)}{H_k^{(2)}(\beta_n^{\mathrm{TE}}r)}+C_{nk}^{\mathrm{TE}}\frac{J_k'(\beta_n^{\mathrm{TE}}r)}{J_k(\beta_n^{\mathrm{TE}}r)},\quad n=1,\ldots,M,\ k=-K,\ldots,K. \qquad \text{(B.12)}
\end{aligned}
$$

Equations (B.11) and (B.12) are summarized as $\boldsymbol{Z}_{21}^k\boldsymbol{A}_k+\boldsymbol{Z}_{22}^k\boldsymbol{B}_k=\boldsymbol{Y}_2^k\boldsymbol{C}_k$, explaining definitions (8.58), (8.59) and (8.60).

Appendix C: Some comments about the orthogonality

Very recently, a similar technique was published in [27]. However, in this paper the scattering matrix of one cylinder is found by weighting the boundary conditions with the *complex conjugate*, denoted by $(\cdot)^*$, of the electric or magnetic fields of the eigenmodes. The authors claim that the following orthogonality relationship is valid for the longitudinal eigenmodes:

$$
\int_0^d[\boldsymbol{E}_m(z)\times\boldsymbol{H}_n^*(z)]\cdot\boldsymbol{u}_y dz \quad=\quad \delta_{mn}. \qquad \text{(C.1)}
$$

From this, it would follow that

$$
\int_S\hat{\boldsymbol{e}}_{mk}(\rho,\phi,z)\times\hat{\boldsymbol{h}}_{nl}^*(\rho,\phi,z)dS, \qquad \text{(C.2)}
$$

with S a circular cylindrical surface parallel with the z-axis, equals zero for two different radial modes. This only holds for lossless layered media without PMLs. In this section, it will be shown with a numerical example that for layered media with PMLs the only correct orthogonality relationships are those given in Appendix A.

Consider the configuration depicted in Fig. 8.12. It comprises a homogeneous medium with constitutive parameters (ϵ, μ) sandwiched between two PEC plates. Let $\tilde{d}=d^{\mathrm{re}}+jd^{\mathrm{im}}$ denote the complex distance between the two PEC plates. The components for the longitudinal TM_z eigenmodes are

$$
\begin{aligned}
E_{z,m}(z) &= \cos\left(\frac{m\pi}{\tilde{d}}z\right), &\text{(C.3)}\\
E_{y,m}(z) &= -\frac{jm\pi}{\tilde{d}\beta_m^{\mathrm{TM}}}\sin\left(\frac{m\pi}{\tilde{d}}z\right), &\text{(C.4)}\\
H_{x,m}(z) &= \frac{\omega\epsilon}{\beta_m^{\mathrm{TM}}}\cos\left(\frac{m\pi}{\tilde{d}}z\right), &\text{(C.5)}
\end{aligned}
$$

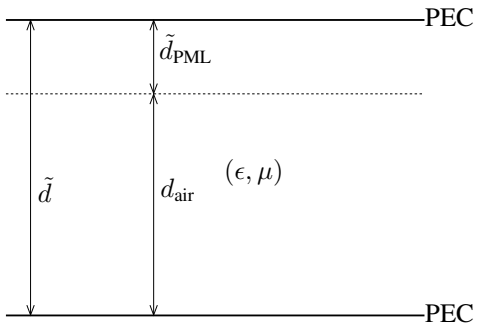

Figure 8.12: Homogeneous PML waveguide.

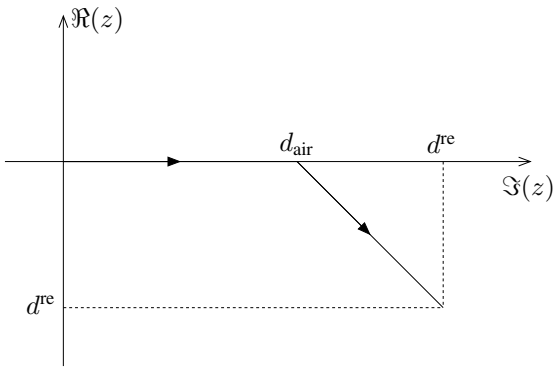

Figure 8.13: Integration path.

m	n	$d_{\text{air}} = 0$	$d_{\text{air}} = 2a$	$d_{\text{air}} = 4a$
0	0	$(6 - 0.3j)a$	$(6 - 0.3j)a$	$(6 - 0.3j)a$
0	1	0	0	0
0	2	0	0	0
0	3	0	0	0
1	1	$(3 - 0.15j)a$	$(3 - 0.15j)a$	$(3 - 0.15j)a$
1	2	0	0	0
1	3	0	0	0
2	2	$(3 - 0.15j)a$	$(3 - 0.15j)a$	$(3 - 0.15j)a$
2	3	0	0	0
3	3	$(3 - 0.15j)a$	$(3 - 0.15j)a$	$(3 - 0.15j)a$

Table 8.1: $\mathrm{I}_1(m, n)$

with $m = 0, 1, 2, \ldots$ Equation (A.1) leads to integrals of the form

$$\mathrm{I}_1(m,n) \quad = \quad \int_0^{\tilde{d}} \cos\left(\frac{m\pi}{\tilde{d}} z\right) \cos\left(\frac{n\pi}{\tilde{d}} z\right) dz, \tag{C.6}$$

and Eq. (C.1) to integrals of the form

$$\mathrm{I}_2(m,n) \quad = \quad \int_0^{\tilde{d}} \cos\left(\frac{m\pi}{\tilde{d}} z\right) \left[\cos\left(\frac{n\pi}{\tilde{d}} z\right)\right]^* dz. \tag{C.7}$$

It is readily seen that $[\cos(z)]^* = \cos(z^*)$. The integrals (C.6) and (C.7) will be calculated according to the following integration path (Fig. 8.13)

$$z \quad = \quad \begin{cases} t & 0 < t < d_{\text{air}}, \\ d_{\text{air}} + \frac{\tilde{d}_{\text{PML}}}{d^{\text{re}}_{\text{PML}}}(t - d_{\text{air}}) & d_{\text{air}} < t < d_{\text{air}} + d^{\text{re}}_{\text{PML}}. \end{cases} \tag{C.8}$$

Here, t is a real parameter; d_{air} is a real thickness smaller the d^{re}; the complex thickness $\tilde{d}_{\text{PML}}$ is defined as the difference between $\tilde{d}$ and d_{air}, viz. $\tilde{d} = d_{\text{air}} + \tilde{d}_{\text{PML}}$. In Tables 8.1 and 8.2, the values of the integrals (C.6) and (C.7) are given for different values of m, n, and d_{air} and this for $\tilde{d} = (6 - 0.3j)a$. The values of the integrals (C.6) are independent of the integration path and the different longitudinal TM_z eigenmodes are orthogonal. This is not true for the integrals (C.7): different integration paths yield different results and the eigenmodes are not orthogonal for most integration paths. Indeed, the function z^* is not analytic.

m	n	$d_{\text{air}} = 0$	$d_{\text{air}} = 2a$	$d_{\text{air}} = 4a$
0	0	$(6 - 0.3j)a$	$(6 - 0.3j)a$	$(6 - 0.3j)a$
0	1	0	$(0.014 + 0.247j)a$	$(0.02 + j0.496)a$
0	2	0	$(-0.004 + 0.125j)a$	$(-0.055 - 0.245j)a$
0	3	0	$(-0.015 + 0.001j)a$	$(0.06 - 0.009j)a$
1	1	$(3 - 0.15j)a$	$(2.964 - 0.119j)a$	$(-78.482 + 12.012j)a$
1	2	0	$(0.015 + 0.248j)a$	$(0.016 + 0.499j)a$
1	3	0	$(-0.013 + 0.072j)a$	$(-0.076 - 0.139j)a$
2	2	$(3 - 0.15j)a$	$(1.793 - 0.074j)a$	$(-61.306 + 9.536j)a$
2	3	0	(0.028+0.358j)	(0.005+0.734j)
3	3	$(3 - 0.15j)a$	$(3.971 + 0.003j)a$	$(2.742 + 0.02j)a$

Table 8.2: $\mathrm{I}_2(m, n)$

Bibliography

[1] J. D. Joannopoulos, R. D. Meade, and J. N. Winn, *Photonic Crystals, Molding the Flow of Light*. N.J.: Princeton Univ. Press, 1995.

[2] A. Mekis, J. Chen, I. Kurland, S. Fan, P. Villeneuve, and J. Joannopoulos, "High transmission through sharp bends in photonic crystal waveguides," *Phys. Rev. Lett*, vol. 77, no. 18, pp. 3787–3790, Oct. 1996.

[3] H. Benisty, C. Weisbuch, M. Agio, M. Kafesaki, C. Soukoulis, M. Qiu, M. Swillo, A. Karlsson, B. Jaskorzynska, A. Talneau, J. Moosburger, M. Kamp, A. Forchell, R. Ferrini, R. Houdré, and U. Oesterle, "Models and measurements for the transmission of submicron-width waveguide bends defined in two-dimensional photonic crystals," *IEEE J. Quantum Electron.*, vol. 38, no. 7, pp. 770–785, July 2002.

[4] M. Koshiba, "Wavelength division multiplexing and demultiplexing with photonic crystal waveguide couplers," *Journal of Lightwave Technology*, vol. 19, no. 12, pp. 1970–1975, Dec. 2001.

[5] S. Boscolo, M. Midrio, and C. G. Someda, "Coupling and decoupling of electromagnetic waves in parallel 2D photonic crystal waveguides," *IEEE J. Quantum Electron.*, vol. 1, no. 38, pp. 47–53, Jan. 2002.

[6] C. Jin, S. Han, X. Meng, B. Cheng, and D. Zhang, "Demultiplexer using directly resonant tunneling between point defects and waveguides in a photonic crystal," *Jounal of Applied Physics*, vol. 91, no. 7, pp. 4771–4773, April 2002.

[7] L. Wu, M. Mazilu, T. Karle, and T. Krauss, "Superprism phenomena in planar photonic crystals," *IEEE J. Quantum Electron.*, vol. 38, no. 7, pp. 915–918, July 2002.

[8] S. Johnson, S. Fan, P. Villeneuve, and J. Joannopoulos, "Guided modes in photonic crystal slabs," *Phys. Rev. B*, vol. 60, no. 8, pp. 5751–5758, Aug. 1999.

[9] F. Olyslager, *Electromagnetic Waveguides and Transmission Lines*, ser. Oxford Engineering Science Series. Oxford: Clarendon Press, 1999.

[10] J. P. Bérenger, "A perfectly matched layer for the absorption of electromagnetic waves," *Journ. Comput. Phys.*, vol. 114, no. 1, pp. 185–200, 1994.

[11] W. C. Chew and W. H. Weedon, "A 3D perfectly matched medium from modified Maxwell's equations in stretched coordinates," *Microwave Opt. Technol. Lett.*, vol. 7, no. 13, pp. 599–604, Sept. 1994.

[12] W. C. Chew, J. M. Jin, and E. Michielssen, "Complex coordinate stretching as a generalized absorbing boundary condition," *Microwave Opt. Technol. Lett.*, vol. 15, no. 6, pp. 363–369, Aug. 1997.

[13] H. Derudder, F. Olyslager, D. De Zutter, and S. Van den Berghe, "Efficient mode-matching analysis of discontinuities in finite planar substrates using perfectly matched layers," *IEEE Trans. Antennas Propag.*, vol. 49, no. 2, pp. 1985–195, Feb. 2001.

[14] H. Derudder, F. Olyslager, and D. De Zutter, "An efficient series expansion for the 2D Green's function of a microstrip substrate using perfectly matched layers," *IEEE Microwave Guided Wave Lett.*, vol. 9, no. 12, pp. 505–507, Dec. 1999.

[15] F. Olyslager and H. Derudder, "Series representation of green dyadics for layered media using PMLs," *IEEE Trans. Antennas Propag.*, vol. 51, no. 9, pp. 2319–2326, Sep. 2003.

[16] H. Derudder, D. D. Zutter, and F. Olyslager, "A new way to analyse waveguide discontinuities using perfectly matched layers," *IEE Electronic Letters*, vol. 34, no. 22, pp. 2138–2140, Oct. 1998.

[17] P. Bienstman, H. Derudder, R. Baets, F. Olyslager, and D. De Zutter, "Analysis of cylindrical waveguide discontinuities using vectorial eigenmodes and perfectly matched layers," *IEEE Trans. Microwave Theory Tech.*, vol. 49, no. 2, pp. 349–354, Feb. 2001.

[18] D. Pissoort, B. Denecker, P. Bienstman, F. Olyslager, and D. De Zutter, "Comparative study of three methods for the simulation of two-dimensional photonic crystals," *J. Opt. Soc. Am. A*, vol. 21, pp. 2186–2195, Nov. 2004.

[19] S. Shi, C. Chen, and D. Prather, "Plane-wave expansion method for calculating band structure of photonic crystal slabs with perfectly matched layers," *J. Opt. Soc. Am. A*, vol. 21, no. 9, pp. 1769–1774, Sep. 1999.

[20] A. Z. Elsherbeni, "A comparative study of two-dimensional multiple scattering techniques," *Radio Science*, vol. 29, no. 4, pp. 1023–1033, 1994.

[21] D. Pissoort, D. De Zutter, and F. Olyslager, "Efficient semi-analytical analysis of two-dimensional photonic crystals," in *IEEE AP-S Int. Symp.*, vol. 3, Columbus, OH, USA, June 2003, pp. 994–997.

[22] R. F. Harrington, *Time-Harmonic Electromagnetic Fields*, ser. Electrical and Electronic Engineering Series. New York: McGraw-Hill, 1961.

[23] W. C. Chew, J. M. Jin, E. Michielssen, and J. Song, *Fast and Efficient Algorithms in Computational Electromagnetics*. Boston: Artech House, 2001.

[24] P. Bienstman and R. Baets, "Advanced boundary conditions for eigenmode expansion models," *Opt. Quantum Electron.*, vol. 34, pp. 523–540, 2002.

[25] ——, "Optical modelling of photonic crystals and VCSELs using eigenmode expansion and perfectly matched layers," *Opt. Quantum Electron.*, vol. 33, pp. 327–341, 2001.

[26] "http://camfr.sourceforge.net."

[27] S. Boscolo and M. Midrio, "Three-dimensional multiple-scattering technique for the analysis of photonic-crystal slabs," *IEEE J. Lightwave Technol.*, vol. 22, no. 12, pp. 2778–2786, Dec. 2004.

Chapter 9

Conclusions – Future research

In this doctoral thesis, several fast and efficient simulation techniques for analyzing wave propagation in 2D ECs and EC slabs have been presented.

9.1 Eigenmodes in periodic waveguides

In Chapter 2, the main properties of the eigenmodes of general periodic waveguides were obtained from the Lorentz reciprocity theorem. Such a consistent analysis of the eigenmodes of periodic waveguides seemed to be missing in the literature. Besides the orthogonality relation that is satisfied by the modal fields in a periodic waveguide, also an original proof of the bidirectionality property of these waveguides was given. Most often, when periodic waveguides are studied in optical literature, the bidirectionality property is not discussed, but it is just assumed without motivation that the periodic waveguides are bidirectional. Also the excitation of a periodic waveguide was considered. By starting from the Lorentz reciprocity theorem, one obtains immediately compact expressions for the excitation coefficients of the eigenmodes as a function of the exciting source densities or incident fields, without first having to solve the full scattering problem of an incident wave on a waveguide. Moreover, the whole analysis was generalized to periodic waveguides composed of reciprocal and non-reciprocal, anisotropic and bianisotropic materials.

9.2 Analysis of 2D EC structures

To efficiently design EC circuits, many different computational schemes for the characterization of EC devices have been proposed. In Chapter 3, three efficient simulation techniques, namely, the FDTD-ROM technique, the vectorial eigenmode expansion technique, and the multiple scattering technique, have been compared on their efficiency and overall merits. The main advantages and disadvantages of each method are summarized below.

9.2.1 FDTD-ROM

Advantages

- The algorithm is very simple and it is very flexible regarding the structure and the materials.
- As FDTD operates directly in the time-domain, it permits the wideband characterization of an EC device via a single simulation.
- If subcell models are used, the time step is dictated mainly by a coarse grid.
- The computational complexity and the memory requirements scale linear in the number of cylinders.
- The computational complexity does not change when non-circular objects are considered.

Disadvantages

- A staircase approximation has to be used for circular cylinders.
- This technique often suffers from so-called late-time instabilities.
- It is more difficult to control the accuracy.
- The simulation domain must be finite, which necessitates the use of absorbing boundary conditions.
- FDTD inevitably suffers from accumulation of phase errors for larger structures.
- If there are many different objects that are not repeated frequently, FDTD remains computationally expensive.

9.2.2 Vectorial eigenmode expansion

Advantages

- Because propagation through the layers can be handled analytically, the computational complexity scales linearly in the number of layers. Moreover, when modeling EC devices with a finite number of repetitions of a basic period, the calculation time is even rather logarithmic in the number of layers.
- As for mode-matching a discrete set of eigenmodes is required, the entire structure has to be enclosed in a metal box. By invoking the complex coordinate interpretation of a PML, parasitic reflections can be reduced drastically and, hence, structures with radiation losses can be handled.
- The reflection matrix of a semi-infinite EC waveguide and its eigenmodes easily can be calculated, which permits easy calculation of the S-parameters of an EC device.

Disadvantages

- The application of this method becomes unwieldy when many different layer types are involved.
- A staircase approximation has to be used for circular cylinders.
- This technique relies on an absorbing boundary condition.
- Considerable performance is lost if the EC devices comprises waveguides that run along different directions.

9.2.3 Multiple scattering technique

Advantages

- By expanding the surface currents in angular Fourier series, the cylinders' circular nature can be exploited. This permits the fields to be cast in terms of Bessel/Hankel functions. By consequence, high accuracy can be obtained with only a few unknowns per cylinder.
- No absorbing boundary conditions are required when analyzing finite EC structures.
- Cylinders with arbitrary losses, ranging from dielectric cylinders to PEC cylinders, can be handled.

Disadvantages

- This technique requires the solution of a dense linear system of equations whose dimension scales linearly with the number of cylinders. The cost of directly solving this system scales cubically in the number of cylinders.
- To extract the EC device S-parameters, computational de-embedding methods have to be used.
- Non-circular scatterers can be treated as well by characterizing their interactions via scattering matrices. However, as $2K + 1$, the number of azimuthal harmonics per cylinder, will then have to be larger, considerable performance is lost.

9.3 Complex coordinates

In Chapter 4, a new PML based absorbing boundary condition to terminate periodic waveguides for integral equation solvers was presented. In this way, it is possible to model EC structures that end in semi-infinite EC waveguides. Exploiting the complex coordinate interpretation of a PML, the EC waveguides are continued for a number of periods in the complex plane. Although there will always be a disturbance in the periodicity of the EC waveguide by entering into the complex space, the resulting reflections can be very low if the waveguide enters the complex plane in a smooth way, while at the same time

significant absorption is achieved. The performance of the proposed boundary condition was tested for two different ways to enter the complex plane, namely, a linear and a circular PML, via its application to the analysis of a straight EC waveguide. The simulation results were compared with the exact solution, calculated with the formulas obtained in Chapter 2. From this, it became clear that the circular PML outperforms the linear PML.

9.4 Classical fast multiplication schemes

To reduce the computational complexity of the classical multiple scattering technique, the dense linear system of equations can be solved iteratively. If a classical matrix-vector multiplication scheme is employed, both the computational complexity and the memory requirements scale quadratically in the number of cylinders, denoted by N_c. In Chapter 5, the basic principles of two fast and efficient matrix-vector multiplication schemes for the analysis of 2D EC devices were described, namely, the multilevel fast multipole algorithm (MLFMA) and a Fast Fourier Transform (FFT) based scheme.

With MLFMA, the computational complexity scales as $O(N_c \log_2^2 N_c)$ for sparsely filled EC devices and as $O(N_c)$ for densely filled EC devices. The corresponding memory requirements scale as $O(N_c \log_2 N_c)$ and $O(N_c)$. As this scheme makes no assumptions about the EC device, it is widely applicable. This method was even extended to the use of the complex coordinates that appear when the EC devices is terminated by the new PML based absorbing boundary condition. The coordinates of the box centers are allowed to be complex. However, they are chosen such that they follow the path according to which the coordinates of the cylinders' centers become complex in the PML region. Therefore, a new real coordinate is introduced that follows this path. The boxes are first constructed based on this real coordinate and after that the corresponding complex coordinates of the box centers are calculated. The accuracy and the versatility of the MLFMA were demonstrated via its application to the characterization of an EC waveguide coupler and an array of EC horn antennas.

For finite EC devices in which all cylinders are arranged according to a regular grid, the matrix-vector multiplications can be re-expressed as two-dimensional convolutions. With FFTs, the computational complexity can be reduced to scale as $O(N_c \log_2 N_c)$, while the memory requirements scale as $O(N_c)$.

9.5 Preconditioning

The overall cost when solving the linear system iteratively also scales proportional to the total number of iterations required by the iterative solver to reduce the residual error below a preset threshold. As for realistic EC devices the number of iterations can be high, preconditioning is a must. In Chapter 6, the effectiveness of three types of preconditioners, namely, a diagonal, block-diagonal, and shielded-block preconditioner, was tested on two simple EC devices, namely, a rectangular, defect-less EC and a straight EC waveguide. For both configurations, the shielded-block preconditioner outperforms the other two. Unfortunately, the reduction of the iteration count is much less for the EC waveguide than for the defect-less EC. A deeper understanding of the physics behind this

different convergence behavior was obtained by observing the distribution of the eigenvalues of both the unpreconditioned and the preconditioned interaction matrix. From this, it became clear that, even with a state-of-the-art preconditioner, the number of iterations required for the analysis of an EC device comprising EC waveguides will be higher than for the analysis of a defect-less EC. To overcome this problem, the waveguiding character of the EC device has to be resolved, which is not possible using the MST technique in conjunction with an iterative solver.

9.6 Analysis of 2D EC devices using a periodic Green function approach

In Chapter 7, a novel and fast multiple scattering technique for simulating wave propagation in two-dimensional EC devices that, a small number of other defects aside, are formed by removing cylinders from infinite, doubly periodic, and defect-less ECs, was presented. Contrary to the conventional multiple scattering technique, the novel method solves integral equations in terms of equivalent currents that reside on the surfaces of the removed cylinders. The interactions between these currents are described via a Green function that is innate to the infinite EC. For frequencies in the electromagnetic bandgap, this EC Green function decays exponentially with distance. As a result, each and every removed cylinder only interacts with its near neighbors. Hence, now the interaction matrix is essentially sparse. Because of its typical form, the sparse linear system can be solved using a dedicated direct method, thereby avoiding the convergence problems encountered when analyzing EC devices using an iterative solver. Contrary to the free-space Green function, used in the conventional multiple scattering technique, the EC Green function cannot be evaluated analytically. Its pre-computation is achieved using the conventional multiple scattering technique by considering a centrally excited, finite, and small EC. The dense linear system for this configuration can be solved efficiently by using an iterative, preconditioned, and FFT-accelerated method. If the EC device also contains other defects than removed cylinders, a different Green function must be used for interactions between currents residing near a special defect. If there are only a few irregular defects, these special Green functions are only low-rank perturbations of that of the defect-less EC. Moreover, the propagating eigenmodes of an EC waveguide can be very easily calculated. This makes that the new multiple scattering technique is ideally suited to extract the S-parameters of an EC device, as it permits the implementation of exact modal excitations and absorbing boundary conditions. The versatility and computational efficiency of the proposed method was demonstrated via its application to the analysis of two multiplexer-demultiplexer devices, a filter, and a bended waveguide.

Figure 9.1 gives an overview of the applicability of the different 2D techniques.

9.7 Analysis of EC Slabs

Finally, in Chapter 8, the conventional multiple scattering technique was extended to the analysis of wave propagation in EC slabs comprising air holes etched through a layered medium. The open layered medium is characterized by a closed one with (almost) the

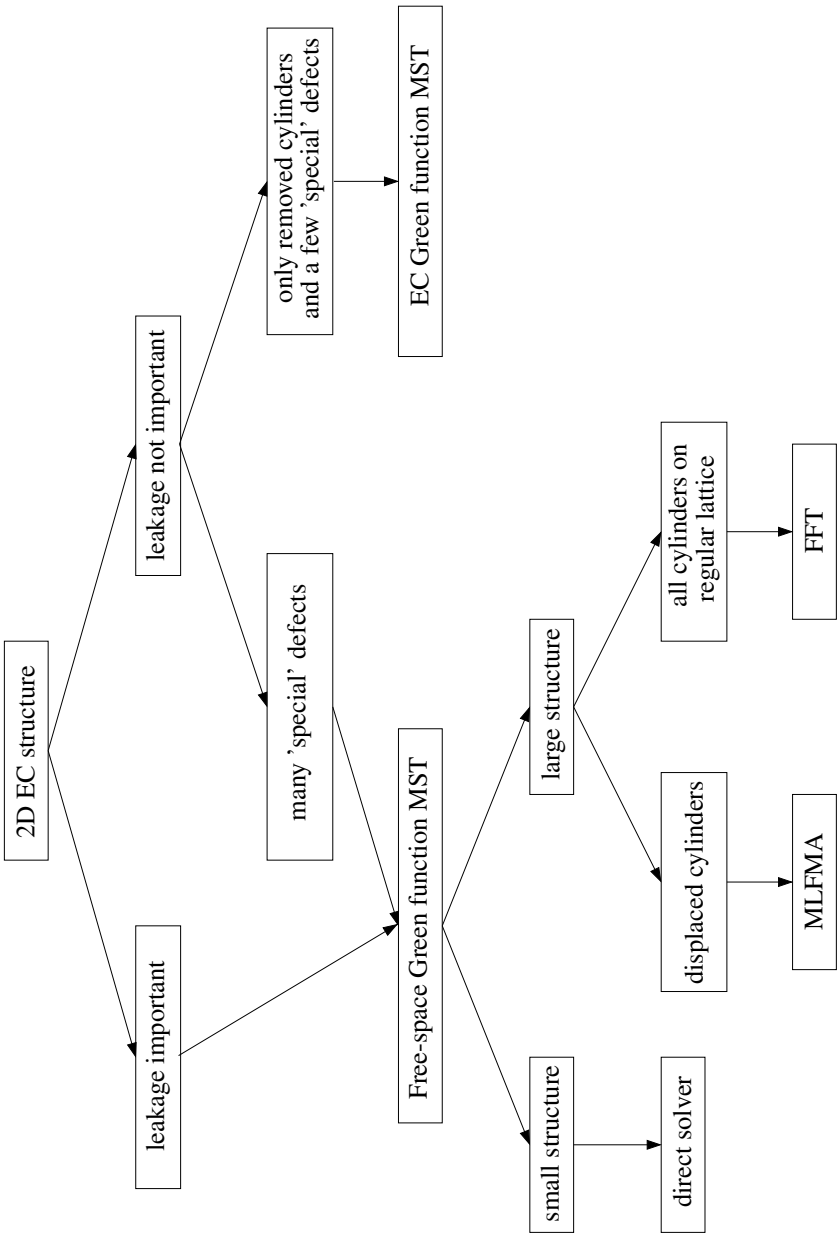

Figure 9.1: Overview 2D techniques.

same electromagnetic behavior by terminating the outermost layers with PMLs, backed by perfectly conducting plates. Using a cylindrical mode-matching, the scattering matrix of every air hole can be easily computed. The matrix elements describing the interactions between the different air holes are very similar to those of the 2D multiple scattering technique. Although the number of unknowns for a realistic EC slab is very large, the computational complexity and the memory requirements can be kept low by solving the resulting linear system of equations iteratively and by performing the necessary matrix-vector multiplications in two steps. The first step corresponds to $2M$ smaller, 2D matrix-vector multiplications, for which the computational complexity and the memory requirements can be reduced by using the multiplication schemes of Chapter 5. In the second step, the unknowns of every air hole are multiplied with the corresponding scattering matrix. For the vast majority of EC slabs, the same air hole will be repeated frequently, so only a few different scattering matrices have to be calculated and stored. The usefulness of the proposed method was demonstrated via its application to the simulation of wave propagation through a straight hexagonal EC waveguide and a hexagonal EC waveguide with two 60^{o} bends.

9.8 Future research

9.8.1 Extensions of the 2D techniques

All examples presented in Chapters 3–7 involve 2D ECs composed of circular cylinders. In literature, also 2D ECs comprising other types of objects are studied [1]. As already mentioned at the end of Chapter 7, non-circular scatterers can be treated as well with the free-space Green function MST and with the EC Green function MST by characterizing their interactions via scattering matrices, similar to what is applied in the 3D technique of Chapter 8. This scattering matrix can be calculated, e.g., via a finite-element method, leading to a hybrid simulation technique.

In Chapter 5, two classical fast multiplication schemes were introduced. The FFT based scheme is very attractive for EC devices in which all cylinders snap to a regular grid. For these devices, the FFT based scheme will outperform the MLFMA as the FFT based scheme does not require as many precalculations as the MLFMA. Unfortunately, it does not apply to EC devices that contain displaced cylinders. For such devices, it can be attractive to apply a so-called FMM-FFT algorithm [2]. The main idea behind this scheme is that all the group centers in the MLFMA are chosen according to a regular lattice. Then the translation operator becomes convolutional and can be applied in $O(N \log N)$ operations using the FFT.

9.8.2 Integrated iterative solver for finite 2D EC devices

A major drawback of the classical fast multiplication schemes of Chapter 5 is that they do not exploit the main property of an EC: for frequencies inside the bandgap no wave propagation is allowed through the crystal. The EC Green function multiple scattering technique, presented in Chapter 7, does explicitly use this property. Unfortunately, this method cannot model radiation effects caused by truncation of the EC, nor can it analyze EC devices that contain many irregular defects. However, it is possible to develop a

novel integrated iterative solver for finite EC devices that cannot be analyzed with the novel multiple scattering technique. This iterative solver is called an *integrated* solver because it offers at the same time a rapid convergence and a cheap multiplication cost. The proposed scheme leads to a rapid convergence because it is based on the use of the shielded-block preconditioner. Because of the bandgap character of the EC, the use of this type of preconditioner also leads to a fast multiplication scheme following a so-called rank revealing scheme, this contrary to the classical fast multiplication schemes.

Similar to the MLFMA, the EC device is divided into boxes and the matrix-vector multiplications are performed in a multilevel way. For two boxes i and j that are sufficiently separated on a certain level, the rank of the part of the *preconditioned* interaction matrix that describes the interaction between these two boxes, denoted by $\tilde{\boldsymbol{Z}}_{ij}$, is low if the frequency lies within the EC bandgap. This fact will be demonstrated via numerical examples in the next paragraph. The rank deficiency of $\tilde{\boldsymbol{Z}}_{ij}$ implies that the corresponding part of the matrix-vector multiplication can be evaluated faster by retaining only the M largest singular values of $\tilde{\boldsymbol{Z}}_{ij}$, denoted by $\tilde{\sigma}_{ij}(m)$, $m = 1, \ldots, M$, along with their left and right eigenvectors:

$$\tilde{\boldsymbol{Z}}_{ij} \approx \tilde{\boldsymbol{U}}_{ij} \tilde{\boldsymbol{S}}_{ij} \tilde{\boldsymbol{V}}_{ij}^{H}. \tag{9.1}$$

Here, $\tilde{\boldsymbol{S}}_{ij}$ is a $(M \times M)$ diagonal matrix containing the M largest singular values of $\tilde{\boldsymbol{Z}}_{ij}$; the matrices $\tilde{\boldsymbol{U}}_{ij}$ and $\tilde{\boldsymbol{V}}_{ij}$ contain the corresponding left and right eigenvectors; $(\cdot)^H$ denotes the Hermitian conjugate. To find the M largest singular values and their eigenvectors, a statistical approach has to be followed, thereby avoiding that the complete preconditioned interaction matrix has to be computed. All interactions that are not sufficiently separated on the lowest level constitute the near interactions and have to be computed in the classical way.

The submatrix $\tilde{\boldsymbol{Z}}_{ij}$ for two well-separated boxes i and j is indeed rank-deficient. First consider the situation depicted in Fig. 9.2. Suppose that $\tilde{\boldsymbol{Z}}_{ij}$ describes the interaction between a dense source box and a dense observation box as indicated in this figure. Figure 9.2 shows the evolution of the largest singular values of $\tilde{\boldsymbol{Z}}_{ij}$ for increasing thickness of the shield. It is observed that all the singular values decrease with increasing thickness of the shield. It follows that the rank of $\tilde{\boldsymbol{Z}}_{ij}$ is in fact zero if the shield is taken large enough. The gray-scaled subfigures, showing the corresponding eigenvectors, prove that the shield prevents that electromagnetic fields can enter into the observation box. This is obviously a consequence of the bandgap character of the EC. Second, consider the situation depicted in Fig. 9.3. Both the source and observation box contain an EC waveguide. The behavior of the singular values of $\tilde{\boldsymbol{Z}}_{ij}$ is similar as above, except that the first singular value stays fixed with increasing thickness of the shield. So the rank of $\tilde{\boldsymbol{Z}}_{ij}$ is one. Physically this rank corresponds to the sole waveguide mode through which electromagnetic fields can couple into the observation box. As a final example, consider the situation depicted in Fig. 9.4. As in the first example, both the source and observation boxes are densely filled, but now they are both residing at the edge of the EC. By consequence, the observation box is only surrounded by the shield for three of its four edges. It is observed that the largest singular values first decrease for increasing thickness of the shield. However, from a certain thickness every singular value stays fixed. More complicated situations can be considered, but the final conclusion is that the rank of the

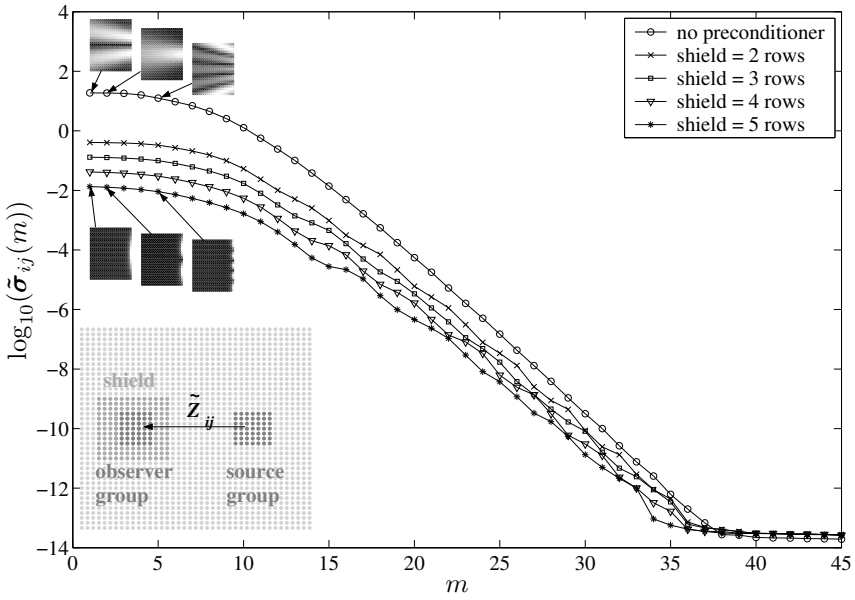

Figure 9.2: Singular values for two dense groups.

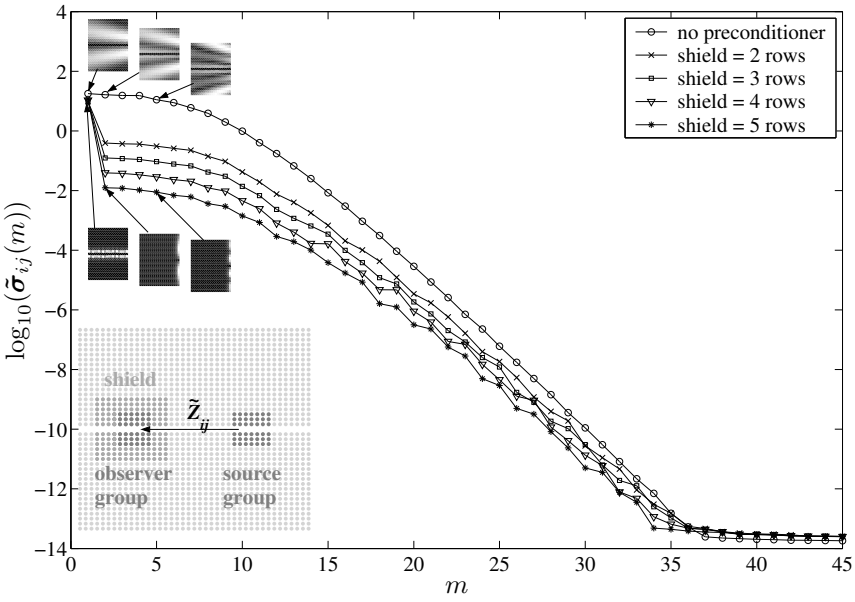

Figure 9.3: Singular values for two groups containing an EC waveguide.

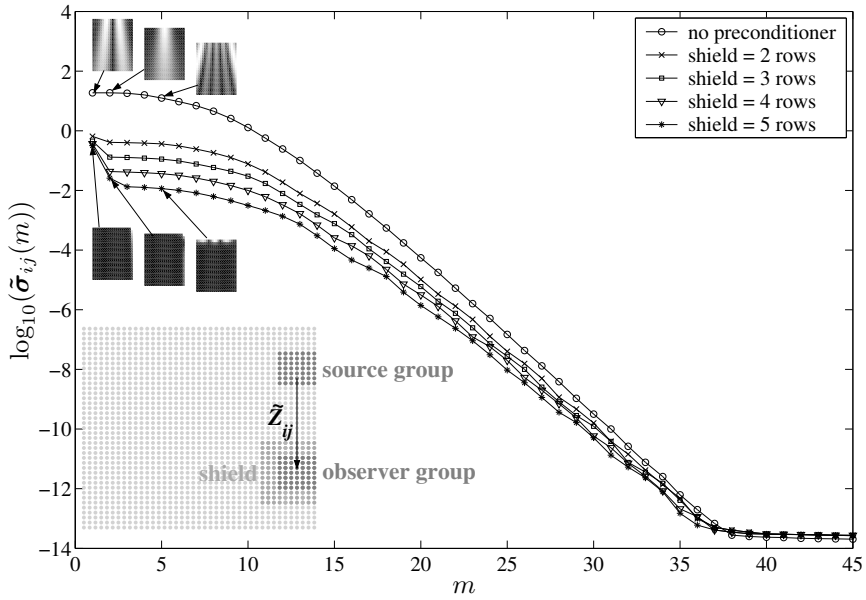

Figure 9.4: Singular values for two dense groups at the edge of an EC structure.

different preconditioned submatrices is very low.

9.8.3 Extensions of the 3D technique

It is clear that the development of the new technique to analyze EC slabs, introduced in Chapter 8, has not yet reached a final point. For example, it could be examined if the EC Green function approach can also be applied to these EC slabs. Therefore, the whole 3D technique has to be re-interpreted in terms of equivalent currents residing on the surfaces of the air-holes to fully understand the similarities/differences to/from the 2D MST.

In Chapter 8, it is assumed that all EC slabs are perfect. In practice, these EC slabs are fabricated using advanced CMOS technologies [3]. Unfortunately, there are some significant differences between typical CMOS components and EC slabs. As in CMOS components each layer contains only critical structures of a certain type (e.g., transistor gates, contact holes,...), the process for each layer can be optimized separately. In contrast to this, an EC slab has to be fabricated completely during the same step. Moreover, EC slabs have to be fabricated with a much higher accuracy than CMOS components: for CMOS components a tolerance of 10% is acceptable, for EC slabs a tolerance of less than 5% is required. Indeed, at the one hand, the behavior of devices in EC slabs is very sensitive to the exact parameters (radius, depth, position...) of the air holes, on the other hand, imperfect etching introduces extra loss mechanisms. In [3], the main loss mechanisms in realistic EC slabs are studied. These losses comprise:

(i) Out-of-plane scattering losses: in EC slabs, the electromagnetic waves are confined vertically because of by means of total internal reflection. Using a simplified point-

of-view, this loss mechanism can be understood as follows: in the holes the layered structure is disturbed and, hence, the electromagnetic waves are no longer confined there. From the perspective of out-of-plane scattering, a distinction can be made between *high-index contrast* (i.e., the permittivity of the core layer is much higher then that of the surrounding layers, e.g., Silicium-On-Insulator) and *low-index contrast* (i.e., the permittivity of the core layer is only slightly higher than that of the surrounding layers, e.g., AlGaAs/GaAs/AlGaAs) EC slabs. In high-index contrast EC slabs, a straight waveguide may have a lossless propagating mode, which means that no electromagnetic waves are scattered out of the layered medium for a straight waveguide. Unfortunately, at places where the periodicity is broken, e.g., in a bend, much of the electromagnetic energy is lost there due to out-of-plane scattering. In low-index contrast EC slabs, no lossless mode exist, but the out-of-plane scattering losses at, e.g., a bend are not much higher than for a straight waveguide.

(ii) Substrate leakage: most often, the bottom layer (the *substrate*) has the same permittivity as the core layer. Because the layer between the core layer and the substrate only has a finite thickness, electromagnetic waves can leak from the core layer to the substrate.

(iii) Scattering at the bottom of the holes: when the holes are not etched deep enough, electromagnetic wave can scatter away at the bottom of the holes.

(iv) TE_z/TM_z interaction: many EC slabs only have an electromagnetic bandgap for one polarization. Unfortunately, because of the possible coupling between both polarizations, extra losses are introduced.

(v) Un-identical and/or displaced holes: in a real EC slab, not all holes will be identical nor will they all be exactly on a lattice point. This changes the position of the electromagnetic bandgap and the dispersion relation of the guided waveguide mode. As a result, the guided mode may couple to the radiation modes of the layered medium, causing extra losses.

(vi) Imperfect etching: when etching holes through a layered medium, it is unavoidable that some roughness is introduced at the sidewalls of the holes. Of course, electromagnetic waves will scatter at these irregularities. Sidewall roughness is one of the most important sources of loss in EC slabs. Moreover, as the holes have to be etched deep into the layered medium, their sidewalls are sloped and the holes become narrower towards the bottom. Hence, the effective permittivity of the layer beneath the core layer increases. As a consequence, the electromagnetic fields will extend much deeper in this layer, possibly causing higher losses due to substrate leakage.

Loss mechanisms (i)-(v) are automatically accounted for or can be easily accounted for in the proposed simulation technique. The influence of sidewall roughness and/or sloped sidewalls can be studied by calculating the scattering matrix of such imperfect holes with, e.g., a finite-element method, again leading to a hybrid technique.

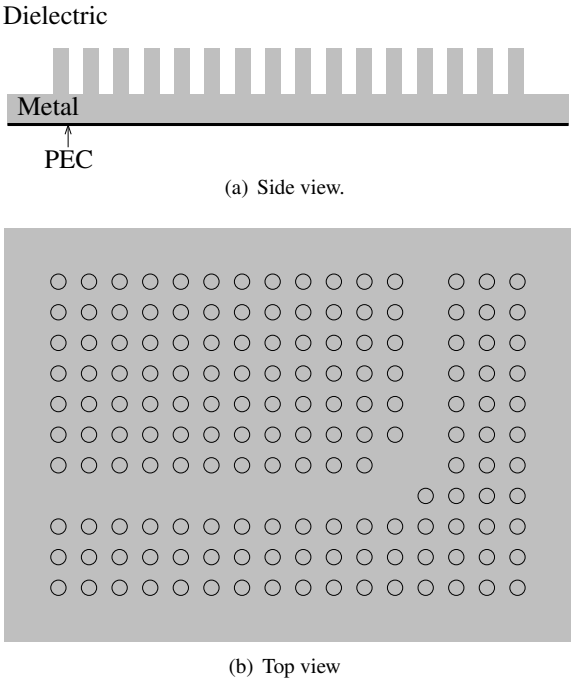

(a) Side view.

(b) Top view

Figure 9.5: Bended SPPBG waveguide.

9.8.4 Surface plasmon polariton bandgap waveguide structures

The 3D technique presented in Chapter 8 could also be applied to other configurations. Recently, a new type of optical waveguide, based on the existence of so-called surface plasmon polaritons (SPP) on metals in the optical regime, was introduced [4, 5]. Surface plasmon polaritons are surface electromagnetic waves that propagate along a metal/dielectric interface and that have an exponentially decaying amplitude in both media. A surface plasmon polariton bandgap (SPPBG) structure results upon introducing a doubly periodic perturbation in the planar metal/dielectric interface. If these perturbations are carefully designed, the SPPs can no longer propagate along the interface, similar to the bandgap effect for electromagnetic waves in classical ECs. By introducing defects, SPPBG waveguides may result. A side and top view of a bended SPPBG waveguide is shown in Fig 9.5. Up to now, FDTD has been the most popular technique to simulate wave propagation in these SPPBG waveguides [6]. However, it is difficult to correctly model the metal region because of its high, frequency-dependent losses and it is precisely the very small penetration of the field in the conductor that is of importance to create the surface plasmon polariton. This problem might be overcome when analyzing these structures with the new 3D technique. To avoid unstabilities due to the high conductivity of the metal, the scattering matrix should be obtained using another type of weighting. In Chapter 8, the equations expressing continuity of the tangential electric field (B.7) and the continuity of the tangential magnetic field (B.8) are both weighted with the radial eigenmodes of the outer layered medium. For SPPBG structures, it is preferable to weight

(B.7) with the radial eigenmodes of the outer layered medium and (B.7) with the radial eigenmodes of the inner layered medium. This can be understood as follows: if the metal would be a perfectly electric conductor, the tangential electric field has to be continuous over the whole boundary of the cylinder. As the tangential magnetic field does not have to be zero at a perfectly electric conductor, the magnetic field only has to be continuous above the metal.

9.9 Overview publications

The results obtained during the PhD research are subject of several publications. The list can be found at the end of this chapter. Other papers are still in preparation.

Bibliography

[1] T. Vallius and M. Kuittinen, "Novel electromagnetic approach to photonic crystals with use of the C method," *J. Opt. Soc. Am. A*, vol. 20, no. 1, pp. 85–91, Jan. 2003.

[2] R. Wagner, J. Song, and W. Chew, "Monte carlo simulation of electromagnetic scattering from two-dimensional random rough surfaces," *IEEE Trans. Antennas Propag.*, vol. 45, no. 2, pp. 235–245, Feb. 1997.

[3] W. Bogaerts, "Nanophotonic waveguides and photonic crystals in silicon-on-insulator," Phd thesis, INTEC-Ghent University, Ghent, Belgium, 2003-2004.

[4] S. Kitson, W. Barnes, and J. Sambles, "Full photonic band gap for surface modes in the visible," *Physical Review Letters*, vol. 77, pp. 2670–2673, 1996.

[5] S. Bozhevolnyi, "Waveguiding in surface plasmon polariton band gap structures," *Physical Review Letters*, vol. 86, pp. 3008–3010, 2001.

[6] M. Lu, M. Lu, P. Carney, and E. Michielssen, "FDTD simulation of 3D surface plasmon polariton band gap waveguide structures," in *IEEE AP-S Int. Symp.*, vol. 3, Monterey, CA, USA, June 2004, pp. 3155–3158.

Overview Publications

[1] D. Pissoort and F. Olyslager, "Termination of periodic waveguides by PMLs in time-harmonic integral equation like techniques," *Antennas and Wireless Propagation Letters*, vol. 2, pp. 281–284, 2003.

[2] ——, "Study of eigenmodes in periodic waveguides using the Lorentz reciprocity theorem," *IEEE Trans. Microwave Theory Tech.*, vol. 52, pp. 542–553, 2004.

[3] D. Pissoort, B. Denecker, P. Bienstman, F. Olyslager, and D. De Zutter, "Comparative study of three methods for the simulation of two-dimensional photonic crystals," *J. Opt. Soc. Am. A*, vol. 21, pp. 2186–2195, Nov. 2004.

[4] D. Pissoort, E. Michielssen, F. Olyslager, and D. D. Zutter, "Fast analysis of 2D electromagnetic crystal structures using a periodic Green function approach," accepted for publication in IEEE Journal of Lightwave Technology.

[5] D. Pissoort and F. Olyslager, "Study of the mode excitation from sources in periodic waveguides," in *URSI Forum*, Brussels, Belgium, Dec. 2002.

[6] D. Pissoort, D. De Zutter, and F. Olyslager, "Efficient semi-analytical analysis of two-dimensional photonic crystals," in *IEEE AP-S Int. Symp.*, vol. 3, Columbus, OH, USA, June 2003, pp. 994–997.

[7] F. Olyslager, H. Derudder, D. D. Zutter, H. Rogier, D. Pissoort, D. V. Ginste, P. Bienstman, and L. Knockaert, "Perfectly matched layers in semi-analytical techniques," in *Workshop on Advanced Computational Electromagnetics*, Ghent, Belgium, May 2003.

[8] D. Pissoort, D. Vande Ginste, F. Olyslager, D. D. Zutter, and E. Michielssen, "A multilevel fast multipole algorithm for the simulation of wave propagation in 2D electromagnetic crystals," in *Proceedings of Piers*, Pisa, Italy, March 2004, pp. 28–31.

[9] D. Pissoort, D. Vande Ginste, F. Olyslager, and E. Michielssen, "Efficient simulation of 2D electromagnetic crystal structures with the multilevel fast multipole algorithm," in *Proceedings of the URSI-EMT Conference*, vol. 2, Pisa, Italy, May 2004, pp. 751–753.

[10] ——, "Different preconditioning techniques for the efficient simulation of 2D EC structures," in *IEEE AP-S Int. Symp.*, vol. 2, Monterey, CA, USA, June 2004, pp. 2131–2134.

[11] F. Olyslager, J. De Zaeytijd, K. Cools, I. Bogaert, L. Meert, D. Vande Ginste, and D. Pissoort, "Applications of complex coordinates to the MLFMA," in *Proceedings of 2004 USNC/URSI National Radio Science Meeting*, Monterey, CA, USA, June 2004, p. 206.

[12] I. Bogaert, J. De Zaeytijd, D. Vande Ginste, D. Pissoort, F. Olyslager, and E. Michielssen, "Simulation of extremely large 2D electromagnetic problems," in *5th UGent-FTW PhD Symposium*, Ghent, Belgium, Dec. 2002, proceedings available on CD-ROM.

[13] K. Cools, L. Meert, D. Vande Ginste, D. Pissoort, F. Olyslager, and E. Michielssen, "Simulation of metamaterials," in *5th UGent-FTW PhD Symposium*, Ghent, Belgium, Dec. 2002, proceedings available on CD-ROM.

[14] D. Pissoort and F. Olyslager, "Fast and efficient simulation of electromagnetic crystal devices," in *URSI Forum*, Brussels, Belgium, Dec. 2004.

[15] D. Pissoort, F. Olyslager, and E. Michielssen, "Fast and efficient computation of wave propagation in electromagnetic crystal slabs," Washington DC, USA, July 2005, submitted to the 2004 USNC/URSI National Radio Science Meeting.

Dit werk kwam tot stand in het kader van een mandaat als aspirant bij het Fonds voor Wetenschappelijk Onderzoek (FWO) - Vlaanderen.